



HAL
open science

Chemical and mineralogical signatures of oxygenic photosynthesis in Archean and Paleoproterozoic sediments

Axelle Hubert

► **To cite this version:**

Axelle Hubert. Chemical and mineralogical signatures of oxygenic photosynthesis in Archean and Paleoproterozoic sediments. Earth Sciences. Université d'Orléans, 2015. English. NNT : 2015ORLE2053 . tel-01362055

HAL Id: tel-01362055

<https://theses.hal.science/tel-01362055>

Submitted on 8 Sep 2016

HAL is a multi-disciplinary open access archive for the deposit and dissemination of scientific research documents, whether they are published or not. The documents may come from teaching and research institutions in France or abroad, or from public or private research centers.

L'archive ouverte pluridisciplinaire **HAL**, est destinée au dépôt et à la diffusion de documents scientifiques de niveau recherche, publiés ou non, émanant des établissements d'enseignement et de recherche français ou étrangers, des laboratoires publics ou privés.

ÉCOLE DOCTORALE 549 - SSBCV

Centre de Biophysique Moléculaire, CNRS Orléans

Thèse présentée par :

Axelle Hubert

A soutenir le : **16 décembre 2015**

Pour obtenir le grade de : **Docteur de l'Université d'Orléans**

Discipline, Spécialité : Sciences de la Terre, de l'Univers et de l'Environnement

**Chemical and mineralogical signatures of
oxygenic photosynthesis in Archean and
Paleoproterozoic sediments**

THÈSE codirigée par :

Dr. Frances WESTALL
Dr. Alexandre SIMIONOVICI

Directrice de Recherche, CNRS Orléans
Professeur, Université de Grenoble

RAPPORTEURS :

Dr. Kurt O. KONHAUSER
Dr. Nicholas T. ARNDT

Professeur, University of Alberta, CA
Professeur classe exceptionnelle, Université de Grenoble

JURY

Dr. Michel FAURE
Dr. Michel VISO

Professeur, Université d'Orléans
Responsable Exobiologie, CNES Paris

*To my aunt Marie-Claire,
To my grandfather Marcel,*

*and
To SAS*

Acknowledgements

First, I would like to thank my co-advisors.

I am grateful to Frances Westall for welcoming me in her group, and I thank her for having given me the opportunity to explore strange new techniques, to seek out ancient life and ancient photosynthetic microbial civilizations, to boldly go where only a few men have gone before...

I am grateful to Alexandre Simionovici for the 42 thousand scientific discussions over the years and for the slightly less scientific discussions too, and for having guided me through photosynthetic life, universe, synchrotron radiation techniques and everything; for having permitted me to hitchhike across galaxies of XRF spectra and for having made the interstellar space between physics and me a little less... spacious.

I am also very grateful to Laurence Lemelle for her continuous and precious support and advice.

I would like to thank sincerely Pr. Kurt Konhauser and Pr. Nicholas Arndt for agreeing to review this manuscript.

I thank all members of the 'Equipe Exobiologie' and especially Marylène Bertrand for her continuous encouragement.

I would like to extend my thanks to all members of the Centre de Biophysique Moléculaire.

I would also like to gratefully acknowledge members of other lab and facilities, for their precious help during these last years. At the ISTO : Colin Faugerolles, Pascale Gautret, Charles Guimau, Leïla Hashim, Sylvain Janiec, Alexandra Kushnir, Claire Ramboz, Max Vidal; at the ISTERRE Grenoble: the members of the "Mineralogie et Environments" group, and also Morgane Ledevin, Valentina Batanova, Valérie Magnin ; at the CME Orléans : Annie Richard, Audrey Sauldubois, Caroline Andrezza ; at the SIMAP Grenoble: Edouard Biguereau, Didier Bouvard, Paul Claud Carry; at the IEMN Lille: David Troadec; at the CP2M Marseille: Guillaume Amiard; at the ESRF: Armando Solé, and the members of the ID21 and I22NI beamlines; at the Bessy II synchrotron: Ivo Zizak; CRPG Nancy: Claire R-B, Etienne Deloule, Nordine Bouden; Barbara Cavalazzi (University of Bologna), Nathalie Grassineau (RUHL), Sasha Verchovsky (Open University).

I would like to warmly thank the "EJC'13 conference" team: Muriel Gargaud, Hervé Cottin, Vassilissa Vinogradoff, Kafila Saiagh, Thomas Gautier, as well as Michel Viso, who also agreed to be a member of the jury for present work.

Very special thanks go to my friends and colleagues: Marion Bonel, Wissem Deraredj, Safia Ezzine, Alexandra Foucault-Collet, Mathieu Galibert, Joan Leclerc, Manon Leturcq, Liane Loïselle, Andre Martins, Mahdi Nadim, Virginie Placide, Mateja Remenaric, Victor Terrier, Nadia Uwurukundo, Alexandra Vuillamy. Thank you all. And for those of you whose PhD has yet to be finished, « may the Force be with you ».

A particular thanks goes also to Emile Bravo, author and cartoonist, who first introduced me to the marvelous field of astrobiology.



"Umh... An astrobiologist?
It's a person who studies ext..."

"...Who will study extraterrestrial life
once we found it."

*« L'imparfait du futur – Une épatante aventure de Jules », Emile Bravo, 2006. Editions Dargaud.
Reproduced with the permission of the author.*

I would like to gratefully thank my parents who awoken me to the passion of Space sciences through Science-Fiction books and movies and night skies full of stars, and for continuous and multi-type support during all these years.

Finally, a huge thank you to Thomas Dufresne, Duf, the calmest and most patient man on Earth (who might actually come from a galaxy far far away...).

This thesis was funded by ANR-09-BLAN-0219-01, CNRS-MI-2014 grants to to Frances Westall, and travel support to the Goldschmidt 2013 conference was provided by ED SSBCV.

Abstract

The evolution of oxygenic photosynthetic bacteria (OPB) is probably the most important biological event of Earth's history since the emergence of life itself. OPB first emerged as a mutation from anoxygenic photosynthetic bacteria (APB) within microbial mats. The release of their by-product O₂ in the environment, which was globally anoxic, fundamentally changed the face of the Earth and led to the development of complex life. However, the specific timing of this evolutionary step remains unclear. The variations in atmospheric O₂ levels through time display a 'roller coaster' trend in which putative peaks of O₂ are recorded around ~2.95 billion years (Ga) ago and ~2.5 Ga ago, followed by what is called the *Great Oxidation Event* (GOE) around 2.4 Ga ago, the moment in time at which the atmosphere of our planet remained permanently oxygenated. To date, attempts to date the appearance of OPB have been based on analysis of general proxies for O₂ in the atmosphere, for example, the presence of rounded pebbles of uraninite in subaerial sedimentary deposits. In the study presented here, we have adopted a more local approach to constrain the timing of the emergence of OPB more precisely. Since OPB appeared as a mutation within APB, we have based our study on *in situ* chemical signatures of OPB at the microbial (μm) scale, within fossilized microbial photosynthetic mats in Archean and Paleoproterozoic sediments dated between 3.45 Ga and 1.88 Ga, *i.e.* spanning the anoxic Earth to the aftermath of the GOE. We used optical microscopy, Raman spectroscopy, SEM/EDS, EPMA, synchrotron radiation μ-XRF, and isotope analytical techniques in order to find, at the μm scale, chemical signatures in the biological and/or mineralogical parts of the mats that would be specific to the presence and metabolic activity of OPB. Results obtained by EPMA and μXRF show that, under certain depositional contexts, enrichment in lanthanides (such as Sm, La and Gd) in individual cells, as well as enrichment in Cu of diagenetic pyrites formed in association with OPB, may represent chemical signatures of OPB. We propose that OPB evolved sometime between 3.33 Ga and 2.98 Ga. Also, we argue that EPMA and μ-XRF, operating at the μm and sub-μm scales, are the most suitable techniques to find chemical signatures of OPB and constrain the timing of their emergence. Importantly, the μXRF results were further improved by the use of a new sample preparation method and a new quantification method, both developed during this study.

Résumé

L'émergence des bactéries photosynthétiques oxygéniques (BPO), aujourd'hui appelées cyanobactéries, est probablement l'évènement le plus important de l'histoire de la biologie, depuis l'apparition de la vie elle-même. Les BPO sont le fruit de la mutation de bactéries photosynthétiques *anoxygéniques* (BPA) dans des tapis bactériens, il y a plusieurs milliards d'années (Ga). Par la libération d'O₂ dans l'environnement, le plus utiles des "déchets" biologiques, les BPO ont conduit à l'oxygénation de notre planète, jusqu'alors anoxique, et au développement de la vie complexe. Cependant, le moment précis de cette évolution n'est toujours pas daté. L'évolution de la concentration d'O₂ dans l'atmosphère au cours du temps peut permettre une première estimation : de possibles pics d'O₂ sont enregistrés aux environs de ~2,95 et de ~2,5 Ga, suivis d'une Grande Oxygénation (*Great Oxidation Event*, GOE) il y a environ 2,4 Ga, marquant l'oxygénation permanente de notre planète. A ce jour, les essais entrepris pour dater l'émergence des BPO concernent l'utilisation de proxies indiquant la présence d'O₂ dans l'atmosphère. Lors de l'étude présentée ici, nous avons adopté une approche plus locale, afin de positionner plus précisément dans le temps l'émergence des BPO. Nous nous sommes concentrés sur l'identification de signatures chimiques spécifiques aux BPO, *in situ* à l'échelle micrométrique, dans des tapis microbien fossiles archéens et paléoprotérozoïques datant de 3,45 à 1,88 Ga, recouvrant ainsi une période allant de la Terre anoxique à la Terre oxygène après le GOE. Nous avons utilisé un large éventail de techniques analytiques telles que la microscopie optique, la spectroscopie Raman, la microscopie électronique couplée à des analyses EDS, des analyses EPMA, μ -XRF à rayonnement synchrotron (SR-XRF), et des analyses isotopiques. Les résultats obtenus par EPMA et μ -XRF montrent que, dans certains contextes de déposition, un enrichissement en lanthanides (par exemple La, Sm, Gd) de cellules fossiles, et un enrichissement en Cu de pyrites diagénétiques formées en association avec des BPO, pourraient représenter des signatures chimiques spécifiques aux BPO. Suite à ces résultats, nous proposons que les BPO ont évolué entre 3,33 et 2,98 Ga. De plus, nous soulignons que l'EPMA et la μ -XRF sont les techniques les plus appropriées pour trouver des signatures chimiques spécifiques aux BPO et contraindre leur émergence dans le temps. Notons que cette étude a aussi contribué à mettre une nouvelle méthode de quantification élémentaire pour SR-XRF, ainsi qu'une nouvelle méthodologie de préparation d'échantillons pour ces mêmes analyses, qui a permis d'optimiser la qualité des résultats obtenus.

Table of contents

INTRODUCTION (FRANÇAIS)	1
Preuves concernant l'augmentation du niveau d'oxygène dans l'atmosphère il y a 2,45-2,32 Ga.....	3
Les causes du « Great Oxidation Event » : le rôle de la photosynthèse oxygénique	6
INTRODUCTION	11
<i>The role of oxygenic photosynthesis in the "Great Oxidation Event"</i>	13
Evidence for the rise of oxygen in the atmosphere 2.45-2.32 Ga ago	13
Causes of the Great Oxidation Event: the role of oxygenic photosynthesis	15
SCIENTIFIC APPROACH AND OBJECTIVES	22
PART I: INTRODUCTION TO BACTERIAL PHOTOSYNTHESIS AND ITS EARLY EVOLUTION	25
CHAPITRE I : RESUME.....	26
CHAPTER I: BACTERIAL PHOTOSYNTHESIS AND EVOLUTION IN ARCHEAN AND PALEOPROTEROZOIC ENVIRONMENTS	28
<i>I.1. Anoxygenic and oxygenic bacterial photosynthesis</i>	28
I.1.1. Anoxygenic photosynthesis	30
I.1.2. Oxygenic photosynthesis	33
I.1.3. From anoxygenic to oxygenic photosynthesis	36
a. Evolution of the reaction centers	39
b. Origin of the Water Oxidizing Complex	41
<i>I.2. Geological context of photosynthesis evolution: Archean and Paleoproterozoic shallow-marine sediments</i>	44
I.2.1. Setting the stage: Archean and Paleoproterozoic environments and sedimentary record	45
a. The Archean period (4.0-2.5 Ga)	45
b. The Paleoproterozoic (2.5-1.6 Ga).....	49
I.2.2. Silicification processes in Archean and Paleoproterozoic aqueous environments	50
I.2.3. Influence of silicification and secondary processes on sediment preservation	52
a. Influence of early silicification	52
b. Influence of hydrothermal activity	54
c. Influence of diagenesis and metamorphism	55
<i>I.3. Emergence of oxygenic photosynthesis: the search for signatures the search for signatures in Archean and Paleoproterozoic sediments</i>	56
I.3.1. A brief history of photosynthesis	58
a. Microfossils and stromatolites	59
b. Hydrocarbon biomarkers.....	66
c. Isotope fractionations	68
d. REE patterns, redox-sensitive elements and minerals	74
e. Biominerals.....	78
I.3.2. Different approaches to the same quest	82
<i>I.4. Conclusions on the search for signatures: biochemistry of modern cyanobacteria versus the Precambrian geological record</i>	85
PART 2: MATERIAL AND METHODS	87
CHAPITRE II : RÉSUMÉ.....	88
CHAPTER II: SAMPLES, ANALYTICAL METHODS AND EXPERIMENTAL PARAMETERS	90
<i>II.1. Samples</i>	90
II.1.1. Criteria for sample selection	90
a. Age of the samples	90
b. Geomorphological context	91
c. Preservation state	92

d. Previous analyses	93
II.1.2 Description of the samples	94
II.2. <i>Sample preparation</i>	94
II.3. <i>Petrographical studies</i>	96
II.3.1. Optical microscopy.....	96
II.3.2. Raman spectroscopy.....	97
a. Principle.....	97
b. Raman spectroscopy analyses.....	98
II.4. <i>Elemental analyses – Excitation by electrons</i>	101
II.4.1. Coupled Scanning Electron Microscopy and Energy-Dispersive X-ray spectroscopy	101
a. Principle.....	101
b. Coupled SEM/EDS analyses	104
II.4.2. Electron-probe microanalysis	105
a. Principle.....	105
b. Electron-probe microanalyses.....	106
II.5. <i>Elemental analyses – Excitation by photons</i>	107
II.5.1. Principle of synchrotron radiation XRF and XANES.....	107
II.5.2. Synchrotron beamlines used in this work	111
a. ID 21 and ID 22 NI at the ESRF, Grenoble	113
b. MySpot beamline, Bessy II, Berlin	115
c. Note on the XANES analyses	116
II.6. <i>Isotope analyses</i>	116
II.6.1. Carbon and sulfur isotopes - In situ measurements by Secondary Ion Mass Spectrometry	117
a. Principle.....	118
b. S and C in situ isotope analyses by SIMS	118
II.6.2. Nitrogen and Carbon isotopes - Stepped-combustion static mass spectrometry.....	119
a. Principle.....	119
b. N and C isotopes analyses by stepped-combustion static MS.....	119
II.7. <i>Preliminary conclusions on analytical methodology</i>	120
PART 3: RESULTS	121
CHAPITRE III : RESUME	122
CHAPTER III: PETROGRAPHICAL STUDY	124
III.1. <i>Sample presentation – Petrographic observations</i>	124
III.1.1. Josefsdal Chert, Kaapvaal Craton, South Africa	124
III.1.2. Pongola stromatolites, Kaapvaal Craton, South Africa	128
III.1.3. Gunflint Iron Formation, Animikie Basin, Canada	132
a. Schreiber Beach Locality.....	135
b. Kakabeka Falls Locality	141
c. Mink Mountain Locality.....	144
III.2. <i>Preservation of the geochemical composition of the sediments through post-depositional processes</i>	149
III.3. <i>Conclusions regarding sample selection</i>	153
CHAPITRE IV: RESUME	156
CHAPTER IV: MORPHOLOGY AND TRACE METAL CONTENT OF SEDIMENTARY PYRITE AND BASE-METAL SULFIDES ASSOCIATED TO PRESERVED TRACES OF LIFE IN ARCHEAN AND PALEOPROTEROZOIC SHALLOW MARINE SEDIMENTS	158
IV.1. <i>Trace element incorporation in sedimentary pyrite</i>	158
IV.2. <i>Sample descriptions</i>	161
IV.3. <i>Methodology: classification of pyrite</i>	165
IV.3.1. Types of pyrite	165
IV.3.2. Identification criteria	169

<i>IV.4. Petrographical results</i>	170
IV.4.1. Pyrites in the Hooggenoeg sample	172
IV.4.2. Pyrite and Ni-pyrite from the Josefsdal Chert, Kromberg Formation	176
IV.4.3. Pyrite and chalcopyrite in the Pongola stromatolites	177
IV.4.4. Pyritization in the Schreiber Beach samples, Gunflint Formation	181
IV.4.5. Pyrite in the samples of the Kakabeka Falls locality, Gunflint Formation	182
IV.4.6. Pyrite in the Mink Mountain hematite-rich stromatolites, Gunflint Formation	182
<i>IV.5. Elemental analyses results</i>	183
IV.5.1. Detrital and diagenetic pyrite in the Hooggenoeg Formation	187
IV.5.2. Diagenetic pyrite in the Josefsdal Chert	189
IV.5.3. Diagenetic pyrite and hydrothermal chalcopyrite in Pongola stromatolites	190
IV.5.4. Diagenetic pyrite in the Kakabeka Falls stromatolites, Gunflint Formation	193
IV.5.5. Sulfarsenides in the Mink Mountain stromatolites, Gunflint Formation	195
<i>IV.6. Discussion</i>	196
IV.6.1. Influence of global redox conditions	197
IV.6.2. Influence of fluid circulation during post-depositional processes	200
IV.6.3. Influence of the surrounding mineralogy and of the local chemistry of microbial colonies on the TE content of diagenetic pyrite	204
a. Microbial mats and microbial clots in the 3.45 Ga-old Hooggenoeg Chert	204
b. Microbial clots in the 3.33 Ga-old Josefsdal Chert	210
c. Reworked kerogenous stromatolitic layers in the ~2.95 Ga-old Pongola stromatolites	213
d. Reworked kerogenous stromatolitic layers in the ~1.88 Ga-old Kakabeka Falls stromatolites	220
e. Additional remarks about replacive pyrite in the ~1.88 Ga-old Schreiber Beach stromatolites, Gunflint Formation, Canada	224
<i>IV.7. Conclusions</i>	225
IV.7.1. Conclusions on the TE content of sedimentary pyrite	225
IV.7.2. Conclusions on SEM/EDS and EPMA	228
CHAPITRE V: RESUME	230
CHAPTER V: SYNCHROTRON RADIATION μ-XRF MAPPING OF FOSSILIZED TRACES OF LIFE OLDER THAN 1.8 GA	232
<i>V.1 Revision of FIB preparation methods for the in situ elemental study by XRF of microfossils in Precambrian cherts</i>	233
V.1.1 Rationale for the necessity of thinning petrographical thin-sections for coupling soft and hard SR-XRF analyses	233
V.1.2. Rationale for choosing the holder of the FIB sample for soft and hard SR-XRF analyses	235
a. Light element composition	236
b. The sample must be inseparable from its support	236
c. Possibility of "cleaning"	237
d. Conductivity	239
V.1.3. Experimental investigations of different holders for the FIB samples for soft and hard SR-XRF analyses	239
a. Beryllium half-grids	241
b. Diamond slot-grids	242
c. Comparison of the mounting of FIB slices on Beryllium and diamond holders	243
<i>V.2 Development of Rayleigh/Compton (R/C) method for the quantification of low Z elements</i>	249
V.2.1. Principle of the R/C analytical method	249
V.2.2. Measurement of the R/C calibration curve	251
V.2.3. Application of the R/C calibration curve to the study of a FIB section in a biofilm of the 3.33 Ga-old Josefsdal Chert	253
a. Presentation of the set of XRF data recorded on a FIB sample of a biofilm in Josefsdal Chert	253
b. Choice of the matrix composition based on the XRF-maps	256
c. Calculation of the Z_a of the selected zone and R/C ratio	257
d. Effect of the composition	259
e. Quantification and correction using the R/C method in this work	261
<i>V.3 Preliminary quantitative XRF analyses of fossilized traces of life older than 1.8 Ga</i>	264

V.3.1 Material and methods	264
V.3.2 Results	269
a. Analyses of the Josefsdal samples	269
b. Analyses of the Gunflint samples	277
V.3.3 Discussion	279
V.4. <i>Conclusions of μ-XRF analyses</i>	287
CHAPITRE VI : RESUME.....	289
CHAPTER VI: CARBON, NITROGEN AND SULFUR ISOTOPE ANALYSES	291
VI.1. <i>Carbon and Sulfur isotope in situ analysis by SIMS</i>	292
VI.1.1. Development of new standards for C and S isotopes analyses of Precambrian microbial sediments by SIMS	292
a. Arguments in favor of the need for new standards	292
b. Experimental section	294
VI.1.2. Preliminary results and discussion.....	296
VI.1.3. Conclusions on the development of new standards for SIMS analyses.....	298
VI.2. <i>C and N isotope analyses by stepped-combustion mass spectrometry</i>	299
VI.2.1. $\delta^{13}\text{C}$ and $\delta^{15}\text{N}$ results	300
a. Josefsdal Chert	300
b. Pongola stromatolites	301
c. Gunflint stromatolite – Schreiber Beach locality.....	302
VI.2.2. Discussion	303
a. Silicification and Si-metasomatism.....	304
b. Microbial degradation during diagenesis	305
c. Long-term maturation and metamorphism	306
VI.2.3. Conclusions on C and N isotope analyses by stepped combustion static mass spectrometry	308
VI.3. <i>Conclusions on the study of C, N and S by isotope analytical techniques</i>	309
CONCLUSIONS	313
CONCLUSIONS (FRANÇAIS)	318
BIBLIOGRAPHY	323
ANNEX	344
1. Anoxygenic photosynthesis	344
2. Oxygenic photosynthesis	347

Introduction (Français)

Lorsque l'on parle de photosynthèse, nous pensons surtout aux plantes et à leurs feuilles vertes, connues pour produire de l'oxygène en utilisant l'énergie apportée par les photons de la lumière solaire. Cependant, les racines de la photosynthèse sont ancrées bien plus profondément dans l'histoire de la vie sur Terre, bien avant l'émergence des Eucaryotes, domaine auquel appartiennent les plantes. L'émergence de la photosynthèse oxygénique peut être décrite comme l'évènement le plus important de l'histoire de la Terre après l'apparition de la vie. Avec une taille de seulement quelques microns, les bactéries photosynthétiques oxygéniques et leur capacité à produire de l'oxygène et à le relâcher dans l'environnement ont conduit, directement et indirectement, à des changements environnementaux irréversibles à l'échelle globale, avec des répercussions fondamentales sur la biosphère et la géosphère. Ces bactéries de part leur activité métabolique ont entraîné l'oxygénation de notre planète, jusqu'alors anoxique, et ont ainsi complètement remodelé les cycles biogéochimiques et climatiques. L'émergence de conditions oxydatives sur Terre a engendré l'essor de la biodiversité, et le passage d'un monde microbien à l'évolution d'organismes plus complexes tels que les eucaryotes (Blankenship & Hartman, 1998; Catling *et al.*, 2005; Payne *et al.*, 2011), l'Homme y compris, ainsi que l'explosion de la diversité minéralogique avec la formation de ~58% des espèces minérales connues à ce jour (Hazen *et al.*, 2008).

En se basant sur les indices offerts par l'enregistrement géologique, des hypothèses ont été émises pour dater l'émergence de ces microorganismes. L'évolution de la photosynthèse oxygénique s'est supposément produite entre 3,8 et 2,4 milliards d'années (Ga) dans le passé. Cet intervalle de temps est cependant encore bien trop vaste pour définir un phénomène aussi important. En effet, contraindre dans le temps l'évolution de ces organismes reste une tâche difficile pour plusieurs raisons: les échantillons géologiques correspondants aux âges d'intérêt sont rares, les échelles de temps et

d'espace à prendre en compte sont considérablement étendues, et l'interconnexion des processus liés à la coévolution du monde biologique et du monde géologique est extrêmement complexe. En effet, les bactéries photosynthétiques évoluent à l'échelle micrométrique, et il en va de même pour les processus chimiques impliqués, où engendrés par leur activité métabolique. Cependant, la composition du sédiment et du milieu aqueux (eau de mer, mare, lagon) dans lequel ces communautés bactériennes se sont développées est contrôlée directement par des processus chimiques et physiques se produisant de l'échelle microbienne à l'échelle mondiale, et par des interactions entre l'atmosphère, les océans et les terrains émergés, à l'échelle globale également.

Ainsi, comprendre l'histoire de la photosynthèse nécessite une étude méticuleuse de l'enregistrement géologique ancien, qui reste la seule archive des histoires partagées de la Vie et de la Terre. Cependant, lorsque les sédiments étudiés sont âgés de plusieurs milliards d'années, ce qui est le cas dans cette étude, ils deviennent rares du fait de l'activité tectonique qui recycle continuellement le matériel géologique. De plus, des sédiments aussi anciens ont subi plusieurs milliards d'années d'altération chimique et mécanique. C'est pourquoi, trouver des échantillons adéquates (sédiments déposés dans un milieu aqueux peu profond, ayant subi le moins de dégradations possibles, et contenant des microfossiles et/ou des restes syngénétiques de matière organique) nécessite un travail de terrain de grande ampleur. D'autre part, même lorsque des échantillons appropriés sont sélectionnés, la matière organique qu'ils contiennent, ainsi que leur minéralogie et leur composition chimique initiale, ont été retravaillées par des processus secondaires tels que la diagénèse, la silicification et le métamorphisme. Ces processus rendent l'étude des traces de vie dans les échantillons délicate, et encore plus lorsque l'on cherche à identifier les restes d'un type de bactérie particulier, comme les bactéries photosynthétiques oxygéniques. Dans un tel cas de figure, les critères « classiques » d'identification de traces de vie ne suffisent plus. Il est donc

nécessaire de trouver de nouvelles signatures chimiques permettant de réaliser ce travail.

Les paragraphes suivant décrivent plus en détail les mécanismes, l'importance et les répercussions de ce saut évolutif, ainsi que les approches scientifiques utilisées jusqu'à maintenant pour tenter de déchiffrer l'histoire de la photosynthèse oxygénique.

Le rôle de la photosynthèse oxygénique dans la Grande Oxygénation de notre planète

Preuves concernant l'augmentation du niveau d'oxygène dans l'atmosphère il y a 2,45-2,32 Ga

Dans l'enregistrement géologique, de nombreux indices suggèrent une hausse du niveau d'oxygène dans l'atmosphère au Paléoproterozoïque (le Protérozoïque s'étend de ~2,4 à ~0,5 Ga). Par exemple, les paléosols latéritiques (dans lesquels le fer est retenu sous sa forme oxydée Fe^{3+}) et les vastes dépôts d'oxydes de manganèse (en particuliers ceux de la formation de Hotazel, Supergroupe du Transvaal, Afrique du Sud) ne sont présents dans l'enregistrement géologique qu'à partir de ~2,3 Ga. Ces dépôts sont une démonstration directe de la présence d'oxygène dans l'environnement puisque Mn a un fort potentiel redox (oxydoréduction) et nécessite donc de grandes quantités d'oxygène pour être oxydé. De plus, la présence de galets bien arrondis d'uraninite (UO_2), de pyrite (FeS_2) et de sidérite (FeCO_3) déposés dans des environnements fluviaux ou marins peu profonds, ne sont documentés qu'avant 2,3 Ga (Rasmussen & Buick, 1999; Roscoe, 1996; England *et al.*, 2002; Hofmann *et al.*, 2009). Ces minéraux sont instables en conditions oxydatives (Holland, 1984), par conséquent, leur transport (qui a entraîné l'arrondissement de ces galets) et leur dépôt dans des sédiments requiert un environnement anoxique, ou très pauvre en oxygène. En effet, dans le cas contraire, la pyrite aurait été oxydée en magnétite (Fe_3O_4) ou

hématite (Fe_2O_3) et l'uraninite en cations d'uranyle (UO_2^{2+}), par exemple. L'absence de ces minéraux dans l'enregistrement géologique après 2,3 Ga suggère donc que l'environnement était oxygéné.

D'autres auteurs utilisent des données géochimiques telles que la distribution et la concentration de certains métaux traces comme le rhénium et le molybdène, mesurées dans des roches sédimentaires marines Archéennes (~4,0-~2,4 Ga). La mobilisation de ces éléments sur les terrains émergés et leur transport vers l'océan nécessite la présence d'oxygène dans l'environnement, même en très petites quantités (Bertine & Turekian, 1973; Holland, 1984; Collier, 1985). Cette caractéristique fait de ces métaux de très bons indicateurs des conditions paléo-redox. Siebert *et al.* (2005) ont décrit l'augmentation des niveaux d'oxygène dans l'environnement dès 2,7 Ga, et Anbar *et al.* (2007) ont reporté un enrichissement temporaire de l'atmosphère en oxygène à ~2,5 Ga. Ces derniers ont introduit le concept de "whiffs of oxygen" qui propose la présence de "pics" d'oxygène dans l'atmosphère et l'environnement bien avant la considérable augmentation de la concentration d'oxygène dans l'atmosphère il y a ~2,4 Ga.

Cependant, une autre approche géochimique semble être plus adéquate pour contraindre dans le temps cette grande oxygénation. L'analyse des isotopes de soufre dans des minéraux soufrés tels que la pyrite ou la barytine (BaSO_4), dans des sédiments datant de l'Archéen jusqu'à aujourd'hui, montre une transition entre un fractionnement isotopique indépendant de la masse (*mass-independent fractionation*, MIF) et un fractionnement dépendant de la masse (*mass-dependent fractionation*, MDF) des isotopes ^{33}S et ^{34}S il y a ~2,45 Ga. La Figure 1a présente les données de $\Delta^{33}\text{S}$ (rapport isotopique indiquant le fractionnement de type MIF du soufre) collectées par plusieurs auteurs (Farquhar *et al.*, 2000; Ono *et al.*, 2003; Kasting, 1993; Mojzsis *et al.*, 2003 ; et Hu *et al.*, 2003). Ces données suggèrent fortement qu'avant ~2,45 Ga, les gaz soufrés expulsés dans l'atmosphère par l'activité volcanique étaient remaniés par la photolyse créée par le rayonnement UV en l'absence d'oxygène atmosphérique (Farquhar *et*

al., 2000). La cessation du signal de type MIF au profit d'un signal de type MDF suggère qu'à l'époque de cette transition, le niveau d'oxygène dans l'atmosphère était suffisamment important pour permettre la création d'une couche d'ozone et empêcher la photolyse par les UV. Il a été estimé que la transition entre ces deux types des fractionnements se fait pour une concentration de $O_2 \geq 10^{-5}$ fois son niveau actuel dans l'atmosphère (Pavlov & Kasting, 2002). En particulier, Bekker *et al.* (2004) ont montré qu'à ~2,32 Ga, la concentration d' O_2 dans l'atmosphère était déjà plus élevée que cette valeur.

Ce phénomène est appelé “*Great Oxidation Event*” (GOE) pour “Grande Oxygénation” et fait référence au passage de conditions anoxiques à oxiques dans l'atmosphère et les océans à l'échelle globale (voir Fig. 1b). Le GOE est daté entre ~2,45 and ~2,32 Ga (Bekker *et al.*, 2004). Les raisons de cette augmentation de la concentration d'oxygène font cependant encore l'objet de discussions. La Terre étant une machine complexe impliquant l'interconnexion continue de processus biologiques et géologiques, il serait dangereusement ambitieux d'attribuer à cet évènement d'échelle globale un seul phénomène biologique ou géologique isolé. Ainsi, il serait plus correct de chercher *LES* causes du GOE et non pas *LA* cause.

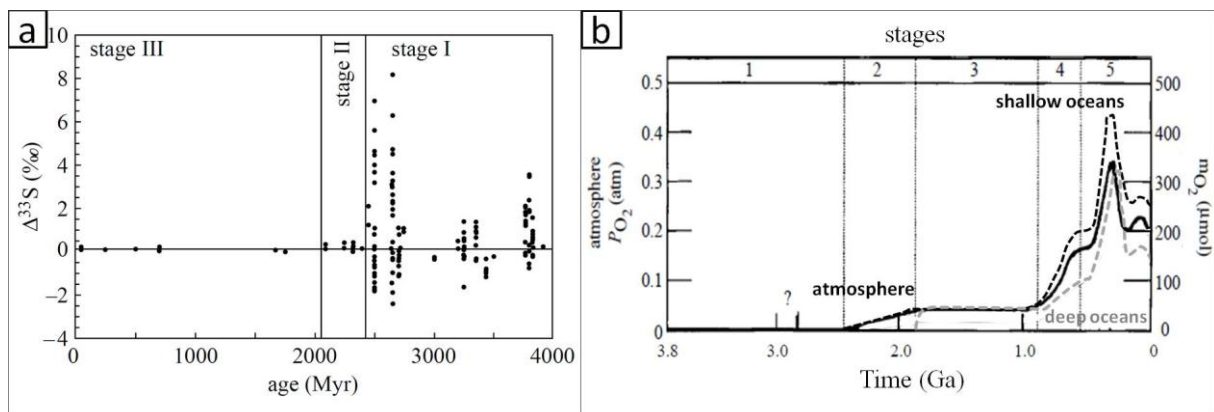
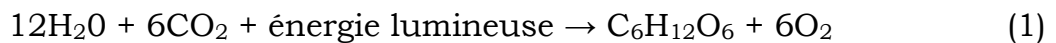


Figure 1. La Grande Oxygénation de l'atmosphère et des océans : estimation du niveau d'oxygène dans l'atmosphère et les océans à partir des isotopes de soufre. a) Valeurs de $\Delta^{33}S$, montrant l'évolution du fractionnement indépendant de la masse du soufre dans des pyrites et des barytines depuis 4 milliards d'années. (Holland, 2006) (Données compilées par S. Ono à partir de Kasting, 1993; Farquhar *et al.*, 2000; Ono *et al.*, 2003; Mojzsis *et al.*, 2003; Hu *et al.*, 2003); b) Estimation de l'évolution de la PO_2 atmosphérique et de la concentration en O_2 des océans profonds et peu profonds. Modifié à partir de Holland, 2006.

Les causes du « Great Oxidation Event » : le rôle de la photosynthèse oxygénique

Parmi les processus biologiques, il existe une façon de produire directement de l'oxygène. En effet, au cours de la photosynthèse oxygénique, la production d'oxygène fait partie de la chaîne de réaction métabolique. Les organismes assurant la photosynthèse oxygénique sont capables d'utiliser les photons de la lumière solaire comme une source d'énergie pour oxyder les molécules d'eau, produisant ainsi de l'O₂ qui est ensuite libéré dans le milieu. Cette réaction peut être exprimée de façon simplifiée comme suit :



L'enregistrement géologique contient des indices suggérant que la photosynthèse oxygénique, en tant que métabolisme bactérien, était déjà en place bien avant le GOE, probablement autour de ~2,7 Ga (Brocks *et al.*, 1999, 2003a; Lepot *et al.*, 2008), et éventuellement, mais non sans susciter de controverses, dès 3,8 Ga (Canfield *et al.*, 2006).

Cette hypothèse a été utilisée comme argument à l'encontre d'un rôle majeur de la photosynthèse oxygénique dans le GOE. Holland (2002) a proposé que ce métabolisme ne pouvait pas être responsable du GOE puisqu'il pouvait avoir émergé plus de 300 millions d'années avant cet événement. Cependant, il est possible que la concentration d'O₂ produit par la photosynthèse n'ait pu augmenter dans l'atmosphère que lorsque les principaux réservoirs géologiques consommant de l'oxygène à l'Archéen et au Paléoproterozoïque n'aient été saturés. En effet, l'environnement Archéen était anoxique, avec l'apport continu de gaz volcaniques, phases minérales et fluides hydrothermaux réduits. Dans un tel contexte, la concentration d'oxygène n'aurait pu augmenter dans l'atmosphère que lorsque les produits de ces sources réductrices furent oxydés, ce qui aura pu prendre des millions d'années.

Un résumé des différentes hypothèses liant l'émergence de la photosynthèse oxygénique au GOE est donné par Buick (2008):

1. La photosynthèse oxygénique a évolué plusieurs centaines de millions d'années avant le GOE. Les puits à oxygène, répartis à l'échelle globale, auront dû être saturés pour que le niveau d'oxygène augmente dans l'atmosphère, expliquant ainsi le délai entre l'apparition de ce métabolisme et le GOE (Catling & Claire, 2005).
2. La photosynthèse oxygénique a évolué autour de 2,4 Ga, causant le GOE et des changements environnementaux et climatiques immédiats (Kopp *et al.*, 2005; Kirschvink & Kopp, 2008).
3. La production d'oxygène par des procédés biologiques a débuté très tôt dans l'histoire de la Terre, et peut-être même avant le début de l'enregistrement géologique. L'atmosphère Archéenne contenait des niveaux importants d'oxygène bien avant le GOE (Ohmoto, 1997). Cependant, il a récemment été suggéré que cette oxygénation Archéenne était plutôt présente sous forme d'« oasis » et que l'atmosphère et les océans à cette époque n'étaient que temporairement oxygénés et à des échelles régionales ou locales (Ohmoto *et al.*, 2008).

Ces nouvelles conclusions, faites par Ohmoto (2008), montrent la nécessité d'introduire une quatrième hypothèse. En effet, bien que la plupart des indices corroborent une augmentation considérable de la concentration d'O₂ dans l'atmosphère autour de ~2,45-2,32 Ga (Bekker *et al.*, 2004), de nombreux indices supportent également la possibilité de fluctuations du niveau d'O₂ dans l'atmosphère à l'Archéen. Plusieurs hypothèses ont été proposées pour expliquer ces variations (e.g. Ohmoto *et al.*, 2006; Kirschvink & Kopp, 2008). De nombreux auteurs les ont interprété comme des « pics » d'oxygénation enregistrés tout au long de l'Archéen (Anbar *et al.*, 2007; Frei *et al.*, 2009; Wille *et al.*, 2007) et dès ~2,95 Ga (Crowe *et al.*, 2013; Planavsky *et al.*, 2014; Large *et al.*, 2014). Ces « pics » pourraient représenter les premiers pas de la photosynthèse oxygénique dans un monde anoxique où

les puits à O₂ auraient empêché l'O₂ produit de s'accumuler durablement dans l'atmosphère.

Bien que la dissociation de la molécule d'eau par les bactéries photosynthétiques oxygéniques soit une des raisons majeures ayant causé l'augmentation de la concentration d'O₂ dans l'atmosphère, l'implication de certains processus géologiques ne doit pas être écartée.

Par exemple, un processus complètement abiotique a été proposé, qui pourrait en partie expliquer le GOE. Plusieurs auteurs proposent que l'état d'oxydation des gaz volcaniques dépend de l'état d'oxydation du manteau terrestre. Ainsi, ils relient l'état d'oxydation de l'atmosphère à l'oxydation des gaz volcaniques, elle-même dépendante de l'évolution de l'état redox du manteau pendant la différenciation de la Terre (Kasting *et al.*, 1993; Kump *et al.*, 2001). Gaillard *et al.* (2011) proposent qu'un changement d'état d'oxydation du soufre due à une baisse de la pression moyenne du dégazage volcanique aurait pu engendrer l'oxygénation de l'atmosphère.

Ces hypothèses sont associées à l'évolution de la composition chimique du manteau pendant l'étape de différenciation de notre planète. Dans ce contexte, Konhauser *et al.* (2009) proposent une interprétation à l'hypothèse de Zahnle *et al.* (2006). Ces derniers avancent que le GOE est le résultat d'un appauvrissement en méthane dans l'atmosphère dû au déclin de l'activité des méthanogènes –un métabolisme procaryote produisant du méthane- en faveur des bactéries sulfato-réductrices permettant ainsi à l'atmosphère de passer d'anoxique à oxique. Konhauser *et al.* (2009) ont montré qu'un déclin de l'activité des méthanogènes à l'échelle globale pourrait être dû à un appauvrissement en nickel (un métal-clé pour ces microorganismes) des roches volcaniques après 2,7 Ga à la suite de changements dans la chimie du manteau. Ces études montrent que les processus géologiques et biologiques sont étroitement liés et qu'ils s'influencent l'un l'autre, mais montrent aussi l'importance des organismes vivants sur l'influence de phénomènes globaux.

Le GOE semble donc être le résultat de l'émergence de la photosynthèse oxygénique, entretenu par des processus abiotiques qui ont permis à la concentration d'oxygène d'augmenter dans l'atmosphère et les océans avec le temps.

Il a été montré que la photosynthèse oxygénique a évolué à partir de la photosynthèse anoxygénique (Olson & Pierson, 1986; 1987; Blankenship, 1992; Blankenship & Hartman, 1998; Xiong & Bauer, 2002), une forme plus ancienne de photosynthèse. La photosynthèse anoxygénique se sert également de la lumière solaire comme source d'énergie, mais mène à la production de composés de soufre et de fer par exemple, à la place de l'oxygène (voir Chapitre I). Cependant, le moment précis de cette évolution biologique n'est pas encore connu, et les trois grandes questions de l'histoire de la photosynthèse (Figure 2), restent pour le moment sans réponse : (i) Quand est apparue la photosynthèse ? (ii) Quand la photosynthèse oxygénique a-t-elle émergé ? (iii) Combien de temps s'est écoulé entre l'émergence de la photosynthèse oxygénique et le GOE ?

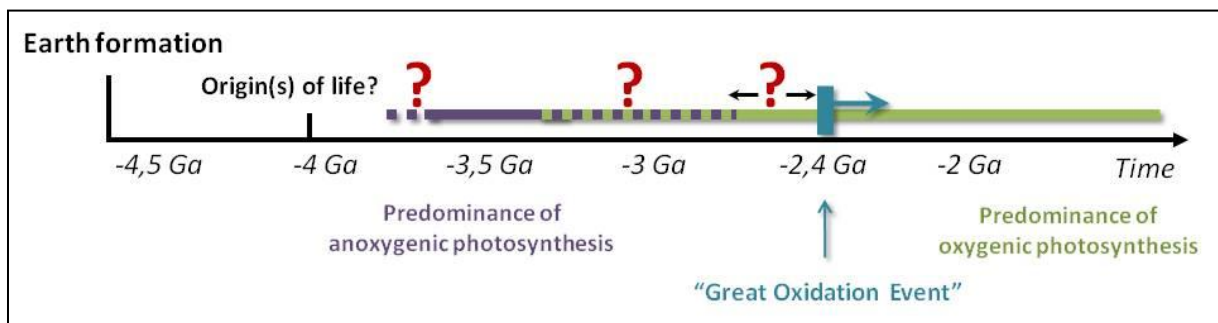


Figure 2. Les trois grandes questions de l'histoire de la photosynthèse. En terme de chronologie, les points clés de l'histoire de la photosynthèse qui restent encore à déterminer sont : (i) l'émergence de la photosynthèse, en tant que photosynthèse anoxygénique, (ii) l'émergence de la photosynthèse oxygénique, et (iii) le temps écoulé entre (ii) et le GOE.

L'objectif de cette étude est de tenter de répondre à la question (ii), elle-même nécessaire pour répondre à la question (iii). Afin de contraindre dans le temps l'évolution de la photosynthèse oxygénique, il est nécessaire de trouver, dans l'enregistrement géologique, des signatures chimiques et

minéralogiques spécifiques à ce type de bactéries. Ces signatures permettront de différencier les bactéries des autres types de microorganismes, mais aussi des bactéries photosynthétiques anoxygéniques. Pour cela, il est nécessaire de connaître les mécanismes du métabolisme photosynthétique (anoxygénique et oxygénique), afin de détecter et d'identifier, les traces chimiques potentielles qu'auraient pu laisser les bactéries photosynthétiques oxygéniques et qui indiqueraient leur présence et leur activité.

Introduction

Photosynthesis evokes plants and their green leaves, known for their ability to produce oxygen using energy from sunlight. The roots of photosynthesis are however, deeply embedded in the primitive history of Earth and of life itself, long before the rise of Eukaryotes such as plants. The evolution of oxygenic photosynthesis can be referred to as the most extraordinary event in the history of Earth, once life has emerged. Only a few microns in size, oxygenic photosynthetic bacteria with their ability to produce oxygen and release it to their environment yielded, directly and indirectly, irreversible local to global scale changes, with fundamental implications for the bio- and geospheres. These particular bacteria and their metabolic activity triggered a transition from an anoxic to an oxic world, thus completely reworking Earth's biogeochemical cycles and climates. The emergence of oxic conditions on Earth directly influenced the blossoming of biodiversity from the bacterial world to the evolution of complex eukaryotic organisms (Blankenship & Hartman, 1998; Catling *et al.*, 2005; Payne *et al.*, 2011), humans included, and an explosion in the diversity of minerals with the formation of *ca* 58% of the total mineral species known today (Hazen *et al.*, 2008).

Hypotheses concerning the timing of the emergence of oxygenic photosynthesis based on clues found in the geological record are numerous. This process is thought to have occurred sometime between 3.8 and 2.4 billion years (Ga) ago. This time interval is, however, overly long for such an important phenomenon that remodeled the face of the Earth. Nevertheless, constraining the evolution of oxygenic photosynthesis in time constitutes a particularly delicate task because of the rarity of suitable samples of this age, the extent of the spatial and temporal scales involved, and the complexity of the interlinked processes related to the co-evolution of the biological and the geological worlds. Indeed, photosynthetic bacteria have the same micrometric (μm) scale as the chemical processes involved in, or

triggered by their metabolic activity. Although the composition of the sediments, and that of the aqueous medium in which these bacterial communities developed, was directly controlled by physical and chemical processes occurring at the microbial to local scale, there was also interaction at the global scale between the oceans, the atmosphere, and emerged terrains.

Understanding the history of oxygenic photosynthesis requires meticulous study of the ancient geological record, the only archive of the joint histories of Earth and Life. Consequently, it is necessary to take into account nanometric to kilometeric chemical heterogeneities. Furthermore, when the sediments studied are several billions of years old, samples become scarce because of the continuous recycling of geological material by tectonic activity. Sediments of this age have undergone deformation, alteration and weathering over billions of years. Finding relevant samples (sedimentary origin, deposited in a shallow aqueous environment, low degree of degradation and metamorphism, containing syngenetic organic matter and/or microfossils) requires dedicated field work. In addition to these obstacles, when suitable samples are found, the organic matter, mineralogy, and chemical composition have been reworked by post-depositional processes, such as diagenesis, alteration, silicification, and metamorphism, so that the study of traces of life becomes challenging, and even more so when trying to identify the remains of a particular metabolic type of bacteria such as oxygenic photosynthetic bacteria. In this scenario, “traditional” recognition criteria for the identification of life are insufficient or no longer usable. Other chemical signatures must be found.

The following paragraphs of this introduction attempt to describe the mechanisms, importance and repercussions of this evolutionary leap, as well as the scientific approaches and tools used to decipher the history of oxygenic photosynthesis.

The role of oxygenic photosynthesis in the “Great Oxidation Event”

Evidence for the rise of oxygen in the atmosphere 2.45-2.32 Ga ago

Some geological features younger than 2.32 Ga strongly suggest a Paleoproterozoic rise of oxygen levels in the atmosphere (Proterozoic: from ~2.4 to ~0.5 Ga). The first appearance of red beds (which form under dry oxidized conditions), lateritic paleosols (in which iron is retained as its insoluble oxidized Fe^{3+} form), and large deposits of Mn-oxides (particularly those from the Hotazel Formation, Transvaal Supergroup, South Africa) occur in the geological record after 2.3 Ga. These deposits are a direct demonstration of the presence of oxygen in the environment since Mn has a high redox (for reduction-oxidation) potential and thus requires significant quantities of oxygen to be oxidized. Furthermore, well-rounded pebbles of uraninite (UO_2), pyrite (FeS_2), and siderite (FeCO_3) deposited in fluvial or shallow-marine environments are found only in sediments older than 2.3 Ga (Rasmussen & Buick, 1999; Roscoe, 1996; England *et al.*, 2002; Hofmann *et al.*, 2009). These minerals are unstable under oxidizing conditions (Holland, 1984), therefore transport (during which the rounded shape developed) and deposition require very low levels of oxygen, otherwise pyrite would have been oxidized to magnetite (Fe_3O_4) or hematite (Fe_2O_3), and uraninite to uranyl cations (UO_2^{2+}), for example. Their absence in the geological record after 2.3 Ga suggests that oxygen was present in the environment at that time.

The concentrations of the transition metals rhenium and molybdenum have been measured in Archean (~4.0-~2.4 Ga) marine sedimentary rocks. The mobilization of these elements requires at least small quantities of oxygen in the environment (Bertine & Turekian, 1973; Holland, 1984; Collier, 1985), hence their usefulness as proxies for paleo-redox conditions.

Re, PGE (Platinum Group Elements) data and Mo concentrations as well as measurements of Mo isotopes in clastic sediments and black shales from the Manjeri Formation (Belingwe Greenstone Belt, Zimbabwe) (Siebert *et al.*, 2005), suggest an increase in oxygen concentration in the environment by 2.7 Ga. Anbar *et al.* (2007) studied Re, Os, Mo, S and U geochemical data from the Mount McRae Shale (Hamersley Basin, Western Australia) deposited ~2.5 Ga ago and report a temporary oxygen enrichment at this time. The concept of “whiffs of oxygen” introduced by this group suggests pulses of oxygenation before a substantial rise in oxygen levels in the environment around 2.3 Ga, as indicated by the evidence mentioned above.

However, the timing of this rise of oxygen might be better constrained by the use of another geochemical approach. Sulfur isotope analyses of Archean to modern sedimentary sulfur minerals, such as pyrites and barites (BaSO₄), record a transition from mass-independent fractionation (MIF) to mass-dependent fractionation (MDF) of the ³³S and ³⁴S isotopes around 2.45 billion years ago. Figure 1a shows the collected data of $\Delta^{33}\text{S}$ (indicator of Sulphur MIF) compiled from Farquhar *et al.*, 2000; Ono *et al.*, 2003; Kasting, 1993; Mojzsis *et al.*, 2003 and Hu *et al.*, 2003. MIF-S signals strongly suggest that, before 2.45 Ga, sulfurous gases injected in the atmosphere via volcanic activity were reprocessed by UV photolysis in the absence of atmospheric oxygen (Farquhar *et al.*, 2000). The loss of the MIF-S signal implies a rise of O₂ atmospheric levels, with a concentration sufficient to allow the formation of an ozone “shield” against UV. The transition from MIF-S to MDF-S occurs for a concentration of O₂ $\geq 10^{-5}$ times the present atmospheric level (PAL) (Pavlov & Kasting, 2002). Bekker *et al.* (2004) show that by 2.32 Ga, the concentration of oxygen in the atmosphere was higher than this specific value.

This phenomenon has been called the “Great Oxidation Event” (GOE) as it refers to the transition from anoxic to oxic conditions in the atmosphere and oceans at the global scale (see Fig. 1b). It is dated between 2.45 and 2.32 Ga (Bekker *et al.*, 2004). The reason for this rise, however, remains

difficult to determine. Earth is a complex machine involving continuously linked biological and geological processes. It would be dangerously ambitious to attribute any single biological or geological cause to such a global event. The cause of the GOE might be better expressed as “the *causes*”.

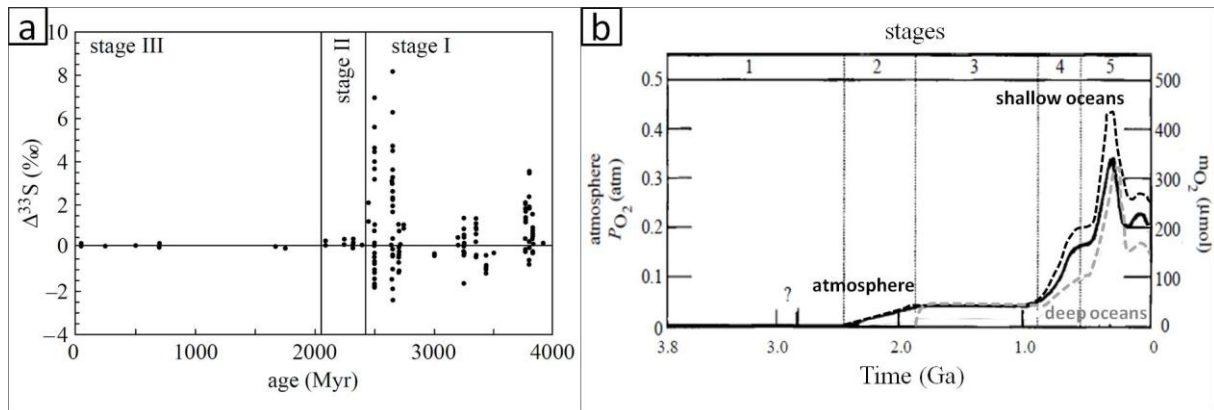
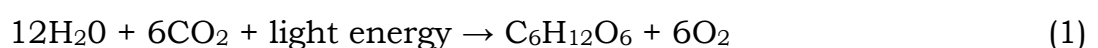


Figure 1. The Great Oxidation Event: indications from S isotopes and estimations of O₂ levels in atmosphere and oceans. a) $\Delta^{33}\text{S}$ values, indicator of mass-independent fractionation of sulfur in pyrites and barites during the past 4.0 Ga. (Holland, 2006) (Data were compiled by S. Ono from Kasting, 1993; Farquhar *et al.*, 2000; Ono *et al.*, 2003; Mojzsis *et al.*, 2003; Hu *et al.*, 2003); b) Estimated evolution of atmospheric PO₂ and the concentration of O₂ in the shallow and deep oceans. Modified from Holland, 2006.

Causes of the Great Oxidation Event: the role of oxygenic photosynthesis

Among biological processes, there is one that directly produces oxygen. Indeed, during oxygenic photosynthesis, oxygen production is part of the metabolic chain of reactions. Oxygenic photosynthetic organisms are able to use photons provided by sunlight as an energy source to oxidize the water molecule (H₂O), producing and releasing oxygen during the process. This reaction can be summarized as follows:



The geological record contains clues suggesting that oxygenic photosynthesis, as a bacterial metabolism, had already evolved long before

the GOE, most likely around 2.7 Ga (Brocks *et al.*, 1999, 2003a; Lepot *et al.*, 2008), and potentially, although not without controversy, as early as 3.8 Ga (Canfield *et al.*, 2006) (see the section below: *Evolution of oxygenic photosynthesis: The search for signatures*).

This evidence has been used as an argument against the important role of the oxygenic photosynthesis in the GOE. Holland (2002) proposed that oxygenic photosynthesis cannot be responsible for the GOE, as it possibly emerged more than 300 Ma before this event. However, it is possible that the concentration of photosynthetically produced oxygen was not able to rise in the atmosphere until oxygen production had saturated the global oxygen sinks available during the Archean and Early Proterozoic. Indeed, the Archean environment was reduced, with a continuous input of reduced volcanic gases, hydrothermal fluxes and crustal minerals. For the atmosphere to become oxygenated, the products of all these reducing sources had to be oxidized, which can take millions of years.

A classic example is related to the occurrence of a particular type of sedimentary deposit called Banded Iron Formations (BIFs), widely distributed around the globe, and dated between 3.8 and 0.8 Ga. These rocks were formed in aqueous marine environments and exhibit alternating Fe-rich and Fe-poor but silica-rich layers. The peak of BIF deposition is dated between 2.7 and 2.4 Ga. For this reason, and because they contain both Fe²⁺ and Fe³⁺ minerals, their depositional mechanisms have been linked to the presence of oxygen in the environment. In particular, Cloud (1965, 1968, 1973) showed that, in an Archean ocean rich in reduced iron Fe(II), the O₂ released by potential oxygenic photosynthetic bacteria would have only oxidized the superficial layer of the ocean, then would have been mixed by marine currents to the reduced layers underneath. This process could have allowed the precipitation of Fe-oxides by oxidizing ferrous iron Fe(II) to insoluble ferric iron Fe(III), which precipitated to BIFs. As oxygen is consumed in this process, O₂ could have started to accumulate in the atmosphere only when all the Fe(II) was oxidized.

This mechanism is not the only one that could explain the delay between an early evolution of oxygenic photosynthesis and the GOE. A change in tectonic style has been documented across the Archean and Proterozoic boundary, between ~2.7-2.4 Ga ago. Barley *et al.* (2005) review the controls and consequences of these changes. This period saw the formation of supercontinents and tectonic plates similar in size and in thickness to those observed today, with the formation of continental plateaus. This had two implications that could have finally allowed the increase of oxygen in the atmosphere:

- This change in tectonic style could have triggered the formation of more elevated reliefs, increasing the availability of more mineral nutrients for photosynthetic microorganisms and other prokaryotes, and thus, increasing the oxygen productivity of potential oxygenic photosynthetic bacteria.
- Also, if the atmosphere started to accumulate oxygen, the enhanced erosion rate triggered by the formation of such elevated reliefs would have increased the burial efficiency of degraded carbon (Campbell & Allen, 2008), avoiding its oxidation and thus making this particular sink for oxygen unavailable, allowing the increase of oxygen levels in the atmosphere to continue.

Buick (2008) summarized the three main hypotheses to explain the time relation between the evolution of oxygenic photosynthesis and the GOE.

4. Oxygenic photosynthesis evolved hundreds of millions of years before the GOE. The widespread oxygen sinks had to be filled in order for oxygen levels to increase in the atmosphere, hence the delay between the emergence of oxygenic photosynthesis and the rise of oxygen in the atmosphere (Catling & Claire, 2005).
5. Oxygenic photosynthesis arose around 2.4 Ga, causing the GOE and immediate environmental change (Kopp *et al.*, 2005; Kirschvink & Kopp, 2008).
6. Oxygen production via biogenic processes began very early in Earth's history, even before the start of the geological record. The Archean

atmosphere was highly oxygenated, long before the GOE (Ohmoto, 1997). More recently however, it was suggested that this oxygenation could have occurred as oxygen oases (Ohmoto *et al.*, 2008).

However, new findings might trigger the need for a fourth hypothesis. Indeed, even though most of the evidence converges towards a remarkable rise on O₂ around 2.45-2.32 Ga ago (Bekker *et al.*, 2004), there was nevertheless significant fluctuations in atmospheric O₂ levels in the Archean. Several hypotheses have been proposed to explain these variations (e.g. Ohmoto *et al.*, 2006; Kirschvink & Kopp, 2008). Many authors have interpreted them as 'pulses' of oxygenation, recorded throughout the Archean (Anbar *et al.*, 2007; Frei *et al.*, 2009; Wille *et al.*, 2007) and as early as ~2.95 Ga (Crowe *et al.*, 2013; Planavsky *et al.*, 2014; Large *et al.*, 2014). These 'pulses' could represent the early stages of oxygenic photosynthesis, and oxygen sinks available at this time would have prevented the permanent accumulation of oxygen in the atmosphere.

Furthermore, although the splitting of water by oxygenic photosynthetic bacteria may be one of the main reasons for the rise of oxygen in the atmosphere, geological processes should not be discounted.

The continuous hot and reduced fluid flux provided by intense hydrothermal activity during the Archean could have triggered the production of small, localized quantities of O₂ by boiling of the hot, pressurized fluids as they reach vents at the surface of the Earth (C. Ramboz, personal communication). Kirschvink & Kopp (2008) have proposed that photochemically-produced H₂O₂ on glacier surfaces could have lead to the production of O₂ when mixed with the H₂O of the ocean (after Liang *et al.*, 2006). However, these authors use this process to propose a source of oxygen pre-dating the GOE that could have allowed a biological adaptation to the toxicity of oxygen, but they do not suggest that it could have triggered the GOE. Alternatively, in shallow marine environments, UV radiation can drive the photooxidation of dissolved Fe(II) (Braterman *et al.*, 1983; Braterman & Cairns-Smith 1987), and locally produce Fe(III) cations that

later form ferric hydroxides via hydrolysis. These ferric hydroxides could be taken as indications of the presence of oxygen. However, experiments on this subject led Konhauser *et al.* (2007a) to discount this hypothesis. They show that, in fluids similar in composition to the Archaean ocean with a high dissolved content of Fe(II), Si and HCO_3^- , the oxidation effects of UV light are negligible compared to the precipitation of ferrous-iron-silicates and ferrous carbonates.

Other more plausible abiotic processes have been proposed to explain the GOE. Several authors suggest that the oxidation state of volcanic gases depends on the oxidation state of the mantle. Thus, they link the oxidation of the atmosphere to the oxidation of volcanic gases related to the evolution of the redox state of the mantle during Earth's differentiation (Kasting *et al.*, 1993; Kump *et al.*, 2001). Gaillard *et al.* (2011) suggest that a change in the oxidation state of sulfur due to a decrease in the average pressure of volcanic degassing could have triggered the oxygenation of the atmosphere.

These hypotheses are associated with the evolution of the chemical composition of the mantle during Earth's differentiation. In this context, Konhauser *et al.* (2009) proposed an alternate interpretation of the hypothesis of Zahnle *et al.* (2006). The latter postulated that the GOE was caused by a depletion of methane in the atmosphere triggered by a decline of methanogenic microbial activity -a prokaryotic metabolism producing methane- in favor of sulfate-reducing bacteria (SRB) thus allowing the atmosphere to evolve from anoxic to oxic conditions with the decrease of methane levels. Konhauser *et al.* (2009) have shown that the decline of global methanogenesis may be the result of a depletion of nickel, a key-metal used by methanogens, in volcanic rocks after 2.7 Ga, following changes in mantle chemistry. These studies demonstrate that geological and biological processes are closely interlinked and strongly influence each other, and show the importance of the role of life in prompting global phenomena.

In summary, the GOE seems to be the result of the emergence of oxygenic photosynthesis, sustained by abiotic processes that allowed oxygen levels to increase in the atmosphere and oceans with time.

It has been shown that oxygenic photosynthesis evolved from *anoxygenic* photosynthesis (Olson & Pierson, 1986; 1987; Blankenship, 1992; Blankenship & Hartman, 1998; Xiong & Bauer, 2002), an older form of the photosynthetic pathway also involving the use of sunlight as an energy source, but leading to the production of iron and sulfur compounds, for example, instead of oxygen (see next, *Bacterial anoxygenic and oxygenic photosynthesis*). The timing of this biological evolution is however, still debatable, and the “Big Three” questions illustrated in Figure 2, still remain: (i) When did photosynthesis appear? (ii) When did oxygenic photosynthesis emerge? (iii) How much time passed between the inception of oxygenic photosynthesis and the GOE?

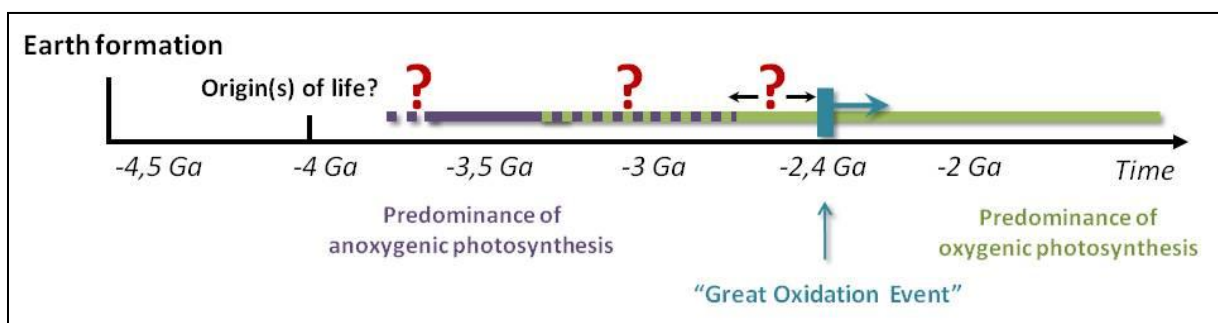


Figure 2. The “Big Three”: three critical questions remain to complete the history of photosynthesis. Indeed, in terms of timing, the key points that still need to be constrained are: (i) the emergence of photosynthesis, initially as an anoxygenic metabolism, (ii) the emergence of oxygenic photosynthesis, and (iii) the period of time between (ii) and the GOE.

The study presented here concentrates on question (ii), which is needed for answering question (iii). To constrain the evolution of oxygenic photosynthesis in time, it is necessary to find mineralogical and chemical signatures in the geological record allowing the differentiation of anoxygenic and oxygenic photosynthesis. For this purpose, the metabolic mechanisms and chemistry of photosynthesis, both anoxygenic and oxygenic, must be

well understood in order to detect any trace that photosynthetic bacteria may have left in the geological record indicating their presence and metabolic activity.

Scientific approach and objectives

Did oxygenic photosynthetic bacteria leave signatures of their presence and activity at the local scale in Archean and Paleoproterozoic sedimentary rocks that would allow tracing their emergence through time? If they did, what are these signatures and which analytical techniques are suitable for their detection and identification?

At the heart of these working hypotheses is the fact that the emergence of oxygenic photosynthesis has been strongly influenced by lateral gene transfer (Raymond *et al.*, 2002; Mulkidjanian *et al.*, 2006; Allen & Martin, 2007) within microbial communities, such as microbial mats. This evolutionary leap must thus have taken place at the very local, micrometric scale before the evolutionary-advantaged, oxygenic photosynthetic bacteria could spread and affect their environment on regional to global scales. If preserved, the first signatures of oxygenic photosynthesis should be found at the micrometric scale.

With the aim of constraining the emergence of oxygenic photosynthesis in time, I chose to use *in situ* analyses at the cellular and microbial mat scale to seek mineralogical and geochemical signatures of this particular metabolism in Precambrian sediments. The signatures sought are of two types:

- Type A signatures: they relate to the intrinsic biochemistry of the oxygenic photosynthetic pathway itself. They involve the chemical characterization of the carbonaceous matter remaining in fossilized bacteria and bacterial mats.
- Type B signatures: they relate to the local environmental impact of oxygenic photosynthesis. They consist of identifying preserved changes in the local mineralogy and chemistry around photosynthetic microfossils that would have been induced by the metabolic activity of oxygenic photosynthetic bacteria, and particularly by the release of oxygen.

The search for these potential chemical signatures of oxygenic photosynthesis is based on the collection and use of new geochemical and mineralogical data obtained from fossilized photosynthetic biofilms and cells ranging in age from the anoxic Archean Earth to the aftermath of the GOE. The rarity of the samples used in this study, and the scientific case itself, pose several constraints that limit the choice of analytical techniques usable. Indeed, the scale of interest of this study requires micrometric to elemental-scale techniques, but proscribes to a certain extent, the use of bulk analytical techniques since the spatial distribution of chemical elements has a key role in this study. Nevertheless, bulk chemical analyses are needed to place the samples in the broader scale in terms of environmental context. Furthermore, the rarity of the samples implies the use of non-destructive techniques as much as possible. These requirements encourage the use of complementary analytical techniques and a top-down approach to study the chemistry and mineralogy associated with photosynthetic microfossils at the local scale. The first step is to determine the suitability of the available techniques, taking into account the fact that the sediments studied have been submitted to a series of chemical changes that include degradation of the organic matter of the primary producers by heterotrophic microorganisms (which also affects the morphology of organic matter remains), silicification, diagenesis, and lower greenschist metamorphism. Therefore, the particularity of this study is the *in situ* investigation at the microorganism scale of chemically modified Precambrian sediments by means of a series of complementary analytical techniques operating at the micrometric scale. This approach thus involves the adjustment and improvement of sample preparation and that of standards, when necessary.

Therefore, the content of this manuscript is as follows: first, Part 1 reports the current scientific knowledge on bacterial photosynthesis and on Precambrian environmental context allowing to appreciate the extent of information retrievable from Archean and Paleoproterozoic fossilized photosynthetic life. Part 2 presents the sample selection methodology and the analytical techniques used in this study, with respects to the

assessments made in Part 1. Then, Part 3 evaluates these analytical techniques with respect to their ability to provide type A and/or type B signatures, through the presentation of the results obtained by optical microscopy and Raman spectroscopy, Scanning electron microscopy and Electron-probe microanalyses, X-ray Fluorescence spectrometry, and isotope measurements.

Part I: Introduction to bacterial
photosynthesis and its early
evolution

Chapitre I : résumé

La photosynthèse bactérienne et son évolution dans les environnements de l'Archéen et du Paléoprotérozoïque

Ce chapitre a pour objectif de décrire les principaux mécanismes de la photosynthèse bactérienne en se basant sur les connaissances réunies sur les bactéries photosynthétiques modernes, et de décrire l'environnement des milieux marins peu profonds de l'Archéen et du Paléoprotérozoïque dans lesquels ces microorganismes se sont développés.

Parmi les bactéries, la photosynthèse anoxygénique est pratiquée par les bactéries vertes du soufre, les bactéries vertes non-sulfureuses, les bactéries pourpres sulfureuses, les bactéries pourpres non-sulfureuses et les Héliobactéries (Ormerod, 1992). La photosynthèse oxygénique est, elle, pratiquée par un seul type de bactéries, les cyanobactéries.

La principale différence entre ces deux types de microorganismes photosynthétiques est que les cyanobactéries utilisent la molécule d'eau comme donneuse d'électrons pour la réduction du CO₂, rejetant de l'O₂ par ce procédé, tandis que les bactéries photosynthétiques anoxygéniques utilisent d'autres composés, à base de soufre et de fer (par exemple : H₂S, S⁰, Fe²⁺, H₂), conduisant à leur oxydation (par exemple SO₄²⁻, Fe(OH)). Afin d'être capable, non seulement d'oxyder la molécule H₂O, mais aussi de réduire le CO₂ pour accomplir la fixation du carbone, les cyanobactéries utilisent, en série, les deux types de centres réactionnels de la machinerie photosynthétique présents séparément chez les bactéries anoxygéniques. Toutefois, la principale amélioration chez les cyanobactéries est l'acquisition du complexe d'oxydation de l'eau, appelé *Water-Oxidizing Complex* (WOC), ou *Oxygen-Evolving Complex* (OEC). Il s'agit d'un complexe de formule Mn₄CaO₅ (Yano *et al.*, 2006 ; Umena *et al.*, 2011) qui héberge la dissociation de la molécule d'eau à travers le « cycle de Kok ».

Il a été montré que l'émergence des cyanobactéries est issue de mutations par transfert horizontal de gènes à partir de bactéries photosynthétiques anoxygéniques. Ce phénomène aurait eut lieu dans des consortia de types tapis microbiens, très représentés à l'Archéen (Nisbet & Fowler, 2011).

A cette époque, les colonies bactériennes photosynthétiques de type benthique se développaient dans des environnements aqueux peu profonds de type plage ou lagon dans une eau sursaturée en silice (SiO_2), conséquence d'une activité volcanique et hydrothermale intense et continue. Cette sursaturation en silice engendre le processus de silicification par lequel la composition initiale du sédiment est remplacée en majeure partie par SiO_2 , perdant ainsi la chimie et la minéralogie initiales du sédiment et des traces de vie qu'il contient. Cependant, ce processus permet la préservation de certaines molécules, agissant comme une robuste fossilisation, et conservant fidèlement la morphologie des tapis microbiens et cellules bactériennes fossiles.

Les principaux indices offerts par l'enregistrement géologique et utilisés pour tracer l'évolution de la photosynthèse oxygénique sont donc très variés, allant de l'identification de microorganismes fossiles, de molécules organiques fossiles, à l'utilisation d'analyses chimiques au niveau élémentaire pour suivre l'évolution du taux d' O_2 dans l'atmosphère au cours du temps (variations des concentrations d'éléments sensibles aux changements de conditions redox, variations du fractionnement isotopique de certains éléments tels que le soufre).

Un tour d'horizon des résultats obtenus grâce à ces indices, publiés dans la littérature, indique que les interprétations faites quant à la datation de l'émergence de la photosynthèse oxygénique restent sujet à controverses. Il apparait donc nécessaire de trouver de nouveaux types de signatures, chimiques et/ou minéralogiques, spécifiques à ce métabolisme.

Chapter I: Bacterial photosynthesis and evolution in Archean and Paleoproterozoic environments

This Chapter first outlines the current scientific knowledge on both anoxygenic and oxygenic bacterial photosynthetic metabolisms. Although a simplified description of the biochemical photosynthetic mechanisms is given here, more detailed information can be found in the Annex of this manuscript. The depositional context of shallow-marine sediments in Archean and Paleoproterozoic environments in which photosynthesis emerged and evolved is then described. This is followed by a summary, from the literature, of the features found in the geological record used as clues to identify the relics of oxygenic photosynthetic bacteria or their past metabolic activity. Finally, conclusions are drawn as to the extent and type of information on oxygenic photosynthesis that can be retrieved from Archean and Paleoproterozoic sediments.

I.1. Anoxygenic and oxygenic bacterial photosynthesis

The tree of life is divided in three branches: Archaea, Bacteria (together constituting the Prokaryota) and Eukaryota. For the purpose of this study, we focus here exclusively on bacterial photosynthesis.

Phylogenetic and geological evidence suggest that the origin of photosynthesis occurred very early in the history of Earth and of life itself. Two schools of thought exist. One school places the evolution of photosynthetic molecular complexes coupled with the origin of life during the prebiotic phase (Mauzerall, 1992; Hartman, 1998), and the other, based on more recent molecular phylogenetic analyses, sees these complexes evolving from primitive microorganisms such as Chemotrophs (Nisbet *et al.*, 1995). These microorganisms are considered to be primitive, not in terms of

metabolic complexity, but rather in the sense that they are certainly among the most ancient forms of life on Earth. Nisbet *et al.* (1995) consider early chemotrophs as being generally confined to deep-sea hydrothermal vents where they use the mineral substrate as electron donors to fix CO₂ through redox reactions and synthesize their own biomass. With the acquisition of pigments in their membrane, they could have developed the ability to detect heat sources at first (thermotaxis) and, concurrently with the evolution of pigments, they could have evolved subsequently the ability to use infrared light (Nisbet *et al.*, 1995; for an interesting view on the early evolution of metabolisms, see also Nisbet & Fowler, 1999). Intracellular proteins could have then adapted to allow an electron transport chain and the synthesis of ATP via photophosphorylation. Thus photosynthesis could have appeared. With the evolution of pigments, these microorganisms could have extricated themselves from the deep ocean and conquered shallow marine environments. The detailed molecular aspects of photosynthesis origin have been reviewed by Xiong & Bauer (2002).

The basis of photosynthesis is the conversion of light energy into chemical energy by the means of light-sensitive pigments, such as chlorophyll or bacterial chlorophyll (called bacteriochlorophyll). The molecular structure of these pigments consists of a porphyrin ring structure with a central magnesium atom. The chemical energy produced is used for the biosynthesis of carbonaceous molecules from inorganic carbon. Photosynthesizers are thus autotrophic organisms able to fix carbon from CO₂ in order to produce organic matter (via Calvin cycle reactions for most bacteria) that is later used by these same organisms.

Among prokaryotes, photosynthesis is restricted to a few bacterial lineages: several types of colored bacteria (green, purple) that are *anoxygenic* (*i.e.* unable to evolve oxygen) and cyanobacteria, the only prokaryotic phylum known to use oxygenic photosynthesis. The evolutionary step from anoxygenic to oxygenic photosynthesis and the related new metabolic abilities required the acquisition of key components. The purpose of this section is to describe both anoxygenic and oxygenic photosynthetic

metabolisms from a chemical and biological point of view. Since the remains of organic matter in Archean and Paleoproterozoic microfossils are rare, and since they are never *intact* considering their age (*i.e.* they are chemically and mechanically degraded), little is known about ancient photosynthetic biochemistry. Thus, it should be emphasized that the biochemical descriptions below are based on modern photosynthetic bacteria.

Furthermore, to avoid digressing from the main plot of this study, simplified terms were used in the following paragraphs to present the relevant photosynthetic processes, although a more detailed version of this section is found in Annex 1.

1.1.1. Anoxygenic photosynthesis

Among the Bacteria, anoxygenic photosynthesis is carried out by the following groups, classified based on their pigment content and the type of electron donor they use: green sulfur bacteria, green non-sulfur bacteria, purple sulfur bacteria, purple non-sulfur bacteria and heliobacteria (Ormerod, 1992).

At the core of their photosynthetic machinery, all photosynthetic bacteria possess a molecular complex called “photosystem”, located in the cell membrane. Anoxygenic photosynthetic bacteria possess either one or the other of the two existing kinds of photosystems, called type 1 and type 2. In both cases, photosynthesis is ensured by an electron transport chain by which the primary physiological reactions are accomplished, such as the reduction of CO₂ to organic carbon and the synthesis of ATP. The electron transport chain involves (i) a reaction center, where the conversion of light energy to chemical redox energy takes place by means of bacteriochlorophyll pigments; electrons excited by this photochemical event are then cycled between (ii) a pool of mobile electron carriers and (iii) an end-member transmembrane complex allowing the recycling of electrons.

During anoxygenic photosynthesis, photons are collected by light-harvesting bacteriochlorophylls located in the membrane of the cell and are

then transferred to the bacteriochlorophylls of the reaction center (henceforth called RC-bacteriochlorophylls). After this photochemical event, RC-bacteriochlorophylls become good electron donors. Excited electrons are transferred to the photosynthetic membrane where electron acceptor molecules act as carriers and diffuse to the end-member transmembrane molecular complex. The latter contains iron able to alternate between the Fe(II) and Fe(III) states and possesses redox reactions sites to host both oxidation and reduction reactions on the electron carriers molecules allowing the transfer of electrons back to the pool for another cycle. This cycle has the effect of creating a proton gradient from the periplasm to the cytoplasm that supplies the ATP synthase enzyme, generating energy for the cell under the ATP form, via photophosphorylation.

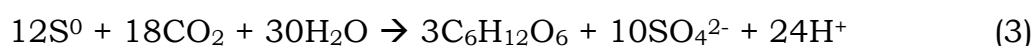
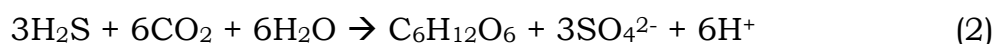
The process by which ATP is generated differs between type 1 and type 2 photosystems. In the type 2 photosystem, electrons are continuously cycled without any net input or consumption. The process is called cyclic photophosphorylation. In type 1 photosystem, the reaction center needs the input of electrons coming from external donors to become oxidized again and complete another cycle. In this case, the photophosphorylation is called noncyclic.

Apart from this, the principal difference between type 1 and type 2 photosystems lies in the composition of the acceptor molecule in charge of taking up the electrons transferred from the bacteriochlorophyll of the reaction center (RC-bacteriochlorophyll) after photo-oxidation.

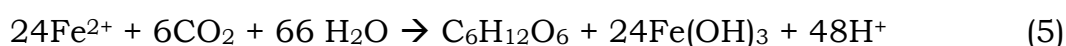
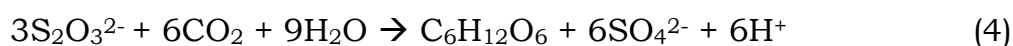
Type 1 photosystem. In the case of green sulfur bacteria and heliobacteria that use a type 1 reaction center, acceptor molecules are iron-sulphur proteins. Via these Fe-S proteins, electrons excited from the RC-bacteriochlorophyll are directly transferred to an enzyme allowing the generation of the reductant required for the reduction of CO₂ to organic carbon. Then, external electron donors step in so that the RC-bacteriochlorophyll molecule does not remain in an oxidized state after this electron transfer. Sulfur compounds such as H₂S, S⁰, S₂O₃²⁻ are thus used

as electron donors to supply the reaction center with electrons. As it becomes reduced again, the reaction center is ready for another cycle.

Green sulfur bacteria, such as the *Chlorobium* genus, develop in sulfide-rich environments and are able to oxidize H₂S and elemental sulfur (S⁰) when H₂S is limiting. The reactions are as follows, with the intervention of light energy:

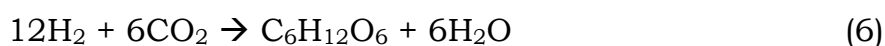


Chlorobium is also capable of using thiosulfate and ferrous iron through the following reactions:



Type 2 photosystem. For purple bacteria and green non-sulfur bacteria that possess a type 2 reaction center, the excited electron is transferred from the RC-bacteriochlorophyll to another molecule of the reaction center and is then taken up by an electron carrier which diffuses to the end-member transmembrane complex. In this complex, electrons are ‘recycled’ either by returning to the electron carriers or are transferred via a Fe-S protein to a ‘shuttle’ molecule located in the periplasm, which transfers the electrons back to the reaction center for a new cycle.

In bacteria using this type of photosystem, the production of the reductant required for the reduction of CO₂ to organic carbon is made possible by external electron donors. In an anoxic environment, electrons are stripped from H₂ (equation (6)), H₂S, S⁰, S₂O₃²⁻ and Fe²⁺, fed to the pool of electron carriers or directly to the end-member transmembrane complex and are then transferred to the reaction center.



Green non-sulfur bacteria, e.g. the *Chloroflexus* genus, are filamentous and are often associated with cyanobacteria in microbial mats in the photic zone (PZ). Purple sulfur bacteria, such as *Chromatium*, however, are able to grow in deeper waters. This is made possible because their bacteriochlorophylls absorb at high wavelengths and because their red and purple carotenoids pigments allow them to use different wavelengths of light than those only penetrating the PZ. Even if they are very similar to purple sulfur bacteria, purple non-sulfur bacteria cannot develop in environments with a high concentration of H₂S. Genera such as *Rhodomicrobium* and *Rhodobacter* have the ability to use Fe²⁺ and H₂ as electron donors.

1.1.2. Oxygenic photosynthesis

The particularity of oxygenic photosynthesis lies in the fact that the electron donor used for the reduction of CO₂ is the water molecule. This “*small step for a bacterium, but a giant leap for biology and geochemistry*”, as rightly described by Allen & Martin (2007), completely revolutionized the photosynthetic pathway and the oxygenic photosynthesis by-product, oxygen gas, reworked the geobiochemical cycles of the entire planet.

To carry out oxygenic photosynthesis, the photosynthetic machinery must involve a reaction center capable, not only of oxidizing the H₂O molecule, but also of being sufficiently reducing to achieve carbon fixation from CO₂. Taken separately, the type 1 and type 2 photosystems involved in anoxygenic photosynthesis and described above do not have these abilities. Two coupled photosystems are necessary to carry out oxygenic photosynthesis. They are called photosystem I and photosystem II (PSI and PSII).

The other major improvement of the oxygenic photosynthetic machinery is the acquirement of the Water-Oxidizing Complex (WOC), also called Oxygen-Evolving Complex (OEC), in PSII. It consists of a manganese-calcium oxide

cluster of the form Mn_4CaO_5 , housed in a protein complex. Umena *et al.* (2011), have presented a high-resolution structure of this inorganic cluster with a resolution of 1.9 Å, shown in Figure I.1.

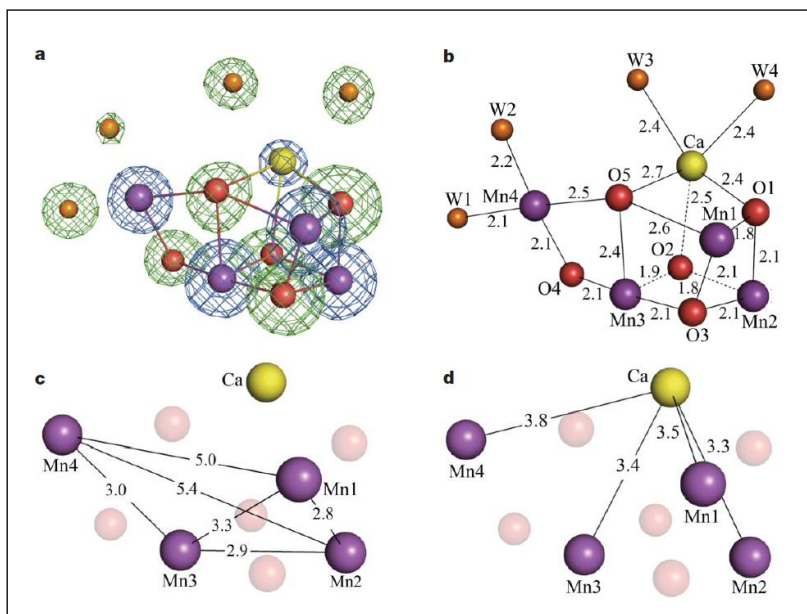


Figure I.1. High-resolution structure of the Mn_4CaO_5 cluster of the WOC in PSII. Distances are in angstroms. Calcium: yellow, oxygen: red, manganese: purple, water molecules: orange. From Umena *et al.*, 2011.

This Mn cluster is the active site for binding H_2O and splitting it into electrons and oxygen gas through what is known as the “Kok cycle” (Kok *et al.*, 1970; Fig. I.2). Mn atoms play the role of positive charge accumulators and are cycled between five different oxidation states called the S_i states ($i = 0 - 4$), S_0 being the less oxidized state and S_4 the most stable oxidized state. The release of O_2 occurs at the transition between S_4 and S_0 states (Fig. I.2). The structure of this cluster and the mechanisms for water splitting and oxygen release have been extensively studied by X-Ray spectroscopy analytical techniques (Yachandra *et al.*, 1996; Ananyev, 2001; Cinco *et al.*, 2002; Yano *et al.*, 2006; Sauer *et al.*, 2008; Umena *et al.*, 2011; Kolling *et al.*, 2012; Yano & Yachandra, 2014; Tran *et al.*, 2014) and are the subject of recent reviews (Sauer *et al.*, 2008; Yano & Yachandra, 2014; Najafpour *et al.*, 2014). However, whether the first cyanobacteria possessed an identical WOC remains unknown (discussed below in the section I.1.3.a).

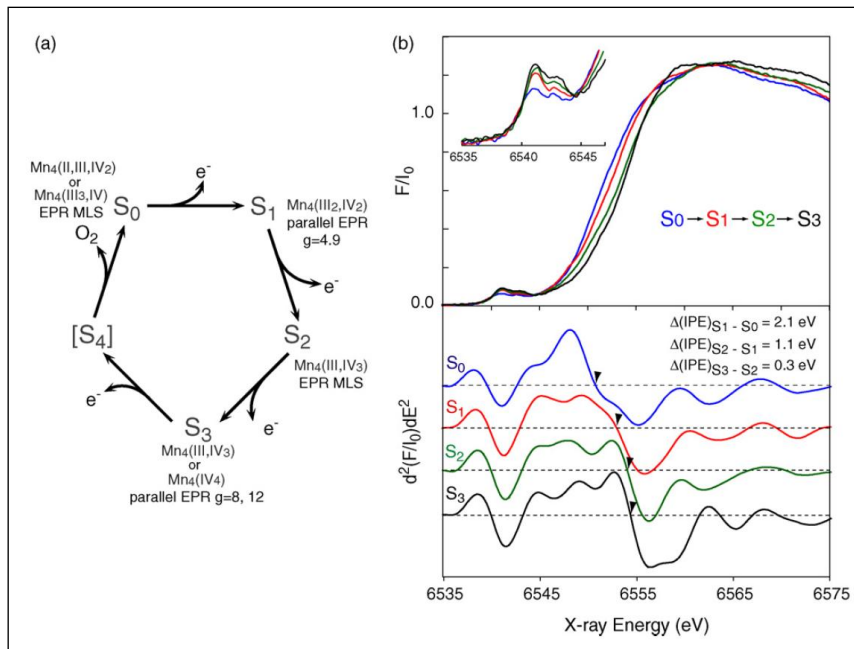


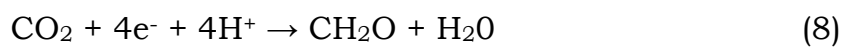
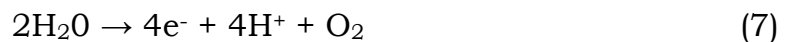
Figure I.2. The S-state Kok cycle and oxidation states of manganese monitored by X-ray absorption spectroscopy. From Sauer *et al.*, 2008.

Oxygenic photosynthesis begins in PSII when the chlorophyll *a* of the reaction center (RC-chlorophyll), called P680, receives the electrons coming from the splitting of water. This has the effect of producing O₂ via the Mn cluster of the WOC (through the S-state Kok cycle, Fig. I.2) and of transforming the chlorophyll into a reductant. Not unlike the anoxygenic photosynthetic process in type 2 photosystem, electrons are firstly taken up by an acceptor molecule within the reaction center and then transferred to the pool of electron carriers. The end-member of the electron transport chain of PSII, however, is a copper-containing molecule. This is where the process departs from anoxygenic photosynthesis. These Cu-molecules do not return the electrons to the reaction center of PSII for another cycle. Instead, they are passed to the photo-oxidized RC-chlorophylls of PSI and dragged, along with newly donated electrons, into another transport chain involving chlorophyll and type 1 photosystem-like components such as electron carriers, Fe-S proteins, and ferredoxins, the point at which electrons are used for the generation of the reductant involved in CO₂ reduction.

Just as in anoxygenic photosynthesis, ATP is synthesized as a result of the proton motive force generated by the diffusion of electron carriers in the photosynthetic membrane. As electrons do not return to the reaction center

due to the coupled PSII/PSI configuration, this method of making ATP is called noncyclic photophosphorylation.

In Bacteria, cyanobacteria are the only phylum representative of oxygenic photosynthesis. The overall reaction of oxygenic photosynthesis is reported by equation (1), but it can be decomposed as follows, where equation (7) represents the oxidation of water by the WOC, and equation (8) the generation of biomass via carbon fixation.



As photosynthesizers, cyanobacteria are necessarily restricted to the photic zone, where they develop either as cyanobacterial plankton in the open ocean, or as stratiform microbial mats or stromatolites in shallow aqueous environments, sometimes associated with anoxygenic photosynthesizers and other types of autotrophic and heterotrophic bacteria. With the splitting of the water molecule, cyanobacteria gained access to an unlimited source of electrons. The continuous input of O₂ in the environment led to the GOE, the reworking of Earth's geochemical cycles, the explosion of biodiversity, and of mineralogical diversity.

The following paragraph summarizes the evolutionary hypotheses on the emergence of oxygenic photosynthesis.

1.1.3. From anoxygenic to oxygenic photosynthesis

The evolution of anoxygenic to oxygenic photosynthesis required several innovations, the most important being the coupling of PSI and PSII linked in a sequential series in one organism, and the acquisition of the WOC in PSII.

Studies involving whole-genome analyses, together with comparisons between the representatives of the different groups of photosynthetic bacteria, have shown that the phylogenetic relationships between these groups are unclear and that no classical tree of life can explain them (Raymond *et al.*, 2002; Mulkidjianian *et al.*, 2006). This can, however, be explained if we considered that genes responsible for coding the photosystems moved across species boundaries during evolution (Raymond *et al.*, 2002; 2003). This process is called lateral gene transfer (or horizontal gene transfer) and refers to the transmission of genetic material from one organism to another, through a process other than genetic heredity between the parental generation and offspring. The frequency of lateral gene transfer (LGT) among Bacteria, lead McInerney *et al.* (2008) to introduce the term of “web” of life (Fig. I.3), rather than “tree” of life to describe their phylogenetic relationships throughout evolution.

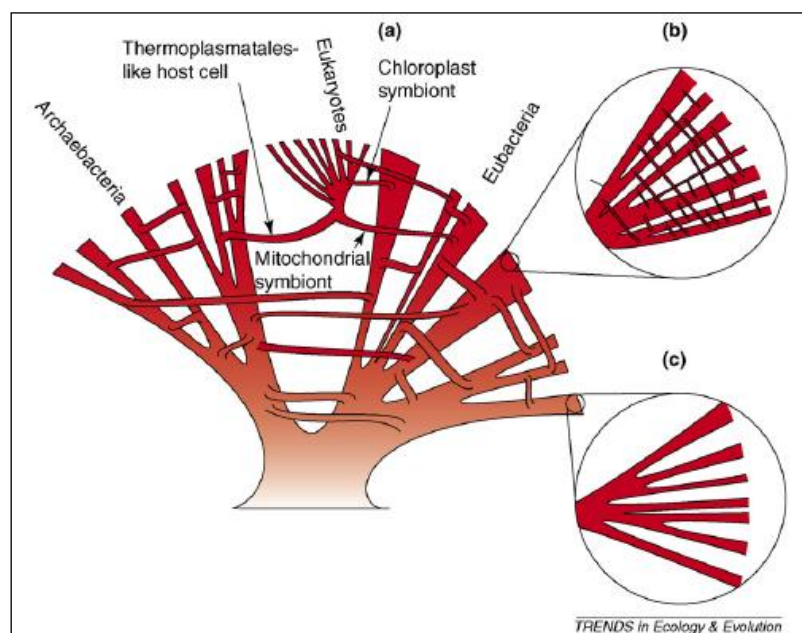


Figure I.3. The “web of life” represented by McInerney *et al.*, 2008. The lateral gene transfer is showed as connections between “branches”.

The frequent intervention of LGT in the evolution of bacteria suggests that they must have developed and evolved in a shared environment (Raymond *et al.*, 2003). This is not surprising as many studies document the close

associations of microorganisms in microbial mats, for example. Furthermore, microbial mats and stromatolite structures have been documented in the geological record going back to the Paleoproterozoic and Archean (Cloud, 1965; Grotzinger & Knoll, 1999; Westall *et al.*, 2001, 2011a, 2011b; Noffke *et al.*, 2003, 2013; Tice & Lowe, 2004; Lepot *et al.*, 2008; Planavsky *et al.*, 2009; and reviews of Schopf *et al.*, 2007; Nisbet & Fowler, 2011; see the section *Evolution of oxygenic photosynthesis: the search for signatures*). In Figure I.4, Nisbet & Fowler (2011) describe the possible micro-habitats of microorganisms during the Archean.

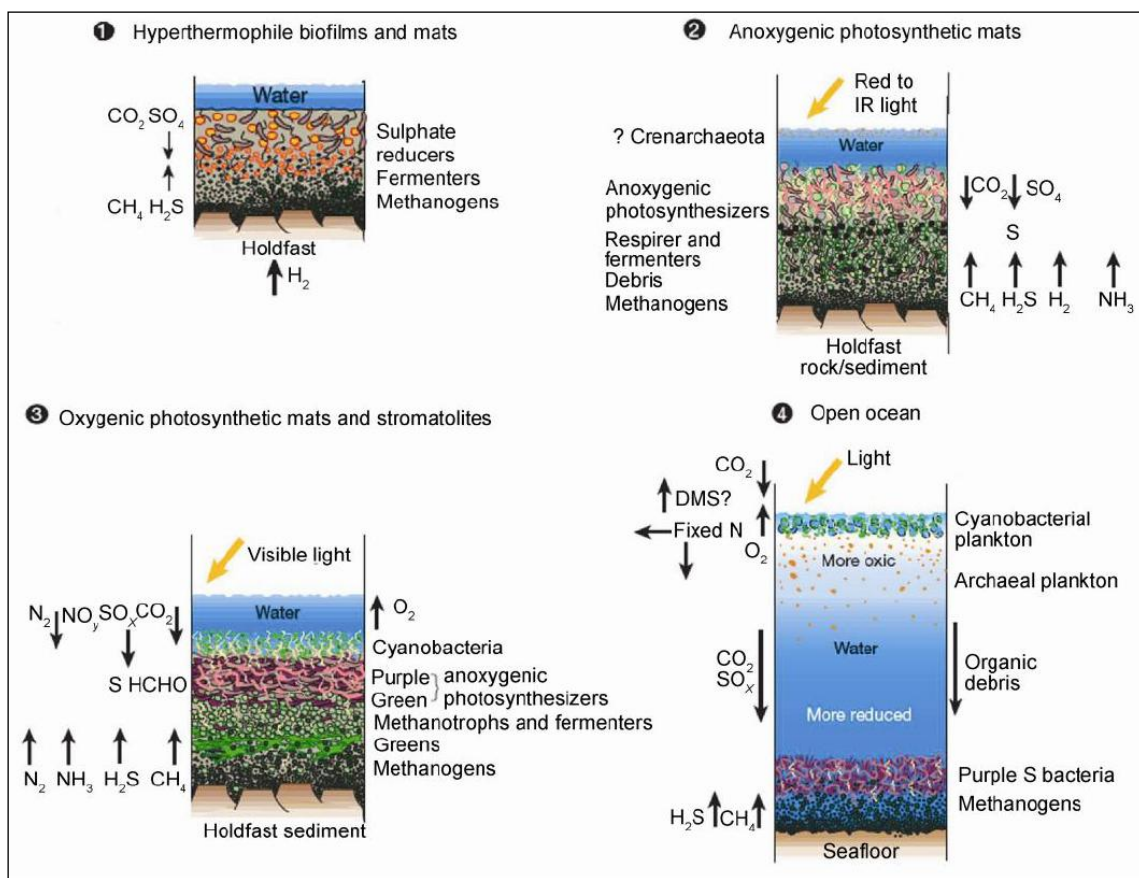


Figure I.4. Nisbet & Fowler (2011) view of Archean local micro-habitats and microbial mats configurations.

Knowing that LGT intervened in the evolution of photosynthetic bacteria raises further questions. Indeed, there is consensus on the fact that the transition from anoxygenic to oxygenic photosynthesis, strictly speaking, occurred when the photosynthetic bacterium possessing PSI and PSII

acquired the WOC and learned how to use the water molecule as an electron donor; however, the process explaining how the two types of photosystems came to be combined in one organism remains debatable.

a. Evolution of the reaction centers

Did a bacterium containing PSI acquire PSII (reviewed by Baymann *et al.*, 2001), or the reverse (Mathis, 1990; Xiong *et al.*, 2000)? Or alternatively, were both photosystems present in an ancient anoxygenic photosynthetic bacterium, called “protocyanobacterium” or “procyanobacterium” in literature, and transferred to other lineages by LGT (Allen, 2005; Mulkidjanian *et al.*, 2006; Allen & Martin, 2007)? In this scenario, illustrated in Figure I.5, loss of one photosystem or the other could have lead to the evolution of different branches of anoxygenic photosynthetic bacteria.

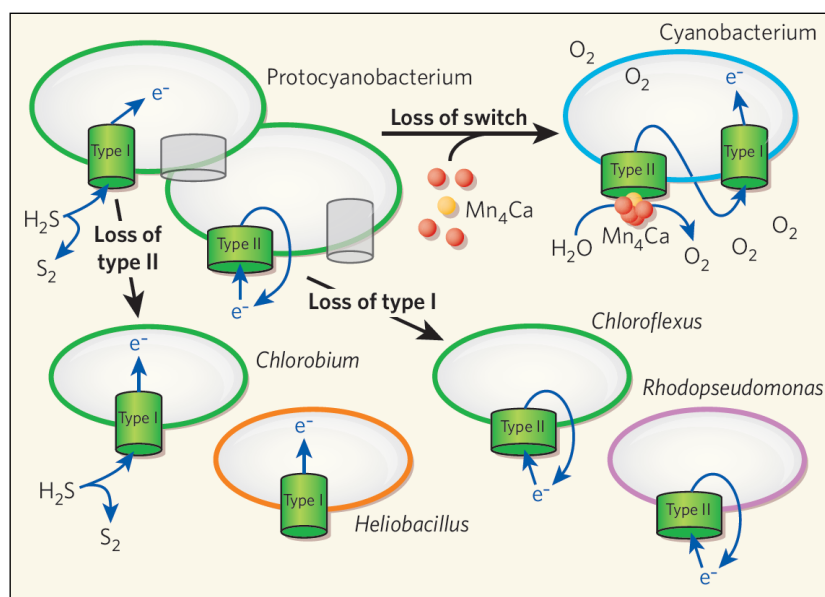


Figure I.5. Possible scenarios for the evolution of photosynthetic bacteria. From Allen & Martin, 2007.

These three hypotheses are still valid today. Numerous studies support the fact that the different molecular components of the two photosystems (reaction centers, pigments, Fe-S proteins, etc.) have their own evolutionary history (Blankenship, 1992; Raymond *et al.*, 2002; Raymond *et al.*, 2003).

Hence, opinions differ depending on whether the studies concern whole-genome analyses or phylogenetic analyses of one molecular complex at a time.

If a “protocyanobacterium” were found in nature, it would be the missing link needed to decipher the complicated history of photosynthesis evolution. This bacterium should possess both type 1 and type 2 photosystems and be able to switch between them depending on changes in environmental conditions (Allen, 2005). Among the cyanobacteria, *Oscillatoria limnetica* has the ability to switch to anoxygenic photosynthesis by de-activating the functionality of its PSII in the presence of sulfide compounds (H_2S , Na_2S), thus using a type-1 reaction center photosynthesis, as seen in *Chlorobium* (Cohen *et al.*, 1975; Garlick *et al.*, 1977; Oren & Padan, 1978). Furthermore, Jørgensen *et al.* (1986) have shown experimentally that a cyanobacterial colony of *Microcoleus chthonoplastes* has the ability to use anoxygenic and oxygenic photosynthesis simultaneously with a gradual transition (in terms of O_2 production and H_2S take up) in the predominance between the two types of metabolisms depending on variations in H_2S concentration in the medium. Thus, *M. chthonoplastes* is able to express both types of photosynthesis without completely inhibiting PSII. These authors have postulated that *M. chthonoplastes* could be of interest in the evolutionary history of oxygenic photosynthesis, as it shows the capacity to continue the practice of oxygenic photosynthesis by means of PSII even under highly sulfidic conditions (unlike *O. limnetica* in which PSII and oxygen evolution are blocked even for low concentrations of sulfide).

However, as both these microorganisms are fully capable of oxygen evolution when they are not repressed by environmental conditions, their capacity to practice anoxygenic photosynthesis based on sulfide compounds seems to be an adaptive response to chemical changes in the medium that occurred later in their evolution, rather than an echo of a potential protocyanobacterium (Blankenship, 1992).

Independent of the evolutionary history of the reaction centers, the acquisition of the WOC in PSII is the key point in evolution, marking the transition from anoxygenic to oxygenic photosynthesis.

b. Origin of the Water Oxidizing Complex

Tamura and Chéniaie (1987) have shown experimentally that in modern oxygenic photosynthetic organisms, assembly and activation of the WOC requires only light and soluble Mn^{2+} ions (photoactivation), even if water oxidation efficiency is enhanced when Ca^{2+} ions are available. However, the processes that lead to the formation of the Mn_4CaO_5 cluster for water oxidation in the first cyanobacteria remain unknown. Several hypotheses exist to explain the origin of the WOC. Most of them concur for the need of transitional electron donors before the use of H_2O .

In 1970, Olson proposed that nitrogen-based compounds such as NO and NO_2^- could have served as transitional electron donors and that the precursor of the WOC could have been a Mn(III)-containing molecular complex that evolved from an Fe-containing molecular complex (such as that found in the end-member transmembrane complex of anoxygenic photosynthesizers). However, more than thirty years later (Olson, 2001), he reconsidered this hypothesis since no evidence was found for the availability of these N-compounds in the reduced Archean ocean (Navarro-González, *et al.*, 2001). Furthermore, increasing knowledge of the structure of the WOC revealed that Mn is localized in an inorganic Mn_4CaO_5 cluster (Umena *et al.*, 2011; Fig. I.1), which makes the hypothesis of a WOC derived from a transmembrane molecular complex rather questionable.

Other pre-existing Mn-based molecules have been proposed as WOC precursors. Blankenship & Hartman (1998) hypothesized that a Mn-containing catalase enzyme could have been a precursor of the WOC, and that it would have used hydrogen peroxide (H_2O_2) as a transitional electron donor. In fact, many authors propose H_2O_2 as a transitional electron donor (see the review of Olson & Blankenship, 2004). However, no similarities between Mn-catalase and the proteins of PSII have been shown by

phylogenetic or structural studies, and there is no evidence that a sufficient amount of H₂O₂ was available in the Archean ocean (Blankenship & Hartman, 1998; Sauer & Yachandra, 2002). It remains possible that hydrogen peroxide was locally available (Blankenship & Hartman, 1998; Balk *et al.*, 2009) and served as a transitional electron donor toward the evolution of the Mn-cluster WOC as we know it today (Blankenship & Hartman, 1998).

Other hypotheses postulate that the WOC Mn₄CaO₅ cluster is derived from a Mn-based mineralogical compound, available in the environment, and later incorporated in PSII (Russell & Hall, 2006; Russell *et al.*, 2008), thus raising the following question: could the Mn-cluster of the WOC be representative of the environment in which water oxidation arose (Allen & Martin, 2007)? Sauer & Yachandra (2002) proposed that Mn-oxide minerals are relevant candidates for this purpose. However, although Mn-oxides can form via photo-oxidation of Mn²⁺ by UV light in aqueous environments (Anbar & Holland, 1992), Earth's environment was generally deprived of Mn-oxides before the rise of oxygen (Roy, 1997; 2006). Najafpour (2011) offers an interesting alternative where calcium-manganese oxides similar in structure to the WOC could be considered as precursors. He argues that the precipitation of such compounds from the aqueous medium requires changes in pH conditions that could have been caused by the activity of protocyanobacteria (mentioned above in I.1.3.a), hydrothermal reactions, short wavelength UV light, all of which are consistent with what is known about Archean environment. However, this also involves the precipitation of Mn-oxides which, except in local environments influenced by hydrothermal reactions and UV light, were not common on the early Earth.

In 2013, Johnson *et al.* postulated that the deposition of sediments enriched in Mn in a 2.415 Ga-old formation in South Africa (Kogias Supergroup, Kaapvaal Craton) were influenced by the metabolic activity of anoxygenic photosynthetic bacteria using Mn(II) as an electron donor, which was subsequently precipitated under its oxidized form. This was supported only a few months later by experimental evidence (Khorobrykh *et al.*, 2013). This process would be very similar to the photoferrotrophic metabolism proposed

for the precipitation of iron in Archean BIFs (Konhauser *et al.*, 2002). Thus, these observations might reveal a transitional photosynthetic metabolism involving Mn photooxidation, and offer an alternative hypothesis for the origin of the WOC of PSII. Moreover, these observations approach for the first time the mechanisms of assembly and activation of the WOC which, in modern oxygenic photosynthetic organisms, only requires light and Mn²⁺ ions (Tamura & Chénia, 1987).

For more detailed information on the genetic and molecular aspects of the evolution of the WOC and that of oxygenic photosynthesis, the interested reader should consult the following reviews: Xiong & Bauer (2002), Olson & Blankenship (2004), Raymond & Blankenship (2008), Björn & Govindjee (2009), Allen & William (2011).

The Mn-cluster of PSII has been the center of numerous studies for decades and its mechanisms continue to intrigue today (Yano & Yachandra, 2014), not only for evolutionary and biological repercussions, but also for sustainable development and clean energy purposes (Najafpour *et al.*, 2014). Being responsible for the evolution of the world's most useful waste-product, O₂, the WOC is often referred to as the most extraordinary accomplishment in the history of biology. Although information for deciphering the molecular evolution of PSI and PSII and the origin and evolution of the WOC is becoming available, the time at which the transition from anoxygenic to oxygenic photosynthesis occurred is still unclear, and the “Big Three” questions still remain (see Introduction Fig. 2).

The geological record is the only record of Earth's history. The following sections describe the depositional context of shallow-marine sediments in Archean and Paleoproterozoic environments and outline the kinds of clues found in this great archive that are used to decrypt the history of oxygenic photosynthesis.

I.2. Geological context of photosynthesis evolution: Archean and Paleoproterozoic shallow-marine sediments

In order to select the most suitable samples of Archean and Paleoproterozoic shallow marine sediments for this study, it is important to understand the environmental conditions that prevailed during these periods, as well as the processes of deposition, lithification, and the nature and degrees of the modifications that these sediments have undergone since their formation. The following paragraphs report this information.

Together with the Hadean, the Archean and Proterozoic eons constitute the longest period of Earth's history: the Precambrian, from the accretion of our planet 4.56 Ga ago to 0.541 Ga.

The Hadean eon is characterized by the almost complete absence of geological record. The Hadean is thus the period of time extending from Earth's accretion 4.56 Ga ago, to the beginning of the geological record around 4.0 Ga. Little is known about the Hadean Earth since there is no archive of this period, with the exception of a few detrital zircons found in younger metamorphosed Archean sediments (Mt Narryer and Jack Hills locations, Yilgarn Craton, Western Australia) and dated, for the oldest, at 4.404 Ga (Wilde *et al.*, 2001). However, together with the study of lunar rocks, these few grains of zircon allowed to retrace the major events of post-accretion Earth's history: the formation of the Moon following the collision of the young Earth with a planetesimal (Canup & Asphaug, 2001; Chambers, 2004), differentiation of the core-mantle (Kleine *et al.*, 2002), and internal differentiation of the mantle leading to a global magmatic ocean (Wood *et al.*, 1970; Boyet & Carlson, 2005), allowing formation of a "proto-crust" (Caro *et al.*, 2005) as early as 4.40 Ga. Further evidence from these detrital zircons suggests that a robust liquid hydrosphere was present on Earth's surface as early as 4.4-4.3 Ga (Wilde *et al.*, 2001; Mojzsis *et al.*, 2001). Finally, the Hadean-Archean transition is marked by an intense meteoritic bombardment called the "Late Heavy Bombardment" (LHB) from 4.1 to 3.9 Ga.

1.2.1. Setting the stage: Archean and Paleoproterozoic environments and sedimentary record

a. The Archean period (4.0-2.5 Ga)

The Archean eon marks the beginning of the geological record and with it, the possibility to search for the early evolution of life on Earth. Evidence points to the fact that liquid water was present at the surface under the form of stable oceans at least 4.3 Ga ago (Wilde *et al.*, 2001).

The Archean rock record has been influenced by metamorphism. However, the chemical and isotopic composition of highly metamorphosed rocks still provides crucial information on contemporaneous environmental conditions, at least at the regional or global scales. Additionally, some Archean geological formations have only been affected by low degrees of metamorphism (greenschist facies or lower). Sediments that belong to these particular formations have conserved their structural integrity and thus carry geomorphological information irretrievable from highly metamorphosed rocks. Their exceptional preservation state also allowed them to conserve the most ancient traces of early life.

Figure I.6 shows the geographical distribution of Archean terrains on the modern Earth. The oldest geological formation known today is the Acasta Gneiss (Canada), dated at 4.031 Ga (Bowring & Williams, 1999). Like most of the rocks constituting Archean cratons, this gneiss is the metamorphosed form of fractionated magmatic rocks belonging to the TTG group, standing for "trondhjemites, tonalites, granodiorites". The geodynamical environment in which these magmas were formed is characteristic of the Archean Earth, but no longer exists. Study of these rocks documents the geodynamic mechanisms that occurred on Earth at this period. However, in the study of the earliest traces of life and best case scenario, preserved fossils, sedimentary rocks deposited in water are essential because they formed under less extreme pressure-temperature conditions than magmatic rocks and are more suitable to harbor life. Within this scope, the Nuvvuagittuq

gneisses (Canada), dated at ~3.8 Ga (David *et al.*, 2009), could be of interest because they formed from volcano-sedimentary rocks and may be as old as 4.2 Ga (O'Neil *et al.*, 2008), although this date is controversial (for example Roth *et al.*, 2013). This applies also to the Isua Gneiss (Greenland), a metasediment dated at ~3.78 Ga (Rosing, 1999). However, the degree of metamorphism that both these geological formations have undergone is too high to expect the preservation of relics of micro-organisms or to interpret unequivocally the origin of any remnant carbonaceous matter.

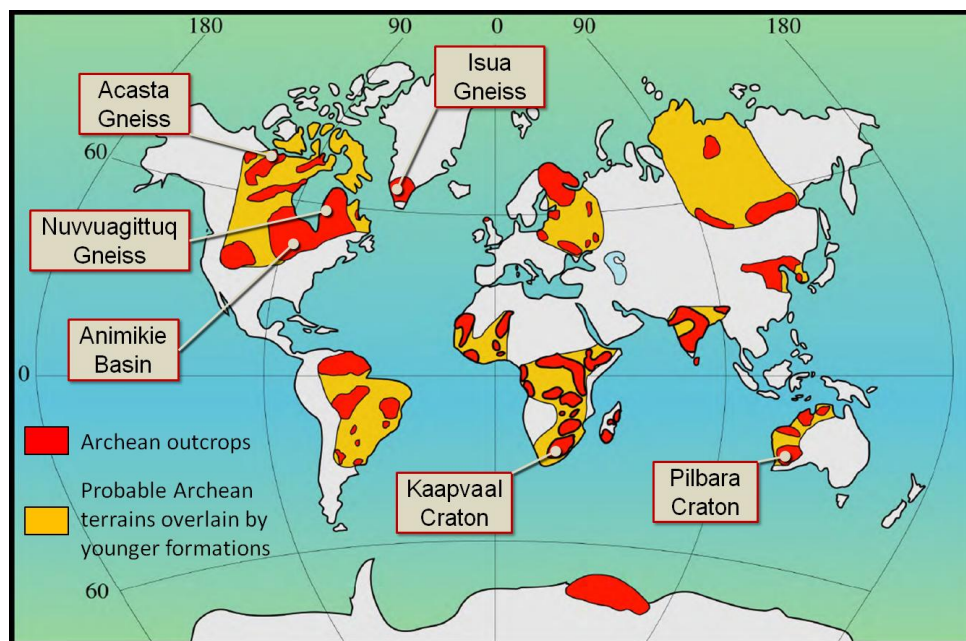


Figure I.6. Simplified location of Archean cratons on the modern distribution of emerged lands. Courtesy of Pr. Hervé Martin, Blaise Pascal University, Clermont-Ferrand, France; slightly modified.

Some of the oldest, well-preserved sediments are found in the Kaapvaal and Pilbara cratons, located in South Africa and Western Australia, respectively, and date back to ~3.5 Ga. These sediments were deposited in shallow to deep (sub-wavebase) ocean environments, overlying magmatic rocks of komatiitic and basaltic compositions formed on the seafloor. They are composed of the products of intense volcanic activity, such as ashes as well as coarse to fine-grained volcanoclastic deposits, and products of the erosion of volcanic rocks.

Figure I.7 shows a comparison of the shape and distribution of modern and probable Archean lithospheric plates, highlighting the differences of the surface of Earth at these two ages. This figure helps to perceive the Archean environment, and the depositional context of the shallow marine sedimentary rocks described here. In a global ocean, the young continental crust formed oceanic platform-like features consisting of emerged volcanic edifices (from a mafic/ultra-mafic composition to a more acid composition and finally, a granitic composition after ~3.0 Ga), surrounded by their erosion products, creating gently sloped morphologies and thus shallow marine environments, such as sand beaches and protected environments such as lagoons, impact basins, volcanic craters, favorable to the development of subaqueous bacterial colonies. Also, in this geomorphology, the photic zone (PZ) directly overlies the sediment, creating a favorable environment for the development of benthic photosynthetic bacteria in the form of bacterial biofilms and mats. Chemical nutrients (such as H_2 , H_2S , S, Fe^{2+} , CH_4) were provided to autotrophic microorganisms by the alteration and weathering of surrounding volcanic edifices, subaqueous volcanism, the input of rivers and the intense marine hydrothermal activity (see Canfield *et al.*, 2006).

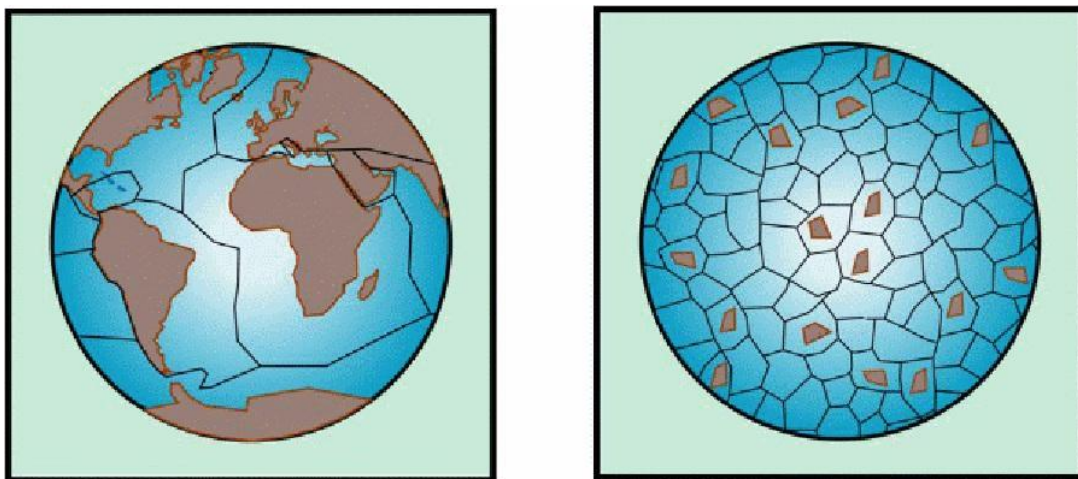


Figure I.7. Comparison of modern (left) and probable Archean (right) size of lithospheric plates. Courtesy of Pr. Hervé Martin, Blaise Pascal University, Clermont-Ferrand, France. Adapted from de Wit & Hart, 1993.

Archean marine sediments were continuously soaked by silica, due to the saturation of sea-water with respect to this compound, and to the intense Si-rich hydrothermal activity during this period. Silica infiltration and saturation of the sediment (silicification) would occur during sedimentation and diagenesis, resulting in rocks called cherts composed mainly of quartz (SiO_2) under the form of micro and megacrystalline quartz (respectively made of $\leq 20\mu\text{m}$ and $\geq 20\mu\text{m}$ crystals; Folk & Weaver, 1952), mesocrystalline quartz (same texture as microquartz but with $\geq 20\mu\text{m}$ crystals; Maliva *et al.*, 2005), and chalcedonic quartz. Sediment silicification can happen rather quickly (see the review by Perry & Leticariu, 2014; Westall *et al.*, 2015), hence contributing to the preservation of the sedimentary structures, the morphology of microfossils, and that of organic matter against deformation and compaction, acting as a robust fossilization process. The processes of silicification and thus, chert formation, are described in more detail below (section I.2.2). In addition, Archean sedimentary cherts and especially those formed at, or near the water-sediment surface, are considered to be good environmental indicators. They carry important information on oceanic and also atmospheric compositions and can thus inform on redox changes in atmosphere and oceans.

Furthermore, the particularity of the sedimentary cherts from the Kaapvaal and Pilbara cratons is that, in addition to effective preservation by silicification, most of them have only undergone a low grade metamorphism of greenschist facies ($< 500^\circ\text{C}$; < 10 kbar), or lower (burial metamorphism to $\sim < 350^\circ\text{C}$ greenschist facies, Xie *et al.*, 1997; Tice *et al.*, 2004). Even if this type of metamorphism is able to rearrange the lattice of certain minerals and carbon chains, there is no deformation of the sedimentary structures and traces of life that are still recognizable. The consequence is a unique structural and chemical preservation that provides valuable insight to Archean environmental contexts, such as the intensity and the type of volcanic activity, the composition of the ocean, as well as crucial information on the forms of life that developed in these environments. Thus, these Archean sedimentary cherts contain the oldest, well-preserved fossils and traces of life known today (for example: Walter *et al.*, 1980; Ueno *et al.*, 2001;

Van Kranendonk *et al.*, 2003; Allwood *et al.*, 2006; Westall *et al.*, 2011a; Westall *et al.*, 2011b; Westall *et al.*, 2015).

The Archean sedimentary rock record also includes carbonate reefs and platforms, the oldest dated at ~3.4 Ga (Allwood *et al.*, 2006). Neoproterozoic stromatolites are widely documented, for instance in the Pongola Supergroup (~2.95-2.98 Ga, South Africa) and the Belingwe Greenstone Belt (~2.7 Ga, Zimbabwe), located respectively in the Kaapvaal and Zimbabwe cratons, as well as in the Steep Rock group (~2.9 Ga, Canada), where the outcrop length reaches several kilometers. As a result of their biomineralization abilities, and in comparison with modern bacterial calcification mechanisms, oxygenic photosynthetic bacteria have long been held responsible for the deposition of these large carbonate formations (e.g. Vasconcelos *et al.*, 2006), and by extension, for the formation of older stromatolites as well, some as old as 3.5 Ga (Awramik, 1992; Altermann *et al.*, 2006). However, it was shown that these Mesoarchean (and older) carbonate reefs and stromatolites may also be related to the activity of anoxygenic photosynthetic bacteria (Bosak *et al.*, 2007), anaerobic heterotrophic bacteria (such as sulfate-reducing bacteria) (e.g. Dupraz *et al.*, 2004; Baumgartner *et al.*, 2006; Bontognali *et al.*, 2008), and also abiotic processes (Grotzinger & Knoll, 1999; Bosak & Newman, 2003; Kopp *et al.*, 2005) (see the paragraph on carbonates in the Introduction).

b. The Paleoproterozoic (2.5-1.6 Ga)

The Paleoproterozoic is the first era of the Proterozoic eon and extends from ~2.5 Ga to ~1.6 Ga. The continuous evolution of the geo- and biospheres since the accretion of Earth and throughout the Archean led to significant changes, characteristic of the Paleoproterozoic. Namely, the transition from an anoxic to an oxic Earth (GOE, ~2.4-2.3 Ga) largely driven by the evolution of oxygenic photosynthesis and sustained by geological processes (review of Farquhar *et al.*, 2011; and references in the Introduction), led to the flourishing of the biological world toward more

complex bacterial life-forms, more complex biological structures, that are unambiguously identifiable in the rock record (well preserved, individual micrometric filamentous and spherical cells; see Fig. I.11). The evolutionary advantaged cyanobacteria spread and conquered the marine world. This was accompanied by a global glaciation, the ~2.3-2.2 Ga Makganyene “snowball Earth”, due to the decline of the methane greenhouse as the atmosphere became oxygenated (see Kopp *et al.*, 2005). However, there is mounting evidence that the oxygenation of the deep oceans occurred in stages and that ferrous Archean bottom waters evolved toward a sulfidic composition in the Paleoproterozoic and thus remained anoxic, until a second rise of oxygen in the atmosphere around ~0.8-0.5 Ga (Canfield, 1998; Hannah *et al.*, 2004; Poulton *et al.*, 2004, Frei *et al.*, 2009; Planavsky *et al.*, 2009; Williford *et al.*, 2011, Canfield *et al.*, 2013).

Paleoproterozoic iron formations were documented in the Animikie Basin of the Lake Superior Region in Canada (see Fig. III.6) that contain stromatolitic cherts bearing a unique assemblage of various well-preserved fossilized microorganisms (in particular, samples from the ~1.88 Ga-old Schreiber Beach locality, Gunflint Formation, Canada). The formation process of these iron formations remains controversial. Indeed, the precipitation of soluble ferrous iron in an anoxic ocean requires either contact with oxic surface waters, or the influence of anoxygenic photosynthetic iron-oxidizing bacteria (Konhauser *et al.*, 2002). Thus, the involvement of either or both oxygenic and anoxygenic photosynthetic bacteria in the origin of these formations is admissible.

1.2.2. Silicification processes in Archean and Paleoproterozoic aqueous environments

In modern oceans, the silica cycle is controlled by biological activity. Silica-secreting marine eukaryotes organisms such as diatoms, radiolarians and sponges use the dissolved silica (henceforth noted DSi) available in the ocean to secrete siliceous skeleton, cell walls or spicules. At least some of

these organisms could have evolved as early as the Neoproterozoic. However, there is no evidence that such organisms were present in the Archean and Paleoproterozoic oceans. Archean and Paleoproterozoic silica precipitation in aqueous environments and thus, chert formation, were controlled by abiogenic processes (Siever, 1957). The continuous Si-rich hydrothermal flux and the alteration of volcanic material provided the ocean with substantial quantities of DSi. However, no sink was available to balance the silica input. As a result, oceans were saturated with respect to silica, with a possible concentration of ~60 ppm or more (Siever, 1992), leading to its precipitation at the water-sediment interface, and within the sediment and underlying igneous rocks via fluid circulation in fractures and veins.

Since sea water composition was likely continuously influenced by hydrothermal activity, and because hydrothermal fluids circulating in the oceanic crust and overlying sediments carried sea water chemical signature as well, the composition of siliceous precipitates in Precambrian sedimentary cherts is in most cases a mixture between sea water and hydrothermal fluids compositions (e.g. Hofmann & Bolhar 2007; Hofmann & Harris, 2008).

Several definitions (for instance: Folk, 1980; Knauth, 1994) and nomenclatures were established to characterize the different types of chert. The most recent was proposed by Ledevin, 2013 and Ledevin *et al.*, 2014, modified from van den Boorn *et al.*, 2007 who were the first to propose a classification based on the type of formation processes. Through the thorough petrographical and geochemical study of the diversity of Archean cherts in the Barberton Greenstone Belt in South Africa, Ledevin and co-authors showed that three main processes were responsible for Archean chert formation: (i) the primary chemical precipitation (C-chert) of silica to the seafloor, from marine Si-saturated waters; this precipitation takes the form of pure siliceous ooze layers or that of cement between particles when mixed with clastic components; (ii) the chemical precipitation of silica in fractures and veins from Si-rich circulating hydrothermal fluids within the oceanic crust (F-cherts); (iii) and the replacement by Si-metasomatism of a magmatic or sedimentary protolith under the influence of Si-rich fluid circulation (S-cherts). In this case, fluid circulation includes oceanic,

hydrothermal, diagenetic or metamorphic fluids. The nomenclature of Ledevin *et al.*, 2014 is illustrated in Figure I.8.

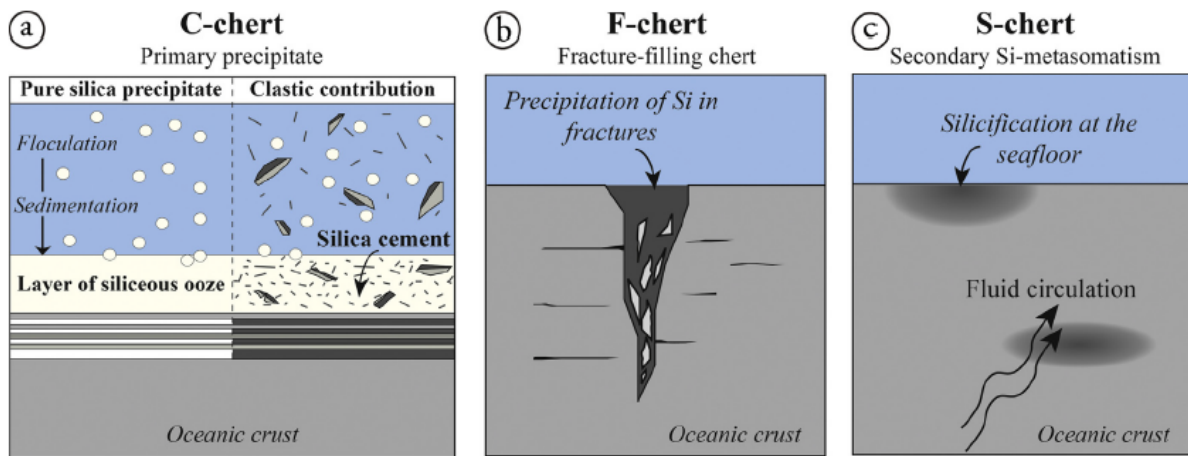


Figure I.8. Nomenclature of cherts based on their formation processes. a) C-cherts refer to the primary precipitation of silica to the seafloor, from marine Si-saturated waters. This precipitation takes the form of pure siliceous ooze or of cement between particles when mixed with clastic components. b) F-cherts refer to the chemical precipitation of silica in fractures and veins from Si-rich circulating hydrothermal fluids within the oceanic crust. c) S-cherts are the replacement by Si-metasomatism of a magmatic or sedimentary protolith under the influence of Si-rich fluid circulation. In this case, fluid circulation includes oceanic, hydrothermal, diagenetic or metamorphic fluids. From Ledevin *et al.*, 2014.

I.2.3. Influence of silicification and secondary processes on sediment preservation

a. Influence of early silicification

In addition to the process of silicification itself, the timing and the rate at which it occurs play an important role in the preservation of the sedimentary structures and that of the morphology of microfossils. A rapid precipitation of silica within the sediment, early after deposition (no later than early diagenesis) allows excellent morphological preservation. Conversely, late silicification, for example due to secondary processes such as late pervasive hydrothermal fluids infiltration or Si-metasomatism occurring after compaction (diagenesis, metamorphism), would not allow the

preservation of the original structural features of the sediment and the morphology of microfossils.

The timing of silicification can be determined by petrographical studies. Several features are characteristic of early silicification, such as microcrystalline quartz, or the absence of compaction features in zones of detrital clasts accumulation, or on soft components like organic matter (Maliva *et al.*, 2005; Perry & Lefticariu 2014; Westall *et al.*, 2001, 2006, 2011b, 2015). Also, preserved, deformation features on microbial mats (for example, roll-up and tear-apart features, Fig. I.9), as well as soft sediment deformation structures indicating contemporaneous infiltrations of silica-rich fluids, show that silicification took place before microbial mats were solidified by lithification and probably while they were still active (for example, Westall *et al.*, 2015). In these cherts, the preservation of microfossils is directly influenced by silica grain size. Archean sedimentary cherts are composed mostly of microcrystalline quartz, which allows preservation of the morphology of microfossils, contrarily to silica precipitated as meso- to megacrystalline quartz, which by their larger grain size, would deform the original morphology. Thus, the presence of morphologically well-preserved micro-organisms in Precambrian cherts itself is also an indicator of early silicification. Furthermore, it has been documented that the presence of organic matter in the sediment can influence the precipitation of silica by providing nucleation sites (Knoll, 1985; Westall *et al.*, 1995; Westall, 1997; Yee *et al.*, 2003; Benning *et al.*, 2004a,b; Orange *et al.*, 2009). Thus, bacterial colonies themselves can trigger primary early silicification.

Although early silicification enhances the preservation of the sediment, this process also triggers chemical 'leaching' of the original material toward a composition of >90 wt.% of SiO₂. Indeed, in highly silicified sediments, petrographical observations reveal that primary minerals (carbonates, clays, detrital grains) have been replaced by microcrystalline quartz. In the case of chemical analyses, this is reflected by a 'dilution' of the chemical signal by the high concentration of the SiO₂ phase. Conversely, in less extensively

silicified sediments, or sediments silicified at later stages, the original mineral composition of the sediment can still be observed, or deduced from the resulting metamorphosed mineralogical phases. However, after deposition, these sediments were more inclined to be subjected to diagenetic and metamorphic deformation, compaction, and fluid circulation. Thus, carbonaceous matter and traces of life in these rocks are often not well preserved (c.f. Pongola stromatolites).

b. Influence of hydrothermal activity

The influence of continuous hydrothermal activity subsequent to early silicification is shown by macroscopic to microscopic signs of Si-rich fluids infiltration. Optical microscopy observations reveal numerous meso- to megacrystalline quartz-filled features affecting the already silicified but still soft, microcrystalline quartz sediment and associated microbial mats. These features are (i) transversal cross-cutting veins, (ii) horizontal infiltrations reflected by fluid-filled lenses (vugs). The timing of the veining is determined, both at the micro and macroscopic scales, by the type of contact between the vein and the bedding planes. For instance, optical microscopy shows that certain infiltrations are highlighted by soft-deformation features on silicified microbial mats (tear-apart, roll-up features). In this case, the soft-deformation may also indicate the direction of the fluid circulation. The example of the 3.33 Ga-old Josefsdal Chert (South Africa) and associated fossilized photosynthetic mats is described in detail in Westall *et al.*, 2015, and more specifically in figure DR4, reported below (Fig. I.9). In some cases, this type of vein contact also shows some microcrystalline quartz and organic matter from the mats dragged in the veins. This suggests that the sediment and mats were silicified but not consolidated when this hydrothermal infiltration took place. In this case, it is attributed to a syn-sedimentary or early diagenetic stage.

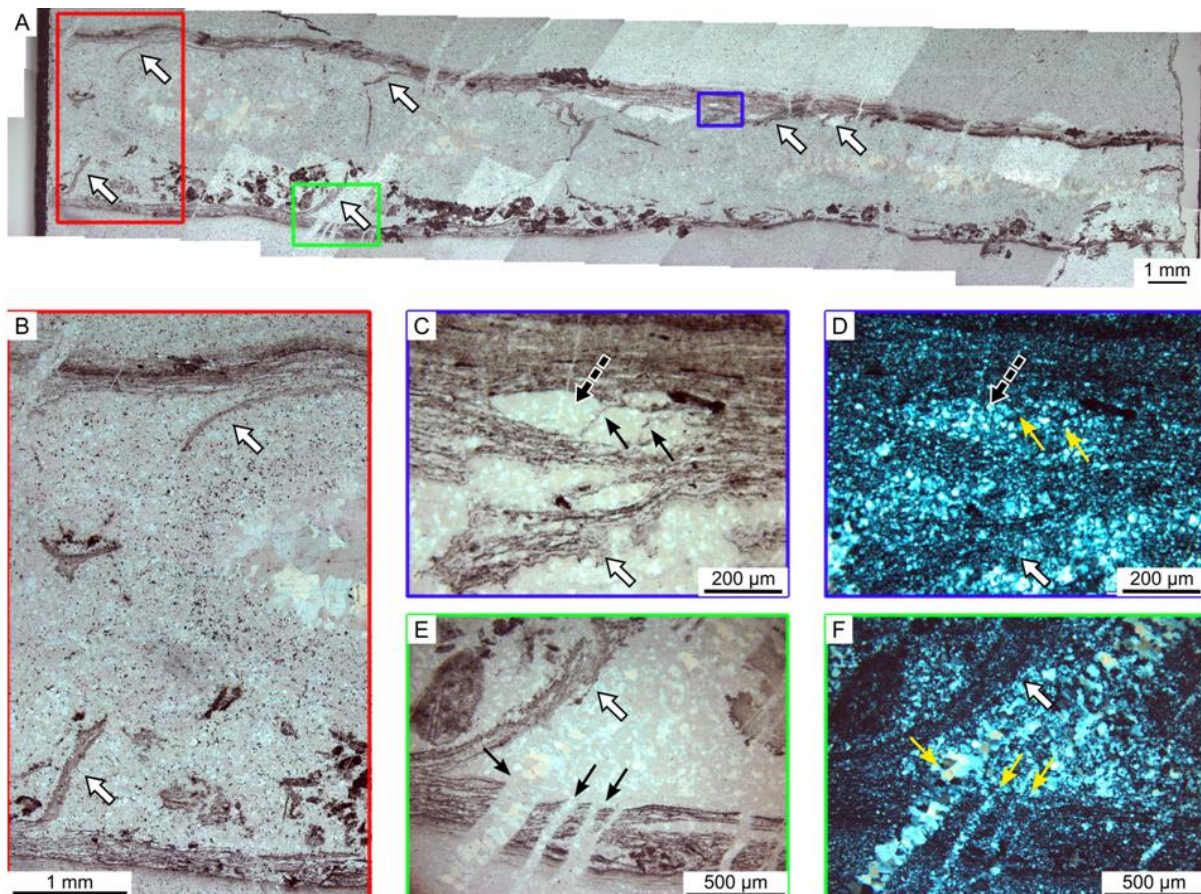


Figure I.9. Soft deformation of a living phototrophic biofilm. A. Optical micrograph view of a finely laminated photosynthetic biofilm that has been forcefully torn apart while it was still soft and probably living. White arrows indicate clearly visible torn fragments. The boxes denote details shown in B-F. B. The orientations of these biofilm fragments, one facing down and the other stretched upwards, gives an idea of the dynamic nature of the deformation. C, D. Transmitted and crossed polar views of a portion of the biofilm showing a torn fragment (white arrow) and fluid infiltration causing opening of an oval, fluid-filled space (vug) in the biofilm (dashed black arrow). The small black arrows point to thin portion of the organic film stretched between the walls of the vug. E, F. Transmitted and crossed polar views of a portion of the biofilm showing a torn fragment (white arrow) and later, brittle cross-cutting quartz veins (small black arrows). From Westall *et al.*, 2015.

c. Influence of diagenesis and metamorphism

Another generation of veins shows brittle contacts with the sediment and often cross-cuts the veins that create soft deformation contacts, described above. This veining occurs at a stage when the sediment is already lithified (brittle contact) and possibly reflects the filling of fractures created by deformation processes, by contemporaneous hydrothermal fluids and Si-

rich sea water precipitation. These veins are thus often attributed to late diagenesis or metamorphism stages.

The impact of diagenesis and metamorphism mostly depends on the extent and timing of silicification (e.g. Walsh, 2004). Compaction due to these processes is limited or inexistent for sediments that have been highly silicified early after deposition, or even during deposition. Metamorphism is expressed by the occurrence of certain metamorphic minerals such as chlorite, muscovite (metamorphosed clays and ash) but there is no deformation of the sedimentary structures (for instance, bedding planes, stromatolitic structures).

I.3. Emergence of oxygenic photosynthesis: the search for signatures the search for signatures in Archean and Paleoproterozoic sediments

Considering the descriptions on the photosynthetic metabolism made above in section I.1, several characteristics specific to photosynthetic bacteria can be considered for their identification in the natural environment. Planktonic photosynthesizers live in at the surface of the water column, in the photic zone (PZ). Planktonic organisms only integrate the sediment post-mortem by sedimentation of their degraded dead cells, which do not offer a particularly recognizable macrostructure in the sediment. Morphologically speaking, benthic photosynthesizers offer the most common and recognizable expression of bacterial photosynthetic life in sediments. Benthic photosynthesizers develop on solid surfaces such as sediments or rocks in the PZ, and form mat-like, laminated structures sometimes macroscopically observable. In these photosynthetic microbial mat, a typical cross-section reveals layers of green and purple colors relating to different types of photosynthetic bacteria distinguished by their pigments (green top layer for cyanobacteria and green as well as purple for anoxygenic

photosynthesizers underneath) (Fig. I.10a). Although optical and electron microscopy observations are often sufficient to identify the types of microorganisms involved, advanced biochemical and genetic analyses can provide more detailed information. For example, the fluorometry technique known as FIRE (Fluorescence Induction and Relaxation System), used to detect the fluorescence emission of chlorophyll-like pigments, allows the distinction between the anoxygenic and oxygenic bacteria in a microbial colony. Furthermore, the release of O₂ can be monitored in the medium of growth of a bacterial community and represents a straightforward indicator of the presence and activity of cyanobacteria. These are fast, unambiguous methods to detect photosynthetic activity and to identify the kinds of photosynthetic bacteria involved.

However, since the sedimentary deposits in which we seek photosynthetic bacteria are several billion years-old, the process of identification becomes more challenging, and even more so when trying to distinguish the anoxygenic and the oxygenic kinds. Sediments this old have generally undergone varying degrees of alteration, deformation, and weathering over billions of years, which makes the preservation of traces of life a real issue. Furthermore, owing to the lower amount of energy produced during anaerobic photosynthesis, mats developed by the early phototrophs were not as well-developed (in terms of size and biomass) as those produced by oxygenic photosynthetic bacteria. Although probably as widely distributed as the environments allowed, they were thinner (millimetric to sub-millimetric) and characterized by less biomass (Fig. I.10b) (Westall *et al.*, 2011b, 2015). Apart from the size and biomass considerations, hydrocarbon chains making up the molecules of all organisms are easily degraded, starting with diagenesis. Rapid mineral encasement (fossilization) that protects the organics from a harsh (e.g. oxygenating) environment can increase the chance of preservation of organic molecules, but in any case, with time, secondary processes such as diagenesis and metamorphism are still able to at least rearrange the C-chains into kerogen (amorphous sedimentary organic matter). Even if preserved and identified, a putative microbial mat may be difficult to interpret. These factors constitute

additional difficulties to finding ancient photosynthetic life in Precambrian rocks (from Earth's formation around 4.56 Ga to the end of Proterozoic ~0.5 Ga). The remains of carbonaceous matter in Archean sediments are present in the form of brownish structures (laminations, clots, clusters) observable in optical microscopy (Fig. I.10b). Although their mat-like structures are generally recognizable given specific environmental contexts, such as shallow water surfaces, other chemical signatures must be found to distinguish the type of photosynthetic metabolism.

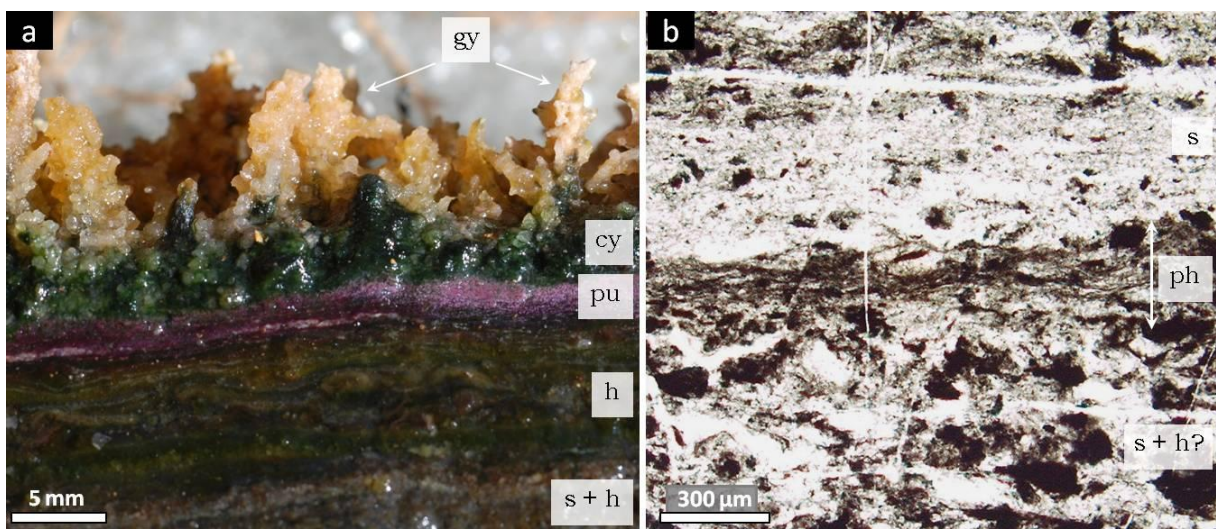


Figure I.10. Modern versus Archean microbial mats. (a) Cross section of a modern photosynthetic bacterial mat from Chiprana Lake, Spain. The green layer at the top consists of cyanobacteria (*Microcoleus chthonoplastes*) and green non-sulfur bacteria (*Chloroflexus-like*). Purple sulfur bacteria constitute the layer underneath. The thick brownish layer probably consists of sediment and heterotrophic bacteria. (Courtesy of Pascale Gautret, CNRS Orléans, France). (b) Transmitted light, photomicrograph of a 30µm-thick thin section of the 3.3 Ga-old Josefsdal Chert, Barberton Greenstone Belt, South Africa, displaying an anaerobic photosynthetic mat in cross section in the silicified sediment (Westall *et al.*, 2011b). Gy: gypsum, cy: cyanobacteria, pu: purple bacteria, h: heterotrophs, s: sediment, ph: photosynthetic mat.

I.3.1. A brief history of photosynthesis

The purpose of this section is to outline the features found in the geological record that are used as clues to identify the relics of oxygenic

photosynthetic bacteria or that of their past metabolic activity. The concern for biogenicity (proof for biological origin) is not addressed here. Several lists of criteria for the identification of biosignatures (Westall & Cavalazzi, 2011) and microfossils (Buick, 1990; Westall *et al.*, 2006; Westall & Southam, 2006) in rocks have been established. These lists are the result of the combination of years of work and expertise and, although constantly updated on the base of new findings, they offer robust criteria for the authenticity of traces of life in rocks.

a. Microfossils and stromatolites

The Archean fossil record is meager, and consists mostly of the remains of degraded, concentrated or diffuse, organic matter, while the Proterozoic period is characterized by a better preserved and diverse archive of life. The structure and the chemical and isotopic compositions of Precambrian organic matter can reveal precious information. Tice & Lowe (2006) made a truly structural “encyclopedia” of carbonaceous matter found in Early Archean sedimentary rocks with a meticulous optical microscopy study of the 3.416 Ga-old Buck Reef Chert (Barberton Greenstone Belt, South Africa) as a case study to hypothesize on the origin and depositional processes for the organic matter observed. Other features can give useful information about ancient life. This is the case for “microbially induced sedimentary structures” also called MISS. Although they are not considered as fossils, strictly speaking, MISS represent the response of microbial communities to the dynamics of the sedimentary environment in which they grow. Thus, they reveal the presence and activity of microbial communities. Fossilized MISS have been reported in Archean sediments (Noffke, 2008; Noffke *et al.*, 2003), some as old as 3.48 Ga (Noffke *et al.*, 2013). They can be indicators of ancient life and provide information on paleoenvironments.

Occasional morphological microbial fossils have been identified in particularly well preserved, Archean and Proterozoic sedimentary deposits. The fossil record of photosynthesis may extend as far back as ~3.5 Ga,

according to the latest reports (Walter *et al.*, 1980; Ueno *et al.*, 2001; Van Kranendonk *et al.*, 2003; Allwood *et al.*, 2006; Westall *et al.*, 2011a). Precambrian photosynthetic fossils are of various scales and take the form of metric to centimetric stromatolites, centimetric to millimetric microbial mats, and individual microscopic cells of only few microns in diameter (Fig. I.11), or less than a micron in diameter (Westall *et al.*, 2006, 2011a). Carbon isotopes data from preserved contemporaneous organic matter consistent with the photosynthetic pathway of carbon fixation (with $\delta^{13}\text{C}$ generally between -5 and -35‰, Schidlowski, 2000; see Fig. I.13) can also be considered as photosynthetic fossil, although abiotic carbon can exhibit isotopic fractionation in this range (e.g. Sephton, 2002; Pearson *et al.*, 2006; Pizzarello *et al.*, 2010).

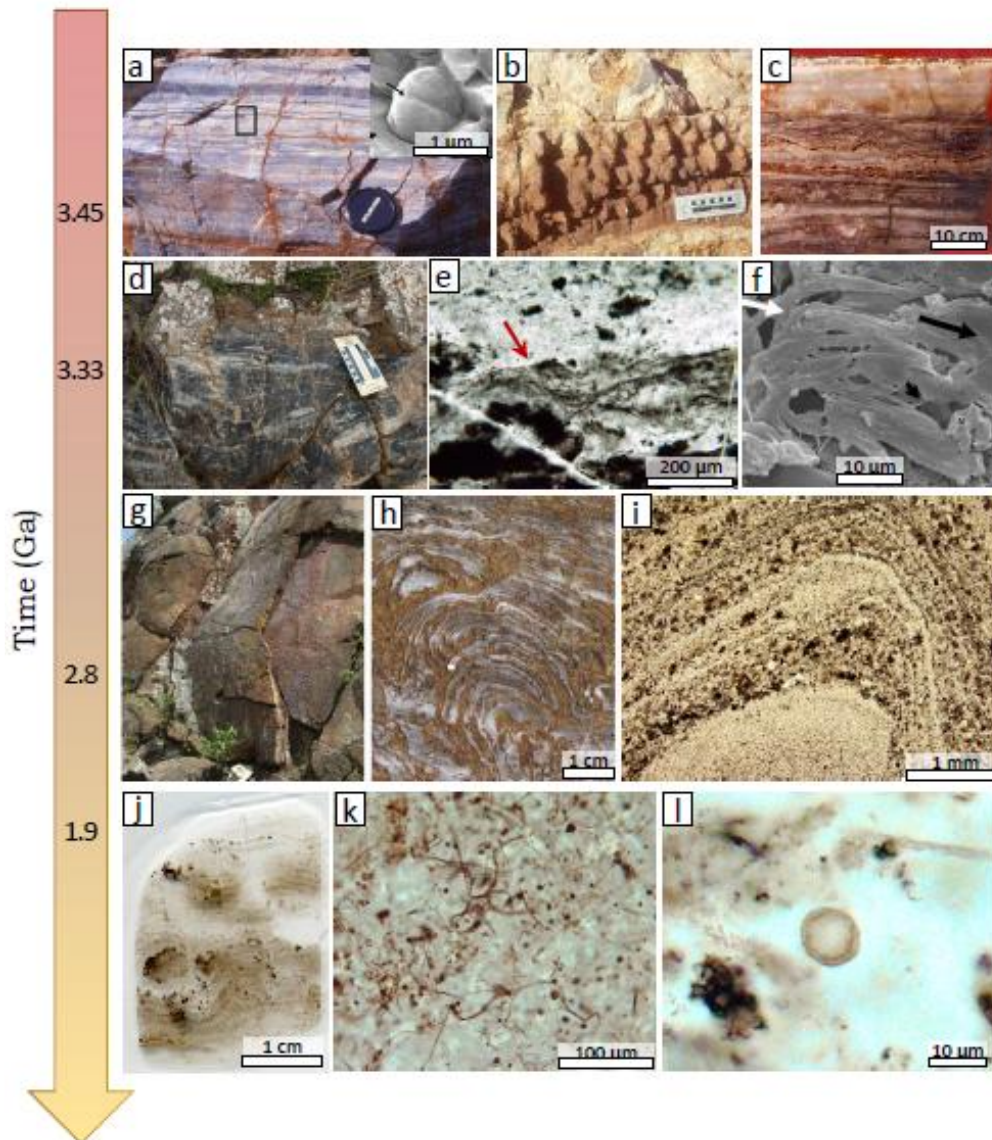


Figure I.11. The Precambrian fossil record of photosynthesis. A. Silicified sediments of the ~3.5 Ga-old Kitty's Gap chert (Australia) and silicified dividing coccoidal cell (SEM image), from [Westall et al., 2011a](#). B. Conical stromatolites from the ~3.38 Strelley Pool chert (Australia), from [Allwood et al., 2004](#). C. Stratiform stromatolites from the ~3.49 Ga-old Dresser Formation (Australia), from [Buick et al., 1981](#). D-F. Silicified sediment from the ~3.33 Ga-old Josefsdal Chert (South Africa) and fossilized life: D. Field photograph (this study), E. Photomicrograph (this study) of a preserved silicified microbial mat, F. SEM image of silicified filaments in a microbial mat, from [Westall et al., 2006](#). G-H. Field view of the >2.8 Ga stromatolites, Steep Rock Lake, Ontario, Canada. The white hat at the bottom of the picture (G) gives the scale. ([Riding et al., 2014](#)). H. Small irregularly laminated superimposed domical stromatolites, iron carbonates emphasize the layering ([Riding et al., 2014](#)). I. Photomicrograph of a cross section within the ~2.98 Ga-old Pongola stromatolites (this study). J-L. ~1.88 Ga-old Gunflint stromatolites from the Schreiber Beach locality (this study): J. Scan of a polished thin section cut through centimetric silicified stromatolites (brown areas) and practically pure chert layers (white areas). K-L. Photomicrographs of numerous filamentous (K) and spherical (L) iron-coated fossilized bacteria, probably from the *Gunflintia-Huroniospora* assemblage. Note that the cell walls are still visible on L.

Fossilized stromatolites constitute a large part of the Precambrian photosynthetic life record (Fig. I.11). The 3.496 Ga-old stromatolites of the Dresser Formation in Western Australia (Warrawoona Group, Pilbara Craton) reported for the first time by Walter *et al.* in 1980, are at the present time the oldest evidence for photosynthesis, based on morphological criteria. Stromatolites are microbially influenced organosedimentary laminated bioconstructions. They form in shallow water and consist of alternating layers of microbial mats and layers of sediment such as carbonates and detrital grains. Many authors have postulated that in Archean and Paleoproterozoic stromatolites, the layers of carbonates were most likely precipitated *in situ* by bacterial activity, whereas in younger Proterozoic stromatolites, they were the result of carbonates sedimentary accretion by bacterial ‘trapping and binding’ to the sticky bacterial extracellular polymeric substances (EPS) (for example: Grotzinger & Knoll, 1999; see the review by Altermann, 2008). The involvement of photosynthetic bacteria in the construction of such structures is revealed by this typical layered configuration. Indeed, to carry out their light-driven metabolism, photosynthetic bacteria have to move upward through the newly deposited or precipitated layer of sediment, in order to develop another mat on the free surface. Modern stromatolites are mostly exclusively built by cyanobacterial communities; hence, fossil stromatolites have long been taken for a proxy for oxygenic photosynthetic activity. However, Bosak *et al.* (2007, 2013) have shown experimentally that stromatolites could equally be formed by anoxygenic photosynthetic bacteria. This clearly reassesses the line of thought that used to systematically link stromatolites to the presence of cyanobacteria. Another issue concerning stromatolites arises from the fact that they are generally deprived of microfossils and show only diffuse organic matter in the mat layers. This severely challenges the biogenicity of these structures, especially as Grotzinger & Rothman (1996) have proposed a functional, completely abiotic model for the growth of early Precambrian stromatolites. However, the lack of evidence for the presence of a microbiota can be explained by secondary processes, such as diagenesis, undergone by the sediment. Indeed, as these structures are originally comprised of

carbonates, such as aragonite, or Mg-calcite (Grotzinger & Knoll, 1999), growth of carbonate crystals during diagenesis and re-arrangement during lithification could have damaged the microbial mats, erasing all morphological evidence, with only degraded organic matter remaining (Schopf *et al.*, 2007). Furthermore, while showing that stromatolite growth can be explained by abiotic processes, Grotzinger & Rothman (1996) question the extent of the involvement of bacteria in the construction of stromatolites, rather than questioning the biogenicity of these structures. In addition, Altermann (2008) has pointed out that abiogenic models for stromatolite formation can be refuted with basic field observations: the morphological complexity of sediment accumulation is evidence for biogenicity, as it reflects a strategic adaptation against sediment fluxes and deposition. Overall, stromatolites, as a whole, are considered as an indication for bacterial photosynthetic activity, but these physical structures are, for now, insufficient to constrain the emergence of oxygenic photosynthesis in time.

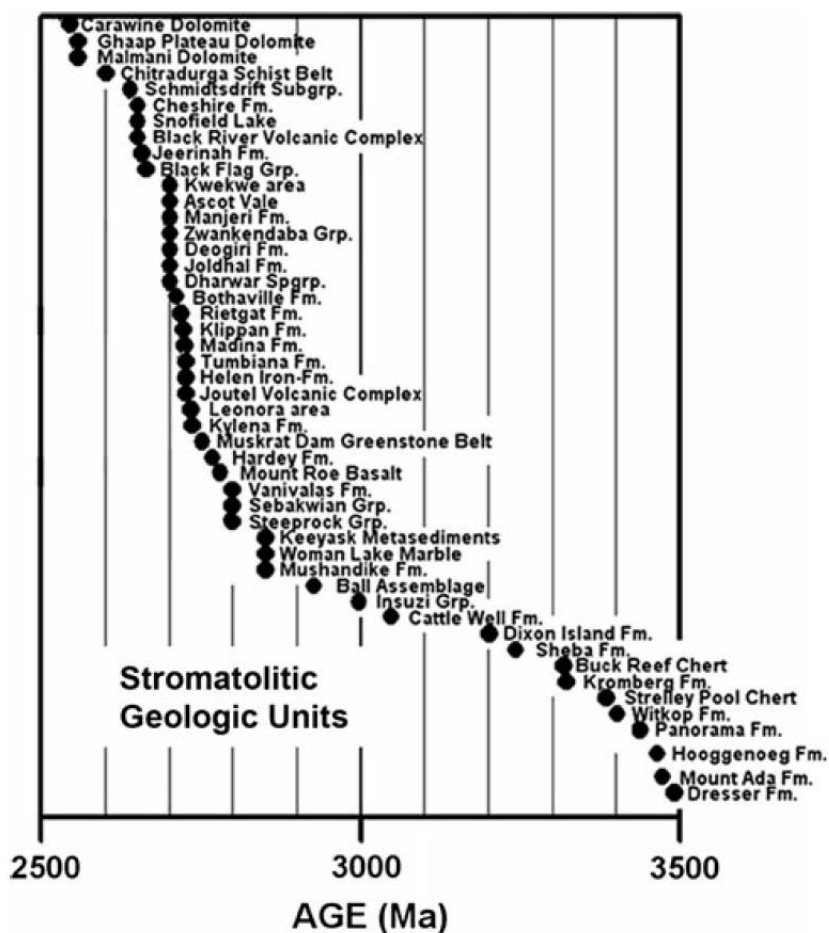


Figure I.12. The Archean record of stromatolites. Vertical axe gives arbitrary cumulative occurrences. From Schopf, 2011, after Hofmann, 2000 and Schopf, 2006.

In 1993, Schopf reported putative filamentous microbial fossils interpreted as oxygenic photosynthesizers in the 3.465 Ga-old Apex cherts (Warrawoona Group) in Western Australia, promoting them, at the time, to the rank of the oldest microfossils. However, in 2002, Brasier *et al.* showed that these micro-structures are secondary artifacts of abiotic organic matter formed under the influence of intense hydrothermal activity, rather than microfossils. These debates are a direct result of the difficulties encountered in micropaleontology and show the necessity of rigorous, complementary, multi-techniques analyses in this field. Indeed, compared to eukaryotic life, the recognition of fossilized bacterial life is likely to be more controversial because of obvious differences in the size and complexity of the preserved structures; large, complex structures, such as dinosaur skeletons being

more easily recognizable as a biological feature than a simply-shaped, 1-5 μm sized fossilized cell. Thus, although based on morphological criteria and microscopic observations, a rigorous quest for microfossils requires advanced, complementary geochemical analyses to prove their legitimacy.

Less controversial Precambrian photosynthetic fossils have been identified. Since the discovery of the first Precambrian microbiota interpreted as photosynthetic life in the 1.9 Ga-old Gunflint Chert of the Animikie Basin (Canada) by Barghoorn & Tyler in 1965 (first reported by Tyler *et al.*, 1957), new discoveries have flourished. Stromatolites have been documented as a continuous record from the early Archean (Walter *et al.*, 1980) to Proterozoic (Goodwin, 1956) (Fig. I.12), fossilized photosynthetic microbial biofilms and mats have been reported as old as 3.446 Ga-old (as detrital fragments in the Kitty's Gap Chert, Westall *et al.*, 2011a), 3.43 Ga-old (Strelley Pool Chert, Wacey *et al.*, 2011), 3.416 Ga (Buck Reef Chert, Tice & Lowe, 2004), 3.33 Ga (Josefsdal Chert, Westall *et al.*, 2001, 2006, 2011b), some of them containing fossilized bacteria. Finally, well-developed and diverse, noncontroversial photosynthetic microbiota occur in the 1.9 Ga-old Gunflint Chert of the Animikie Basin (Canada) (Barghoorn & Tyler, 1965; Cloud, 1965; Awramik & Barghoorn, 1977). Although it should be stressed that each of these findings represents years or even decades of investigations and analyses, the Precambrian fossil record seems to hold substantial remains of early life on our planet, many of which are photosynthetic. Figure I.11 reports a selection of these findings. For many of these microfossils, essentially those that are pre-GOE, there is still a debate as to whether they are fossils of anoxygenic or oxygenic photosynthesizers.

The oldest uncontested cyanobacterial fossils however, are dated at 2.15 Ga, from the Belcher Islands in Canada (Hofmann, 1976), which is still ~300 Ma younger than the GOE, itself marking the youngest boundary for the evolution of oxygenic photosynthesis. Thus, based on this evidence, all that can be said is that photosynthesis had evolved at least 3.5 Ga ago and that by ~2.1 Ga, oxygenic photosynthesis had emerged. The fossil record of photosynthesis does not allow dating the emergence of oxygenic photosynthesis from anoxygenic photosynthesis, for two main reasons: (i) the

oldest uncontested fossils of cyanobacteria post-date the rise of oxygen in the atmosphere and (ii) making the distinction between anoxygenic and oxygenic bacteria remains very challenging in such ancient geological material.

b. Hydrocarbon biomarkers

Molecular fossils, also called biomarkers, could help to resolve the limitations of the microfossil record. A brief but complete definition has been given by Buick (2008):

"Hydrocarbon biomarkers are the defunctionalized and fully saturated molecular skeletons of lipid and pigment biomolecules which are specific enough in their structure and biological distribution to be useful as taxonomic and environmental indicators [...]."

Two types of biomarkers are used as proxies for direct or indirect evidence of oxygenic photosynthesis: hopanes and steranes (for more detailed chemical characteristics, see Buick, 2008). Among hopanes, 2 α -methylhopanes are used as indicators for cyanobacterial activity (Summons *et al.*, 1999) since their unmodified, non-degraded precursors (2-methyl-bacteriohopanepolyol) are produced almost exclusively by modern cyanobacteria. Steranes are derived from sterols that are produced by eukaryotes and they require the presence of O₂ to be synthesized (Summons *et al.*, 2006). Thus, by comparison to hopanes, steranes are possible indirect indicators of oxygenic photosynthesis.

Biomarkers can be preserved in kerogen in Precambrian sedimentary rocks. In 1988, Summons *et al.* reported both of these biomarkers in 1.69 Ga-old sediments from the McArthur Basin, Northern Australia. However, since they are destroyed by oxidative weathering and metamorphism (Brocks & Pearson, 2005), biomarkers can only be retrieved from subsurface samples (e.g. drill-cores samples) in rocks that have only been submitted to low-grade metamorphism. Archean rocks have generally suffered from at least

greenschist facies metamorphism, with temperatures ranging from ~250°C to ~500°C, if not higher grades of metamorphism. It seems difficult to imagine that molecular fossils could survive these conditions. Unexpectedly however, Brocks *et al.* (1999, 2003a) reported biomarkers from 2.45 Ga-old and 2.78 Ga-old shales from the Pilbara Craton, Western Australia. While recognizing that the possibility of post-depositional contamination cannot be completely excluded, the authors presented arguments supporting an indigenous and syngenetic origin for the biomarkers found. However, Rasmussen *et al.* (2008) challenged their interpretations and postulated that the molecular fossils found post-date the age of the shales by at least 500 million years. Recently, Brocks (2011) has confirmed this possibility of post-depositional contamination. He showed that the studied molecules were anthropogenic and that previous interpretations concerning the Archean evolution of oxygenic photosynthesis were thus not valid.

The study of Precambrian biomarkers can be precarious. In most cases, the concentrations of biomarkers recovered are too low to categorically rule out the possibility of post-depositional contamination by infiltration of more recent biomolecules (Brocks, 2001). Furthermore, these studies rely on the ability to evaluate the degree of consistency between specific molecules comprising modern photosynthetic organisms, and what should remain of these molecules in Archean kerogen when parameters of degradation (aging via secondary processes such as metamorphism) have been taken into account. Thus, even if evidence suggests that biomarkers are syngenetic to their Precambrian host rocks, it should be stressed that these extrapolations from modern to Archean have to be considered with caution (Kopp *et al.*, 2005). Apart from concentration and syngeneity issues, the use of hopanes as a proxy for oxygenic photosynthesis has also been challenged. Fisher *et al.* (2005) reported that the anaerobic sulfur-reducing bacteria *Geobacter sulfurreducens* could synthesize various hopanols. Hence, hopanes, the fossilized derivatives of these compounds, do not necessarily imply oxygenic photosynthesis bacteria. In addition, Mulkidjanian *et al.* (2006) have proposed that the presence of the putative 'protocyanobacteria' (see above:

From anoxygenic to oxygenic photosynthesis) could be responsible for the cyanobacteria-specific biomarkers such as 2 α -methylhopanes found in Archean kerogen, consequently challenging once again the use of hopanes as proxies for oxygenic photosynthesis.

However, there is evidence for syngenetic, non-contaminated biomarkers in kerogens of the 2.45 Ga-old Matinenda Formation (Huronian Supergroup, Canada) (see Buick, 2008), the ~2.5 Ga-old sediments of the Transvaal Supergroup (Kaapvaal Craton, South Africa) (Waldbauer *et al.*, 2009). Although thorough analyses of these hydrocarbons need to be undertaken and complementary geochemical evidence must be found to support these reports, the study of biomarkers has the potential to push the oldest evidence for oxygenic photosynthesis back to ~2.5 Ga.

c. Isotope fractionations

Isotope fractionation occurs during a phase transition and relates, within a molecule, to the variations in the relative abundances of isotopes, revealed by the 'heavy' to 'light' isotope ratios. Isotope ratios are measured by mass-spectrometry and are used as indicators for the chemical processes responsible for the fractionation.

Carbon. Living organisms carry out isotope fractionations naturally during their metabolic activity. Since the pioneer work of Nier and Gulbransen in 1939, it is known that autotrophic organisms preferentially take up the light isotope of carbon ^{12}C during carbon fixation, rather than the heavier isotope ^{13}C . Photosynthetic organisms are no exception to the rule and it has been shown that the discrimination against ^{13}C is the result of kinetic effects occurring during photosynthetic CO_2 fixation (Park & Epstein, 1960). Since heterotrophic organisms use the carbonaceous matter primarily produced by these autotrophic organisms for their own metabolic activity, all living organisms consist of ^{12}C -enriched organic matter, while the ^{13}C is retained in other reservoirs such as oceans, under the form of 'inorganic' carbon

contributing to the composition of dissolved carbonate ions or as carbonate minerals. The isotopic ratio of carbon is a strong indicator of biogenicity and is given by $\delta^{13}\text{C}$, calculated as follows:

$$\delta^{13}\text{C} = \left(\frac{^{13}\text{C}/^{12}\text{C}}{^{13}\text{C}/^{12}\text{C}}_{\text{standard}} - 1 \right) \times 1000 \quad (9)$$

The standard usually used is the Pee Dee Belemnite standard ($^{12}\text{C}/^{13}\text{C} = 88.99$; PDB). Figure I.13 shows the compilation of $\delta^{13}\text{C}$ for the major groups of autotrophic microorganisms, plants and carbonate minerals.

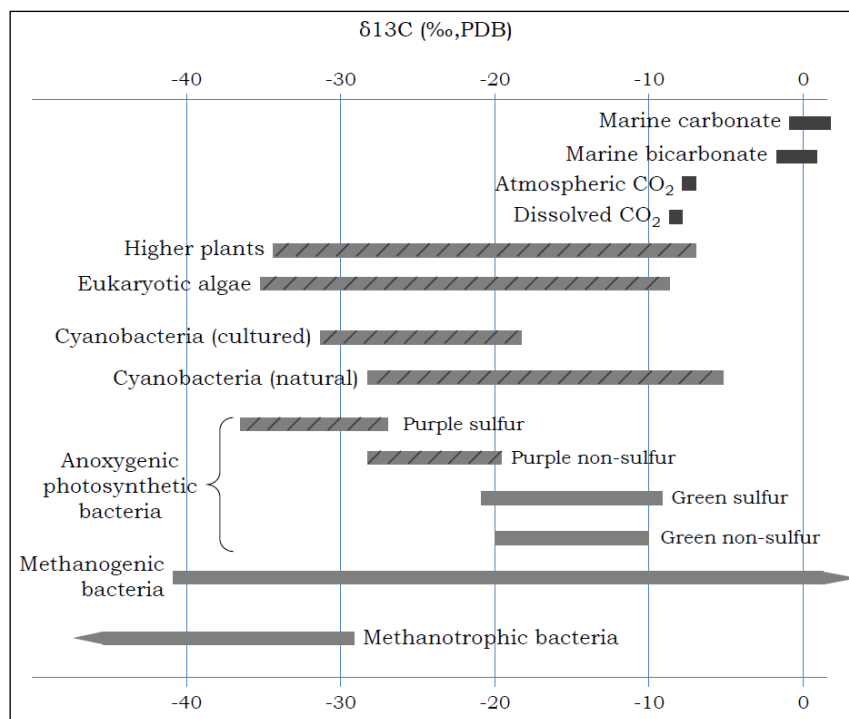


Figure I.13. Diagram of $\delta^{13}\text{C}$ isotopic variations in the major groups of autotrophic microorganisms, plants and inorganic carbon compounds. Dashed areas correspond to organisms using the Calvin cycle as CO_2 fixation pathway. Modified from Konhauser, 2007, after Schidlowski, 2000.

$\delta^{13}\text{C}$ can be calculated for any carbonaceous matter found in rocks and is particularly interesting especially for putative traces of life. The oldest relics of carbonaceous matter of biological origin strongly suggestive of a photosynthetic pathway were discovered by means of this method (Mojzsis *et al.*, 1996; Falkowski, 2011). However, although helping the characterization of the organic matter, this method has no decisive impact to the particular

issue under discussion in this study, since the $\delta^{13}\text{C}$ ranges of anoxygenic and oxygenic bacteria overlap with $\delta^{13}\text{C}$ values generally ranging from \sim -35‰ to 5‰ (Fig. I.13). Furthermore, abiotic carbon such as the one found in some meteorites that usually displays highly negative $\delta^{13}\text{C}$ values can sometimes reach a $\delta^{13}\text{C}$ of -30‰. Despite this, analyses of $\delta^{13}\text{C}$ are necessary to exclude or at least considerably restrict the possibility of an inorganic origin for the carbon observed when biogenicity is questioned. The microfossils reported in the last paragraph have been tested by this method.

Sulfur. Sulfur isotopes are equally widely used in the study of the Precambrian period. Their relevance is twofold: (i) the isotope ratio of ^{34}S to ^{32}S , $\delta^{34}\text{S}$ (equ.10), provides biological (in a similar way to carbon biological fractionation) and environmental indications, and (ii) $\Delta^{33}\text{S}$ (involving both $\delta^{34}\text{S}$ and $\delta^{33}\text{S}$, equ.12) is an indicator of mass-independent fractionation (MIF) which correlates with the presence of significant levels of oxygen in the atmosphere (see the section '*Evidence for a rise of oxygen in the atmosphere 2.45-2.32 Ga ago*' in the Introduction, and Fig. 1). The standard commonly used for the calculation of isotopic ratios given below is the Canyon Diablo Troilite (CDT; troilite is an iron sulfide mineral with the formula FeS).

$$\delta^{34}\text{S} = ((^{34}\text{S} / ^{32}\text{S})_{\text{sample}} / (^{34}\text{S} / ^{32}\text{S})_{\text{standard}} - 1) \times 1000 \quad (10)$$

$$\delta^{33}\text{S} = ((^{33}\text{S} / ^{32}\text{S})_{\text{sample}} / (^{33}\text{S} / ^{32}\text{S})_{\text{standard}} - 1) \times 1000 \quad (11)$$

$$\Delta^{33}\text{S} = 1000 \times ((1 + \delta^{33}\text{S}/1000) - (1 + \delta^{34}\text{S}/1000)^{0.515} - 1) \quad (12)$$

Figure I.14 compares the $\delta^{34}\text{S}$ variations for natural S-containing reservoirs. With respect to the search for signatures of oxygenic photosynthesis, $\Delta^{33}\text{S}$ can thus be considered as an indirect proxy, but a direct indicator of an oxygenated atmosphere.

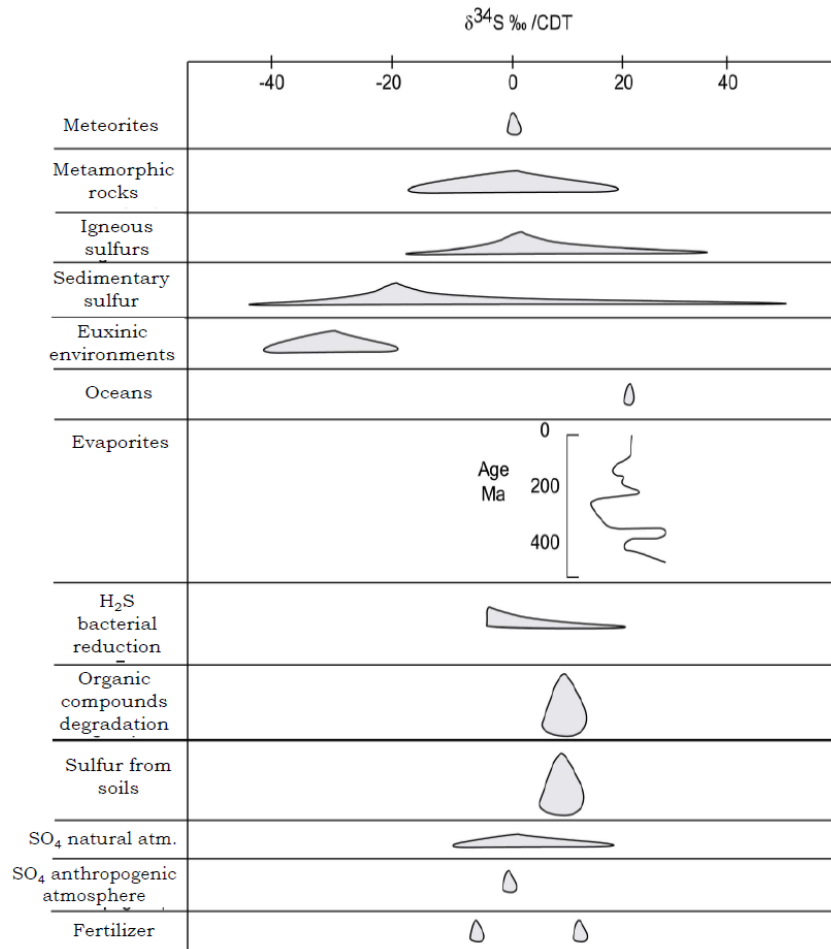


Figure I.14. $\delta^{34}\text{S}$ compositions in major groups of organic and mineral sulfur compounds. Modified from Pisapia, 2006 after Thode, 1991.

Nitrogen. Nitrogen isotope composition is a great complementary indicator for the evolution of oxygenated conditions. Indeed, in modern oxygenated oceans, the N cycle is controlled by the biological reduction of atmospheric N_2 to NH_4^+ (by N fixation), and the return of the fixed N to the atmosphere via denitrification and anaerobic ammonia oxidation. Intermediate compounds, nitrate (NO_3^-) and nitrite (NO_2^-), are produced respectively by nitrification (oxidation of NH_4^+ to NO_2^- and NO_3^-) and by nitrification and nitrate reduction, both of these processes requiring at least some free oxygen. Nitrification and denitrification processes yield to positive $\delta^{15}\text{N}$ (average values of 6‰ and 7‰), the organic matter in sediments being enriched in ^{15}N .

In anoxic oceans, before the evolution of cyanobacteria and the production of oxygen, the N cycle would have been solely controlled by

atmospheric N₂ fixation and regeneration of NH₄⁺ after the burial of the N-fixing organic matter in sediments. This process yield negative δ¹⁵N values (as low as -6 ‰) since the organic nitrogen produced is depleted in the heavier isotope, ¹⁵N, relatively to atmospheric N₂.

The isotopic values of nitrogen can thus be used to trace the evolution of oxygen levels in the oceans through time, and across the GOE. This is confirmed by the geological record. Numerous studies have documented negative δ¹⁵N values from samples pre-dating the GOE (see the review of Papineau *et al.*, 2005) and positive after the GOE (Peters *et al.*, 1978; Sweeny *et al.*, 1978). In particular, the first report of changes in the δ¹⁵N values through Archean and Proterozoic marine kerogen was made by Beaumont and Robert (1999). They documented a switch to positive δ¹⁵N values of marine kerogen between ~2.5 and 2.1 Ga. Positive δ¹⁵N values were reported before the GOE, in sediments as old as ~2.67 Ga-old (Garvin *et al.*, 2009; Godfrey & Falkowski, 2009). However, the quantity of oxygen necessary for N isotopic values to switch to positive values has yet to be established. Thus, it remains uncertain whether these positive values account for extensive global oxygenation or whether they indicate the onset of low-levels of oxygen in the atmosphere, or an oxidation event of the surface ocean.

Transition metals - iron. In addition to the light elements, such as carbon and sulfur, predominantly comprising organic matter it is important to mention that stable isotope geochemistry of heavier elements is currently in development, with great implications for the understanding of the Precambrian environment and early life. Elements concerned are the transition metals such as iron, molybdenum, chromium (see Fig. I.15) and some elements of the lanthanides and actinides series based on chemical behavior similarities. The narrow range of variations of their isotope ratios (see the review by Anbar & Rouxel, 2007) postponed the investigation of their isotope fractionation for decades since analyses with higher precision and sensitivity were required. Concurrent with recent advances in mass spectrometry however, particular interest has grown around these transition

metals as their potential for understanding many natural processes operating in the geo- and biosphere has been revealed.

In particular, iron stable isotope geochemistry is currently being developed, and the extent of its applications is under close investigation (see Anbar, 2004). In the context of the present study, the relevance of Fe isotopes is plural. As a transition metal, Fe can have multiple oxidation states. Its mobility is controlled by redox conditions in aqueous systems, influenced by biological and abiotic processes, and leading to significant variations of its abundance in both time and space. Furthermore, Fe is also a key element in photosynthesis biochemistry as it is an important external electron donor for anoxygenic bacteria (see *Bacterial anoxygenic and oxygenic photosynthesis*). Since Fe isotopes can be fractionated both abiotically and biologically, their relevance here is twofold:

- The variations in Fe isotope ratio ($\delta^{56/54}\text{Fe}$) in sedimentary rocks have been shown to express the fractionation of Fe during abiotic oxidation, which could reflect the progressive oxygenation of the ocean and atmosphere through time (Rouxel *et al.*, 2005). Johnson *et al.* (2008) argued that this record could be directly linked to the onset of oxygenic photosynthesis.
- The $\delta^{56}\text{Fe}$ of iron oxides formed in well-oxygenated aqueous environments is supposed to reflect the $\delta^{56}\text{Fe}$ of the original water source because of near complete iron oxidation and then precipitation, with $\delta^{56}\text{Fe}$ values from 0 to -1‰ (e.g. Zhu *et al.*, 2000). Conversely, if oxidation is partial, as in oxygen-depleted environments, iron oxides will have near zero to positive $\delta^{56}\text{Fe}$ values relative to the Fe^{2+} source (e.g. Croal *et al.*, 2004; Rouxel *et al.*, 2005). Both of these processes can occur abiotically, but they can also be reconciled with the conditions prevailing in the surrounding environments of cyanobacterial mats (Severmann *et al.*, 2004), or anaerobic Fe-oxidizing bacterial mats (e.g. Planavsky *et al.*, 2009) (such as some anoxygenic photosynthetic bacteria), respectively.

Stable isotope geochemistry of transition metals is a nascent field that is currently in a development-improvement phase. Additional data and studies

are currently piling up and are needed to fully understand the mechanisms and causes of isotope fractionation of such elements. However, the future of Fe isotope study appears promising as it is already possible to postulate that the variations of $\delta^{56/54}\text{Fe}$ in the sedimentary record are able to trace the oxidation of oceans through time. The record of Fe isotopic variations supplements those of S, as well as Mo and Cr isotope data in the study of the GOE, and even in the emergence of oxygenic photosynthesis (see the reviews by Anbar & Rouxel, 2007; Farquhar *et al.*, 2011; Lyons *et al.*, 2014).

d. REE patterns, redox-sensitive elements and minerals

Fluctuations in atmospheric O_2 levels have strongly influenced the distributions and concentrations of redox-sensitive elements in aqueous sediments through time, making them good indicators of paleoredox conditions in ocean and atmosphere.

The transition metals mentioned above and presented in Figure I.15 are more sensitive to changes in redox conditions than other elements of the periodic table. This is due to their ability to readily assume multiple oxidation states which affects their behavior and mobility when conditions change from anoxic to oxic, or conversely. Since their mobility and thus, their transport to seawater is defined by the quantities of O_2 in the environment, the content and distribution of transition metals in sedimentary rocks serve as robust proxies for the paleoredox state of the atmosphere and oceans.

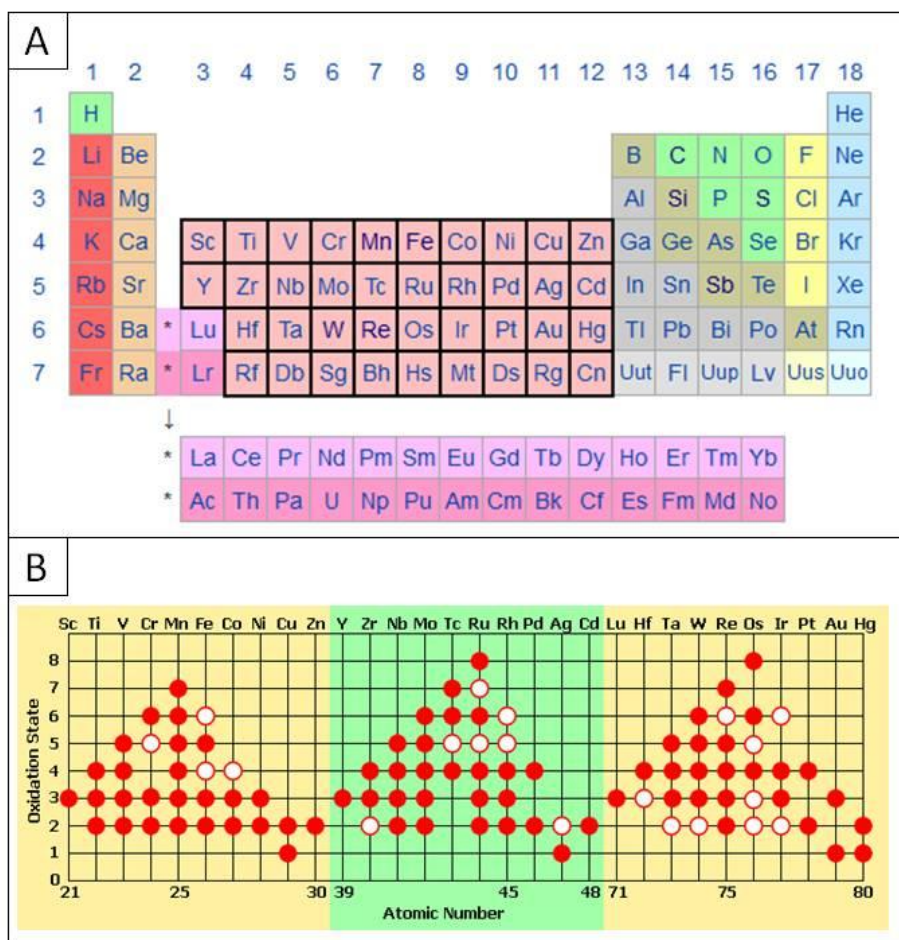


Figure I.15. Transition metals in the periodic table (A) and their oxidation states (B).

In this context, the abundances of the redox-sensitive transition metals molybdenum and rhenium in Precambrian sediments have been the subject of numerous geochemical studies (Siebert *et al.*, 2005; Algeo & Lyons, 2006; Scott *et al.*, 2008; Tissot *et al.*, 2012; McKay & Pederson, 2014). In 2007, Anbar *et al.* reported an enrichment in Mo and Re in the ~2.5 Ga-old Mount McRae Shale in Western Australia. They interpreted this enrichment as a consequence of oxidative weathering of crustal sulfide minerals on emerged terrains, resulting in the supply of Mo and Re to the Archean ocean. This demonstrates the presence of signs of atmospheric oxygenation around ~2.5 Ga already.

Conversely, the absence of certain redox-sensitive elements in marine sediments can also be an indication for an oxygenated atmosphere. This is the case of cerium, for instance, which reacts inversely to oxidation, and its relevance in terms of paleoredox proxy is better expressed by patterns in the

measurements of REE (rare earth elements, lanthanide series) and Yttrium in marine sedimentary rocks. Under oxic conditions, the behavior of Ce diverges from that of the other rare earth elements: Ce^{3+} is oxidized to Ce^{4+} and its solubility decreases, leading to its depletion in sea water as it is removed from continental input fluxes. Negative Ce anomalies in REE+Y patterns of sedimentary rocks are thus indicators of oxidative weathering on emerged lands, and are used as a proxy for oxygenated conditions. This indicator has proved very useful in following the fluctuations of redox conditions in oceans and atmosphere through time. Kato *et al.* (2006) reported negative Ce anomalies in Banded Iron Formations dated throughout the Archean and as far back as 3.8 Ga, and thus support an early rise of oxygen levels, while other authors have shown that aqueous environments were still globally anoxic during the Archean and that only Proterozoic sediments show Ce-depleted REE+Y patterns (Alexander *et al.*, 2008; Allwood *et al.*, 2010; Planavsky *et al.*, 2010), with a transition from anoxia to an oxic environment around 2.3 Ga (Tang *et al.*, 2013), and a potential, temporary mid-Paleoproterozoic oceanic and atmospheric anoxia event (Bau & Alexander, 2006).

Despite these debates, the nature of chemical properties of Ce make negative Ce anomalies true indicators of oxic conditions. It is thus possible that negative Ce anomalies could be interpreted at the local scale.

The record of such redox-sensitive trace elements in the Precambrian ocean has recently gained a new dimension as Large *et al.* (2014) proposed an original approach involving their content in sedimentary pyrites. Indeed, as long as Fe^{2+} ions and H_2S are available, pyrite (FeS_2) can precipitate in the water column or during early diagenesis in the top few meters of sediment, during which it incorporates simultaneously trace elements available in the water, either as micro-inclusions or directly in their crystal lattice. On the same basis as Mo, Re and Ce studies described above, redox-sensitive trace elements content and distribution in sedimentary pyrites constitute small 'black boxes' of the chemical composition of the water column at the time and location of pyrite formation and deposition. This is on the strict

condition that the pyrites studied are not of hydrothermal or metamorphic origin, otherwise they would not reflect oceanic composition but rather that of the hydrothermal and metamorphic fluids. The results of LA-ICPMS measurements of Large *et al.* (2014) on pyrites from Precambrian to modern black shales are reported in Figure I.16. They show that pulses of trace elements in pyrites occurred at least twice before the GOE (called here GOE1) at ~2.45 Ga. Their results have strengthened previous studies (Anbar *et al.*, 2007; Kaufman *et al.*, 2007; Wille *et al.*, 2007; Frei *et al.*, 2009 ; Crowe *et al.*, 2013; Planavsky *et al.*, 2014) that support “whiffs” of oxygen in Earth’s environment from 50 million to half a billion years before the GOE. The general variations in atmospheric O₂ level might thus be more rightly schematized in Figure I.16 than in Figure 1b (Introduction). Therefore, these temporary increases in atmospheric O₂ might represent the timid dawn of oxygenic photosynthesis.

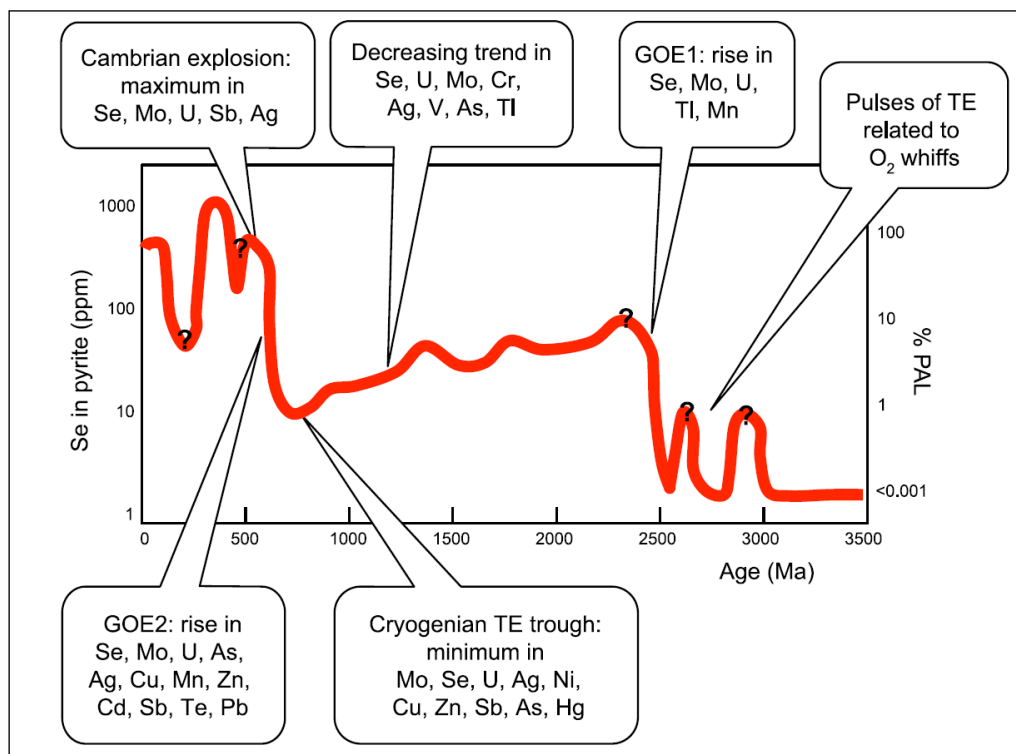


Figure I.16. Variations of redox-sensitive trace elements content in sedimentary pyrites and oxygenation of the atmosphere and ocean. Note that atmosphere oxygenation (red curve) is estimated by the Se content in pyrite. TE : trace elements. From Large *et al.*, 2014.

Although the distributions and concentrations of redox-sensitive elements in marine sediments and sedimentary pyrites are robust proxies for environmental oxygenation, minerals comprising these particular elements are also relevant as they are easily subject to changes in redox conditions. Such is the case of minerals such as uraninite (UO_2), siderite (FeCO_3) and pyrite. Under oxidizing conditions, pyrite (FeS_2) is oxidized and forms SO_4^{2-} and Fe^{3+} ions, uraninite is dissolved and forms soluble U^{6+} ions and siderite is oxidized in Fe^{3+} ions (Holland, 1984; Krupp *et al.*, 1994). Well-rounded pebbles of these minerals have been reported in Archean sediments, but not beyond ~ 2.3 Ga (for example: Roscoe, 1996; Rasmussen & Buick, 1999; England *et al.*, 2002; Hofmann *et al.*, 2009). The rounded shapes of the pebbles indicate long transport an aqueous mediated over large distances typical of river transportation. These reports thus demonstrate that the Archean atmosphere must have contained very low levels of oxygen, otherwise these minerals would have not survived in river waters mixed with oxic air (Holland, 1984; Rasmussen & Buick, 1999). Well-rounded pebbles of redox-sensitive minerals help to constrain the timing of the GOE and allow the evaluation of oxygen concentrations in the Archean atmosphere (>0.1 PAL) (summarized in Catling & Zahnle, 2002).

e. Biominerals

Biominerals are mineral phases synthesized by living organisms. Biomineralization can be ‘induced’ or ‘controlled’. Indeed, certain organisms can trigger the precipitation of minerals owing to interactions between their metabolic activity and the surrounding aqueous environment: this is called induced biomineralization (Lowenstam, 1981); others can precipitate them deliberately within their cells or on the cell walls as part of an evolutionary strategy: controlled biomineralization. With respect to both anoxygenic and oxygenic photosynthetic bacteria, the biomineralization is induced (see Frankel & Bazylinski, 2003).

This chapter focuses on biominerals precipitated by photosynthetic activity that are observed in this context in Precambrian sediments. Some

modern cyanobacteria are able to precipitate gypsum ($\text{CaSO}_4 \cdot 2\text{H}_2\text{O}$) and stromatolitic gypsum deposits have been documented as far as Messinian (Rouchy & Monty, 2000) (~7.2-5.3 Ma, Upper Miocene). However, bioprecipitated gypsum is not documented in Precambrian sediments. Westall *et al.* (2006, 2011b) reported gypsum precipitated in association with a photosynthetic microbial biofilm formed in an evaporitic, shallow water environment. The observed gypsum, however, appears to be purely evaporitic in origin and shows no signs of biological origin.

Sulfate minerals will thus not be discussed here.

Iron oxides. A significant example of induced biomineralization is the massive precipitation of iron oxides that formed the Precambrian Banded Iron Formations (BIFs). In 1968, Cloud proposed that the oxidation of soluble Fe^{2+} ions in the ocean by photosynthetically produced O_2 could have been the main process responsible for Precambrian BIFs formation. However, many authors argue in favor of the involvement of anoxygenic photosynthetic bacteria (Garrels *et al.*, 1973; Hartman, 1984, Widdel *et al.*, 1993; Konhauser *et al.*, 2002; Kappler & Newman, 2004; Kappler *et al.*, 2005; Posth *et al.*, 2010; Wu *et al.*, 2014). Indeed, some anoxygenic photosynthetic bacteria use ferrous iron as an electron donor for their metabolism (cf. above: *Bacterial anoxygenic and oxygenic photosynthesis*), during which they oxidize it to insoluble ferric iron, triggering its precipitation as iron hydroxides ($\text{Fe}^{3+}(\text{OH})_3$) at first, that later form iron oxides. Fe^{2+} ions are available in the anoxic parts of the ocean and can be provided by soluble ferrous iron minerals such as siderite (FeCO_3) and ferrous monosulfides (FeS). On the other hand, poorly soluble minerals such as pyrite (FeS_2), vivianite ($\text{Fe}_3(\text{PO}_4)_2$) or magnetite (Fe_3O_4) are unused by these bacteria (Kappler & Newman, 2004).

In the scope of the present study, it should thus be noted that the presence of iron-oxides is neither an exclusive indicator of oxygenic photosynthesis nor that of the presence of molecular O_2 since they can be precipitated by both oxygenic bacteria and anaerobic Fe-oxidizing bacteria. However, $\delta^{56}\text{Fe}$ measurements on Fe-oxides of Iron Formations allow to go further in

differentiating between the involvements of both of these types of bacteria (e.g. Planavsky *et al.*, 2009).

Carbonates. The metabolic activity of modern cyanobacteria influences the pH conditions and the local chemistry of their close surrounding environment. In addition to CO₂, cyanobacteria are capable of using the carbon of HCO₃⁻ available in ocean water. This HCO₃⁻ uptake has the overall effect of moving the carbonate equilibrium equation toward the precipitation of carbonates. The result is the precipitation of calcite, or aragonite (polymorph of calcite) both with the formula CaCO₃. Biological and chemical conditions of biomineralization processes as well as microfabrics of bioprecipitated calcium carbonates in the geological record have been reviewed by Riding (2000), while Merz-Preiß (2000) has focused on cyanobacterial calcification and especially environmental controlling factors. Modern cyanobacteria can be encrusted by fine carbonate crystals (micrite) precipitated in their cell wall and extracellular polymeric substances (EPS) (the importance of EPS in carbonates bio-precipitation mechanisms has been raised by several authors, e.g. Westall *et al.*, 2000, Dupraz *et al.*, 2004, Bontognali *et al.*, 2008, and reviewed by Tourney & Ngwenya, 2014). In addition, several authors have recently shown that some cyanobacteria are also capable of precipitating amorphous calcium carbonates intracellularly (Couradeau *et al.*, 2012; Benzerara *et al.*, 2014).

As a result of their biomineralization abilities, and in comparison with modern bacterial calcification mechanisms, cyanobacteria are of great interest as principal contributors for the formation of Precambrian carbonate sediments, the latter being used as proxies for the presence and activity of oxygenic photosynthetic bacteria (e.g. Vasconcelos *et al.*, 2006). Supported by numerical models evaluating CaCO₃ saturation state in modern to Precambrian cyanobacterial mats (Aloisi, 2008), many authors have evoked the involvement of cyanobacteria in the formation of the ~2.9 Ga-old large carbonate platforms from Steep Rock (Canada), Pongola Belt (South Africa) and Mushandike (Zimbabwe) (see Nisbet & Fowler, 2011). Cyanobacteria are also held responsible for the deposition of early Archean to Proterozoic

carbonate sediments and particularly for the formation of the stromatolites they contain (Beukes & Lowe, 1989; Buick, 1992; Grotzinger & Knoll, 1999; Kamber & Webb, 2001; Golubic & Seong-Joo, 2012; Riding *et al.*, 2014), including some stromatolites as old as 3.5 Ga (Awramik, 1992; Altermann *et al.*, 2006).

Nanocrystals of aragonite have been reported in the ~2.7 Ga-old carbonated stromatolites from the Tumbiana Formation (Australia) (Lepot *et al.*, 2008) and in a ~3.33 Ga-old calcified and silicified photosynthetic microbial mat of the Josefsdal Chert, Kromberg Formation (South Africa) (Westall *et al.*, 2006, 2011b). However, although admitting the bioprecipitation of these nanocrystals within photosynthetic bacterial mats, and the strong possibility that these nanocrystals are specifically related to anaerobic sulfate-reducing bacteria (SRB) activity, none of these authors have observed evidence allowing them to attribute these aragonite occurrences to the activity of oxygenic photosynthesizers. These observations made at the sub-micrometric scale show that the connection between carbonates and cyanobacteria is far from being systematic.

Alternatively, several studies report that *in situ* carbonate biomineralization in modern microbial mats and stromatolites can be strongly influenced by the metabolic activity of heterotrophic bacteria such as SRBs (e.g. Dupraz *et al.*, 2004; Baumgartner *et al.*, 2006; Bontognali *et al.*, 2008), or else, by dead microbial cell material offering nucleation sites for heterogeneous nucleation of calcite (Bosak & Newman, 2003).

Interestingly, modern anoxygenic photosynthetic bacteria as well are capable of inducing the precipitation of carbonates via HCO_3^- uptake and changes in pH conditions. For example, Bundeleva *et al.* (2012) have shown experimentally that *Rhodovulum* strains (purple non sulfur bacteria) are able to precipitate CaCO_3 with bulk rates similar to cyanobacteria and heterotrophic bacteria, and significantly higher than some coralline algae. Similar to carbonate biomineralization conducted by SRBs, the metabolic activity of *Rhodovulum* induces a rise in pH that allows calcite precipitation, the latter being facilitated on supports such as dead cells or the EPS of living

bacteria. Additionally, Bosak *et al.* (2007) reassessed the overlooked role of anoxygenic photosynthetic bacteria in the construction of Precambrian stromatolites by demonstrating that they can equally stimulate the precipitation of carbonates but also incorporate carbonate grains in protolamina as a way of increasing the solidity of the structure (akin to the “trapping and binding” process). This is in line with the ability of anoxygenic photosynthetic bacteria to induce *in situ* carbonate precipitation and to form at least small-scale stromatolites, such as those found in the Early Archean.

Overall, carbonate biomineralization is not automatic evidence for cyanobacterial activity. However, biomineralization of calcite and aragonite is a documented process that may have occurred as early as ~3.5 Ga in stromatolites and photosynthetic microbial mats, whether under the influence of photosynthetic activity, or associated heterotrophic activity, or indirectly as a result of changes in pH conditions triggering heterogeneous nucleation. Thick Precambrian carbonate deposits could in fact be a proxy for oxygenic photosynthesis, since Bundelewa *et al.* (2012) have noted that a lower efficiency of anoxygenic photosynthetic carbonate bioprecipitation is expected, which could not allow the formation of such large platforms. Nevertheless, there is still debate as to which type of bacteria is involved in the formation of Precambrian carbonate sediments, and to what proportion. Altermann *et al.* (2006), for instance, concluded that since at least 3 Ga, carbonate rock deposits are the result of the activity of cyanobacterial and heterotrophic microbial consortia.

In all cases, *in situ* carbonate bioprecipitation remains a possible proxy for the presence of photosynthetic bacteria in Precambrian stromatolites and microbial mats, but is not specific to cyanobacteria.

1.3.2. Different approaches to the same quest

From these reports emerge two fundamentally different approaches in the great quest for oxygenic photosynthesis signatures. One approach consists in seeking signs of environmental oxygenation, on the assumption

that an oxygenated micro or global environment is direct evidence for oxygenic photosynthesis activity.

However, several studies have shown that environmental oxygenation and its link to oxygenic photosynthesis might be more complex. On the basis that (i) the availability of dissolved O₂ in water can lead to the formation of hydroxyl radicals which are harmful to DNA, and that (ii) the OEC of PSII itself requires O₂-mediating enzymes to counter oxygen toxicity, Kirschvink and Kopp (2008) (after Cloud, 1973) argued that a source of oxygen must have been available to drive the biological evolution of oxygen tolerance, before the emergence of oxygenic photosynthesis. A hypothesis was proposed that describes the production of O₂ by the interaction of photochemically-produced H₂O₂ on glacier surfaces with the H₂O of the ocean (Liang *et al.*, 2006; Kirschvink & Kopp, 2008). According to these authors, this hypothesis could also explain the “whiffs” of oxygen documented before the GOE, around 2.9 Ga and 2.5 Ga (Anbar *et al.*, 2007; Kaufman *et al.*, 2007; Wille *et al.*, 2007; Frei *et al.*, 2009 ; Crowe *et al.*, 2013; Planavsky *et al.*, 2014).

Furthermore, geological processes, such as plate tectonics (Barley *et al.*, 2005) or O₂ removal by reduced species of the mantle (Canfield *et al.*, 2006) (see *Causes of the Great Oxidation Event: the role of oxygenic photosynthesis*), could have prevented the accumulation of photosynthetically-produced oxygen in the atmosphere. This implies that the lack of oxygenation signs in the atmosphere during the Archean does not necessarily prove that oxygenic photosynthesis had not already evolved (Björn & Govindjee, 2009).

The history of atmospheric and oceanic oxygen fluctuations does not seem to assure a precise timing for the emergence of oxygenic photosynthesis.

The other approach consists of *in situ* local investigations where morphological evidence, biomarkers and multi-technique geochemical studies of organic matter and the surrounding sedimentary matrix, including the evaluation of atmospheric and oceanic oxidation state at the time of the deposition, are gathered to identify microfossils of oxygenic photosynthetic bacteria at the millimeter to sub-micrometer scale. This process has proved

its worth since the oldest evidence for photosynthesis, if not the oldest evidence for oxygenic photosynthesis, stems from this meticulous complementary approach.

Nevertheless, the “complementary” component is obligatory since the aim is no longer the bulk study of the behavior of one or several redox-sensitive elements to infer the global redox state, but rather the accumulation of *in situ* morphological and geochemical evidence proving that the observed structures are, in fact, the remains of cyanobacterial cells, mats or remnants of their metabolic activity. Taken separately, these arguments could lead to the wrong interpretations. The debates between J. W. Schopf and M. D. Brasier about the authenticity of structures morphologically similar to cyanobacteria recovered in the Apex chert (Western Australia) constitute a good example of these difficulties (Schopf, 1993 and Brasier *et al.*, 2002). Another issue relates to the significance of biomarkers. For instance, Mulkidjanian *et al.* (2006) raised the possibility that biomarkers such as 2 α -methylhopanes suggestive of cyanobacterial activity could rather indicate the presence of protocyanobacteria, the putative non-oxygenic cyanobacteria that potentially possessed both photosystems and pre-dating the first oxygenic photosynthesizers. This could have deep implications on the timeline of the history of photosynthesis since the analyses of certain biomarkers recovered in Archean kerogens from Canada and South Africa have helped pushing the oldest evidence for cyanobacteria back to 2.5 Ga and over (see Buick, 2008; Waldbauer *et al.*, 2009).

Within these different approaches, it is clear that the inferred timing of emergence of oxygenic photosynthesis is strongly influenced by the kinds of chemical or mineralogical clues investigated. Figure I.17 schematically outlines the studies reported above and illustrates this variability.

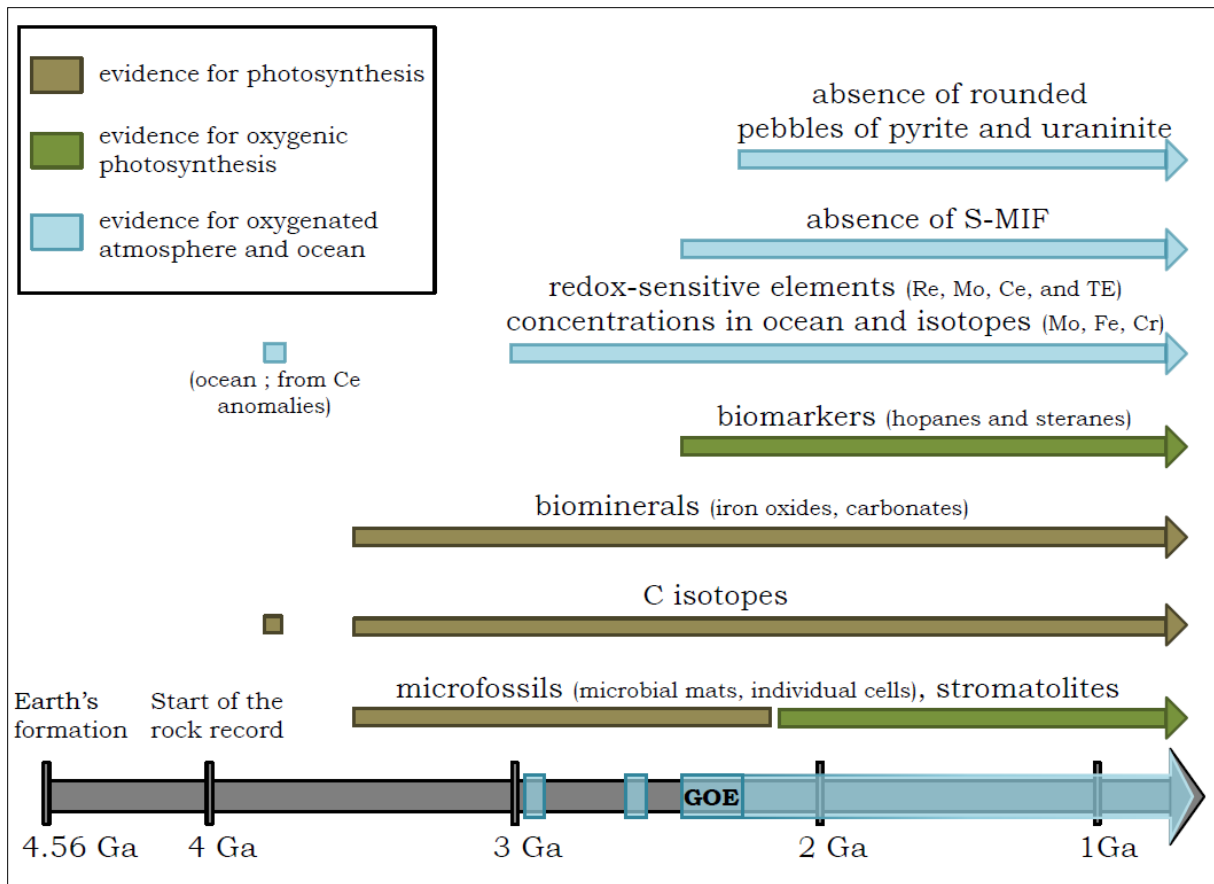


Figure I.17. Evidence for the emergence of photosynthesis (anoxygenic and oxygenic photosynthesis taken together), oxygenic photosynthesis, and signs of oxygenated atmosphere and oceans, from the different kinds of mineralogical and chemical clues investigated. Note that green areas indicate evidence for oxygenic photosynthesis, taking into account the continued existence of anoxygenic photosynthesis that continues to exist today. References are in the text.

I.4. Conclusions on the search for signatures: biochemistry of modern cyanobacteria versus the Precambrian geological record

The phylogenetic variety of modern anoxygenic and oxygenic photosynthetic bacteria, as well as the biochemical mechanisms of their metabolisms and their environmental impacts from local to global scales are generally well known. Moreover, continuous technological improvements further improve the possibilities of studying these two families of organisms. Nevertheless, despite these advances and the joint efforts of the scientific

community to combine new findings, the timing of the emergence of cyanobacteria remains elusive for two primordial reasons: (i) the degree of similarity between modern and the first oxygenic photosynthetic bacteria is uncertain and, even if they are in fact, very similar, (ii) the specific compounds constituting cyanobacteria (such as the chlorophyll pigments) or the signatures of their local environmental impact have little or no chance of surviving in the sparse and generally extensively reworked, Precambrian rock record.

Furthermore, the combination of these two points has further impact on the possibility to interpret all the potential evidence found in the geological record: point (i) jeopardizes the reliability of using microfossils, stromatolites, biominerals and biomarkers as evidence, and because of point (ii), in particular chemical leaching during hydrothermal silicification (common in the early sedimentary horizons), as well as compositional changes and deformations during diagenesis and metamorphism, the integrity of all the morphological, mineralogical and chemical signatures is being mistrusted.

With the aim of precisely constraining the time of emergence of oxygenic photosynthesis, it seems evident that new geochemical data should be added to the extant collection, thereby statistically increasing the value of previous interpretations. More importantly, new signatures must be found and suitable analytical techniques have to be selected and improved for this particular purpose.

Part 2: Material and Methods

Chapitre II : résumé

Echantillons, méthodes analytiques et paramètres expérimentaux

Ce chapitre décrit dans un premier temps la méthodologie utilisée pour sélectionner les échantillons les plus appropriés pour cette étude, puis présente l'éventail de techniques analytiques utilisées dans le but de trouver de nouvelles signatures chimiques de la photosynthèse oxygéniques.

Les échantillons sélectionnés doivent respecter les contraintes suivantes : ils doivent d'être d'origine sédimentaire, déposés dans des milieux aqueux peu profonds, à l'intérieur de la zone photique et ils doivent avoir un âge compris entre 3,5-3,3 et 1,9-1,8 milliards d'années (Ga) en ayant toutefois subi le moins de déformation et d'altération possible. De plus, les échantillons caractérisés du point de vue de leur pétrographie, de leur contenu en termes de traces de vie, et de leur composition chimique, en amont de cette étude, ont été privilégiés.

La liste des techniques analytiques utilisées dans cette étude est elle-même restreinte par plusieurs contraintes. En effet, compte-tenu de la rareté des échantillons, ces techniques doivent être non-destructrices. De plus, elles doivent pouvoir être capables de réaliser des analyses *in situ* à haute résolution spatiale dans les tapis microbiens et cellules fossiles, à l'échelle micrométrique, puisqu'il s'agit de l'échelle d'intérêt de cette étude.

Nous avons utilisé la microscopie optique, la spectroscopie Raman, la microscopie électronique couplée à des analyses élémentaires, la microsonde électronique et la spectrométrie de fluorescence X à rayonnement synchrotron. De plus, bien que destructrices, nous avons également utilisé des techniques d'analyses isotopiques. En effet, ces techniques restent essentielles pour caractériser la matière organique fossile. Cependant, nous les avons utilisés en dernier dans la chaîne analytique, afin de ne pas gêner l'utilisation des techniques mentionnées ci-dessus.

Dans la Partie III de ce manuscrit, chacune de ces techniques est évaluée afin de déterminer leur pertinence vis-à-vis du sujet, c'est-à-dire leur capacité à détecter et caractériser de possibles signatures chimiques spécifiques à la photosynthèse oxygénique.

Chapter II: Samples, analytical methods and experimental parameters

The first part of this Chapter focuses on presenting the methodology used for the selection of the samples, based on the list of relevant criteria, and then describes the samples analyzed in this study. As mentioned in the Objectives section, the scientific question of this study carries several constraints regarding analytical techniques: they should be able to provide *in situ* geochemical and mineralogical information at the μm or sub- μm scales and they should be non-destructive as much as possible. The second part of this Chapter presents the significant range of analytical techniques selected with respect to the aforementioned constraints. Concerning the type A signatures (chemical characteristics of the remaining organic matter) and type B signatures (local environmental impact at the micrometric scale) of oxygenic photosynthesis (defined in the ‘*Scientific approach and objectives*’ section), the ability of each of these techniques to provide answers in differentiating relics of anoxygenic and oxygenic photosynthesis activity in Precambrian sedimentary cherts will then be assessed in *Part 3: Results* of this work.

II.1. Samples

II.1.1. Criteria for sample selection

a. Age of the samples

With the aim of finding chemical and mineralogical signatures of oxygenic photosynthesis to determine when it arose from its precursor anoxygenic form, selected samples must primarily correspond to **specific**

periods of time in the evolutionary history of photosynthesis, through the Archean (4.0-2.5 Ga) to the Paleoproterozoic (2.5-1.6 Ga). They should represent a time range broad enough to include three situations: (1) photosynthetic life has evolved and is predominantly anoxygenic, (2) oxygenic photosynthetic life has evolved and spread and is predominant, and (3) the transition period between these two end members. To this end, and with reference to the timeline defined by the gathering of geochemical evidence presented in Chapter I Figure I.17, I chose to study samples comprised between ~3.5-3.3 and ~1.9-1.8 Ga, hence beginning at a time when several lines of evidence point to active photosynthetic life but without decisive proof of cyanobacterial evolution, to a time when cyanobacteria-like microfossils have been documented, thus covering the period of the GOE.

b. Geomorphological context

Considering that photosynthetic bacteria are the micro-organisms of interest in this study, the selection process should satisfy geomorphological criteria that constrain a **particular environmental context of deposition** for the chosen rock samples. Paleosols are often involved in the study of Earth's oxygenation because they provide information on the redox state of the atmosphere. However, they do not contain relics of photosynthetic bacteria since they did not form in an aqueous medium and are thus not relevant for this study. BIFs, possibly formed under the activity of photosynthetic microorganisms, might carry evidence of planktonic oxygenic photosynthetic bacteria, or more likely, anoxygenic iron-oxidizing photosynthetic bacteria (cf. Posth *et al.*, 2011). However, since planktonic microorganisms live in the water column, they enter the sediment post-mortem, by sedimentation of their degraded, dead cells. The remains of these particular photosynthetic microorganisms are thus found in Archean rocks under the form of degraded carbonaceous matter with no particular morphology. Morphologically speaking, photosynthesizers living at the sediment surface (benthic microorganisms) offer the most common and recognizable expression of bacterial photosynthetic life in sediments, forming

microscopic to macroscopic structures (such as mat-like colonies and stromatolites) and interacting with sediment surface to form microbially-induced sedimentary structures (MISS; Noffke *et al.*, 2003). The samples of choice should be obtained from sediments able to support the development of benthic photosynthetic life and thus, should be deposited in shallow aqueous environment, **within the photic zone**.

c. Preservation state

Furthermore, given the required age for the samples, the selection must involve **deformation, alteration and weathering criteria**. To the extent possible, samples should have undergone minimum degrees of alteration and **metamorphism**. In order to avoid the influence of post-deposition to modern contamination by weathering and chemical alteration, samples have all been taken far from apparent fractures to avoid infiltration of non-contemporaneous organic matter (cf. Westall & Folk, 2003), and several centimeters below the open surface of the outcrop, subjected to the modern environment (precipitations, oxidation). Since the scope of this study is a chemical and mineralogical investigation at the microbial scale, sedimentary structures and microstructures, mineralogical textures, distribution and morphology of the organic matter (OM) and that of fossils, and chemical compositions at the micro-scale must be well preserved. Highly metamorphosed sedimentary rocks such as the metasediments of the Isua supracrustal belt (~3.8 Ga, Greenland) would not provide relevant information to this study. The degree of metamorphism that these rocks have been submitted to is too high (up to amphibolite facies) and did not allow such preservation. In this type of rock, major-to-trace element analyses and isotope analyses might still provide valuable information on the formation of these rocks, on the regional geological context, and on the global chemical processes involved at the time (for example, Mojzsis *et al.*, 1996; Furnes *et al.*, 2007), but all microstructures and microscale geochemical data are lost.

Furthermore, since **hydrothermal fluid circulation** can create significant chemical 'leaching' (see Chapter I.2.3), selected samples must have been as little influenced by intrusive hydrothermal fluxes as possible. During the Archean and also Paleoproterozoic, sea water and sediments were constantly influenced by hydrothermal activity (for example, Archean: Hofmann & Bolhar, 2007; Hofmann & Harris, 2008; Westall *et al.*, 2015; Alexander *et al.*, 2008; Paleoproterozoic: Klein & Beukes, 1992; de Wit & Hart, 1993). Thus, hydrothermal and mixed marine-hydrothermal chemical signatures were unavoidably transmitted to the chemical composition of the sediment. However, samples were selected with the aim of avoiding close contact between the sediment and major signs of high intensity hydrothermal infiltrations that disrupt the sediment and were thus sampled as remotely as possible from macroscopic hydrothermal breccias and fractures.

d. Previous analyses

Finally, the nature of analyses made on the samples prior to this study influenced the selection process. Detailed **optical and electron microscopy observations** were conducted on the collection of Precambrian samples available at the Centre de Biophysique Moléculaire, CNRS Orléans (France), which allowed the identification of photosynthetic microfossils (mats and cells) and stromatolites. These interpretations were supported by detailed field work (field campaigns and literature research; see the references in Chapter III, for each Precambrian formation considered in this study) focused on the depositional context of the sediments that indicates deposition in a shallow marine environment. The carbonaceous matter of the selected samples have all been previously analyzed by **Raman spectrometry**, and show a Raman signature of mature kerogen (insoluble relics of carbonaceous matter) coherent with the age of sediment deposition and subsequent metamorphic condition, with no indication of post-depositional contamination. **Carbon isotope analyses** were also carried out and suggest a biological origin for the carbon, consistent with photosynthetic

pathways. Thus, prior to this study, evidence was gathered to interpret the traces of life found in the samples as photosynthetic and contemporaneous to their host rock.

II.1.2 Description of the samples

The preselected samples are rock samples and polished thin sections of shallow marine sedimentary cherts ranging from ~3.33 Ga to ~1.88 Ga in age. They come from the Kaapvaal Craton (South Africa) and the Animikie Basin (Canada) and belong to several collections. Samples belonging to Frances Westall, CNRS Orléans, France, are: samples from the Josefsdal Chert, from the Pongola stromatolites (Barberton Greenstone Belt, South Africa), and samples from the Gunflint Formation (Animikie Basin, Canada). Other samples (samples GF55-1 and GF55-1b) from the Schreiber Beach locality of the Gunflint Formation were provided by Andrew Knoll, Department of Earth and Planetary Sciences, Harvard University (Cambridge, Massachusetts). The sediments studied have all undergone low degrees of metamorphism, the highest being greenschist facies.

From this list of preselected samples, a thorough study combining petrographical investigations and an extensive literature research was carried out in order to understand the depositional context of each of these samples and to ascertain their relevance with respect to this study. The results are reported in Chapter III.

II.2. Sample preparation

Samples were prepared from handsamples of sedimentary cherts from the Kaapvaal Craton in South Africa, and the Animikie Basin in Canada, and were cut in 30 µm-thick thin sections of approximately 2.5x3.5 cm at the Institut des Sciences de la Terre d'Orléans (ISTO), Orléans, France. These polished thin sections were used, at first, for petrographical investigations

(optical microscopy and Raman spectroscopy), as well as for Scanning Electron Microscopy (SEM), Electronic-Probe Micro-Analysis (EPMA) and Secondary Ion Mass Spectrometry (SIMS) analyses, after being coated with carbon (SEM and EPMA) or gold (SIMS). Electronic techniques and especially EPMA and SIMS require a perfectly smooth surface. Thin sections were abraded with 40 μm abrasive cloths under water at the ISTO, and then polished using the Logitech polisher at the same institute, with felt discs soaked in diamond abrasive pastes. Each thin section was subsequently polished using 9 μm , 3 μm and then 1 μm diamond pastes. In addition to meeting analytical constraints, this preparation method is useful to avoid the possible effects of modern environment on the thin sections. Indeed, in the specific case of this study, where micrometric evidence of oxidation is sought in order to detect past oxygenic photosynthesis activity, abrasion of the top few nanometers of the thin sections allows removing potential surface mineralogical changes due to modern oxidation (e.g. oxidation of reduced minerals phases such as metal-sulfides).

Ultra thin sections with micrometric dimensions required for the penetrative synchrotron radiation analyses were cut within these same polished thin sections. They carry the name of the technique used to manufacture them, and are henceforth called 'FIB sections', with reference to the *Focused Ion Beam* (FIB) technique. They were made at the Institut d'Electronique, de Microélectronique et de Nanotechnologies (IEMN) in Lille, France, and at the Centre Pluridisciplinaire de Microscopie électronique et de Microanalyse (CP2M) in Marseille, France. This preparation method is the subject of a dedicated part in Chapter V.

Destructive isotopic analyses were either conducted on separate centimetric pieces of the handsamples (nitrogen and carbon stepped-combustion mass spectrometry analyses), or directly on the polished thin sections (sulfur and carbon *in situ* isotope analyses by SIMS). However, when conducted directly on thin sections, isotope analyses were performed last in the analytical suite.

II.3. Petrographical studies

Petrographical observations and analyses allow a detailed characterization of each sample with respect to mineralogy, history of deposition of the sediment at the centimeter and millimeter scales (sedimentology, secondary processes) and study of the organic matter and microfossils (morphology, fossilization mode). They also provide a robust database of microscopic observations for the selection of specific micrometric zones within each thin section that will be used to conduct *in situ* specialized measurements and to provide locations for the manufacture of FIB sections.

II.3.1. Optical microscopy

Optical microscopy observations were made on an Olympus BX-51 at the Centre de Biophysique Moléculaire, CNRS Orléans, France (Fig. II.1A). The device offers the possibility to observe the sample in plane and cross polarized light and in reflected light. Samples previously coated with graphite or gold were systematically cleaned in order to avoid the artifact metallic reflection of graphite or gold under reflected light. In plane-polar mode, a condenser system allows focusing the transmitted light on opaque zones (where mineral or organic material is densely packed), in order to increase the luminosity and the quality of observation. The magnification capacity of the objective lenses ranges from 25 to 1000 times. The microscope is coupled to an Olympus camera connected to an image acquisition software, allowing taking photomicrographs at various magnifications and illumination modes.

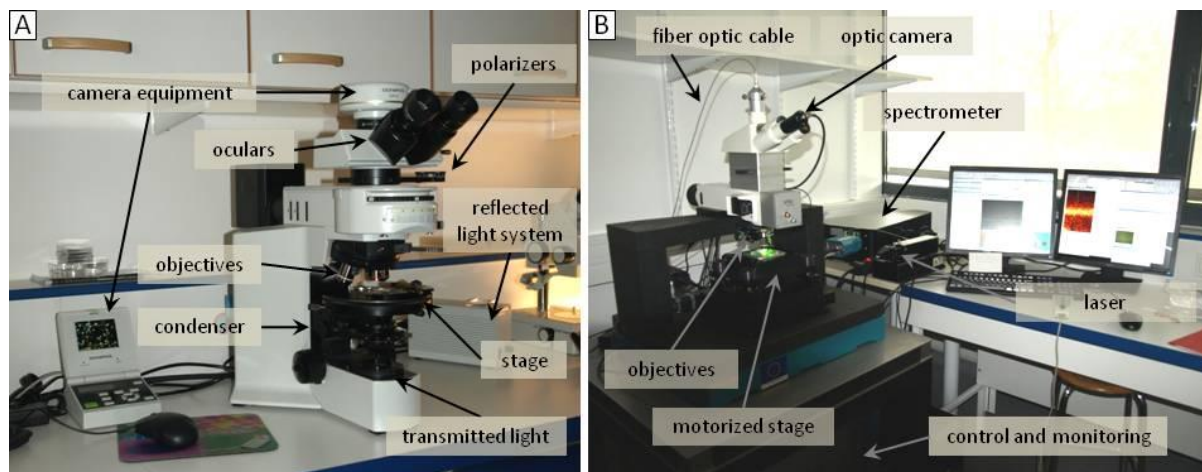


Figure II.1. Optical microscopy (A) and Raman spectroscopy (B) platform at the CBM, CNRS Orléans, France.

Optical microscopy studies provide crucial sedimentary and mineralogical information that is necessary to conduct further investigation at smaller spatial scales. The degree of silicification of the samples makes difficult to establish the paragenesis sequences due to the extensive SiO₂-replacement. However, this process also uniquely preserved the sedimentary structures, even at the micrometric scale, which allows at least reconstituting the successive depositional steps, but also studying the environmental context of deposition via the remaining primary mineralogical phases, the extent of the influence of hydrothermal activity, the distribution of organic matter, the morphology of microfossils, and the general preservation state of the sample.

Complementary information on mineralogical phases and the nature of the carbonaceous matter are obtained by Raman spectroscopy analyses.

II.3.2. Raman spectroscopy

a. Principle

During the scattering of light by matter, photons are converted into vibrational energy before being reconverted into photons. Most of the time, the excited atomic bonds return to their initial vibration modes in such a

way that the reemitted photons have the same energy than that of the incident photons. This elastic scattering of photons is called Rayleigh scattering. However, although lower, the probability exists that the excited bonds do not return to their initial states. In this case, photons are reemitted with a shift of energy. This phenomenon corresponds to the inelastic scattering, also referred to as Raman scattering in the visible spectrum. Molecules or crystals have generally several vibration modes of distinct energy thus allowing a specific Raman scattered light to be representative of a given material. The Raman signal being very low in comparison with reflected or elastically scattered light, it is necessary to spread the photons in energy using a spectrometer to separate the Raman photons from the others. Since Raman spectroscopy requires the use of a high intensity monochromatic light source, its use particularly expanded after the advent of the laser. A Raman spectrum corresponds to the number of photons collected by a detector (now a CCD camera) versus their shift in energy from the incident light, generally displayed in wavenumbers (in cm^{-1}). A Raman spectrum is thus made of several bands, each being specific to the vibration mode of a particular molecule or crystal.

Raman spectroscopy affects any type of materials (solid, liquid or gas). Since it is sensitive to the atomic bounds symmetry, it can distinguish polymorphs. Finally, this non-destructive technique is able to provide *in situ* compositional information at the micrometric scale, on mineralogy as well as carbonaceous matter, regardless of their mineralogical or biological origin.

b. Raman spectroscopy analyses

Raman spectroscopy analyses were carried out on a WITec Alpha 500 RA at the Centre de Biophysique Moléculaire, CNRS Orléans, France (Fig. II.1B) using a green laser at 532 nm. The device is able to make spot analyses but also transects and maps by means of an automated stage. The in plan resolution reaches less than 0.5 μm depending on the numerical aperture of the objective used. Samples coated for techniques requiring

metallization were systematically cleaned prior to Raman analyses in order to avoid the dominant artifact signal of carbon or gold.

Raman spectroscopy analyses intervene as a complementary method to study the mineralogy. This technique is able to identify fine micrometric mineral phases that are too small to be observed and to be identified with optical microscopy petrographical criteria, especially if these micrometric grains were extensively replaced by SiO₂ during silicification and are thus optically indistinguishable from the surrounding siliceous matrix.

Apart from assisting in mineralogical analyses, the principal interest of Raman spectroscopy is its ability to provide information on carbonaceous matter (CM) that optical microscopy cannot provide. Raman spectra of CM are characterized by two main bands: a peak D, for disordered carbon (located around 1350 cm⁻¹) and a peak G, for graphite (around 1580 cm⁻¹) (Fig. II.2A). The maturity of the carbon can be determined by the intensity (noted I) ratio of these two peaks, that is correlated to the degree of structural order (Tuinstra & Koenig, 1970). However, when the carbon analyzed is very poorly ordered, determining its maturity requires other spectral parameters, namely the precise positions and widths of the D and G bands (e.g. Ferrari & Robertson, 2000; Busemann *et al.*, 2007).

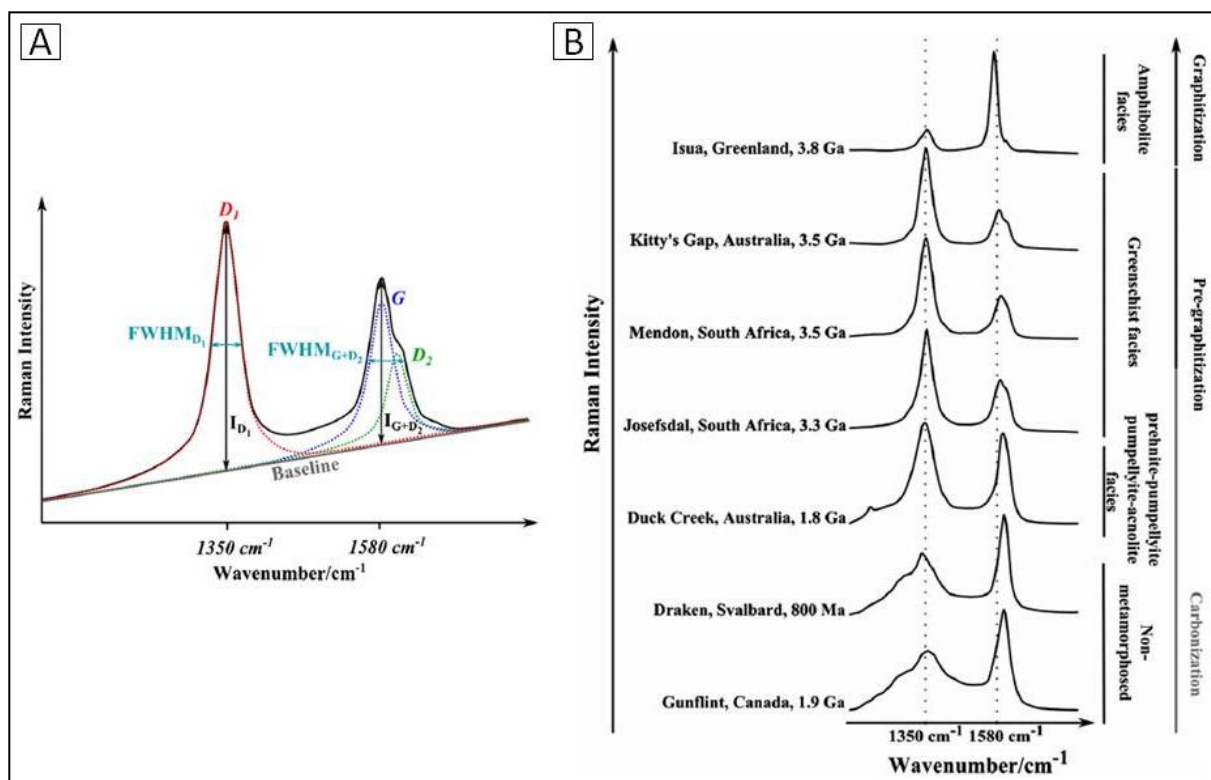


Figure II.2. Raman spectrometry of carbonaceous matter. A. Characteristics of a Raman spectra of carbon. B. Average Raman spectra of carbon in various Precambrian sediments and relation with the degree of degradation. From Foucher *et al.*, 2015.

Spectral profiles of mature, insoluble relics of CM called *kerogens* that are found for instance in Precambrian rocks, were extensively studied (e.g. Tice *et al.*, 2004; Schopf *et al.*, 2007; Sforza *et al.*, 2014) and allow correlating the degree of maturity of the CM to the highest temperature it was submitted to (Beysac *et al.*, 2002; Rouzaud *et al.*, 2012), and thus, to the experienced metamorphism (Fig. II.2B; and for example: Jehlicka *et al.*, 2003). Hence, it is possible to estimate if a particular carbon spectrum is coherent with the conditions (heating) sustained by CM hosted by a Precambrian sediment that was metamorphosed, thereby eliminating the possibility of modern but also post-depositional contamination if the sediment was sealed early by silicification. Furthermore, it was recently shown that the variations in CM spectra resulting from Raman mapping can provide insight into the biogenicity of the kerogen in low grade metamorphic rocks (Foucher *et al.*, 2015).

The study of CM spectral profiles by Raman spectroscopy is a fledged field of study in constant progress. Detailed information can be found in the aforementioned references that have shown the extent of the information provided by Raman CM spectra processing. However, to avoid deviating from the main subject of this study, it is worth mentioning that carbon Raman spectra obtained were used with the sole aim of controlling the consistency of the CMs analyzed in Archean and Paleoproterozoic biological relics, in order to proceed to further relevant analytical techniques, with respect to the aim of this work. This control being complete, Raman analyses were focused on the compositional study of the samples.

The main petrographical observations by optical microscopy and complementary analyses by Raman spectroscopy are reported in Chapter III.

II.4. Elemental analyses – Excitation by electrons

Scanning Electron Microscopy (SEM) coupled with Energy-Dispersive X-ray Spectroscopy (EDX or EDS), and Electron-Probe Micro-Analysis (EPMA) both carry the dual functionality of an observational and an analytical tool, able to provide electron-based imagery, as well as spot elemental analyses and elemental mapping.

II.4.1. Coupled Scanning Electron Microscopy and Energy-Dispersive X-ray spectroscopy

a. Principle

Scanning Electron Microscopy (SEM) is a little-destructive technique able to reach a spatial resolution in the range of the micrometer. The principle of SEM is based on the interaction between a focused electron beam and the atoms constitutive of a sample. The electron beam scans the

sample, producing at each point several types of signals (Fig. II.3) that are specific to the nature of the interaction. The detected signals are then used to produce different modes of imagery (Fig. II.4) and to perform elemental analyses.

For instance, Secondary Electron Imagery (SEI) is provided by the detection of Secondary Electrons (SE) ejected from an atomic shell by ionization following the total energy transfer of an incident (primary) electron (Fig. II.3A) after collision. Secondary electrons have a low energy and their range in solids is quite small, on the order of a few microns. Only those emitted from the top hundreds of nanometers of the sample reach the detectors. The slightest variation in the surface topography will change the quantity of secondary electron collected. The variations of contrast on SE images correspond to the differences in the intensity of the detected signal and thus, to variations of topography. This characteristic makes SEI useful to study the surface structure of the sample, and the morphology of small 3D objects.

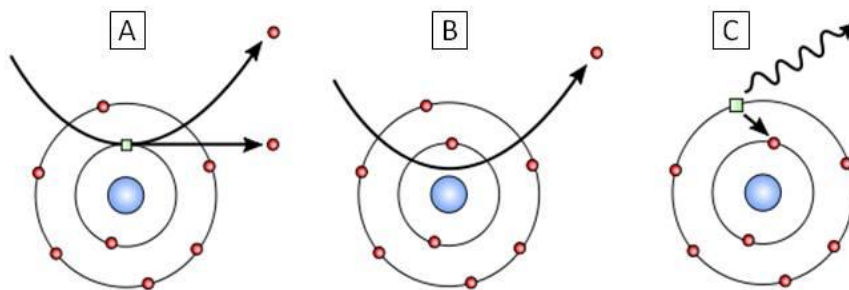


Figure II.3. Illustration of some electron-matter interactions induced during electron microscopy. A. Ionization and ejection of a secondary electron. The incident electron transfers some of its energy to another electron. If the energy transferred by the incident electron is sufficiently high, the atomic electron is ejected from the electronic cloud into the continuum. B. Quasi-elastic interaction: the incident electron interacts with the nucleus and is back-scattered, with a slight loss of energy that can be linked to the number of protons of the nucleus, and thus, to the chemical element. C. Ionization and emission of X-rays. A high-energy incident electron collides with an electron of an inner shell and ejects it. The electron hole created is filled by an electron from an outer shell. This electronic transition produces an X-ray with an energy equal to the difference between the two atomic shells, thus specific to the involved element. Reproduced with permission, according to the CC BY-SA 3.0 license.

The second imagery mode used in this study is based on the collection of Back-Scattered Electrons (BSE). BSE are emitted as a result of the *quasi-elastic* interaction between incident electrons and atomic nuclei (Fig. II.3B). Emitted electrons are detected with only a slight loss of energy with respect to the incident electron beam. The shift in energy of the detected BSE depends on the atomic number (Z , number of protons in the nucleus) of the emitting atom. The ‘heavier’ the atom (with a high Z), the more electrons are released, leading to a high intensity signal. Thus, in BSE images, areas containing high Z phases will appear brighter than areas with low Z phases (Fig. II.4 right). BSE imagery gives information on the composition of the scanned area, through a contrast of relative intensities between ‘light’ and ‘heavy’ chemical phases.

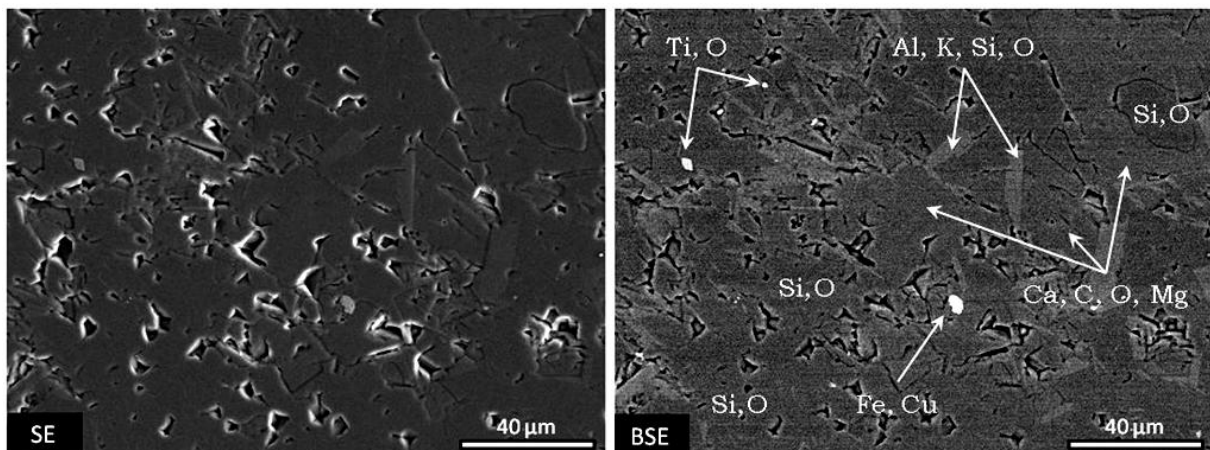


Figure II.4. Comparison between SE (left) and BSE (right) imagery modes by SEM, in the same zone of a thin section cut in a Pongola stromatolite. The SE image shows the surface topography, which, in this case, shows mainly the porosity remaining in the silica matrix. The BSE image highlights the differences in the chemical composition of the mineralogical phases. The heaviest phase, a grain of chalcopyrite CuFeS_2 (approximate average $Z = 22$) appears in bright white, while the lightest phase, the SiO_2 matrix (approximate average $Z = 10$), corresponds to the darkest regions.

If the SEM is equipped for Energy-Dispersive X-ray Spectroscopy (EDX or EDS) analyses, it is possible to obtain the elemental composition, for major to minor elements, at the surface of the sample. SEM/EDS analyses rely on the type of signal emitted after the ionization. A high-energy incident electron can excite an electron from an inner shell, leading to its ejection out of the

electronic cloud. This has the effect of creating an electron vacancy at the location of the ejected electron. In order for the atom to regain its stable state, an electron from a higher energy shell fills the vacancy. This electronic transition releases energy in the form of an X-ray, characteristic of the atom involved (Fig. II.3C). The different types of electronic transitions are illustrated in Figure II.5. The EDS spectrum shows the intensity of the signal versus the energies of the collected X-rays (in keV). By reading its position on the energy axis, each X-ray peak can be correlated to an electronic transition that is specific to a particular chemical element. The higher the atomic number, the higher the energy of the released X-ray. Light elements produce low-energy X-rays which are strongly absorbed in the sample before reaching the detectors. However, if the SEM operates under vacuum conditions, low *Z* elements such as carbon and oxygen can also be detected. If the sample is well polished, the EDS detector is also able to perform quantitative analyses of the detected element.

b. Coupled SEM/EDS analyses

Analyses were conducted on a Hitachi S4500 SEM fitted with an Oxford energy dispersive spectrometer equipped with a SATW Si(Li) detector (resolution 136 eV, 10 mm²) at the Centre de Microscopie Electronique (CME) de l'Université d'Orléans, France. Samples used were polished thin sections, coated beforehand with carbon at the same institute, and FIB sections. Measurements were performed at an accelerating voltage of 15 kV and a working distance of 25 mm (distance between the bottom of the objective lens and the sample). Elemental compositions were obtained in spots, averaged from rectangular zones, along profile lines, or by means of elemental mapping. Elemental quantification was performed with a 0.5% uncertainty, by means of single-element standards.

SEM/EDS analyses during this study were used for the following purposes:

- to perform a primary chemical characterization by mapping and quantification of the zones of interest previously identified by

petrographical observations and analyses, at the elemental level and for major to minor elements.

- SEM SE images assisted in the preparation of the FIB ultra-thin sections for synchrotron radiation analyses. Since the micrometric zones intended for FIB manufacturing were selected by optical microscopy, SEI was used to locate these zones a second time, with the same imagery system as the FIB setup.
- After synchrotron experiments, FIB sections were analyzed by SEM/EDS in order to map under vacuum the light elements virtually invisible by SR-XRF analyses at high energy, such as C, N, O and F.

The thin sections used were: Josefsdal 99SA07d, Pongola 07SA01, 07SA02A, 07SA03, Gunflint Schreiber Beach GF-55-1, and Gunflint Mink Mountain 07CA16. After synchrotron experiments, elemental mapping by SEM/EDS was made on the FIB sections. One of them was cut in a small 3D sample of the Josefsdal Chert in which the microbial mat is apparent at the surface and that is called “Josefsdal 3D”. Mapping by SEM/EDS was performed on several other FIB sections as well, cut in the following thin sections: Josefsdal 99SA07d, 12SA16, Pongola 07SA02, and Gunflint Schreiber Beach GF-55-1 and GF-55-1B.

II.4.2. Electron-probe microanalysis

a. Principle

Electron-probe microanalysis (EPMA) is a powerful, little-destructive technique based on the same physical principle and electron-matter interactions as the SEM. The elements of the sample emit characteristic (in energy and wavelength) X-rays when bombarded with a high-energy electron beam. In the same way as SEM, EPMA is capable of performing high-resolution EDS analyses and elemental mapping. However, its particularity relies on its capacities of detection and complete quantification of major to

trace elements as well by WDS (Wavelength-Dispersive X-ray spectroscopy), with a detection limit giving concentrations down to tens of part per million (ppm). Quantification is performed by comparing the intensities of the detected X-rays to the intensities of X-rays generated by reference materials.

b. Electron-probe microanalyses

Electron-probe microanalyses (EPMA) were conducted with the aim of studying the content and spatial distribution of trace elements in metal-sulfides. These analyses fall within the search for type B signatures through the petrographical and chemical study of metal-sulfides associated with fossilized photosynthetic microfossils. The complete study is reported in Chapter IV.

EPMA were performed at the Institut des Sciences de la Terre (ISTerre), Grenoble, France, on a JEOL JXA-8230 electron microprobe. Measurements were performed at an accelerating voltage of 15 kV and working distances of 11.3 mm and 11.2 mm. The micro-probe was calibrated for sulfide analyses and for the detection of S (K α), Fe (K α), Co (K α), Ni (K α), Cu (K α), As (L α), Se (L α), Mo (L α), Ag (L α), Cd (L α), Sb (L α) and Te (L α). Table II.1 summarizes the experimental conditions (detection limit (DL), acquisition time and standards). “T_{acq}” refers to the acquisition time at the element peak, and “Bckgrd T_{acq}” to the acquisition time on the background, which was measured before and after the peak. Quantitative measurements were performed on the standards listed below (see Table II.1; Pentl.: pentlandite, (Fe,Ni)₈S₉), systematically analyzed before and after each set of measures. Thin sections used were Pongola 07SA01, 07SA03, Gunflint Kakabeka Falls 07CA13, and a thin section named 03SA04 from the Hooggenoeg Formation, (Onverwacht Group, South Africa), that will be described in Chapter IV.

Table II.1: Detection limit (DL), acquisition time (T_{acq}) and standard used for each element considered during EPMA analyses.

Element	S	Fe	Co	Ni	Cu	As	Se	Mo	Ag	Cd	Sb	Te
DL (ppm)	49	38	59	73	85	35	22	59	38	37	45	42
T_{acq} (s)	40	30	40	30	20	60	30	30	30	30	30	30
Bckgrd T_{acq} (s)	20	15	20	15	10	30	15	15	15	15	15	15
Standard	CuFeS ₂	CuFeS ₂	CoO	Pentl.	CuFeS ₂	InAs	Se	Mo	Ag ₂ Te	CdS	Sb	Ag ₂ Te

II.5. Elemental analyses – Excitation by photons

X-ray Fluorescence (XRF) spectrometry and X-ray Absorption Near-Edge Structure (XANES) spectroscopy are non-destructive, penetrative, powerful techniques, allowing an *in situ* elemental investigation at the scale of only few-nanometers.

II.5.1. Principle of synchrotron radiation XRF and XANES

XRF and XANES rely on the interactions between a monochromatic X-ray beam and matter. The XRF technique is based on the photoelectric effect produced when an incident X-ray is absorbed by an atom, leading to the ejection of an electron (photoionization) from an inner shell (for example K, L, or M shell). As a result of this process, electronic transition mechanisms (Fig. II.3) take place, in order for the ionized atom to regain its stable state.

The transition of an electron from an outer shell (of lower atomic binding energy) toward the shell where an electronic vacancy is left after photoionization (Fig. II.5) induces the emission of a fluorescence photon. Since each electronic shell within an atom has its own characteristic binding energy, the resulting energy of the emitted fluorescence photon will depend on both the shells involved in the transition, and is thus specific of the emitting atom. Hence, the fluorescence signal collected during XRF analyses allows identifying the detected elements for each individually analyzed point or points of a map area. The XRF spectrum (Fig. II.6) shows the intensity of

the signal (in fluorescence counts) as a function of the fluorescence energy (in eV or keV). Each peak of fluorescence can be attributed to a chemical element by reading its corresponding energy, and using tables of X-ray emission energies.

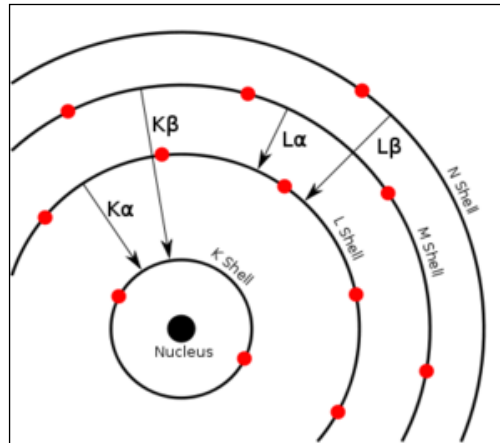


Figure II.5. Illustration of some of the electronic transitions occurring after photoionization, and their designations. K lines correspond to electronic transitions toward the K shell ($K\alpha$ for $L \rightarrow K$; $K\beta$ for $M \rightarrow K$, etc.), L lines to electronic transitions toward the L shell, etc.

Other mechanisms are involved when the incident photon beam interacts with the sample. The ‘elastic scattering’ also called Rayleigh scattering represents the portion of incident X-rays that have only superficially interacted with matter. These photons ‘bounced’ on atoms without any energy transfer to the atoms and are thus detected at various scattering angles without loss of energy with respect to the incident energy. Hence, on the XRF spectrum, they form a peak at the energy corresponding to the incident beam.

Compton scattering occurs when an incident photon collides with a loosely bound electron from the outer shell of an atom. The incident photon transfers part of its energy to an electron, so-called ‘recoil electron’ of lower energy. The amount of energy exchanged during this process depends on the scattering angle. The energy of the scattered photon, or Compton energy, can be calculated as follows:

$$E_c = E' = \frac{E}{1 + \frac{(1 - \cos\theta)E}{m_e c^2}}$$

where E_c is the Compton energy, or scattered energy (E'), E_0 is the incident energy (also corresponding to the Rayleigh scattering energy), θ is the scattering angle, and $m_e c^2$ is the electron rest mass energy (= 511 keV).

Multiple Compton scattering can be detected, leading to several Compton peaks on the spectrum, each time decremented by a different energy loss (C^* in Fig. II.6). The energies of the multiple Compton events can be calculated with the same equation than above, by replacing E_0 by E_c for the second Compton E_{C2} , and then E_c by E_{C2} for the third event, and so forth, provided the specific scattering angles are known.

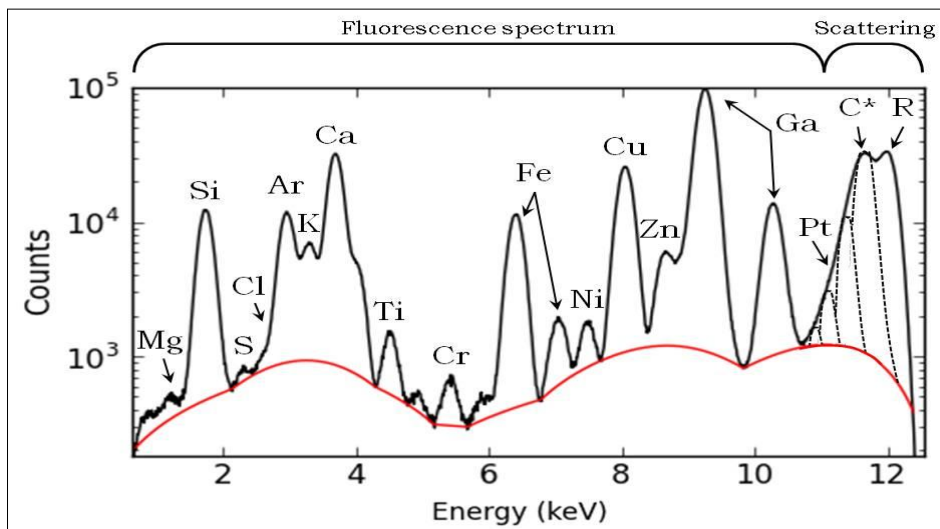


Figure II.6. XRF spectrum exhibiting fluorescence peaks and scattering peaks. The $E_{inc}=12$ keV. The sample analyzed here is a $\sim 10 \times 30 \times 3 \mu m$ FIB section cut through a microbial mat in the 3.33 Ga-old Josefsdal Chert. R: Rayleigh scattering, C^* : multiple Compton scattering, represented by schematic dashed line peaks. PyMCA software, ESRF Grenoble (Solé *et al.*, 2007).

These scattering peaks are considered as noise on the XRF spectrum. However, they can be of great interest in certain aspects of quantification since they indirectly relate to the average Z (atomic number) of the medium

crossed by these photons. During this work, I contributed to the development of a new quantification method for SR-XRF analyses using Compton and Rayleigh scatterings, exposed in Chapter V.

XANES is based on the same physical principle and interactions X-ray-matter as XRF. However, while XRF mapping is conducted at fixed incident energy and gives the spatial distribution of any detected element in the map area, XANES analyses are conducted with a variation of the incident energy around the inner shell electron binding energy (K, L or M shell) and on a localized spot. This technique allows determining the chemical speciation of a specific element at a precise, localized spot, by progressively varying the incident energy around the energy corresponding to the ionization threshold of the specific shell of the considered atom. In a sample that is heterogeneous at the micrometer scale, XRF mapping and transect analyses are required prior to XANES to accurately pinpoint the spot where the element of interest is the most concentrated. Figure II.7 shows an example of XANES spectrum for a titanium compound (from Bare, 2005). The position in energy of the inflection point (Fig. II.7), also called the edge (here K edge) or threshold, gives the oxidation state of the considered element when compared to XANES spectra of standards that can be organic or inorganic compounds.

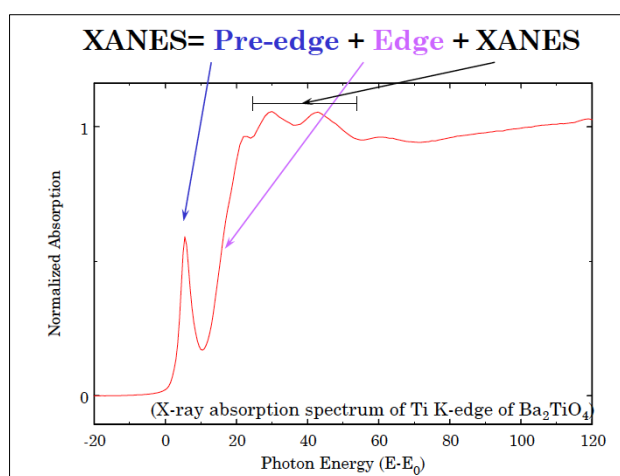


Figure II.7. An example of XANES spectra. The case study here is titanium, from Bare, 2005, UOP LL. The incident beam energy varies between 4.95 keV and 5.1 keV. Reproduced with permission of the author.

For instance, Figure II.8 shows the XANES spectrum at the sulfur K-edge of the cell-wall of a microfossil in a sample of sedimentary conglomerate of the 700-800 My-old Draken Formation, Svalbard (Lemelle *et al.*, 2008). Comparison with the energy of the edges of several sulfur standards, both organic and inorganic, allowed the authors to conclude that organic compounds persisted in the cell-wall of these 700-800 My-old microfossils since the analyzed sulfur displayed the same edge energy as the organic heterocyclic sulfur dibenzothiophene, or DBT.

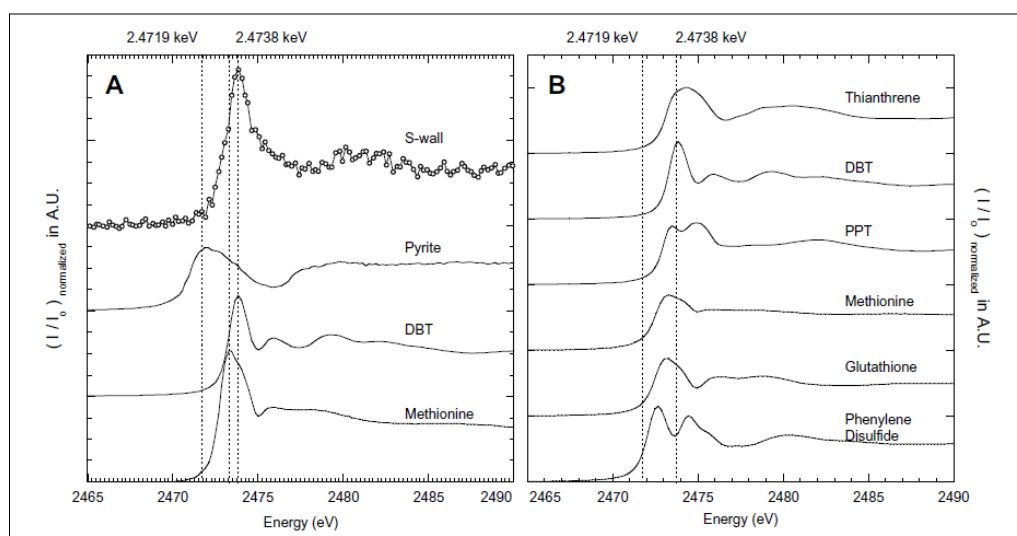


Figure II.8. XANES at the sulfur K-edge of the cell-wall of a microfossil (dotted line spectrum in A) in a sample of sedimentary conglomerate of the 700-800 My-old Draken Formation, Svalbard and comparison with standards (B). From Lemelle *et al.*, 2008.

II.5.2. Synchrotron beamlines used in this work

X-rays were traditionally produced by X-ray tubes, ever since their discovery, by W. Roentgen, in 1995. With the advent of synchrotrons, 1947 dedicated “X-ray factories” have been designed and built, spanning the gap from 1st generation synchrotrons, mainly used for nuclear physics electron beam experiments, where X-rays were used in parasitic modes, to 3rd generation synchrotrons (Fig. II.9). The latter were dedicated, high intensity, high energy machines of exceptional advantages, such as fluxes up to a few

million times higher than an X-ray tube. Another advantage is the natural spatial focusing of the X-rays generated in the specially designed new synchrotron sources, called “insertion devices”, which can be further focused by appropriate devices such as X-ray lenses or Kirkpatrick-Baez bent mirrors to nanometer scale beams. On these 3rd generation synchrotrons, dedicated beamlines were built, making use of various properties of the beams produced by the insertion devices (ID).



Figure II.9. Distribution of the synchrotrons of 1st (yellow), 2nd (orange) and 3rd (in progress) generations.

For the present work, synchrotron radiation experiments were carried out at the ID21 and ID22 NI beamlines of the European Synchrotron Radiation Facility (ESRF) in Grenoble, France, and at the mySpot beamline of the Bessy II synchrotron, Helmholtz Zentrum Berlin (HZB), Berlin, Germany.

Access to these beamlines is highly competitive and authorized by international beamtime allocation committees which rate the proposals based on scientific and technical criteria. Overbooking reaches 800% at ID22 NI and about 300% at mySpot. Both flux and focusing beamline

characteristics of mySpot are more modest but they are quite sufficient for some of our analyses.

a. ID 21 and ID 22 NI at the ESRF, Grenoble

ESRF is a 3rd generation source which features beamlines producing extremely high fluxes (1×10^{13} ph/s) of white ($E < 50$ keV) or monochromatic energy ($1 < E < 120$ keV) focused down to tens of nanometer scales. Experiments are performed on specific beamlines, optimized for the properties of the wanted elements or compounds. Beamlines are available for instance for investigating X-ray fluorescence of low ($6 < Z < 14$), or high ($14 < Z < 92$) atomic number elements, X-ray diffraction of various crystalline compounds, tomography for 3D morphology imaging of various materials, or speciation (XAS) for probing the chemical environment of a specific atom in a compound.

The ID21 beamline (Fig. II.10) was chosen for its capacity to perform low energy low Z XRF imaging then XANES on low Z edges (sulfur K edge ≈ 2.47 keV, performed under vacuum), with fairly high resolution ($0.3\text{--}1 \mu\text{m}$).

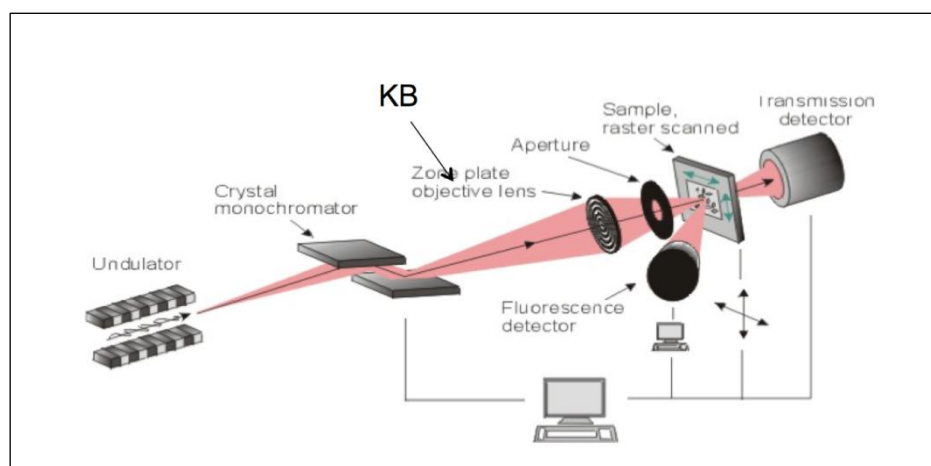


Figure II.10. ID21 low energy imaging beamline schematics. KB: Kirkpatrick-Baez bent mirrors.

Focusing on ID21 is performed either by Fresnel Zone lenses or by double bent mirrors (Kirkpatrick-Baez; KB in Fig. II.10) for energies up to the Ni K edge. Measurements are made under vacuum, which requires dry samples,

of low porosity which can be easily pumped down to 1×10^{-6} bars. Minimum Detection Limits (MDLs) are in the 200 ppm range for a 1 second exposure.

ID22 NI (Fig. II.11) was used for nanoimaging of light to heavy elements, at high energy 17-17.5 keV and at high spatial resolution (100 - 200 nm) in our stromatolite and sandy sediments samples, yielding distributions of the elements from ~Mg-Al to ~As, thus including life-related elements such as S, Mg, K, elements contained in biominerals such as Ca, or in the siliceous matrix such as Si and redox-sensitive transition metals. As the beam is used in PINK mode (low energy resolution, high flux, $\Delta E/E \approx 100$), intensity in the few hundred nanometer spots reaches 1×10^{12} which imposes a limit on the sample resistance to beam damage. However, MDLs are in the tens of ppm for a 1 second exposure. Experiments are performed in the air, allowing fast sample changes and easy access.

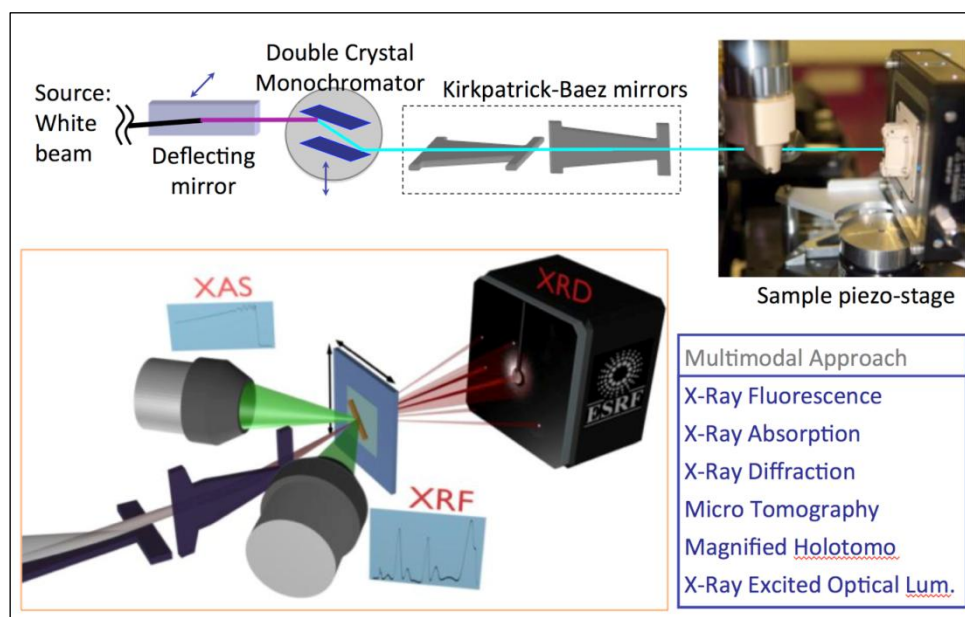


Figure II.11. ID22 NI high energy imaging beamline schematics.

Fluxes on these beamlines during analyses were in the 1×10^9 - 1×10^{11} photons/second range in the beam spot, at energies between 2.4 and 17 keV.

b. MySpot beamline, Bessy II, Berlin

The mySpot beamline offers a $>1 \mu\text{m}$ resolution and a flux of $<5 \times 10^9$ photons/second. This beamline uses a Si (110) monochromator and monocapillary focusing optics which are extremely stable and cover the monochromatic energy range from 4 to 20 keV. XRF ($14 < Z < 92$) and XANES ($Z \geq \text{Ca}$) analyses can easily be performed in the air, but low Z element quantification is more difficult. MDLs which are linearly dependent on the flux are thus higher, reaching 100-500 ppm for most elements between Ca and Zn. Figure II.12 shows the experimental setup at the mySpot beamline.

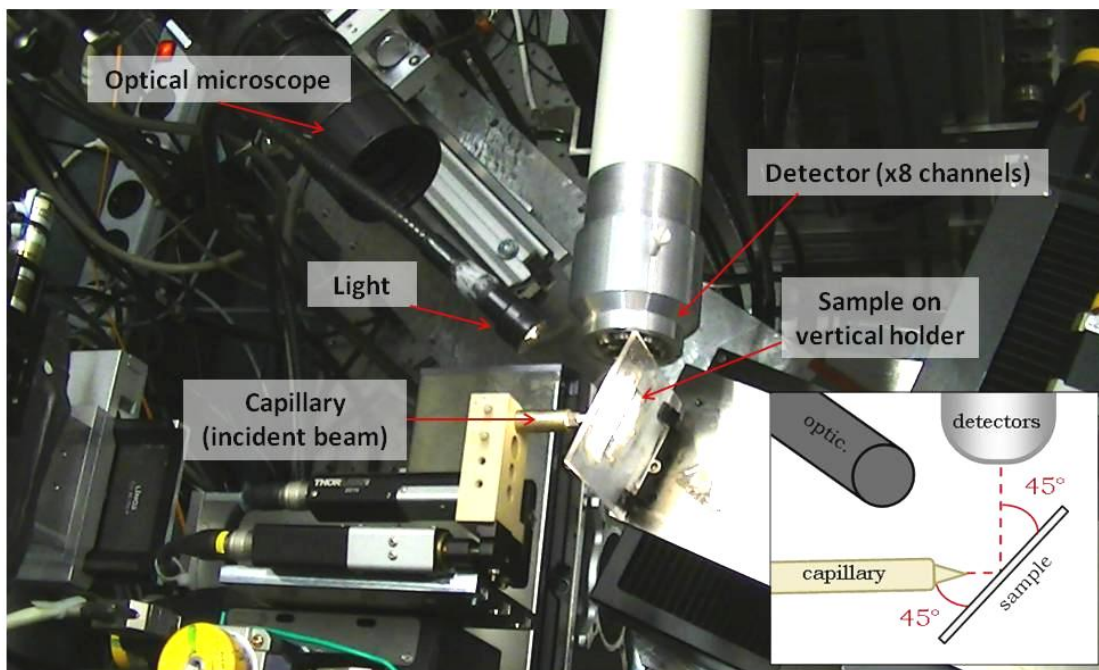


Figure II.12. Experimental setup at the 'mySpot' beamline, BessyII HZB, seen from above, and schematic representation (box).

Synchrotron radiation μ -XRF analyses were focused on samples from the 3.33 Ga-old Josefsdal Chert and the 1.88 Ga-old Gunflint Chert (Schreiber beach locality). The FIB sections used were cut through silicified biofilms from the thin sections 99SA07d, 12SA16 and from sample 'Josefsdal 3D' of the Josefsdal Chert, and through individual fossilized cells from the thin section GF-55-1 of the Gunflint Chert. A detailed description of these FIB samples is given in Chapter V.

c. Note on the XANES analyses

The ability of XANES analyses, which are non-destructive, to provide insights into the oxidation states of light to heavy elements at the micrometric scale makes this technique relevant for the topic of this study. Indeed, determining the oxidation state of light elements such as sulfur allows differentiating between organic and mineralogical compounds (e.g. Lemelle *et al.*, 2008) and thus allows characterizing remains of organic matter. The oxidation state of transition metals such as Fe and Mn in both mineralogical and biological parts of our samples may provide information on the redox conditions in the immediate environment of the microfossils, and possibly on the associated biochemical processes (e.g. biomineralization, use of Fe compounds as electron donors for the functioning of the photosynthetic machinery). Therefore, XANES analyses at the Fe K-edge were conducted at the mySpot beamline on a FIB sample cut through a fossilized microbial mat from the Josefsdal Chert. However, preliminary results highlighted the need for further calibration, probably due to the insufficient concentration of iron in the analyzed sample. Preliminary Fe-XANES results are thus inconclusive at this stage of the study. Nonetheless, sample preparation and the thorough selection of zones of interest were continued in view of conducting XANES at the Fe and Mn K-edges again during next synchrotron analyses campaigns.

II.6. Isotope analyses

Carbon isotope analyses were made prior to this study and already established that carbon was biogenic and consistent with the photosynthetic pathway (e.g. for the Josefsdal biofilms: Westall *et al.*, 2006, 2011b, 2015; for the Gunflint stromatolites at Schreiber Beach: Williford *et al.*, 2013; see Chapter I). The late diagenetically altered Pongola stromatolites yield $\delta^{13}\text{C}$ values consistent with marine carbonates rather than biological carbon. However, differentiating between anoxygenic and oxygenic photosynthetic

bacteria on the sole basis of the isotopic composition of carbon is not possible since they have overlapping $\delta^{13}\text{C}$ signatures. In addition, as Precambrian microbial remains are found in mat-like arrangements, the isotopic signature of photosynthetic bacteria is likely to be mixed with that of other autotrophic and even heterotrophic microbes preserved in the same mats. With the aim of overcoming this challenge, a first step would be to couple carbon isotopes analyses with the isotope analyses of other biologically-related elements, and the isotopic analytical techniques used should be able to discriminate, to a certain extent, between the different types of microbes present in the samples analyzed, either spatially, or by means of carbonaceous compounds separation. To this purpose, we used (i) Secondary Ion Mass Spectrometry (SIMS) for the *in situ* measurement of $\delta^{13}\text{C}$ and $\delta^{34}\text{S}$ within polished thin sections, and (ii) stepped-combustion mass spectrometry (MS) to obtain the $\delta^{13}\text{C}$ and $\delta^{15}\text{N}$ values of carbonaceous compounds extracted from small rock samples.

Since they involve the pulverization or the gasification and collection of material from the sample, isotopic analyses are destructive techniques. The interest of S and C *in situ* isotope analyses by SIMS relies on the fact that they are conducted directly in the same thin sections that are used for petrographical analyses, SEM/EDS and EPMA, as well as FIB section preparation, allowing determining a precise localization for each spot measurement that will be the most relevant for the study. Because the support used is the same than for the other observational and analytical techniques, *in situ* isotopic analyses were performed at the last stage of the analytical procedure. N and C isotopes analyses by stepped-combustion MS were made separately on small rock samples corresponding to duplicates of the thin sections used for the previously described analyses.

II.6.1. Carbon and sulfur isotopes - In situ measurements by Secondary Ion Mass Spectrometry

Secondary Ion Mass Spectrometry (SIMS) is a chemical analytical technique able to measure isotope distributions directly within a solid

sample by spot analyses. This technique thus offers the possibility to measure the isotopic composition of C and S of targeted areas within fine layers and clusters of organic matter.

a. Principle

The principle of SIMS, also called ion-probe, relies on the detection of the secondary ions ejected when a sample is bombarded with a high-energy focused beam of (primary) ions (generally Cs^+ , or O^-). The contact between a primary ion and the surface of the sample has the effect of displacing atoms that will then collide with the surrounding atoms. Atoms located at the surface of the sample are ejected. When ejected as ions, they are called secondary ions and are collected and analyzed with a mass spectrometer, where the mass to charge (m/q) ratios are measured to determine the elemental and isotopic composition of the material pulverized (few nm^3) during this process. The extent of matter removed by pulverization and the dimensions of the resulting pit depend principally on the spot size of the incident beam.

b. S and C in situ isotope analyses by SIMS

Since secondary ions are ejected from the surface of the sample, SIMS analyses require an uncontaminated surface with respects to the elements of interest in the analysis. Thin sections were thus coated with gold not carbon, at the Centre de Recherche Pétrographiques et Géochimiques (CRPG), CNRS Nancy, France, where SIMS analyses were performed on a Caméca 1280 IMS. Thin sections used were: Josefsdal 99SA07d and Gunflint Schreiber Beach GF-55-1. They were resized to obtain the required dimensions of 22x25 mm of the sample holder at the CRPG. The parameters of the primary Cs^+ ion beam were as follows: a 10 nA intensity, and a 10 kV voltage. Mass resolution (or mass resolving power, MRP, is defined by $M/\Delta M$ where M is the mass and ΔM the width of the peak at 10% of its height) reached 3800 for sulfur and 4500 for carbon. The spot size was 25 μm in diameter.

II.6.2. Nitrogen and Carbon isotopes - Stepped-combustion static mass spectrometry

Stepped-combustion MS is another useful analytical technique to overcome the challenge of mixed-signatures of isotopes analyses within Precambrian microbial mats. If the kerogen analyzed contains several compounds comprising carbon and nitrogen, this technique is able to release the C and the N in a sequential manner, allowing the content and isotope composition of these elements to be determined for each compound separately.

a. Principle

During stepped-combustion mass spectrometry, samples are heated progressively toward higher temperatures in a step-wise manner. Steps usually consist of 50°C to 100°C intervals, for a duration of 30 or 40 minutes. This process can take place under vacuum or in an oxygen atmosphere (respectively called pyrolysis or combustion). At the end of each step, gases produced by the escape of C and N under heating are collected, purified and quantified. Gases are then accepted into the mass spectrometer, where the isotopic composition of each element is measured.

A detailed description of the principles and technical aspects of stepped-combustion MS, as well as applications to C and N isotope analyses, is given in Boyd, 2004.

b. N and C isotopes analyses by stepped-combustion static MS

Analyses were performed by Dr. Alexander B. Verchovsky at the Centre for Earth, Planetary, Space and Astronomical Research (CEPSAR), at the Open University, Milton Keynes, United Kingdom. Samples were analyzed by stepped-combustion and static mass spectrometry simultaneously for C and N on the 'Finesse' instrument in an oxygen atmosphere provided by a CuO-Cu₂O furnace, at a pressure of 10 mbar. Small aliquots from pieces of

handsamples corresponding to the duplicates of the thin sections Josefsdal 12SA09, Pongola 07SA01 and Gunflint Schreiber Beach 07CA05 were used for analyses.

Measurements were performed from 200°C to 1400°C with 100°C increments, and with 50°C increments between 600 and 900°C. A supplementary step at 950 °C was made during the analysis of the Josefsdal sample. Heating intervals were 30 minutes each, extended by an additional 20 minutes in order for the oxygen to resorb on CuO. For all measurements and samples taken together, error bars were comprised between 0.1 and 0.6 ‰ for $\delta^{13}\text{C}$ and 0.2 and 0.8 ‰ for $\delta^{15}\text{N}$. Error values of 3.2 and 5.2 ‰ were recorded for the Josefsdal sample at temperatures 1200°C and 1400°C respectively. Thus, isotope values corresponding to temperatures above 1100°C were not taken into account for the Josefsdal sample.

Standards used for the calculation of $\delta^{13}\text{C}$ and $\delta^{15}\text{N}$ were the $\delta^{13}\text{C}$ value of the Pee Dee belemnite and the $\delta^{15}\text{N}$ value of air.

II.7. Preliminary conclusions on analytical methodology

This Chapter presents a large range of analytical techniques, which are all essential to the current study. Indeed, some of these techniques are necessary to understand the history of the sample and to localize the zones of interest before any other more specialized chemical analyses are made, while others are technically capable of finding type A or type B signatures of oxygenic photosynthesis. However, their ability to do so is evaluated in the following Part of this manuscript.

Overall, they respect the constraints imposed by the topic of this study, namely the ability to provide *in situ* geochemical and mineralogical information at the μm or sub- μm scales, while being as non-destructive as much as possible. The only destructive analyses, the isotopic measurements, were carefully performed last in the analytical suite.

Part 3: Results

Chapitre III : résumé

Etude pétrographique

Ce chapitre présente l'étude bibliographique et les observations pétrographiques faites sur les échantillons disponibles au Centre de Biophysique Moléculaire, CNRS Orléans, France, et discute de leur pertinence concernant le sujet de cette étude.

Les roches datant de l'Archéen et du Paléoproterozoïque sont peu fréquentes et souvent très métamorphisées. Cependant, il a été possible de sélectionner des échantillons de roches sédimentaires formées dans des milieux marins peu profonds datant de 3,33 Ga à 1,88 Ga, qui n'ont été soumis qu'à un métamorphisme de bas degré allant de la diagénèse (métamorphisme d'enfouissement ; par exemple, les échantillons de Gunflint) à un métamorphisme de type schistes verts (par exemple, les stromatolithes de Pongola et le chert de Josefsdal).

Les échantillons sélectionnés couvrent, de par leur âge, la période de temps d'intérêt, c'est-à-dire depuis un milliard d'année avant le GOE, lorsque la Terre était anoxique et que la photosynthèse anoxygénique était en place, jusqu'à ~500 millions d'années après le GOE, lorsque l'atmosphère et les océans étaient globalement oxygénés, et que la photosynthèse oxygénique était très probablement déjà bien développée.

Les échantillons sélectionnés contiennent tous des indices de vie photosynthétique, sous la forme de cellules microbiennes fossiles, de biofilms et tapis microbiens fossiles et de structures stromatolithiques.

Les analyses de la matière organique contenue dans ces échantillons faites en amont de cette étude (par spectroscopie Raman, MEB, MET, ToF-SIMS, μ XRF, analyses *in situ* des isotopes de carbone), supportées par la littérature ainsi que par des analyses chimiques et isotopiques complémentaires faites dans cette étude, indiquent (à l'exception des stromatolithes de Pongola), que le carbone est syngénétique, d'origine biologique, et qu'au moins une partie

de cette matière organique correspond à des restes de microorganismes photosynthétiques.

Ces échantillons ne présentent pas de signes indiquant une contamination secondaire, après lithification. Cela est confirmé par les observations en microscopie (optique et électronique) faites dans cette étude. La plupart de nos échantillons contient, non seulement de la matière organique fossile, mais aussi des cellules microbiennes fossiles bien préservées par une silicification rapide, tôt dans l'histoire de dépôt des sédiments considérés.

Le Tableau III.1 donne les principales caractéristiques pour la liste d'échantillons sélectionnés. Les contraintes mentionnées dans le Chapitre II quant à la sélection des échantillons sont respectées. Les échantillons sélectionnés sont donc pertinents pour cette étude.

Chapter III: Petrographical study

This Chapter presents in a first part the bibliographic research and the results of the petrographical investigations made on the samples available at the Centre de Biophysique Moléculaire, CNRS Orléans, France, in order to discuss their relevance with respect to this study and to the criteria presented in Chapter II. In the second part, the question of the preservation of the chemical and isotopic compositions of the original sediments through post-depositional processes is assessed. Then, selected samples are listed and conclusions are drawn.

III.1. Sample presentation – Petrographic observations

The Josefsdal Chert samples have been well described previously, thus the section on Josefsdal Chert samples is mainly based on published research. Samples from the Pongola and Gunflint stromatolites required further petrographical observations and analyses in order to identify the zones of interest and thoroughly understand the context of formation of these sediments, which is debated in the literature.

III.1.1. Josefsdal Chert, Kaapvaal Craton, South Africa

The Josefsdal Chert (JC) crops out at the top of the Kromberg Formation of the Onverwacht Group volcano-sedimentary sequence, located in the Josefsdal Valley, Barberton Greenstone Belt, South Africa. Further stratigraphic details can be found in Lowe & Byerly 1999. It is mapped as the K3c chert (Lowe & Byerly, 1999) which is dated at ~3.33 Ga (Byerly *et al.*, 1996). These rocks consist of black and blue, banded black and white, and greenish and black silicified sediments deposited on top of pillow basalts, also silicified in their upper parts. The black layers contain organic

matter in the form of deposited detritus as well as remnants of clots and laminated microbial mats (Westall *et al.*, 2001, 2006, 2011b, 2015; Fig. III.1, Fig. III.2). Sedimentary structures indicate that the sediment was deposited in a shallow marine environment ranging from shore face to upper shore face (tidal) in depth (Westall *et al.*, 2015; Fig. III.1D-E). The study of the organic matter (optical microscopy, Raman spectrometry, scanning electron microscopy, *in situ* carbon isotopes measurements) revealed that the JC microbiota was diverse and part of a complex, interacting microbe-sediment system with microbial mats coherent with the activity of anoxygenic photosynthetic bacteria and sulfate-reducing bacteria (SRB) (Westall *et al.*, 2001, 2006, 2011b, 2015), and with associated clotted remnants of chemolithotrophic and chemo-organotrophic bacteria (Westall *et al.*, 2015).

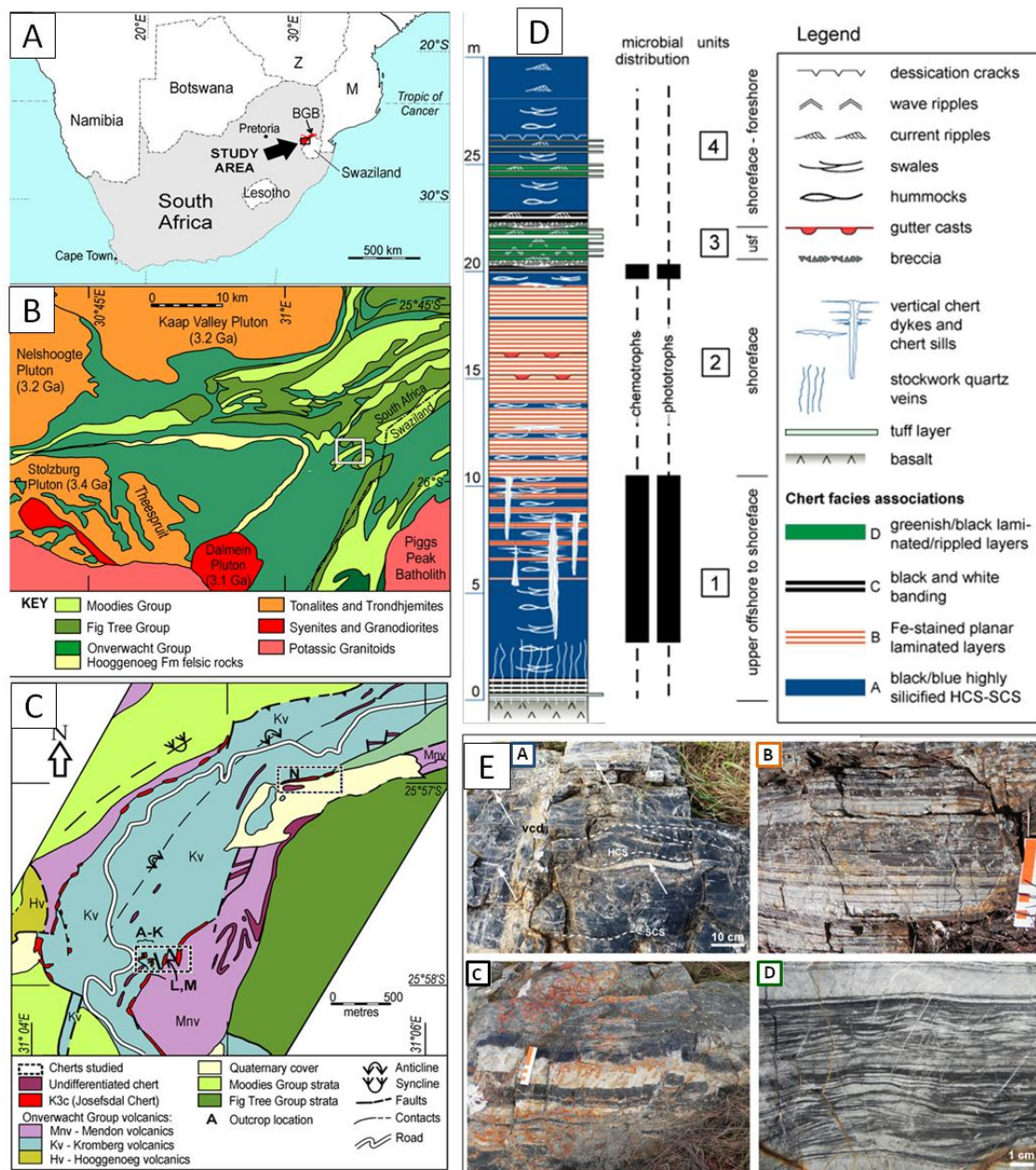


Figure III.1. General location of the Josefsdal Chert in the Kaapvaal Craton, South Africa, and stratigraphic description. Note that phototrophs and chemotrophs have been documented in all facies, and specifically in black/blue and black and white cherts. From Westall *et al.*, 2015.

The uncompacted shape of the clusters of organic matter (detrital or formed by bacterial activity) suggests that the sediment was silicified very early after deposition, preventing its deformation by compaction. The extent of silica replacement (85 to 99% SiO₂) is such that the diversity of the mineralogy of the JC is limited. The JC is composed mostly of microcrystalline quartz (mesocrystalline quartz and megacrystalline quartz in fluid infiltration

features, e.g. veins and vugs), occasionally with remnant muscovite in chert-pseudomorphed volcanic detrital particles, and carbonaceous matter, associated with micrometric grains of pyrite, anatase, and rutile. Some evaporite minerals have also been documented (aragonite, gypsum or anhydrite, Mg-calcite, and halite), as well as nanograins of aragonite (Westall *et al.*, 2001, 2006, 2011b).

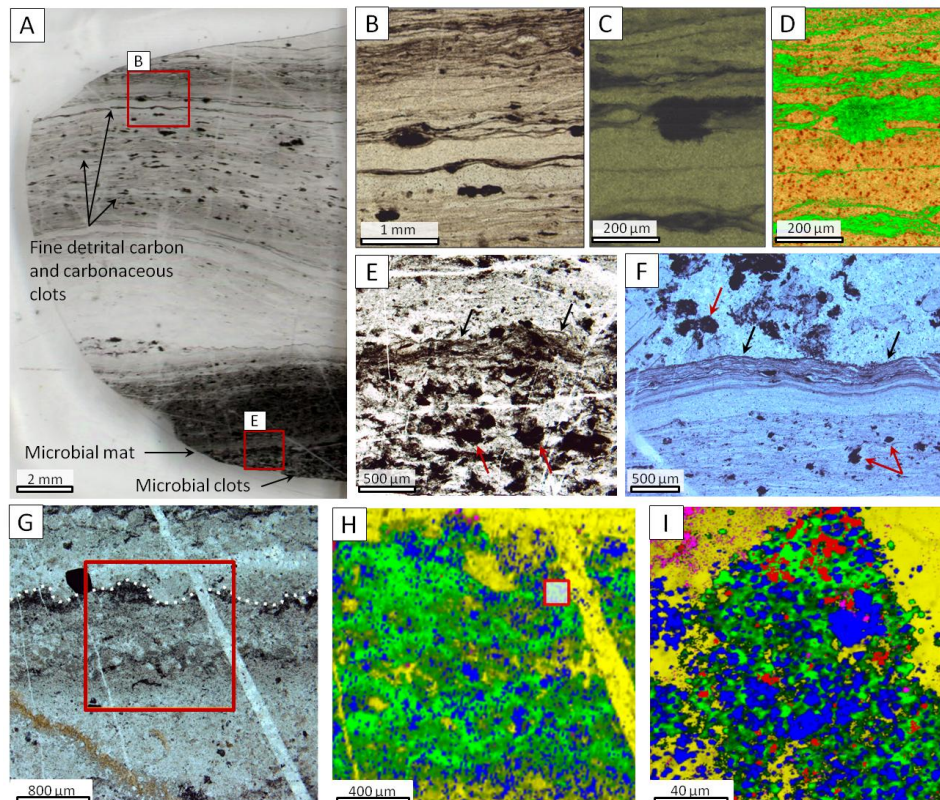


Figure III.2. Distribution and texture of the carbonaceous matter in the Josefsdal Chert. A. Thin section presenting microbial mats and clots in the lower part and detritally-deposited carbon and clots in the upper part. Red boxes denote details of these two carbonaceous matter types shown in B and E. B-D. Detrital carbon and clots. B. Optical micrograph (plane polarized light), detail of detrital carbon and clots from A. C-D. Raman spectrometry map of deposited carbonaceous matter. C. Optical micrograph of the analyzed zone and D. compositional Raman map. Green: carbon, orange: quartz. E-F. Details of microbial mats and clots. Optical micrographs, plane polarized light. Black arrows indicate the photosynthetic mats, red arrows indicate chemotrophic clots. G-I. Modified from Westall *et al.*, 2015. Raman analyses in a zone showing the carbonaceous remains of a poorly preserved photosynthetic biofilm. G. Optical micrograph showing carbonaceous matter and pyrite (euohedral, ~300µm crystal, and microcrystalline) in the phototrophic biofilm (dotted white line). Red box denotes the area of the Raman map in H. H-I. Raman maps showing noticeable concentrations of carbon (green), anatase (blue) and pyrite (red) in a quartz matrix (yellow). Some muscovite is also visible (fuchsia). Red box in H indicates the area of the Raman map in I.

Ten thin sections from the Josefsdal Chert outcrop were studied. Their designations begin with 99SA, 10SA, 12SA.

III.1.2. Pongola stromatolites, Kaapvaal Craton, South Africa

Silicified stromatolites analyzed were sampled in the ~2.98-2.95 Ga Nsuze Group (Mukasa *et al.*, 2013) of the Pongola Supergroup (South Africa). The Nsuze Group is a volcano-sedimentary sequence, predominantly volcanic, which contains minor sedimentary sequences such as the White Mfolozi Formation (Fig. III.3). This particular formation contains silicified dolomite horizons, one of which, the Chobeni Member, displays stromatolites. These carbonates were formed in shallow, low energy environments, such as the tidal zone, during periods of reduced volcanic activity (von Brunn & Mason, 1977; Beukes & Lowe, 1989; Wilson *et al.*, 2013), allowing the development of bacterial colonies. Although microcrystalline quartz is the predominant mineral phase, the Pongola stromatolites exhibit a larger mineralogical variety than the Josefsdal Chert. The siliciclastic nature of the laminae (Fig. III.4) indicates that their formation was strongly influenced by the surrounding volcanic environment. Dolomite is present as ≥ 20 μm crystallites and anhedral altered crystals, and as 50-150 μm subhedral to euhedral crystals. The latter probably formed during diagenetic recrystallization and contain inclusions of the same composition and size than the surrounding sediment (such as anatase, quartz, rutile; Fig. III.5E). The presence of muscovite, sometime associated to dolomite, is indicative of a greenschist facies degree of metamorphism. The stromatolitic layering is highlighted by the grain-size sorting of detrital grains within the laminations and by fine brownish-dark micro layers of altered dolomite crystals (Fig. III.5). Concavities between stromatolitic domes are filled with detrital material: carbonates, siliciclastic grains, and rounded clasts of quartz (Fig. III.4).

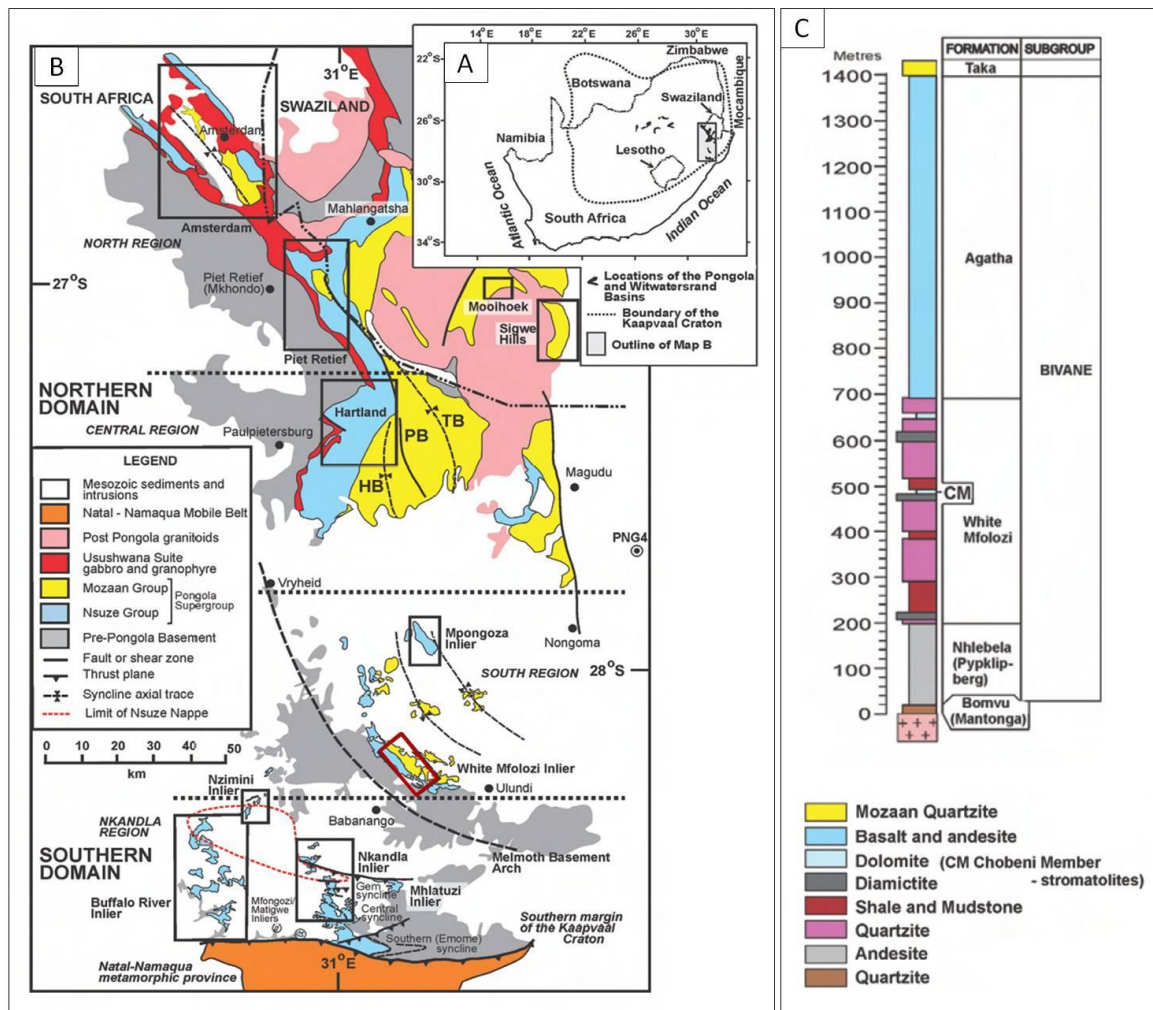


Figure III.3. Geology of the Pongola Supergroup, Kaapvaal Craton, South Africa. A and B. Location of the White Mfolozi Formation (red box) in the Pongola Supergroup. C. Geology and stratigraphy at the red box location showing the stromatolites-bearing Chobeni Member (CM) in the White Mfolozi Formation. Modified from Wilson *et al.*, 2013.

Although fossils of microbial mats and possible mineralized cellular fossils (replaced by chert, pyrite and hematite) were documented in the younger Mozaan Group sediments (Pongola Supergroup) by Noffke *et al.*, 2003 and Noffke 2010, no fossilized bacterial mats or cells were observed in our stromatolite samples from the Chobeni Member of the Nsuzze Group. Carbonate rearrangement and growth during diagenesis is most likely responsible for the alteration of the microbial mats and cells that were already decaying at this stage (Grotzinger & Knoll, 1999; Schopf, 2007). The typical convex-upward doming with thickening of the layers over the flexure

crests shows, however, the implication of trapping and binding by phototactic microorganisms. Thus, the absence of fossilized microbiota in these stromatolites argues in favor of a late silicification rather than an abiotic origin of these structures.

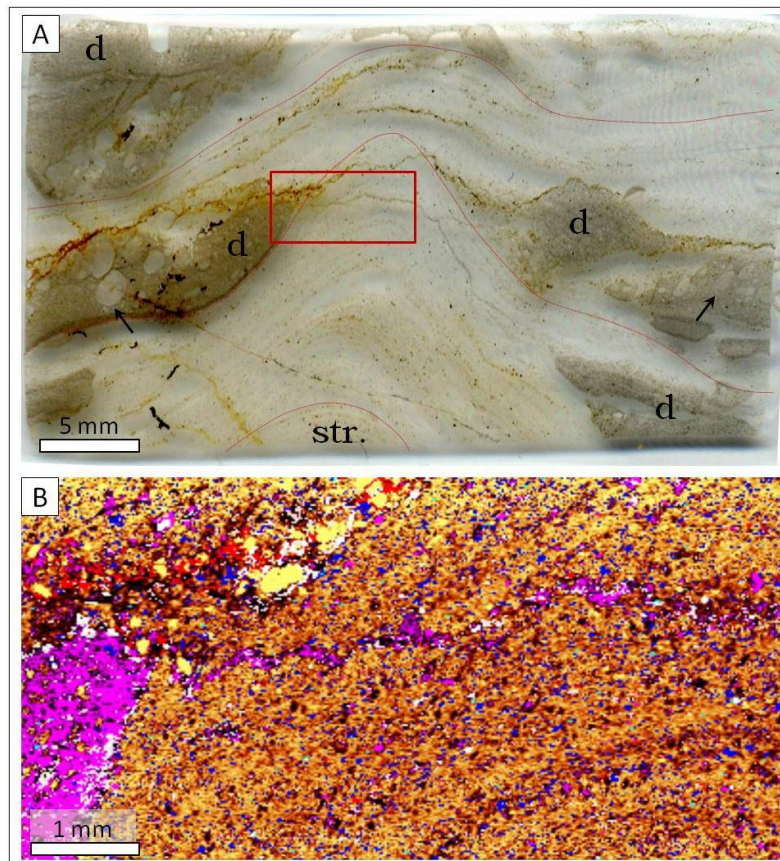


Figure III.4. A. Thin section of sample 07SA01, Pongola stromatolites. Red dashed lines outline the small stromatolitic domical structure; d: detrital material. Black arrows show rounded clasts of quartz. The red box shows the area of the Raman map in B. B. Raman spectrometry map of the stromatolitic laminations, detrital material and probable stylolite. Orange-brown: quartz; fuchsia: dolomite; dark blue: anatase; pale blue: apatite; red: rutile; pale pink: muscovite.

However, there is still an ongoing discussion about the type of photosynthetic bacteria responsible for the formation of the Pongola stromatolites. Several authors argue in favor of the oxygenic photosynthesis hypothesis (for example Beukes & Lowe, 1989; Bosak *et al.*, 2009; for the Mozaan Group: Noffke *et al.*, 2003). Others support this same assumption as an indirect deduction after showing that substantial quantities of free oxygen were present in the water column at that time (Planavsky *et al.*, 2014).

However, since no microfossils were recovered from these particular stromatolites, and because anoxygenic photosynthetic bacteria as well have experimentally proved able to form stromatolites (Bosak *et al.*, 2007), determining the type of micro-organisms involved remains a matter of controversy.

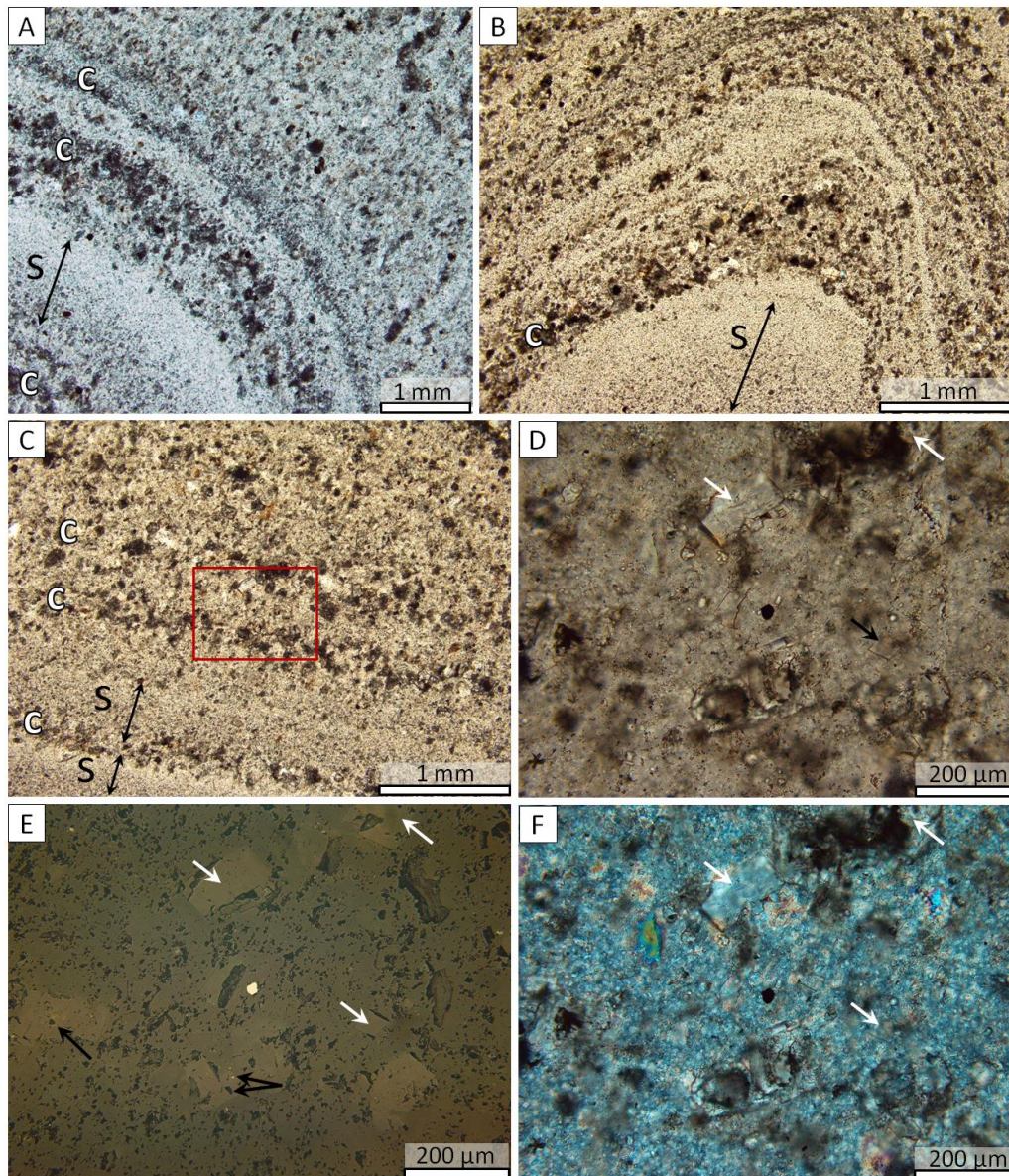


Figure III.5. Optical micrographs of Pongola stromatolites (samples 07SA01 and 07SA02A). A-C. Domical or planar layering, plane polarized light. Laminations are highlighted by detrital grains sorting (s) and dark layers of degraded carbonates (c). Red box in C indicates the position of D-F. D-F. Detail of altered carbonates. Same zone, with from D to F, plane polarized, reflected, and cross polarized light respectively. White arrows show diagenetic subhedral to euhedral dolomites. Black arrows in E point to matrix inclusions in diagenetic dolomites (anatase, rutile, quartz).

Three thin sections from the Pongola stromatolites were studied. Their designations are 07SA01, 07SA02A, and 07SA03.

III.1.3 Gunflint Iron Formation, Animikie Basin, Canada

The marine sediments of the ~1.88 Ga-old Gunflint Iron Formation (Fralick *et al.*, 2002) are exposed in the Animikie Basin of the Lake Superior Region (Ontario, Canada) (Fig. III.6). They overlie continental margin shelf deposits formed on a 2.7 Ga-old peneplaned Archean craton (further details on general geology and stratigraphy in Goodwin 1956 and Ojakangas *et al.*, 2001), and record several transgression-regression cycles. This formation contains a diversity of stromatolitic cherts, in which quartz is more abundant than iron compounds. If there is a consensus of opinion toward a hydrothermal source for the iron (Derry & Jacobsen, 1990; Hamade *et al.*, 2003), the origin of silica in these cherts has long been considered hydrothermal as well, until Hamade *et al.* (2003), using Ge/Si ratios, suggested that silica could have been predominantly provided to the ocean by continental weathering.

Regardless of the silica source, stromatolites from the Gunflint Formation were extensively silicified and are mostly composed of microcrystalline to megacrystalline quartz. Stromatolitic laminations are highlighted by differences in quartz crystal sizes and by variations in the abundance of iron in the chert matrix (Fig. III.6B-G) (Maliva *et al.*, 2005). In some samples, chalcedonic quartz is also present, and occurs as pore-filling (supported by straight boundaries between adjacent growth and triple points where the growths meet), often accompanied by detrital organic matter and iron-oxides (in this case chalcedony displays botryoidal habits) (Fig. III.7).

Samples were taken from the Schreiber Beach, Kakabeka Falls and Mink Mountain localities of the Gunflint Formation (Fig. III.6A, modified from Planavsky *et al.*, 2009). These sediments have undergone low degrees of diagenesis and metamorphism, with a maximal regional metamorphism reaching only sub-greenschist facies (e.g. Mink Mountain samples) (French,

1973; temperature slightly above burial diagenesis: Winter & Knauth, 1992; estimated maximum burial temperature: 100-130°C, Miyano & Klein, 1986), while Schreiber Beach and Kakabeka samples are described as unmetamorphosed (e.g. Shapiro & Konhauser, 2015) (this is supported by Raman spectra of the carbonaceous matter; for instance, Foucher *et al.*, 2015; see Fig. II.2). For these reasons, the Gunflint cherts offer a unique assemblage of well-preserved, morphologically various microfossils.

Gunflint sediments correspond to shallow water, subtidal shelf to intertidal deposits (Awaramik & Barghoorn, 1977; Ojakangas *et al.*, 2001; Fralick *et al.*, 2002; Planavsky *et al.*, 2009). However, the morphology and chemical composition of these stromatolites vary between the three localities. There is a gradual variation from stromatolites with laminations containing abundant microfossils, diffuse organic matter, and iron oxides (e.g. Schreiber Beach), to those with dense, iron-rich laminations, with low organic matter content (e.g. Mink Mountain). Planavsky *et al.* (2009) interpreted these variations of organic matter content as reflecting the control of the original relative abundances of Fe and Si in the sediment on diagenetic alteration and degradation of microorganisms.

Regardless of their carbonaceous matter preservation, Gunflint microbiota systematically exhibit iron-oxides coatings, although the extent varies between the three localities. Two models have been presented to explain the mineralization process of these iron-coatings. The 'biological model' (e.g. Schelble *et al.*, 2004; Planavsky *et al.*, 2009; Wilson *et al.*, 2010) stipulates that it is a primary feature formed under the influence of iron-oxidizing bacteria that stimulated the precipitation of iron oxyhydroxides on their sheaths, later transformed to hematite and preserved by silicification. This model, however, does not account for the differences of preservation (relative proportions of carbonaceous matter and iron-oxide contents of microfossils) of the same bacteria from one locality to another. The 'taphonomic model', recently proposed by Shapiro & Konhauser (2015), proposes that hematitic-coating on microfossils reflects an alteration process, rather than the metabolic activity of bacteria. This model suggests that after primary silicification and during burial, Fe(II) groundwaters

penetrated the porous zones of the stromatolites and adsorbed on the preserved carbonaceous matter of the filaments, and that later (possibly tens to hundreds millions of years), oxygenated groundwaters oxidized both the adsorbed Fe^{2+} and carbonaceous matter, before pores were filled by another stage of silicification. This model is confronted to the observations made on our samples and is discussed below.

The differences observed in the texture, mineralogy, and microfossils preservation of the Gunflint stromatolitic cherts seem to be the result of spatially or temporarily unique environmental conditions. The study of these stromatolites and their microbiota should thus be considered and interpreted as such.

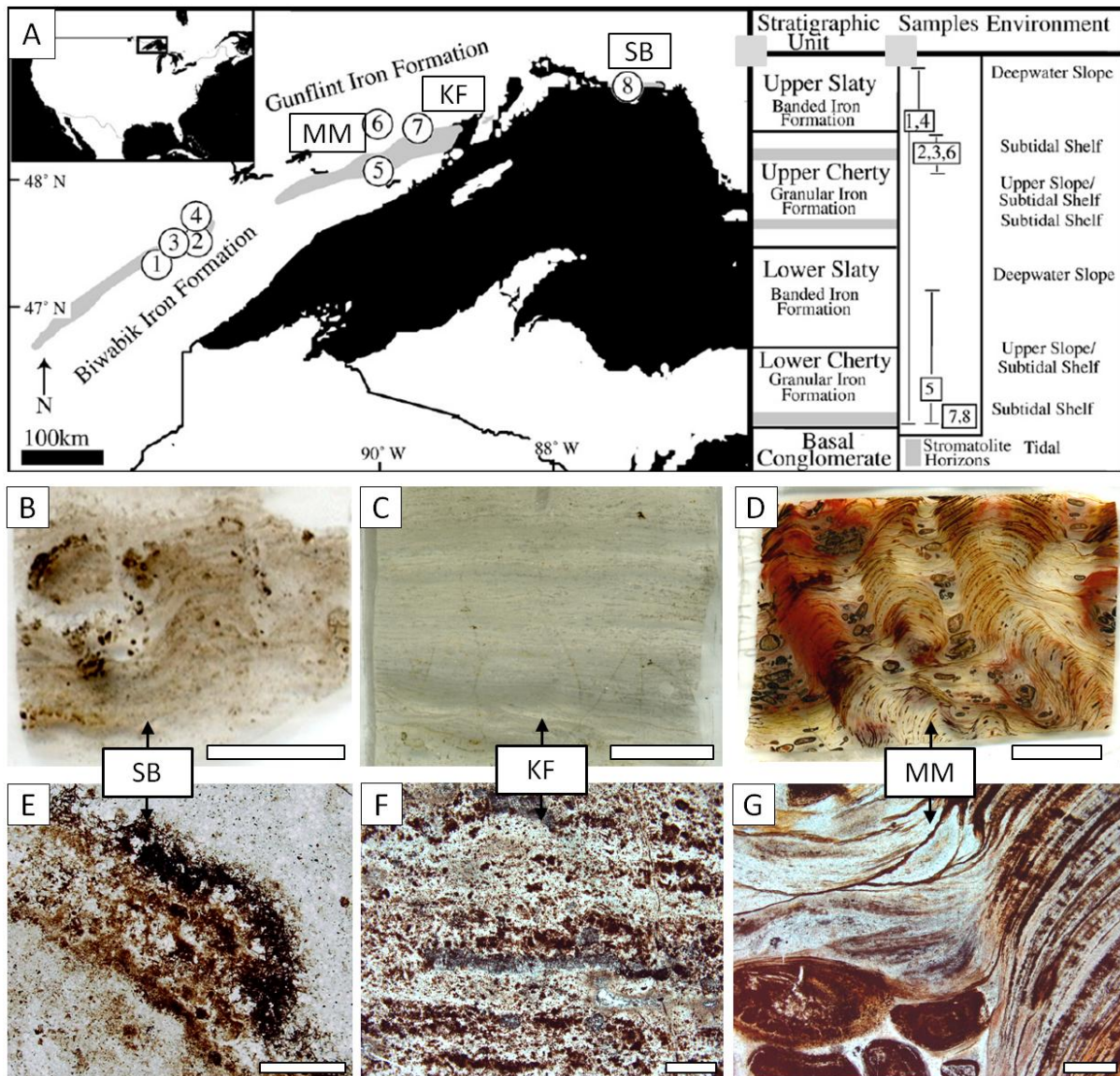


Figure III.6. A. General location of the Gunflint Iron Formation and location of the Mink Mountain (MM), Kakabeka Falls (KF), and Schreiber Beach (SB) localities in the stratigraphy. Modified from Planavsky *et al.*, 2009. (Depositional facies are from Ojakangas *et al.*, 2001). B-D. Scans of 30 μ m-thick thin sections from the three localities. E-G. Optical micrographs of stromatolitic laminations in plane polarized light, illustrating the variations in distribution and contents of organic matter and iron-oxides between the three localities. Scale bars are: 1 cm for B-D and 500 μ m for E-G.

a. Schreiber Beach Locality

Stromatolite samples from the Schreiber Beach locality are small columnar stromatolites formed in shallow water, intertidal environment (Cloud, 1965; Awaramik & Barghoorn, 1977) and are composed mostly of quartz. Microcrystalline quartz precipitated in stromatolitic columns and

bacterial mats, while mesocrystalline and megacrystalline quartz are the result of later infiltration of a Si-rich fluid, or associated with chalcedonic quartz and detrital organic matter in the filling of pores (Fig. III.7). Minor mineral phases are (i) ~100-500 μm euhedral dolomites, likely resulting from metamorphic (Winter & Knauth, 1992) or diagenetic recrystallization of precursor carbonate (Mg-calcite or possibly smaller crystals of dolomite) and (ii) pyrite, occurring as pyritization of isolated (iron-coated) carbonaceous matter (both on bacteria, Fig. III.8, and organic matter dragged in pores). Stromatolitic laminations are highlighted by the well-preserved bacterial mats composed of organic matter and iron-oxides, and by the differences in quartz crystals size between mat layers and silica cement.

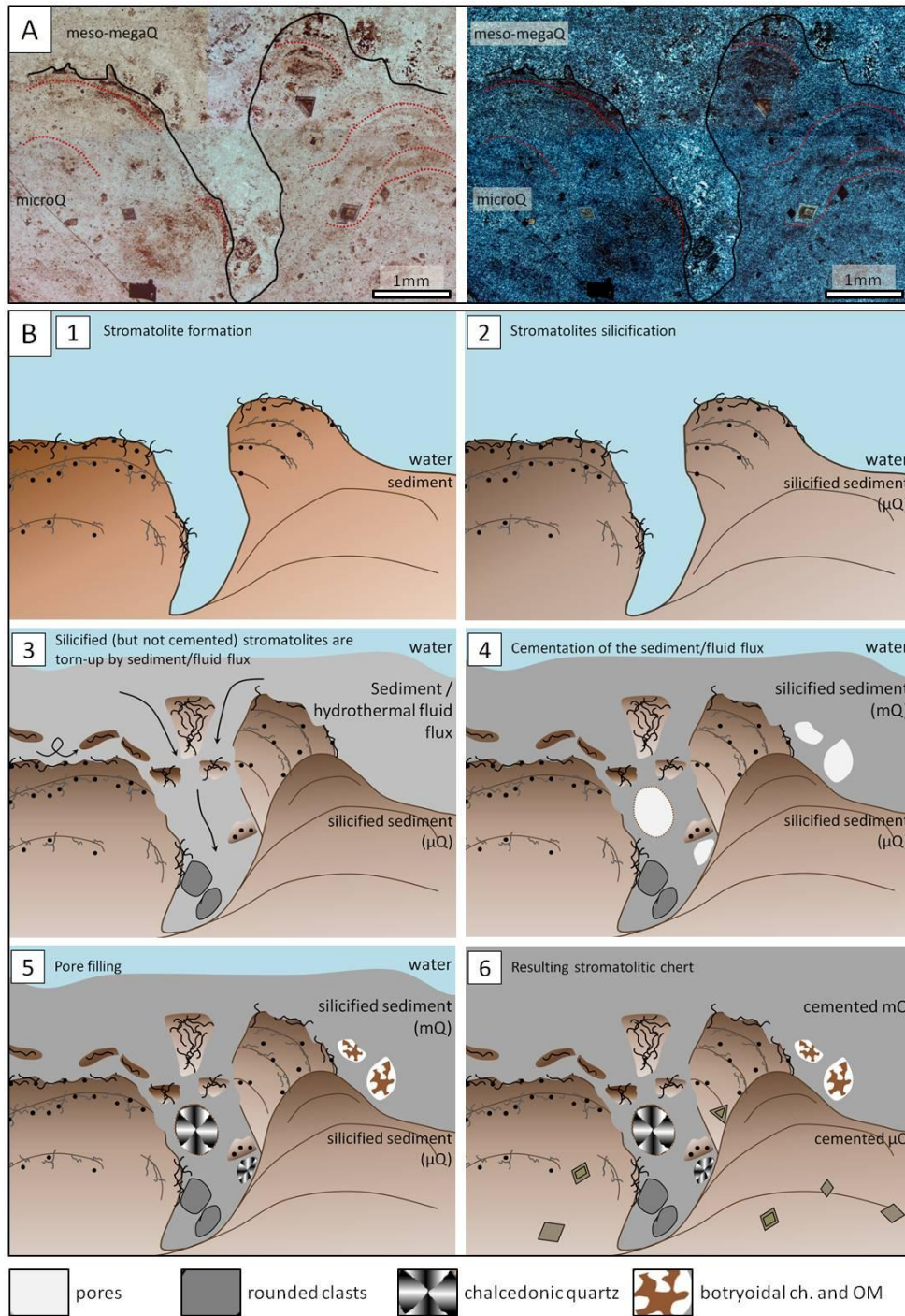


Figure III.7. Reworked stromatolitic columns and hollow between due to a sediment and Si-rich fluid flux in the ~1.88 Ga-old Schreiber Beach stromatolites, Gunflint Iron Formation, Canada. A. Optical micrographs of the hollow between two stromatolitic columns in plane polarized light (left) and cross polarized light (right). Variations in quartz grain size are visible. The black line delimits the microquartzitic stromatolites (including torn up fragments of bacterial top layers) from the meso to megaquartzitic-filled hollow, where chalcedony-filled pores are also visible. The red dashed lines highlight the mat layers of the stromatolitic columns. B. Schematized deposition and chertification process for this zone. Note that the euhedral dolomites resulting from diagenesis or low degree of metamorphism are only present at stage 6. μ Q: microcrystalline quartz; mQ: mesocrystalline quartz; OM: organic matter.

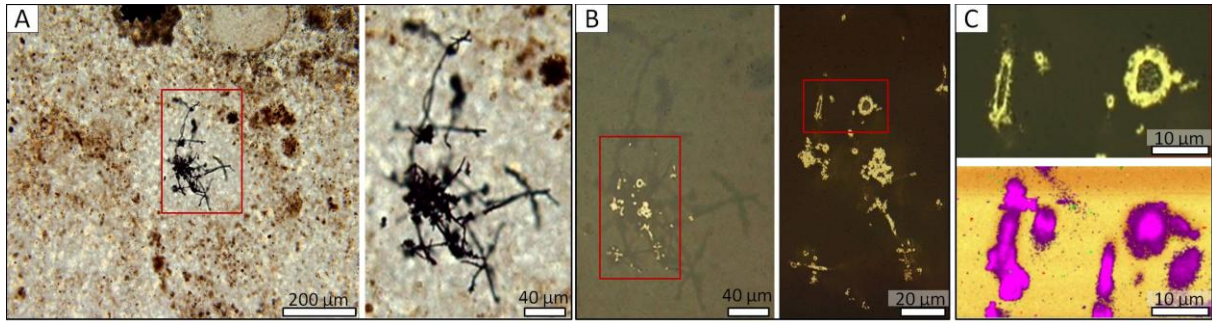


Figure III.8. Pyritized microbial filaments from the ~1.88 Ga-old Schreiber Beach stromatolites, Gunflint Iron Formation, Canada. A. Optical micrographs, plane polarized light. Pyritized filaments occur in small zones of clear chert. B. Optical micrographs, reflected light. Pyrite (yellow) coating is visible on filamentous and spherical hollow cells. C. Optical micrograph in reflected light and corresponding Raman map. Orange: quartz; fuchsia: pyrite; carbon: green (detected locally in association with pyrite).

Sedimentary structures in the samples show no signs of deformation due to compaction. The morphology of mats and filamentous and coccoidal microorganisms is very well-preserved in microcrystalline quartz. This indicates that silicification, lithification and recrystallization to microcrystalline quartz occurred at a very early diagenetic stage. In addition, torn-up, silicified (microcrystalline quartz) mat fragments can be observed in concavities between stromatolitic columns, along with rounded clasts of quartz, iron-oxides and organic matter (Fig. III.9). This suggests that the already silicified stromatolitic columns were destructured and the hollows were infilled as a result of syn-sedimentary reworking, and that mat fragments and clasts were dragged-in by a pervasive, energetic sediment and Si-rich fluid flux that later crystallized as mesocrystalline and megacrystalline quartz (Fig. III.7). This further suggests that the torn-up, top bacterial layers of stromatolites were not yet lithified when transported in the concavities, thus primary silicification occurred very early, during sedimentation, and quartz infilling with further crystallization as mesocrystalline and megacrystalline quartz occurred no later than early diagenesis (Winter & Knauth, 1992). The observation of a Si-rich fluid inflow is consistent with an active hydrothermal activity.

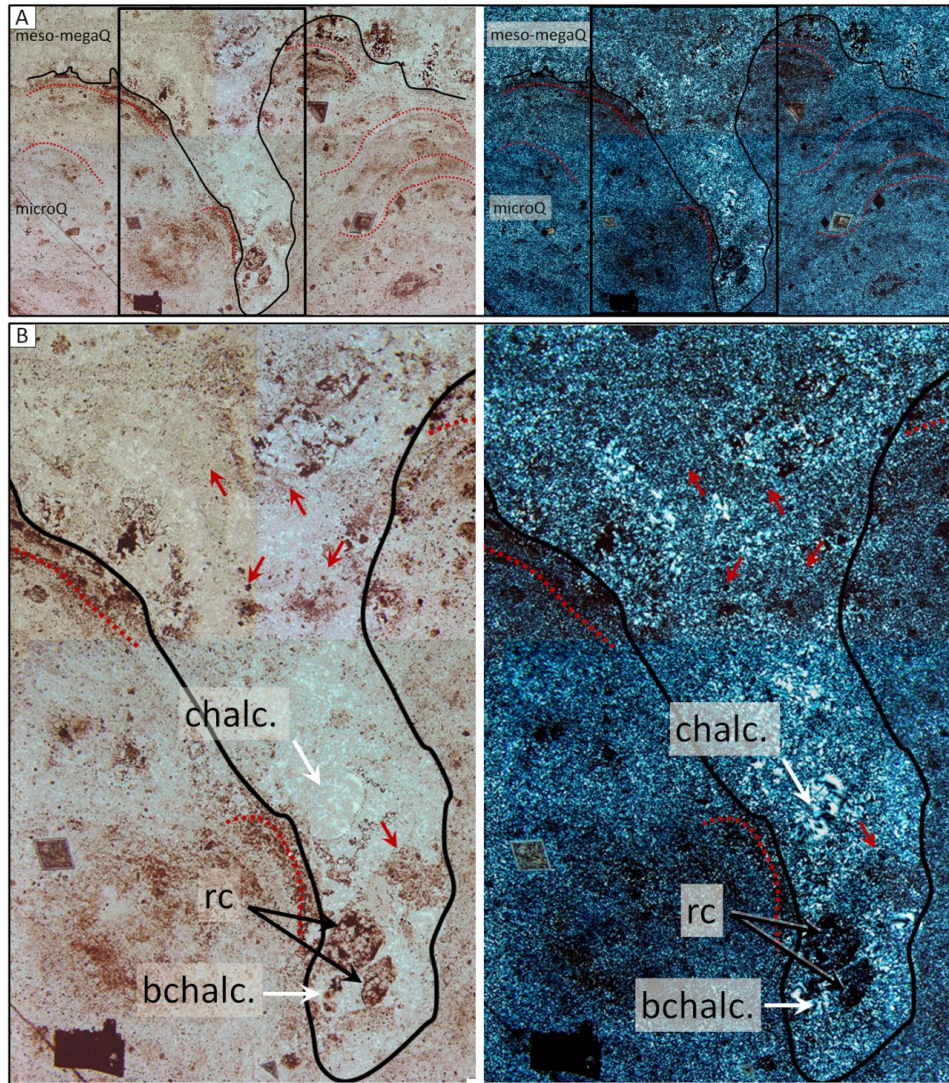


Figure III.9. Details of the infilled concavity in the ~1.88 Ga-old Schreiber Beach stromatolites, Gunflint Iron Formation, Canada, shown in Fig. III.7A. Red arrows indicates torn-up, silicified (microcrystalline quartz) mat fragments dragged in the hollow, surrounded by the meso- to megaquartzitic silicification. White arrows show pores filled by quartz crystallized as chalcedony (chalc.) and botryoidal chalcedony (bchalc.). rc: rounded clasts of quartz, iron-oxides and organic matter.

The dominant component of Schreiber Beach microbiota is the *Gunflintia-Huroniospora* assemblage (Barghoorn & Tyler, 1965), composed of interpreted photosynthetic filamentous (*Gunflintia*) and coccoidal (*Huroniospora*) bacteria (Fig. III.10A-E). This predominant assemblage is associated with other types of micro-organisms, presented in Fig. III.10G-I. The brownish-red coloring of these microfossils is due to a poorly crystallized, hematite coating. Another type of microorganism has been documented in close association with the *Gunflintia-Huroniospora*

assemblage. Recently, Wacey *et al.* (2013) documented the presence of saprophytic heterotrophic bacteria, consuming preformed organic matter (possibly degraded sheaths of *Gunflintia*).

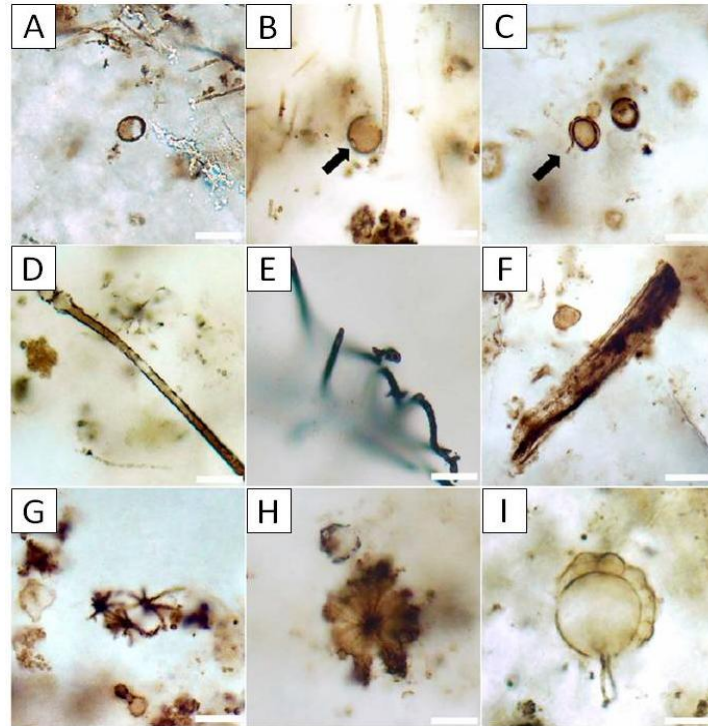


Figure III.10. Photomicrographs of Gunflint microfossils, plane polarized light. Translated into English from Labrot, 2006. a)-c) Spherical cells of *Huroniospora*. Cell wall and intracellular content are organically preserved; d) *Gunflintia* filament; e) pyritized *Gunflintia* filaments; f) Probable detached bacterial mat fragment; g)-i) other microorganisms of the Gunflint microbiota: g) three *Eoastrion* star-shaped cells; h) the umbrella-like shape of *Kakabeka umbellate*; i) incomplete specimen of *Eosphaera tyleri*, which could be affiliated to eukaryotes. Scale bar is 10 μm , except for a) and h): scale bar is 20 μm . Labrot, 2006.

Gunflint microbiota from the Schreiber Beach locality has been the subject of a long-standing study (e.g. Tyler & Barghoorn, 1954), and especially the microfossils of the Schreiber Beach locality, since they are the most well-preserved of the Gunflint Formation. On the basis of carbon stable isotope analyses and morphological similarities between the filamentous microorganisms and the domical structures observed and modern photosynthetic blue-green algae and stromatolites respectively, Barghoorn & Tyler (1965), postulated that oxygenic photosynthetic microorganisms formed the stromatolites at Schreiber Beach. This hypothesis was further

supported by Cloud (1965): “*These microstructures were almost surely autotrophic and in the line of evolution toward green-plant photosynthesis, if not themselves oxygen producers*”; but also by Awaramik & Barghoorn, 1977, who introduced the term ‘cyanophytes’ to designate the different types of bacteria they observed.

Original studies thus relate the Gunflint microbiota (*Gunflintia* filaments and *Huroniospora* spheres) to cyanobacteria-like microorganisms. However, the hematite-coating characteristic of the microfossils led to another theory for the metabolism of the Schreiber Beach microbiota. As early as 1965, Barghoorn & Tyler mentioned the possibility of them being “iron-loving” bacteria. Studies have suggested that hematite was bioprecipitated as a direct result of the activity of Fe(II)-oxidizing bacteria. However, the ‘taphonomic’ model recently proposed by Shapiro & Konhauser (2015) suggests that hematite precipitation on microfossils is not related to bacterial metabolism, but rather to diagenetic processes, involving the infiltration of Fe(II)-rich groundwaters during burial, and later oxidation by percolation of oxygenated waters.

Thus, it is still unclear whether the microbiota harbored by the Schreiber Beach stromatolites corresponds to anoxygenic (Fe(II)-oxidizing) or oxygenic photosynthetic bacteria as primary producers. However, the results of Shapiro & Konhauser (2015) show that iron-oxide coating on filamentous and spherical bacteria is not necessarily relevant as a metabolic recognition criterion and maintain the possibility of a predominant oxygenic photosynthetic microbiota. This is corroborated by the recent *in situ* carbon isotopes analyses made by Williford *et al.*, 2013.

Thin sections from the Schreiber Beach locality are named 07CA05, GF55-1 and GF55-1B.

b. Kakabeka Falls Locality

Stromatolitic cherts from the Kakabeka Falls locality (Fig. III.6A) represent the lower member of the Gunflint Formation, directly overlying

Archean units and the basal conglomerate (Hofmann, 1969; Franklin *et al.*, 1982). Analyzed samples come from domal silicified stromatolites. They show alternating 100-500 μm thick red-brownish layers of iron-oxides (microcrystals of hematite) containing altered (shapeless) and detrital (rounded grains reaching 200-400 μm) carbonates (dolomite, ankerite, siderite) silicified by microcrystalline quartz, and paler layers of mesocrystalline and megacrystalline ‘impure’ chert, containing small amounts of iron-oxides and degraded carbonates (Fig. III.11). Pyrite occurs as a minor mineralogical phase.

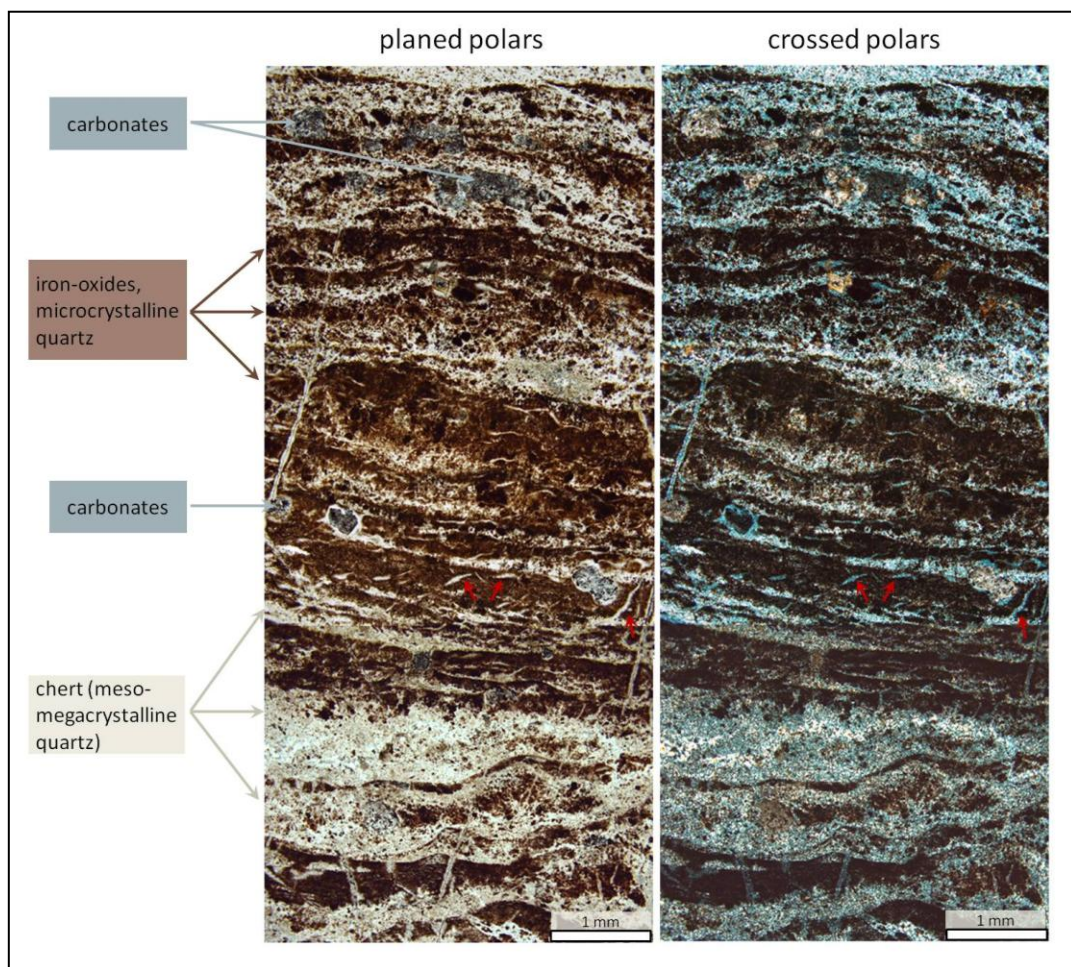


Figure III.11. Optical micrograph views of Kakabeka Falls microbialites. Alternating laminations of chert and dense iron-oxide with degraded and detrital carbonates are shown. Carbonates are dolomite, ankerite and siderite. Red arrows point to microcrystalline quartz lenses, some of which are straightening upward (far right).

The samples are perturbed by numerous veins of varying origins: (i) microcrystalline quartz lenses visible in the iron-oxide layers; (ii) transversal

microcrystalline quartz veins cross-cutting indifferently pale and brownish layer with a smooth contact, creating the fractured texture of the brownish layer; (iii) cross-cutting sub-parallel or transversal meso-megacrystalline quartz fractures, with a marked contact with the sediment are also visible (Fig. III.12). The marked contact between meso- to megacrystalline quartz veins (iii) with the sediment indicates that these veins infiltrated the sediment after lithification. Microquartzitic lenses and veins (i and ii) seem to correspond to the same feature, since some lenses straighten up and cross the laminae (Fig. III.11 and Fig. III.12). These features reveal a dewatering process, whereby silica-rich pore waters escape upward through the compacted sediment. Primary, microcrystalline silicification is a result of the polymerization into a siliceous gel of these silica-rich waters. The contact between the pale, mesoquartzitic layers and these dewatering microquartzitic veins is not clearly discernible but rather seems to reveal a subtle mixing between the two types of quartz crystals sizes (Fig. III.12). These observations suggest that microquartz and mesoquartz zones correspond to the same silicification event. This also suggests that dewatering occurred before lithification and that the sediment was not lithified before compaction. Furthermore, microquartz zones also comprise degraded detrital carbonates, indicating that silicification occurred after the sediment begun to degrade and transform. This would not have favored the preservation of microbial mats or cells, and would have degraded the remaining organic matter. Incidentally, no kerogenous compounds were detected by Raman mapping. The preservation state of the Kakabeka Falls stromatolites could thus resemble that of the ~2.98 Ga-old Pongola stromatolites, in which organic matter is fully degraded due to a late silicification.

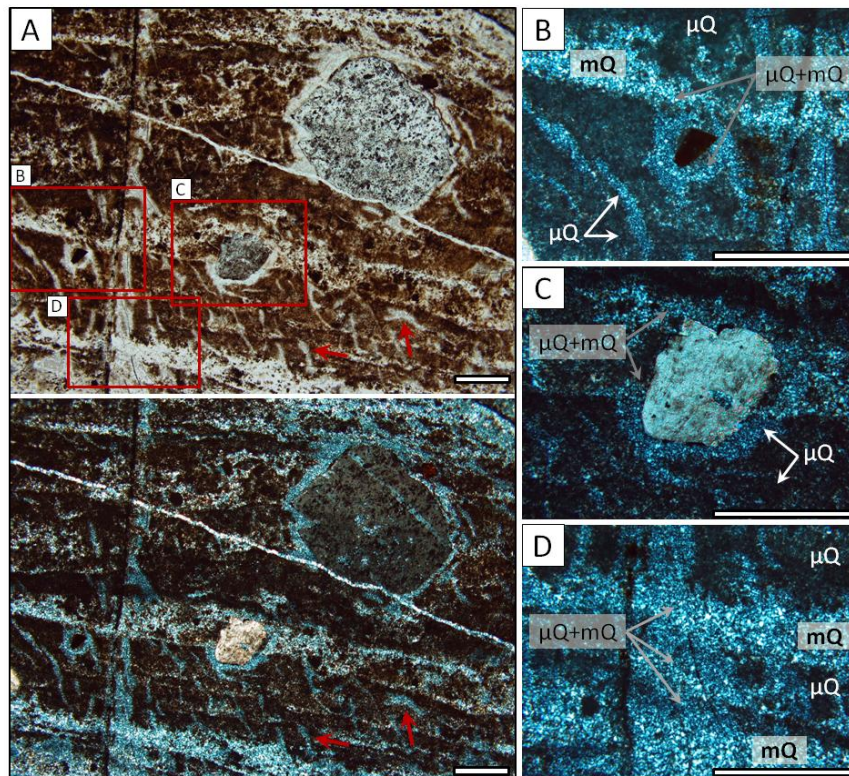


Figure III.12. Details of a layer of iron-oxides in Kakabeka Falls microbialites. A. Optical micrographs in (plane and cross polarized light) of a zone showing ~500 μm microquartzitic iron-oxides layers with straightening upward microquartzitic lenses (red arrows). Carbonates crystals are also visible. A fine, megaquartzitic vein cross-cuts the iron layers with a marked contact. Red boxes indicate the area of the details in B-D. B-D. Optical micrographs in cross polarized light showing mixed micro and mesoquartz in zones where chert layers meet microquartzitic iron-oxides layers and lenses. μQ : microquartz; mQ: mesoquartz. Scale bar: 400 μm .

c. Mink Mountain Locality

Samples from the Mink Mountain locality (Fig. III.6A) are small columnar stromatolites with 100-200 μm -thick alternating chert layers (microcrystalline quartz) and Fe-rich layers consisting of amorphous and microcrystalline hematite (~1-2 μm ; Schelble *et al.*, 2001). Rare 20-50 μm subhedral pyrites are associated with iron oxides layers. Laminations between two columns are flat or concave, but mostly uninterrupted. Intraclasts and ooids cemented by micro- to megaquartz and covered by more recent laminations (Fig. III.13 and III.14A) were deposited in concavities in intercolumnar spaces. Ooids are composed of lithoclasts of

quartz (cores) and layers of iron-minerals (sulfides and oxides) and quartz (cortices). They are described in detail in Maliva *et al.*, 2005 (p.841).

Silicification and lithification of these stromatolites occurred early, before burial diagenesis, as documented for instance, by the loose grain-packing of intraclasts and ooids (Fig. III.13 and III.14A).

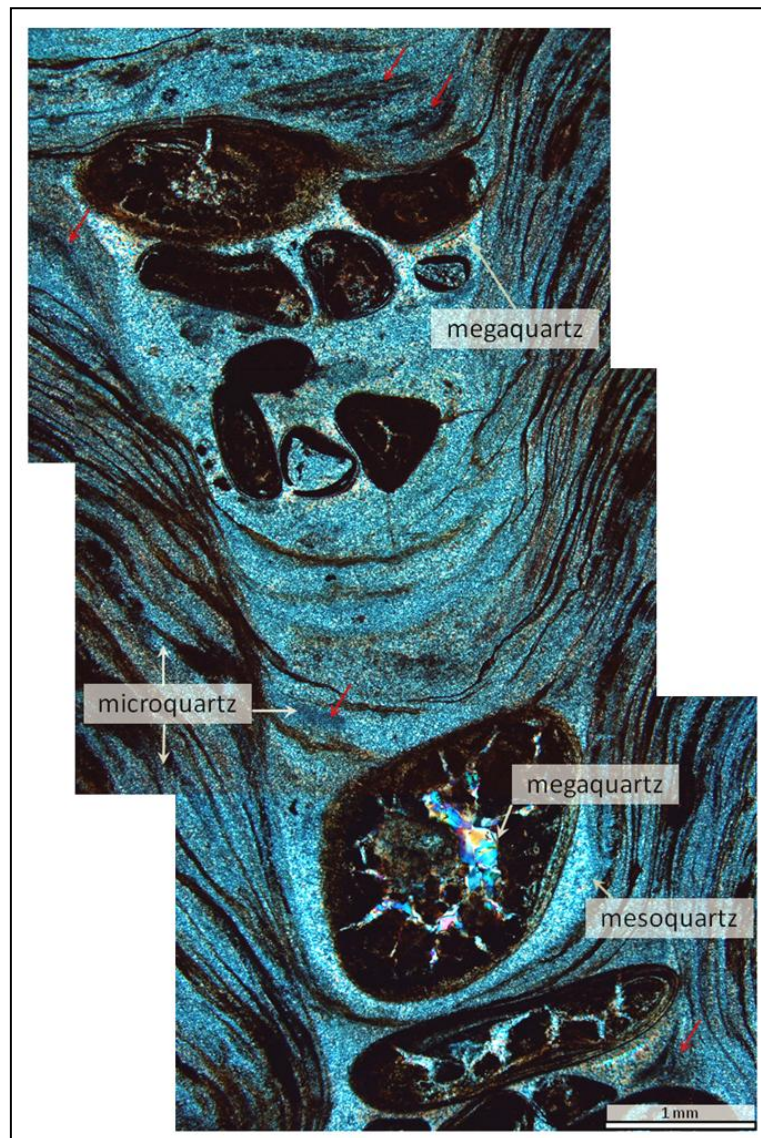


Figure III.13. Optical micrograph view of the intercolumnar space in a thin section of the hematite-rich Mink Mountain stromatolites, cross polarized light. Spaces between ooids and clasts are filled with meso to megaquartz. The low density of grain-packing indicates a low degree of compaction, and that silicification occurred before burial. Red arrows indicates remnant microbial mats.

These samples are poor in organic matter. Planavsky *et al.*, 2009 categorized these stromatolites as “hematite-rich”, as opposed to “microfossil-rich” stromatolites (e.g. Schreiber Beach). Using Ce anomalies and Fe isotopes analyses, they concluded that these hematite-rich stromatolites were formed in a low oxygen environment, probably by chemolithoautotrophic Fe(II)-oxidizing bacteria. This chemolithotrophic-based microbiota could have been spatially widespread in the Animikie Basin, but for a short period of time, reflecting an ecosystem response to unique redox conditions at that time (reduced hydrothermal fluids overtaking the oxygenated Paleoproterozoic oceanic composition, such that oxygenated conditions occurred in the upper water layer only).

Our stromatolite samples from the Mink Mountain locality contain hematitic-coated filaments ~50-100µm long and ~2µm in diameter (Fig. III.14B,M-N), localized at the top edge of hematite-rich layers, coherent with the comparison with modern chemotrophic iron-oxidizing bacteria of the type *Crenothrix* and *Gallionella* made by Barghoorn & Tyler 1965 and Cloud 1965. Nonetheless, in our samples, we observed numerous substructures with a tendency to form small domical structures, alternating dark and brownish 15-30µm layers of filamentous and spherical bacteria-like objects organized in mats. These structures are well-developed when localized in intercolumnar spaces, and between ooids and intraclasts (Fig. III.13, III.14A), probably taking advantage of the protection offered by the porosity. The microfossils within the mats are ~20-50 µm long and 2-3 µm thick filaments, and spheres with a diameter of 5-9 µm, and correspond respectively to *Gunflintia* and *Huroniospora*. They are partially (Fig. III.14I-L) or entirely (Fig. III.14G-H) coated or replaced by micrometric (0.5 to 2-3 µm) crystals of iron-oxides (hematite). In several cases, the cellular outline is preserved (Fig. III.14I). Although the Gunflint Formation as a whole is considered to be non-metamorphosed, samples from the Mink Mountain locality were submitted to at least some degree of metamorphic alteration that could explain the differences in organic matter preservation, and the extent and textures of iron-oxides coatings compared to samples from the Schreiber Beach locality that are non-metamorphosed. Indeed, the ‘taphonomic model’ of Shapiro &

Konhauser (2015) postulates that differences in iron-oxide replacement of bacteria through the Biwabik and Gunflint Formations is a function of varying degrees of post-depositional alteration (e.g. metamorphism). However, in our samples, various textures of iron-oxides coating (Fig. III.14E-F) can be observed for mats that are only few millimeters or even few tens of micrometers (Fig. III.14C) apart. It is doubtful that bacterial mats from the same thin section, separated by few stromatolitic laminations, would be subjected to a completely different post-depositional history. The model of Shapiro & Konhauser (2015) for hematite-coating microfossils proposes that, after primary silicification and during burial, Fe(II) groundwaters penetrated the porous zones of the stromatolites and adsorbed on the preserved carbonaceous matter of the filaments, and that later, oxygenated groundwaters oxidized both the adsorbed Fe²⁺ and carbonaceous matter. Considering the differences of iron-coating observed in our samples between two superposed layers of bacterial mat, and following this model, it is possible to hypothesize that these differences are due to the distribution of the porosity. If porous zones were distributed preferentially one in every two layers of microbial mat, Fe(II) groundwaters would have penetrated more abundantly within the more porous layers. This further suggests that some process made one layer out of two systematically more porous. In such close contact, only differences in bacterial metabolic activity could have created this disparity. Thus, it remains possible that the textural differences of iron-oxides coating reflect, indirectly, varying bacterial metabolisms. However, in our Mink Mountain samples, evidence for an ‘incomplete’ primary silicification that would have let porous zones in which Fe(II)-rich fluids and later oxygenated fluids could have penetrated, is only visible in the intercolumnar spaces between ooids and clasts, with the presence of meso- to megaquartz filling. Microbial mats zones all show evidence for early and rapid primary silicification with the crystallization of microquartz, which unlikely offers the possibility of a porous network.

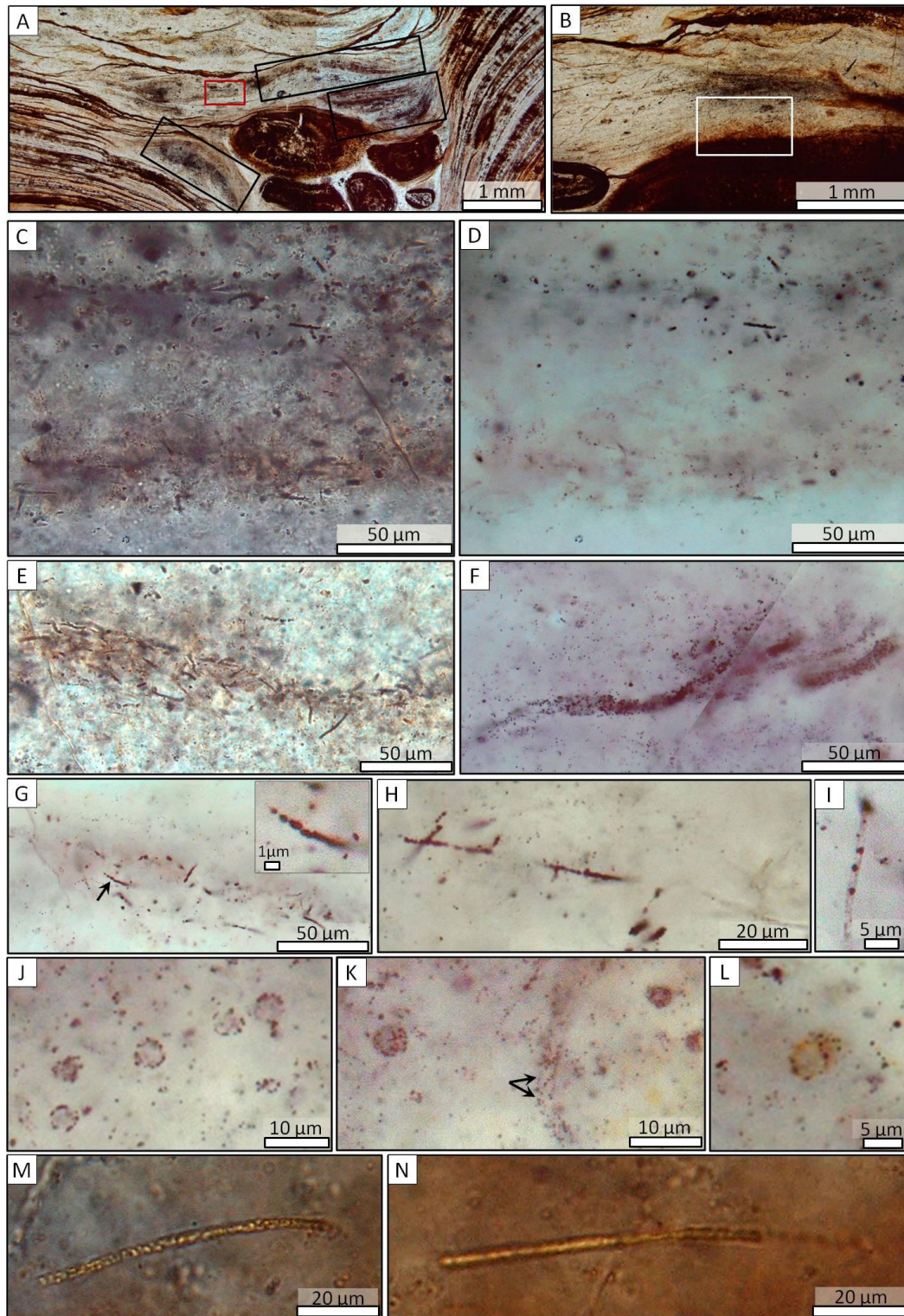


Figure III.14. Microfossil diversity in Mink Mountain hematite-rich stromatolites. Optical micrographs, plane polarized light. A. Ooids and rounded clasts deposited between two stromatolitic columns. Note the loose grain-packing. Boxes show the locations of several microbial mats with dark/brownish alternating layers. The red box indicates the area of the bi-layered mat shown in C-D. B. Location (white box) of the hematitic chemotrophic-like filaments reported in M-N. C. Bi-layered microbial mat with a dark superior layer and a brownish-orange inferior layer. D. Same zone, with condensed transmitted light. These optical micrographs highlight the differences in the extent of microbial mineralization. (End of caption overleaf.)

(Fig. III.14 overleaf.) Darker layers show larger sizes of hematite crystals, or darker crystals, which could be magnetite. E-F. Differences in mat preservation by mineralization. E. Mat exhibiting preserved cellular outlines and microcrystals of hematite. F. Optical micrograph mosaic, with a variation of $\sim 10\mu\text{m}$ in the thin section depth (right). General shape of what appear to be several interlaced filaments of sub- μm crystals of hematite. G-I. : Hematite-coated filaments of *Gunflintia*. G. The black arrow locates the filament in the box. I. Well-preserved cellular outline. J-L. Hematite-coated cells of *Huroniospora*. Black arrows in K indicate cell walls of probable interlaced filaments, enlightened by the microcrystals of hematite. M-N. Probable chemotrophic bacterial filaments.

Five thin sections from the Gunflint Iron Formation were studied. Thin sections GF55-1 and GF55-1b were sampled at the Schreiber Beach locality, 07CA13 at the Kakabeka Falls locality, and 07CA16 and 07CA16A at the Mink Mountain locality.

III.2. Preservation of the geochemical composition of the sediments through post-depositional processes

Post-depositional processes listed in Chapter I.2.3 affect the original chemical and isotopic composition of the sediment. Apart from the Pongola stromatolites, the sediments used in this study show evidence of early silicification (section III.1). In these samples, post-depositional changes in the chemical and isotopic composition of the kerogenous phase and mineralogical environment are significantly influenced by the Si-metasomatism of primary silicification and possibly by microbial activity during early diagenesis rather than by secondary, post-silicification hydrothermal events, late diagenesis and metamorphism. Indeed, the overprinting of these later events is limited once the sediment is 'sealed' by silicification, which limits further chemical migration and exchanges.

The metasomatism due to primary silicification is associated with elemental enrichment-depletion patterns that depend on the temperature and chemical composition of the hydrothermal source responsible for the Si-rich fluid circulation, or on that of the sea water if silica was directly precipitated from water at or just below the water-sediment interface. These

changes in sample chemistry are thus dependent on the local chemistry and depositional environment of each sedimentary sample.

Independently of their age or process of formation however, the sedimentary cherts all display extensive SiO₂-replacement associated with depletion of elements that are mobile during water-rock interactions. These enrichment-depletion patterns of major-to-trace elements are dependent of the conditions of silicification and original chemical composition of the sediment. For instance, Hofmann & Harris (2008) documented a depletion in the major elements Na, Ca, Mg, and metals Ni, Co, Cu and Zn with increasing SiO₂ content in low-temperature hydrothermally silicified volcanic rocks of the Barberton Greenstone Belt, while noticing an enrichment in some other elements, such as K, Rb and Ba.

In order to evaluate the degree of chemical alteration undergone by the presented samples, we here report some complementary geochemical results for major to trace element contents of samples from the Josefsdal Chert, Pongola stromatolites, Gunflint stromatolites (Schreiber Beach locality) and a silicified komatiitic basalt obtained by ICP-OES and ICP-MS analyses (CRPG, CNRS Nancy, France). Since these analytical techniques are both extensively destructive and used for bulk-rock analyses, they are not considered as part of the analytical technique suite used in this study and listed in Chapter II that are evaluated for the research of type A and type B signatures of oxygenic photosynthesis (type A and type B signatures are defined in the '*Scientific approach and objectives*' section). The results obtained are only occasionally referred to in the relevant sections of this manuscript as a complementary source of information.

Bulk chemical analyses show that the samples from the Josefsdal Chert, Pongola stromatolites and Gunflint stromatolites at the Schreiber Beach locality are systematically enriched in SiO₂, with average SiO₂ concentrations of ~96%, ~89% and ~99%, respectively. In association with the SiO-replacement, all samples show a depletion in the major elements (Ti, Fe, Mg, Mn, K, Al, Ca, Na and P), whose concentration generally do not exceed <1%. In some samples with <97% SiO₂, Al₂O₃ and Fe₂O₃ can reach several percent (<4%). Scatter plots of Al₂O₃ and K₂O versus SiO₂ in

particular exhibit a general decreasing trend with increasing SiO_2 concentration (Fig. III.15), while the concentration of other elements remains low and constant independently of the SiO_2 content. The Pongola stromatolites were less extensively silicified, and silicification occurred at a late stage of alteration. These stromatolites display the highest concentrations of Al_2O_3 and K_2O . In these samples, combined SEM/EDS and Raman spectrometry indicates frequent muscovite overgrowths (metamorphosed phase of precursor clay-minerals) on euhedral to subhedral Ca-Mg carbonates (dolomite, possibly diagenetic) (Fig. III.15B). Thus, the general decreasing trend of Al_2O_3 and K_2O contents with increasing SiO_2 concentration supposedly indicates that the process (or the series of processes; hydrothermal event, diagenesis, metamorphism) responsible for the juxtaposition of clay-minerals/muscovite with euhedral recrystallized dolomite in carbonate-containing samples, such as the Pongola stromatolites, is more efficiently prevented in extensively and early silicified samples.

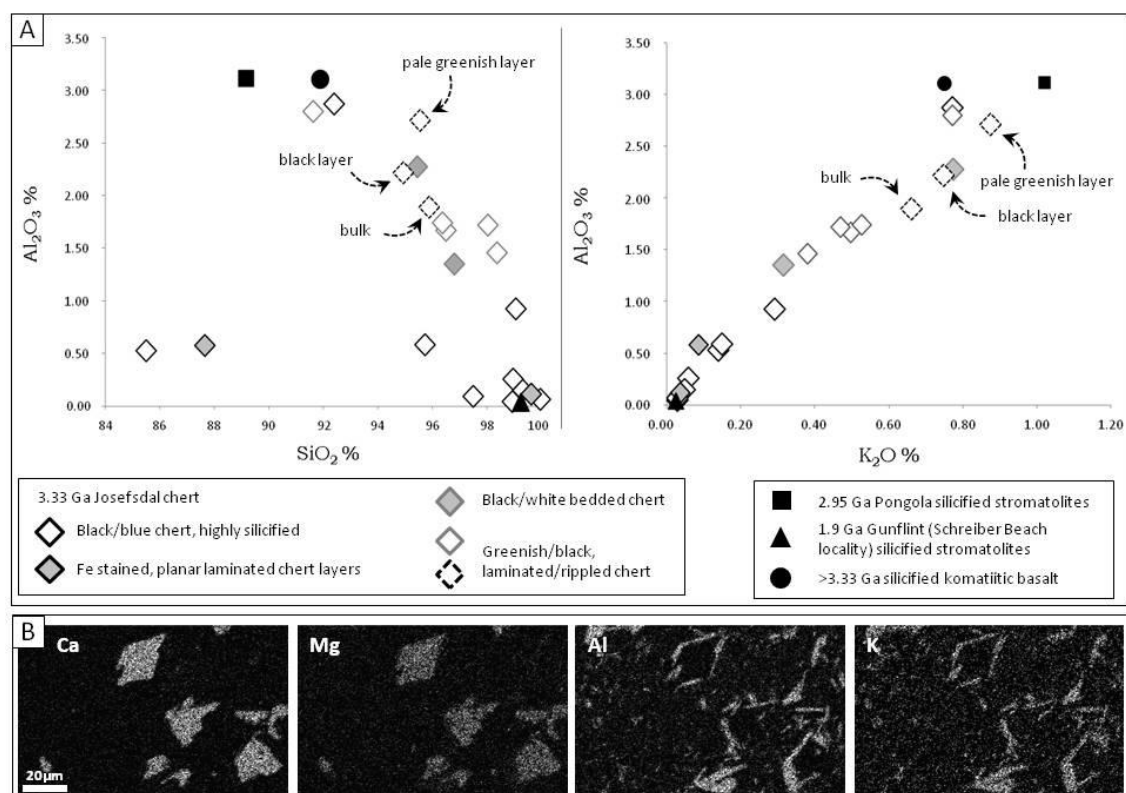


Figure III.15. (caption overleaf.)

Figure III.15 (overleaf). Al₂O₃ and K₂O abundances in sedimentary cherts (from the Josefsdal Chert), silicified stromatolites (from Pongola stromatolites and Gunflint Formation) and a silicified komatiitic basalt. A. Relative abundances of Al₂O₃, SiO₂ and K₂O from bulk ICP-MS data in 19 samples from the Josefsdal Chert, 1 sample from Pongola stromatolites and 1 sample from Gunflint Schreiber Beach stromatolites. Same data are shown for a sample of silicified komatiitic basalt. Facies of the Josefsdal Chert are described in Fig. III.1D-E. B. SEM/EDS maps from a sample of Pongola stromatolite. Al-K overgrowths are visible around Ca-Mg carbonates, determined by Raman mapping as being muscovite (KAl₂(Si₃Al)O₁₀(OH)₂) and dolomite (CaMg(CO₃)₂), respectively.

While they can be used to study the composition of the Si-rich fluid responsible for silicification, these changes in major and minor element compositions raise significant questions for inferring the original chemical composition of the sediment. Rare earth element (REE) patterns, on the other hand, are generally well-preserved during silicification (e.g. Bau & Alexander, 2006) and can be used to study the composition of sea water and the environmental conditions of sediment deposition and silicification via La, Eu, Y, and Ce anomalies. Shale-normalized (Post-Archean Australian Shale standard, McLennan, 1989) REE+Y (yttrium) patterns, Ce/Ce*, Eu/Eu* and Y/Ho ratios show that most of our samples display a marine signal with low to elevated positive La anomalies and Y/Ho ratios, and that they also exhibit positive Eu anomalies (with the exception of Pongola stromatolites), thus indicating a mixed marine-hydrothermal signature.

Numerous authors have documented the shifts in carbon isotope compositions of organic matter that can be induced by the selective preservation of their heavy or light isotopes during post-depositional processes.

The loss of organic carbon triggered by silicification metasomatism affects the relative abundances of carbon isotopes. Ueno *et al.* (2004) have shown that metasomatism created by the infiltration of silica dikes in 3.5 Ga-old basaltic greenstones can trigger a preferential loss of ¹²C resulting in a shift of the δ¹³C values. They estimated a ¹³C-enrichment of ~4‰ for a consumption of >90% of the organic carbon. However, since the kerogens in both the Josefsdal Chert and Gunflint stromatolites (Schreiber beach

locality) exhibit signs of rapid and early silicification and well-preserved mat and cellular structures (section III.1), it is unlikely that the organic matter was consumed to this extent by the associated metasomatism. Further discussion on $\delta^{13}\text{C}$ is reported in Chapter VI.

Major to minor element contents are helpful for understanding the elemental enrichment-depletion patterns associated to the Si-metasomatism responsible for silicification. REE systematics remain informative via the study of La, Ce, Eu and Y anomalies, to decipher the conditions of silicification and the environmental context of sediment deposition.

III.3. Conclusions regarding sample selection

The Archean and Paleoproterozoic sedimentary rock record is scarce and often highly metamorphosed. However, it was possible to select suitable samples of 3.33 to 1.88 Ga-old shallow marine sediments, deposited within the photic zone, that have only been submitted to low degrees of metamorphism ranging from diagenesis (burial metamorphism; e.g. Gunflint samples) to greenschist facies.

The age range of the samples covers the period of time relevant for this study: from one billion years before the GOE, when Earth was anoxic and anoxygenic photosynthesis had probably evolved, to ~500 million years after the GOE, when atmosphere and oceans were globally oxic, and oxygenic photosynthesis was well established.

The samples all display evidence for photosynthetic life, supported by the literature, in the form of cellular fossils, fossilized biofilms and mats and stromatolitic structures. Previous analyses of the carbonaceous matter of these samples (which include Raman spectrometry, SEM, TEM, ToF-SIMS, μXRF , *in situ* carbon isotopes), also supported by the literature and by chemical and isotopic analyses made in the present study (see Chapter VI), indicate (except for Pongola stromatolites samples) that the carbon is

syngenetic, biogenic, and that at least some of it is consistent with photosynthetic activity. No signs of post-lithification or modern contamination were observed. This is confirmed by microscopic observations made in the present study. Most of our samples contain not only fossilized organic matter, but also cellular microfossils that, in relation with the extensive and early silicification of their host sediments, are well-preserved.

Table III.1 summarizes the principal characteristics of the selected samples. The list of samples presented is non exclusive. Twenty-four samples were used for this study, including samples from the ~3.45 Ga Hooggenoeg Formation (BGB South Africa), 2.7 Ga Belingwe stromatolites (BGB South Africa) and 2.7 Ga Joutel stromatolites (Abitibi, Canada) that are not described here since they served to provide complementary information and comparison during this project, but were not the subject of detailed chemical analyses by an extensive suite of analytical techniques.

The constraints on sample selection mentioned at the beginning of this chapter are respected. The suite of samples selected is thus relevant for this study.

Table III.1: Description of the samples.

Locality	Age (Ga)	Name	Mineralogy (main phases)	Environment of deposition*	Description	carbonaceous matter distribution	Photosynthetic remnants*
Josefsdal Chert	3.33	99SA-, 10SA-, 12SA-	chert, minor pyrite, anatase, rutile, muscovite	shoreface to upper shoreface (tidal)	banded blue/black, black/white and green/black chert (finely laminated)	laminated microbial biofilms, mats, clots, and detrital organic matter	photosynthetic bacterial biofilms
Pongola stromatolites	2.98	07SA01, 07SA02A, 07SA03	chert, pyrite, dolomite, muscovite, rutile, anatase, hematite	upper shoreface (tidal)	silicified dolomite, cm domical stromatolites	altered carbonates	domical stromatolites
Gunflint <i>Schreiber Beach</i>	1.88	07CA05, GF55-1, GF55-1B	chert, hematite, minor dolomite, pyrite	foreshore (intertidal)	iron-poor chert, small columnar stromatolites	microbial cells, biofilms and detrital carb. matter	columnar stromatolites, cellular microfossils and fossilized photosynthetic
Gunflint <i>Kakabeka Falls</i>	1.88	07CA12, 07CA13	chert, iron-oxides, siderite, dolomite, ankerite, minor pyrite	shoreface (subtidal)	finely laminated domical stromatolites	altered carbonates	flat-laminated stromatolitic layers
Gunflint <i>Mink Mountain</i>	1.88	07CA16, 07CA16A	chert, hematite, minor pyrite, magnetite	shoreface (subtidal)	hematite-rich small columnar stromatolites associated with ooids	diffuse or absent	columnar stromatolites, microfossils, possibly of photosynthetic bacteria**

*References are in the text. ** Ongoing debate involving chemotrophic bacteria rather than phototrophic bacteria (e.g. Planavsky *et al.*, 2009).

Chapitre IV: résumé

Morphologie et contenu en métaux traces de pyrites et sulfures métalliques sédimentaires associés à des traces de vie dans des sédiments marins peu profonds de l'Archéen et du Paléoprotozoïque

Ce chapitre présente les résultats d'une étude détaillée de la morphologie et du contenu en métaux traces de pyrites et sulfures métalliques sédimentaires associés à des traces de vie, entreprise par microscopie optique, MEB/EDS et EPMA.

Les analyses pétrographiques et élémentaires montrent qu'à l'intérieur d'un même échantillon, il existe des différences de morphologie et de composition chimique des pyrites diagénétiques, et que ces différences sont fonction de leur distribution spatiale dans le sédiment. En effet, ces différences de morphologie sont observées suivant que les pyrites considérées se trouvent en association avec un tapis microbien, un amas de matière organique, de la matière organique détritique ou encore avec des couches de silice pratiquement pure.

De plus, il est intéressant de noter que les différences observées dans ces pyrites diagénétiques en ce qui concerne leur composition en éléments traces (TE), n'ont pas pu être entièrement expliquées par des changements dans les conditions redox globales au cours du temps, ni par l'influence d'arrivée de fluides épigénétiques. Nous proposons que ces variations sont plus probablement dues à des processus locaux, à l'échelle micrométrique, affectant ainsi la composition des fluides diagénétiques, responsables de leur précipitation, à la même échelle. Nous proposons également que la présence d'activité microbienne dans l'environnement immédiat des ces pyrites (dizaines de μm ou moins), ainsi que le type de métabolisme impliqué, sont responsable de ces différences.

Ainsi, nous proposons que les microorganismes du chert de Hooggenoeg, daté à 3,45 Ga (H3c; Lowe & Byerly, 1999) consistent en une association de bactéries photosynthétiques anoxygéniques oxydant le fer, et de microorganismes chimiotrophes capables d'utiliser de façon périodique l'As et le Se apportés par l'activité hydrothermale et volcanique, à la place du soufre, dans un environnement anoxique pauvre en sulfates. De plus, en se basant sur le contexte géomorphique de dépôt, sur la composition du sédiment et le contenu en TE des pyrites diagénétiques, nous proposons que les microorganismes du chert de Josefsdal, daté à 3,33 Ga, devaient être de nature similaire à ceux du chert de Hooggenoeg.

Les résultats obtenus pour les stromatolites de Pongola datés à ~2.98 Ga sont cohérents avec une atmosphère oxygénée ou faiblement oxygénée, et avec la présence d' « oasis » d'O₂ dans la zone photique. Nous suggérons que la présence d'O₂ est le résultat de l'activité émergente de bactéries photosynthétiques oxygéniques, associées à des microorganismes chimiotrophes dans ces stromatolithes. Cette production d'O₂ dans un environnement d'autre part anoxique aura pu engendrer l'utilisation de Cu-protéines chez les bactéries présentes, afin de se défendre contre le stress oxydatif créé.

Les résultats obtenus pour les stromatolithes de Kakabeka Falls datés à 1,88 Ga, sont cohérents avec l'activité de bactéries photosynthétiques oxygéniques et de SRB dans un environnement oxygéné, et avec une activité réduite, ou une absence, de méthanogènes. Les concentrations élevées en Cu dans les pyrites diagénétiques de ces échantillons supporterait alors notre proposition donnée ci-dessus, suggérant que de fortes concentrations en Cu dans les pyrites diagénétiques de certains sédiments Précambriens pourraient indiquer indirectement un fort taux d'oxygène dans le milieu, et potentiellement l'activité dans l'environnement anoxique local, de bactéries photosynthétiques oxygéniques.

Chapter IV: Morphology and trace metal content of sedimentary pyrite and base-metal sulfides associated to preserved traces of life in Archean and Paleoproterozoic shallow marine sediments

In this Chapter, we present optical microscopy, SEM/EDS and EPMA results. The aim of this study was to evaluate the amount of chemical information provided by pyrite precipitated within microbial colonies in Archean and Paleoproterozoic sediments. The first part of this Chapter presents the relevance of the trace element content of sedimentary pyrite in the study of the Precambrian evolution of photosynthesis. In the second part, we describe the samples used for this work. The experimental parameters for optical microscopy, SEM/EDS and EPMA analyses are given in Chapter II. Thus, the methodology section of this chapter focuses on describing the method used to identify and select the pyrite grains of interest within the samples. Finally, the petrographical and elemental results are reported and discussed.

IV.1. Trace element incorporation in sedimentary pyrite

Constraining the appearance of oxygenic photosynthetic bacteria (that later became cyanobacteria) from their anoxygenic precursors, would allow better understanding of the importance of their involvement in the GOE.

Assuming that it is photosynthetically-produced, one possible way to proceed is to determine precisely the variations in the concentration of O₂ in the atmosphere through time. In this context, numerous studies have used

bulk-rock analytical techniques on ancient marine sediments to monitor, through geological time, the fluxes into the ocean of redox sensitive elements such as Mo, U and Re, sensitive to oxidative weathering (Siebert *et al.*, 2005; Algeo & Lyons, 2006; Anbar *et al.*, 2007; Scott *et al.*, 2008; Tissot *et al.*, 2012; McKay & Pederson, 2014). Another way to determine the timing of the appearance of oxygenic photosynthesis is to conduct thorough micropaleontological investigations at the micrometer scale within Archean and Paleoproterozoic shallow marine sediments, in order to identify microbial photosynthetic remains, to characterize their morphology, their chemical and isotopic compositions, and their possible impact on the immediate (μm) surrounding mineral matrix, such as signs of oxidation resulting from the release of O_2 . Although important for understanding the global context, bulk-rock analyses are not sufficient in this case. These investigations require imaging, mineralogical and elemental analytical techniques, functioning at the micrometric and sub-micrometric scale.

Although complementary, these two lines of investigation are most of the time conducted separately by the scientific community. Nevertheless, the trace element content of pyrite (FeS_2) in Archean to Paleoproterozoic shallow-marine sediments could be a key component in bringing the two together. Indeed, pyrite that precipitates during sedimentation or during diagenesis (hereafter called sedimentary pyrite) has received growing interest due to its ability to incorporate redox-sensitive, major-to-trace elements available in the aqueous medium during its growth. In anoxic sediments, pyrite forms by the precipitation of Fe(II) with H_2S , the latter being available in the medium or produced by the reduction of marine sulfates resulting from the activity of sulfate- or sulfur-reducing bacteria (SRBs), either syngenetically with sedimentation or during diagenesis. In an oxygenated aqueous environment, pyrite forms during diagenesis, and begin to grow at or below the sediment-water interface where the medium is depleted in oxygen, and Fe^{2+} and H_2S are available. In either case, trace elements (TE) such as As, Se, Mo, Co, Cu, Mn, Ni, Cr, Pb, Zn and Cd available in seawater, pore water, or released from other sedimentary compounds, such as metal-oxides, commonly coprecipitate with Fe sulfides (Moore *et al.*, 1988), or form their own metal-

sulfides (particularly As, Co, Cu, Ni, Pb) (Luther *et al.*, 1980). Since many of these TE are redox-sensitive, oxidative weathering on land has a strong influence on their alteration and transport to the ocean and thus on their availability to co-precipitate with pyrite. Furthermore, even when submitted to high grade metamorphism (low pressure but temperatures up to 742°C), such as that undergone by some Archean sediments, the refractory nature of pyrite allows its TE content to be retained (particularly Co, Ni, As and Se) making the TE content of sedimentary pyrite a robust proxy to retrace the evolution of oxygen concentration in the atmosphere through geological time as far back as the Early Archean (e.g. Tribovillard *et al.*, 2006; Williford *et al.*, 2011; Large *et al.*, 2014). For instance, on the basis of the variations of Se concentrations in diagenetic pyrite in marine sediments, Large *et al.* (2014) refined the model of the GOE originally proposed by Holland (2006) and suggested the occurrence of peaks of oxygen before the GOE (Fig. IV.1).

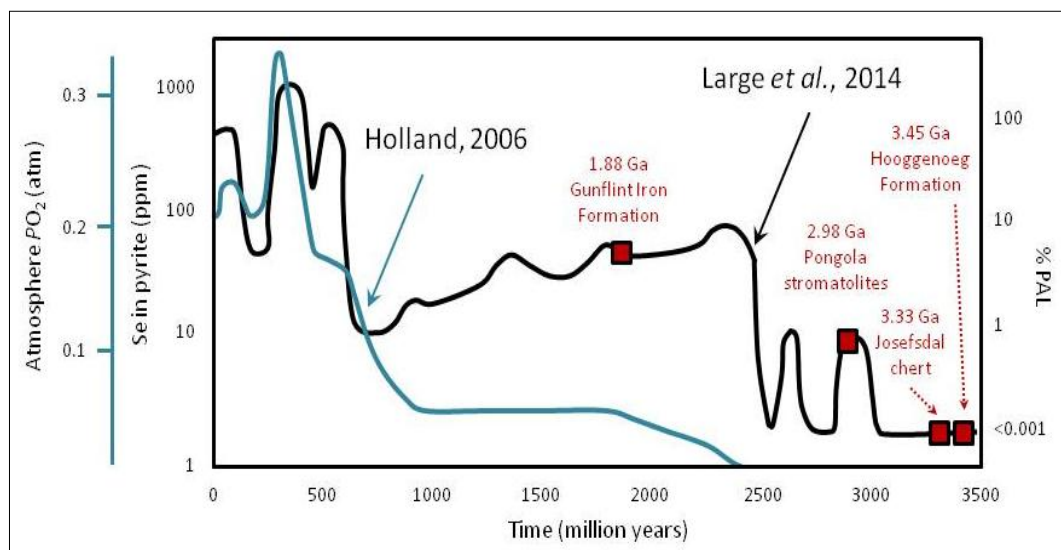


Figure IV.1. Variations in atmospheric O₂ content through time. In blue, the model for the Great Oxidation Event by Holland (2006) based on $\Delta^{33}\text{S}$ data. In black, the model of Large *et al.* (2014) for the evolution of atmospheric O₂ concentrations based on the TE contents of sedimentary pyrite (note that the left scale is Se concentrations), joining the “Whiffs of oxygen” model of Anbar *et al.*, 2007. Red squares indicate the age and designations of the samples used in this study.

In addition to global redox conditions, the TE content of sedimentary pyrite may provide information on local processes related to the presence of organic matter and microbial communities within the sediment. For

instance, numerous studies have documented that, in organic-rich anoxic sediments, organic matter scavenges trace metals such as Co, Ni, Cu, As, Se, V, Mo (Volkov & Fomina, 1974; Raiswell & Plant, 1980; Dill & Kemper, 1990; Kohn *et al.*, 1998; Large *et al.*, 2007; Perkins *et al.*, 2008; Piper & Calvert, 2009), that are subsequently partitioned into pyrite during diagenesis (e.g. Large *et al.*, 2007, 2009). Also, the degradation of organometallic complexes during diagenesis can lead to the release of trace metals into the medium that can be readily incorporated in the diagenetic pyrite composition (e.g. Tribovillard *et al.*, 2006; Large *et al.*, 2007, 2009). Furthermore, certain TE such as As and Se are used as electron donors or acceptors in a variety of microbial metabolisms (Zehr & Oremland, 1987; Oremland *et al.*, 1989; Dowdle & Oremland, 1998; Kirk *et al.*, 2004; Kulp & Pratt, 2004; Kulp *et al.*, 2008; and review of Stolz *et al.*, 2006), hence controlling their oxidation state in the medium and thus their incorporation in pyrite.

Therefore, the TE content of sedimentary pyrite in Precambrian shallow marine sediments could be of dual-use in constraining the evolution of oxygenic photosynthesis in time, allowing simultaneous monitoring of the global redox conditions prevailing at the time of deposition of a specific sediment, as well as the local (micrometric) chemistry of trace metals associated to the microbial communities.

By studying their morphological characteristics and TE content, we propose to investigate the relevance of sedimentary pyrites and metal-sulfides located within the immediate (μm) vicinity of Archean and Paleoproterozoic photosynthetic microbial remains for providing information on local microbial activity.

IV.2. Sample descriptions

We used thirteen 30 μm -thick polished thin sections cut through rock samples from the ~3.45 Ga Hooggenoeg chert, the 3.33 Ga Josefsdal chert, the 2.98 Ga Pongola stromatolites and the 1.88 Ga Gunflint chert (sampled from the Schreiber Beach, Kakabeka Falls and Mink Mountain localities). These thin sections are presented in Figure IV.2. Prior to petrographical

observation and elemental analyses, the 13 thin sections were abraded with 40 μm abrasive cloths under water at the Institut des Sciences de la Terre d'Orléans (ISTO), CNRS Orléans, France, and then polished using the Logitech polisher at the same institute, with felt discs soaked with diamond abrasive pastes. Each thin section was subsequently polished by 9 μm , 3 μm and then 1 μm diamond pastes. In addition to meeting the analytical requirements of SEM and EPMA (smooth surfaces), this preparation method is useful to avoid the possible effects of modern environment on the thin sections (e.g. modern oxidation of preexisting hematite and pyrite to goethite).

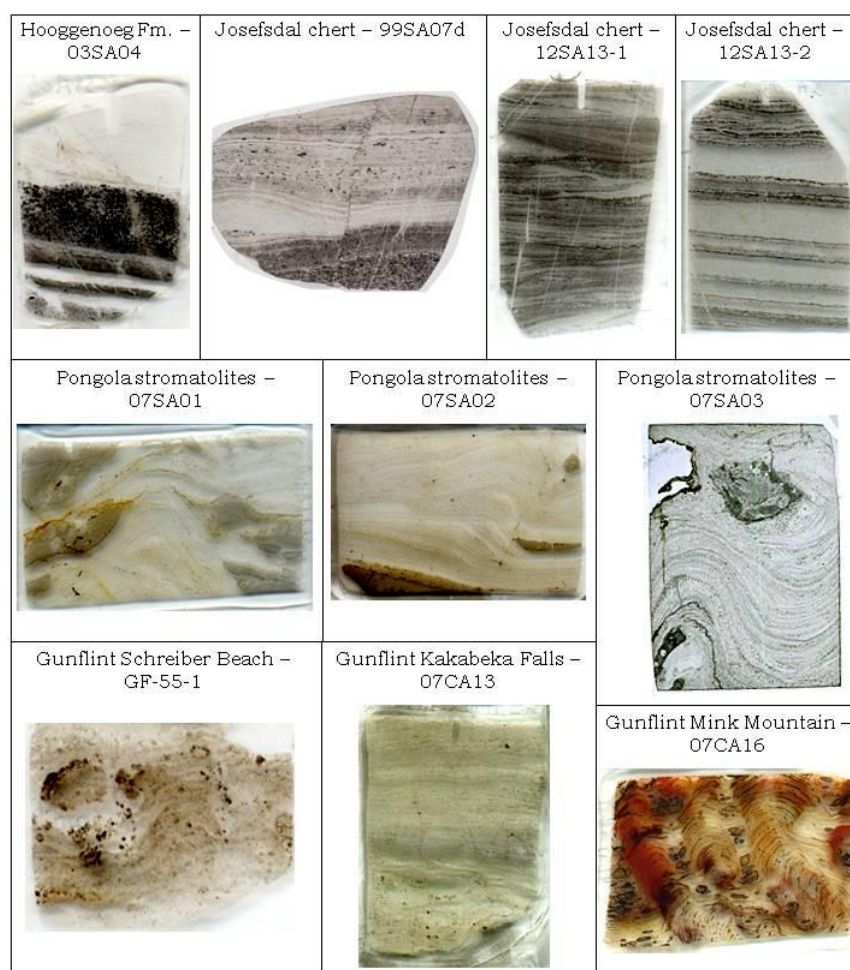


Figure IV.2. High resolution scans of the 30 μm -thick polished thin sections used in this study. Dimensions are approximately 2x3cm. Not represented: duplicates of the following thin sections: GF-55-1, 07CA13 and 07CA16.

The principal characteristics of the samples are listed in Table IV.1. The depositional context, post-depositional processes (e.g. silicification, metamorphic grade) mineralogy and microfossil contents of these samples were described in Chapter III. This is with the exception of sample 03SA04 from the Hooggenoeg chert and samples 12SA13-1 and 12SA13-2 from the Josefsdal chert that were only used for the present investigation. These samples are briefly described in the following paragraphs.

Additional samples: thin sections 03SA04 from the Hooggenoeg chert and 12SA13-1 and 12SA13-2 from the Josefsdal chert, Onverwacht Group, South Africa

The Onverwacht Group is a stratigraphic unit of the Swaziland Supergroup, Barberton Greenstone Belt, South Africa that consists of ultramafic to mafic and dacitic volcanic rocks, and sedimentary rocks that were formed in deep to shallow marine settings. Samples 03SA04 and 12SA13-1/12SA13-2 belong to the H3c chert (Lowe & Byerly, 1999a) of the ~3.45 Ga-old Hooggenoeg Formation (de Wit *et al.*, 1987; Armstrong *et al.*, 1990; Krüner *et al.*, 1991; Lowe & Byerly 1999a) and the Josefsdal Chert (JC) of the ~3.33 Ga-old (Byerly *et al.*, 1996) Kromberg Formation (lateral equivalent of the K3c chert, Lowe & Byerly, 1999a), respectively. These sediments were deposited in shallow-marine environments (Hooggenoeg: Lowe, 1999; JC: Westall *et al.*, 2001, 2015). They consist of highly silicified volcanic dust, ash, accretionary lapilli and volcanoclastics debris, and carbonaceous sediments. They are underlain by silicified pillow basalts and komatiitic basalt (Lowe & Byerly, 1999b).

Table IV.1. Main characteristics of the samples.

Sample name, locality and age	Description and depositional settings	CM, microfossil	Stage of silicification	Metamorphic grade
<i>Hooggenoeg, 3.45 Ga</i>				
03SA04	Black carbonaceous chert. Volcaniclastic debris, accretional lapilli, ash. Shallow-water, subaerial.	Photosynthetic mats Chemio- organotrophic clots Detrital CM	Early diagenesis (before compaction)	Lower greenschist facies
<i>Josefsdal chert, 3.33 Ga</i>				
99SA07d	Black/white banded carbonaceous chert. Finely laminated sandstone, rippled, volcanic accretionary lapilli and ash. Upper shoreface.	Photosynthetic mats Chemolithotrophic and chemo-organotrophic clots Detrital CM	Sedimentation/Early diagenesis (before compaction)	Lower greenschist facies
12SA13-1	Green/black laminated chert. Same composition. Rippled	Detrital CM	Early diagenesis	Lower greenschist facies
12SA13-2	Same, planar	Detrital CM	Early diagenesis	Lower greenschist facies
<i>Pongola stromatolite, 2.98 Ga</i>				
07SA01	Small domical stromatolites. Silicified dolomites in volcano-sedimentary sequence. Tidal deposits.	OM reworked by carbonates.	Late, possibly syn-metamorphic	Greenschist facies
07SA02	Same	OM reworked by carbonates.	Late, possibly syn-metamorphic	Greenschist facies
07SA03	Same	OM reworked by carbonates.	Late, possibly syn-metamorphic	Greenschist facies
<i>Gunflint chert, 1.88 Ga</i>				
SB : GF-55-1, GF-55-1b	Small columnar stromatolites - Hematite-poor. Intertidal deposits.	Large variety of OM-rich variously-shaped microfossils	Very early, during sedimentation or earliest stages of diagenesis	Unmetamorphosed
KF : 07CA13, 07CA12	Columnar stromatolites - Hematite-dense layers. Subtidal shelf to intertidal deposits.	OM-poor: diffuse in carbonate-hematite layers, or absent	Late diagenesis	Unmetamorphosed
MM : 07CA16, 07CA16A	Small columnar stromatolites - Hematite-rich. Subtidal shelf to intertidal deposits.	Large variety of hematite-rich filamentous microfossils	Early diagenesis (before compaction)	Sub-greenschist facies

References can be found in Chapter III.

Samples 12SA13-1 and 12SA13-2 are laminated greenish/black chert (Fig. IV.2 and Fig. IV.3F,G) and belong to the Josefsdal chert of the Kromberg Formation. These samples have the same mineralogical composition as that of the other samples from the Josefsdal chert used in this study and described in Chapter III, although the sediment grain size is coarser. Furthermore, in these two samples, microbial mats are poorly preserved (Westall *et al.*, 2015), displaying only laminations of compacted CM (Fig. IV.3F,G).

Sample 03SA04 (Hooggenoeg Formation) is a banded black and white chert showing alternating organic-rich layers (black) consisting in microbial biofilms (Fig. IV.3A,B), microbial clots (Fig. IV.3C), and organic-poor layers (pale layers) of practically pure chert (Fig. IV.3A) crystallized as meso to megaquartz from silica-rich fluids infiltrations. In the Hooggenoeg formation, filaments and mats were interpreted as photosynthesizing (Walsh, 1992; Westall *et al.*, 2001 and “Note added in proof”). The uncompacted shape of the clusters of organic matter (detrital or formed by bacterial activity) in samples 03SA04 (Fig. IV.3A-C) suggests that the sediments were silicified early after deposition, preventing their deformation by compaction. The metamorphic grade undergone by these sediments is lower greenschist facies (<~350°C, Xie *et al.*, 1997; Tice *et al.*, 2004).

IV.3. Methodology: classification of pyrite

IV.3.1. Types of pyrite

For the purpose of this study, focus was made on the identification of sedimentary pyrite precipitated in close contact (micrometric scale) with fossilized photosynthetic microbial mats and cells when present, or with the originally biological layers of stromatolite samples. However, in order to be thorough, and whenever possible, sulfides occurring in contact with microbial clots that were described as probable colonies of chemolithotrophic or chemo-organotrophic microorganisms (e.g. Westall *et al.*, 2015), as well as sulfides occurring in organic-poor layers of the samples or associated with

detrital carbonaceous matter (CM) were also considered, to provide comparative information. Figure IV.3 and Figure IV.4 describe and locate these zones of interest (microbial colonies, detrital CM and organic-poor layers) in the samples used (from the thin sections presented in Figure IV.2); for the Hooggenoeg chert: Fig. IV.3A-C; for the Josefsdal chert: Fig. IV.3D-G; for the Pongola stromatolites: Fig. IV.3H-I; for the Gunflint chert at the Schreiber Beach locality: Fig. IV.4A-C; at the Kakabeka Falls locality: Fig. IV.4D-E; and at the Mink Mountain locality: Fig. IV.4F-G.

Furthermore, pyrites with a detrital origin were also considered in this study since their presence or absence in marine sediment is in itself an indicator of atmospheric redox conditions (e.g. Holland, 1984; Rasmussen & Buick, 1999). Independent of their condition and context of formation in igneous rocks, detrital pyrites along with various other detrital particles are easily trapped in the extracellular polymeric substance of biofilms due to the adhesive nature of the latter. When oxygenic photosynthesis first arose, reducing conditions must still have prevailed in the atmosphere and oceans (see the review of Buick, 2008). In such anoxic environments, pyrite expelled by, or eroded from, volcanic edifices is easily transported and deposited in marine sediments. If it is deposited in a sediment where oxygenic photosynthetic bacteria were locally active, these pyrite grains could bear textural evidence of oxidation by the putative oxygen-rich microbial medium before being preserved by a rapid silicification of the sediment or by posterior pyrite overgrowths. Under weakly oxidizing atmospheric conditions, detrital pyrite could still be deposited in the proximal, tidal environment in which the sedimentary samples selected for this study were deposited. However, it should be noted that a strongly oxidative atmosphere would not allow the transport of reduced minerals such as pyrite into the ocean (e.g. Holland, 1984; Rasmussen & Buick, 1999). Thus, in some cases, the absence of detrital pyrite in a given sediment may serve as a complementary indication to the presence of oxygen in the environment.

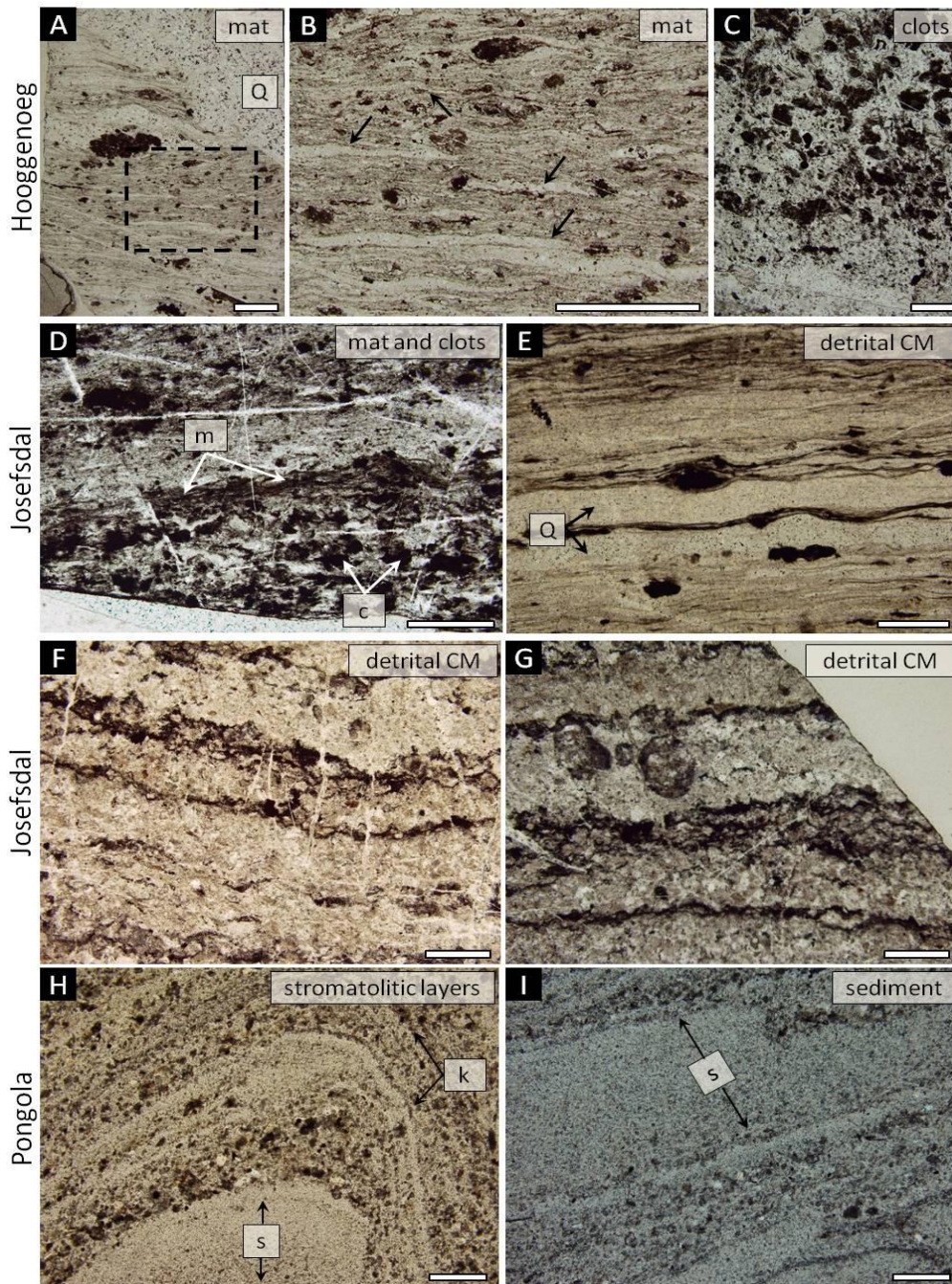


Figure IV.3. Optical photomicrographs of samples from the chert H3c of the Hooggenoeg Formation (A-C), the Josefsdal chert (K3c, Kromberg Formation) (D-G), and Pongola stromatolites (H-I). A. Finely laminated mat layers and clots of detrital CM. The apparent localized compaction of the mat laminae is due to the infiltration of siliceous fluids. The mat has been torn by silica-rich fluids, recrystallized into meso/megaquartz (Q). The dashed black box shows the location of the magnification in B. B. Black arrows point to the megaquartz lenses resulting from post-depositional Si-rich fluid infiltration. C. Probable chemolithotrophic or chemoorganotrophic colonies organized in clots. D. Microbial mat (m) on top of microbial clots (c). E. Fine layer and clots of detrital CM. Layers of practically pure quartz are also visible (Q). F-G. Coarsely grained sandy sediment and poorly preserved, compacted microbial mats. H-I. Ancient stromatolitic layers (k) now composed of degraded carbonates and layers of sediment deposition, displaying grain sorting (s). Scale bar is 500 μ m.

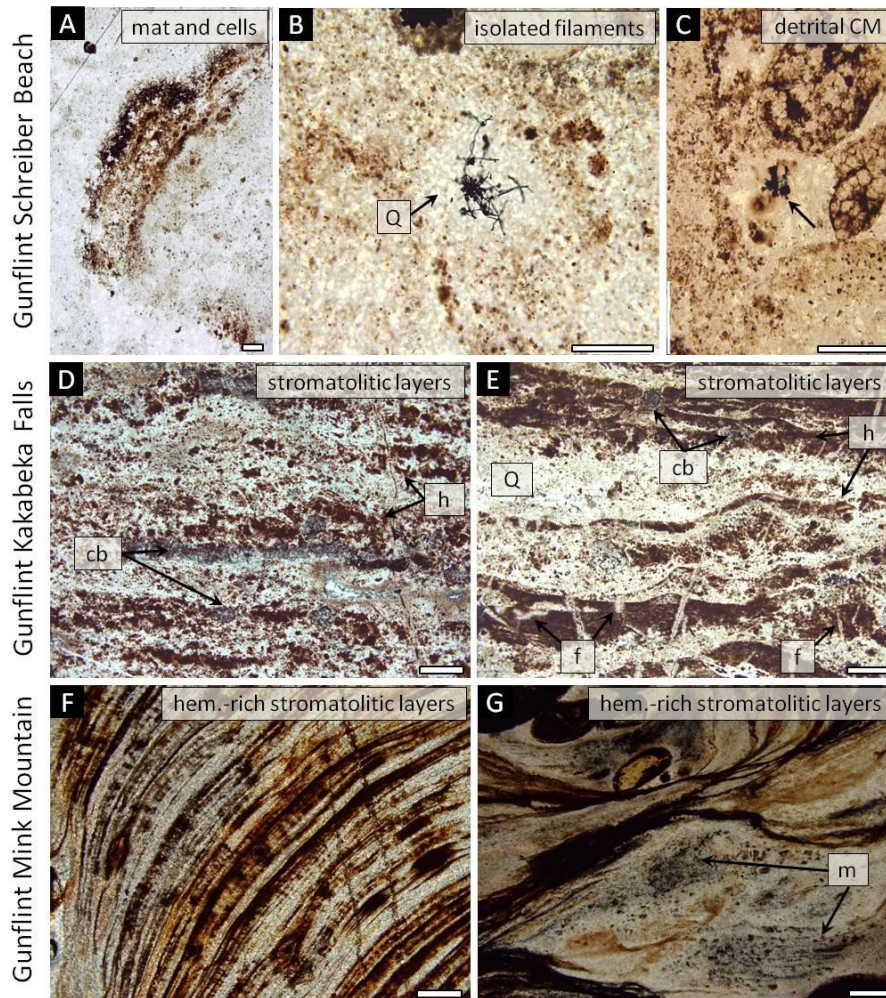


Figure IV.4. Optical photomicrographs of samples from the Gunflint chert at the Schreiber Beach (A-C), Kakabeka Falls (D-E) and Mink Mountain (F-G) localities, and the corresponding microfossils and contexts of sediment deposition. A. Microfossil-rich stromatolitic layer, hematite-coated, and surrounding organic-poor chert. B. Isolated pyritized microbial filaments in a practically pure cherty pore filled with meso/megaquartz (Q). C. Pyritized detrital OM in a pore filled with hematite-coated OM and silica spherules, located in an intercolumnar cavity. D-E. Stromatolitic layers showing alternating hematite-rich (h) and degraded carbonate (cb) layers and chert layers (Q). Fluid escape lenses (f) are also visible. F. Finely laminated hematite-rich stromatolitic layers. G. Microbial mats (m) located in the intercolumnar space, between hematite-rich stromatolitic layers.

Epigenetic pyrites form during hydrothermal or metamorphic events and provide information about epigenetic fluids rather than on the composition of seawater or diagenetic fluids. However, as they may occur as overgrowths on, or replacements of precursor pyrites (sedimentary pyrite, detrital pyrite), epigenetic pyrites may hamper the identification of the

pyrites of interest and lead to their under-estimation in the samples. It is thus important to also consider epigenetic pyrite.

Overall, the TE content of sedimentary pyrite is of primary interest. In this study, it is thus crucial to differentiate between sedimentary pyrite and detrital, and to identify epigenetic overgrowths.

IV.3.2. Identification criteria

Morphological and textural criteria for the recognition of sedimentary versus hydrothermal and metamorphic (epigenetic) pyrite have been extensively studied (e.g. Rasmussen & Buick 1999; Large *et al.*, 2007; Guy *et al.*, 2010; Large *et al.*, 2014). In particular, we used the paragenetic and morphological classification described by Guy *et al.* (2010) to differentiate between detrital, sedimentary and epigenetic pyrite.

Detrital pyrites are generally rounded, but may be subhedral or angular when too small to be mechanically abraded. Since they were deposited in the sediment and did not grow *in situ*, their distribution follows the basic rules of sedimentation. For instance, their distribution in the sediment is concentrated on bedding planes or erosional surfaces. Also, in samples where grain size sorting is visible, detrital pyrite generally has similar size and rounding degree relatively to other surrounding grains of the same stratigraphic level (although they may be somewhat smaller due to their heavier mass). Detrital pyrite can be inclusion-free or inclusion-rich, but in the latter case, inclusions should be different in size and composition compared to the surrounding mineral matrix. Detrital pyrite may also occur in the form of lithoclasts representing the erosion and transport of a lithified rock or particle of various origins: sedimentary (precipitated by microbial activity or during diagenesis) or epigenetic.

Sedimentary pyrite may occur as framboidal pyrite and microcrystal aggregates. In particular, diagenetic pyrite can occur as small subhedral to euhedral crystals aligned parallel to bedding planes, or as fine, disseminated crystals distributed homogeneously in the sample. Diagenetic pyrite can also

form clusters that can be aggregates of small euhedral pyrite crystals, inclusion-free anhydral displacive nodules formed as the sediment was still highly plastic, or inclusion-rich cement concretions formed by the filling of pore spaces between the detrital particles composing the sediment. Diagenetic pyrite can occur as replacement of mineralogical and organic compounds. Occurrences of replacive pyrite were observed on Archean and Paleoproterozoic pyritized microfossils and detrital CM (for instance, Schieber, 2002; Wacey *et al.*, 2013). Another frequent feature of diagenetic pyrite is as inclusion-free to inclusion-rich overgrowths on pre-existing detrital or earlier diagenetic pyrites and metal-sulfides.

Epigenetic pyrite is not aligned with bedding planes. Its distribution can be influenced by fractures, veins, or other signs of fluid circulation. Epigenetic pyrite growth influenced by hydrothermal or metamorphic events can yield the formation of inclusion-free overgrowths on diagenetic pyrite. Large euhedral crystals containing crystallographically aligned pores suggesting rapid growth (e.g. Ramdohr, 1958; Craig *et al.*, 1998) are also a common feature of epigenetic pyrite.

From a chemical point of view, the Co/Ni ratio of pyrite helps distinguishing between diagenetic and epigenetic phases. Pyrites displaying $\text{Co/Ni} \approx 1$ and $\text{Co/Ni} < 2$ are considered diagenetic, while epigenetic pyrite have higher Co values and Co/Ni ratios (Bajwah *et al.*, 1987; Large *et al.*, 2014; Guy *et al.*, 2010).

IV.4. Petrographical results

In the 13 thin sections, circa 140 metal-sulfides were found and studied. The first observation is that in all samples, pyrite and other metal-sulfides are rare and very small, with an average size of 25 μm overall, and 23 μm for sedimentary pyrites alone. Petrographical results are reported in the following paragraphs and summarized in Table IV.2. In the following paragraphs, bracketed numbers indicate the number of sulfides observed for the considered type.

Table IV.2. Petrographic description of pyrite types and paragenetic textural phases, according to their associations with microbial remains, detrital organic matter or kerogen-free deposits.

Sample name	Sulfide type	Association	Description			Paragenesis-morphology*
			Phase 1	Phase 2	Phase 3	
<i>HG 03SA04</i>	HG-1	Microbial mat	Anhedral to subhedral, 25-100 µm, small inclusions (<1 µm)	Subhedral inclusion-free overgrowths or fine rims of pyrite		DET / DIA
	HG-2	Microbial clots	Anhedral to subhedral pyrite (10-100 µm), inclusion-free (or rare <1 µm inclusions)	Euhedral, inclusion-free pyrite overgrowth		DET / DIA / + EPI?
	HG-3	Fractures/fluid circulation (equally in 'pure' cherty zones or cots zones)	Anhedral, subhedral pyrite	Euhedral hematite overgrowth	(Central pyrite is sometimes fully replaced by FeOx or completely oxidized (void))	DET/ (DIA) replaced by FeOx / EPI
<i>JOS 99SA07d</i>	JOS-1	Microbial clots just underneath the photosynthetic microbial mat	Anhedral, small (10-20 µm) rare, pyrite and Ni-pyrite. Small (~1 µm) inclusions.	Anhedral syngenetic overgrowth		DIA / DIA
	JOS-2	Microbial clots	Anhedral, small (10-20 µm), rare, pyrite and Ni-pyrite. Small (~1 µm) inclusions.	Anhedral syngenetic overgrowth		DIA/ DIA
	JOS-3	Sedimented OM layers	Subhedral to euhedral, small (5-15 µm) pyrite			DIA
<i>JOS 12SA13-1, 12SA13-2</i>	JOS-4	Poorly preserved mat and sedimented compacted OM layers	Euhedral, small (1-5 µm) abundant disseminated pyrite			DIA
	JOS-5	Sedimented ash, volcaniclastics layers	Aneydral to rounded 10-20 µm pyrite, rare	Euhedral inclusion-free pyrite overgrowth		DET / DIA
	JOS-6	Sedimented ash, volcaniclastics and compacted OM layers and fluid circulation	Euhedral, large (50-150 µm) pyrite, include DIA pyrite and present crystallographically aligned pores			EPI
<i>PON 07SA01, 07SA02, 07SA03</i>	PON-1	Altered carbonate layers	Anhedral to subhedral pyrite, with numerous small dolomite inclusions (<1-5 µm)	Euhedral pyrite overgrowth	FeOx replacement	DIA / DIA / EPI
	PON-2	Altered carbonate and iron oxides layers	Anhedral (± rounded) to subhedral chalcopyrite, with small (<10 µm) phyllosilicates (muscovite) and dolomite inclusions	Peripheral overgrowth with inclusions of FeOx and covellite, and other compounds		DIA / EPI
	PON-3	Altered carbonate layers	Subhedral to euhedral, small (20 µm) chalcopyrite, with small (<10 µm) phyllosilicates (muscovite) and dolomite inclusions	FeCuOx replacement, plus other compounds		DIA / EPI
<i>SB GF-55-1, GF-55-1b</i>	SB-1	Isolated microbial filamentous cells	Replacive pyrite, anhedral			DIA
	SB-2	Isolated fibrous OM	Replacive pyrite, fibrous	Cement pyrite	Subhedral inclusion-free fine pyrite overgrowth	DIA / DIA / EPI
<i>KF 07CA12, 07CA13</i>	KF-1	Degraded OM layers (carbonates and hematite)	~500 µm cluster of anhydral inclusion-free pyrite, surrounded by carbonates and FeOx			DIA
	KF-2	Cherty layer	Small (15 µm) anhedral to rounded, inclusion-free pyrite			DIA
<i>MM 07CA16, 07CA16a</i>	MM-1	Stromatolitic hematitic layers	Euhedral or subhedral, 20-60 µm rare metal-sulfides, contain small inclusions (<1-3 µm) that have the same morphology and size as the rough patches and hematite grains of the matrix			EPI

*Following Guy *et al.*, 2010. HG: Hooggenoeg. JOS: Josefsdal; PON: Pongola; Gunflint; SB: Schreiber Beach; KF: Kakabeka Falls; MM: Mink Mountain. DET: detritic, DIA: diagenetic; EPI: epigenetic (hydrothermal or metamorphic replacements).

IV.4.1. Pyrites in the Hooggenoeg sample

Two main morphological types of pyrite were observed in the 03SA04 sample of the Hooggenoeg Formation, depending on their association with microbial mats or microbial clots.

HG-1. [4] Detrital pyrite and diagenetic overgrowths in microbial mats.

Subhedral to euhedral pyrites ranging from 40 to 60 μm were observed in association with microbial mats, trapped between the laminae. These pyrites exhibit inclusion-poor to inclusion-rich, angular to rounded cores (Fig. IV.5A,B). Inclusions in these cores do not exceed 2 μm , thus remaining largely inferior in size to the grains of the siliceous sedimentary matrix. These core pyrites may be either detrital grains, or may have been syngenetically precipitated by microbial activity. However, the fact that the inclusions are largely inferior in size compared to the grains of the matrix suggests that these pyrites did not grow *in situ*. Also, the rounded edges suggest that these pyrite cores were transported. Thus, we interpreted these core pyrites as detrital grains. However, the presence of numerous small inclusions of probable light composition (black in EPMA BSE; Fig. IV.5A) suggest that these detrital grains may originally come from a rock in which pyrite was precipitated by microbial activity or during diagenesis. The majority of these pyrites exhibits a smooth, inclusion-free, euhedral overgrowth probably diagenetic (Fig. IV.5A-C).

HG-2 and HG-3. [20] Detrital pyrite and diagenetic and epigenetic overgrowths in the microbial clots.

The other type of pyrite is observed in association with the layer of microbial clots. These grains are euhedral and range from 50 to 100 μm in size (Fig. IV.5D-F). A large number of these pyrites display extensive replacement by iron oxides (HG-3), especially when located on fluid circulation features such as veins, or late filling by a SiO_2 -rich fluid (now megaquartz). Replacement by Fe-oxides identified as hematite is euhedral with a preserved pyrite grain in the center (Fig. IV.5E). However, the grain

may be fully replaced by hematite in which case the core pyrite itself was oxidized and replaced by late Fe-oxides (Fig. IV.5F). In the former case, a vacant space is visible between the preserved core pyrite and the hematitic replacement (Fig. IV.5E). This possibly results from hydrothermal replacement of magnetite by hematite, resulting in a volume decrease, thus increasing permeability and the possibility of fluid circulation (Ohmoto, 2003). Furthermore, the preserved core pyrite displays angular to rounded edges, and in some case, a well-rounded morphology (Fig. IV.5E box). We used the same arguments as above to suggest that these core pyrites are detrital grains (see HG-1 above). Pyrites associated with clots may thus be angular to rounded, detrital pyrites such as those found in the microbial mats, with well-developed inclusion-free euhedral diagenetic overgrowths, that were later replaced by Fe-oxides when the grain was located on the path of fluid circulation during a late epigenetic event.

Grains that are fully-replaced by hematite were also observed in the pure cherty zones of the samples, where no microbial mats, clots, or detrital CM are visible, but only a mesoquartz to megaquartz cement. This supports the possibility that hematite-replacement is concomitant to or results from Si-rich fluid circulation during a hydrothermal event. This Fe-oxide replacement was not observed on pyrite associated with the microbial mats, neither were hydrothermal and epigenetic overgrowths. It is possible that the morphology of the clots itself, with their approximate rounded shape, allowed porosity to remain even after primary silicification, hence resulting in a higher permeability compared to the mat layers. This is supported by the fact that the clots are coated with joined isopachous, layered, rims of silica. Similar textures were reported in the Buck Reef Chert (K1 of the Kromberg Formation, Onverwacht Group) on detrital clots of CM, and were interpreted by Tice & Lowe (2004) as the earliest generation of silica. The remaining porosity would have facilitated the circulation of fluids after silicification. In fact, in our sample, late silica infiltration, recrystallized as meso- to megaquartz, fills the spaces left between the silica-coated clots. If this is true, then Fe-oxide replacements are a result of the circulation of a secondary fluid, probably oxygenated, containing at least some Fe³⁺ ions.

Under the reducing conditions prevailing at 3.45 Ga (e.g. Holland, 2006; Fig. IV.1), the availability of small quantities of Fe^{3+} could result from the photooxidation of Fe^{2+} in the photic zone (PZ) by the high ultraviolet flux reaching Earth's surface, since the protective ozone layer was not in place at that time (Cairns-Smith, 1978; Braterman *et al.*, 1983). Although, Konhauser *et al.* (2007) have shown experimentally that the quantity of ferric iron produced by this process in a medium with high dissolved Fe(II), Si and HCO_3^- would have been negligible compared to ferrous silicates and ferrous carbonates precipitation, this may have been sufficient to precipitate small quantities of magnetite.

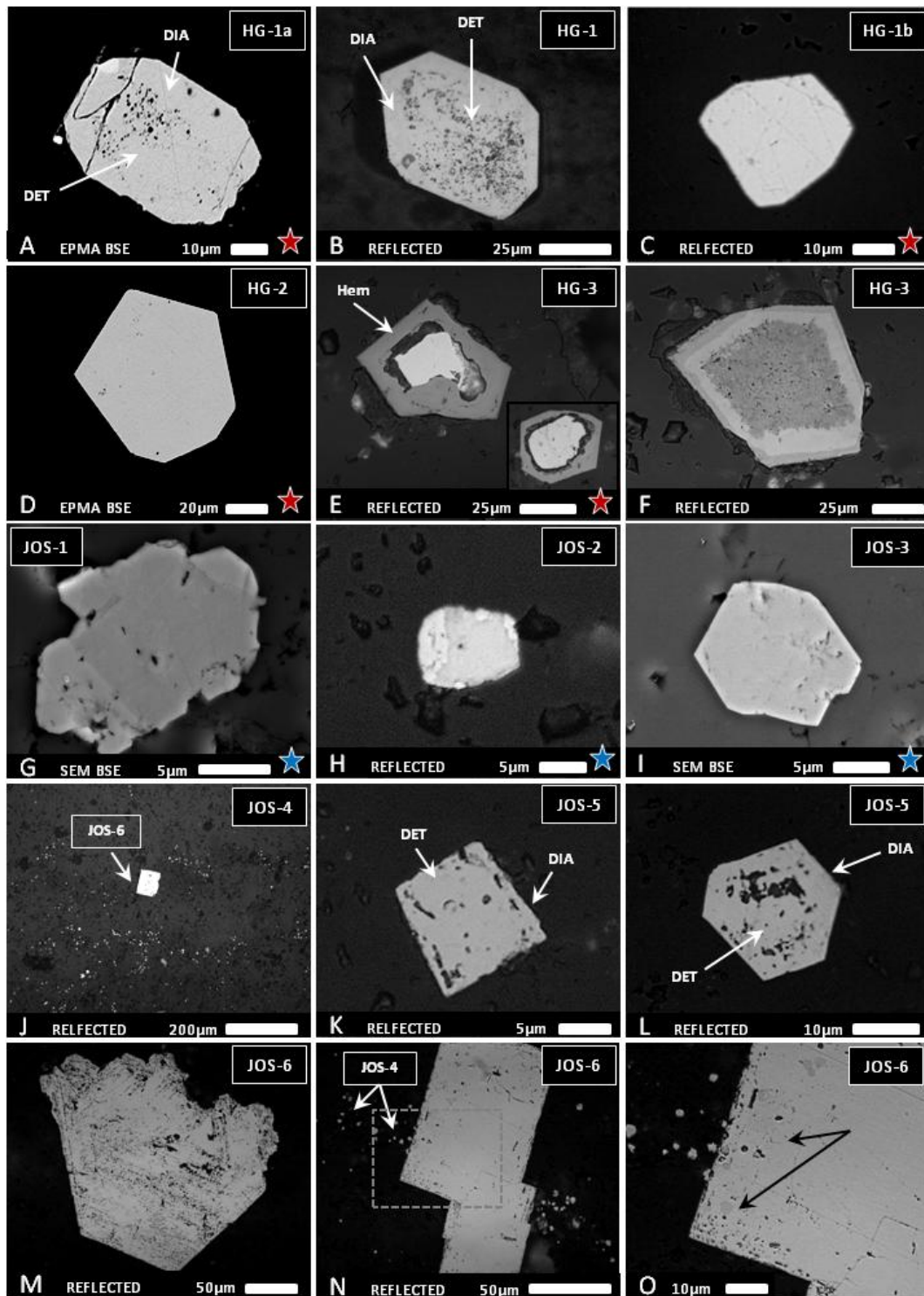


Figure IV.5. Photomicrographs of metal-sulfides found in the Middle Marker and Josefsdal samples. Red stars refer to sulfides that were analyzed by spot measurements and/or mapped by EPMA, blue stars to sulfides analyzed by spot measurements by SEM/EDS. Designations correspond to the pyrite types listed in Table IV.2. DET: detrital; DIA: diagenetic. E. The grain in the box shows the rounded morphology of the remaining pyrite. The grain (pyrite and Fe-oxides overgrowth) measures 100 μm . N. Dashed grey box shows the location of the magnification in O. Black arrows in O indicate micrograins of diagenetic pyrite (JOS-4) and anatase trapped in the epigenetic pyrite JOS-6 during the growth of the later.

IV.4.2. Pyrite and Ni-pyrite from the Josefsdal Chert, Kromberg Formation

Pyrite grains in Josefsdal sample 99SA07d are rare and very small, with grain sizes ranging from 10 to 25 μm , whether they occur within the microbial clots, some of them near the photosynthetic microbial mat (tens of μm below), or within the detrital CM. However, characteristic morphological and optical differences were observed between the grains associated with microbial communities (mat and clots) and grains associated with detrital CM.

JOS-1 and JOS-2. [6] Diagenetic pyrite in the microbial mat and microbial clots.

Grains found in microbial mats and clots are anhydral. In reflected light, they display two distinct sulfide phases, one showing a deeper yellow color with brownish shades compared to the pale yellow of pyrite that appears to have overgrown them (Fig. IV.5G-H). The deeper yellow color of these grains is attributed to significant amounts of metals other than Fe (such as Ni, As...) (Deer *et al.*, 1966).

JOS-3. [7] Diagenetic pyrite in the detrital CM.

Grains associated with detrital CM are anhydral to euhedral, but mostly euhedral, and display the characteristic color of pyrite in reflected light.

JOS-1, JOS-2 and JOS-3 are probably diagenetic, as indicated by the evidence for *in situ* growth provided by numerous small ($\sim 1\mu\text{m}$) inclusions that have the same size and texture as those in the surrounding matrix.

Samples 12SA13-1 and 12SA13-2 (JOS-4 to JOS-6) from the Josefsdal chert are used as comparison since, just as 99SA07d they were formed by the sedimentation of coarse to fine volcanoclastic grains, ashes, and detrital CM, although microbial traces are poorly preserved and the CM is compacted between two successions of grain-sorted coarse to fine

volcaniclastics deposits, suggesting later silicification compared to sample 99SA07d.

JOS-4. Diagenetic microcrystalline pyrite.

In these samples, pyrite is also rare, although diagenetic microcrystalline subhedral to euhedral pyrite is well represented, following the CM layers (Fig. IV.5I,N,O).

JOS-5. [7] Diagenetic overgrowths on precursor pyrite.

Small, 10-20 μm euhedral pyrites following bedding planes display inclusion-free fine overgrowths on anhydral to rounded pyrite (Fig. IV.5K-L). These grains may represent small diagenetic overgrowths on either: (i) detrital grains deposited in the sediment and frequently associated with the poorly preserved and compacted laminae of CM probably because of their adhesive nature, or (ii) microbial pyrite precipitated by the activity of SRBs during the degradation of organic matter from the poorly preserved mats.

JOS-6. [4] Epigenetic pyrite.

Several significantly larger (50-150 μm) euhedral crystals of pyrite were documented in these samples (Fig. IV.5M-O). In several cases, these crystals have overgrown diagenetic microcrystalline pyrite and anatase and show crystallographically aligned pores, suggesting rapid growth (Fig. IV.5N-O). These pyrites result from a post-diagenetic episode of growth and are thus considered epigenetic. This is supported by their close relationship to veins and fluid escape features.

IV.4.3. Pyrite and chalcopyrite in the Pongola stromatolites

The Pongola samples display *prima facie* various sulfide morphologies and textures that can be used to classify them in two main types: pyrite and chalcopyrite. Pyrite and chalcopyrite are widely distributed in these stromatolite samples, although they are generally associated with the layers of altered carbonates.

PON-1. [9] Diagenetic pyrite.

Pyrite occurs as 50-100 μm subhedral inclusion-rich grains (Fig. IV.6A-B). The inclusions are small ($<5 \mu\text{m}$) and correspond in size and morphology to the siliciclastic surrounding matrix composed of volcanoclastics and dolomite grains, suggesting that they grew *in situ*. These pyrites display fine euhedral overgrowths that are partially replaced by Fe-oxides in some cases. This suggests that pyrites are more likely diagenetic and that euhedral overgrowths and Fe-oxides correspond to one or several epigenetic event(s).

The morphology and texture of the PON-1-type diagenetic pyrite is similar to the cement concretions described by Guy *et al.* (2010; their DIA-5 pyrite), which form by the infill of pore spaces between detrital particles present in the sediment. The growth of these diagenetic pyrites depends on the amount of porosity and thus, on the burial depth (Carstens, 1986). However, PON-1 pyrites bear some similarities with Guy's diagenetic displacive nodules as well (also called DIA-5 pyrite in Guy *et al.*, 2010), since some of these grains display very few matrix inclusions. These displacive nodules form at the sea floor or shallow burial depth (Guy *et al.*, 2010; Selles-Martinez, 1996), where the sediment is still highly plastic, hence allowing pyrite precipitation and growth without the incorporation of detrital particles. Thus, the formation of PON-1 may have occurred at an advanced stage of diagenesis but not far at relatively shallow depths, where compaction was still limited and the sediment was still porous.

PON-2 and PON-3. [9] Hydrothermal chalcopyrite.

In these samples, chalcopyrite is recognizable by its deep yellow color in reflected light, and its systematic association with Cu-rich phases (Cu-rich Fe-oxide replacement, covellite crystals; Fig. IV.6C-E) revealed by dark purple-blue shades. Chalcopyrite is subhedral to euhedral with grain sizes ranging from 10 to 100 μm . With the exception of few small grains (10-15 μm ; Fig. IV.6D), chalcopyrite contains inclusions of phyllosilicates (micas) and dolomite (Fig. IV.6C, E) consistent in morphology and size with the crystals of same composition found in the matrix. This suggests that chalcopyrite

grew *in situ* as well. However, in some cases, direct contact between large euhedral dolomite crystals and PON-3 show that growth of chalcopyrite was hindered by the presence of these dolomite crystals. Since large dolomite crystals probably formed by neomorphic growth of precursor dolomite grains or high Mg-calcite during early diagenesis (Schopf *et al.*, 2007), this further suggests that the growth of PON-2 and PON-3 chalcopyrite is posterior to the growth of large euhedral dolomite during early diagenesis. Considering that these sulfides grew *in situ* but that they are highly enriched in Cu compared to PON-1, their precipitation may result from the circulation of a Cu-rich hydrothermal fluid that penetrated the sediment after the earliest stages of diagenesis.

All chalcopyrite grains show signs of chemical alteration, although two distinct groups are identified: (i) some grains display peripheral recrystallization (still chalcopyrite in composition) in which angular crystals of covellite and Fe-oxides are visible (Fig. IV.6C), (ii) while in most chalcopyrites, chemical alteration occurs as fine (<5 μ m and frequently <2 μ m) rims of Cu-rich (purple-blue shades under reflected light) Fe-oxide (hematite) replacement (Fig. IV.6D,E). Type (i) and (ii) are called PON-2 and PON-3 respectively.

It is possible that the epigenetic overgrowth on PON-1 and the precipitation of PON-2/PON-3 result from the same hydrothermal event. Therefore, PON-2 and PON-3 precipitation occurred after PON-1 and thus after the earliest stages of burial diagenesis. PON-2 and PON-3 likely precipitated from a late Cu-rich hydrothermal infiltration made possible by the absence of silicification at this stage. The further oxidation would thereby result from a secondary epigenetic event that affected primarily the Cu-rich phases such as PON-2 and PON-3 and possibly the overgrowth on PON-1.

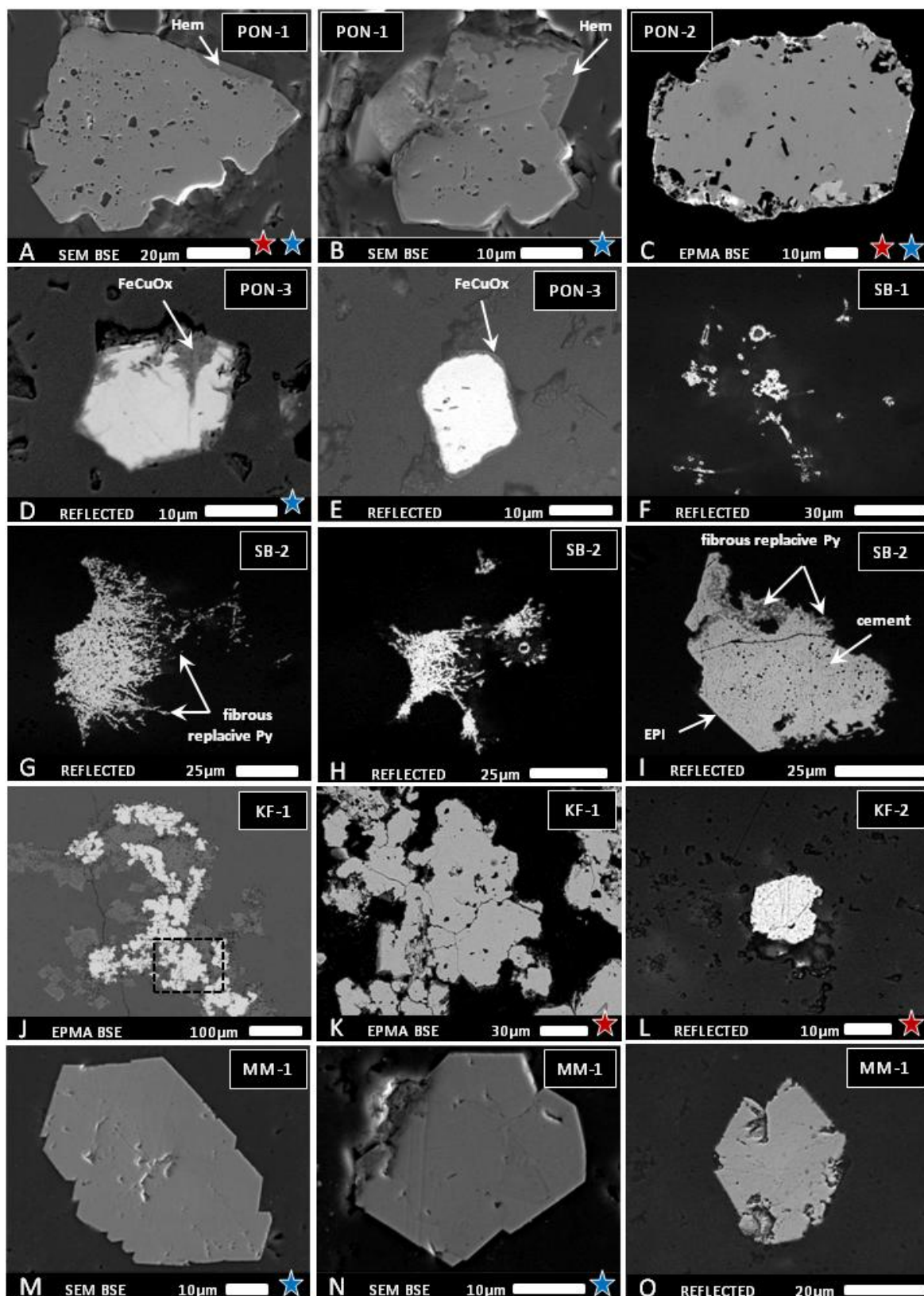


Figure IV.6. Photomicrographs of metal-sulfides found in the Pongola stromatolites and Gunflint samples. Red stars refer to sulfides that were analyzed by spot measurements and/or mapped by EPMA, blue stars to sulfides analyzed spot measurements by SEM/EDS. Hem: hematite; FeCuOx: Cu-rich Fe-oxides; Py: pyrite; EPI: epigenetic. J. Dashed black box indicates the location of the magnification in K.

IV.4.4. Pyritization in the Schreiber Beach samples, Gunflint Formation

SB-1 and SB-2. [13] Replacive pyrite on microbial cells.

Pyrites found in the Schreiber Beach locality samples of the Gunflint Formation were exclusively replacive pyrite. Numerous transported CM clusters located in pores (SB-2; Fig. IV.6G-H) as well as microbial filamentous fossils located in practically pure cherty zones (SB-1; Fig. IV.6F), both coated with hematite, were reported pyritized (see Fig. IV.4). There was no occurrence of detrital grains of pyrite, possibly indicating an oxygenated atmosphere. Replacive pyrite results either from diagenetic processes (e.g. Frizzo *et al.*, 1991) or epigenetic processes such as hydrothermal sulfidation (e.g. Barnicoat *et al.*, 1997). It has been shown that hydrothermal activity had no or little influence on these particular sediments (Hamade *et al.*, 2003), and that silicification occurred as a result of Si-rich seawater precipitation, very early after deposition. Thus, pyritization in these samples may result from the diagenetic solubilization of Fe-oxides present on microbial filaments and detrital OM when isolated in anoxic zones enriched in H₂S. If true, these replacive pyrites could be of great interest for the purpose of this study since they are precipitated directly on the microfossils and may have absorbed the TE released during the breakdown of organic molecules. However Shapiro & Konhauser (2015) proposed that hematite mineralization of these microfossils occurred during late diagenesis, making pyritization the result of chemical processes occurring later than diagenesis, or, the result of a hydrothermal event, isolating some filaments and OM in anoxic veins and pores enriched in H₂S. This is supported by the fact that pyritized CM and microbes occur within meso-megaquartz zones, suggesting late infill of pores by a SiO-rich fluid and that some extensively pyritized CM displays well-developed euhedral growths of inclusion-free pyrite typical of epigenetic pyrite (Fig. IV.6I). These pyrites were thus dismissed for further elemental investigation. However, this is debated in the Discussion section below.

IV.4.5. Pyrite in the samples of the Kakabeka Falls locality, Gunflint Formation

KF-1 and KF-2. [4] Diagenetic pyrite.

Pyrite in the Kakabeka Falls samples is rare, anhydral and ranges from individual 15 μ m grains to several hundreds of μ m large clusters. Distinct differences are observed between pyrite in hematite-rich and carbonate-rich layers and pyrite in cherty layers. KF-1 (Fig. IV.6J-K) refers to large clusters (~500 μ m) found in association with degraded, hematite-rich stromatolitic layers, while KF-2 (Fig. IV.6L) refers to the significantly smaller (10-20 μ m) anhedral grains found in cherty layers (see Fig.IV.4). Large clusters contain occasional small inclusions of carbonates and chert. It is likely that these clusters grew *in situ*, since they contain inclusions of the matrix. However, this must have occurred at a stage where the sediment was still highly plastic since these inclusions are rare. These clusters correspond to the displacive pyrite nodules described by Guy *et al.* (2010) and interpreted as being precipitated just below the water-sediment interface (see the paragraph on Pongola diagenetic pyrite above). Small pyrite grains bear the same characteristics as the large clusters, although they are too small to have incorporated matrix inclusions. Pyrite in the Kakabeka Falls samples is thus most likely early diagenetic. No detrital pyrite was found, suggesting that atmosphere and possibly ocean were oxygenated at that time.

IV.4.6. Pyrite in the Mink Mountain hematite-rich stromatolites, Gunflint Formation

MM-1. [8] Epigenetic pyrite in hematite-rich laminae.

Pyrite in the Mink Mountain stromatolites is rare and restricted to the hematite-rich stromatolitic laminae. The grains are subhedral to euhedral crystals, with grain sizes ranging from 10 to 60 μ m (Fig.IV.6M-O). They contain small inclusions that correspond in size and distribution to (i) the

micro/nanocrystals of hematite present in the matrix, and to (ii) the microporosity of the matrix. In reflected light, the color of the grains is either deep-brownish yellow or white, suggesting that metals other than Fe are also part of the composition as major elements (such as As, Co, Ni) (Deer *et al.*, 1966). Evidence for *in situ* growth, euhedral morphology and high content of metals such as Co, As points to an epigenetic origin.

IV.5. Elemental analyses results

Point elemental analyses were performed by SEM/EDS and EPMA in order to quantify the major to trace element composition of the paragenetic phases identified by petrographical observations (detrital, diagenetic and epigenetic). The results are reported in Table IV.3, where chemical composition is cross-referenced with grain type designation (e.g. Hg-1, Hg-2, etc.) and the paragenetic association (detrital, diagenetic and epigenetic) presented in Table IV.2. Precise locations of the analytical spots numbered in Table IV.3 are given in Figure IV.7-10 and Figure IV.12-15. Except for the epigenetic pyrites of the poorly-preserved mat Josefsdal chert samples (12SA13-1 and 12SA013-2) and the replacive pyrite in the stromatolites of the Schreiber Beach locality, Gunflint Formation, each type of pyrite studied was submitted to quantitative elemental analyses. EPMA mapping is reported in Figures IV.7 to IV.10 and was performed on selected grains in order to assess the spatial distribution of the TE within these phases. Apparent zoning in Fe and S maps (and sometimes Cu, Se and Ni) near the grain boundary is an edge effect related to secondary fluorescence (Fournelle *et al.*, 2005; Williford *et al.*, 2011).

The combined TE zoning and Co/Ni ratios obtained by quantitative analyses allows differentiating between detrital, diagenetic and epigenetic origins (Bajwah *et al.*, 1987; Large *et al.*, 2014; Guy *et al.*, 2010).

Table IV.3. Major to trace elements content of the described metal-sulfides.

Sample name	Sulfide name	Sed./growth stage	Analytical techniques	Chemical composition								Co/Ni	Spot on picture*
				Fe (wt%)	S (wt%)	Cu (ppm)	Co (ppm)	Ni (ppm)	As (ppm)	Se (ppm)	Other		
<i>HG 03SA04</i>	HG-1a	Detrital grain	EPMA	46.18	52.81	0	0	0	271	544		-	1
		Detrital grain	EPMA	46.44	53.05	0	<D.L.	<D.L.	283	515		-	3
		Diagenetic overgrowth	EPMA	46.32	52.88	88	382	214	327	577		1.79	2
	HG-1b	Detrital grain	EPMA	45.97	53.07	<D.L.	0	0	179	531	Cd	-	1
		Detrital grain	EPMA	45.87	53.01	<D.L.	0	<D.L.	262	538		-	2
		Diagenetic overgrowth	EPMA	45.65	52.62	97	460	445	359	637		1.03	3
	HG-2	Detrital grain	EPMA	46.37	53.16	<D.L.	<D.L.	<D.L.	409	625	Ag	-	2
		Detrital grain	EPMA	46.34	52.99	191	0	0	173	498		-	3
		Diagenetic overgrowth	EPMA	45.95	52.71	90	151	1836	3151	474	Te	0.08	4
		Hydrothermal	EPMA	45.78	52.81	249	5032	1018	634	468	Ag	4.94	1
		Hydrothermal/metam.	EPMA	46.25	53.02	<D.L.	408	<D.L.	277	427		-	5
	HG-3	Detrital grain	EPMA	46.54	52.71	120	0	<D.L.	304	610		-	1
		Detrital grain	EPMA	46.44	52.87	156	<D.L.	<D.L.	607	432		-	2
	<i>JOS 99SA07d</i>	JOS-1	Diagenetic	SEM/EDS	20.43	46.28			32.76 wt%				-
Diagenetic			SEM/EDS	18.41	43.19			29.3 wt%			O, Si	-	2
Diagenetic			SEM/EDS	19.43	44.77			30.38 wt%			O, Si	-	3
Diagenetic			SEM/EDS	20.42	32.45			33.98 wt%			O, Si	-	4
Diagenetic			SEM/EDS	20.39	31.55			34.76 wt%			O, Si	-	5
Diagenetic			SEM/EDS	14.34	22.31			24.74 wt%			O, Si	-	6
Diagenetic			SEM/EDS	13.33	21.8			21.73 wt%			O, Si	-	7
JOS-2		Diagenetic	SEM/EDS	10.75	39.5			49.17 wt%				-	1
		Diagenetic	SEM/EDS	21.63	39.29			38.69 wt%				-	2
		Diagenetic	SEM/EDS	34.36	52.18			13.01 wt%				-	3
		Diagenetic	SEM/EDS	29.69	48.49			21.38 wt%				-	4
		Diagenetic	SEM/EDS	38.92	55.9			4.76 wt%				-	5
		Diagenetic	SEM/EDS	40.72	57.58			1.24 wt%				-	6
JOS-3		Diagenetic	SEM/EDS	42.02	57.98							-	1
		Diagenetic	SEM/EDS	40.74	57.17			1.58 wt%				-	2
		Diagenetic	SEM/EDS	40.87	57.52			1.61 wt%				-	3

		Diagenetic	SEM/EDS	39.21	57.52			2.73 wt%		-	4		
		Diagenetic	SEM/EDS	39.93	57.49			1.94 wt%		-	5		
		Diagenetic	SEM/EDS	39.81	57.2			2.17 wt%		-	6		
		Diagenetic	SEM/EDS	40.85	56.13			2.05 wt%		-	7		
		Diagenetic	SEM/EDS	40.06	57.01			1.97 wt%		-	8		
<i>PON 07SA01</i>	PON-1	Diagenetic stage	EPMA	44.19	50.19	260	65	419	14938	514	0.16	~1	
		Diagenetic stage	EPMA	45.00	51.06	285	339	761	11942	621	0.45	~1	
		Diagenetic stage	EPMA	45.27	51.70	282	233	827	10175	567	0.28	1	
		Diagenetic stage 2	EPMA	45.43	52.24	207	611	1451	3761	515	0.42	2	
		Diagenetic stage 2	EPMA	45.47	52.56	94	764	4797	2457	566	Ag	0.16	~5
		Diagenetic stage 2	EPMA	45.98	53.11	0	1157	4144	2042	460		0.28	5
		Diagenetic stage 2	EPMA	45.7	52.87	<D.L.	1319	3329	1616	518	Ag	0.40	3
		Hydrothermal	EPMA	46.02	52.64	430	2488	1932	4256	462		1.29	6
		Hydrothermal	EPMA	45.44	51.93	357	3173	1772	2486	479		1.79	4
	PON-2	Hydroth. CuFeS ₂	EPMA	30.49	35.06	34.46 wt%	<D.L.	0	254	574	-	1	
		Hydroth. CuFeS ₂	EPMA	30.31	35.25	34.38 wt%	<D.L.	<D.L.	291	568	-	2	
		Hydroth. CuFeS ₂	EPMA	30.18	35.26	34.78 wt%	<D.L.	118	223	602	Cd	-	3
		Hydroth CuFeS ₂	EPMA	30.25	34.94	34.39 wt%	0	<D.L.	241	591	-	4	
		Epigenetic CuS	EPMA	2.64	34.06	55.51 wt%	173	165	238	3363		1.05	5
		Fe-oxide	EPMA	44.87	3.13	5.38 wt%	276	2369	0	517	Sb	0.12	6
		Epigenetic CuFeS ₂ +PbZnNiAsCo	EPMA +SEM/EDS	7.28	32.40	35.31 wt%	19664	61693	208	3293	Pb, Zn, Ag, Cd, Te	0.32	7
	PON-3	Hydroth. CuFeS ₂	EPMA	29.74	35.00	34.44 wt%	<DL	<DL	180	528	-	1	
		Hydroth. CuFeS ₂	EPMA	29.57	34.83	33.99 wt%	64	<DL	136	489	Ag, Sb	-	2
		Hydroth. CuFeS ₂	EPMA	29.45	34.73	34.28 wt%	323	497	262	505		0.65	3
Hydroth. CuFeS ₂		EPMA	29.05	34.32	34.95 wt%	320	361	172	537	Ag	0.89	4	
Epigenetic CuFeS ₂ +PbZnNiAsCo		EPMA +SEM/EDS	27.69	32.01	35.14 wt%	646	2716	214	598	FeOx, Ag	0.24	5	
Epigenetic CuFeS ₂ +PbZnNiAsCo		EPMA +SEM/EDS	26.53	19.98	31.12 wt%	2003	13745	186	1345	FeOx, Ag, Cd	0.15	6	
Epigenetic FeCuOx +PbZnNiAsCo		EPMA +SEM/EDS	9.35	11.06	13.83 wt%	2410	3171	139	644	Ag	0.76	7	
<i>KF 07CA13</i>	KF-1	Diagenetic stage 1	EPMA	45.98	52.29	258	185	174	9279	476	1.06	6	

		Diagenetic stage 2	EPMA	46.32	52.58	699	206	0	4177	446	-	3	
		Diagenetic stage 2	EPMA	46.52	52.95	411	121	<D.L.	1140	468	-	1	
		Diagenetic stage 3	EPMA	46.18	52.51	1598	139	151	3752	442	Ag	0.92	5
		Diagenetic stage 3	EPMA	46.16	52.61	1565	147	<D.L.	3011	419	-	8	
		Diagenetic stage 3	EPMA	46.09	52.56	1048	0	0	2285	436	-	7	
		Diagenetic stage 4	EPMA	45.88	52.50	2901	146	251	3742	465	0.58	9	
		Diagenetic stage 4	EPMA	46.01	52.88	1302	415	256	2124	462	Cd	1.62	4
		Diagenetic stage 4	EPMA	46.27	52.94	461	103	<D.L.	1507	359	-	2	
KF-2		Diagenetic stage 1	EPMA	45.74	52.54	2830	0	79	5667	462	-	2	
		Diagenetic stage 2	EPMA	45.64	52.27	2365	0	<D.L.	5025	484	-	1	
		Diagenetic stage 3	EPMA	45.73	52.35	2737	<D.L.	<D.L.	5520	357	-	7	
		Diagenetic stage 3	EPMA	45.64	52.24	2174	0	<D.L.	4460	381	-	6	
		Diagenetic stage 3	EPMA	45.94	52.50	1884	0	<D.L.	3683	457	-	3	
		Diagenetic stage 3	EPMA	45.22	51.45	1066	0	0	2628	402	-	5	
		Diagenetic stage 4	EPMA	45.73	52.61	1793	0	0	3025	328	-	8	
		Diagenetic stage 4	EPMA	45.21	51.60	1804	144	317	1583	371	0.45	4	
		Diagenetic stage 4	EPMA	45.91	52.39	1446	<D.L.	0	3049	365	-	9	

<i>MM 07CA16</i>	MM-1a	Hydrothermal	SEM/EDS	6.78	24.34	25.49 wt%	3.6 wt%	39.33 wt%	7.08	
		Hydrothermal	SEM/EDS	7.35	21.75	25.73 wt%		41.69 wt%	Hem.	-
		Hydrothermal	SEM/EDS	4.33	20.39	21.99 wt%	6.06 wt%	44.85 wt%	Hem.	3.63
		Hydrothermal	SEM/EDS	5.93	24.31	24.84 wt%	3.87 wt%	38.24 wt%	Hem.	6.42
		Hydrothermal	SEM/EDS	6.08	25.42	23.75 wt%	3.38 wt%	38.85 wt%	Hem.	7.03
	MM-1b	Hydrothermal 1	SEM/EDS	6.39	24.53	27.68 wt%		41.41 wt%	-	
		Hydrothermal 2	SEM/EDS	6.29	21.83	34.31 wt%	6.81 wt%	28.94 wt%	5.04	
		Hydrothermal 2	SEM/EDS	2.61	22.75	23.73 wt%	4.48 wt%	41.43 wt%	5.30	
		Hydrothermal 2	SEM/EDS	3.52	21.16	25.46 wt%	5.42 wt%	39.42 wt%	4.70	

*See Figures IV.7 to IV.10 and IV.12 to IV.15.

Sample and sulfide names, as well as growth stages are found in Table IV2.

HG: Hoogenoeg; JOS: Josefsdal; PON: Pongola; Gunflint; SB: Schreiber Beach; KF: Kakabeka Falls; MM: Mink Mountain.

IV.5.1. Detrital and diagenetic pyrite in the Hooggenoeg Formation

Elemental mapping confirmed the petrographical observations and deductions regarding the paragenetic origin of the pyrites found in the microbial mats and clots. Indeed, EPMA maps, and especially Co maps (Fig. IV.7) reveal an internal chemical zoning indicating detrital grains overgrowth by diagenetic and epigenetic precipitation phases. Two pyrites occurring in the microbial mat (HG-1a and HG-1b) and two from the microbial clots (HG-2 and HG-3), with one displaying significant Fe-oxide replacements (HG-3), were quantitatively analyzed.

In all cases, the recurrent TE in detrital pyrite are As and Se with respectively 172-607 ppm and 427-637 ppm. Co and Ni are absent, or below detection limit (D.L.). Cu may occur as Cu-sulfide micro-inclusions since it is detected locally, although reaching only 191 ppm.

The chemical composition of the diagenetic overgrowths is characterized by the presence of Co and Ni. However, the TE content of the diagenetic phase differs between microbial mats pyrites and microbial clots pyrites. For HG-1a and HG-1b, As and Se contents slightly increase compared to the detrital grain (+40-50 ppm), and Co, Ni and Cu are detected exclusively in this diagenetic overgrowth, with respectively 382-460 ppm, 214-445 ppm and 88-97 ppm. Co/Ni ratios are 1.79 and 1.03.

The diagenetic overgrowth of HG-2 displays high contents of Ni (1836 ppm) and As (3151 ppm), and lower levels of Co (151 ppm), Cu (90 ppm) and Se (474 ppm). The Co/Ni of this phase is 0.08 (Fig. IV.8). The HG-2 diagenetic phase is overgrown by two more euhedral precipitation phases, one being hydrothermal with high Co contents (~5000 ppm) and Co/Ni = 4.94, the other being probably hydrothermal and/or metamorphic, characterized by low TE contents generally resulting from the liberation of TE during recrystallization processes (Large *et al.*, 2007).

HG-3 post-detrital overgrowths were not analyzed since all that is remaining is an Fe-oxide replacement.

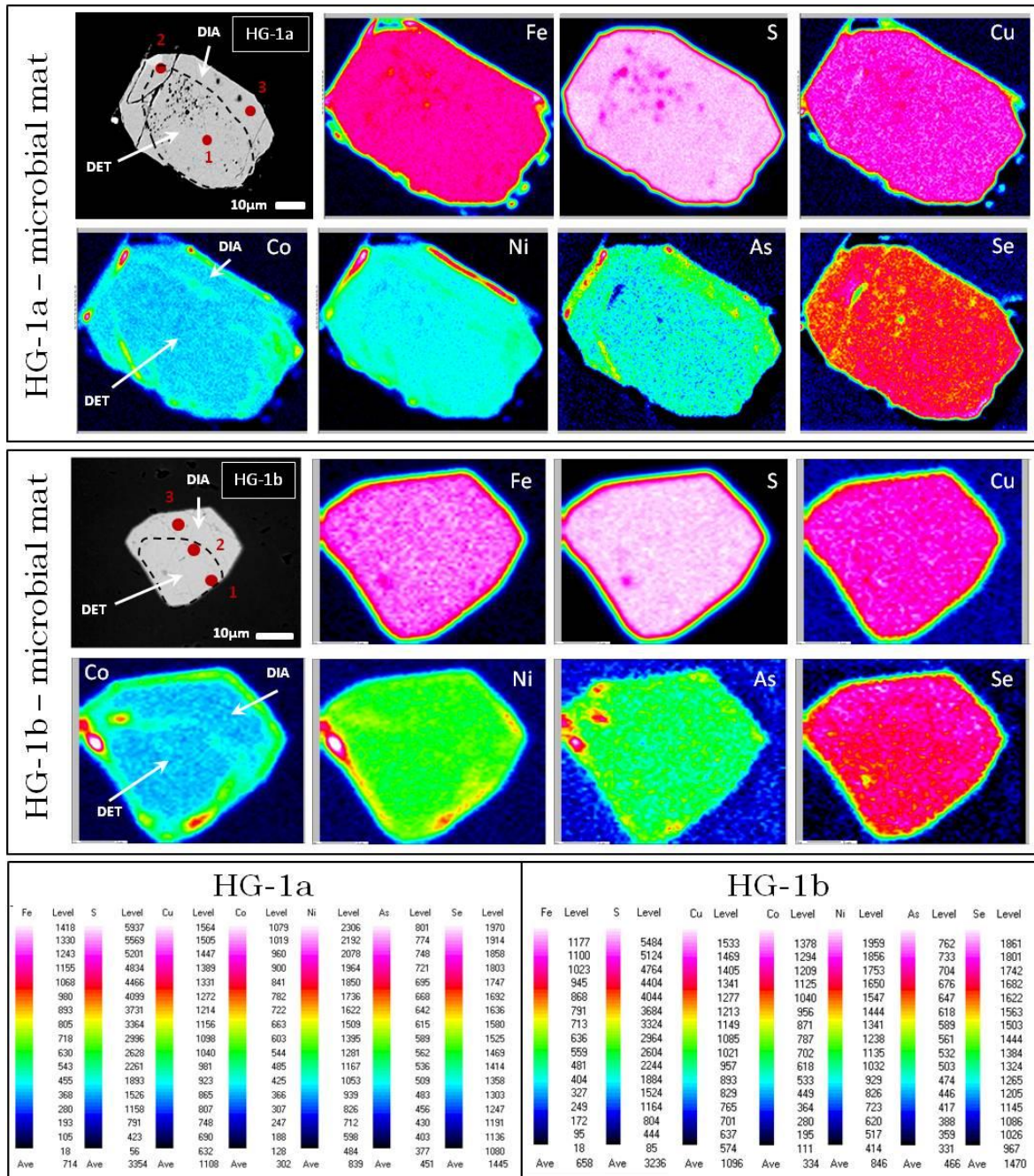


Figure IV.7. EPMA elemental mapping of diagenetic pyrites HG-1a and HG-1b located within the microbial mat in the Hooggenoeg Chert.

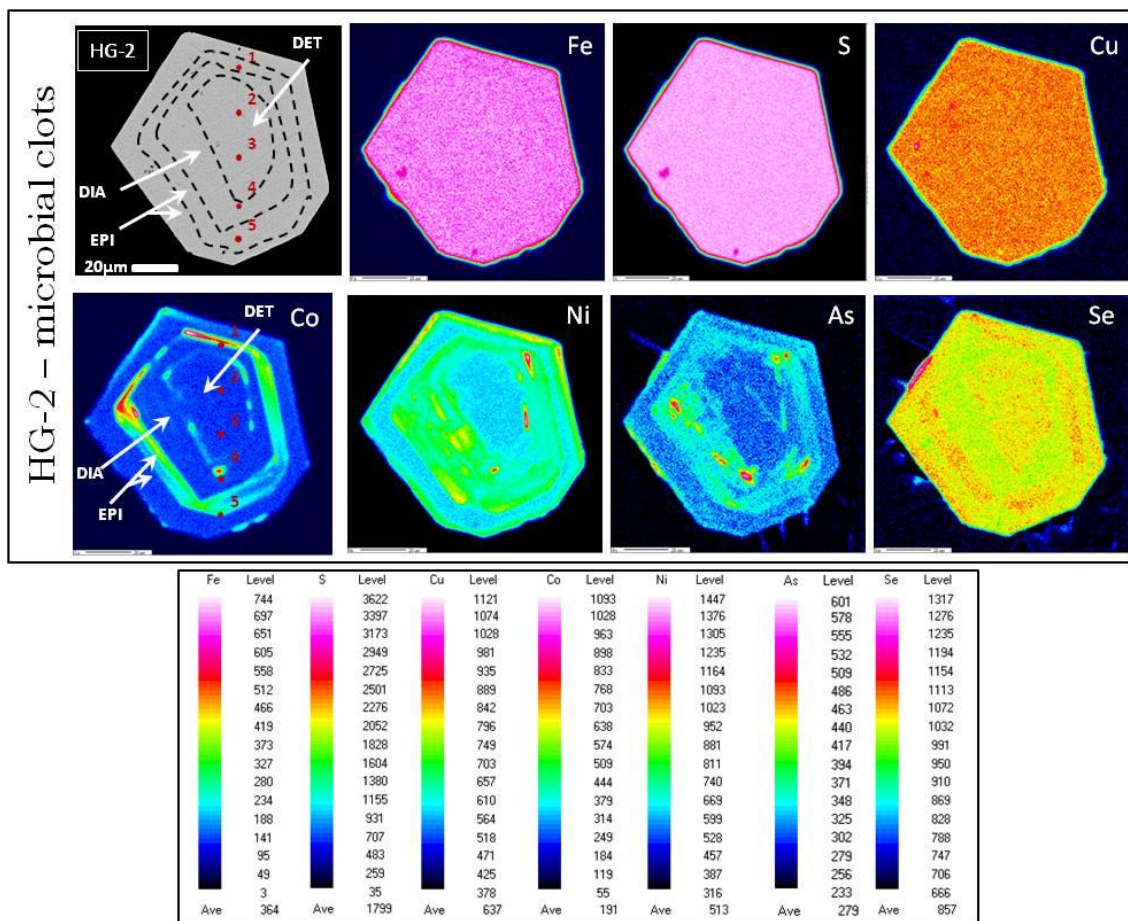


Figure IV.8. EPMA elemental mapping of pyrites HG-2 located within the microbial clots in the Hooggenoeg Chert.

IV.5.2. Diagenetic pyrite in the Josefsdal Chert

The chemical compositions of diagenetic sulfides in the sample 99SA07d of the Josefsdal Chert were determined by SEM/EDS spot analyses (see Table IV.3). Note that, with this technique, TE with concentrations <1000 ppm are not detected. However, high levels of Ni were measured, and the variations in the content of this element alone allow interesting observations to be made.

The first observation that can be made is that, in the anhydral diagenetic pyrites found in the microbial clots (JOS-2) and near the microbial mat (JOS-1), Ni contents range between ~30 and ~50 wt.%, at least in the first stages of their growth (central part of the grain, spot n°1), while

Ni is absent from the central part of the euhedral diagenetic pyrite associated with detrital CM (JOS-3, spot n°1), and Ni contents at the other analytical spots within the grain are only <3 wt.%. The relative abundances of Fe, S and Ni in the central part of JOS-1 are coherent with pentlandite (Fe,Ni)₉S₈. However, since Ni contents are highly variable in these grains (between two grains, and within one grain, from the center to the edges), we prefer to refer to them as Ni-rich pyrites.

The chemical variations that yield the subtle color changes at the extremities of JOS-1 (analytical spots n°4-7) and JOS-2 (spots n°2-6) are of two types: (i) progressive introduction of SiO₂ in the composition (up to ~43 wt.%), with only a slight decrease in Ni content (~-10wt.%) toward the edge and (ii) progressive decrease in the Ni content (~-50wt.%) toward a pure FeS₂ composition at the edges, respectively.

IV.5.3. Diagenetic pyrite and hydrothermal chalcopyrite in Pongola stromatolites

Combined elemental mapping and quantification reveal that diagenetic pyrite is enriched in As (up to ~1.5 wt.%), which is also present in early diagenetic euhedral dolomite (PON-1 and PON-2 maps, in Fig. IV.9). This supports the fact that pyrite grew concomitantly with early diagenetic dolomite, from the same diagenetic fluid, although As was preferentially concentrated in pyrite. Co/Ni ratios of diagenetic pyrite range from 0.16 to 0.45. The fine euhedral pyritic overgrowth in PON-1 is composed of high contents of Co (2488-3173 ppm), Ni (1772-1932 ppm) and As (2486-4256 ppm). Co/Ni ratios are 1.29 and 1.79, consistent with hydrothermal pyrite (Bajwah *et al.*, 1987). Fe-oxide replacement is also enriched in Co, Ni, and SEM/EDS revealed the presence of Zn. Compared to the diagenetic phase, the hydrothermal overgrowth is slightly enriched in Cu (~390 ppm against ~220 ppm) and elemental mapping revealed the presence of a Cu-rich phase containing high levels of Fe, Co, Ni, As and Se that seems to be linked to the euhedral hydrothermal overgrowth.

The TE in PON-2 and PON-3 are depleted in the original chalcopyrite (Co, Ni and As <500 ppm, Se 500-600 ppm) and enriched in the peripheral alterations zones. In PON-2, the peripheral zone is composed of an amorphous chalcopyrite phase and crystals of covellite and Fe-oxides. Covellite is enriched in Se (~3000 ppm), while Fe-oxides display high levels of Cu (5 wt.%), S (3 wt.%) and Ni (~2300 ppm). The amorphous chalcopyrite phase displays high contents of Ni (~6 wt.%), Co (~2 wt.%) and Se (~3000 ppm). SEM/EDS detected Zn, along with high contents of Pb (1-3 wt.%) concentrated in micro-inclusions of galena (PbS). In PON-3, TE follow the same preferential chemical associations although, in this case, the peripheral alteration does not show separate Fe-oxides and Cu-sulfides mineral phases (observed in PON-2), but is gradual from a practically pure chalcopyrite composition at the center with low TE content, toward an Fe-oxide rich amorphous chalcopyrite enriched in Ni (~2700 ppm to ~1.4 wt.%) and Co (~2000 ppm), and finally to Cu-S-rich Fe-oxide replacement rim enriched in Pb (3-6 wt.%), Ni (~3000 ppm) and Co (~2400 ppm).

Where Co and Ni concentrations are sufficiently high, the calculation of Co/Ni in chalcopyrite gives 0.65-0.89, which is a little less than the average Co/Ni for hydrothermal chalcopyrite found by Bajwah *et al.* (1987). However, they noted that the lack of Co in this case could be due to preferential partitioning of Co in pyrite due to the compatible electronic spin state of Co²⁺ and Fe²⁺. Also, if the epigenetic euhedral overgrowth on PON-1 and the chalcopyrites PON-2 and PON-3 precipitated from the same fluid, as hypothesized earlier, this may explain the Co-rich, Cu-poor composition of PON-1 overgrowth and the concentration of Cu in a separate grain. Furthermore, Co/Ni in Fe oxide-rich phases of PON-2 and PON-3 yield respectively 0.12 and 0.15-0.76. This is consistent with the values given by Bajwah *et al.* (1987) for hydrothermal magnetite.

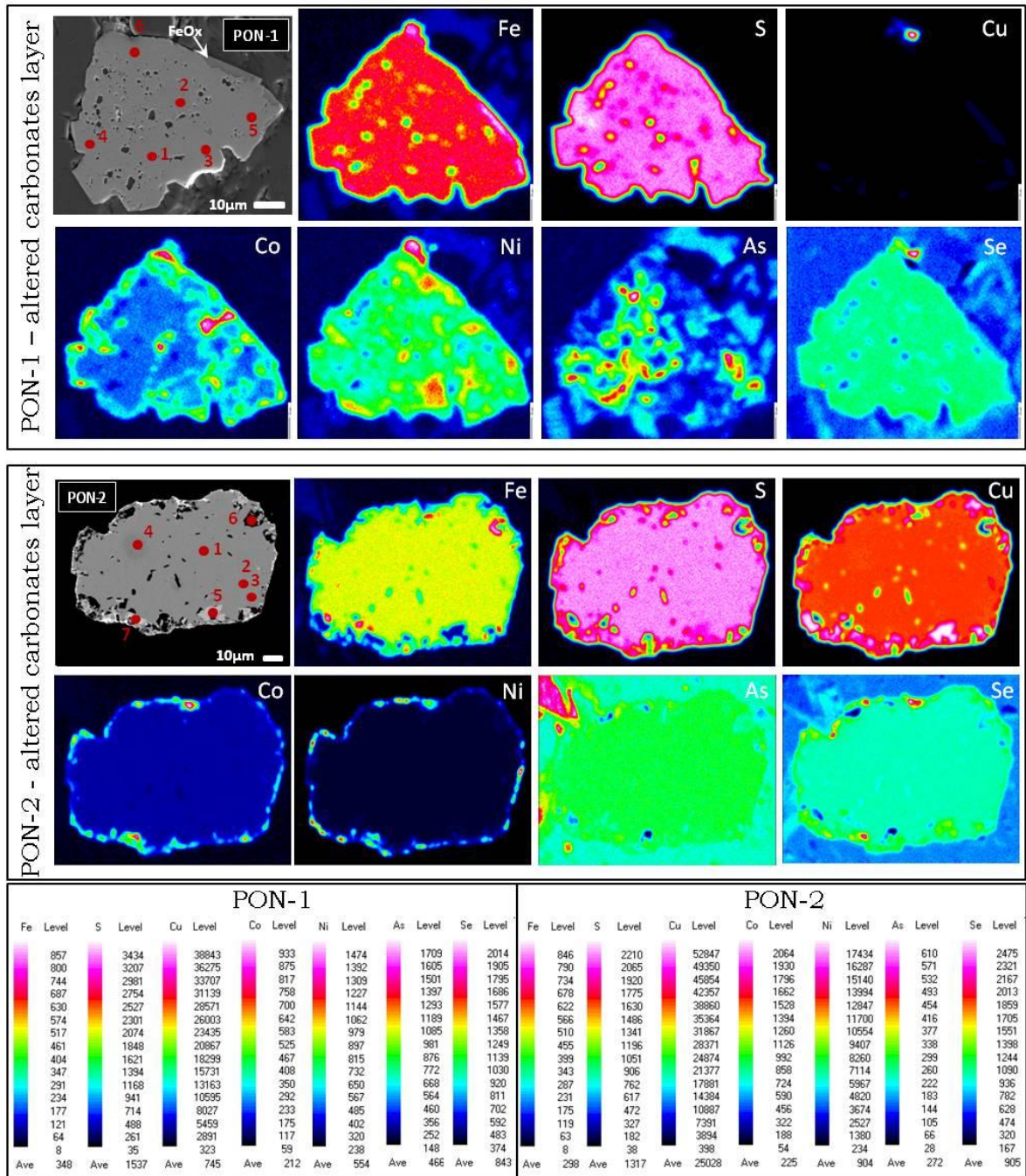


Figure IV.9. EPMA elemental mapping of PON-1 diagenetic pyrite and PON-2 chalcopyrite in the Pongola stromatolites.

The differences between the PON-1 and PON-2/PON-3 chemical compositions suggest that they precipitated from two different fluids. PON-1 precipitated during diagenesis concomitantly with the euhedral dolomite crystals from an As-rich fluid. Chalcopyrite, whose growth was hindered by diagenetic euhedral dolomite, precipitated later from a fluid rich in Cu (and

other metals: Co, Ni, Zn, Pb) and depleted in As (top left of As and Fe maps of PON-2). It is possible that the distribution of Co, Ni, Zn and Pb in these chalcopyrites results from a metamorphic or a later hydrothermal event, responsible for the liberation of these TE from the original chalcopyrite and their concentration and recrystallization in a peripheral zone, as well as their partition into separate sulfide and Fe-oxide phases (PON-2) or incorporation in a solid solution (PON-3) (Large *et al.*, 2007). Although it has been noted that, while Zn and Pb are easily expelled during recrystallization events and Co and Ni tend to be retained, this occurs in pyrite, which is refractory, and does not apply to chalcopyrite. Furthermore, the euhedral overgrowth and Fe-oxide replacement on PON-1, and the peripheral alterations on PON-2 and PON-3 (respectively made of CuS-rich Fe-oxides and CuS, Fe-oxide and CuFeS), all contain Ni, Pb and Zn suggesting that they correspond to the same event. This hydrothermal fluid was, together with Cu and Co, enriched in Pb, Ni and Zn that preferentially co-precipitated with sulfides.

We propose that the recrystallization of these phases occurred concomitantly with silicification as trace amounts of Si are detected by SEM/EDS in Fe(CuS)-oxide phases. Thus, the chronological events that Pongola stromatolites were submitted to, inferred from these sulfides, confirm that silicification occurred late in these samples. Cautions must thus be used when interpreting the TE content of these sulfides, although early diagenetic PON-1 pyrites remain relevant to the study. However, all the pyrites/chalcopyrites were observed in altered carbonate layers, which challenges the possibility of making comparison with sulfides precipitated remotely from original microbial layers of the stromatolites.

IV.5.4. Diagenetic pyrite in the Kakabeka Falls stromatolites, Gunflint Formation

The chronology of the growth stages of the diagenetic pyrites in Kakabeka Falls stromatolites is difficult to interpret, at least for large crystals, because of the dendritic and concretionary nature of their

morphology (KF-1). However, EPMA revealed that both KF-1 and KF-2 are characterized by high contents of As (1500-9000 ppm and 1500-5600 ppm, respectively) and Cu (258-2900 ppm and 1000-2800 ppm), moderate levels of Se (although slightly lower in average than the Se content reported in the older sediments in this study; >300 ppm but <500 ppm for both), and generally very low levels of Co and Ni, with higher spot concentrations of 178 ppm and 204 ppm respectively. Co/Ni ratios range from 0.45 to 1.62, and are thus consistent with sedimentary pyrite, and more specifically, with the “diagenetic pyrite concretions from Fe-poor host-rock” (Guy *et al.*,2010).

There is a general co-variation of As and Cu content in both KF-1 and KF-2 with stable As/Cu values between 1 and 3, although KF-1 incorporated more As than Cu in the earlier stages of its growth (spots n°3,6; Fig.IV.10) with As/Cu ratios of 35 to 5. This suggests that KF-1 and KF-2 precipitated from a diagenetic fluid enriched in As and Cu, but that the growth of KF-1 was initiated by a different fluid in which As was 35% more abundant than Cu and represented 90% of the detected TE content.

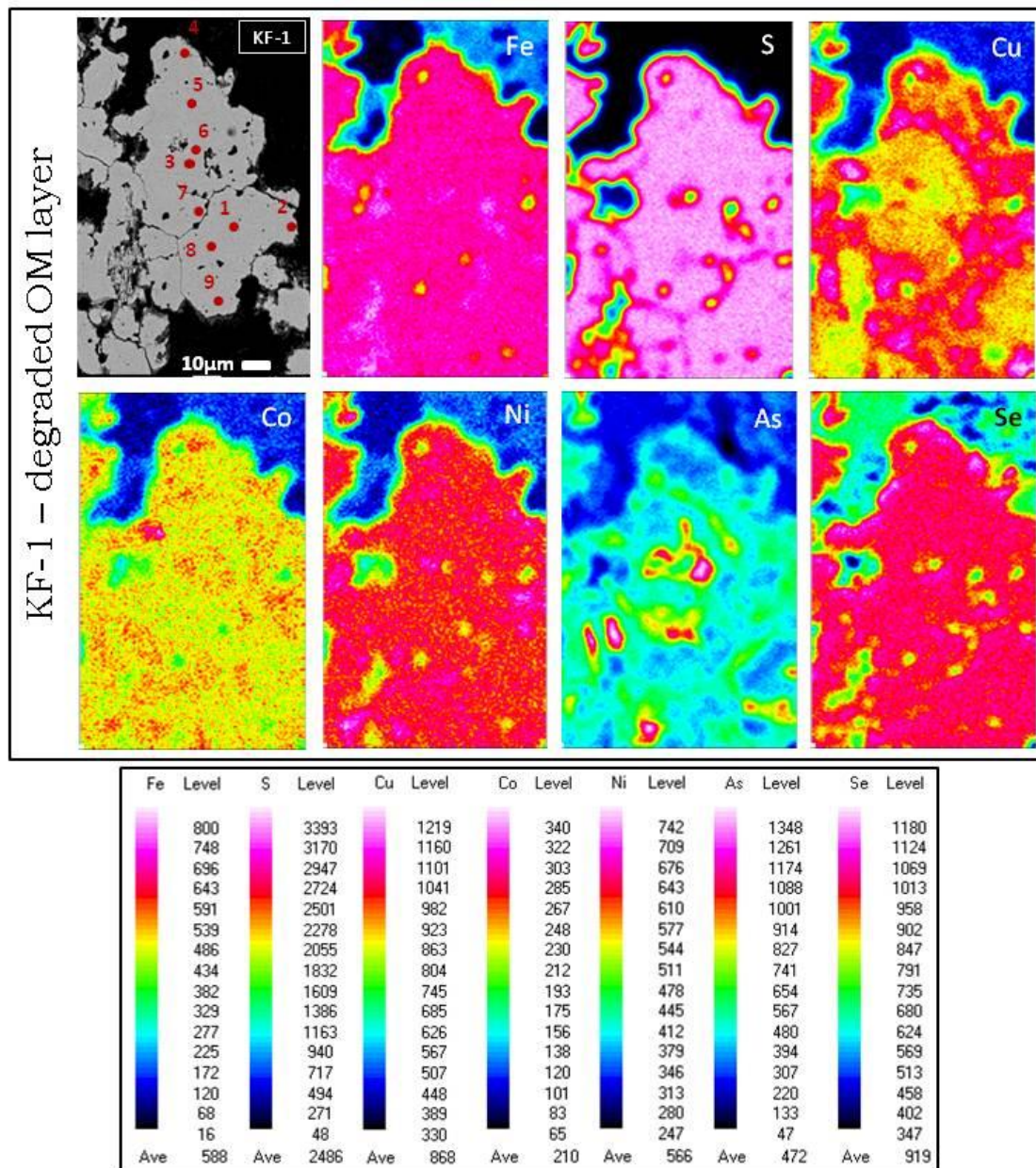


Figure IV.10. EPMA elemental mapping of diagenetic pyrite KF-1 located in a layer of degraded OM and carbonates in the Kakabeka falls stromatolites.

IV.5.5. Sulfarsenides in the Mink Mountain stromatolites, Gunflint Formation

Elemental results were obtained by localized spot analyses by SEM/EDS (see Table IV.3). Sulfides in the Mink Mountain stromatolites are subhedral to euhedral and grew *in situ* as indicated by numerous small (~1µm) inclusions similar in size and morphology to the surrounding matrix.

SEM/EDS revealed that some of the inclusions in the sulfides of the Mink Mountain hematite-rich stromatolites are micrometric grains of hematite making up the stromatolitic laminae and probably precipitated during early diagenesis (Planavsky *et al.*, 2009). Elemental quantification reveals that they contain high levels of Co and As, as major elements, reaching ~34 wt% and ~45 wt% respectively, with minor variable amounts of Fe and Ni, between 2.61-7.35 wt.% and 3.36-6.81 wt%, respectively. Evidence for *in situ* growth after diagenesis (from inclusions, euhedral morphology, see IV.4.6), coupled with high levels of Co and As, point to a hydrothermal origin for these Co-Fe-Ni-sulfarsenides. In comparison, bulk-rock analyses show that the sample is highly depleted in Co (2 ppm). We propose that these sulfides precipitated at a late diagenetic stage from a hydrothermal fluid rich in Co, As and Ni, and that they are not representative of the early diagenetic fluid composition that may provide information on microbial activity.

IV.6. Discussion

Petrographical observations, combined with elemental distributions, quantification and Co/Ni ratios show that, with the exception of the sulfides found in the Mink Mountain stromatolites, all samples contain diagenetic pyrite in association with microbial mats or clots, stromatolitic layers, or detrital CM, either in the form of concretions, clusters, or as overgrowths on detrital precursors. We conclude that HG-1, HG-2, JOS-1, JOS-2, JOS-3, PON-1, KF-1 and KF-2 are pyrites precipitated from diagenetic fluids and thus relevant for the purpose of this study.

Interestingly, we observed systematic differences in the morphology, texture and TE content of diagenetic pyrite in microbial mats (HG-1, ~JOS-1, KF-1) compared to their counterparts, formed during the same diagenetic stage, but in association with microbial clots (HG-2, HG-3, JOS-2), detrital CM (JOS-3), or cherty layers (KF-2). In Figures IV.12 to IV.15, the elemental results reported previously and listed in Table IV.3 are represented as a function of paragenetic stages, in order to evaluate the evolution of the TE contents during diagenesis for each pyrite.

We found no effect of epigenetic processes on the TE content of diagenetic pyrite. According to previous studies, Co, Ni, As and Se are retained in the pyrite structure even at high metamorphic grades (up to 742°C at low pressure), with the exception of hydrothermal dissolution-reprecipitation causing Co, Ni, As and Se to be released (Craig *et al.*, 1998; Vaughan & Rosso, 2006). However, among our samples, such processes are relevant only for PON-2 and PON-3 that are not diagenetic pyrites but rather two-stage hydrothermal chalcopyrites. Also, Large *et al.* (2007) have shown that Cu, Pb, Zn, Ag, Cd and Te can be lost at metamorphic grades above lower greenschist facies. For our samples, only the Pongola stromatolites were submitted to a higher metamorphic grade than lower greenschist facies. In these samples, expulsion of Cu, Zn and Pb was observed in the hydrothermal chalcopyrites but not the diagenetic pyrites. Metamorphism, dissolution under pressure and hydrothermal dissolution and redeposition are thus dismissed as potential influences on the TE content of the selected diagenetic pyrites.

The TE content of diagenetic fluids depends on the composition of (i) seawater, itself influenced by global redox conditions and the input of ambient hydrothermal activity and (ii) pore waters, influenced by the composition of groundwaters, by the alteration products of the mineralogical and organic compounds of the sediment, as well as by biological reduction/oxidation processes during sedimentation and during diagenesis. These aspects are discussed below. During the discussion, ICP-MS results (Annex 2) are mentioned when appropriate to provide complementary information.

IV.6.1. Influence of global redox conditions

In this study, detrital pyrite was documented in the ~3.45 Ga Hooggenoeg chert, in the 3.33 Ga Josefsdal chert (at least in the samples 12SA13-1 and 12SA13-2), and was absent in the ~2.95 Ga Pongola and ~1.88 Ga Gunflint samples. Since pyrite is oxidized under oxygenated conditions (Holland, 1984; Rasmussen & Buick, 1999), this is consistent

with a rise of oxygen in the atmosphere between 2.45-2.32 Ga (Bekker *et al.*, 2004; Holland, 2006) and the hypothesis of whiffs of oxygen before the GOE (Anbar *et al.*, 2007) and particularly at 2.95 Ga (Large *et al.*, 2014) (see Fig.IV.1). These observations are in disagreement with some of our elemental data. Indeed, while Large *et al.* (2014) reported that the contents of Ni, Co and Cu in sedimentary pyrite were not dependent on the oxygenation of the atmosphere and further supply to the ocean by oxidative continental weathering, they also demonstrated that elements such as Mo, Se, and indirectly As, are robust proxies for environmental redox conditions. However, none of the analyzed pyrites contained Mo, even in samples post-dating the GOE, yet Mo is responsive to the oxidative weathering and would have been provided to the ocean under oxygenated conditions and readily incorporated in pyrite. However, since the Mo concentrations reported by Large *et al.* (2014) for the period between 3.45 Ga and 1.88 Ga are ≤ 50 ppm, the apparent absence of Mo may be due to its very low content, falling below the D.L. (here 59 ppm). Furthermore, in the diagenetic pyrites studied here, the average Se concentration is 560 ppm at 3.45 Ga, 540 ppm at 2.95 Ga and 420 ppm at 1.88 Ga. Thus, we see no significant evolution of the Se content through time, apart from a slight decrease with decreasing age. Large *et al.* (2014) have used the variations of the Se content of sedimentary pyrite to trace the evolution of atmospheric oxygen through time (see Fig.IV.1), on the basis that the Se input into oceans is enhanced under an oxygenated atmosphere (oxidative weathering of sulfides on land). Thus, not only the Se content reported here is systematically and significantly higher than that reported by Large *et al.* (2014) at any given time from the Archean to the Paleoproterozoic, but the slight decrease observed is in contradiction with their observations. Thus, the Se content in our samples cannot be explained solely by changes in global redox conditions.

The absence of detrital pyrite in the Pongola and Gunflint samples however, correlates with the As content in these pyrites. Indeed, the As content can be linked, although indirectly, to the evolution of atmospheric and oceanic oxygen levels (Arvestål, 2013; Large *et al.*, 2014). Several models

were proposed to explain the evolution of oceanic composition through the Precambrian. These models propose evolution from an anoxic Fe^{2+} -dominated ocean before the GOE, to oxic surface water and anoxic Fe^{2+} -enriched bottom waters after the GOE, and the development around 2.1-1.9 Ga until ~ 1 Ga of euxinic sulfidic layer between the oxic and anoxic layers (Poulton *et al.*, 2004; Poulton & Canfield, 2011; Canfield *et al.*, 2007). Others proposed an anoxic $\text{Fe}^{2+}/\text{H}_2\text{S}$ -dominated deep ocean during most of Precambrian history until the oxygenation of surface and bottom waters ~ 0.5 Ga-ago (Planavsky *et al.*, 2011). However, the sediments used in the present study were deposited exclusively in tidal environments within the photic zone (PZ) and thus changes in the behavior of As are related principally to the oxygen levels of surface water and its transition from anoxic to oxic. Before the rise of oxygen, the principal source of As in the reducing oceans would have been hydrothermal vents from which As was released as As^{3+} , the most stable form of As in these environmental conditions. During the Archean, the removal of As in the anoxic environment was mainly ensured by its adsorption on photosynthetically-produced Fe-oxides (by Fe(II)-oxidizing anoxygenic photosynthetic bacteria), and incorporation in pyrite precipitated from Fe(II) and H_2S present in the medium or produced by bacterial activity (SRBs). During putative periods of whiffs of oxygen at 2.95 Ga (Large *et al.*, 2014) and 2.5 Ga (Anbar *et al.*, 2007) and after the GOE at ~ 2.4 Ga (e.g. Bekker *et al.*, 2004), the oxidative weathering of sulfides on land would have supplied the oceans with large amounts of sulfates and As^{5+} . As^{5+} would have been present in the upper oxygenated layer, while hydrothermal vents continued to deliver As^{3+} , dominating the lower anoxic part of the oceans. In these conditions, the supply of As would have exceeded its removal, particularly since Fe^{2+} would have been restricted to bottom waters, hence preventing photoferrotrophy and the production of Fe-oxides onto which As could have been adsorbed (Arvestål, 2013). As^{5+} would have partly stayed in solution in the oxic PZ while As^{3+} could form abiotically from the large amounts of As^{5+} in water and be incorporated into pyrite under the redox boundary during early diagenesis, since this boundary would have coincided with the bottom of the oxygenated PZ at that time. The

high As content in the diagenetic pyrite of Kakabeka Falls stromatolites may be explained by this process. This may also explain the high levels of As in the Pongola diagenetic pyrite, hence reinforcing the hypothesis of an O₂ whiff at 2.95 Ga. This process however, is not sufficient to explain the differences in As content of diagenetic pyrites within the same section and separated by only a few millimeters, such as the differences observed between the diagenetic pyrite in the microbial mat and in the microbial clots in the Hooggenoeg chert. Furthermore, this paragraph demonstrates that, although the supply of As to the ocean strongly depends on the oxygenation of the atmosphere, its concentration in pyrite is also dependent on the microbial activity.

Therefore, the TE content in diagenetic pyrites of Se and As, representing respectively direct and indirect proxies for the levels of oxygen in the atmosphere, cannot be explained here solely by variations of global redox conditions.

IV.6.2. Influence of fluid circulation during post-depositional processes

It was demonstrated above that all the variations of TE content of diagenetic pyrites analyzed here could not be explained by the influence of global redox conditions alone. Furthermore, since pyrites analyzed in this study are separated by only few millimeters or tens of micrometers within a thin section, vertically or horizontally, it is unlikely that they were submitted to different post-depositional histories, such as silicification or pervasive hydrothermal fluid circulation. The same applies to the downward seawater infiltrations and upwelling hydrothermal fluids and groundwaters that aliment pore waters during diagenesis, because the composition of these fluids depends on the nature of the igneous and sedimentary rocks they go through, and thus can be of various compositions at the regional scale but not at the millimeter scale. However, we still observed significant differences

in Co, Ni, Cu, As and Se relative abundances in diagenetic pyrite separated by only a few tens of microns.

Large *et al.* (2014) reported that the contents of Ni, Co and Cu in sedimentary pyrite were not dependent on the oxygenation of the atmosphere: Ni and Co concentrations generally decrease through time, while Cu displays a relatively flat pattern. Rather, Ni and Co supply to the ocean and incorporation in pyrite correlate with periods of eruptions of komatiitic ultra-mafic or mafic lavas (Large *et al.*, 2014) in which these elements are particularly enriched. The general decrease of the concentration of these elements in the ocean, especially Ni, from the Archean to the Paleoproterozoic, follows the cooling of the upper mantle and a decrease in this particular type of lava (Konhauser *et al.*, 2009). The Ni and Co content shown here is in general agreement with these reports, although Co displays higher concentrations at 3.45 Ga and 1.88 Ga compared to Large's data. Also, Ni concentrations are abnormally high in all samples, suggesting that another process contributed to their enrichment in pyrite. Furthermore, the Cu content increases drastically through time in our diagenetic pyrites with a maximum of ~3000 ppm in the Kakabeka Falls stromatolites (Fig. IV.11), thus not following the trend proposed by Large *et al.* (2014).

Furthermore, bulk-rock analyses show that our samples are highly depleted in Co, Ni and Cu compared to their concentration in pyrite. This suggests an efficient partitioning of these metals in diagenetic pyrite. If the variations in the content of these elements in sedimentary pyrite were only related to the content of the ocean or circulating groundwater, then Co, Ni and Cu concentrations would fall into the same order of magnitude as those reported by Large *et al.* (2014) and be similar regardless of the location of the pyrite in the sediment, which is not what is observed here. Hence, this suggests that another process is responsible for the partitioning of Co, Ni and Cu in pyrite.

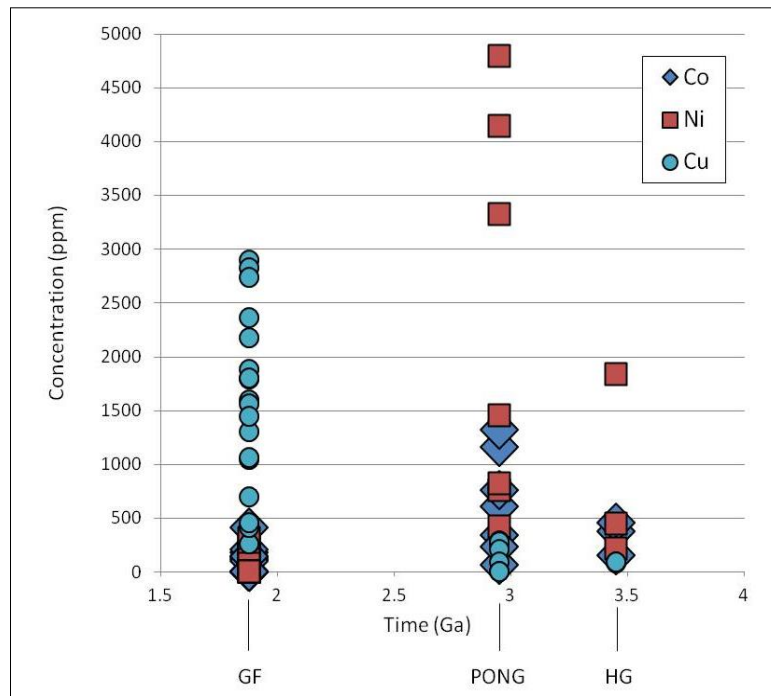


Figure IV.11. Distribution of Co, Ni and Cu content (ppm) in diagenetic pyrite in the different samples. GF: Gunflint chert; PONG: Pongola stromatolites; HG: Hooggenoeg chert. For scale reasons, the high contents of Ni (1 to 50%) in diagenetic pyrites in the 3.33 Ga Josefsdal chert are not represented.

For instance, in the Hooggenoeg sample, HG-1 diagenetic pyrites located in the microbial mat are enriched in Co, Ni, Cu and slightly enriched in As and Se, while HG-2 in the microbial clots is highly enriched in As and Ni, slightly enriched in Co, but depleted in Cu and Se (Fig. IV.11). The enrichment in Co, Ni and Cu could be explained by silica alteration processes. Hofmann & Bolhar (2007) and Hofmann & Harris (2008) proposed that in this region, silica alteration by hydrothermal fluxes may have yielded an enrichment in these particular elements of the sedimentary cherts, compared to the silicified basalts underneath (Hofmann & Harris, 2008). However, the enrichment of Co, Ni and Cu was reported in carbonaceous cherts deposited on the sea floor and stratigraphically under the H3c. Silicification of the H3c by Si-saturated seawater and Si-rich circulating fluids in the underlying sediments and basalts may itself have enriched the sediment in Co, Ni, Cu. However, if the diagenetic fluid was highly hydrothermal, pyrites should have more elevated Co/Ni ratios, as is the case for the hydrothermal overgrowth on HG-2, especially since Co^{2+} tends to

readily substitute for Fe^{2+} in pyrite (Bajwah *et al.*, 1987). Although hydrothermal input may explain the constant and low Cu concentrations in HG-1a, HG-1b and HG-2 (88, 97 and 90 ppm), it does not explain the variations in Co, Ni, As and Se (to a lesser extent) between the HG-1 and the HG-2 pyrites.

In the Josefsdal Chert, diagenetic pyrites have significantly variable contents of Ni from their core to their edges (Fig. IV.13): stable 20-35 wt.%, decreasing from 49 wt.% to 1.2 wt.% and increasing from 0 wt.% to 2.7 wt.%, respectively in JOS-1, JOS-2 and JOS-3. These differences in Ni content can be explained neither by regional post-depositional processes such as silica alteration, metamorphism, nor by local silicification or hydrothermal events which still affect the whole sediment. Furthermore, ICP-MS analyses (Annex 2, sample 99SA07d) revealed that, compared to the carbon-poor (white) layers of the sample, Ni is particularly enriched in the carbon-rich layers, where microbial mats and clots are found, indicating a specific scavenging of Ni by organic matter, but also possibly by micrograins of pyrite in these layers.

In the Kakabeka Falls stromatolites, both KF-1 and KF-2 pyrites display high contents of As and Cu, with relatively stable As/Cu of ~1-3. KF-1, however, shows a primary diagenetic stage during which it incorporated 35% more As than Cu. Again, this cannot be explained by differences in the chemistry of sea water or the circulating groundwaters during diagenesis since these two pyrites are located on layers separated by only few millimeters.

Therefore, the differences observed in the TE contents and relative abundances in diagenetic pyrite within a single thin section cannot be entirely explained by differences in the composition of seawater (with both global redox conditions and hydrothermal influences), or by post-depositional processes that affected the whole rock such as silicification, silica alteration, or the influence of circulating hydrothermally-charged groundwaters. Rather, they may result from differential local chemistry and

pore water composition at the mm to μm scale. We propose to investigate the input of surrounding matrix mineralogy and the effect of OM and microbial colonies on the TE content of these diagenetic pyrites.

IV.6.3. Influence of the surrounding mineralogy and of the local chemistry of microbial colonies on the TE content of diagenetic pyrite

a. Microbial mats and microbial clots in the 3.45 Ga-old Hooggenoeg Chert

In the sample from the Hooggenoeg chert, silicification occurred before compaction and thus during the earliest stages of diagenesis. Krajewski & Luks (2003) showed that burial diagenesis had the effect of restricting the supply of reactive iron, sulfate and OM, thus limiting the trace metal substitution in pyrite. Silicification would have the same effect. During silicification, the sediment is soaked in Si-saturated water which fills the porosity and precipitates preferentially on OM and micro-organisms (Knoll, 1985; Westall *et al.*, 1995; Konhauser *et al.*, 2002; Orange *et al.*, 2009). This has the overall effect of limiting the reactivity of OM and the mobility and circulation of trace metals liberated from OM degradation and desorbed from matrix minerals. Thus, the TE in diagenetic HG-1 and HG-2 were incorporated before silicification, *i.e.* during the earliest stages of diagenesis at or near the water-sediment interface.

We established that Cu concentrations are low and relatively constant between the diagenetic overgrowths of HG-1a, HG-1b, and HG-2 (~90 ppm). The Cu content probably represents the background hydrothermal contribution to the diagenetic fluid. Focus is made on the Co, Ni, As and Se content. HG-1a and HG-1b, located within the microbial mats, display more Co and slightly more Se but less As and Ni (Co: 380-460 ppm, Se: 570-640 ppm, As: 327-359 ppm, Ni: 214-445 ppm) in comparison with HG-2 located within the microbial clots that have particularly elevated As and Ni concentrations and less Co and Se (Co: ~150 ppm, Se: 474 ppm, As: 3151 ppm, Ni: 1836 ppm).

Thus, HG-1 is characterized by incorporation of Co, as well as by moderate As and Se concentrations, while HG-2 is characterized by high As and Ni contents.

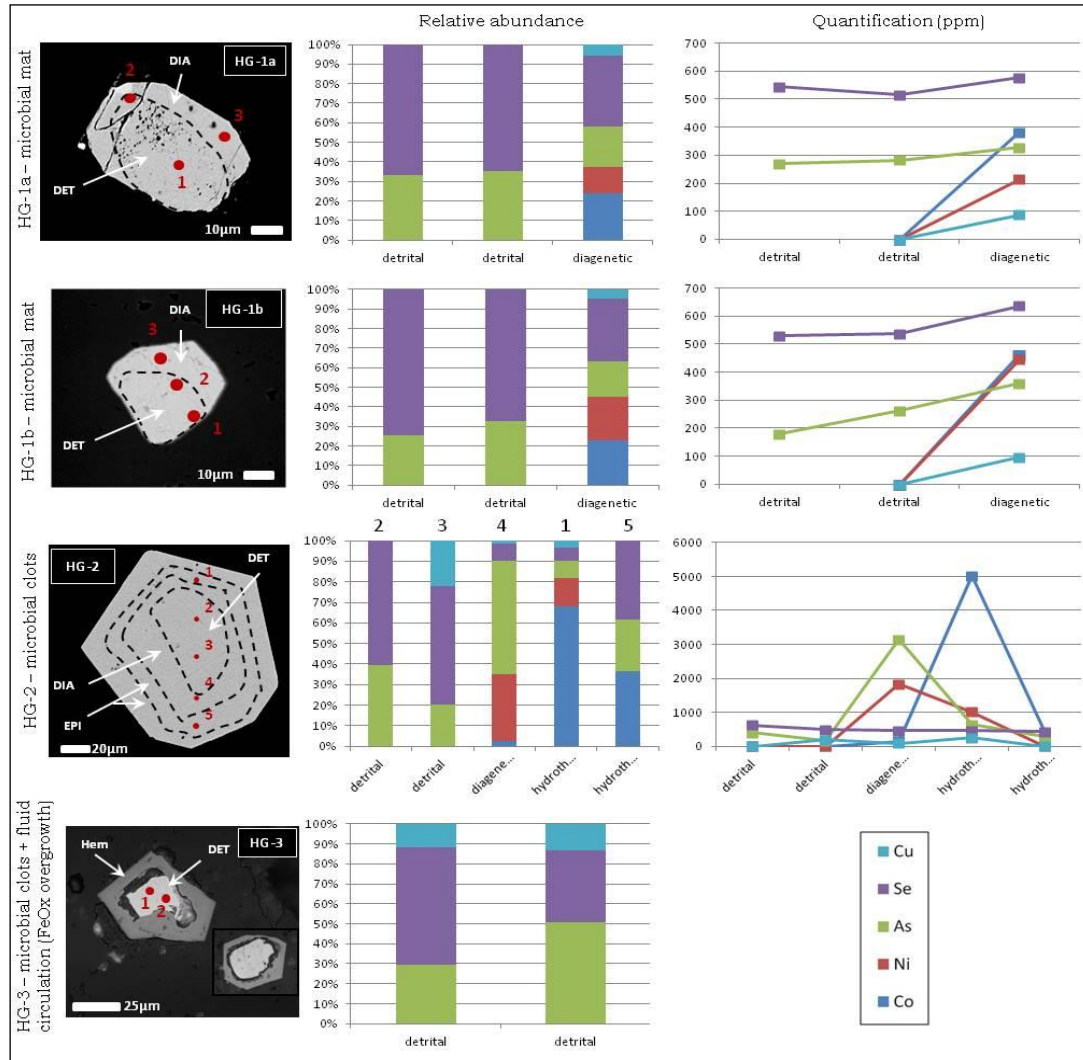


Figure IV.12. Relative abundances and concentrations of Cu, Ni, Co As and Se in pyrites from the 3.45 Ga Hooggenoeg chert H3c, Onverwacht Group, South Africa, from detrital to epigenetic stages. Columns in the relative abundance bar diagrams are in increasing order with regards to the analytical spots numbers reported in Table IV.3, or are specified (HG-2).

Nickel

At 3.45 Ga, Ni was primarily provided to the ocean by the alteration of Ni-rich ultramafic rocks on the seafloor. Several authors have documented the scavenging of Ni by organic matter in organic-rich sediments as it is an

essential metal for chemotrophic microorganisms, such as methanogens, sulfate-reducing bacteria and anaerobic methanotrophs (e.g. Krüger *et al.*, 2003; Konhauser, 2007; Konhauser *et al.*, 2009). Additionally, Zerkle *et al.* (2005) proposed that Ni could be a possible biosignature for methanogens (together with tungsten). Also, it was shown that Ni contained in such metalloenzymes is released and partitioned into sedimentary pyrite during early diagenesis (Tribovillard *et al.*, 2006; Large *et al.*, 2007, 2009, 2014; Guy *et al.*, 2010). The high Ni content in HG-2 located within the microbial clots is consistent with Westall *et al.* (2015) who interpreted the microbial clots in the Josefsdal chert of the Kromberg Formation as chemotrophic colonies.

Cobalt

Furthermore, like Ni and Cu (although here Cu was linked to the background hydrothermal component), Co is detected only in the diagenetic overgrowths in HG-1 pyrites. Note that it is a metalloenzyme element that can be released from organic matter during the diagenetic breakdown of organic molecules. These metals are necessary to any living organism in trace amounts, but may be toxic in larger amounts. According to Zerkle *et al.* (2005), Co was possibly the third most important trace metal (after Fe and Zn) in metalloenzymes since the origin of life and until the rise of oxygen (see their Figure 9A). Furthermore, these authors argued that:

‘Cobalt and nickel-containing enzymes are most commonly used in metabolisms based on methane, carbon monoxide, and hydrogen, such as those likely operating on early Earth.’ [Zerkle *et al.*, 2005]

Hence, it is not unlikely that Co in HG-1 pyrites come from the degradation of such metalloenzymes present within the laminae of the microbial mats but absent from the microbial clots. However, the present data do not allow further interpretation of the Co content in these pyrites.

Arsenic and selenium

Unlike Ni and Co, the concentrations of Se in HG-1 and of As in HG-2 seem to be the direct or indirect result of oxidation-reduction processes

conducted by phototrophic and chemotrophic microbial colonies prior to diagenesis and during diagenesis by non-phototrophic microbes. As and Se are biologically important because they fuel certain microbial metabolisms by acting as electron donors and/or acceptors due to their multiple oxidation states. In fact, numerous studies have reported microbial metabolisms able to use As and Se over S (see the review of Stolz *et al.*, 2006) often due to the energetic advantage they offer (Ahmann *et al.*, 1994; Oremland *et al.*, 1989). Due to their proximity with volcanic edifices, the anoxic tidal sediments of the Hooggenoeg chert may have been frequently affected by continental hydrothermal vents, in addition to marine hydrothermal vents, both releasing fluids enriched in H₂S, Fe²⁺ and virtually depleted in SO₄²⁻ (Guy *et al.*, 2010). Since As³⁺ would have been enriched in these fluids, it would have been available in both seawater and circulating groundwaters, pervasively infiltrating the sediment. Simultaneously, Se was supplied to the sediment as a product of the intense volcanic activity. Indeed, it was reported that Se is volatilized in the magma chamber and is thus enriched in volcanic emissions, such as ash and atmospheric particles (see the review in Floor & Roman-Ross, 2012). Kulp & Pratt (2004) reported that, in organic-rich sediments, Se occurs preferentially in association with organic carbon and S due to similarities in the biochemical pathways of these elements and similarities in the chemical behavior of Se and S. The proximity of the Hooggenoeg chert with volcanic edifices would have favored the enrichment of shallow marine sediments in Se from ash fall deposits. In the reducing Archean conditions, Se would have been ejected by volcanic activity and deposited in the sediment as elemental Se (Se⁰), Se⁻ or selenide (Se²⁻). Se²⁻ would have concentrated in association with organic carbon, and specifically in organo-Se compounds and proteins, which is why Se²⁻ is also the oxidation state of selenium found in kerogen.

The simultaneously elevated concentrations of As and Ni in HG-2 during diagenesis (Fig. IV.12) suggests that they substitute for different elements in the pyrite lattice. As can substitute for Fe as well as for S (e.g. Lowers *et al.*, 2007; Deditius *et al.*, 2008). Since Ni most likely replaces Fe, it is possible that As replaces S here. In this case, As entered pyrite in a

reduced form, such as As^- or As^{2-} (review of Wang & Mulligan, 2008); or, if present in sufficiently high concentrations in the diagenetic fluid, Ni and As may also have co-precipitated to form minute NiAs inclusions in which case As is present as arsenide As^{3-} . In the anoxic oceans of the Archean, the stable oxidation state of As would have been As^{3+} . This suggests that As^{3+} naturally present in the ocean was reduced, a phenomenon difficult to explain by abiotic processes. A number of microorganisms are able to reduce arsenate As^{5+} to arsenite As^{3+} . In particular, Hoefft *et al.* (2004) reported that a strain of chemolithoautotrophic bacteria is able to reduce As^{5+} to As^{3+} while oxidizing sulfide to sulfates. Ahmann *et al.* (1994) have shown that the use of As^{5+} as a terminal electron acceptor instead of sulfate is energetically favorable for a number of SRBs. Furthermore, Westall *et al.* (2015) argued that in the Josefsdal chert, which is very similar in composition, depositional context and microbial remains to the Hooggenoeg chert, some rounded clots of OM were chemotrophic colonies that would have fed on these hydrothermal inputs. This is consistent with the morphology of the clots observed here in the Hooggenoeg chert. Chemotrophic bacteria functioning with sulfur may have partially used As instead of S in such an environment. An ancient form of the chemotrophic metabolism described by Hoefft *et al.* (2004) could have used directly the available As^{3+} for As reduction instead of As^{5+} thus producing reduced forms of As that would have entered pyrite composition. The chemotrophic metabolism described by Hoefft *et al.* (2004) may thus have been a key factor to provide substitutes of SO_4^{2-} to SRB activity in the clots. Note that Westall *et al.* (2011, 2015) proposed that the chemotrophic microbes in the clots of the Josefsdal Chert may be chemo-organotrophic SRBs. Such bacteria would require organic compounds, which may have been provided by methanogens. Methanogens are consistent with both clot-like colony morphology and the sequestration and release of elevated Ni content as discussed above.

Overall, the high Ni and As concentrations in the diagenetic pyrites located in the microbial clots may stem from the activity of chemolithotrophic microbes, probably an association of methanogens and SRBs.

The low As content in diagenetic pyrites located in the mats compared to that in the clots can be simply explained by the As desorption from Fe-oxides (Arvestål, 2013; Smedley & Kinniburgh, 2002; Koschinsky & Hein, 2003). This implies the activity of Fe-oxidizing anoxygenic photosynthesizers coherent with the mat-like structure. However, it is unlikely that the Se incorporated by HG-1 pyrites during diagenesis comes from the desorption of Se from minerals of the matrix. Indeed, only the oxidized form selenite Se^{4+} is known to adsorb onto oxyhydroxides and clays, and only selenate Se^{6+} remains in solution (Kulp & Pratt, 2004). In a reduced environment, these selenium sources would have existed only if microbial activity was responsible for the oxidation of reduced forms of Se, and they would then have been incorporated into pyrite only if these oxidized forms were reduced to Se^{2-} again, thus strongly indicating a biological activity. Microorganisms that could have oxidized selenium may be Se^0 -oxidizing chemoheterotrophs and chemoautotrophs (Dowdle & Oremland, 1998). These microbes could have led to the production of SeO_4^{2-} , thus sustaining the activity of SeO_4^{2-} -reducing bacteria such as SRBs using Se instead of S (Zehr & Oremland, 1987; Oremland *et al.*, 1989), in the same way as described above for As. It is also tempting to postulate that, if in these sediments Se was indeed partially used instead of S, then anoxygenic photosynthetic bacteria using sulfur may also have used Se^0 , producing SeO_4^{2-} as well. SeO_4^{2-} -reducing bacteria would, in term, have reduced Se allowing a Se cycle to develop at that time. Thus, either these oxidized forms of Se did not exist in the Hooggenoeg sediments and could not be involved in the Se content of diagenetic pyrite, or they were produced and then reduced by microbial activity. In either case, the Se content of HG-1 is likely to be controlled by microbial activity, and principally by chemotrophic activity.

A scenario that does not involve selenite and selenate would be as follows. In the microbial mat, the availability of aeriually-deposited Se would have favored its use over As, used preferentially by the underlying microbes in the clots, where Se would have been depleted. During diagenesis, the Se concentrated in organic carbon would have desorbed and been incorporated into pyrite where it substituted for S under the form Se^{2-} as well (Kulp &

Pratt, 2004; Matamoros-Veloza *et al.*, 2014). If Se was mostly supplied as Se⁰ by volcanic activity, it is possible that Se²⁻ was produced by microbial activity. These microbes located in the mat would have slightly increased the Se²⁻ concentrations of the selenium bulk, thus resulting in an enrichment of Se in HG-1 compared to HG-2 in the clots. In fact, Herbel *et al.*, 2003 have shown that some anaerobic bacteria in anoxic sediments have the capacity to reduce Se⁰ to Se²⁻.

The slightly higher Se concentrations in diagenetic pyrites located in the mats compared to those in the clots may thus be explained by the activity of chemotrophic microbes, associated with degradation of the OM primarily produced by the anoxygenic photosynthesizers, able to use Se instead of S.

If this is true, then combined As and Se contents in both HG-1 and HG-2 and inferred putative microbial metabolisms suggest that at 3.45 Ga the hydrothermally-influenced sediments of the tidal environment were periodically deprived of SO₄²⁻ but enriched in As and Se, enabling SRBs and other chemotrophs in microbial mats and clots to use As and Se, two energetically favorable elements, over S for their metabolism. This is consistent with the results of Zehr & Oremland (1987) who concluded that SRBs are more inclined to carry out selenate reduction to H₂Se instead of sulfates to H₂S when the environment is depleted in sulfates.

b. Microbial clots in the 3.33 Ga-old Josefsdal Chert

Microbial sediments of the Hooggenoeg Chert and Josefsdal Chert are very similar in terms of mineralogical composition, geomorphological context of deposition and composition of the hydrothermal fluids. Also, they both harbor mat-like and associated clot-like microbial colonies. Like the Hooggenoeg Chert, sample 99SA07d from the Josefsdal Chert shows signs of early silicification (Westall *et al.*, 2006, 2011b), supported by the lack of compaction of easily deformable organic structures. Silicification occurred

before compaction and thus during the earliest stages of diagenesis. In this sample, diagenetic pyrite JOS-1 located in the microbial clots and 50 μm below a photosynthetic mat contains between 30 and 20 wt.% of Ni, with a decrease of Ni content from the center to the edges of the grain, where it shows progressive replacement by SiO_2 . JOS-2, located within the microbial clots contains between 50 and 1 wt.% Ni, again, with a decrease from center to edges. JOS-3, located in the detrital CM contains between 0 and 3 wt.% of Ni. Despite its proximity to the microbial mat, we see no evidence in the chemical composition of JOS-1 that may indicate differential trace-metal input released from the degradation of this microbial structure. However, it should be noted that SEM/EDS analyses would not have detected TE elements with concentration less than 1000 ppm.

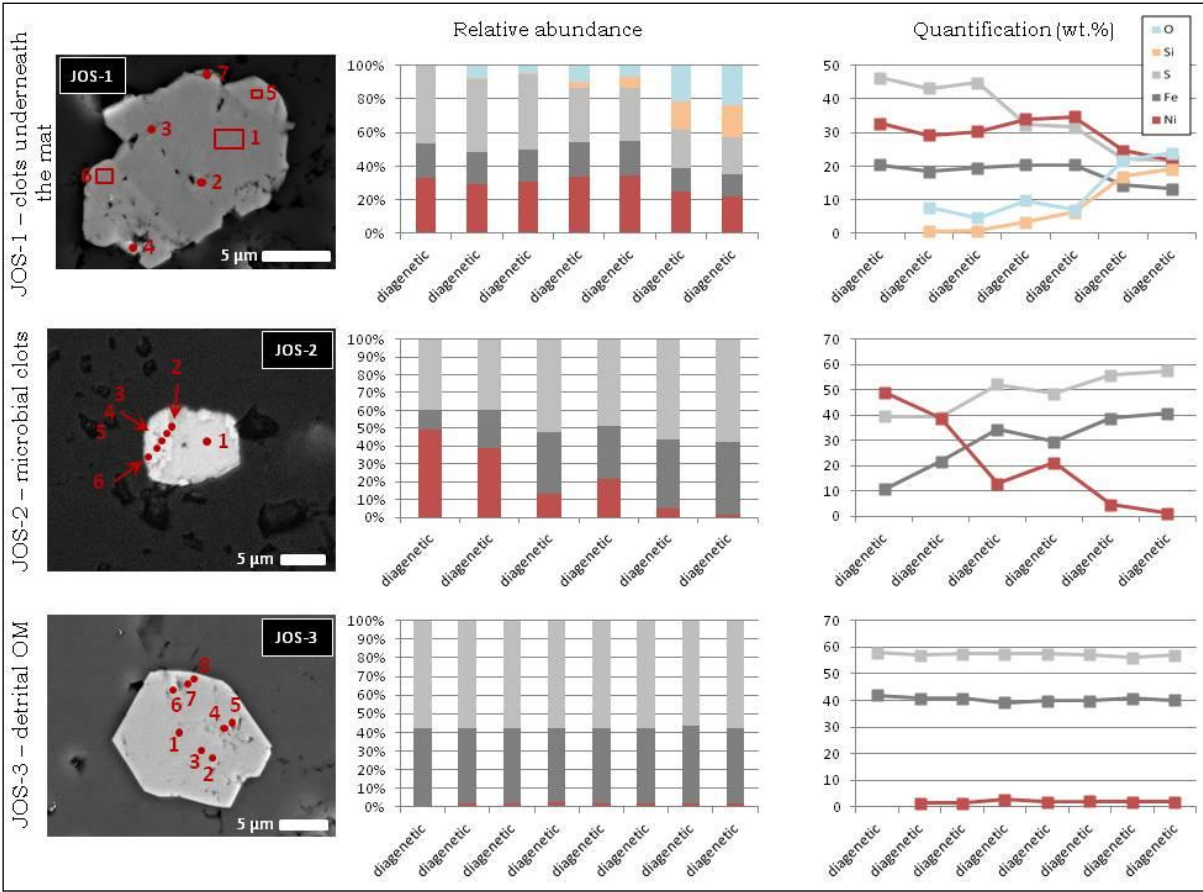


Figure IV.13. Relative abundances and concentrations of Fe, S, Ni and Si and O in diagenetic pyrites from the 3.33 Ga Josefsdal chert K3c of the Kromberg Formation, Onverwacht Group, South Africa. Columns in relative abundance bar diagrams are in logical order regarding to the analytical spot numbers.

The composition of the diagenetic fluid in this sample may have been highly influenced by hydrothermal activity, as reported for instance by Westall *et al.*, 2015, with an input in both seawater and groundwater. However, if the enrichment in Ni results from hydrothermal activity, these pyrites should have even higher concentrations of Co with respect to Ni (Bajwah, 1987; Large *et al.*, 2007, 2009, 2014; Guy *et al.*, 2010), as well as other metals, and should display a euhedral habit. These characteristics are not observed here. The elevated Ni content of the diagenetic pyrites in this sample is most likely due to the circulation of groundwaters in the underlying ultramafic basalts and komatiites enriched in this element (e.g; Konhauser *et al.*, 2009). Nonetheless, the JOS-3 pyrite located in detrital CM, although displaying several percent of Ni (0-3 wt. %), is highly depleted in Ni compared to JOS-1 and JOS-2 located in the microbial clots. Furthermore, complementary ICP-MS analyses show that Ni is specifically enriched in the organic-rich layers compared to organic-poor layers (see Annex 2; sample 99SA07d). This suggests preferential uptake of Ni by the microbial colonies, and thus possibly a significant release of Ni contained in organic matter during diagenesis, followed by efficient partitioning of this element in diagenetic pyrites. In this case, the low Ni concentration in JOS-3 can be seen as the “blank” concentration representing only the contribution of upwelling groundwaters during diagenesis, with no or little contribution from organic matter degradation. This is consistent with the fact that detrital CM was transported and degraded and had probably already released its TE content before deposition.

Differences observed between JOS-1 and JOS-2 may be explained as follows: the growth of JOS-1 occurred during silicification, supported by the increasing concentrations of Si and O detected from the center to the edges of the grain, which in turn stopped its growth, while the growth of JOS-2 may have occurred before silicification, allowing it to grow into a more subhedral habit and toward a pure FeS₂ composition as immediate pore waters became depleted in Ni.

In this sample, Ni is thus likely to have been provided by the degradation of the surrounding, omnipresent, organic matter of the

microbial clots. This is in agreement with the observed TE content of HG-2 which also displays high levels of Ni in microbial clots. The fact that pyrites in the Josefsdal chert are smaller and scarcer than in the Hooggenoeg chert, may explain the higher Ni content, as high inputs of Ni would have been partitioned in a lower volume of diagenetic pyrite material.

c. Reworked kerogenous stromatolitic layers in the ~2.95 Ga-old Pongola stromatolites

Pongola stromatolites were silicified after diagenesis, probably during a late epigenetic event such as hydrothermal pervasive infiltration or possibly concurrently to metamorphism. The remains of what used to be the microbial mat layers of the stromatolites are identifiable by their brownish-black color coming from the concentration of carbonates and the products of their degradation that reworked the organic signature of the original organic carbon. Indeed, since silicification occurred late, the mats and cells were unprotected during diagenetic reworking. Instead, carbonate alteration and neomorphic growth had the effect of degrading the organic-rich layers. Due to compaction, diagenetic CO₂-rich fluids mediated exchange of carbon between the residual organic matter and the carbonates. This explains why the $\delta^{13}\text{C}$ data in the Pongola stromatolites yield almost exclusively marine carbonates values.

Since the microbial layers were submitted to extensive degradation during diagenesis, the TE content of diagenetic pyrite may be the only record able to chemically characterize the unpreserved microbial colonies. In PON-1, the diagenetic growth is characterized by high levels of As (up to ~15000 ppm) that decrease concurrently to the increase of Ni (up to ~4800 ppm), and to a lesser extent, to the increase of Co (up to ~1300 ppm), and also by moderate amounts of Se (450-620 ppm) and noticeable amounts of Cu (200-280 ppm).

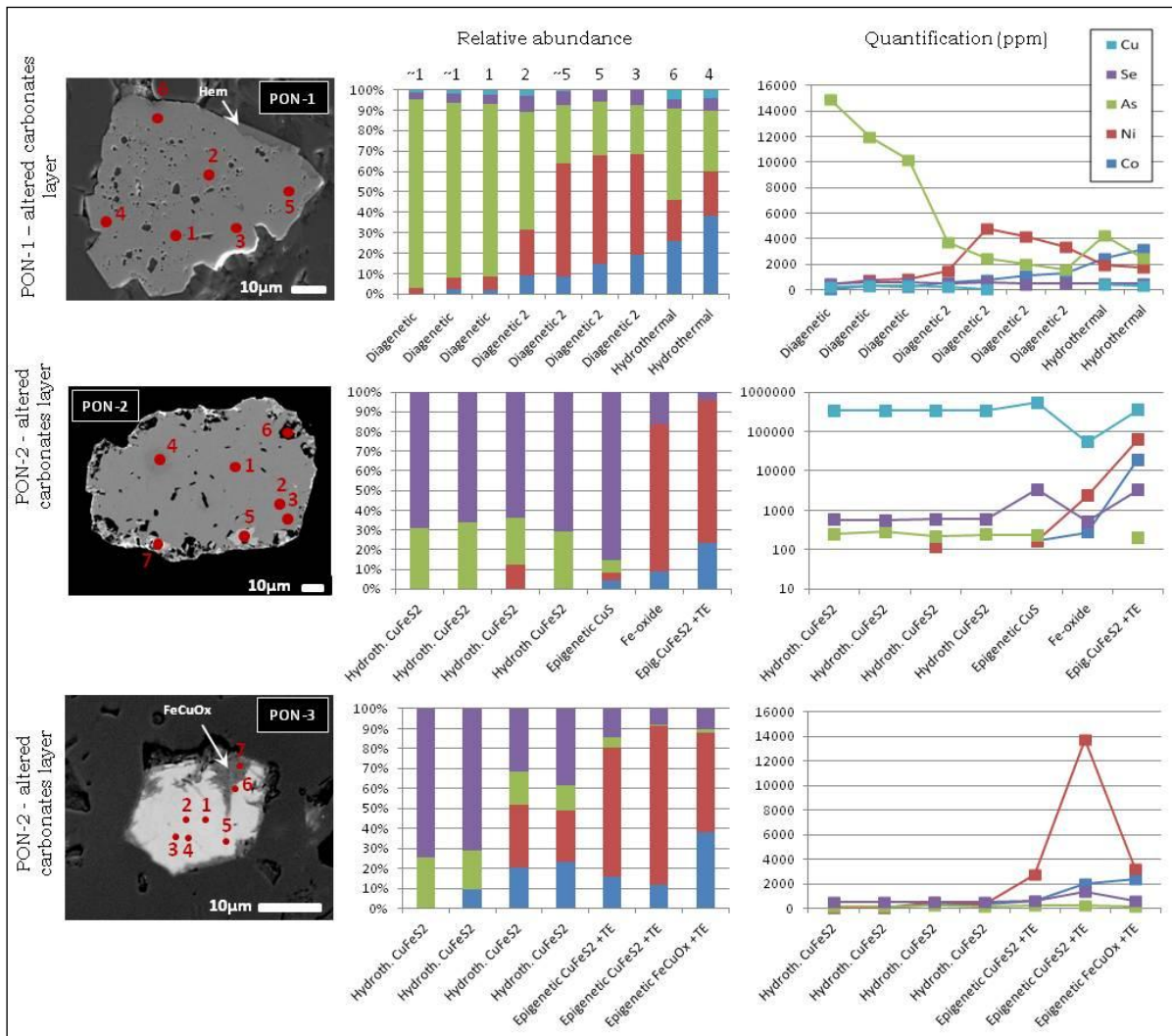


Figure IV.14. Relative abundances and concentrations of Cu, Ni, Co, As and Se in diagenetic pyrites from the 2.95 Ga Pongola stromatolites, Pongola Supergroup, South Africa. Columns in relative abundance bar diagrams are in logical order regarding to the analytical spot numbers or they are specified if not. Note that in PON-2 right diagram the scale is logarithmic because the Cu content has been added.

Arsenic and nickel

Since no detrital pyrite was observed in the Pongola samples, and because diagenetic pyrite precipitated not earlier than burial diagenesis, it is possible that these stromatolites formed in an (at least partially) oxygenated environment. Furthermore, the high As content in diagenetic pyrite PON-1 supports an oxygenated atmosphere at that time. Oxidative weathering on land could have supplied large amounts of As^{5+} into the ocean, abiotically reduced to As^{3+} under the redox-boundary during diagenesis. This boundary may have been very shallow if only low levels of oxygen were present in the

surface ocean. The As and Ni content in PON-1 show complementary variations (Figure IV.14 right), suggesting that they substitute for the same element, here, Fe. The variations of As and Ni concentrations can be explained as follows. First (stage 1), a low temperature, As-rich, diagenetic solution in pore waters allowed diagenetic pyrite to incorporate high amounts of As³⁺ (O'Day *et al.*, 2004). This was possibly enhanced by the affinity of As with clays, an important component of the sedimentary matrix of these stromatolites, and the further desorption of As from these minerals (Smedley & Kinniburgh, 2002; Koschinsky & Hein, 2003). Then (stage 2), the deficiency of Fe in the pyrite lattice created by As substitution allowed the Ni (and lesser Co) enriched in the pore waters by a secondary diagenetic fluid to enter the composition of pyrite while As was partly adsorbed in recrystallized dolomite, which contains traces of Fe (see Fe and As maps of PON-1 in Fig. IV.9). During a third stage, a Cu-rich hydrothermal fluid (Fig. IV.14: spots 6 and 4), responsible for the precipitation of PON-2/PON-3 chalcopyrites, precipitated a Co-enriched overgrowth in which was incorporated the As coming from dissolution of the detrital pyrite under hydrothermal conditions and from its desorption from clays and dolomite.

Thus, stages 1 and 2 should provide some information about the TE released during the degradation of surrounding organic matter, although stage 2 would be more suitable to evaluate the TE content because of the decrease incorporation of As. Regardless of As, diagenetic stages 1 and 2 of PON-1 contain, from high to low concentrations: Ni (400 to 3300 ppm), Co (65 to 1320 ppm), Se (stable between 460 and 620 ppm) and, for the first time compared to diagenetic pyrites in the Hooggenoeg and Josefsdal cherts, noticeable amounts of Cu (200-280 ppm) that bear no relation to silica alteration or other hydrothermal influence. As noted above, these elements are strongly absorbed by organic matter in anoxic sediments and released and partitioned into pyrite during diagenesis (among others: Volkov & Fomina, 1974; Raiswell & Plant, 1980; Dill & Kemper, 1990; Kohn *et al.*, 1998; Large *et al.*, 2007; Perkins *et al.*, 2008; Piper & Calvert, 2009). Pongola stromatolites may not have been entirely anoxic since we argued above that

the environment could have contained at least some free oxygen, which could have limited the absorption of these metals in OM. However, at least small concentrations of the total detected Co, Ni and Cu content could come from the degradation of metallo-proteins necessary for microbial metabolisms. For instance, the low Cu concentrations suggest that this element may have been released and incorporated in the pyrites by this process. This is supported by bulk-rock ICP-MS measurements (Annex 2, sample 10SA01) that yield a Cu concentration of 28 ppm. This bulk Cu content may be largely due to the late Cu-rich hydrothermal event responsible for PON-2 and PON-3 precipitation, suggesting that bulk Cu during diagenesis was less than 28 ppm. Hence, this further suggests efficient partitioning of Cu in diagenetic pyrite (200-280 ppm).

Cobalt, nickel and copper

The significantly higher concentrations of Co and Ni in PON-1, on the other hand, may result from a complementary process. An alternate explanation is that Co and Ni were not entirely released from OM but from another component of the stromatolitic sediment during diagenesis. Guy *et al.* (2010) reported the occurrence of Co-rich pyrites in sedimentary rocks from the 3.0 to 2.8 Witwatersrand Supergroup in South Africa. They interpreted the Co-enrichment of diagenetic pyrite as a result of the reductive dissolution of Mn-oxyhydroxides and further expulsion of trace metals (e.g. Co, Ni) efficiently adsorbed in these minerals, while Mn preferentially enters the composition of authigenic carbonates (Algeo & Maynard, 2004; Johnson *et al.*, 2013). As the same phenomenon was reported in samples from the Pongola Supergroup (Smith, 2007), it is possible that it explains the Co and Ni content of PON-1. In our samples, the presence of Mn-oxides from which Co and Ni could have desorbed is supported by ICP-MS analyses (Annex 2, sample 10SA01) that show bulk-rock depletion of Co and Ni (respectively 4.5 and 19 ppm). The enrichment of pyrite regarding Co and Ni without bulk-rock enrichment in these metals suggests an efficient partitioning of these metals in diagenetic pyrite possibly during this process. Furthermore, although Mn-oxides tend not to be

preserved in ancient rocks, and despite the extensive SiO₂ replacement (SiO₂: 89.15 wt.%), the bulk-rock composition of Pongola stromatolites displays 0.05 wt.% of MnO (for comparison, MnO in the bulk Josefsdal Chert is < D.L. and only 0.002 wt.% in the organic-rich layers). This may suggest that disseminated Mn-oxyhydroxides were indeed present in the Pongola stromatolites. Furthermore, Planavsky *et al.* (2014) also reported the presence of Mn-oxides in the ~2.95 Ga Sinqeni Formation of the Pongola Supergroup and proposed that evidence for the presence of Mn-oxides in such ancient sediments indicates that oxygen-producing photosynthesis was ongoing. Several studies have indeed shown that the oxidation of Mn(II) in marine settings requires significant quantities of dissolved O₂ or a high-potential photosystem (e.g. Tebo *et al.*, 2005; Clement *et al.*, 2009; Kopp *et al.*, 2005), which is consistent with oxygenic photosynthesis.

Our previous interpretations suggesting that at least some O₂ was present in the atmosphere and in the PZ at 2.95 Ga support the possibility that Mn-oxides related to oxygenic photosynthesis were present in the Pongola stromatolites. Furthermore, this is consistent with the presence, for the first time compared to the Hooggenoeg and Josefsdal chert samples, of noticeable amounts of Cu desorbed from organic matter during diagenesis. Indeed, Ridge *et al.* (2008) have shown that organisms that live in oxygen-rich environments use Cu, contrarily to the majority of anaerobic microorganisms. Several authors demonstrated that organisms including Prokaryotes and numerous photosynthetic bacteria use Cu proteins for electron transport, but also as a defensive response against oxidative stress (e.g. Osman & Cavet, 2008; Rademacher & Masepohl, 2012; and review of Huertas *et al.*, 2014). This is also consistent with proteome and metallome studies that have linked the increasing use of Cu-based proteins in organisms with the appearance of oxygenic photosynthesis and the rise of oxygen (e.g. Zerkle *et al.*, 2005; Ridge *et al.*, 2008). Hence, in 2.95 Ga-old sediments, the noticeable release of Cu from OM and partitioning into diagenetic pyrite may indicate oxygenation of the surrounding medium and possibly oxygenic photosynthetic activity.

Above, we argued that at least some part of the Co and Ni content could be derived also from the degradation of OM. Stromatolites are generally a consortium of different types of microbial colonies consisting in oxygenic and/or anoxygenic photosynthesizers and chemotrophic microorganisms, both autotrophic and heterotrophic. The high concentration of Ni over Co and Cu in these stromatolites is not surprising since Ni is an important component of metalloenzymes in several of these microbiota, such as sulfate-reducing bacteria and methanogens (e.g. Krüger *et al.*, 2003; Konhauser *et al.*, 2009) and a possible biosignature for methanogens (together with tungsten, Zerkle *et al.*, 2005). Although by 2.95 Ga volcanic rocks had evolved toward a K-rich granitic composition due to the formation of the differentiated crust, they still displayed a high proportion of ultramafic components (Wilson *et al.*, 2013), thus providing the required Ni content.

Fe-oxides

We found no evidence suggesting that the fine to well-developed Fe-oxide replacement, either on pyrite or chalcopyrite, are a result of modern oxidation. Rather, Fe-oxide replacement corresponds to a specific spatial distribution within the sediment since they were documented only on grains located in the path of fluid circulation. The lack of softly deformable compounds (such as carbonaceous matter) in the stromatolitic layers makes it difficult to determine the direction of fluid circulation, i.e. from the overlying seawater or upwelling groundwaters. However, petrographical observations suggest that this fluid circulation occurred concomitantly with silicification (traces of Si in Fe-oxides, no brittle contact between veins and silicified sediment) suggesting that it occurred late in the sediment history. At this post-depositional stage, no bacterial activity remained that could have caused Fe-oxide replacement. Therefore, Fe³⁺ was made available either by the photooxidation of Fe²⁺ by UV light in the PZ (Cairns-Smith, 1978; Braterman *et al.*, 1983), or by the presence of at least small quantities of O₂, or both. At 2.95 Ga, the fact that some O₂ was present in the environment is not unlikely, since several authors documented “whiffs” of oxygen before the GOE (Anbar *et al.*, 2007), and especially around 2.95 Ga (atmosphere: Large

et al., 2014; ocean: Planavsky *et al.*, 2014). Incidentally, this would coincide with the high As content of the diagenetic fluid reported here. Furthermore, if diagenetic fluids were depleted in H₂S, precipitation rates of pyrite would have been low thus enhancing the extent of As incorporation (Arvestål, 2013).

Arsenic and selenium

If oxygen was indeed present in the atmosphere at 2.95 Ga, the oxidative weathering of sulfides on land may, in the same way as for As, account for the Se concentrations reported for PON-1. However, the concentrations of Se reported are still >50 times higher than that proposed by Large *et al.* (2014) for the same time period. Although formed during periods of reduced volcanic activity, the composition of Pongola stromatolites was highly influenced by the products of this activity (von Brunn & Mason, 1977; Beukes & Lowe, 1989; Wilson *et al.*, 2013). Furthermore, Wilson *et al.* (2013) described these volcanic episodes as ‘*cyclic [...] many of which were of an explosive nature*’. Thus, Se would have been supplied to seawater also from ash fall in these sediments. In this case, Se⁰-reducing chemotrophs (Herbel *et al.*, 2003) within the stromatolites may have increased the Se²⁻ availability and absorption in organic matter as in the Hooggenoeg chert and probably the Josefsdal chert, and the Se²⁻ would have been partitioned into pyrite during diagenesis. Another explanation is that the differentiation of the crust was accompanied by the formation of elevated relief more subjected to weathering. This would, in turn, have supplied high quantities of erosional products to the ocean, such as As and Se. However, under an oxygenated atmosphere, the eroded Se would have entered the ocean as selenite and or selenate. Thus, in any case, if the aqueous environment around the Pongola stromatolites was oxygenated as well, microbial Se-reduction would have been necessary for Se²⁻ to absorb into OM. Metabolisms that reduce selenite and selenate to Se⁰ and Se²⁻ are more diverse than those reducing only elemental Se, and include SRBs and other chemotrophs (Zehr & Oremland, 1987; Herbel *et al.*, 2003; review of Stolz *et al.*, 2006).

Although no evidence of fossilized oxygenic photosynthetic bacteria was found in our samples from the Pongola stromatolites, the absence of detrital pyrite, the possible presence of Mn-oxides, coupled with high levels of As during diagenesis, and the presence of Cu released from OM tend to indicate that certain amounts of O₂ were present in the atmosphere and surface waters and that oxygen-producing photosynthetic bacteria may have been present and active. It should be noted though, that SRBs reduce selenate only when sulfate concentrations are very low (Zehr & Oremland, 1987). Thus, the atmosphere was more likely only weakly oxidative at that time, which would have limited the sulfates supply to the oceans (low sulfate content supported by e.g. Canfield, 1998; Planavsky *et al.*, 2011), enabling the bacterial reduction of Se.

d. Reworked kerogenous stromatolitic layers in the ~1.88 Ga-old Kakabeka Falls stromatolites

The numerous fluid escape features observed in the Kakabeka Falls stromatolitic layers (Fig. IV.4) are filled with microquartz suggesting that silicification in these samples took place at the same time as the fluid escape and thus during compaction associated with burial diagenesis. The fact that no fossilized microorganisms or biofilms are preserved is consistent with complete degradation of organic compounds. Furthermore, as in the Pongola stromatolites, the recrystallization of detrital and syngenetic carbonates (dolomite, ankerite, and siderite) may have reworked the biogenic carbonaceous material. The TE content of diagenetic pyrite may be the only way of recovering information on the biochemical processes that took place in these stromatolitic layers, even more so since they precipitated before burial diagenesis (very rare inclusions even in the large clusters, suggesting a high degree of porosity and plasticity of the sediment at the time of precipitation; see Petrographical results), thus concurrently to OM degradation.

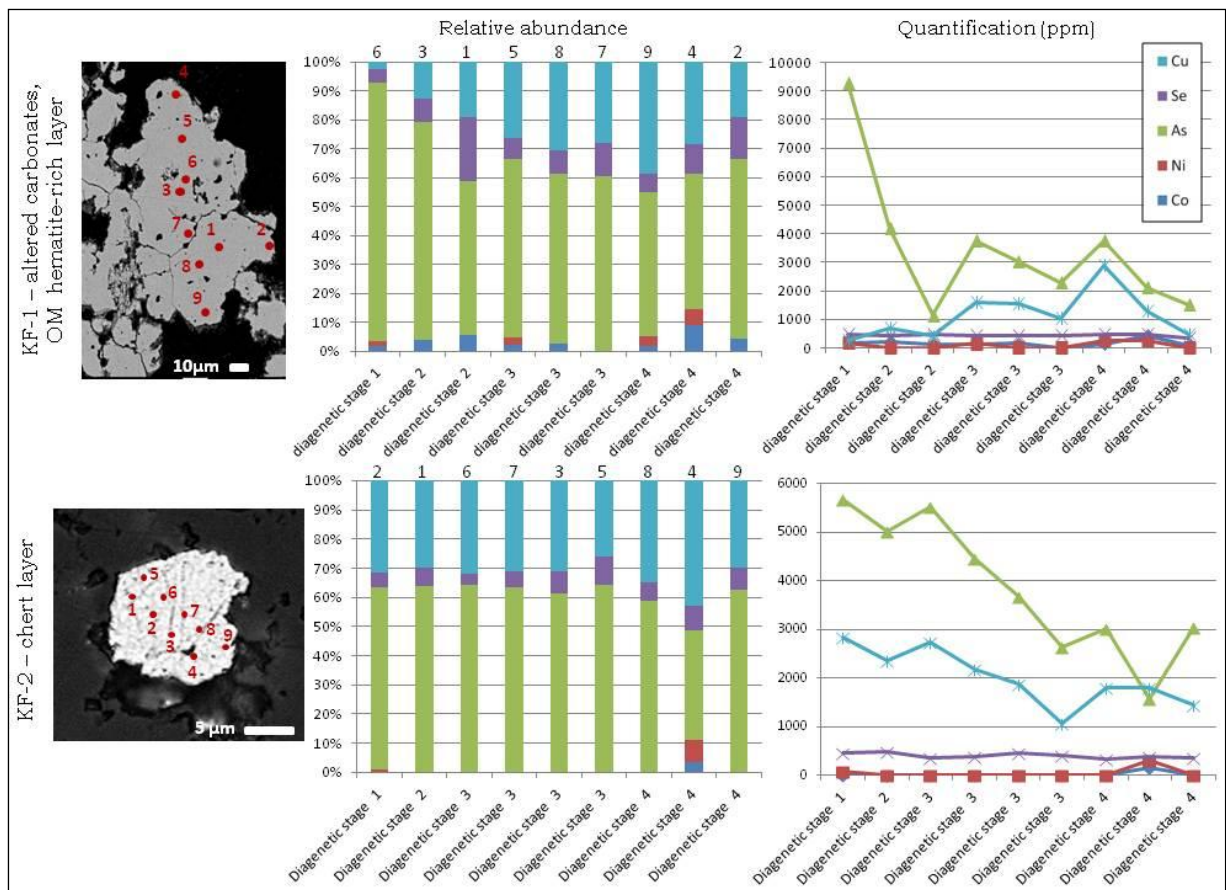


Figure IV.15. Relative abundances and concentrations of Cu, Ni, Co, As and Se in diagenetic pyrites from the 1.88 Ga Kakabeka Falls stromatolites, Gunflint Formation, Canada. Columns in relative abundance bar diagrams refer to the analytical spots on SEM and optical images (left).

The diagenetic pyrites in these stromatolites are characterized by low levels of Ni (<D.L., or 110 ppm average), low Co (160 ppm in average, and detected only at spot n°4 in KF-2), moderate levels of Se (420 ppm average), but high As and Cu concentrations (1000-9000 ppm). KF-1 is challenging to interpret because of its dendritic morphology and the fact that all Co/Ni ratios are <1 except one, which does not help reconstructing the timing of the successive growths.

In KF-1, the variations in As and Cu contents suggest at least two main diagenetic stages:

- Stage 1: the diagenetic fluid is highly enriched in As available directly from seawater and desorbed from clays and carbonates (that include

siderite) and high levels of As are rapidly incorporated in pyrite in the OM layer.

- Stage 2: the deficiency in Fe resulting from the As incorporation allowed other metals to enter the pyrite lattice, such as Cu.

The co-variations in As and Cu contents (Fig. IV.15) could suggest that they substitute for different elements in the pyrite lattice, as in HG-2. During Stage 1, As could have substituted for Fe, then for S thus allowing Cu to substitute for Fe. However, in an environment where oxidative weathering of sulfides on land was ongoing, sulfates would have been readily available in the ocean, which goes against the need and opportunity for the use of As instead of S by microbial colonies. Thus, As would not have been reduced from As^{5+} to As^{3+} by microbial activity and As^{3+} would have been present in low levels in the medium (provided only by marine hydrothermal vents and possibly by inorganic reduction of As^{5+} to As^{3+}). In this case, As and Cu would not have been in competition to incorporate pyrite. Hence, in KF-1 and KF-2, it is more likely that As and Cu both substitute for Fe.

Arsenic

At 1.88 Ga, the atmosphere and oceans were probably oxygenated (Holland, 2006; Large *et al.*, 2014). This explains the high levels of As which would have been provided in large amounts under the form As^{5+} to the ocean by oxidative weathering of sulfides on land. In a stratified ocean, significant amounts of As would have stayed in solution in the oxic PZ due to the depletion in Fe^{2+} , thus limiting photosynthetically-mediated precipitation of Fe-oxides onto which As could adsorb. Thus, it is possible that part of the As content results from the diagenetic release of As^{5+} adsorbed on clays and carbonates, as well as directly from the incorporation of the As^{5+} that remained in solution, rather than from its desorption from Fe-oxides. However, to enter pyrite, As^{5+} would have to be reduced to As^{3+} . This could have been possible abiotically under the redox boundary during early diagenesis since this boundary should have coincided with the bottom of the PZ at that time. Indeed, abiotic processes for the reduction of As and incorporation into early diagenetic pyrite suggest that the oxic layer was thin

and directly overlay the anoxic layer where Fe^{2+} and H_2S were present. This is consistent with the model of Planavsky *et al.* (2011) describing persistent anoxic bottom waters containing both H_2S and Fe^{2+} under the oxygenated mixing zone, from the Archean to ~ 0.5 Ga. Also, H_2S could have been present directly in the stromatolitic layers and could have resulted from the activity of SRBs feeding on the large amounts of sulfates present in seawater.

Copper

We already established that the high Cu contents in KF-1 and KF-2 were neither related to epigenetic events, nor enriched in seawater. Furthermore, ICP-MS results (Annex 2, sample 07CA13) show that the bulk-rock is depleted in Cu compared to the pyrites studied here, indicating effective partitioning of this metal into pyrite during diagenesis. It is possible to hypothesize that the high Cu contents are related to the reductive dissolution of Mn-oxides, as in the Pongola stromatolites. However, Co rather than Cu would have preferentially adsorbed onto these oxides (Guy *et al.*, 2010), which is difficult to reconcile with the present data. Thus, the enrichment in Cu results from another phenomenon. We propose that the Co, Ni and Cu contents are the degradation products of metalloenzymes, which may explain the rare detection and lower contents of Co and Ni in KF-2 since it is located in the organic-poor layer. The characteristic low levels of Ni in the Kakabeka Falls diagenetic pyrites, compared to those in the older sediments described in this study may stem from the depletion of Ni in seawater due to reduced Ni-rich mafic-ultramafic emissions, thus triggering a decline in the activity of methanogens (Konhauser *et al.*, 2009). Hence, the low levels of Ni may represent the absence of methanogens in these stromatolites.

As discussed for PON-1, we argue that the high Cu contents reported here relate to the degradation of Cu-proteins within the microbial mats, and that may be related to the presence of oxygen and to the activity of oxygenic photosynthetic bacteria. The similar concentrations of Cu in KF-1 and KF-2 may result from the migration of the liberated Cu from one layer to another,

suggesting efficient pore water circulation which may have been enhanced by escaping oxygen during the earliest stage of diagenesis.

Selenium

Contrary to the older samples presented in this study, the Se content in Kakabeka Falls diagenetic pyrites may correspond to the interpretations of Large *et al.* (2014) and be a proxy for atmospheric oxygenation. Indeed, for the same time period, the concentrations of Se in these samples are only six times higher than Large's data. Se may have been supplied to the ocean by an effective oxidative weathering of sulfides on emerged land and further incorporated pyrite directly as Se^{2-} or after microbially-mediated Se reduction. Since the pyrites analyzed by Large *et al.* (2014) were not located in organic-rich sediments within the remains of microbial colonies, we attribute the higher Se concentrations in our pyrites to the efficient absorption of Se in OM and use by microbial activity, followed by further desorption during diagenesis.

e. Additional remarks about replacive pyrite in the ~1.88 Ga-old Schreiber Beach stromatolites, Gunflint Formation, Canada

Replacive pyrites on unicellular fossils in the Schreiber Beach samples (Gunflint Formation) were not selected for elemental analyses at first because, at 1.88 Ga under oxygenated atmospheric and oceanic conditions, the Fe^{2+} and H_2S necessary for pyrite precipitation would have been both available only when the sediment was infiltrated by hydrothermal fluids or when it was influenced by an anoxic medium, for instance during late burial diagenesis, when degradation of OM was already complete. However, similarly to published studies (e.g. Planavsky *et al.*, 2011), the present study shows that the anoxic ocean layer could have reached shallow depths at that time, hence allowing pyrite to precipitate at shallow burial depths also. Thus, if the Fe-oxide coatings on these individual microfossils indeed resulted from taphonomic processes (Shapiro & Konhauser, 2015), the degrading OM could have released TE (such as As, Co, Ni, Cu) that could have been

incorporated into the Fe-oxides by substituting for Fe. Since pyrite nucleated on, and replaced Fe-oxide coatings, these TE could have been further transmitted to the replacive pyrite. Thus, further elemental analyses will include the replacive pyrites of the Schreiber Beach samples.

IV.7. Conclusions

IV.7.1. Conclusions on the TE content of sedimentary pyrite

Petrographical and elemental analyses show that, within the same sample, differences exist in the morphology and chemical content of diagenetic pyrite and that these differences are a function of spatial distribution. Indeed, morphological differences are observed between the inventoried diagenetic pyrites when located in microbial mats, microbial clots, detrital CM or organic-poor layers. Interestingly, the differences observed in their TE content could not be entirely explained by changes in global redox conditions through time, or by the influence of epigenetic events (e.g. Si-metasomatism during silicification, late hydrothermal fluid infiltrations). We found that these variations are more likely a function of local processes, occurring at the micrometric scale and affecting the chemical composition of the diagenetic fluid at the same scale. We argue that the absence or presence of microbial activity in the immediate surroundings (tens of μm or less) of the considered diagenetic pyrite and the involved metabolisms (when applicable) are responsible for these differences.

We propose that the microbiota of the 3.45 Ga-old Hooggenoeg chert considered here (H3c; Lowe & Byerly, 1999) consists of an association of Fe-oxidizing anoxygenic photosynthetic bacteria and chemotrophic microbes (probably SRBs and methanogens) that were able to periodically use As and Se supplied by hydrothermal and volcanic activity instead of S in an anoxic environment and under low concentrations of sulfates. In the microbial mats, Fe-oxidizing anoxygenic photosynthetic bacteria could have resulted in

the precipitation of Fe-oxides onto which seawater As^{3+} could have adsorbed. These photosynthetic bacteria may have been associated with Se-oxidizing bacteria using the Se^0 and/or Se^{2-} supplied by volcanic activity instead of S, such as chemotrophs or possibly sulfur-oxidizing anoxygenic photosynthetic bacteria, and Se^{6+} -reducing chemotrophs such as SRBs, or simply Se^0 -reducing chemotrophs. In this case, a Se cycle could have existed. In the microbial clots, there could have been an As cycle implicating chemolithoautotrophic bacteria that reduced As^{3+} while oxidizing H_2S to SO_4^{2-} and SRBs that used the SO_4^{2-} produced or the available As. The presence of an As cycle in anoxic Archean marine sediments was in fact reported by Sforza *et al.* (2014b), in the ~2.7 Ga-old Tumbiana stromatolites (Australia). If the SRBs were chemoorganotrophs as proposed by Westall *et al.* (2011) for the Josefsdal chert, then they could have used the CH_4 produced by methanogens. This would be coherent with the TE results (high Ni content). Based on the geomorphological context of deposition, sediment composition and TE content of diagenetic pyrite, we argue that the microbiota of the 3.33 Ga-old Josefsdal chert (K3c; Lowe & Byerly, 1999) was of a similar nature.

The results obtained from the 2.98 Ga-old Pongola stromatolites are consistent with an oxygenated or weakly oxygenated atmosphere, and oxygen oases in the PZ. We propose that the presence of oxygen is a result of the activity of emerging oxygenic photosynthetic bacteria, which were associated with chemotrophic microbes such as SRBs and methanogens in these stromatolites. The production of O_2 in an otherwise anoxic medium may have triggered the use of Cu-proteins in the microbiota as a defensive response against oxidative stress.

The results from the Kakabeka Falls stromatolites are consistent with the activity of oxygenic photosynthetic bacteria and SRBs in an oxygenated environment but with a reduced activity or absence of methanogens. The high levels of Cu in the diagenetic pyrite of Kakabeka Falls would thus be consistent with our proposition that Cu in diagenetic pyrite in microbial Precambrian sediments could indirectly reflect oxygenated conditions, or the nearby activity of oxygenic photosynthesis in an anoxic environment.

In light of these promising results, we conclude that the TE content of diagenetic pyrite precipitated in close contact (μm) with microbial remains provides important information on the biochemistry of the considered microbial colonies.

In the Pongola and Kakabeka Falls stromatolites, we interpreted the Cu content of diagenetic pyrites as coming from the degradation of Cu-enriched proteins used in metabolisms involving electron transport as well as defense mechanisms against oxidative stress, thus corresponding to photosynthetic metabolisms adjusting to, and evolving in, a newly oxygenated environment. The release of Cu during diagenesis in these samples may come from the diagenetic degradation of anoxygenic photosynthetic bacteria and chemotrophic bacteria, the latter using Cu-proteins as a defense mechanism against the oxidative stress created by the activity of cyanobacteria, and not the from cyanobacteria themselves. However, if at 2.95 Ga, cyanobacteria were just emerging, they may have used the same defense mechanism against their own by-product, oxygen. This would be consistent with the fact that, conversely to methanogens, cyanobacteria do not have a unique metal biosignature, but that under certain conditions, they could express different cellular metal contents (Zerkle *et al.*, 2005).

Thus, the principal outcome of this study is the possibility to use the Cu content of diagenetic pyrite associated with microbial remains as a way of identifying the presence of oxygenic photosynthesis, provided that Cu was not brought in by epigenetic fluids.

Further investigations should include repeated TE analyses on diagenetic pyrites for the time periods considered in this study, including pyritized microfossils in Paleoproterozoic sediments, as well as on Archean sediments comprised between 3.33 Ga and 2.98 Ga, since we suggest here that oxygenic photosynthesis probably emerged between these two time periods. Also, since the speciation of As and Se in microbial sediments influences their chemical affinity with mineralogical compounds of the matrix and with organic compounds, as well as strongly depending on global

redox conditions and microbial activity, X-Ray Absorption Near Edge Structure spectroscopy of As and Se in these elements could provide a necessary input in deciphering precisely the biochemistry of Precambrian microbiota.

IV.7.2. Conclusions on SEM/EDS and EPMA

SEM/EDS and EPMA are little-destructive, elemental techniques with a resolution reaching the micrometer scale. They allow obtaining the *in situ* distribution of major-to-minor (SEM/EDS) and major-to-trace elements (EPMA) at the surface of selected zones within the samples, and offer the possibility of precise quantifications down to tens of ppm (EPMA).

These techniques permit the study of the elemental composition of the kerogen, that is, the chemical elements associated to carbon, for low to high Z elements. They also provide elemental maps, allowing study of the relation of carbon to associated elements within the kerogenous zones. These techniques are thus able to provide insight into the search for type A signatures, since the elemental composition of the kerogen may bring information on the microbial metabolisms involved before degradation of the carbonaceous matter.

Furthermore, SEM/EDS and EPMA show great potential in finding type B signatures. With these techniques, the elemental composition of mineral phases close to the bacterial remains can be mapped as well, allowing detection of the potential chemical impact of microbial activity on the surrounding mineral environment at the micrometric and sub-micrometric scales. In this context, we have shown in the present work that the study of sulfide phases associated with the mats and cells is of great interest. Although the identification of textural changes on these sulfides that could be due to the release of oxygen-producing microorganisms was not possible from petrographical investigation, the study of trace elements content and distribution within sulfide phases by EPMA allows further information to be

obtained. For instance, the content and distribution of these trace elements in sedimentary pyrite can account for the trace elements available in the aqueous medium during their growth (in reducing conditions, e.g. diagenesis) and thus enables determining the local chemistry of the sediment, and that of the local aqueous medium, influenced by the oxygen content of the atmosphere and by local microbial activity.

Chapitre V: résumé

Analyses élémentaires en μ -XRF par rayonnement synchrotron de microfossiles datés à plus de 1,8 Ga

Ce chapitre présente les efforts méthodologiques faits dans le but d'améliorer la qualité des résultats obtenus par analyses μ -XRF. Nous présentons une nouvelle méthode de préparation d'échantillons, impliquant l'utilisation de grilles diamant et d'une soudure en forme de « drapeau » pour fixer l'échantillon de type FIB à la grille diamant. De plus, nous présentons une nouvelle méthode de quantification élémentaire appliquée à ce type d'analyses et utilisant les raies de diffusion Rayleigh et Compton du spectre XRF, qui permet d'améliorer considérablement le calcul des concentrations des éléments détectés. Aussi, ce chapitre donne les résultats obtenus pour la caractérisation de la composition chimique à l'échelle élémentaire de restes microbiens dans des échantillons du chert de Josefsdal daté à 3,33 Ga et des stromatolites de Gunflint datés à 1,88 Ga.

A partir de la distribution de samarium, lanthane et gadolinium en association avec le matériel cellulaire de cellules individuelles de l'assemblage *Gunflintia-Huroniospora*, les interprétations faites proposent que la présence de lanthanides dans ces cellules du chert de Gunflint pourrait représenter une réponse métabolique des bactéries photosynthétiques de ces sédiments contre une insuffisance du milieu en certains métaux, pourtant nécessaires à l'activité photosynthétique. De plus, il a été montré que, pour pratiquer leur activité métabolique, les cyanobactéries requièrent des quantités plus importantes de métaux traces par rapports à d'autres procaryotes (Merchant & Helmann, 2012; Huertas *et al.*, 2014). Ainsi, il est possible de suggérer que, dans un contexte de famine en termes de métaux, les bactéries photosynthétiques oxygéniques seraient alors plus disposées à utiliser des éléments de substitution comme les lanthanides. La présence de lanthanides dans les cellules bactériennes

fossiles de Gunflint pourrait donc indiquer, dans un certain contexte, la présence de bactéries photosynthétiques oxygéniques.

Aussi, la capacité des analyses μ -XRF à étudier à la fois la composition élémentaire de biofilms et cellules fossiles, ainsi que celle de la matrice minérale qui les entoure, perfectionnée par les améliorations méthodologiques présentées dans cette étude, font de cette technique analytique un atout prometteur dans la recherche de signatures chimiques spécifiques à la photosynthèse oxygénique dans les sédiments du Précambrien.

Chapter V: Synchrotron radiation μ -XRF mapping of fossilized traces of life older than 1.8 Ga

Synchrotron radiation X-Ray Fluorescence spectrometry (SR-XRF) is a powerful non-destructive, analytical technique able to provide information on the composition, spatial distribution and concentration of the detected chemical elements. Although this analytical method is today suitable and powerful enough for pursuing this kind of study, the methods usually applied needed to be revised to fit the constraints of this particular study. These constraints arise from the effective SiO_2 replacement of the original chemical composition, the high chemical heterogeneity at the μm and sub- μm scale, and the need to study biologically-related light elements (e.g. C, N, O, F, P, S, Mg) and also heavy elements, such as transition metals (V, Mn, Fe, Co, Cu, Mo), that enter the composition of microfossils as trace metals as well as the sedimentary matrix since these elements were present in seawater and hydrothermal fluids. The small amount of chemical information remaining after the extensive replacement by silica must be efficiently extracted if interpretations are to be rigorous. We indeed found that the quantification method applied to evaluate compositions from photon counts could be significantly optimized. Methodological work was made in an effort to improve the quality of the XRF analyses of highly silicified Precambrian samples containing traces of life.

In the first part of this chapter, we present the tests made to improve sample preparation. The implications of the choice of the sample holder and the FIB protocol used to prepare the micrometric samples that were explored are summarized here. In the second part, we present a new method for quantitative SR-XRF analyses optimized for the study of both light and heavy elements in organic matter of microfossils in Precambrian cherts. Preliminary analyses of XRF measurements are discussed in the third part of this chapter.

V.1 Revision of FIB preparation methods for the in situ elemental study by XRF of microfossils in Precambrian cherts

V.1.1 Rationale for the necessity of thinning petrographical thin-sections for coupling soft and hard SR-XRF analyses

Since XRF is a penetrative technique, elemental quantification is made on the whole volume traversed by the beam, whether the targeted surface to analyze is a point or an area. In such samples displaying chemical and structural heterogeneities at the micrometric and sub-micrometric scales, it is important to understand whether the element quantified is localized in the fossilized mat, in a microcrystal or in the silica matrix. Hence, the thickness of the sample must be reduced to roughly the beam resolution in order to minimize this uncertainty.

The thickness of the sample must also be rigorously controlled to perform accurate XRF analyses. Biologically-related elements such as Na, Mg, P, S, K are considered as light elements, producing low-energy fluorescence photons. These low-energy photons are difficult to detect because they are strongly auto-absorbed in the thickness of the sample before they can reach the detectors. Figure V.1 shows XRF estimates of the transmission of fluorescence photons of elements with fluorescence lines of energy comprised between 2 keV and 15 keV in a SiO₂ matrix and for various thicknesses. In this figure, the green areas highlight the energies at which transmission will be optimal (>90%) for the corresponding photons, and red areas highlight critical transmission (<50%).

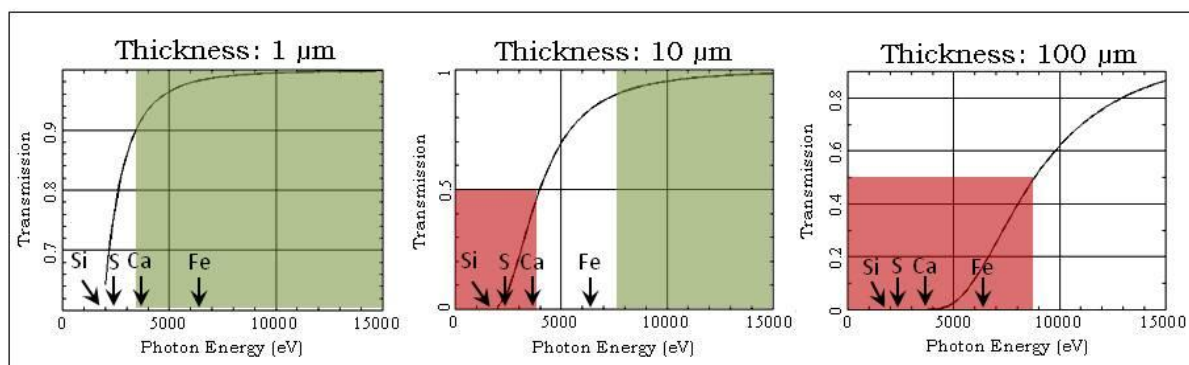


Figure V.1. Transmission estimates of the fluorescence signal in a hypothetical pure SiO_2 sample, for various sample thicknesses. Database software available online on the website of the Center for X-Ray Optics (www.cxro.lbl.gov) was used; reference: Henke *et al.*, 1993. Photons for which transmission will be optimal ($\geq 90\%$) are highlighted by the energy ranges in green, while a poor transmission $\leq 50\%$ corresponds to the red areas.

From these calculations, it becomes apparent that low Z element fluorescences are efficiently collected only for thin samples. For instance, for a $1\ \mu\text{m}$ -thick sample, Ca and heavier element fluorescences are transmitted at 90% and more, and light elements (Si, S) fluorescences still have a $>50\%$ transmission. However, for a $10\ \mu\text{m}$ -thick sample, the transmission of light element fluorescences and even Ca falls below 50% . Furthermore, it should be noted that these calculations are made for a material with an idealized 100% SiO_2 composition, and that our samples contain heavier phases that should decrease the estimated transmissions.

The $30\ \mu\text{m}$ -thick polished thin sections used for petrographical analyses and electron microscope analyses are too thick for a good escape of the fluorescence lines of light elements and even for transition elements. Thus, in samples that are heterogeneous at the micrometer scale, the study of light to heavy, major to trace elements requires the use of ultra-thin sections. Since, at a thickness of $10\ \mu\text{m}$, light elements are poorly transmitted ($<50\%$), and that $1\ \mu\text{m}$ -thick samples would not provide enough material, especially in the case of diluted samples presenting poorly concentrated kerogen, we chose a thickness ranging from 2 to $3\ \mu\text{m}$ for our samples.

V.1.2. Rationale for choosing the holder of the FIB sample for soft and hard SR-XRF analyses

FIB techniques are *a priori* optimal to analyze sample zones a few μm thick in a petrographical thin-section. The preparation of the FIB sections is a little destructive step, since only $\sim 10\text{-}20 \times 3 \mu\text{m}$ of the observable surface is removed, and $\sim 10\text{-}20 \times 10 \times 3 \mu\text{m}$ volume overall. Through the observation of a polished thin section from the Josefsdal Chert, Figure V.2 shows that the impact of FIB sampling is very limited and does not interfere with optical observations. Furthermore, since all non-destructive observations and analyses (optical microscopy, Raman, SEM, EPMA) that require an intact sample surface have already been conducted by the time the FIB sections are prepared, this sub-sampling does not affect the quality of these previous analyses.

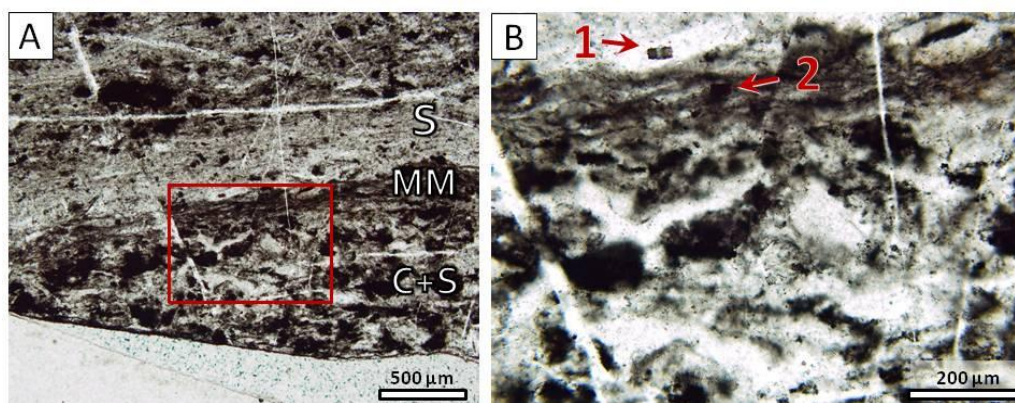


Figure V.2. Optical micrographs of the thin section 99SA07d from the Josefsdal Chert after FIB sections preparation. A. Sandy sediment (S), clots of organic matter (chemotrophs, see Westall *et al.*, 2015; (C) and a photosynthetic microbial mat (MM) are visible. B. FIB sections were cut through a siliceous lens (1) and through the kerogen constituting the finely layered microbial mat (2).

However, FIB techniques are very demanding regarding the type of support used to hold the sample. Since SR-XRF is a penetrative technique, the only way to ensure accurate elemental quantification is by using samples with limited thickness, thus decreasing the compositional heterogeneities due to the sample thickness. The samples hereafter referred to as 'FIB' samples

are few μm -sized and μm -thick sections obtained by cutting across the original sample (usually 30 μm -thick polished thin sections) with the *Focused Ion Beam* technique (FIB), using a Ga beam.

In the following paragraphs, we list the characteristics required for a SR-XRF sample support in order to improve the quality of the analysis. Also, we test the adequacy of commonly used supports in this respect.

a. Light element composition

Firstly, the support should preferably have a light elemental composition to be transparent to X-Rays even at low incident energy and not emit its own fluorescence lines which may contaminate the spectra. For this reason, the supports commonly used such as electron microscopy grids of various metals (Cu, Au) are not suitable. However, other types of supports such as windows of silicon compounds (Si_3N_4 , Si-Oxide or Si), and also carbon grids and diamond grids may be more appropriate. Here we also propose to study the suitability of the lightest element solid support, not routinely used for electron microscopy analyses: the Beryllium half-grids. All these materials synthesized in laboratory are supposed to be pure material (99%) but traces contents are unknown.

b. The sample must be inseparable from its support

When using windows, the FIB section is simply placed on a fine Si_3N_4 membrane. Only electrostatic forces assure the bond between the sample and the support. In contact with these windows, the highly silicified FIB samples will have an unpredictable behavior. They may charge under in-vacuum photon irradiation and jump away from the membranes. Thus, in order to reduce to a minimum the possibility of sample loss, it is preferable to weld the FIB section to the support, such as it is done for electron microscopy analyses where FIB sections are welded with Platinum or a specific SEM glue to a TEM grid.

c. Possibility of “cleaning”

Also, while choosing a support, it is important to take into account the possibility that Ga and Pt ions will contaminate the sample during the preparation and that these undesirable elements must be removed as much as possible. Gallium ions used to cut during the FIB sectioning bounce against the sample walls in the pit (Fig. V.3A) and can redeposit on the FIB section (Fig. V.3B). They also embed in the first few hundred nanometers of the sample. Likewise, during the welding of the FIB to the support, Pt ions can be deposited on the section and on the support around the welding site or be embedded in the section.

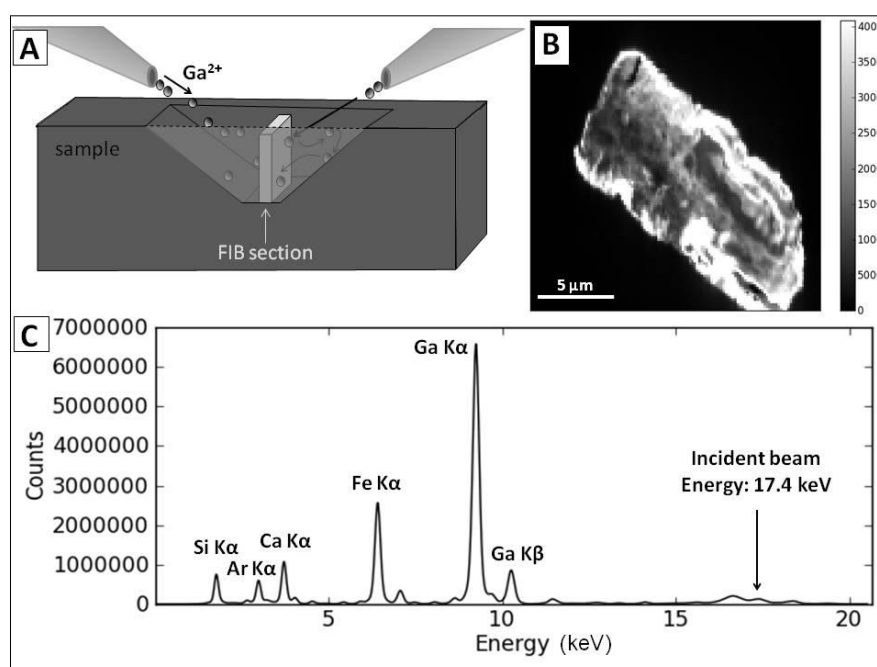


Figure V.3. Ga ions deposition phenomenon and consequences on XRF imagery and XRF spectrum. A. Bouncing of the Ga ions on the walls of the pit during FIB cutting, and deposition on the FIB sample in central position. B. SR-XRF imagery, Ga distribution on an example of partially cleaned FIB sample supported by a Si₃N₄ membrane window, color bar: fluorescence counts. C. SR-XRF sum-spectrum of the same FIB sample and support, note that Ga signal is higher than Si signal by a factor of 7.5, even though Si comprises most of the FIB sample and of the silicon nitride window underneath.

In XRF analyses, these two particular elements are considered “heavy” (atomic number Z of Ga: $Z = 31$, Pt: $Z = 78$) with respect to the lighter (biologically-related) elements (C: $Z = 6$; P: $Z = 15$; S: $Z = 16$). Compared to light elements, these heavy elements produce high energy fluorescence

photons under excitation that efficiently go through the thickness of the sample and reach the detectors. This high energy signal interferes with the signal coming from the sample (Fig. V.3C) leading to an under-estimation of the elements of interest during quantification. The Pt and Ga signals do so by saturating the detectors and causing a “dead time” compensation of the acquisition electronics leading to counting time losses of up to 30-40%. Furthermore, Pt M-lines fluorescence peaks in XRF spectra (~2.05 keV) cover the energy range of P and S, two very important elements in the study of fossilized traces of life. Thus, Pt will overlap P or S lines and will prevent the proper investigation of the sample.

For these reasons, Ga and Pt ions deposited/embedded on/in the sample must be removed. This can be done by an ion milling procedure using an argon ion beam. Figure V.4 shows the effect of this procedure. This also applies to tungsten (W: $Z = 74$) that is sometime used in FIB section preparation as well. Indeed, the L and M-order fluorescence peaks of this element can hinder the proper detection of Si, but also of certain metals such as Cu and Zn. Hence, the support used to hold the samples must allow the FIB sections to be free on both their sides for an efficient ‘cleaning’ of Ga, Pt and/or W by ion milling. Neither Si-windows nor C-grids can enable this configuration. In the cases where Si_3N_4 windows and C-grids are used as supports, the cleaning of the Ga ions is made before extraction of the FIB section from the pit, which easily leads to the redeposition of bouncing Ga in the same way as in Figure V.3A.

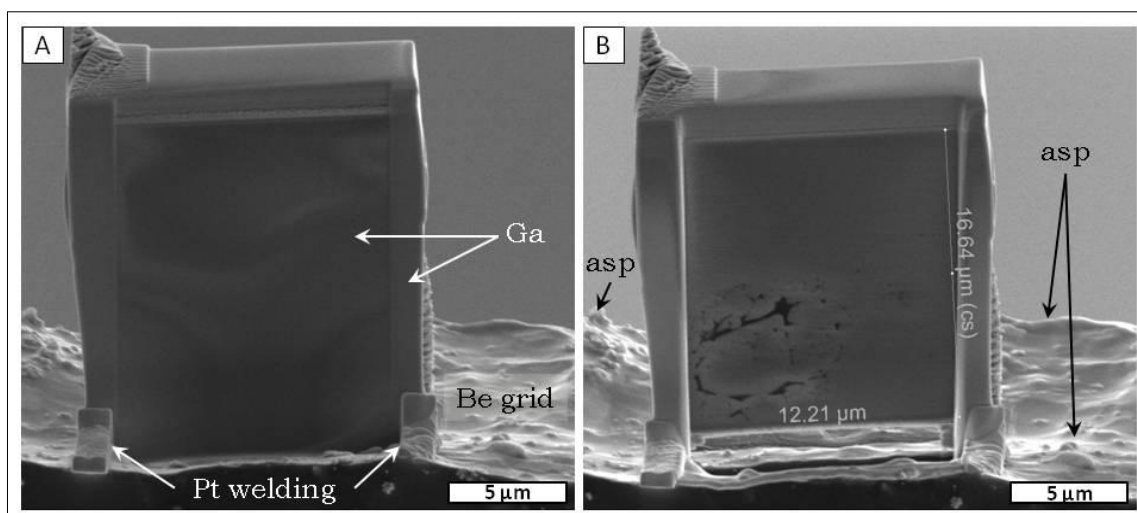


Figure V.4. Effect of ‘cleaning’ of the FIB sample surface by ion milling. SEM imagery before (A) and after (B) ion milling of a FIB section cut through an individual cell from the Gunflint stromatolites, Schreiber Beach locality. In B, a crystallized structure appears, which corresponds to the mineralized bacterial cell. ‘asp’ shows the asperities of the inner edge of the Beryllium grid used to support this FIB sample.

d. Conductivity

Preferably, the support needs to be conductive to allow preliminary or complementary analyses with electron microscopy techniques without any need for carbon or gold metallization. Indeed, it is always preferable to avoid any addition of carbon on the sample when studying fossil carbonaceous matter. Also, as Pt, Au ($Z = 79$) M-peaks (2.12 keV) will overlap with the nearby P and S peaks and Au L-peaks around 9.7 keV and 11.5 keV will saturate the detectors.

V.1.3. Experimental investigations of different holders for the FIB samples for soft and hard SR-XRF analyses

Since they are initially targeted for electron microscopy analyses, the pre-sorted supports with a light composition are all conductive materials. Table V.1 summarizes the properties of the discussed supports concerning the technical requirements.

Table V.1. Properties of the selected supports with respect to the requirements.

Requirements	Si-windows	Carbon grids	Diamond slot-grids	Beryllium half-grids
Light element composition	✓	✓	✓	✓
Robust bond to the support	X	X	✓ (Pt welding)	✓ (Pt welding)
Possible cleaning of the FIB section sides	X	X	✓	✓
Conductivity of the support	✓	✓	✓	✓

The diamond slot-grids and beryllium half-grids (Fig. V.5) possess all the required characteristics. We decided to test both of these preparation methods. SEM/EDS imagery and elemental analyses were performed at the Centre de Microscopie Electronique (CME), Université d'Orléans, France. SR-XRF analyses presented here were performed at the 'mySpot' beamline of the Bessy II synchrotron, Helmholtz-Zentrum, Berlin, Germany, at the incident energy of 12 keV. At this energy, the fluorescence $K\alpha$ - $K\beta$ of Ga and $L\beta$ of Pt are highlighted on the raw maps (Fig. V.8).

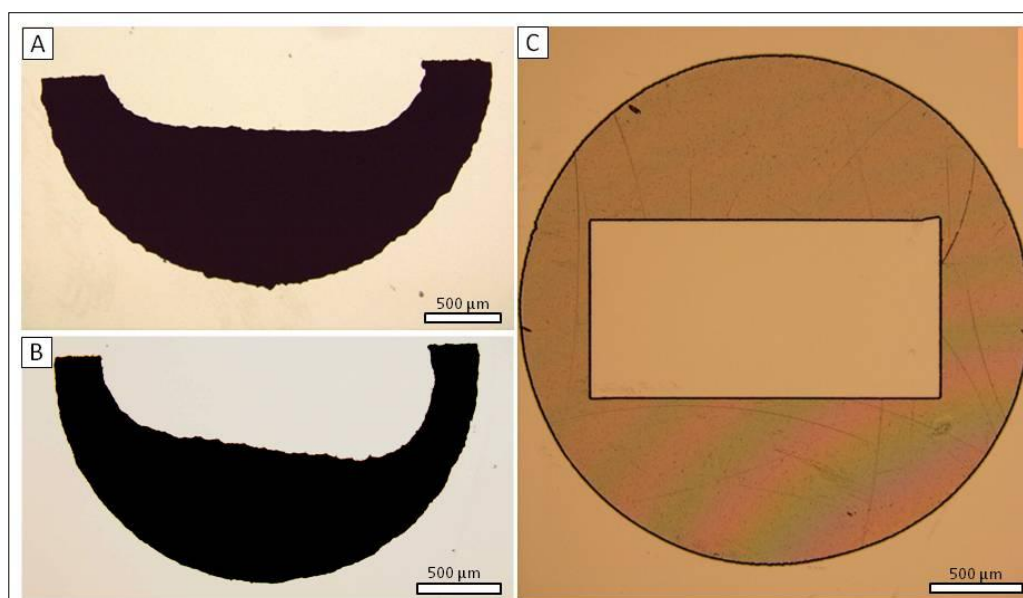


Figure V.5. Optical microscopy images of Beryllium half-grids and Diamond grids. A and B. Be half-grids. Note the irregularity of both internal and external edges. C. Diamond slot-grid.

a. Beryllium half-grids

The advantage of using beryllium grids is that Be is the lightest element from which a solid support can be made and used for FIB section preparation. Beryllium half-grids (Be-grids) are made from grids with 1x2mm slots obtained by sintering and were purchased from SPI Supplies under the reference 412BGH-BA. SEM/EDS analyses show that in the light elements range, the grid only displays Al and O, and little Be and C (Fig. V.6). However, the physical properties of Be make precise-shape modeling challenging. The edges of the slot are irregularly shaped and both faces of the grid bear many asperities and allochthonous grains (Fig. V.6B and Fig. V.6C) that are enriched in C (Fig. V.6D). These conditions are unsuitable for FIB welding, which requires plane and smooth surfaces as much as possible.

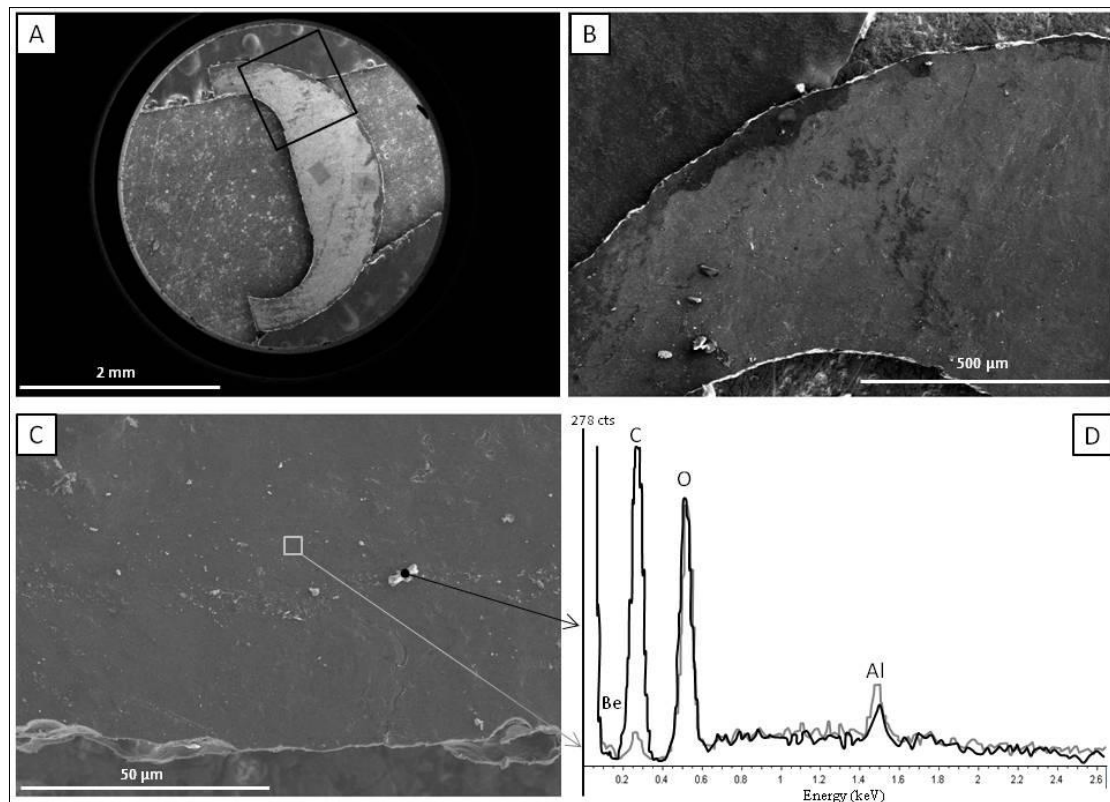


Figure V.6. SEM imagery and EDS analyses of a Beryllium half-grid. A and B: electronic imagery of the half-grid of beryllium, and zoom (black box). Note the irregularities of both the surface and edges of the half-grid. Trails of dust particles and cracks are also visible. C. Close-up on a region near the inner edge of the half-grid. Note the trail of dust particles, and the very irregular edge. D. EDS spectra of a dust particle (black line) and a clean zone (grey line), incident energy: 5 keV, acquisition time: 30 s/spectrum.

For this purpose, we performed ion milling (CME, Orléans) on the edges of the slot in order to create suitable surfaces for FIB welding (Fig. V.7). After thinning, edges and near-edge surfaces are abraded and smoothed enabling the fixation of FIB samples. However, even after this procedure, the edges are neither perfectly smooth nor planar in their thickness (~30 μm) (Fig. V.4 'asp' and Fig. V.8A SEM image) and the welding process remains challenging. A robust weld is thus necessary and is achieved by means of two Pt dots, directly on the edge of the grid. FIB samples were cut and welded to the grid at the Centre Pluridisciplinaire de Microscopie électronique et de Microanalyse (CP2M), Université d'Aix-Marseille, France using a dual beam FIB system.

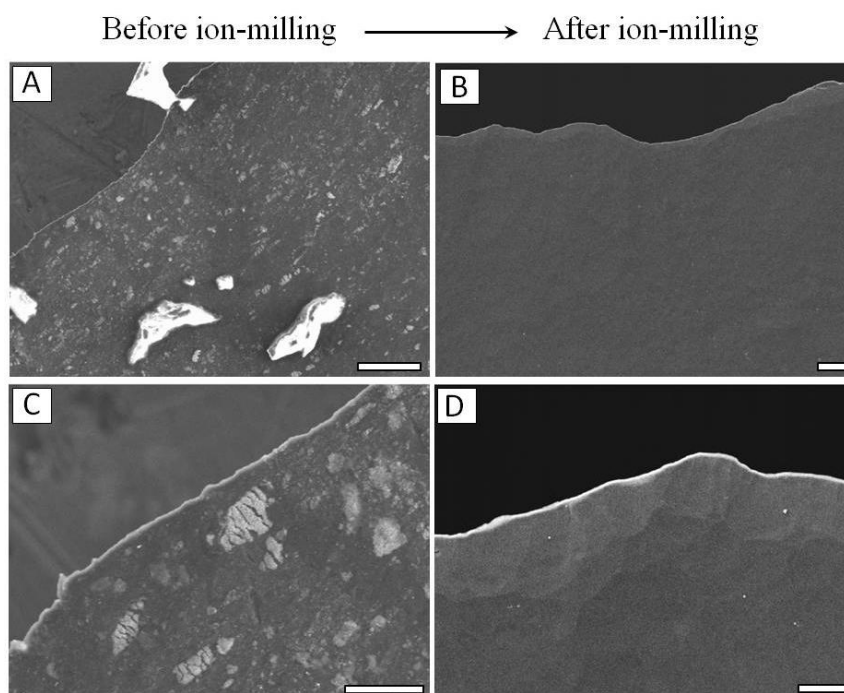


Figure V.7. Ion milling of the edges of the Be-grids. Scale bars are, for A and B: 20 μm , for C and D: 5 μm .

b. Diamond slot-grids

Diamond grids (D-grids) have a diameter of 3mm and 1x2mm slots. They were purchased from SPI Supplies under the reference 402DG-AB. The clean and precise cut of the edges does not require supplementary preparation such as ion milling and abrasion as mentioned above for the Be half-grids. In order to reduce the influence of the Pt signal and the grid

signal over the signal of the sample during XRF analyses, FIB samples were fixed to the D-grid not by two Pt dots, but by means of a narrow Pt ‘pole’, thus moving the sample away from the grid and from the Pt deposited on the grid (Fig. V.8B). Also, to increase this effect, we chose to cut the FIB sections in a more elongated, rectangular form. FIB cutting and welding to the D-grid were performed at the Institut d’Electronique de Microélectronique et de Nanotechnologie (IEMN), CNRS Villeneuve d’Ascq, France.

c. Comparison of the mounting of FIB slices on Beryllium and diamond holders

Figure V.8 shows optical and electron microscopy images, as well as XRF maps of the FIB sections and grids configurations for both Be-grids and D-grids.

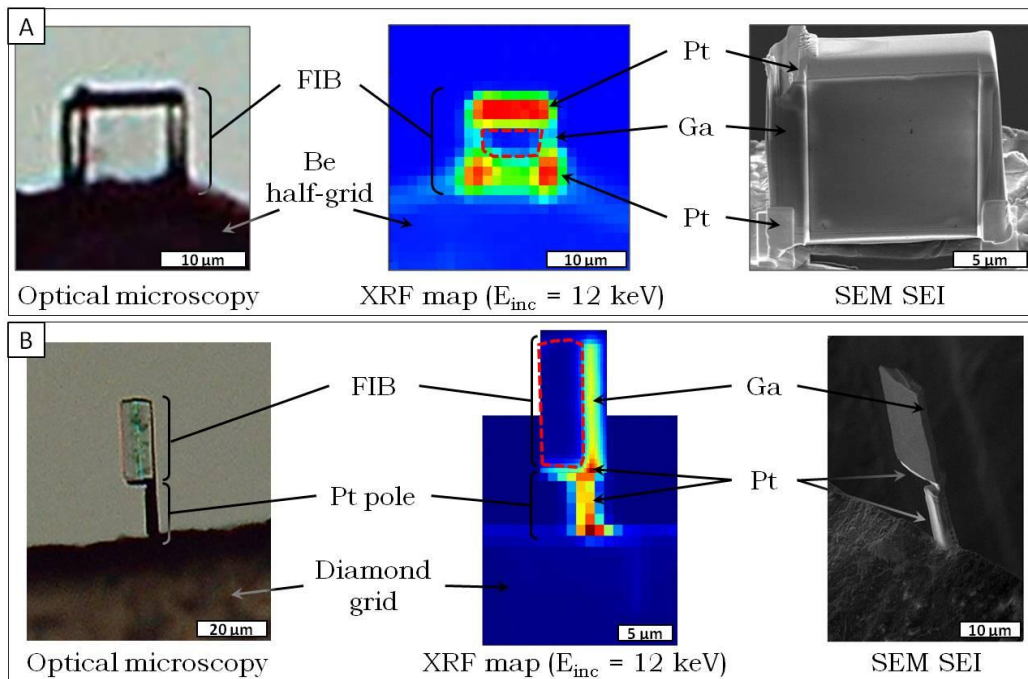


Figure V.8. Optical microscopy, XRF and electron microscopy imagery of the configurations of sample preparation with Be-grids (A) and D-grids (B). XRF map were performed with an incident energy (E_{inc}) of 12 keV, which highlights the distribution of Pt and Ga. Red dashed lines on the XRF maps delimit the areas of the FIB samples that are not affected by the signal of Ga and Pt. Note that with the D-grid configuration, the usable area is greater.

Compared to the configuration used for Be-grids, the surface of the FIB section that is not influenced by the fluorescence signal of Pt and Ga (red dashed lines) is significantly greater in the case of the D-grids preparation method. Furthermore, depending on the FIB-grid angle, the asperities remaining in the thickness of the edges of the Be-grids as well as the two Pt dots may be in the trajectory of the incident beam during XRF analyses and may emit a fluorescence signal that is detected along with the signal of the FIB sample. Thus, in the case where Be-grids are used as supports, it is necessary to characterize the chemical composition of the grid itself and that of Pt-Ga zones as their XRF signals are likely to interfere with the signal of the sample.

Figure V.9 shows the XRF spectra of a Be-grid and a D-grid at $E_{inc}=12k$ keV, obtained from the grid areas that are visible on the maps in Figure V.8. The Be-grid spectrum was obtained over an area of 104 pixels normalized to 1 pixel, with an acquisition time (T_{acq}) of 1 second/pixel, while the D-grid spectrum was obtained over an area of 105 pixels normalized to 1 pixel, with a T_{acq} of 2 seconds/pixel. The XRF spectrum of the Be-grid reveals the presence of significant amounts of several metals constituting the grid such as Fe, Ni, Cu and Zn (Fig. V.9A), while the composition of the D-grid (Fig. V.9B) displays a higher purity (detected elements do not exceed 15 counts, even for a longer acquisition time, $T_{acq}=2s/pixel$ instead of $1s/pixel$). The presence of Ga and Pt is not surprising since these spectra are derived from selected areas located only several microns from the location of the FIB sections.

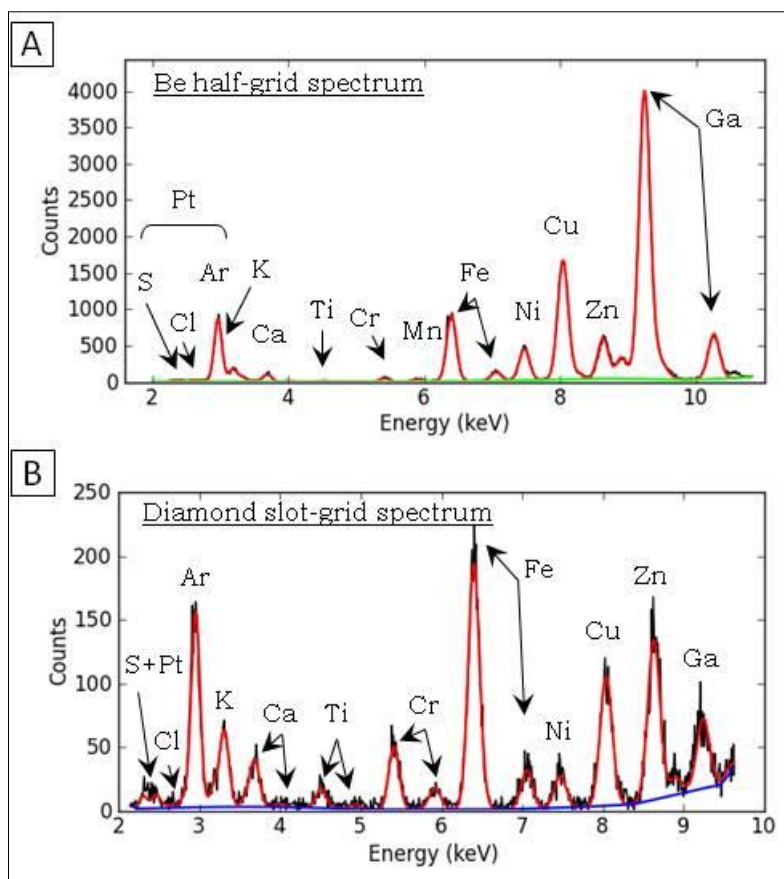


Figure V.9. XRF sum-spectra of a Be half-grid (A) and a diamond slot-grid (B), obtained from the maps in Fig.V.8 from selected zones of 104 pixels and 105 pixels respectively, and normalized to one pixel. These zones are located several microns under the locations of the FIB sections, thus explaining the presence of Pt and Ga. A. Spectrum acquired over 104 pixels at $E_{inc} = 12$ keV with an acquisition time (T_{acq}) of 1s/pixel. B. Spectrum acquired over 105 pixels at $E_{inc} = 12$ keV $T_{acq}=2$ s/pixel. Note the order of magnitude difference of the fluorescence counts between the two grids: even with $T_{acq} = 2$ s, the fluorescence count of ultra-trace elements in the D-grid is less than 15 cts.

We studied the XRF signal of five Be-grids and two D-grids. The average XRF signal for both grid-types is reported in Table V.2, along with the XRF signal of the FIB areas within the red dashed lines in Figure V.8. Table V.2 also reports the remaining signal for each detected element after the signal of the grid was subtracted from the signal of the sample. We propose that the usable remaining data for typical samples correspond to the points with counts larger than their variance (error) after subtraction of this parasitic signal (bold font in Table V.2).

We found that not only the use of Be-grid as a support requires supplementary preparation (ion-milling), but the XRF analyses of these grids

reveal that their low average atomic number is compromised by the presence of significant amounts of metals (such as Fe, Ni, Cu, Zn) in their composition. XRF from these metals interfere with the signal of the sample. In addition, the irregular morphology of the edges of these grids forces to use Pt dots for a robust weld of the FIB samples. Since XRF is a penetrative technique, the frequent lumps created by the irregularity of the edges (visible in the background of Fig. V.4B: 'asp') are likely to be on the trajectory of the incident beam to the FIB sections, and the signal from the grid easily mixes with the signal of the samples. Furthermore, since Pt is a heavy element, the two Pt dots at the base of the FIB samples also strongly influence the signal coming from the sample, at both low and high incident energy. Therefore, except for highly concentrated elements such as Si, the elemental signal of sample Jos1 is thus difficult to extract from these parasitic signals.

On the other hand, XRF analyses show that D-grids have a highly pure carbon composition with only ultra-trace amounts of other elements. Apart from Ga, the usable data in the case of the D-grids include Si, S, K, Ca, Sc, Ti, Fe, Co, Zn and As. These elements cover two groups: the light elements (C, N, O, F, P, S, Mg...) as well as the heavy elements such as transition metals (V, Mn, Fe, Co, Cu, Mo...) that make up the composition of microfossils. Furthermore, the precision of D-grids manufacturing does not necessitate intermediate preparation before FIB welding. The smooth, clear edges of these grids allow using a narrow Pt-pole to fix the FIB sample remotely to the D-grid. Combined with a Pt-pole configuration for FIB welding that reduces to a minimum the influence of the XRF signal of the heavy elements Ga and Pt, the D-grids have no or little influence on the sample signal. In addition, this particular preparation method ensures a robust bond between the FIB sample and its support, while allowing both faces of the FIB section to be free, thus offering the possibility to 'clean' the Ga and possibly the Pt deposited on the samples.

Finally, we propose that Diamond-grids, combined with a Pt-pole for FIB welding and the removing of Ga and Pt on the sample using an argon ion

beam, are the preferred choices of support for FIB samples in the context of the chemical characterization of early traces of life.

Table V.2: Comparison of the extent of useable XRF data (in fluorescence counts) between samples supported by a Be-grid and samples supported by a D-grid. All results are normalized to $T_{\text{acq}}=1\text{s}$ and to 1 pixel.

Be-grid (A)		FIB sample (B)		B-A		D-grid (A)		FIB sample (B)		B-A			
Fit	peak area	sigma	peak area	sigma	peak area	sigma	Fit	peak area	sigma	peak area	sigma	peak area	sigma
Al	/	/	1.49E+01	5.83E+01	1.49E+01	5.83E+01	Al	4.96E-02	1.06E+00	8.17E-01	4.60E-01	7.67E-01	1.52E+00
Si	7.77E+00	1.15E+01	1.42E+02	1.48E+01	1.34E+02	2.63E+01	Si	6.93E-02	7.47E-01	7.78E+01	3.16E+00	7.77E+01	3.91E+00
P	5.49E+00	1.13E+01	1.21E+01	8.95E+00	6.61E+00	2.03E+01	P	/	/	/	/	/	/
S	1.79E+02	2.59E+01	6.47E+01	7.40E+00	<i>-1.14E+02</i>	<i>3.33E+01</i>	S	3.74E-01	1.00E+00	7.65E+00	1.54E+00	7.28E+00	2.54E+00
Cl	5.99E+01	7.40E+01	5.44E+01	6.15E+00	<i>-5.50E+00</i>	<i>8.02E+01</i>	Cl	2.42E+00	1.95E+00	1.84E+00	1.59E+00	<i>-5.80E-01</i>	<i>3.54E+00</i>
K	2.97E+02	5.45E+01	3.54E+02	7.35E+01	5.70E+01	1.28E+02	K	1.24E+00	1.09E+01	2.97E+01	1.36E+01	2.85E+01	2.45E+01
Ca	7.27E+02	3.16E+01	5.73E+02	1.37E+01	<i>-1.54E+02</i>	<i>4.53E+01</i>	Ca	7.58E+00	9.76E+00	3.51E+01	2.51E+00	2.75E+01	1.23E+01
Sc	/	/	/	/	/	/	Sc	/	/	2.36E+00	1.04E+00	2.36E+00	1.04E+00
Ti	1.20E+02	1.83E+01	5.27E+01	4.75E+00	<i>-6.73E+01</i>	<i>2.31E+01</i>	Ti	3.01E+00	2.21E+00	1.30E+01	1.75E+00	9.99E+00	3.96E+00
V	4.74E+01	2.39E+01	1.27E+01	9.05E+00	<i>-3.47E+01</i>	<i>3.30E+01</i>	V	/	/	1.96E-02	2.08E+00	1.96E-02	2.08E+00
Cr	7.09E+02	2.43E+01	2.12E+02	8.88E+00	<i>-4.97E+02</i>	<i>3.32E+01</i>	Cr	5.73E+00	3.00E+00	9.33E+00	1.39E+00	3.60E+00	4.39E+00
Mn	4.21E+02	2.66E+01	5.49E+01	7.93E+00	<i>-3.66E+02</i>	<i>3.45E+01</i>	Mn	1.93E+00	1.95E+00	4.46E+00	1.53E+00	2.53E+00	3.48E+00
Fe	1.16E+04	1.23E+02	2.23E+03	2.53E+01	<i>-9.37E+03</i>	<i>1.48E+02</i>	Fe	1.09E+02	9.03E+00	9.73E+02	1.22E+01	8.64E+02	2.12E+01
Co	/	/	9.24E-01	8.00E+00	9.24E-01	8.00E+00	Co	/	/	5.86E+00	3.46E+00	5.86E+00	3.46E+00
Ni	6.38E+03	7.08E+01	4.71E+02	1.77E+01	<i>-5.91E+03</i>	<i>8.85E+01</i>	Ni	1.79E+01	4.19E+00	1.15E+01	2.20E+00	<i>-6.40E+00</i>	<i>6.39E+00</i>
Cu	1.70E+05	3.20E+02	3.32E+03	3.58E+01	<i>-1.67E+05</i>	<i>3.56E+02</i>	Cu	3.55E+02	1.37E+01	4.56E+01	5.76E+00	<i>-3.09E+02</i>	<i>1.95E+01</i>
Zn	8.12E+03	8.37E+01	3.13E+03	3.60E+01	<i>-4.99E+03</i>	<i>1.20E+02</i>	Zn	5.68E+01	6.20E+00	9.47E+01	7.44E+00	3.79E+01	1.36E+01
Ga	1.30E+04	8.91E+01	1.92E+05	2.73E+02	1.79E+05	3.62E+02	Ga	1.00E+02	6.49E+00	1.26E+03	1.45E+01	1.16E+03	2.10E+01
Ge	5.70E+01	3.10E+01	/	/	<i>-5.70E+01</i>	<i>3.10E+01</i>	Ge	/	/	/	/	/	/
As	1.92E+03	4.71E+01	5.11E+00	2.95E+00	<i>-1.91E+03</i>	<i>5.01E+01</i>	As	/	/	1.70E+01	4.54E+00	1.70E+01	4.54E+00

Font code: italic: negative data; normal: positive data; normal bold: positive data larger than their sigma = rigorous, usable data.

V.2 Development of Rayleigh/Compton (R/C) method for the quantification of low Z elements

V.2.1. Principle of the R/C analytical method

It was shown in previous studies that undetected light elements were erroneously neglected and did not contribute to the quantification of the detected elements (Bos & Vrieling, 2005). Omitting absorbing light elements, particularly in Earth Sciences where C, N, O, Si are major elements in the quantification process, underestimates the concentration of the detected elements which leads to distorted interpretations. In order to obtain a reliable quantification of low Z elements in our stromatolite samples, I contributed to the study of a novel quantification methodology, which changes the treatment of fluorescence data containing contributions of the low Z element undetected fluorescences (Simionovici *et al.*, 2010, 2012 and 2015 in preparation). This method is based on the scattering of X-rays from the atoms in the sample, which produces both elastic (Rayleigh) and inelastic (Compton) contributions at an energy close to the incident one (Fig. V.10). At this high energy, all atoms of the illuminated column traversed by the beam produce scattering, and that can be semi-quantitatively treated to obtain an estimate of the average low Z content of a sample. This low Z contribution cannot be directly attributed to elements as is done with fluorescence, which has a Z^{3-4} dependence, which strongly separates neighboring Z atoms. One can use the ratio of elastic to inelastic scatterings, Rayleigh/Compton (R/C) which have a Z^{2-3} respectively Z dependence to obtain a calibration curve. The curve will represent a straightforward way to characterize an “average” atomic number of a sample, as a function of the elements recorded in fluorescence but also of the “undetected” elements. We define this “average” atomic number Z_a of the whole sample as the Z_i element atomic numbers weighted by the n_i atomic densities as:

$$Z_a = \frac{\sum_i n_i Z_i + n_u Z_u}{\sum_i n_i + n_u} \quad \text{with} \quad n_{i,u} \left(\frac{\text{at.}}{\text{cm}^3} \right) = c_{i,u} \frac{A_0 \left(\frac{\text{at.}}{\text{mole}} \right) r_{i,u} \left(\frac{\text{g}}{\text{cm}^3} \right)}{A_{i,u} \left(\frac{\text{g}}{\text{mole}} \right)} = c_i \frac{A_0 r_{i,u}}{A_{i,u}}$$

with A_0 Avogadro's number, Z_i the atomic numbers of fluorescing elements, Z_u the average atomic number of the undetected elements, $\rho_{i,u}$ the volume densities of elements and $A_{i,u}$ the element atomic masses. The sum is taken over all “ i ” elements detected in fluorescence plus one average “undetected” element “ u ”.

Using a calibration curve linking the ratio of Rayleigh to Compton scatterings of a spectrum measured in every point of a sample to the average atomic number of that spectrum, one can directly extract the “average” atomic number Z_a of that sample. As shown earlier, Z_a depends on the “undetected” atomic number Z_u and its concentration c_u . If one has a priori knowledge of the sample and knows that there are some elements of low Z present in the sample, one can calculate the average atomic number Z_u . One has then to solve an equation to extract the c_u concentration of the undetected phase of atomic number Z_u . As an example, for our chert samples primarily composed of SiO_2 , one can calculate the undetected element “ u ” labeled “Oxycon” for oxygen-silicon as:

SiO_2 chert composition

$$Z_{\text{Oxycon}} = c_S \times Z_S + c_O \times Z_O$$

$$c_S = \frac{A_S}{A_S + 2 \times A_O} = \frac{28}{28 + 2 \times 16} \gg 0.46$$

$$c_O = \frac{2A_O}{A_S + 2 \times A_O} = \frac{32}{28 + 2 \times 16} \gg 0.54$$

The Z of the undetected Oxycon is then 10.8, and one has to calculate its concentration c_{Oxycon} using the « Solver » function in an Excel spreadsheet. This is done in an iterative loop starting from the previously estimated c_i concentrations of the fluorescing elements in the sample, from the average Z equation:

$$Z_a = \frac{\sum_i \frac{c_i r_i Z_i}{A_i} + \frac{c_u r_u Z_u}{A_u}}{\sum_i \frac{c_i r_i}{A_i} + \frac{c_u r_u}{A_u}}$$

The only unknown here is $\mathbf{c}_{Oxycon} \equiv \mathbf{c}_u$ and Solver calculates it, iterating the equation above. The sum of the \mathbf{i} detected elements and the \mathbf{u} undetected one is then normalized to 1 to estimate the ratio between Oxycon and the other elements in the respective phase.

V.2.2. Measurement of the R/C calibration curve

As mentioned earlier, Rayleigh and Compton contributions are always present in any XRF spectrum obtained on a synchrotron, as scattering is dependent on the photon beam polarization, a property of the photon beam on all synchrotrons. Polarization is roughly the angle between the plane made by the direction of a photon and its perpendicular electrical field vector E with the horizontal plane, and that is almost 0° yielding an almost 100% horizontal polarization for the ESRF storage ring.

The scattering of the incident beam of energy $E_0 = 17.45$ keV at ID22 NI produces a Rayleigh peak at 17.45 keV, and a Compton peak, dependent on the angle between the incident photon and the direction of detection which for our experiment was 105° , by means of the formula:

$$E_{Compton} = \frac{E_0}{1 + \frac{E_0}{511} [1 - \cos(105^\circ)]}$$

where the rest mass of the electron from which the incident photon scatters is, in units of energy, 511 keV.

As Rayleigh and Compton scatterings have high energies, their auto-absorption in the sample will be weak and they will easily be detected, which is the advantage of this method. Their peaks can be fitted by 3 gaussians representing pure Rayleigh at incident energy, pure Compton at the

scattering angle of our measurement (105°) and a larger gaussian representing the series of multiple Rayleigh+Compton, so called Multiple Scattering (MS) at all angles inside the sample which produce an X-ray directed towards the detector. This is illustrated in Figure V.10.

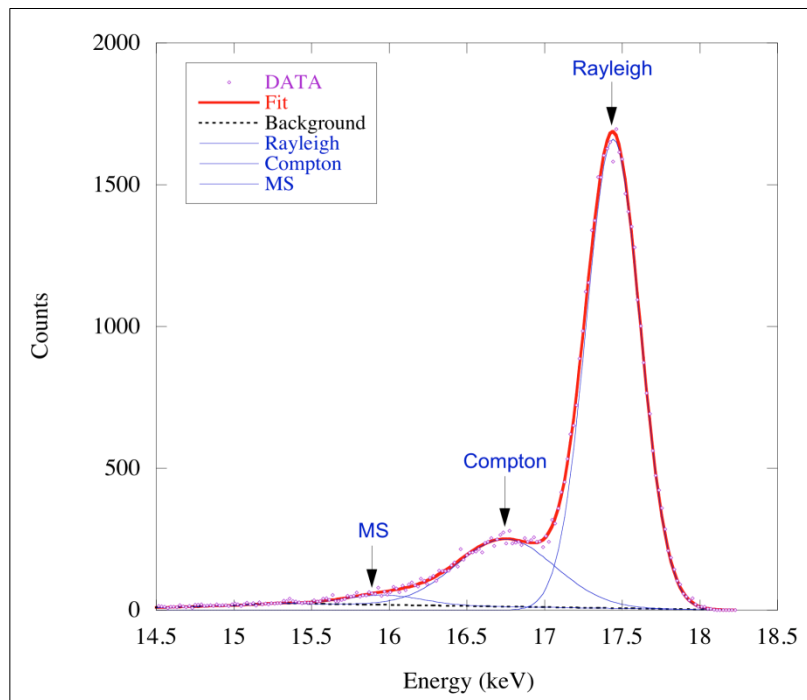


Figure V.10. Gaussian fits of the Rayleigh, Compton and MS scatterings for an incident beam energy of $E=17.45$ keV.

Using a series of thin standards, from Goodfellow Inc. and MicroMaterials Inc. we measured the Rayleigh/Compton ratio as a function of the average Z of the samples. The experiments were performed at ID22 NI during a special calibration campaign in 2013, and the results in the form of a Rayleigh/Compton versus Z graph are reported in Figure V.11.

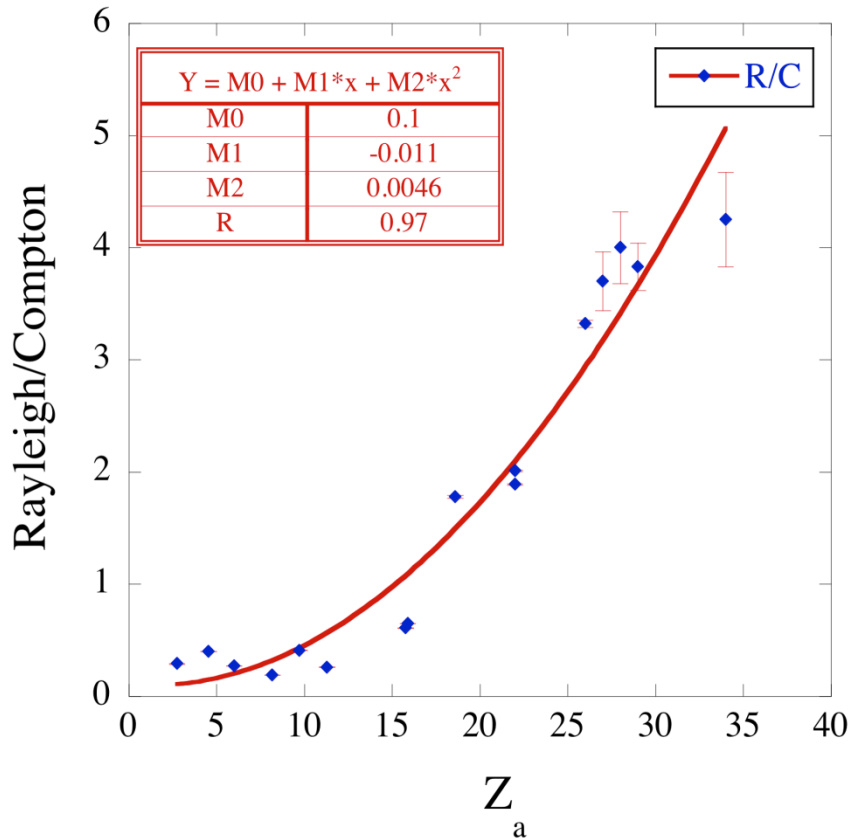


Figure V.11. Calibration curve linking Rayleigh/Compton ratios measured on reference materials to their average atomic number Z_a .

V.2.3. Application of the R/C calibration curve to the study of a FIB section in a biofilm of the 3.33 Ga-old Josefsdal Chert

a. Presentation of the set of XRF data recorded on a FIB sample of a biofilm in Josefsdal Chert

We applied the R/C method to the study of the 3.33 Ga Josefsdal Chert, Barberton Greenstone Belt, South Africa. The remains of a syngenetic bacterial biofilm found in this particular chert were identified by Westall *et al.* (2006; 2011b) and interpreted as representing a consortium of sulfur reducing bacteria and anoxygenic photosynthesizers. A 1-10 μm thick mat-like structure, distributed irregularly over a surface area of 6 mm^2 , was formed by multiple layers of parallel filaments that have a consistent diameter of 0.25 μm along their lengths. These filaments are coated with a

heterogeneously textured film that varies from ropy, granular, smooth to holey, interpreted to be extracellular polymeric substances (EPS). The structure, texture, mineralogy and geochemistry of this bacterial biofilm have been investigated by a large range of analytical techniques that revealed chemical and structural heterogeneities at the micrometer scale within the mat.

These heterogeneities concern the fossilized biological component as well as the mineralogical component of the mat, and they can be observed horizontally along the mat, as well as vertically. The fossilized organic parts of the mat vary in thickness and in texture at a micrometer scale. A kerogen layer of uneven thickness occurs just beneath a thin silica coat along the surface of the mat. Within this layer, the organic sulphur and carbonates (calcite and probable micro to nanocrystals of aragonite) zones, interpreted as remnant of bacterial activity (Westall *et al.*, 2011b), seem to be equally uneven. Furthermore, the mineralogical phases in the mat are diverse and specifically distributed in the few micrometers of thickness. At the bottom, the biofilm has trapped and embedded the detrital volcanic particles on which the microbial mat had grown. Within the thickness of the mat, the degraded kerogen layer contains, in addition to the carbonates mentioned above, micrograins of quartz. Finally, larger mostly euhedral calcite crystals are embedded in the upper part of the mat, as well as a suite of evaporite minerals.

This important heterogeneity was imaged in an XRF experiment carried out at the ID22 NI beamline that provided an ideal set of XRF data to investigate the analytical improvements generated by the R/C method. We used a 3 μm -thick section, cut vertically into the biofilm, prepared with the FIB (Focused Ion Beam) technique using Ga ions. Thus, the sample is thick enough for the signal to traverse the sample and be detected, but sufficiently thin for the multiple secondary Compton scattering to be limited. The 15x10x3 μm FIB section (Fig. V.12) was mounted on a 200 nm-thick Si_3N_4 window and analyzed at the ID22 NI beamline of the European Synchrotron Radiation Facility (ESRF) in Grenoble. The sample was positioned at an

angle of 105° with respect to the incoming beam having an energy of 17.45 keV.

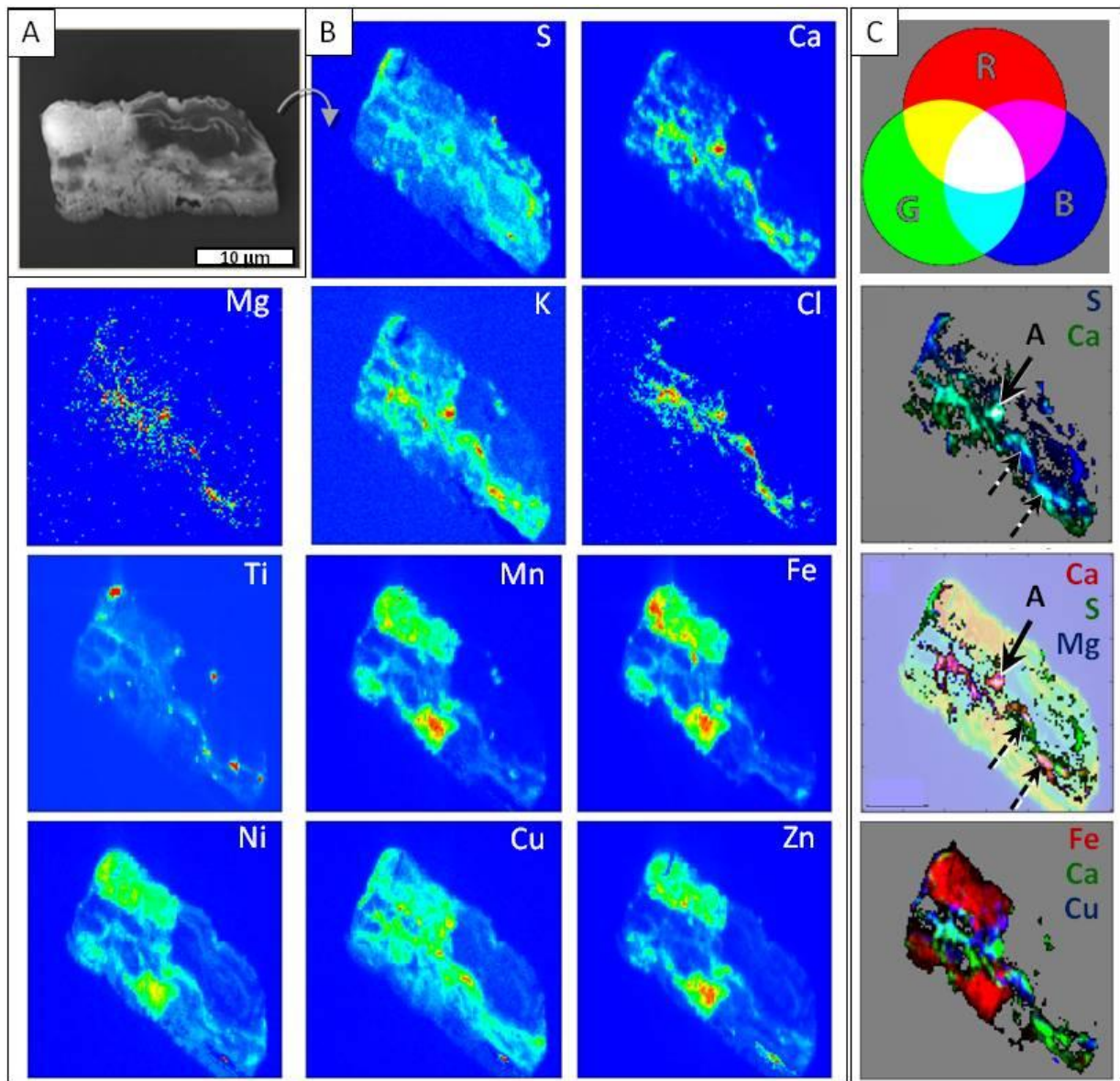


Figure V.12. A. SEM BSE image of a $\sim 12 \times 20 \times 3 \mu\text{m}$ FIB section cut transversally through a mat of microbial filaments formed on a finely grained sandy sediment, from the 3.33 Ga-old Josefsdal Chert (South Africa). B-C. XRF analyses results after data treatment with the PyMCA software (ESRF, Grenoble; Solé *et al.*, 2007). Experimental parameters for the acquisition of the map: $E_{\text{inc}}=17.45 \text{ keV}$, $T_{\text{acq}}=1\text{s/pixel}$, pixel: 250 nm. B. A selection of element maps showing the spatial distribution of light (Mg, S, K) to heavy (Fe, Cu) elements. Ti occurs as micrograins of detrital volcanic particles. C. RGB correlations. Light elements are principally localized in a wavy phase: Mg, S, Cl, K, Ca, while base-metals such as Mn, Fe, Ni, Zn incorporate micrometric mineral grains, with the exception of Cu which is correlated to Ca. Normal and dashed arrows show the micrometric zones where Mg, S and Ca are correlated (white pixels). The normal arrow noted “A” shows the zone of the 15 pixels selected for the application of the R/C method.

The XRF maps of the low Z elements (Mg, S, Cl, K, Ca) and the high Z elements (Ti, Cr, Mn, Fe, Ni, Cu, Zn) were compiled (Fig. V.12B) and their correlations are shown in the Figure V.12C. The distribution of S and Ca is intricately linked in a wavy phase composed of other light elements such as K, Cl as well as Mg. With the exception of Cu, heavier, base-metal elements such as Mn, Fe, Ni and Zn are concentrated in micrometric geometric phases. Cu is concentrated in the light phase with Ca, and thus Mg, S, Cl and K.

b. Choice of the matrix composition based on the XRF-maps

Within these maps, the sum spectrum of 'region A' (located in Fig. V.12C) was extracted from 15 pixels in the Ca-S wavy zone described above. The spectrum reveals the additional presence of Si, Ar, Fe, Ga and Sr, principally (Fig. V.13). As we are interested in consolidating the idea that the bacterial biofilm is photosynthetic and as Mg is a major element of the co-factors of chlorophyll and bacteriochlorophyll molecules, we investigated with special care the spatial distribution of Mg. Although less contrasted, Mg is also distributed in this Ca-S phase (Fig. V.12B-C; Fig. V.13). However, we believe that Mg is most probably linked to the carbonate phase as calcium-magnesium carbonate (high Mg-calcite or dolomite: $\text{MgCa}(\text{CO}_3)_2$). Our reasoning for the choice of the selected phase composition is as follows. The Sr peak is significant in the spectrum. However, as Sr is a heavy element, it does not mean that it is present in great amounts in the sample, it just means that its signal was strongly excited by the nearby incident energy and was able to exit more easily the sample, unabsorbed. Mg on the other hand, is too light to be detected properly. Its peak on the sum spectrum of the raw map and on the spectrum of region A (Fig. V.13) is very small. However, Mg is present in the phase. Thus, we decided to include it in the matrix. Ar, representing the air composition between the sample and the detector, was of course not chosen to be part of the matrix composition. The entire section is coated with an irregular thickness of Ga (the equivalent of approximately 5 nm), used to make the FIB section. This element, although not originally

constitutive of the sample, has to be part of the phase composition. Since the chemical compounds in which Fe and Mg are included are unknown, we decided to keep them as isolated elements, but with a limited thickness (see Table V.3). In this sample, XANES analyses identified organic sulphur as a component close to the thiophene (Westall *et al.*, 2011b). The matrix is thus assumed to be mainly composed of: CaCO₃ (aragonite and/or calcite), SiO₂ (silica), C₄H₄S (thiophene), Ga, Fe and Mg.

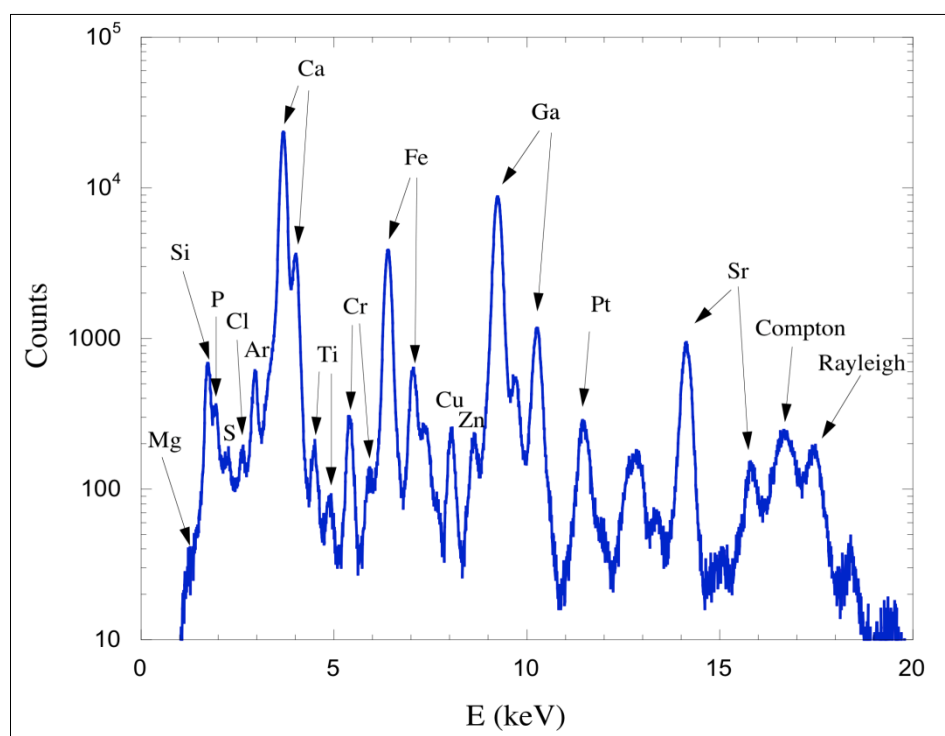


Figure V.13. Sum spectrum generated from the 15 pixels of the selected zone located in Figure V.12C (arrow 'A').

c. Calculation of the Z_a of the selected zone and R/C ratio

The average atomic number (Z_a) of each compound is calculated with the same method as previously used for the standards. The parameters used are listed in Table V.3. The thicknesses are defined and adjusted in order to respect the total 3 μm -thickness of the sample, plus several nanometers of pure Gallium (the equivalent of approximately 5 nm).

Table V.3. List of the proposed compounds of the selected A phase, and parameters used for the average Z calculation.

Compound	Formula	Density (g/cm ³)	Z_a	Atomic mass (g/mol)	Thickness (μm)	Number of atoms
Aragonite	CaCO ₃	2.83	10	100	1.2	2.05E+08
Thiophene	C ₄ H ₄ S	1.051	4,9	84	0.8	6.03E+07
Silica	SiO ₂	2.634	10	60	0.05	1.32E+07
Gallium	Ga ⁺	5.91	31	69.72	0.005	2.55E+06
Elementary Fe	Fe	7.87	26	56	0.55	4.66E+08
Elementary Mg	Mg	1.738	12	24.31	0.4	1.72E+08
<i>Total thickness =</i>					<i>3.005μm</i>	

With these parameters, region A composed of “SiO₂ + Ga + CaCO₃ + C₄H₄S + Fe + Mg” has a Z_a of 20.52. Figure V.14 shows the fit of the Rayleigh and Compton peaks in the sum-spectrum of region A.

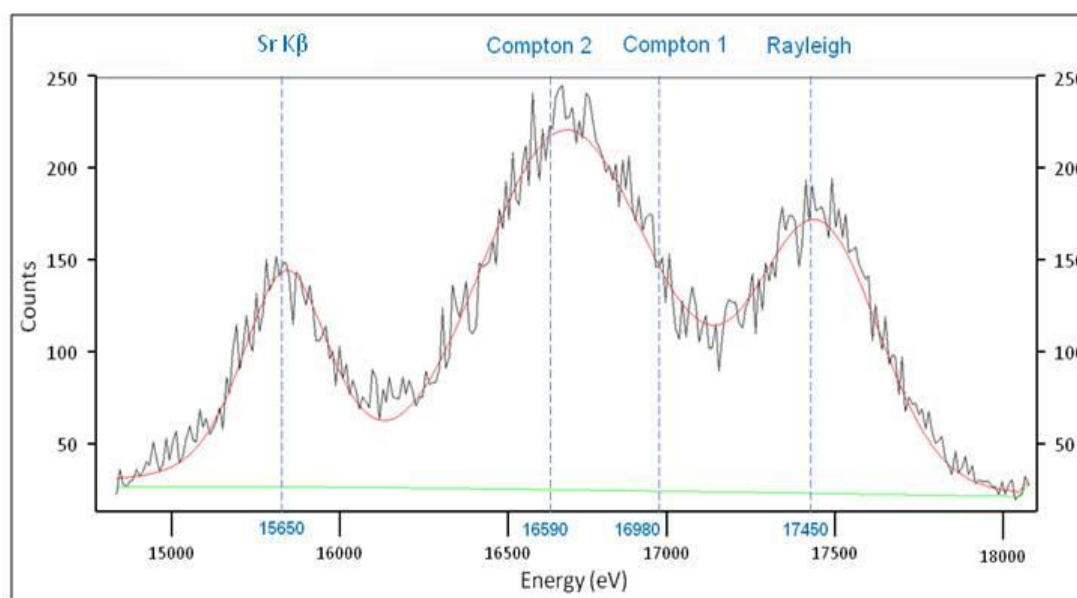


Figure V.14. Fit of the Rayleigh and Compton peaks in the sum-spectrum of the selected ‘region A’ zone (15 pixels). Black: data; red: fit; green: background. The peak on the left, lower than the scattering peaks, is the Sr K β peak.

The calculated R/C is 1.39, and the (Z_a ; R/C) point is (20.52 ; 1.39), reported in Figure V.15. The (Z_a ;R/C) point corresponding to the selected phase of the fossilized microbial mat follows the trend of the R/C- Z_a relation established using thin standards.

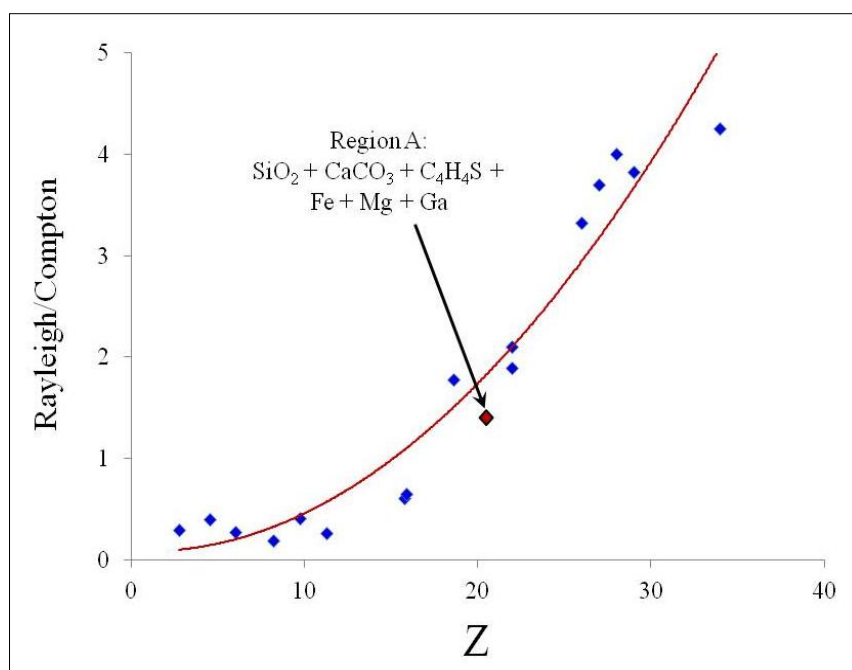
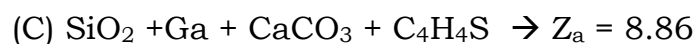
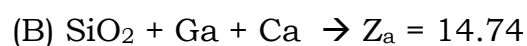
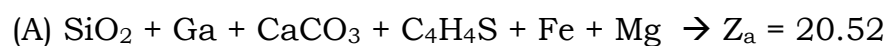


Figure V.15. Rayleigh/Compton and average Z_a trend from thin standards (green). The selected phase from the Josefsdal Chert Microbial Biofilm is in red.

d. Effect of the composition

In order to test our hypothesis to estimate the composition of our selected phase (A), we tried two other compositions named B and C, for the same R/C ratio:



The parameters used are reported in Table V.4 and the results in Figure V.16. The composition correlating with the calibration curve is the one that is the more precise and complete. Note the large variation of the average Z values, showing the importance of the contribution of low Z elements undetected in fluorescence (H, C, O). Furthermore, if Mg was actually part of a dolomite phase that would replace the CaCO_3 and Mg compounds of our hypothesized composition by a $(\text{CaMg})(\text{CO}_3)_2$ compound, the average Z of this new composition would be $Z_a=20.28$, with an acceptable difference of 1.18% with respect to the $Z_a=20.52$ originally calculated for phase A. In other

words, with a composition taking into account dolomite rather than aragonite+Mg, the new (R/C; Z_a) point would still follow the trend of the calibration curve, and the interpretation would roughly be the same.

The $R/C=f(Z_a)$ relation works for this sample and highlights the fact that neglect of one or more determining compounds in the hypothesized composition can lead to a false interpretation. Moreover, if there is an alternative choice for a similar compound made of the same elements, both possibilities have to be tested. It should not affect the average Z strongly enough to change the interpretation, but as a matter of accuracy, this has to be addressed.

The R/C method is thus suitable for organo-mineral material study, as long as the hypothesized composition is a priori defined and homogenous in the selected zone.

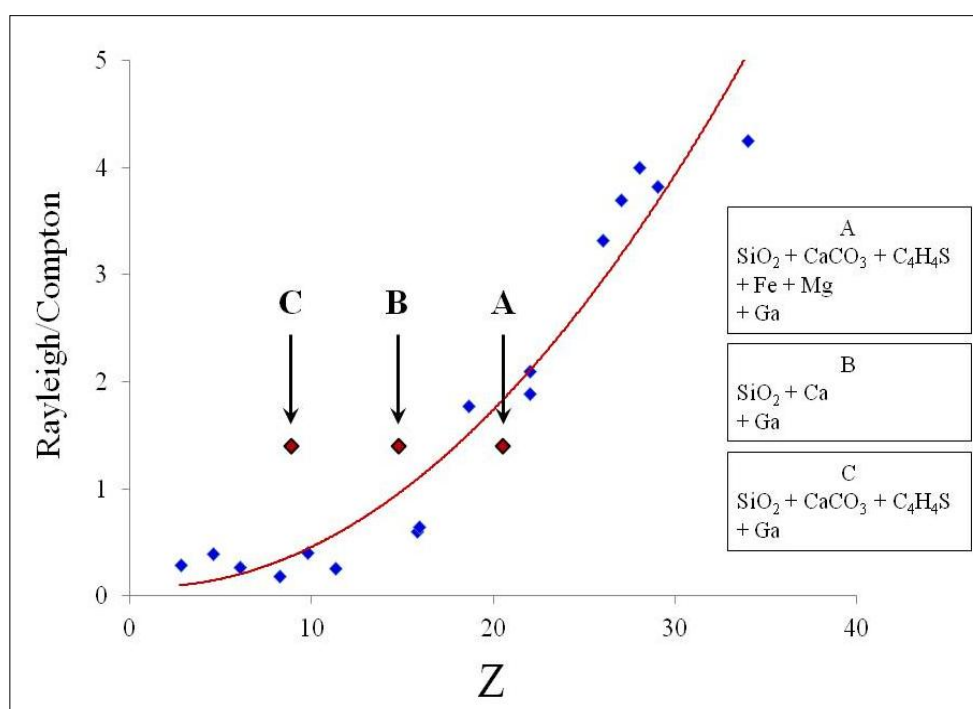


Figure V.16. Rayleigh/Compton as a function of the average Z relation from thin standards (green). Comparison of the proposed composition (A) for the selected phase of the Josefsdal Chert Microbial Biofilm, with two different compositions (B and C).

Table V.4. List of hypothetical phase B and C compounds, and the parameters used for the average Z calculation.

Compound	Formula	Density (g/cm ³)	Average Z	Atomic mass (g/mol)	Thickness (μm)	Number of atoms
Phase B						
Calcium	Ca	1.55	20	40	1.5	3.49E+08
Silica	SiO ₂	2.634	10	60	1.5	3.97E+08
Gallium	Ga	5.91	31	69.72	0.005	2.55E+06
<i>Total thickness =</i>					<i>3.005 μm</i>	
Phase C						
Aragonite	CaCO ₃	2.83	10	100	1.5	2.56E+08
Thiophene	C ₄ H ₄ S	1.051	4.9	84	1.2	9.04E+07
Silica	SiO ₂	2.634	10	60	0.3	7.93E+07
Gallium	Ga ⁺	5.91	31	69.72	0.005	2.55E+06
<i>Total thickness =</i>					<i>3.005 μm</i>	

e. Quantification and correction using the R/C method in this work

With the application of the R/C method to the 3.33 Ga fossilized microbial biofilm from the Josefsdal Chert, it is now possible to estimate the undetected phase, made up of low-Z elements. Hence, the quantification of detected elements can be corrected by taking into account this light phase. In the case of rocks containing traces of ancient life, typically Archean cherts, the light phase is mostly constituted of the following elements (H, C, N, O, F and Na, Mg, P), but also of a very large proportion of SiO₂, since these rocks are highly silicified. Taking into account this light phase in the quantification means several tens of percents correction on a quantification solely based on the detected elements (Simionovici *et al.*, 2010, 2012, 2015 in preparation).

Possible applications: quantification of biological material

With this R/C method, we are now able to precisely quantify the detected elements related to the association of photosynthetic microorganisms and SRBs activity in Precambrian silicified mats (such as Ca, S, Mg). If further quantitative studies show a connection between the activity of

these micro-organisms and the amount of carbonates produced, this could become a strong biosignature.

Furthermore, in addition to carbon and to the principal constitutive elements of life (H, N, O, P), microbial cells require a number of other elements that could potentially provide biosignatures, including bioactive trace metals. These metals, inside the cell, are called “metallomes”. They represent the intracellular metal content and reflect the metabolic requirement of the cell. Zerkle *et al.* (2005) showed that the use of metals in prokaryotes as a group generally follows the hierarchy: Fe >> Zn > Mn >> Mo, Co, Cu >> Ni > W, V. If the fossilized micro-organisms studied display preserved closed cells, it is possible with the R/C method to quantify these metals and see if they follow the previous hierarchy. If this is indeed possible, then the quantification of the metallome of Archean cells with the R/C method, could become a strong biosignature, provided that the analyzed cells are larger than the beam spot size. Zerkle *et al.* (2005) noted that model metallomes vary with metabolism, oxygen tolerance, optimum growth temperature, and phylogeny. Nevertheless, if the previous metals are precisely quantified with the R/C method and correspond to a model metallome well-defined, we could learn much about the metabolism and the environment of growth of the Archean micro-organisms.

Possible applications: insights into the Archean environment

The behavior of certain elements, mobile or immobile, can give information on alteration, fluid circulation, and temperature of hydrothermal activity at the time of the deposit. Depletion and enrichment for an element in our sample can be measured by normalization to an immobile element, such as Al or Ti, considered immobile due to the low solubility of their oxides and hydroxides in low temperature aqueous solutions (Hofmann & Harris, 2008). In this case, precise quantification of these elements is needed. Correctly constrained by the R/C method, these ratios can give useful information on the Archean environment.

Overall, with this original quantification method, it is now possible to correct the concentrations of detected elements by taking into account the undetected ones (e.g. oxygen of SiO₂, carbon...), or “low Z” elements at the sub-micrometer scale.

Thus, in addition to the previous analyses, the application of the R/C method to this particular sample will allow a precise quantification of the chemical elements present in our samples. This method can be extended to any XRF quantification case in Earth and Planetary Sciences, dealing with undetected low Z elements which are often major elements in samples such as fossil-containing rocks, meteorites or alteration phases.

V.3 Preliminary quantitative XRF analyses of fossilized traces of life older than 1.8 Ga

We present below the elemental analyses carried out on the Josefsdal samples and on the Gunflint samples at different energies on several beamlines.

V.3.1 Material and methods

The samples used in this study are described in Chapter I. They come from Precambrian silicified sediments deposited in shallow marine environments: the 3.33 Ga-old Josefsdal Chert (Onverwacht Group, South Africa) and the 1.88 Ga-old Gunflint chert (Schreiber Beach locality, Animikie Basin, Canada). The analyzed samples are 2-3 μm thick micrometric sections prepared by the *Focused Ion Beam* (FIB) technique from petrographic polished thin sections and from a 3D sample of fossilized microbial mat (Josefsdal Chert microbial biofilm, Westall *et al.*, 2006, 2011b; see description above in section V.2). They contain kerogenous and/or mineralized remains of microbial biofilms and cells in a siliceous mineral matrix. Table V.5 describes the FIB sections samples and the preparation methods (sample holders, FIB protocol) used for each.

XRF and XANES experiments were conducted at the ID21 and ID22NI beamlines at the European Synchrotron Radiation Facility (ESRF) in Grenoble, France, and at the mySpot beamline at the BessyII synchrotron, Helmholtz Zentrum Berlin (HZB), Germany. They are described elsewhere in this manuscript (see Chapter II section II.5.2). The experimental conditions and the samples studied are summarized below in the Table V.6. For every sample, we also list the different regions of interest for which the elemental composition were studied and their interpretation based on optical observations and electron microscopy imagery.

Table V.5. Presentation of the FIB samples: location of the FIB cut, FIB protocol and imagery (optical microscopy and electron microscopy).

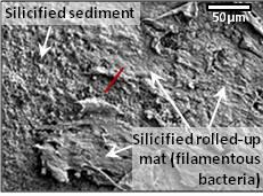
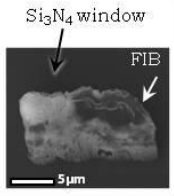
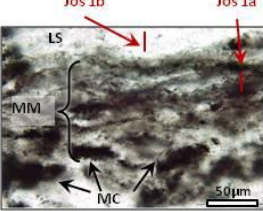

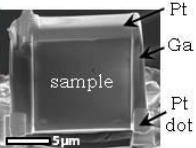
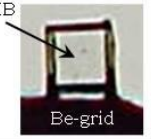
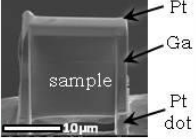
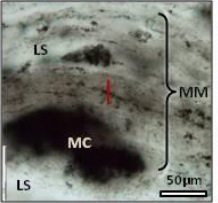
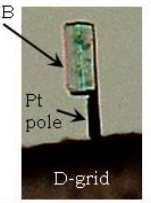
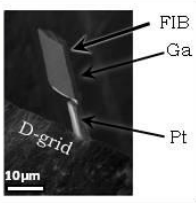
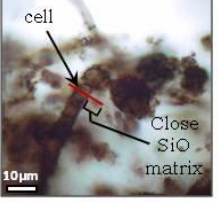
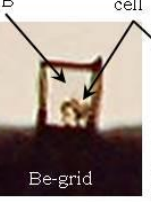
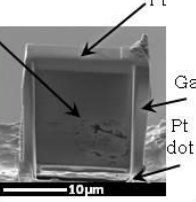
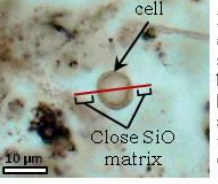
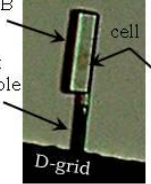
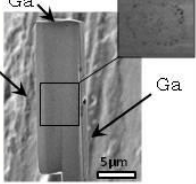
Age	Locations of the FIB samples (red lines, not exactly to scale)	Name of the FIB sample	Holder	FIB protocol		Imagery	
				'Cleaning' of the deposited Ga and/or Pt	Relation sample/holder	Optical microscopy	SEM BSE
Josefsdal chert – 3.33 Ga	 <p>SEM SE imagery. Top view of the Josefsdal Chert microbial mat in Westall <i>et al.</i>, 2006; 2011b)</p>	Jos 3D	Si ₃ N ₄ window	Ion milling was performed in the pit after FIB cutting	Sample is simply placed on the Si ₃ N ₄ window	/	
	 <p>Photomicrograph of a silicified microbial mat (MM), microbial clots (MC) and SiO-lenses (LS) in the thin section 99SA07d.</p>	Jos 1a (microbial mat)	Be half-grid	Ion milling was performed after the FIB was welded to the Be-grid	The FIB sample is welded to the Be-grid with two Pt dots at its base		
	Jos 1b (SiO lense)						
 <p>Photomicrograph of a silicified microbial mat (MM), microbial clots (MC) and SiO-lenses (LS) in the thin section 12SA16.</p>	Jos 2	Diamond grid	Ion milling was performed after the FIB was welded to the D-grid	The FIB sample is welded to the D-grid by means of a Pt 'pole'			
Gunflint chert (Schreiber Beach) – 1.88 Ga	 <p>Photomicrograph of a silicified filamentous bacterium (mineralized <i>Gunflintia</i>) and siliceous matrix in the thin section sample GF-55-1.</p>	Gunf1	Be half-grid	Ion milling was performed after the FIB was welded to the Be-grid	The FIB sample is welded to the Be-grid with two Pt dots at its base		
	 <p>Photomicrograph of a mineralized and silicified spherical bacterium (<i>Huroniospora</i>) and siliceous matrix in the thin section GF-55-1.</p>	Gunf2	Diamond grid	Ion milling was performed after the FIB was welded to the D-grid	The FIB sample is welded to the D-grid by means of a Pt 'pole'		

Table V.6. Experimental conditions, raw maps and regions of interest selected, for each sample. (1/2)

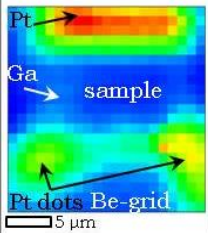
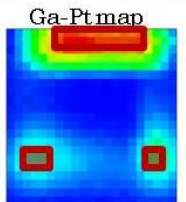
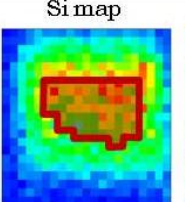
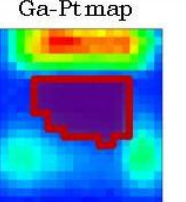
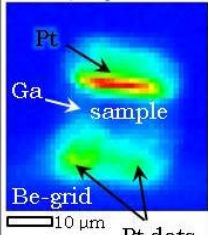
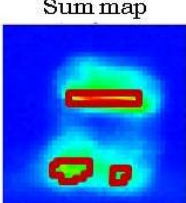
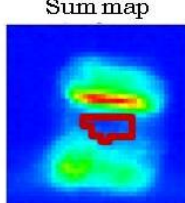
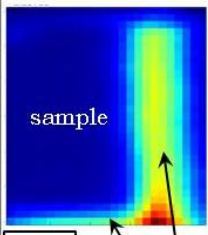
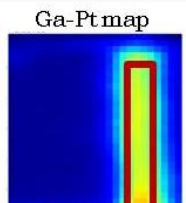
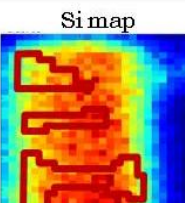
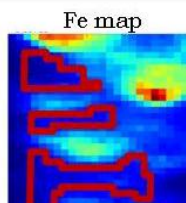
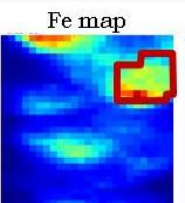
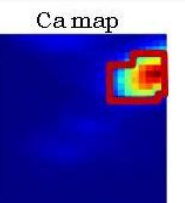
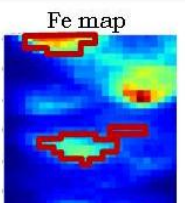
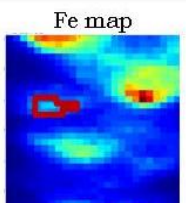
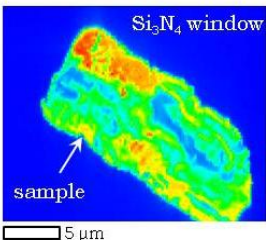
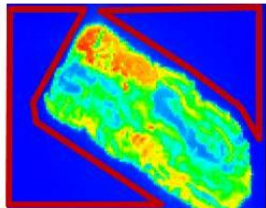
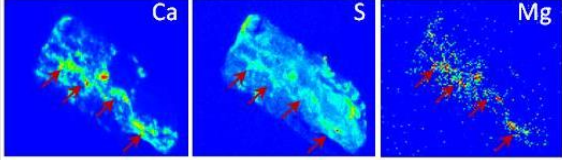
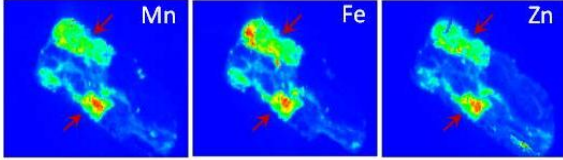
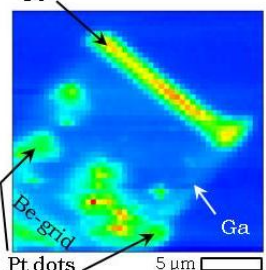
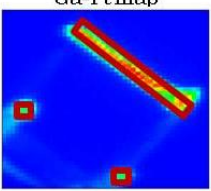
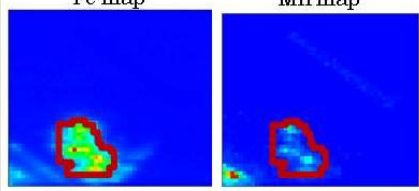
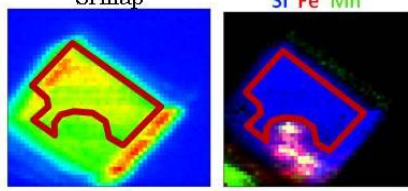
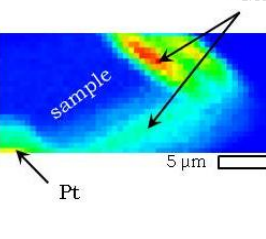
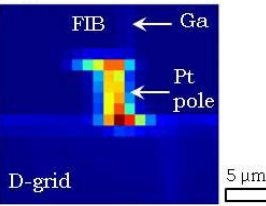
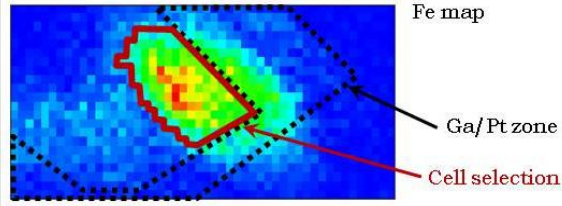
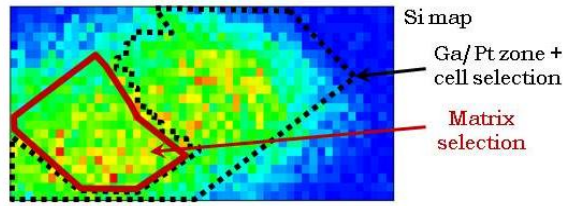
Sample	Beamline Exp./PI E_0	Sum map at E_0	Selected zones (red shapes)				
			Background zone	Zone 1	Zone 2	Zone 3	Zone 4
Jos 1a	mySpot September 2013 /Simionovici 7.5 keV		Background = Ga/Pt + Be-grid 	Si signal - Ga/Pt signal = silicified biofilm + SiO ₂ matrix  	/	/	/
Jos 1b	mySpot September 2013 /Simionovici 10.6 keV		Background = Ga/Pt + Be-grid 	Si signal - Ga/Pt signal = SiO ₂ matrix 	/	/	/
Jos 2	mySpot September 2014 /Hubert 12 keV		Background = Ga/Pt 	Si signal - Fe spots = silicified biofilm  	Ca-rich Fe grain = unidentified microstructure 1  	Fe micrograins with some Ca = unidentified microstructure 2 	Ca-poor Fe micrograins = unidentified microstructure 3 

Table V.6. Experimental conditions, raw maps and regions of interest selected, for each sample. (2/2)

Sample	Beamline Exp./PI E_0	Sum map at E_0	Selected zones (red shapes and arrows)		
			Background zone	Zone 1	Zone 2
Jos 3D	ID22 NI April 2010 /Simionovici 17.45 keV		Background = Si_3N_4 window	'Wavy' Ca-S-Mg zone = biofilm remains	Fe-rich micrograins = mineral matrix
					
Gunf 1	ID21 May 2014 /Lemelle 7.5 keV		Background = Ga/Pt + Be-grid	Fe-Mn-rich microstructure = bacterial cell	Si signal - Fe-Mn-rich cell = close SiO_2 matrix
					
Gunf 2	mySpot September 2014 /Hubert 12 keV		Background = Ga + Pt pole	Fe-rich microstructure = bacterial cell	Si signal - Fe-rich cell = close SiO_2 matrix
					

The same preliminary data treatment was applied to all the spectra, whatever the experimental set-up. We considered that the useable data for typical samples correspond to the spectra with count rates larger than the variance of the initial count rate after subtraction of the background signal. We further took into account the interference between the sample signals measured in the regions of interest (ROI) with those of the specific holder of the FIB section. For sample Jos 3D, the background signal corresponds to the signal of the Si₃N₄ window, since the FIB section is placed directly on this support. For samples Jos 1 and Gunf 1, the XRF lines of both the Be-grid and the Pt dots are considered background since their proximity to the FIB sample causes interference with the signal of the latter. However, in the case of samples Jos 2 and Gunf 2, the background signal consists only of the signal extracted from the Ga-Pt zones. Indeed, D-grids have a low Z composition and their XRF signals have a low intensity. Moreover, since with this preparation method FIB samples are separated by 10 μm from the D-grids, we considered that the background signal is most likely to be influenced by the Pt pole rather than the grid. The zones corresponding to the selected background are shown in Table V.6.

In all the tables reported in the “results” section, useable data are in bold font and defined as positive data larger than the initial variance (error) after subtraction of the background signal (e.g. holder, Ga-Pt zones). All presented data are normalized to 1 second of acquisition time and to 1 pixel, and are expressed in photons count/pixel/second.

In order to be thorough, we took into account the fact that the photon flux (photons/second) varies from one map to the other depending on the beamline and experimental parameters used. Hence, the regions of interest (ROI) corresponding to the background and subtracted from the signal of the sample, were systematically extracted from the same map as that used to study the sample itself (this is the case for samples Jos 1a, Jos 1b, Jos 2, Jos 3D and Gunf 1). On the map used to study Gunf 2, there is a significant overlap between the Ga-Pt zones whose signal is used as background and the silica zone (used to study the sample) (see Table V.6). Since the signal of the background could not be reliably extracted from this map, we used

another map, with similar photon flux ($\pm 5\%$ difference: 4.44×10^{10} ph/s against 4.69×10^{10} ph/s), that shows the Pt-pole and the Ga zones. Therefore, data corresponding to the fossilized microbial remains and to the siliceous matrix are directly comparable if they are located within a same FIB sample (which is the case for samples Jos 2, Jos 3D, Gunf 1 and Gunf 2). Furthermore, since the data are normalized to 1 pixel and 1 second, results from the selected ROIs are also comparable regardless of their sizes, if the experimental set-up, the incident beam energy and the photon flux are the same, which is the case for samples Jos 2 and Gunf 2. Overall, comparisons can be made for the chemical composition of biological remains and that of the mineral and/or siliceous matrix within Jos 2, Jos 3D, Gunf 1 and Gunf 2, as well as between Jos2 and Gunf 2.

V.3.2 Results

Table V.7 to Table V.11 give the XRF signal (in counts/pixels) for each region of interest (biofilm, individual cell, siliceous matrix) presented in Table V.6 in every analyzed FIB section.

a. Analyses of the Josefsdal samples

High energy XRF maps: Jos 2 ($E=12$ keV) and Jos 3D ($E=17.45$ keV)

From these analyses, a large variety of light (Si, S, K, Ca...) to heavy (Mn, Fe, Ni, Cu, Zn, As, Sr...) elements are detected and considered as useable data. Figure V.17 et Figure V.18 show the spectra corresponding to the regions of interest selected for the Jos 2 and Jos 3D maps and described in Table V.6. The XRF signals for each ROI are found in Table V.8 and Table V.9 for Jos 2 and Jos 3D, respectively.

Table V.7: XRF raw results for samples Jos 1a and Jos 1b.

Sample / holder	Jos1a and Jos1b / Be-grid											
Exp. param.	Jos 1a: Einc = 7.5 keV ; Tacq = 10s						Jos 1b: Einc=10.6 keV ; Tacq=3s					
Zone	Background: Ga-Pt and Be-grid		microbial mat (sample Jos 1a)		microbial mat - background		Background: Ga-Pt and Be-grid		SiO matrix (sample Jos 1b)		SiO matrix - background	
Elements	area	sigma	area	sigma	area	sigma	area	sigma	area	sigma	area	sigma
Si			9.19E+01	3.34E+00	9.19E+01	3.34E+00						
P			9.00E+00	4.85E+00	9.00E+00	4.85E+00						
S	4.06E+01	3.00E+00	2.83E+01	3.21E+00	NEG	NEG	3.65E+01	4.33E+00	3.15E+01	3.90E+00	NEG	NEG
Cl	9.45E+01	3.88E+00	3.38E+01	2.43E+00	NEG	NEG						
K			9.83E+01	4.53E+00	9.83E+01	4.53E+00	4.22E+01	8.53E+00	4.78E+01	5.93E+00	5.54E+00	1.45E+01
Ca	1.39E+02	4.44E+00	1.28E+02	4.05E+00	NEG	NEG	1.54E+02	7.60E+00	1.27E+02	7.23E+00	NEG	NEG
Sc									5.88E+00	2.45E+00	5.88E+00	2.45E+00
Ti	1.07E+01	1.44E+00	1.22E+01	1.43E+00	1.51E+00	2.87E+00	8.09E+00	2.52E+00	1.94E+01	3.29E+00	1.13E+01	5.81E+00
V	3.97E+00	1.34E+00	6.33E+00	1.36E+00	2.36E+00	2.70E+00	7.47E+00	2.30E+00	1.98E+00	2.53E+00	NEG	NEG
Cr	4.16E+01	2.66E+00	2.05E+01	2.03E+00	NEG	NEG	4.22E+01	4.63E+00	1.08E+01	3.01E+00	NEG	NEG
Mn	3.34E+01	3.55E+00	6.13E+00	2.41E+00	NEG	NEG	7.57E+01	6.27E+00	8.95E+00	3.12E+00	NEG	NEG
Fe	9.83E+02	1.10E+01	5.36E+02	8.21E+00	NEG	NEG	1.07E+03	1.98E+01	2.81E+02	1.05E+01	NEG	NEG
Co							1.21E+01	5.87E+00			NEG	NEG
Ni							6.03E+02	1.66E+01	7.26E+01	7.83E+00	NEG	NEG
Cu							2.06E+03	2.96E+01	8.55E+02	1.82E+01	NEG	NEG
Zn							6.37E+02	1.80E+01	6.65E+02	1.72E+01	2.71E+01	3.52E+01
Ga							4.72E+04	1.35E+02	3.31E+04	1.13E+02	NEG	NEG
Y			1.30E+02	1.23E+01	1.30E+02	1.23E+01						
Mo	1.00E+01	2.60E+00	1.06E+01	7.12E+00	5.54E-01	9.72E+00	1.41E+01	3.80E+00	1.16E+01	3.12E+00	NEG	NEG
Tc							1.02E+01	3.53E+00			NEG	NEG
Ru							2.22E+01	4.57E+00			NEG	NEG
Pd	1.41E+02	1.35E+01	2.04E+01	1.01E+01	NEG	NEG						
Cd	4.58E+02	1.34E+01			NEG	NEG	1.72E+01	5.93E+00			NEG	NEG
Nd	2.20E+01	3.90E+00	1.23E+01	2.98E+00	NEG	NEG						
Hf							2.72E+01	1.46E+01			NEG	NEG
Pt	2.67E+02	6.10E+00	3.50E+01	1.20E+01	NEG	NEG	5.61E+01	5.30E+00	4.41E+01	6.90E+00	NEG	NEG

Table V.8: XRF raw results for sample Jos 2.

Sample / holder	Jos2 / D-grid																			
Exp. param.	Einc = 12 keV ; Tacq = 20s																			
Zone	Background: Ga-Pt		zone 1: microbial mat + SiO matrix		zone 1 - background		zone 2: Ca-rich Fe micrograins		zone 2 - background		zone 3: Fe micrograins with some Ca		zone 3 - background		zone 4: Ca-poor Fe micrograins		zone 4 - background			
Elements	area	sigma	area	sigma	area	sigma	area	sigma	area	sigma	area	sigma	area	sigma	area	sigma	area	sigma		
Al																	1.94E+01	7.39E+00	1.94E+01	7.39E+00
Si	2.75E+02	3.46E+01	3.73E+02	5.58E+01	9.81E+01	9.04E+01	1.67E+02	2.59E+01	NEG	NEG	2.46E+02	7.65E+01	NEG	NEG	3.07E+02	9.67E+01	3.22E+01	1.31E+02		
S			2.12E+00	4.95E+00	2.12E+00	4.95E+00					9.28E+00	6.20E+00	9.28E+00	6.20E+00						
Cl			4.94E+00	8.57E+00	4.94E+00	8.57E+00														
K	2.14E+02	2.36E+01	8.21E+01	4.72E+01	NEG	NEG	1.77E+02	3.65E+01	NEG	NEG	2.90E+02	3.85E+01	7.61E+01	6.21E+01	3.16E+02	3.75E+01	1.02E+02	6.11E+01		
Ca			2.56E+02	2.06E+01	2.56E+02	2.06E+01	6.59E+03	9.46E+01	6.59E+03	9.46E+01	7.00E+02	3.40E+01	7.00E+02	3.40E+01						
Ti	1.80E+01	6.53E+00	2.02E+01	6.76E+00	2.20E+00	1.33E+01	5.69E+01	1.16E+01	3.89E+01	1.81E+01	9.33E+01	1.27E+01	7.54E+01	1.92E+01	2.97E+01	7.63E+00	1.17E+01	1.42E+01		
V			9.57E-01	4.76E+00	9.57E-01	4.76E+00									7.88E+00	6.29E+00	7.88E+00	6.29E+00		
Cr	9.01E+00	6.46E+00	1.13E+01	5.54E+00	2.31E+00	1.20E+01	1.85E+01	6.95E+00	9.47E+00	1.34E+01	1.52E+01	6.30E+00	6.23E+00	1.28E+01	1.32E+01	5.94E+00	4.17E+00	1.24E+01		
Mn			2.89E+00	4.86E+00	2.89E+00	4.86E+00	1.18E+01	7.04E+00	1.18E+01	7.04E+00	7.61E+00	5.66E+00	7.61E+00	5.66E+00						
Fe	3.32E+02	1.93E+01	2.91E+02	1.87E+01	NEG	NEG	8.50E+02	3.71E+01	5.19E+02	5.64E+01	8.36E+02	3.06E+01	5.04E+02	4.99E+01	5.31E+02	2.43E+01	2.00E+02	4.36E+01		
Co			2.59E+00	7.68E+00	2.59E+00	7.68E+00														
Ni	1.35E+01	8.00E+00	2.87E+01	9.12E+00	1.51E+01	1.71E+01	2.75E+01	1.47E+01	1.40E+01	2.27E+01	5.51E+01	1.13E+01	4.15E+01	1.93E+01	2.36E+01	8.20E+00	1.00E+01	1.62E+01		
Cu	5.98E+01	1.11E+01	5.87E+02	2.66E+01	5.27E+02	3.77E+01	2.95E+03	5.82E+01	2.89E+03	6.93E+01	1.48E+03	4.07E+01	1.42E+03	5.18E+01	6.45E+01	1.03E+01	4.70E+00	2.14E+01		
Zn	1.43E+01	9.69E+00	1.08E+02	1.46E+01	9.41E+01	2.43E+01	5.22E+02	2.86E+01	5.08E+02	3.83E+01	2.92E+02	2.08E+01	2.78E+02	3.05E+01	2.87E+01	8.64E+00	1.44E+01	1.83E+01		
Ga	1.08E+04	1.20E+02	2.36E+03	6.31E+01	NEG	NEG	6.64E+03	8.53E+01	NEG	NEG	1.39E+03	3.96E+01	NEG	NEG	7.82E+03	8.95E+01	NEG	NEG		
As			1.69E+01	1.34E+01	1.69E+01	1.34E+01														
Sr			1.14E+02	5.32E+01	1.14E+02	5.32E+01														
Pt	2.39E+02	7.09E+01	1.11E+02	4.78E+01	NEG	NEG														

Table V.9: XRF raw results for sample Jos 3D.

Sample / holder	Jos3D / Si ₃ N ₄ window									
Exp. param.	Einc = 17.45 keV ; Tacq = 1s									
Zone	Background noise: Si ₃ N ₄ window		microbial mat		microbial mat - background		microcrystals		microcrystals - background	
Elements	area	sigma	area	sigma	area	sigma	area	sigma	area	sigma
Al	1,86E+01	1,16E+01	1,80E+01	1,28E+01	NEG	NEG	2,31E+01	2,18E+01	4,50E+00	3,34E+01
Si	6,62E+02	1,29E+02	4,61E+02	1,14E+02	NEG	NEG	5,16E+02	1,92E+02	NEG	NEG
S			2,26E+01	1,17E+01	2,26E+01	1,17E+01	1,53E+01	1,20E+01	1,53E+01	1,20E+01
Cl	9,95E+01	1,37E+01	6,35E+01	1,40E+01	NEG	NEG	5,21E+01	1,39E+01	NEG	NEG
K			1,16E+02	2,04E+01	1,16E+02	2,04E+01	1,07E+02	2,15E+01	1,07E+02	2,15E+01
Ca	1,85E+01	5,65E+00	4,37E+03	8,47E+01	4,35E+03	9,04E+01	2,87E+03	7,21E+01	2,85E+03	7,78E+01
Sc			1,77E+01	2,76E+01	1,77E+01	2,76E+01	5,33E+00	2,46E+01	5,33E+00	2,46E+01
Ti			1,70E+02	1,83E+01	1,70E+02	1,83E+01	3,35E+02	2,45E+01	3,35E+02	2,45E+01
Cr			1,69E+02	1,58E+01	1,69E+02	1,58E+01	1,37E+02	1,84E+01	1,37E+02	1,84E+01
Mn			5,09E+01	1,30E+01	5,09E+01	1,30E+01	7,07E+02	3,42E+01	7,07E+02	3,42E+01
Fe	9,08E+01	1,00E+01	3,16E+03	5,74E+01	3,07E+03	6,74E+01	3,09E+04	1,78E+02	3,08E+04	1,88E+02
Ni			7,36E+01	1,25E+01	7,36E+01	1,25E+01	3,22E+02	2,19E+01	3,22E+02	2,19E+01
Cu			1,80E+02	1,68E+01	1,80E+02	1,68E+01	2,00E+02	1,98E+01	2,00E+02	1,98E+01
Zn	4,84E+00	3,33E+00	1,71E+02	2,05E+01	1,66E+02	2,38E+01	1,64E+03	4,82E+01	1,64E+03	5,15E+01
Ga	3,39E+02	1,88E+01	2,61E+04	1,91E+02	2,58E+04	2,10E+02	2,54E+04	1,90E+02	2,51E+04	2,09E+02
As			5,81E+01	1,90E+01	5,81E+01	1,90E+01	3,79E+01	2,07E+01	3,79E+01	2,07E+01

Table V.10: XRF raw results for sample Gunf1.

Sample / holder	Gunf1 / Be-grid									
Exp. param.	Einc = 7.5 keV ; Tacq = 2s									
Zone	Background: Ga-Pt and Be grid		microbial cell		microbial cell - background		SiO matrix around cell		SiO matrix - background	
Elements	area	sigma	area	sigma	area	sigma	area	sigma	area	sigma
Al			2.33E+00	1.78E+00	2.33E+00	1.78E+00				
Si	1.62E+02	1.95E+01	7.94E+02	2.03E+01	6.32E+02	3.98E+01	8.28E+02	2.12E+01	6.66E+02	4.07E+01
P	7.18E+02	4.55E+01			NEG	NEG			NEG	NEG
S			3.35E+01	6.00E+00	3.35E+01	6.00E+00	6.51E+00	3.45E+00	6.51E+00	3.45E+00
Cl	4.94E+01	1.21E+01	1.06E+01	6.20E+00	NEG	NEG	4.11E+00	2.90E+00	NEG	NEG
K	3.45E+01	9.30E+00	1.00E+01	4.63E+00	NEG	NEG	6.98E+00	4.03E+00	NEG	NEG
Ca	8.40E+01	1.18E+01	3.35E+01	4.88E+00	NEG	NEG	1.56E+01	3.39E+00	NEG	NEG
Ti	4.72E+01	7.40E+00			NEG	NEG			NEG	NEG
Cr	6.75E+01	1.06E+01	2.29E+01	4.57E+00	NEG	NEG	1.86E+01	3.80E+00	NEG	NEG
Mn	3.68E+01	9.15E+00	2.36E+01	5.35E+00	NEG	NEG	6.09E+00	4.74E+00	NEG	NEG
Fe	1.72E+03	3.32E+01	8.61E+03	7.12E+01	6.89E+03	1.04E+02	6.51E+02	2.01E+01	NEG	NEG
Ga	1.27E+01	3.72E+00			NEG	NEG			NEG	NEG
Y	1.02E+03	7.75E+01			NEG	NEG			NEG	NEG
Zr	9.45E+02	7.30E+01			NEG	NEG			NEG	NEG
Nb	6.02E+01	1.81E+01			NEG	NEG			NEG	NEG
Ru	3.50E+01	1.23E+01			NEG	NEG	4.57E+00	4.04E+00	NEG	NEG
Sm			2.89E+01	1.04E+01	2.89E+01	1.04E+01				
Pt	2.68E+02	6.65E+01	2.86E+02	1.79E+01	1.81E+01	8.44E+01	1.01E+02	9.15E+00	NEG	NEG

Table V.11: XRF raw results for sample Gunf2.

Sample / holder	Gunf2 / D-grid									
Exp. param.	Einc = 12 keV ; Tacq = 2s		Einc = 12 keV ; Tacq = 8s							
Zone	Background: Ga-Pt pole		microbial cell		microbial cell - background		SiO matrix around cell		SiO matrix - background	
Elements	area	sigma	area	sigma	area	sigma	area	sigma	area	sigma
Al			8.17E-01	4.60E-01	8.17E-01	4.60E-01	6.70E-01	4.53E-01	6.70E-01	4.53E-01
Si			7.78E+01	3.16E+00	7.78E+01	3.16E+00	7.56E+01	3.13E+00	7.56E+01	3.13E+00
S			7.65E+00	1.54E+00	7.65E+00	1.54E+00	7.03E+00	1.54E+00	7.03E+00	1.54E+00
Cl			1.84E+00	1.59E+00	1.84E+00	1.59E+00				
K			2.97E+01	1.36E+01	2.97E+01	1.36E+01	3.55E+01	1.40E+01	3.55E+01	1.40E+01
Ca	3.25E+01	2.32E+01	3.51E+01	2.51E+00	2.64E+00	2.57E+01	3.40E+01	2.51E+00	1.54E+00	2.57E+01
Sc			2.36E+00	1.04E+00	2.36E+00	1.04E+00	1.60E+00	1.01E+00	1.60E+00	1.01E+00
Ti			1.30E+01	1.75E+00	1.30E+01	1.75E+00	1.31E+01	1.73E+00	1.31E+01	1.73E+00
Cr			9.33E+00	1.39E+00	9.33E+00	1.39E+00	8.41E+00	1.29E+00	8.41E+00	1.29E+00
Mn			4.46E+00	1.53E+00	4.46E+00	1.53E+00	2.42E+00	1.23E+00	2.42E+00	1.23E+00
Fe	1.37E+01	6.98E+00	9.73E+02	1.22E+01	9.59E+02	1.92E+01	2.41E+02	6.21E+00	2.27E+02	1.32E+01
Co			5.86E+00	3.46E+00	5.86E+00	3.46E+00				
Ni			1.15E+01	2.20E+00	1.15E+01	2.20E+00	1.46E+01	1.94E+00	1.46E+01	1.94E+00
Cu	4.68E+01	1.58E+01	4.56E+01	5.76E+00	NEG	NEG	4.61E+01	6.06E+00	NEG	NEG
Zn			9.47E+01	7.44E+00	9.47E+01	7.44E+00	9.90E+01	7.73E+00	9.90E+01	7.73E+00
Ga	8.49E+03	1.66E+02	1.26E+03	1.45E+01	NEG	NEG	1.22E+03	1.44E+01	NEG	NEG
As			1.70E+01	4.54E+00	1.70E+01	4.54E+00	1.58E+01	4.68E+00	1.58E+01	4.68E+00
Y			1.03E+00	6.45E-01	1.03E+00	6.45E-01				
Mo			1.65E+01	4.49E+00	1.65E+01	4.49E+00	1.70E+01	4.59E+00	1.70E+01	4.59E+00
Cd			3.33E+01	2.01E+01	3.33E+01	2.01E+01	2.75E+01	2.05E+01	2.75E+01	2.05E+01
Sb			1.67E+00	1.24E+00	1.67E+00	1.24E+00				
Ba			4.04E+00	2.44E+00	4.04E+00	2.44E+00				
La			2.86E+00	1.13E+00	2.86E+00	1.13E+00	1.23E+00	9.31E-01	1.23E+00	9.31E-01
Pm			2.18E+00	2.03E+00	2.18E+00	2.03E+00	2.70E+00	1.60E+00	2.70E+00	1.60E+00
Sm			1.91E+01	5.60E+00	1.91E+01	5.60E+00				
Gd			4.01E+00	1.99E+00	4.01E+00	1.99E+00	1.73E+00	1.50E+00	1.73E+00	1.50E+00
Tm			2.97E+01	1.40E+01	2.97E+01	1.40E+01	3.45E+01	1.34E+01	3.45E+01	1.34E+01
Hf			4.97E+01	3.01E+01	4.97E+01	3.01E+01	4.89E+01	3.15E+01	4.89E+01	3.15E+01
W			3.01E+00	2.49E+00	3.01E+00	2.49E+00	3.54E+00	2.49E+00	3.54E+00	2.49E+00
Pt	1.95E+03	1.22E+02								

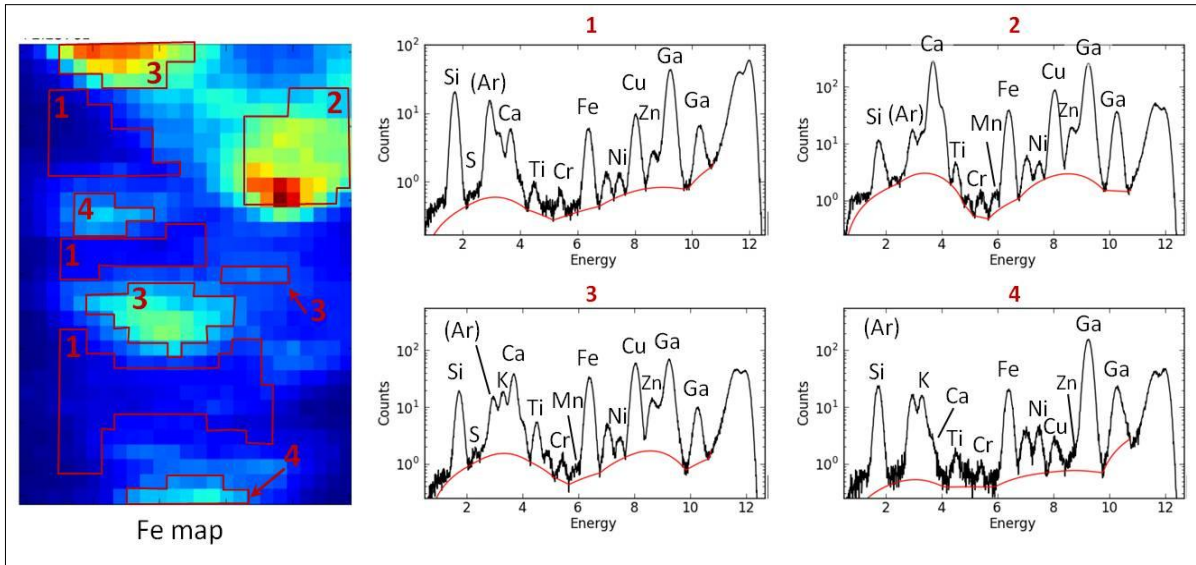


Figure V.17. Selected zones in the Jos 2 map, and corresponding spectra (normalized/pixel) at E=12 keV. Unnamed peaks at the right are Rayleigh and Compton scatterings.

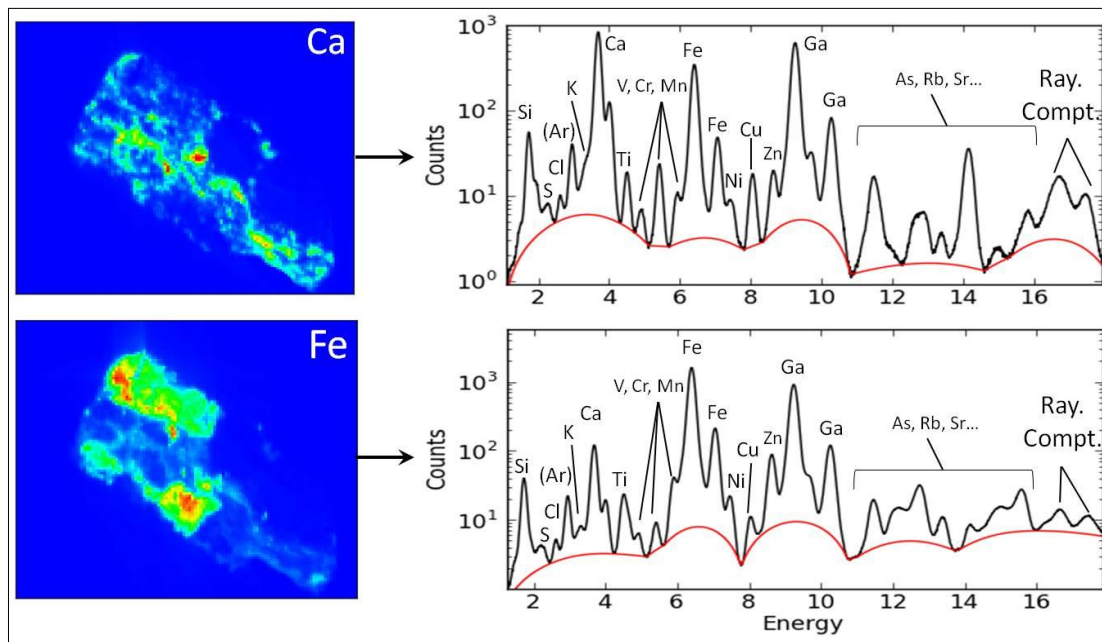


Figure V.18. Selected zones in the Jos 3D map, and corresponding spectra (normalized/pixel), at E=17.45 keV.

In terms of intensity, the major elements in the silicified microbial biofilm of sample Jos 2 are Cu, Ca and Sr, with minor Si, Zn and As. Major elements of the unidentified microstructure of zone 2 are Ca, Cu, Fe and Zn with minor Ti and Mn. The chemical composition of the unidentified microstructure of zone 3 is similar to that of zone 2 with, as major elements Cu, Ca, Fe and Zn, although minor elements consist of K, Ti, Ni, S and Mn.

The major elements of the unidentified microstructure of zone 4 are Fe and K, with minor Al and V.

Compared to the three types of unidentified micrograins (zones 2 to 4, see Table V.6), the silica-rich microbial mat remains are enriched in Si as well as in As and Sr which are only detected in this zone. Microstructures from zone 2 and zone 3 are enriched in Ca, Ti, Mn, Fe, Cu and Zn compared to the microbial mat and the unidentified micrograin of zone 4. In addition, the microstructure from zone 3 is enriched in S and Ni. The microstructure of zone 4 is characterized by significant levels of Fe, and an enrichment in Al, K and V compared to the microbial mat and the microstructures of zones 2 and 3.

From the investigation of sample Jos 3D we obtained the following results: major elements in the biofilm remains are Ca, Fe, significant levels of Cu, Ti, Cr, Zn, K and minor Ni, As, Mn and S, while the microcrystals embedded in the biofilm are principally characterized by Fe, Ca and Zn, significant levels of Mn, Ti, Ni, Cu, Cr, K, and minor As and Cl. In terms of relative intensities, the microbial biofilm is enriched in S, Ca, Cr and As, compared to the microcrystals, while these grains are enriched in Ti, Mn, Ni and Zn and are highly enriched in Fe compared to the biofilm. The intensity of K is similar in both.

Lower energy XRF maps: Jos 1a (E=7.5 keV) and Jos 1b (E=10.6 keV)

Figure V.19 shows the spectra corresponding to the Jos 1a and Jos 1b maps. Since no chemical heterogeneity was observed in these samples, the zones selected for further investigation correspond to the FIB sections themselves, although pixels displaying high Ga and or Pt intensities were dismissed as much as possible. Element intensities are reported in Table V.7.

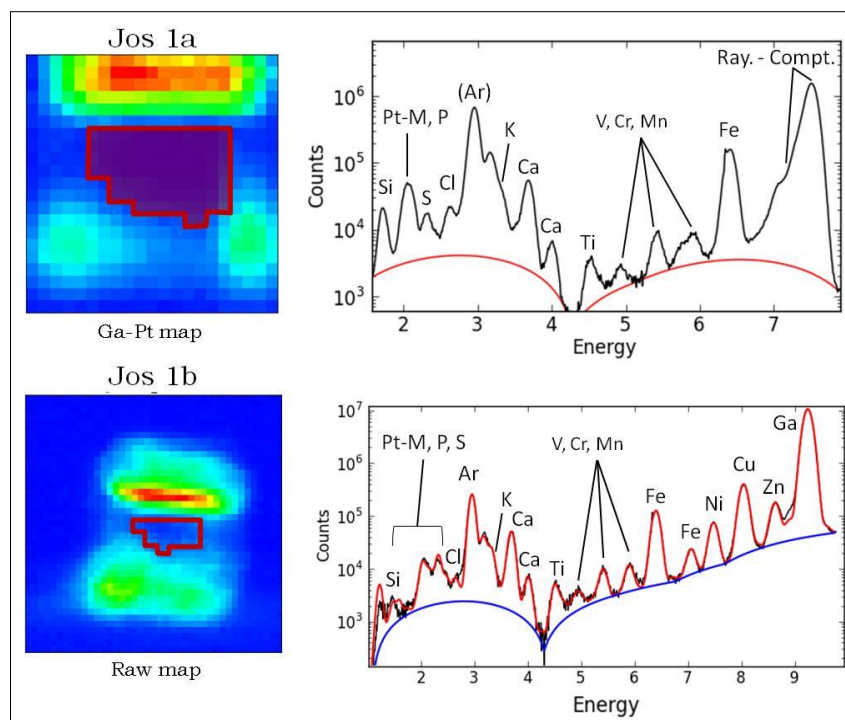


Figure V.19. Selected zones in the Jos 1a and Jos 1b, and corresponding spectra (normalized/pixel), at E=7.5 keV and E=10.6 keV, respectively.

Very few results were obtained from the Jos 1a and Jos 1b maps (Table V.7) as a result of a strong background signal (Ga-Pt zones and Be-grid signal). Indeed, after subtraction of the background, the composition of the samples was characterized by only few elements. The composition of the microbial mat extracted from Jos 1a shows that it primarily consists of Y, K and Si with minor P while the siliceous matrix obtained from Jos 1b displays only low levels of Ti and Sc. Although supposed to compose most of sample Jos 1b, Si is not detected in this FIB section. This is a direct result of the influence of the parasitic signal of heavy elements (Ga, Pt and also Cu, Fe, etc. from the Be-grid) on the transmission of light elements, even if concentrated, such as Si.

b. Analyses of the Gunflint samples

Figure V.20 and Figure V.21 show the spectra corresponding to the regions of interest selected for Gunf 1 and Gunf 2 maps obtained at E=7.5 keV and E=12 keV, respectively. Results reported in Table V.10 and Table V.11 show that the signal of Si is of similar intensity in the individual cells

and the silica matrix in both Gunf 1 and Gunf 2 samples. This is also the case for Ti.

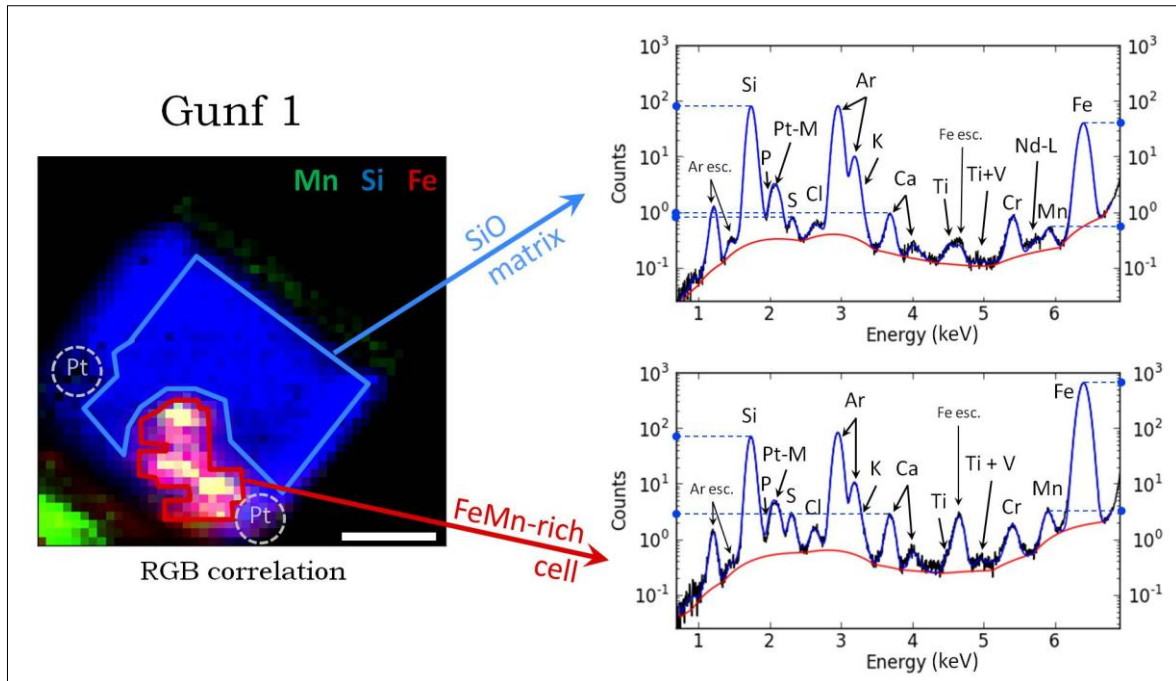


Figure V.20. Selected zones in the Gunf 1 map, and corresponding spectra (normalized/pixel), at E=7.5 keV. Scale: 5 μ m.

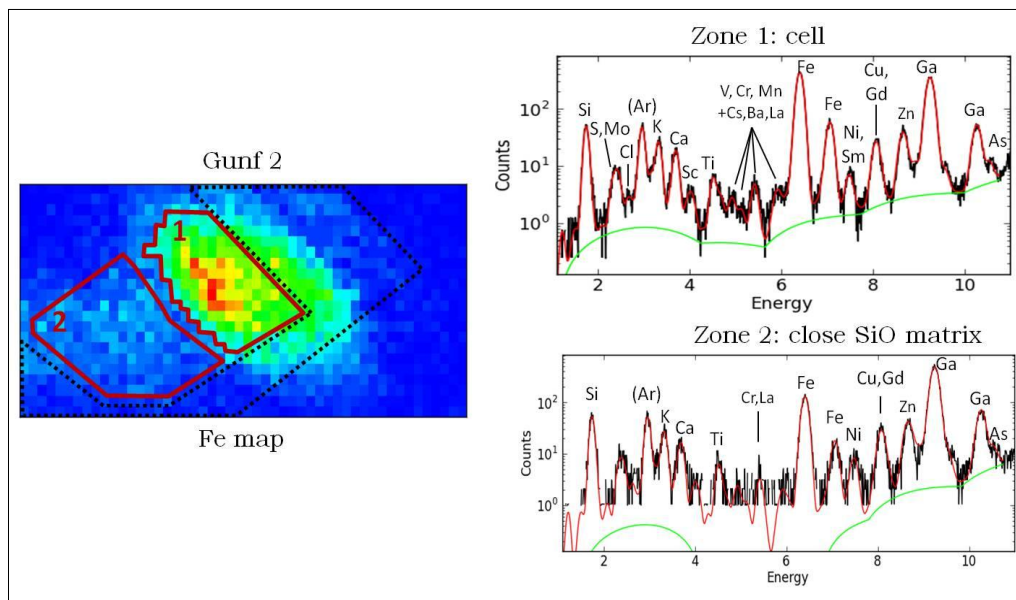


Figure V.21. Selected zones in the Gunf 2 map, and corresponding spectra (normalized/pixel), at E=12 keV. The dashed black line represents the areas of the FIB sample that are influenced by the Ga-Pt signal.

In sample Gunf 1 (Table V.10), the zone corresponding to the cell shows high levels of Fe and Si, with minor S, Sm and Al, while the siliceous matrix only displays high Si and minor S.

In sample Gunf 2, a large diversity of light (Al, Si, S, Cl, K) to heavy chemical elements (transition metals but also Y, Cd, Sb, Ba and lanthanides) was detected with XRF signals that, however, remain useable after subtraction of the background signal (Table V.11). The major elements in the microbial cell consist primarily of Fe, as well as Zn, Si, with significant levels of Cd, Tm, K, Sm, As, Mo, Ni while other elements are Cr, S, Co, Mn, Ba, Gd, W, La, Sc, Cl, Sb, Y and Al. Although of lower intensity with respect to the signal of the cell, the close surrounding siliceous matrix of Gunf 2 also contains primarily Fe. Other major elements are Zn associated with significant levels of Si, and minor elements are K, Tm, Cd, Mo, As, Ni, Ti, Cr, S, W, Mn, Gd, Sc, La and Al. In terms of relative intensities, the cell is enriched in the following light to heavy elements compared to the siliceous matrix: S, Cl, Sc, Cr, Mn, Fe, Co, As, Y, Cd, Sb, Ba, La, Sm and Gd. On the other hand, the siliceous matrix is only slightly enriched in K, Ni, Zn, Tm and W, compared to the cell.

V.3.3 Discussion

A summary table of relative element intensities for the zones corresponding to the microbial mats or cells and for the zones corresponding to the siliceous matrix, in both the Josefsdal and the Gunflint samples is presented in Table V.12. We considered the relative intensities for the metals and the low *Z* elements. In a first approximation, the relative element intensities for the low *Z* and high *Z* group can be interpreted as relative compositions.

Table V.12: Summary table of the characteristic elemental composition of the biofilms, microfossils and mineral matrix in Josefsdal and Gunflint FIB samples.

Sample	Selected zone	Elements (by decreasing intensity)		
		All elements	Metals	Light elements, light metals
3.33 Ga-old Josefsdal microbial mats	Biofilm	Ca>Fe >> Cu>Ti=Cr>Zn>K >> Ni>As>Mn>S	Fe >> Cu > Zn >> Ni > As > Mn	Ca >> Ti = Cr > K >> S
	Biofilm + SiO matrix	Cu>Ca>Sr >> Si>Zn>As	Cu >> Zn > As	Ca >> Si
	Microcrystals	Fe >> Ca>Zn >> Mn>Ti>Ni>Cu>Cr>K >> As>S	Fe >> Zn >> Mn > Ni > Cu >> As	Ca >> Ti > Cr > K >> S
	Unidentified microstructures	1 - Ca>Cu >> Fe>Zn >> Ti>Mn	Cu >> Fe > Zn >> Mn	Ca >> Ti
		2 - Cu >> Ca>Fe>Zn >> K>Ti>Ni >> S>Mn	Cu >> Fe > Zn >> Ni >> Mn	Ca >> K > Ti >> S
3 - Fe>K >> Al >> V		Fe >> V	K >> Al	
1.88 Ga-old Gunflint stromatolites	Filamentous cell	Fe >> Si >> S>Sm >> Al	Fe	Si >> S >> Al
	Spherical cell	Fe >> Zn>Si>Hf>Cd>K>Tm>Sm>As>Mo>Ti>Ni >> Cr>S>Co>Mn>Ba>Gd>W>La>Sc>Pm>Cl>Sb>Y>Al	Fe >> Zn > As > Mo > Ni >> Co > Mn > W	Si > K > Ti >> Cr > S > Cl > Al
	SiO matrix around the cells	Filamentous cell: Si >> S Spherical cell: Fe >> Zn>Si>Hf>K>Tm>Cd>Mo>As>Ni>Ti >> Cr>S>W>Pm>Mn>Gd>Sc>La>Al	Fe >> Zn > Mo > As > Ni >> W > Mn	Si >> S Si > K > Ti >> Cr > S > Al

Table V.13: Characteristic chemical composition for the microbial mats, cells and siliceous matrix, in both the Josefsdal and the Gunflint samples, in terms of few elemental ratios.

	Josefsdal				Gunflint			
E (keV)	12	17.45	12	17.45	7.5	12	7.5	12
Beamline	mySpot	ID22 NI	mySpot	ID22 NI	ID21	mySpot	ID21	mySpot
Exp./PI	September 2014 - Hubert	April 2010 - Simionovici	September 2014 - Hubert	April 2010 - Simionovici	May 2014 - Lemelle	September 2014 - Hubert	May 2014 - Lemelle	September 2014 - Hubert
Zone	fossilized biofilm		microstructures		fossilized cell		close SiO matrix	
Name of the FIB sample	Jos 2	Jos 3D	Jos 2	Jos 3D (microcrystals)	Gunf 1	Gunf 2	Gunf 1	Gunf 2
Fe/Si					11	12.33		3
Fe/S		136	54.34 (zone 3)	2014	206	125.40		32
Ca/Fe		1.42	12.71 (zone 2) 1.39 (zone 3)	0.009				
Ca/Cu	0.49	24.18	2.28 (zone 2) 0.49 (zone 3)	14				
Fe/Zn		18.47		18.84		10.13		2.30

Overall, Table V.13 gives the characteristic chemical composition for the zones corresponding to microbial mats or cells and to the zones corresponding to the siliceous matrix, in both the Josefsdal and the Gunflint samples, in terms of few elemental ratios.

The Josefsdal samples display high levels of Ca and the systematic presence of Cu, both in the silicified biofilms and in the microcrystals. Interestingly, compared to the other metals preferentially distributed in the microcrystals (Mn, Fe, Ni, Zn), Cu is equally distributed in the biofilm and the microcrystals. Also, the biofilm parts of Josefsdal samples contain more S, Ca and As than the mineral matrix (except in micrograins enriched in Ca). A distinction between the composition of the biofilms [1] and that of the microcrystals [2] can be made also from the relative abundances of metals below, obtained by coupling the results from Jos 2 and Jos 3D:

[1] Fe-Cu > Zn > Ni > Mn

[2] Fe > Zn > Mn > Ni > Cu

Following these relative abundances, the composition of the unidentified microstructures 1 and 2 (zone 2 and zone 3) of Jos 2 is coherent with that of the biofilms. Thus, they may represent cross-cut concentrated kerogenous zones of the remaining biofilm, which take a rounded shape in the FIB sample Jos 2. However, they may also represent entrapped detrital micrometric grains of muscovite, pyroxene, plagioclases (alteration products of the surrounding volcanic material), common in the local environment (Westall *et al.*, 2011b). Unidentified microstructure 3 may be a microcrystal of Fe oxide with O undetected, with traces of Al and V. However, the presence of K in this microstructure suggests that it may also represent a micrograin of muscovite.

The Josefsdal sedimentary environment was bathed continuously by hydrothermal fluids, as documented by physical structures and the trace element distributions related to hydrothermal features (Westall *et al.*, 2015). These elements may have included Cu, Fe, Ni, As, and Mn. They would have

been scavenged to varying degrees by the organic matter associated with the microbial structures, as well as by trapped detrital and authigenically precipitated minerals associated with the biofilms. In particular, these elements are known to enter the composition of pyrites (e.g. Moore *et al.*, 1988). Furthermore, it was shown that As has a particular affinity with clays and Fe-oxides (Smedley & Kinniburgh, 2002; Koschinsky & Hein, 2003; Arvestål, 2013), while Mn preferentially enters the composition of authigenic carbonates (Algeo & Maynard, 2004; Johnson *et al.*, 2013). At this stage of the study, it is thus difficult to interpret with certainty the origin of the three microstructures identified in Jos 2. Further investigation should include SEM/EDS analyzes of this FIB section, in order to obtain the distribution of carbon and other light, undetected elements.

Compared to the Josefsdal samples, Gunflint samples are characterized by (i) high levels of Fe, mostly concentrated in the individual cells, (ii) low levels of Ca and Cu, which are virtually absent after subtraction of the background signal (see Table V.10 and Table V.11), and (iii) an enrichment in incompatible elements such as Ba and Sc, Y, La, Sm, and Gd from the Rare Earth Elements series. This enrichment may result from the weathering of the granitic crustal material enriched in incompatible elements and present on emerged landmasses at 1.88 Ga. Interestingly, however, these elements are particularly enriched in the cell, compared to the surrounding SiO matrix, and Y, Ba and Sm are found exclusively in the cell, along with other elements: Cl and Co (Table V.11). Although the XRF signal of sample Gunf1 was difficult to extract leading to only a partial recovery of the information, Sm remains a characteristic element of the cell in this sample as well, suggesting that the detection of Sm in samples Gunf1 and Gunf2 is not an artifact depending on sample preparation which was different for both samples, and that this element must indeed be present in a noticeable quantity in individual fossilized Gunflint cells.

Furthermore, the distribution of La and Gd in the matrix outside the cell is correlated with that of Fe. This is shown in Figure V.22. From the distribution of Fe in Gunf2, three zones were selected, with similar Si

intensities but decreasing Fe intensities: zone 1 represents the composition of the cell, while zones 2 and 3 represents the composition of the matrix near the cell, with Fe intensity of zone 2 superior to Fe intensity of zone 3. The spectra corresponding to each of these three zones were extracted and normalized to 1 pixel. The table in Figure V.22 gives the results of the fits for Si, Fe, La and Gd. While Fe:Si and La:Si ratios decrease from zone 1 to zone 3, the Fe:La ratio is similar in zone 2 and zone 3, and higher in zone 1 which is not surprising since in terms of intensity, $Fe_{cell} > 4 * Fe_{matrix}$, and $La_{cell} > 2 * La_{matrix}$. The distribution of Gd is similar to that of La, although its fit value for zone 3 cannot be taken into account since the error is too large. This however suggests that the intensity of Gd in zone 3 is too low to be correctly fitted, which remains consistent with a co-variation of Fe with La and Gd. Therefore, the chemical association of Fe, Cl, Co, Y, Ba, Sm, La and Gd inside the cell and of Fe, La and Gd in the close surrounding matrix suggests a preferential distribution of these elements in relation to cellular activity. If this is true, the presence of Fe, La and Gd outside the cell may stem from the escape of cellular material from the cell, possibly resulting from silicification, or the preservation of residual Extracellular Polymeric Substances (EPS) in the siliceous matrix.

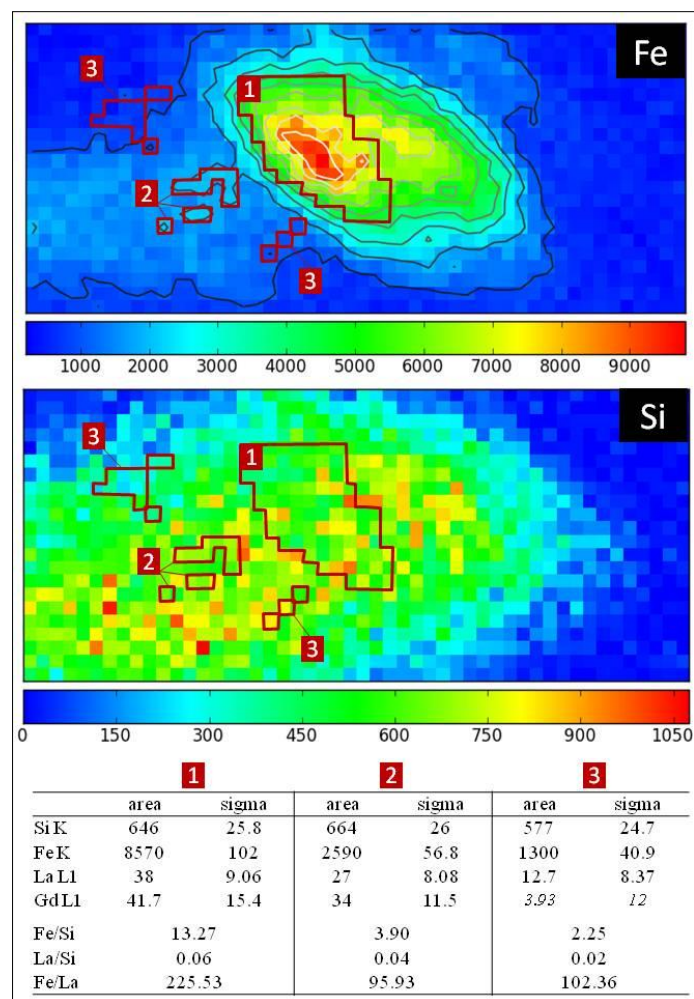


Figure V.22. Correlated raw distributions of Fe, La and Gd in sample Gunf2. Fe and Si maps exhibit three zones of similar Si intensity but decreasing Fe intensity (from 1 to 3). Fit results of these selected zones for Fe, Si, La and Gd are reported in the table below. While the Fe:Si ratio decreases from zone 1 to 3, Fe:La is similar with the exception of zone 1 where Fe is highly concentrated.

It is possible that these elements were enriched in the seawater and entered the cell during early diagenesis and before pervasive silicification. However, this would neither explain the distribution of Y, Ba and Sm that are found in the cell but not in the siliceous matrix, nor the correlated distribution of Fe, La and Gd outside the cell. It was proved that lanthanides ions (e.g. La^{3+} , Gd^{3+} , Ce^{3+} , Nd^{3+} , Eu^{3+} , Dy^{3+}) play an important role on maintaining photosynthetic activity under conditions of photosynthetically-essential metals deficiency, such as a deficiency in Mg^{2+} , Ca^{2+} or Mn^{2+} . Indeed, numerous studies have documented that treatment based on the abovementioned lanthanides with specific optimum concentrations can lead

to stimulatory physiological effects in oxygenic photosynthetic organisms (Bacteria, Algae, Plants), for instance: plant growth, resistance against oxidative stress, PSII activity, O₂ evolution rate, chlorophyll biosynthesis (e.g. Lumsden & Hall, 1975; Bueno *et al.*, 1995; Chen *et al.*, 2001; Zhang *et al.*, 2003; Lancaster *et al.*, 2004; Emmanuel *et al.*, 2010; Wang *et al.*, 2011; and see table 1 in Goecke *et al.*, 2015), depending on the type of organism and metal deficiency.

The association of these particular elements with the fossilized cells in the Gunflint samples may thus stem from their involvement in the substitution of Mg²⁺, Ca²⁺ or Mn²⁺ or other metals in molecules of the photosynthetic apparatus. This would suggest a deficiency in one or several of these elements in the medium. As Mn is detected both in the cells and the siliceous matrix, it is unlikely that this particular element was depleted in the medium. Since Mg is a light element, its fluorescence emission has a very low energy which is difficultly detected. However, at E=7.5 keV with Tacq=2s and at E=12 keV with Tacq=8s (respectively Gunf 1 and Gunf 2 maps), Mg could easily be detected if present in sufficient amounts. The absence of Mg from the data set thus may indeed suggest its deficiency in Gunflint samples. However, as Gunflint samples are characterized by very low levels of Ca and Cu, so low that they are dismissed after subtraction of the background signal (see Table V.10 and Table V.11), it is also possible to suggest that Sm, La and Gd substitute for these elements, which are both involved in molecules of the bacterial photosynthetic apparatus.

Along with Mg, Ca is a biologically-essential metal. Furthermore, Ca is involved in oxygenic photosynthesis as part of the water oxidizing complex of the formula: Mn₄CaO₅ (Yachandra *et al.*, 1996; Umena *et al.*, 2011). In Bacteria, Cu is a trace metal that can be part of proteins involved in electron transport (e.g. transfer of electrons from PSII to PSI in cyanobacteria, see Chapter I.1.2). However, Cu may also be part of proteins involved in the regulation of oxidative stress, which gained importance after the evolution of oxygenic photosynthesis (e.g. Miller, 2012).

Therefore, the presence of lanthanides in relation to cellular activity in the Gunflint samples may represent the metabolic response of

photosynthetic bacteria against a deficiency in Ca, Cu and a general deficiency in trace metals. Furthermore, Zerkle *et al.* (2005) have shown that cyanobacteria do not display a particular trace metals signature, but may express a metal signature when certain metalloenzymes are expressed under specific environmental conditions. Also, since cyanobacterial requirements in terms of trace metals are greater than in other prokaryotes (e.g. Merchant & Helmann, 2012; Huertas *et al.*, 2014), it is possible that in case of metal starvation, oxygenic photosynthetic bacteria would be more inclined to use substitutive elements such as lanthanides. The presence of lanthanides in the Gunflint fossilized cells may indicate the presence of oxygenic photosynthetic bacteria.

V.4. Conclusions of μ -XRF analyses

XRF spectrometry is a non-destructive, penetrative, powerful technique, allowing *in situ* elemental investigation at the scale of a micrometer to only few-nanometers.

However, sample preparation methodology for the analyses of FIB sections is a crucial step toward obtaining rigorous, useable data with respect to major to trace elements and light to heavy elements composing biological remains and the mineral matrix of Precambrian sediments. The data set of XRF results presented here illustrates the efficiency of using the Diamond-grid preparation method developed during this study and presented in section V.1, since the Jos 2 and Gunf 2 samples yielded the most significant useable data over a large series of major to trace, light to heavy elements.

In order to go further, the quantification method based on the Rayleigh and Compton scattering peaks also developed during this investigation will allow calculating precise concentrations for all detected elements, whose number is enhanced by the Diamond-grid sample preparation method.

The ability of μ XRF to analyze both the elemental composition of fossilized biofilms and cells as well as their surrounding mineral matrix, enhanced by the methodological improvements developed in this work, make

this technique a very promising asset in finding type A and type B signatures of oxygenic photosynthesis in Precambrian bacterial mats.

Chapitre VI : résumé

Analyse des isotopes de carbone, azote et soufre

Une grande partie du travail fait durant cette étude a consisté à développer de nouveaux standards pour les analyses isotopiques par SIMS, afin d'améliorer la qualité des résultats obtenus. Ce travail méthodologique est présenté dans une première partie, suivi des résultats préliminaires pour $\delta^{13}\text{C}$ et $\delta^{34}\text{S}$ obtenus grâce à ces standards. Ces analyses ont été effectuées le long d'une ligne de transect à travers un tapis microbien fossile identifié dans le chert de Josefsdal, constitué d'un biofilm microbien photosynthétique (probablement anoxygénique) développé sur des amas de matière organique (possiblement des microbes chimiotrophes). Les valeurs de $\delta^{13}\text{C}$ vont de -26,79‰ à -13,85‰, avec une valeur moyenne de -21,34‰ et sont cohérentes avec un fractionnement de type cycle de Calvin, probablement assuré par l'activité de bactéries photosynthétiques anoxygéniques dans cet échantillon (Westall *et al.*, 2006, 2011), mais sont aussi cohérentes avec l'activité de méthanogènes. Les valeurs de $\delta^{34}\text{S}$ vont de -2,88‰ à 0,79‰ avec une valeur moyenne de -1,64‰, et sont cohérentes avec la réduction bactérienne de H_2S , bien que ces valeurs chevauchent également les valeurs $\delta^{34}\text{S}$ correspondant à d'autres composés soufrés tels que le soufre de roches sédimentaires et ignées.

Ces valeurs isotopiques du carbone et du soufre dans le tapis de Josefsdal sont toutefois cohérentes avec les interprétations précédentes faites à partir d'analyses pétrographiques, chimiques et isotopiques, et qui suggèrent que ce tapis microbien est un consortium de bactéries photosynthétiques anoxygéniques et au moins un type de chimiotrophes tel que des bactéries réduisant le soufre (Westall *et al.*, 2006, 2011b, 2015).

La deuxième partie de ce chapitre est consacrée aux analyses isotopiques du carbone et de l'azote par spectrométrie de masse et chauffage par paliers. Ces analyses ont été réalisées sur des petits morceaux de roche

provenant du chert de Josefsdal, des stromatolithes de Pongola, et du chert de Gunflint. Deux composés carbonés ont été extraits dans l'échantillon de Josefsdal. Le premier pourrait correspondre aux restes microbiens identifiés dans cet échantillon, à savoir des bactéries photosynthétiques et des microbes chimiotrophiques, tandis que le deuxième composé semble correspondre à la matière organique de ces microorganismes, hautement remaniée par des processus secondaires épigénétiques. Dans l'échantillon de Pongola, un seul composé a été extrait. Les valeurs de $\delta^{13}\text{C}$ et de $\delta^{15}\text{N}$ de ce composé correspondent à celle des carbonates marins. Les résultats obtenus pour l'échantillon de Gunflint sont prometteurs. Les valeurs de $\delta^{13}\text{C}$ dans cet échantillon sont cohérentes avec la photosynthèse bactérienne, et ne montrent aucun signe de fractionnement dû à une dégradation de la matière organique par des processus secondaires.

Ainsi, l'échantillon du chert de Josefsdal (Afrique du Sud) daté à 3,33 Ga et l'échantillon du chert de Gunflint (Schreiber Beach, Canada) daté à 1,88 Ga ont été silicifiés tôt dans l'histoire de dépôt du sédiment et montrent des valeurs de $\delta^{13}\text{C}$ and $\delta^{15}\text{N}$ cohérentes avec du carbone et de l'azote dérivés de l'activité microbienne, suggérant que les processus post-dépôts n'ont pas influencé de manière significative les valeurs isotopiques de ces kérogènes. En particulier, les valeurs négatives de $\delta^{15}\text{N}$ obtenues dans les stromatolithes de Gunflint pourraient ainsi représenter le signal de la matière organique d'origine, simplement remaniée par l'activité bactérienne au cours de la diagénèse précoce. Les effets du métamorphisme sont cependant importants dans les stromatolithes de Pongola qui montrent des valeurs de $\delta^{13}\text{C}$ cohérentes avec des minéraux carbonatés, suggérant ainsi une silicification tardive.

Chapter VI: Carbon, nitrogen and sulfur isotope analyses

Stable isotopes analyses in sediments provide significant insights on past microbial life and environmental conditions (for instance: Schidlowski, 2000; Mojzsis *et al.*, 1996; Falkowski, 2011; Papineau *et al.*, 2005; Beaumont and Robert, 1999). The purpose of this study was to focus on characterizing the values of $\delta^{13}\text{C}$, $\delta^{34}\text{S}$ and $\delta^{15}\text{N}$ of microbial remains within the 3.33 Ga-old Josefsdal Chert, the ~2.98 Ga-old Pongola stromatolites and the 1.88 Ga-old Gunflint chert (Schreiber Beach locality).

The recurring challenge of this study is the spatial scale at which analytical techniques must operate to obtain the required information which is the microbial scale. The isotope measurements are also challenging. In Archean and Paleoproterozoic shallow marine sediments, photosynthetic life is mostly found under the form of microbial mats, in which photosynthetic biofilms and sometimes preserved individual cells are juxtaposed within only few microns to other autotrophic and heterotrophic microorganisms. In such samples, the results of bulk isotope analyses yield $\delta^{13}\text{C}$ values corresponding to the mixed-signatures of these metabolisms. In the case of this study, such analyses would lead to meaningless results since they do not provide the isotopic signature of a specifically selected cell or layer of microbial mat. Alternatively, Secondary Ion Mass Spectrometry (SIMS) and stepped-combustion Mass Spectrometry (MS) may be able to partly overcome this challenge. We used SIMS for its capacity to perform spot analyses at the micrometric scale within petrographical thin sections, thus allowing the careful selection of micrometric zones of interest. Since it operates on small rock samples, stepped-combustion Mass Spectrometry (MS) is considered as a bulk analytical technique. However, we put forth that its ability to separate the carbonaceous compounds contained in these small rock samples may be of use in our particular case.

A large part of the work done on isotope analyses during this study consisted in developing new standards for SIMS analyses in order to answer to analytical requirements and improve the quality of the results. This methodological work is presented in the first part of the chapter along with the preliminary *in situ* $\delta^{13}\text{C}$ and $\delta^{34}\text{S}$ SIMS measurements made in order to test these new standards. The second part of this chapter reports the results of $\delta^{13}\text{C}$ and $\delta^{15}\text{N}$ stepped-combustion mass spectrometry analyses. Then, we evaluate the possible involvement of these techniques in finding type A and type B signatures for oxygenic photosynthesis in Archean and Paleoproterozoic sediments.

VI.1. Carbon and Sulfur isotope *in situ* analysis by SIMS

In these highly silicified samples, even if microfossils are well preserved, the quantity of carbon and sulfur is very low with respect to the SiO_2 that constitutes the matrix and >90 wt.% of the total sample. Standards usually used for SIMS analyses are highly concentrated in S and C, allowing a great reproducibility on standards isotopic measurements, and thus a better constraint on isotopic values from the samples. However, with concerns for a rigorous calibration, and without losing sight of the importance of the reproducibility of the measurements, standards were manufactured purposely for these analyses with S, C and SiO_2 relative concentrations simulating those of the Precambrian samples analyzed. This original method for standard preparation is the subject of the following section.

VI.1.1. Development of new standards for C and S isotopes analyses of Precambrian microbial sediments by SIMS

a. Arguments in favor of the need for new standards

We already established that bulk isotopic analyses of our samples would only give a mixed isotopic signature corresponding to the metabolic

diversity of the preserved microorganisms and would not allow characterizing individual microfossils. Determining the isotopic composition of each microbial type separately requires SIMS analyses, able to measure *in situ* the isotopic composition of tens of μm -thick carbonaceous phases with a high spatial resolution.

In addition to the challenge of preventing mixed isotopic signatures, SIMS analyses are hampered by the dilution of C and S concentrations in the highly predominant silica matrix. Indeed, the Precambrian samples used in this study are composed of over 90 wt.% SiO_2 . More specifically, bulk chemical analyses reveal that except for the stromatolites samples from the Pongola Supergroup that have a ~ 89 wt.% SiO_2 composition, the concentration of SiO_2 in samples from Josefsdal and Gunflint reaches >96 % wt. Nevertheless, the chemical diversity of these samples remains important, although other elements are found in trace amounts. In the most concentrated carbonaceous zones, bulk analyses show that S reaches 1% (mostly due to the presence of microcrystals of pyrite) and C only 0.1% (*personal communication, N. Grassineau*).

Nonetheless, the chemical nature of the standards generally used for SIMS analyses is very different to that of our samples. Standards are homogenous and purposely enriched in C and S, with the aim of increasing the reproducibility of the measurements. However, the error on the concentrations of light versus heavy isotopes decreases if the standards and the samples have similar elemental concentrations and isotopic compositions. Furthermore, the instrumental fractionation used to calculate the accurate isotopic ratios strongly depends on the chemical composition of the matrix.

Thus, ideally, standards should contain trace amounts of C and S in a matrix of SiO_2 , in order to (i) reduce the error on the determination of the various isotopes concentrations, thus increasing the accuracy of $\delta^{13}\text{C}$ and $\delta^{34}\text{S}$ values, and (ii) better estimate the effect of the SiO_2 matrix on the instrumental fractionation, again, allowing to increase the accuracy of the calculated isotope ratios.

The preparation method that we developed to obtain such appropriate standards is reported below.

b. Experimental section

Constraints on standards manufacturing were twofold: they had to satisfy (i) specific compositions, similar to that of Precambrian kerogen in cherty matrices, and (ii) technical criteria so that they fit the physical requirements of the SIMS instrument. The development of these standards was the result of a multi-institutional collaboration with the CRPG, CNRS Nancy; the Génie Physique et Mécanique des Matériaux (GPM2) group, SIMaP laboratory Grenoble, in France, and Nathalie Grassineau at the Royal Holloway, University of London (RHUL, United Kingdom).

Standards were prepared from powders of quartz (SiO_2), pyrrhotite (Fe_{1-x}S , with $0 < x < 0.20$) and graphite (C). The compositions of the mixtures were determined with the precious advice of Nathalie Grassineau (RHUL), with respect to the relative concentrations of SiO_2 , C and S found in Archean kerogens (as well as similar $\delta^{34}\text{S}$ and $\delta^{13}\text{C}$ values):

- [1] Quartz + 0.1 % graphite
- [2] Quartz + 0.03 % graphite
- [3] Quartz + 1 % pyrrhotite
- [4] Quartz + 0.03 % pyrrhotite

From a physical point of view, porosity in the standards is prohibited to avoid electrons from charging at the surface during SIMS analyses. Hence, once mixed, powders were sintered (heated under pressure) to limit inter-grains spaces. The manufacture of these standards thus consisted in two steps: powder mixtures and sintering.

Powder mixtures

FeS and C powders were provided by Nathalie Grassineau (RHUL), who also precisely determined the isotope values of S and C, $\delta^{34}\text{S}_{(\text{FeS})} = -1.31\text{‰}$

and $\delta^{13}\text{C}_{(\text{graphite})} = -23.95\text{‰}$. 99.9% pure SiO_2 powder, consisting of $\leq 10\mu\text{m}$ grains (advice from our collaborators at the GPM2: $\leq 10\mu\text{m}$ grains facilitate sintering) was purchased from American Elements® (product reference: SI4-OX-03-P.10UM).

The shape and volume of the standards were determined with respects to the SIMS sample-holders at the CRPG and the GPM2 sintering matrix. Compromise was made on a tablet shape of 8mm diameter and 3mm height, that is a volume of 150 mm^3 . For a standard made entirely of quartz (Q), this corresponds to a quantity of Q=400 mg. We added the graphite and the pyrrhotite to this quantity of quartz. With respect to the compositions mentioned above, this gives the four following mixtures:

- [1] 400 mg Quartz + 0,4 mg graphite
- [2] 400 mg Quartz + 0,12 mg graphite
- [3] 400 mg Quartz + 4 mg pyrrhotite
- [4] 400 mg Quartz + 0,12 mg pyrrhotite

In order to avoid the contamination of the powders by the omnipresent environmental carbon during manipulation, the quartz powder was first mixed to methanol and placed in an ultrasonic bath during 15 minutes. After decantation, methanol supernatant was removed by pipette and the rest by evaporation. The resulting 'clean' quartz powder was then divided in four parts of 400 mg. Pyrrhotite and graphite powders were grinded with an agate mortar and pestle to avoid contamination by other material than SiO_2 . They were then weighted by a precision balance with sensitivity down to $1\mu\text{g}$. When added to the quartz powder, they were finely and extensively mixed to ensure the repartition of S and C in the whole mixture.

Sintering

Sintering was made at the SIMaP laboratory, in the GPM2 group, Grenoble. Test-specimens containing only quartz (400 mg of Q powder) were primarily used to determine the suitable sintering methodology. Different temperature plateaus of sintering, from 800°C to 1450°C , were tested to

determine the appropriate temperature that insures minimum porosity and maximum solidity with minimum graphite deterioration (and isotopic value changes). Test-specimens were then tested by SIMS at the CRPG to control their behavior under the ion beam. We found that the sintering temperature that meets all the technical requirements was 1400°C. At this temperature, graphite is degraded and its isotopic composition changes. However, a 1400°C sintering ensures the solidity of the standards, their adequacy with the SIMS electron beam by providing low porosity, and the possibility to keep approximate Archean concentration for S and C, as required for this study. Thus, we favored these advantages to the fact that C isotopic values might change during the sintering process. This, however, requires to rigorously determining the new $\delta^{13}\text{C}$ values of the standards before SIMS analyses.

Sintering was made under argon atmosphere, with the following thermal cycle: a temperature increase of 10°C/min until 1400°C, then a 1h plateau at this temperature, after which the specimen was cooled.

VI.1.2. Preliminary results and discussion

Measurements on this set of standards have shown that the reproducibility was challenging. $\delta^{13}\text{C}$ values for standards [1] and [2] with instrumental fractionation correction ranged from -38.7‰ to -18.1 ‰ with a mean value of -28.9‰ and for an original bulk value of -23.95‰ (determined by N. Grassineau, RHUL). $\delta^{34}\text{S}$ values for standards [3] and [4] ranged from -5.5‰ to +16.91 ‰ with a mean value of +0.8‰ and for an original bulk value of -1.31‰ (N. Grassineau). Degradation by heating during sintering could account for a shift of isotopic values. However, the low reproducibility of the measurements is here rather considered to be the result of low graphite and pyrrhotite concentrations in the prepared standards.

To test this hypothesis, another set of standards was prepared, with increased graphite and pyrrhotite concentrations up to 10% of each mixture. Powder mixtures were sintered at 1700°C during 25 minutes at the Conditions Extrêmes et Matériaux: Haute Température et Irradiation

(CEMHTI) laboratory, CNRS Orléans (experiment was conducted by R. Michel). $\delta^{13}\text{C}$ values for the graphite standards ranged from -27.72‰ to -18.03‰ with a mean value of -22.58‰, while $\delta^{34}\text{S}$ values for pyrrhotite standards ranged from -12.08‰ to -8.32‰ with a mean value of -9.66‰. Reproducibility of the measurements for this set of standards was significantly improved. This test confirms that the concentrations of pyrrhotite and graphite powders should be increased. The differences observed for this second set of standards between the original isotopic values determined by N. Grassineau and the $\delta^{13}\text{C}$ and $\delta^{34}\text{S}$ values measured here may this time be the result of heating during sintering. This effect could be limited by reapplying the protocol established for sintering and reported above with a maximum temperature of 1400°C, although concentrations of graphite and pyrrhotite in the mixture must be increased by several percents.

Although the development of improved standards for SIMS analyses is still ongoing, some preliminary results of C and S *in situ* isotope analyses obtained with the second set of standards can be discussed. $\delta^{13}\text{C}$ was measured across the 3.33 Ga microbial mat of thin section 99SA07d of the Josefsdal Chert (presented in Chapter III Fig. III.2A,E). The 1 mm-thick mat is composed of a finely laminated biofilm overlaying clots of organic matter. 27 spot analyses were made, distributed in three transect lines each crossing the biofilms and the clots layer. Although no clear gradual shift in isotopic values is observed from the biofilm to the organic matter clots, $\delta^{13}\text{C}$ values range from -26.79‰ to -13.85‰ with a mean value of -21.34‰ and are consistent with photoautotrophy (Calvin cycle) probably insured by anoxygenic bacteria in this sample (Westall *et al.*, 2006, 2011), and with methanogenic bacteria, because of the overlapping values for these two pathways. $\delta^{34}\text{S}$ values range from -2.88‰ to 0.79‰ with a mean value at -1.64‰ and are consistent with H₂S bacterial reduction, although, not unlike $\delta^{13}\text{C}$ values, these values overlap with other S-compound such as sedimentary sulfur, igneous sulfur and sulfur from metamorphic rocks. However, $\delta^{13}\text{C}$ and $\delta^{34}\text{S}$ values are consistent with previous interpretations from petrographical, chemical and isotopic analyses which may suggest that

this particular mat is a consortium of anoxygenic photosynthetic bacteria and at least one type of chemotrophs such as sulfur-reducing bacteria (Westall *et al.*, 2006, 2011b, 2015).

VI.1.3. Conclusions on the development of new standards for SIMS analyses

Precambrian microfossils, whether they are microbial biofilms, microbial clots or individual cells, are composed predominantly of silica-soaked kerogen with only low levels of C and S remaining. Furthermore, they are often arranged in the form of sub-mm to μm -thick microbial mats consisting in a consortium of phototrophic and chemotrophic microorganisms, with both autotrophs and heterotrophs. All these metabolic pathways have a different C isotopic signature range, although overlaps are frequent. In a microbial mat configuration, extracting the isotopic signature of each microbial type separately becomes challenging. This requires not bulk but rather *in situ* isotopic measurements with a high spatial resolution, as offered by the SIMS technique. Here we proposed a new S and C standards preparation method to increase the precision of SIMS results on the isotopic signatures of these ancient microbial colonies, by taking into account the compositional characteristics of Precambrian shallow-marine sediments. We found that the abundances of C and S relatively to SiO_2 in these standards can only approach that of Archean compositions, since in order to ensure a proper reproducibility of the measurements, they should be slightly increased. Although more tests are needed, we are confident that the effort made to develop original standards, similar to the samples in their composition, will allow efficient corrections on the calculated isotopic ratios, and thus provide rigorous insights on the diversity of microbial life during the Precambrian.

VI.2. C and N isotope analyses by stepped-combustion mass spectrometry

The analyses of carbon and nitrogen isotopes by stepped combustion mass spectrometry (MS) were conducted on a small piece of the following samples: 12SA09 from the 3.33 Ga-old Josefsdal Chert, 07SA01 from the ~2.98 Ga-old Pongola stromatolites (described in Chapter III) and 07CA05 from the 1.88 Ga-old Gunflint chert, Schreiber Beach (equivalent of sample GF-55-1 described in Chapter III). Since it is not described before in the manuscript, Figure VI.1 shows a photomicrograph of a representative zone of sample 12SA09, in which a highly silicified sediment, disrupted by multiple quartz veins, displays numerous carbonaceous clots and a probable microbial mat distorted by quartz lenses. Experimental parameters of these stepped-combustion MS analyses are given in Chapter II.

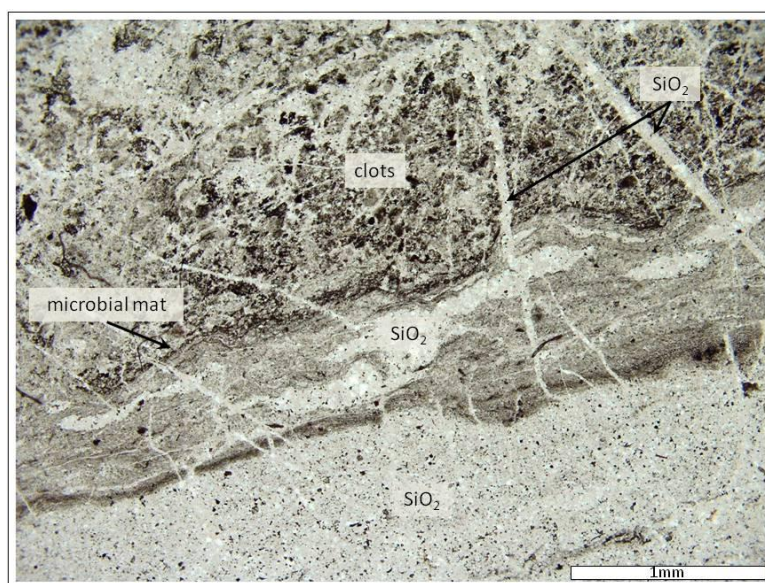


Figure VI.1. Photomicrograph of a representative zone of sample 12SA09, Josefsdal Chert, South Africa. Silica infiltrations parallel and transversal to the bedding plane are visible. A microbial mat, deformed by silica lenses, and probable microbial clots are also visible.

VI.2.1. $\delta^{13}\text{C}$ and $\delta^{15}\text{N}$ results

The results obtained from these analyses are reported in Figure VI.2 to Figure VI.4. Compounds extracted between 200°C and <600°C are considered modern contamination (e.g. Ash *et al.*, 1990; Boyd, 2004).

a. Josefsdal Chert

Combined results for $\delta^{13}\text{C}$ and $\delta^{15}\text{N}$ values show that two main kerogenous compounds were extracted between 700°C and 1200°C (increases in C and N yields; Fig. VI.2).

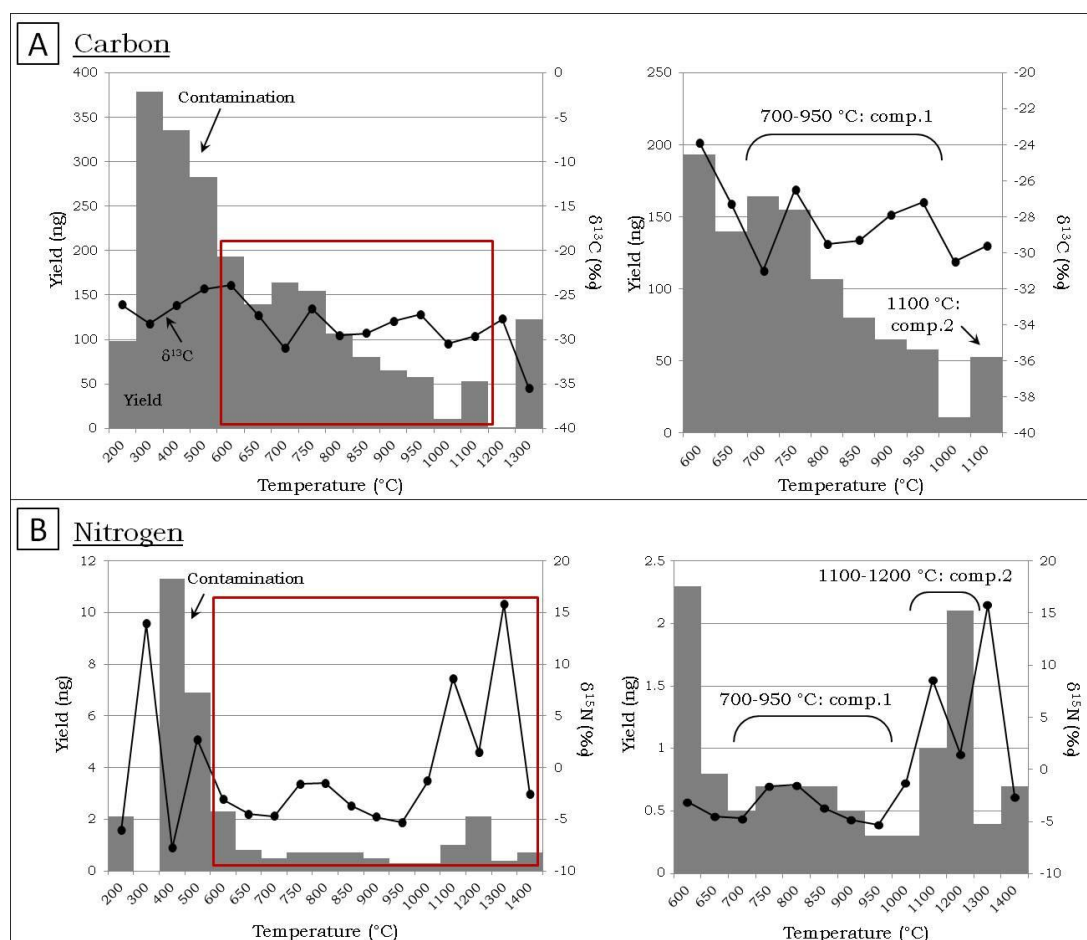


Figure VI.2. Results for Carbon (A) and Nitrogen (B) isotope analysis in sample 12SA09, Josefsdal Chert, South Africa, by stepped combustion mass spectrometry. Red boxes locate the enlargement presented in graphs on the right. Filled grey bars give the quantity of extracted C and N (in ng) as a function of temperature. Black lines give the recorded $\delta^{13}\text{C}$ and $\delta^{15}\text{N}$ (in ‰) also as a function of temperature.

Compound 1 was extracted between 700°C and 950°C. Its $\delta^{13}\text{C}$ values range from $-31\text{‰} \pm 0.2$ to $-26.5\text{‰} \pm 0.1$ with an average value at -28.57‰ , while $\delta^{15}\text{N}$ values range from $-5.3\text{‰} \pm 0.7$ to $-1.5\text{‰} \pm 0.4$ with a mean value at -3.6‰ . Compound 2 was extracted at 1100°C for C and between 1100°C and 1200°C for N. The unique $\delta^{13}\text{C}$ value was $-29.6 \pm 0.7\text{‰}$ while the two $\delta^{15}\text{N}$ values were $+8.6 \pm 0.4\text{‰}$ and $+1.5 \pm 0.4\text{‰}$ with an average value at 5.05‰ .

b. Pongola stromatolites

In the Pongola stromatolite sample, variations in carbon yield as a function of increasing temperature are positively correlated to the variations of $\delta^{13}\text{C}$ values (Fig. VI.3A).

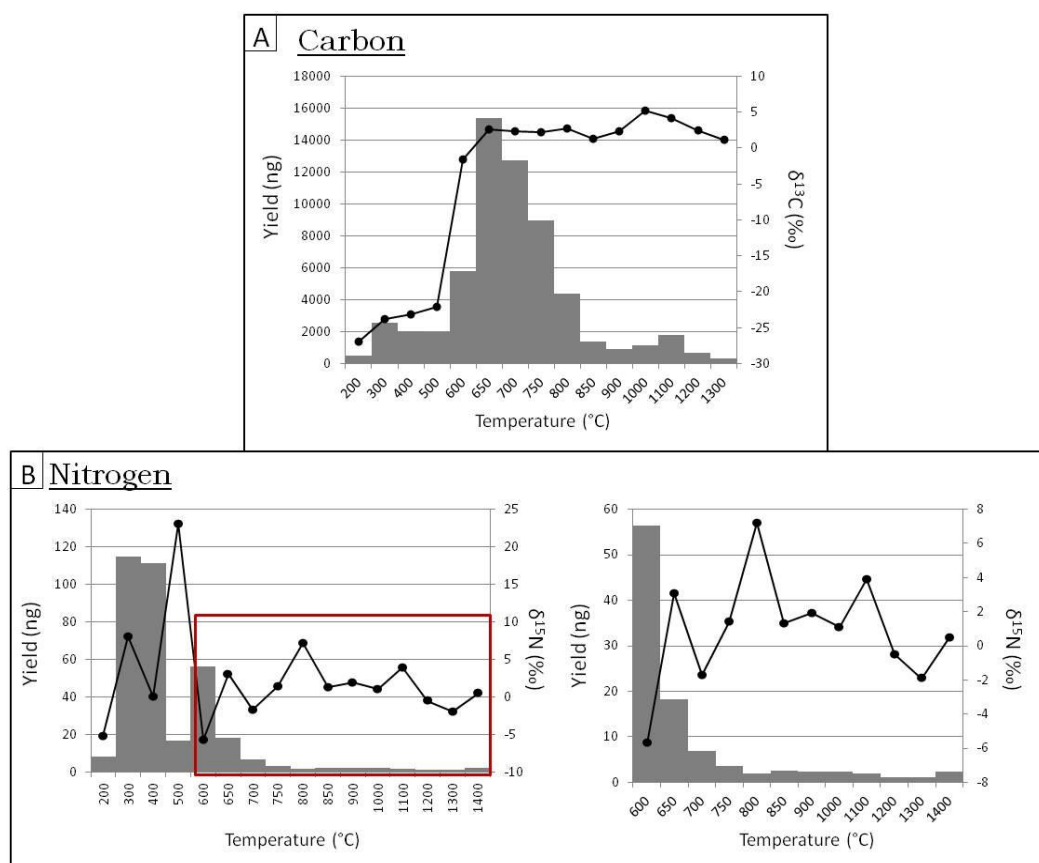


Figure VI.3. Results for Carbon (A) and Nitrogen (B) isotope analysis in sample 07SA01, Pongola stromatolites, South Africa, by stepped combustion mass spectrometry. The red box in B locates the enlargement presented in the right graph. Filled grey bars give the quantity of extracted C and N (in ng) as a function of temperature. Black lines give the recorded $\delta^{13}\text{C}$ and $\delta^{15}\text{N}$ (in ‰) also as a function of temperature.

One main compound is extracted between 600°C and 850°C with $\delta^{13}\text{C}$ values ranging from $-1.6 \pm 0.3\text{‰}$ to $+2.7 \pm 0.3\text{‰}$ and with an average value at $+1.58\text{‰}$, although it is possible that a second compound is extracted between 900°C and 1300°C with $\delta^{13}\text{C}$ values ranging from $+1.2 \pm 0.6\text{‰}$ to $+5.2 \pm 0.3\text{‰}$ and with an average value at $+3.08\text{‰}$. There is no clear correlation between nitrogen yield and variations in $\delta^{15}\text{N}$ values (Fig. VI.3B). From 600°C to 1300°C, $\delta^{15}\text{N}$ values range from $-5.7 \pm 0.3\text{‰}$ to $+7.2 \pm 0.3\text{‰}$, with an average value of $+0.91\text{‰}$.

c. Gunflint stromatolite – Schreiber Beach locality

The $\delta^{13}\text{C}$ values in the Gunflint sample show that two main kerogenous compounds were extracted between 650°C and 1400°C (Fig. VI.4A). Compound 1 is extracted between 650°C and 850°C. Its $\delta^{13}\text{C}$ values range from $-26 \pm 0.2\text{‰}$ to $-23.9 \pm 0.2\text{‰}$ with an average value at -25.28‰ , while compound 2 is extracted between 900°C and 1400°C, with $\delta^{13}\text{C}$ values ranging from $-32.6 \pm 0.2\text{‰}$ to $-29.1 \pm 0.3\text{‰}$ with an average value at -30.3‰ . $\delta^{15}\text{N}$ values range from $-13.4 \pm 0.2\text{‰}$ to $+32.6 \pm 0.3\text{‰}$ between 650°C and 1400°C. Three maximum yields are recorded for nitrogen at 700-750°C, 850°C and 1100-1300°C, with the following $\delta^{15}\text{N}$ average values: -10.3‰ , 1.4‰ and 5.4‰ , respectively.

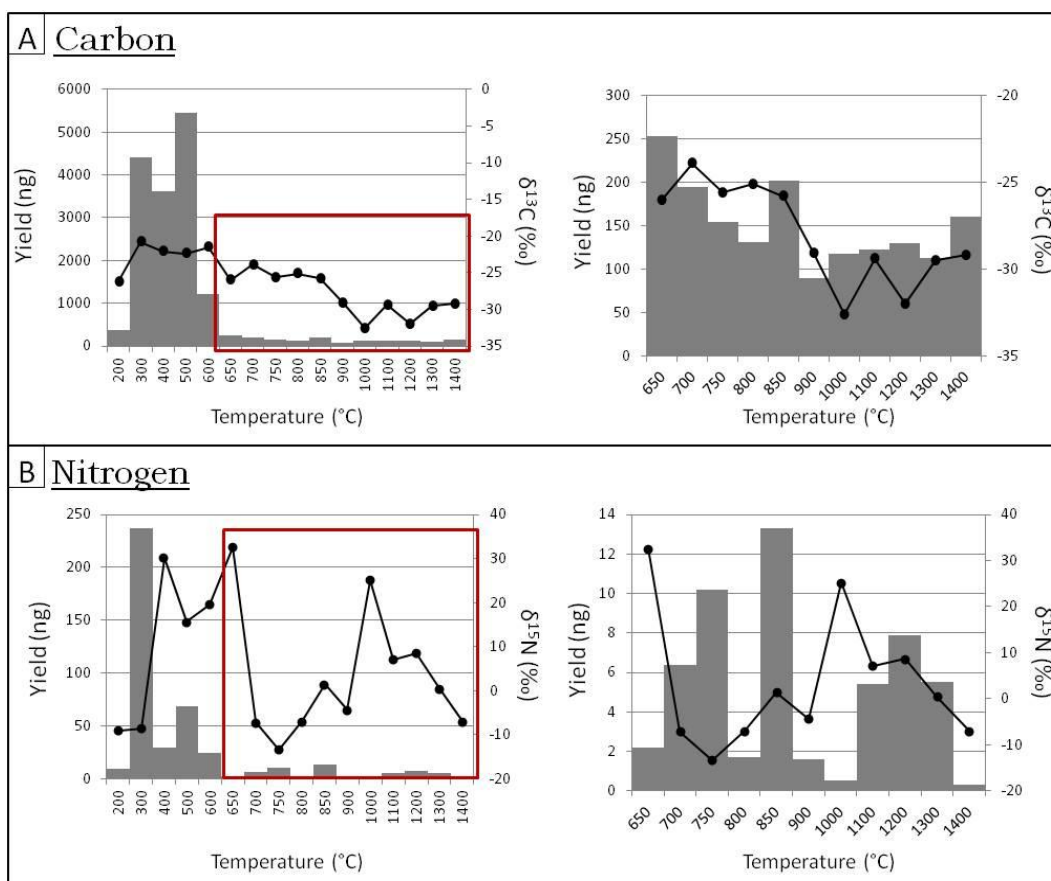


Figure VI.4. Results for C (A) and N (B) isotope analysis in sample 07CA05, Gunflint chert, Schreiber Beach locality, Animikie Basin, Canada, by stepped combustion mass spectrometry. Red boxes locate the enlargement presented in graphs on the right. Filled grey bars give the quantity of extracted C and N (in ng) as a function of temperature. Black lines give the recorded $\delta^{13}\text{C}$ and $\delta^{15}\text{N}$ (in ‰) also as a function of temperature.

VI.2.2. Discussion

Figure VI.5 combines the results reported above in a graph showing $\delta^{15}\text{N}$ versus $\delta^{13}\text{C}$ values. Several studies have shown that $\delta^{13}\text{C}$ and $\delta^{15}\text{N}$ values of kerogens contained in ancient sediments may be influenced by post-depositional processes. In the following paragraphs, we discuss the extent of information provided by the stepped-combustion MS results obtained here with respect to the type of microbial life hosted by the sediments analyzed.

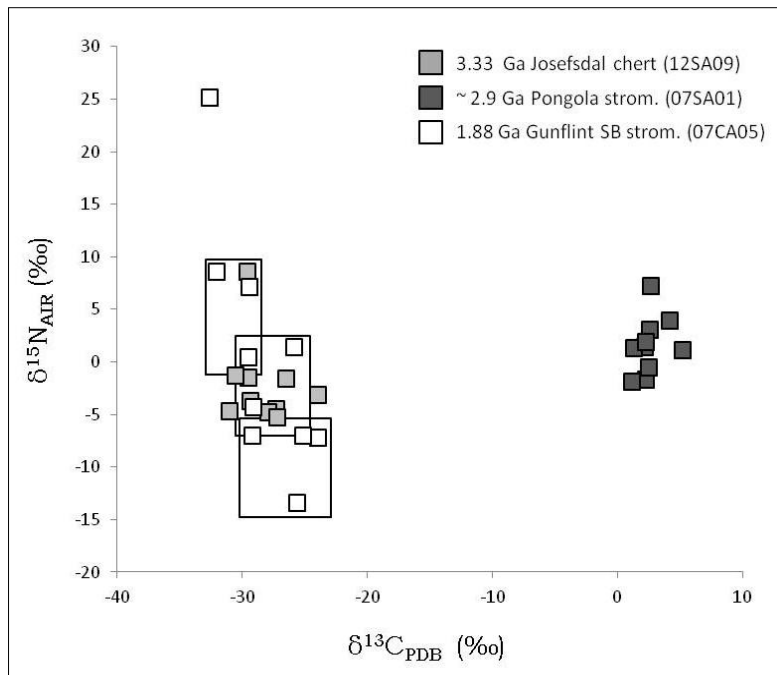


Figure VI.5. Stepped-combustion static mass spectrometry $\delta^{13}\text{C}$ and $\delta^{15}\text{N}$ values for one sample of each of the following formations: 3.33 Ga Josefsdal Chert, ~2.9 Ga Pongola stromatolites (South Africa) and 1.88 Ga Gunflint stromatolites ('SB': Schreiber Beach locality). Black boxes differentiate three compounds separated by this method in the Gunflint sample. Error bars are smaller than the symbols.

a. Silicification and Si-metasomatism

For instance, it was shown that during silicification, the Si-metasomatism can affect the relative abundances of carbon isotopes. Ueno *et al.* (2004) have shown that the metasomatism induced by the infiltration of silica dikes in 3.5 Ga-old basaltic greenstones can trigger a preferential loss of ^{12}C resulting in a shift of the $\delta^{13}\text{C}$ values. They estimated a ^{13}C -enrichment of ~4‰ for a consumption of >90% of the organic carbon. With the exception of Pongola stromatolites, $\delta^{13}\text{C}$ values in these samples range from -31‰ to -26‰ in the Josefsdal Chert and from -32‰ to -24‰ in the Gunflint stromatolites (Schreiber Beach) and are consistent with carbon derived from Calvin cycle reactions, which would still be valid with a ^{13}C -enrichment of ± 4 ‰. Furthermore, since the kerogens in both the Josefsdal Chert and Gunflint stromatolites (Schreiber beach locality) exhibit signs of rapid and early silicification and well-preserved mat and cellular structures

(see Chapter III.1), it is unlikely that the organic matter was consumed to this extent by the associated metasomatism.

b. Microbial degradation during diagenesis

Lehmann *et al.* (2002) reported that organic matter degradation and microbial growth during very early diagenesis can cause a small decrease in $\delta^{13}\text{C}$ and $\delta^{15}\text{N}$ bulk values of 1.6‰ and 3‰ respectively, and that these diagenetic switches in isotope values mostly depend on the redox conditions, with better preservation of organic matter under anoxic conditions. They postulated that these differences can be attributed to the preferential degradation of certain organic compounds by anaerobic or aerobic microbial activity. Ueno *et al.*, 2004 have shown that these early diagenetic shifts would have been smaller than those resulting from metasomatism. However, these very early diagenetic shifts may explain the negative $\delta^{15}\text{N}$ values observed for Gunflint stromatolites (Schreiber Beach) in which two kerogenous phases with a negative $\delta^{15}\text{N}$ can be distinguished, characterized by the following average values for $\delta^{13}\text{C}$ and $\delta^{15}\text{N}$ respectively: (i) -24.9‰ and -9.2‰, and (ii) -26.7‰ and -3.3‰ (Fig. VI.5). This is opposite to the model of Kasting (for instance, Kasting, 1993; Beaumont & Robert, 1999) where $\delta^{15}\text{N}$ values are supposed to increase through geological time toward positive values, following modifications in the nitrogen cycle due to the oxygenation of our planet. Since Gunflint stromatolites present evidence for a very early silicification (Chapter III.1) and no signs of diagenetic compaction or metamorphic alteration, they could have been silicified during the earliest stages of diagenesis. Thus, the isotopic data obtained from the Gunflint kerogen in this study may indeed reflect values of the microbially-altered organic matter alone. If this is the case, it may be tempting to interpret the $\delta^{13}\text{C}$ and $\delta^{15}\text{N}$ values mentioned above (called (i) and (ii)) as resulting from microbial activity and to highlight the consistency of these values with the $\delta^{15}\text{N}$ values of diagenetically altered bacteriochlorophyll (Beaumont & Robert, 1999) and chlorophyll (Chicarelli *et al.*, 1993), respectively for (i) and (ii). However, even if the stepped-combustion method for isotope analyses,

while being a bulk technique, is able to separate C and N of various carbonaceous components, the organic matter in the Gunflint stromatolites contains closely associated microfossils of various metabolisms, and the extracted isotopic values of the organic components during the analyses most likely expresses the mixed-signature of these microorganisms.

c. Long-term maturation and metamorphism

Metamorphic processes can result in the enrichment of the heavy isotope for both carbon and nitrogen remaining in the kerogenous phase.

For instance, carbon isotope composition can be influenced by isotopic exchanges between the carbon of organic material and that of carbonate minerals via CO₂-rich fluid circulation during metamorphism (Schidlowski *et al.*, 1983; Ueno *et al.*, 2002). However, neither the Josefsdal Chert nor the Gunflint samples have $\delta^{13}\text{C}$ values consistent with such an exchange which would lead to positive $\delta^{13}\text{C}$ values. This degradation process was possibly hampered by (i) an insufficient maximal temperature associated with the low degree of metamorphism undergone by these two formations (diagenetic metamorphism and low greenschist facies) and (ii) an efficient 'shielding' provided by early silicification that prevented these exchanges. On the other hand, this process may explain the $\delta^{13}\text{C}$ values of the Pongola stromatolites (Fig. VI.5) ranging from $-1.6 \pm 0.3\text{‰}$ to $+5.2 \pm 0.3\text{‰}$ with a mean average $\delta^{13}\text{C}$ value of $+2.26\text{‰}$. These results are consistent with the $\delta^{13}\text{C}$ range of inorganic carbon from carbonate minerals. Furthermore, since there are evidence for a late silicification of these stromatolites (see Chapter III.1), the exchanges between organic carbon and carbon from the carbonates present in the stromatolitic layers could also have occurred concomitantly with the growth of carbonate grains during diagenesis (Schopf *et al.*, 2007). In this case, the dissolution of primary high Mg-carbonates (dolomites) under pressure (as indicated by frequent stylolites) (see Chapter III Fig. III.4) may have provided the necessary mediation CO₂-rich fluid. Since Pongola stromatolites display $\delta^{13}\text{C}$ values consistent with carbonates and that only one compound was separated by stepped-combustion mass spectrometry, we

conclude that both carbon and nitrogen isotopic compositions from these samples were influenced by metamorphism and thus do not reflect microbial metabolisms.

Apart from isotopic exchanges between inorganic and organic carbon, long-term thermal maturation of kerogen during metamorphism and through geological times can cause a ^{13}C -enrichment of kerogen as well (Schidlowski, 1988; Des Marais, 1997). However, Ueno *et al.* (2004) have shown that this metamorphic overprint would be smaller than the isotopic shift resulting from metasomatism.

The negative $\delta^{15}\text{N}$ values of compound 1 in the Josefsdal sample (see Fig. VI.2) are consistent with the consumption of reduced nitrogen species such as N_2 during global anoxia that limited the concentration of nitrate in the oceans (Beaumont & Robert, 1999). The range of $\delta^{13}\text{C}$ values associated to this compound is consistent with methanogenic bacteria, but also with carbon fixation by Calvin cycle, thus coherent with the photosynthetic pathway. However, although a shift toward positive $\delta^{15}\text{N}$ values in kerogen is documented through geological times in relation to the evolution of redox conditions at the surface, it is unlikely that this process explains the positive $\delta^{15}\text{N}$ values of compound 2 contained in kerogen from the 3.33 Ga-old globally anoxic Earth. These positive $\delta^{15}\text{N}$ values rather result from the long-term maturation of organic matter accompanied by a ^{15}N -enrichment (e.g. Boyd *et al.*, 1993).

Indeed, similarly to carbon, a shift toward positive values of $\delta^{15}\text{N}$ of kerogens due to an enrichment in the heavy nitrogen isotope ^{15}N is documented with increasing maturation degree of the organic matter (e.g. Boyd *et al.*, 1993). However, nitrogen isotope analyses by stepped-combustion mass spectrometry reveal the opposite trend for our samples (Fig. VI.5). Indeed, while samples from the Josefsdal Chert and Pongola stromatolites that have undergone different degrees of greenschist facies metamorphism display similar maximal $\delta^{15}\text{N}$ values of +8.6‰ and +7.2‰ respectively, stromatolites from the Schreiber Beach locality of the Gunflint Formation display a significantly higher maximal $\delta^{15}\text{N}$ value of +25‰ despite

the fact that these rocks have undergone the lowest degree of metamorphism (diagenetic metamorphism). Thus, while this process may still account for the high $\delta^{15}\text{N}$ values of the Josefsdal Chert and Pongola stromatolites, it is unlikely that metamorphic alteration explains the isotopic composition of the ^{15}N -enriched kerogenous compound of the Gunflint stromatolites.

VI.2.3. Conclusions on C and N isotope analyses by stepped combustion static mass spectrometry

Modern carbonaceous contamination (<600°C) identified and set aside, stepped combustion mass spectrometry analyses were able to extract two compounds in the Josefsdal Chert sample 12SA09. Compound 1 may represent the remains of bacterial life identified in this sample: photosynthetic mat and chemotrophic microbial clots, while compound 2 more likely represents highly degraded organic matter, probably sharing the same origin as compound 1 (similar $\delta^{13}\text{C}$ values) but that was less protected against post-depositional processes (hydrothermal infiltrations, metamorphism), possibly due to a less extensive silicification.

From the Pongola stromatolite sample, only one compound was extracted that shows positive $\delta^{13}\text{C}$ values consistent with marine carbonates. The loss of biological isotopic signatures in Pongola samples is coherent with their late silicification and their reworking during secondary processes (such as diagenesis, metamorphism).

Results obtained from the Gunflint sample are however promising. Indeed, their exceptional preservation state yielded particularly interesting discussion. The $\delta^{13}\text{C}$ values from this sample are consistent with bacterial photosynthetic activity and no signs of isotopic shifts resulting from kerogen degradation by secondary, post-depositional processes were evidenced. Furthermore, since the positive $\delta^{15}\text{N}$ values in this sample cannot be explained by these alteration processes, they likely reflect biological production of nitrate (NO_3^-) and thus the rise of oxygen levels in the environment, as documented by Beaumont & Robert (1999).

Overall, samples from the 3.33 Ga-old Josefsdal Chert (South Africa) and from the Schreiber Beach locality of the 1.88 Ga-old Gunflint Formation (Canada) were silicified early and show $\delta^{13}\text{C}$ and $\delta^{15}\text{N}$ values coherent with microbially-derived C and coherent N compounds, suggesting that post-depositional events did not significantly influence the isotope composition of these kerogens. In particular, negative $\delta^{15}\text{N}$ values observed in Gunflint stromatolites that might represent the preservation of early diagenetic OM reworked by bacterial activity argue in favor of a very early silicification. The effects of metamorphism are different in the Pongola stromatolites that display signs of late silicification. Carbon isotopes in these rocks are now completely dominated by the carbonate composition.

VI.3. Conclusions on the study of C, N and S by isotope analytical techniques

Secondary Ion Mass Spectrometry (SIMS) and stepped-combustion mass spectrometry are high-resolution, chemical analytical techniques allowing determining the isotopic composition of biologically essential elements such as C, N and S within kerogens. Since these analytical methods are destructive, they were performed separately on small pieces of the rock samples, corresponding to duplicates of the thin sections used for the whole study, or at the end of the analytical chain when the samples used were the thin sections themselves (this was the case for *in situ* isotope analyses by SIMS).

The implication of isotope analytical methods in this study is concentrated primarily on the search for type A signatures (defined in the *Scientific approach and objectives* section), since during isotopic investigations the focus was made on the characterization of the kerogens. Although stepped-combustion MS is a bulk analytical technique, it remains more relevant than other bulk analyses since it allows separating kerogenous compounds. SIMS analyses allow going further in the isotopic

characterization of Precambrian kerogens by the *in situ* analysis of specific kerogenous structures such as biofilms, microbial clots or cells with a spot size of 25 μ m. This is particularly relevant to overcome the challenges of (i) mixed isotopic signatures induced by the proximity of several bacterial metamorphic types regrouped in the same mat, but also (ii) the possibility of the loss of the original isotopic values of autotrophic microbes resulting from the reworking of organic matter by heterotrophic microbes. For these reasons, the isotopic characterization of kerogens by SIMS is a fundamental step in the search for type A signatures. The necessary development of suitable standards for the study of C and S isotopes of Precambrian kerogen with this technique was conducted in this study and is still ongoing.

Although $\delta^{15}\text{N}$ in kerogens and $\Delta^{33}\text{S}$ of sulfur-compounds (sedimentary pyrites) may provide indirect to direct insights on the oxygenation of the environment at the time of sediment deposition, they may not assist in finding type B signatures (defined in the *Scientific approach and objectives* section), which concerns the impact of oxygenic photosynthetic bacterial activity on its immediate mineralogical surrounding, at the μm scale.

However, further *in situ* $\delta^{34}\text{S}$ analyses at the micrometric scale could be applied to the search of type B signatures. Indeed, measurements of sulfur isotopes in syngenetically grown mineralogical grains surrounding the microfossils, such as pyrite, may provide answers in understanding the intricate metabolic processes occurring in mat-like microbial consortia during the Precambrian.

Conclusions

The emergence of oxygenic photosynthesis yielded direct and indirect fundamental changes at the global scale that lead to the development of the geobiosphere as we know it. Without this evolutionary step, the atmosphere would still be anoxic and life still microbial.

Understanding the mechanisms involved in the evolution of oxygenic photosynthetic bacteria and constraining their emergence in time is essential to deciphering the longest and most impressive part of Earth's history.

Such a research topic requires the involvement of several fields of study such as geology, biology, geomicrobiology, ocean chemistry, geochemistry, within which each scientific community attempts to answer the “Big Three” questions defined in the Introduction: (i) When did photosynthesis appear? (ii) When did oxygenic photosynthesis emerge? (iii) How much time passed between the inception of oxygenic photosynthesis and the Great Oxidation Event (GOE)?

One possible way to proceed is to determine precisely the variations in the concentration of O₂ in the atmosphere through time. Another way is to conduct thorough micropaleontological investigations at the micrometer scale in Archean and Paleoproterozoic shallow marine sediments, in order to identify microbial photosynthetic remains, to characterize their morphology, their chemical and isotopic compositions, and their possible impact on the immediate (µm) surrounding mineral matrix, such as any signs of oxidation resulting from the release of O₂. The aim of this investigation was to contribute to this micropaleontological method and participate in constraining the emergence of oxygenic photosynthetic bacteria in time by means of finding chemical and/or mineralogical signatures of this metabolism at the microbial scale within Archean and Paleoproterozoic sediments.

For this purpose, I defined two main types of signatures. Type A signatures which relate to the intrinsic biochemistry of the oxygenic photosynthetic pathway itself; these signatures involve the chemical

characterization of the carbonaceous matter remaining in fossilized bacteria and bacterial mats. Type B signatures relate to the local environmental impact of oxygenic photosynthesis. Type B signatures consist of identifying preserved changes in the local mineralogy and chemistry around photosynthetic microfossils that would have been induced by the metabolic activity of oxygenic photosynthetic bacteria, and particularly by the release of oxygen.

The search for these potential chemical signatures in fossilized photosynthetic biofilms and cells ranging in age from the anoxic Archean Earth to the aftermath of the GOE poses several constraints that limit the choice of suitable analytical techniques. Indeed, the scale of interest of this study requires micrometric to elemental-scale techniques and the rarity of the samples implies the use of non-destructive techniques as much as possible.

Therefore, during this study, the objectives were twofold: to identify possible type A and/or type B signatures and to determine which analytical techniques are the most suitable to detect these signatures.

Chemical signatures for Archean and Paleoproterozoic oxygenic photosynthesis

This study was able to provide probable answers for both signature types.

First, in samples from the 1.88 Ga-old Gunflint Chert (Schreiber Beach locality, Animikie Basin, Canada), we report the presence of Sm distributed specifically inside two Fe-rich individual cells assigned to the photosynthetic (Williford *et al.*, 2013) and probably cyanobacteria-like (Barghoorn & Tyler, 1965; Cloud, 1965; Awaramik & Barghoorn, 1977), *Gunflintia-Huroniospora* assemblage. Furthermore, we report that, within a spherical *Huroniospora* cell, Sm is associated with La and Gd and that the distribution of these two elements outside the cell follows the distribution of Fe. Indeed, in the silica matrix surrounding this cell, the zones depleted in

La and Gd correspond to Fe-poor zones. Since, in these samples, the distribution of Fe possibly represents the post-depositional precipitation of Fe-oxides on organic matter (Shapiro & Konhauser, 2015), we suggest that Sm, La and Gd follow the distribution of organic matter as well. However, we argue against the possibility that these rare earth elements were brought in by the precipitation of Fe-oxides, since this hypothesis would not explain the preferential distribution of Sm exclusively inside the cells and not in the matrix. If these elements were indeed originally contained within the organic matter, then the presence of La and Gd outside the cell may stem from the escape of cellular material from the cell, or the preservation of residual extracellular polymeric substances in the siliceous matrix.

Based on literature and on elemental data from this study for Ca, Cu, Mn and other metals, I propose that, in these samples, the association of Sm, La and Gd with cellular material may stem from the use of lanthanides by photosynthetic bacteria as a metabolic answer to deficiency in the medium of photosynthetically-essential metals (the complete study is reported in Chapter V). Since there is a strong possibility that the *Gunflintia-Huroniospora* assemblage might have been oxygenic photosynthetic bacteria, then the enrichment of lanthanides inside these preserved cells, compared to the siliceous matrix may become, in specific contexts, a signature for this metabolism, provided that there is some evidence for metal deficiency in the medium while the organisms were active.

Therefore, since it contributes to the chemical characterization of the organic matter of these bacteria, this result may provide a possible type A signature.

Secondly, within the 2.98 Ga-old Pongola and the 1.88 Ga-old Gunflint (Kakabeka Falls locality) stromatolites, the detection of significant amounts of Cu in diagenetic pyrites related neither to early silicification nor to later hydrothermal events, was interpreted as resulting from the breakdown of Cu-proteins from degrading organic matter in the surrounding stromatolitic layers (see Chapter IV). The presence of Cu-proteins in bacteria at ~2.98 Ga and 1.88 Ga may stem from the need of using Cu-based, ancestral

equivalent of modern superoxide dismutase enzymes as a metabolic protection mechanism against oxidative stress in an oxygenated environment. I propose that the presence of large amounts of Cu in the diagenetic fluids of Pongola and KF stromatolites and partitioning in diagenetic pyrites is a result of an ongoing oxygenic photosynthesis.

Thus, I propose that, in certain conditions, the Cu content of diagenetic pyrites associated, within few microns, with the remains of photosynthetic bacteria, may suggest the presence and activity of oxygenic photosynthetic bacteria in the local environment, if not in the considered stromatolitic layers.

This result may be relevant for type B signatures, since it may indicate the influence of oxygenic photosynthesis on its local environment at the micrometric scale.

Suitable analytical techniques for the search of signatures

The conclusive results presented above were obtained by SEM/EDS, EPMA, and by synchrotron radiation μ -XRF analyses. In particular, the sample that yielded the most pertinent μ -XRF results was prepared following the sample preparation method developed during this investigation and reported in Chapter V.

Therefore, I argue that the analytical techniques most suited to finding signatures of oxygenic photosynthesis (of both type A and type B) in Precambrian sediments are non-destructive, elemental techniques powerful enough to perform high resolution mapping at the micrometric to sub-micrometric scales and to detect and quantify major to trace elements down to tens of ppm.

The new quantification method for synchrotron radiation μ XRF analyses based on the Rayleigh and Compton scatterings that this study contributed to develop (see Chapter V) thus further enhances the ability of μ XRF analyses to find signatures of oxygenic photosynthesis.

Overall, in the interest of constraining in time the emergence of oxygenic photosynthesis, we can say from this investigation that this metabolism had probably not evolved at 3.33 Ga but was probably ongoing by at least 2.98 Gyr ago.

Conclusions (Français)

L'émergence de la photosynthèse oxygénique a engendré des changements fondamentaux directs et indirects à l'échelle globale, qui ont mené au développement de la géobiosphère telle que nous la connaissons. Si ce saut évolutif n'avait pas eu lieu, l'atmosphère de notre planète serait encore anoxique aujourd'hui, et la vie, encore au stade microbien.

Comprendre les mécanismes impliqués dans l'évolution des bactéries photosynthétiques oxygéniques et dater leur émergence est essentiel afin de lever le voile sur la plus longue et la plus impressionnante période de l'histoire de notre planète.

Un tel sujet de recherche nécessite l'implication de multiples domaines d'études comme la géologie, la biologie, la géomicrobiologie, la chimie océanique, la géochimie, dans lesquels chacune des communautés scientifiques concernée essaie de répondre aux trois grandes questions suivantes : (i) Quand la photosynthèse est-elle apparue ? (ii) Quand la photosynthèse oxygénique a-t-elle émergé ? (iii) Combien de temps s'est-il écoulé entre (ii) et la Grande Oxygénation de notre planète (*Great Oxidation Event*, GOE) ?

Une des façons de procéder est de déterminer précisément les variations de la concentration d'O₂ dans l'atmosphère et au cours du temps. Une autre façon est de réaliser des études précises de micropaléontologie à l'échelle micrométrique dans les sédiments marins peu profonds Archéens et Paléoprotozoïques afin d'identifier des restes de micro-organismes photosynthétiques, de caractériser leur morphologie, leur composition chimique et isotopique, et l'éventuel impact de leur activité métabolique sur leur environnement minéral (à l'échelle micrométrique toujours), comme par exemple, des signes d'oxydation dûs à la libération d'O₂. L'objectif de cette étude était de contribuer, de par cette méthode micropaléontologique, à situer dans le temps l'émergence des bactéries photosynthétiques oxygéniques, en trouvant des signatures chimiques et/ou minéralogiques de

ce métabolisme, à l'échelle microbienne, et dans des sédiments Archéens et Paléoprotérozoïques.

Pour cela, j'ai défini deux types de signatures. Les signatures de type A sont liées à la biochimie du métabolisme photosynthétique oxygénique. Ces signatures impliquent la caractérisation de la matière carbonée préservée dans les microfossiles. Les signatures de type B concernent l'impact local environnemental de la photosynthèse oxygénique. Ces signatures consistent donc à identifier, localement autour des microfossiles photosynthétiques, des changements dans la minéralogie et la chimie du sédiment qui auraient été préservés et qui pourraient avoir été engendrés par l'activité de ces bactéries.

La recherche de ces potentielles signatures chimiques dans des biofilms et cellules photosynthétiques fossiles datant de la Terre Archéenne anoxique jusqu'à la Terre oxique au lendemain du GOE, pose des contraintes qui limitent les possibilités d'utilisation de certaines techniques analytiques. En effet, l'échelle micrométrique d'étude imposée par le sujet nécessite des techniques capables d'opérer de l'échelle micrométrique à élémentaire, et la rareté des échantillons requiert l'utilisation de techniques non-destructrices autant que possible.

Ainsi, les objectifs de cette étude comportaient deux volets : identifier de potentielles signatures de type A et B, et déterminer quelles techniques analytiques sont le plus appropriées pour détecter ces signatures.

Signatures chimiques pour la photosynthèse oxygénique à l'Archéen et au Paléoprotérozoïque

Cette étude a permis de trouver deux potentielles signatures. Dans les échantillons de Gunflint (Schreiber Beach) datant de 1,88 Ga, nous avons détecté la présence de samarium distribué spécifiquement à l'intérieur de deux cellules individuelles riches en fer correspondant aux bactéries photosynthétiques (Williford *et al.*, 2013) et probablement de type cyanobactéries (Barghoorn & Tyler, 1965; Cloud, 1965; Awaramik & Barghoorn, 1977), de l'assemblage *Gunflintia-Huroniospora*. De plus, à

l'intérieur de la cellule *Huroniospora*, le Sm est associé à du lanthane et du gadolinium, et la distribution spatiale de ces deux éléments à l'extérieur de la cellule suit la distribution du Fe. En effet, dans les quelques microns de matrice siliceuse qui bordent la cellule, les zones appauvries en La et Gd correspondent aux zones pauvres en Fe. Puisque dans ces échantillons, la distribution du Fe représente très probablement la précipitation secondaire d'oxydes de fer sur la matière organique (Shapiro & Konhauser, 2015), nous proposons que Sm, La et Gd suivent également la distribution de la matière organique. Il semble peu probable que ces terres rares (REE) aient été apportées par la précipitation des oxydes de fer, puisque ceci n'expliquerait pas la distribution de Sm à l'intérieur des cellules et non dans la matrice. Si ces éléments étaient originellement contenus dans la matière organique, alors il est possible que la présence de La et Gd à l'extérieur de la cellule représente l'échappement de matériel cellulaire ou la préservation d'EPS (pour « *extracellular polymeric substances* ») dans la matrice siliceuse.

En me basant sur des recherches publiées, ainsi que sur les données élémentaires concernant Ca, Cu, Mn et d'autres métaux obtenus dans cette étude, je propose que dans ces échantillons, l'association de Sm, La et Gd avec le matériel cellulaire des microfossiles de Gunflint pourrait représenter l'utilisation de lanthanides par les bactéries photosynthétiques en substitution à des métaux essentiels pour l'activité bactérienne et/ou photosynthétique, dans un milieu appauvri en ces métaux (voir Chapitre V). Puisqu'il est fort probable que l'assemblage *Gunflintia-Huroniospora* ait réalisé la photosynthèse oxygénique, alors l'enrichissement en lanthanides à l'intérieur de ces cellules fossiles par rapport à la matrice pourrait devenir, dans un contexte particulier, une signature de ce métabolisme, à condition qu'il y ait des indices montrant l'appauvrissement du milieu en certains métaux essentiels durant leur période d'activité.

Cette possible signature contribue à la caractérisation chimique de la matière organique de ces bactéries. Ce résultat pourrait donc fournir une potentielle signature de type A.

Dans les échantillons de stromatolithes de Pongola et de Gunflint (Kakabeka Falls) datant respectivement de ~2,98 Ga et 1,88 Ga, la détection d'importantes concentrations de cuivre dans les pyrites diagénétiques, qui n'aurait été apporté ni par la silicification ni par la circulation plus tardive de fluides hydrothermaux, a été interprété comme résultant de la dégradation de protéines de Cu durant la dégradation de la matière organique contenue dans les couches stromatolithiques (Chapitre IV). La présence de potentielles Cu-protéines dans des bactéries à ~2,98 Ga et à 1,88 Ga pourrait représenter le besoin d'utiliser d'anciennes formes d'enzymes équivalents aux modernes Cu superoxyde dismutases dans le contexte d'un mécanisme de protection métabolique contre le stress oxydatif dans un environnement oxygéné. Je propose que la présence de grandes quantités de Cu dans les fluides diagénétiques des stromatolithes de Pongola et de Kakabeka Falls et sa répartition dans les pyrites diagénétiques pourrait trahir le fait que la photosynthèse oxygénique était en place à ces époques. Je propose que dans certaines conditions, le contenu en cuivre de pyrites associées, à l'échelle micrométrique, à des restes de bactéries photosynthétiques, pourrait témoigner de la présence et l'activité de bactéries photosynthétiques oxygéniques dans l'environnement local, si ce n'est dans les couches stromatolithiques concernées elles-mêmes.

Ce résultat pourrait être intéressant pour la recherche de signatures de type B, puisqu'il pourrait indiquer l'influence de la photosynthèse oxygénique sur son environnement local à l'échelle micrométrique.

Techniques analytiques appropriées à la recherche de ces signatures

Les résultats présentés ci-dessus ont été obtenus par MEB/EDS, EPMA, et par μ -XRF à rayonnement synchrotron. En particulier, l'échantillon qui a permis d'obtenir le plus de résultats par μ -XRF a été préparé suivant la méthode de préparation d'échantillons développée dans cette étude et présentée dans le Chapitre V.

Je conclus donc que les méthodes analytiques les plus appropriées pour trouver des signatures chimiques de la photosynthèse oxygénique dans

des sédiments Précambriens sont les techniques élémentaires, non ou très peu destructrices, comme celles mentionnées ci-dessus, ayant la capacité de réaliser des cartographies élémentaires à haute résolution (μm et $<\mu\text{m}$) et de détecter et quantifier les éléments majeurs à traces jusqu'à la dizaine de ppm.

La nouvelle méthode de quantification élémentaire pour analyses de μ -XRF par rayonnement synchrotron que cette étude a contribué à développer et qui est basée sur les diffusions Rayleigh et Compton (Chapitre V) permet donc d'augmenter la capacité des analyses μ -XRF déjà prometteuses à trouver des signatures de la photosynthèse oxygénique.

Pour conclure, et afin de contribuer à contraindre dans le temps l'émergence de la photosynthèse oxygénique, les résultats obtenus au cours de cette étude suggèrent que ce métabolisme n'avait probablement pas évolué à 3,33 Ga mais qu'il était probablement déjà actif il y a $\sim 2,98$ Ga.

Bibliography

A

- Ahmann D., Roberts A. L., Krumholz L. R., Morel M. M., 1994. Microbe grow by reducing arsenic. *Nature*, 371, 750.
- Alexander B. W., Bau M., Andersson P., Dulski P., 2008. Continentally-derived solutes in shallow Archean seawater: Rare earth element and Nd isotope evidence in iron formation from the 2.9 Ga Pongola Supergroup, South Africa. *Geochimica et Cosmochimica Acta*, 72, 378–394.
- Algeo T. J., Lyons T. W., 2006. Mo–total organic carbon covariation in modern anoxic marine environments: Implications for analysis of paleoredox and paleohydrographic conditions. *Paleoceanography*, 21.
- Algeo T. J., Maynard J. B., 2004. Trace-element behavior and redox facies in core shales of Upper Pennsylvanian Kansas-type cyclothems. *Chemical Geology*, 206, 289–318.
- Allen J. F., 2005. A redox switch hypothesis for the origin of two light reactions in photosynthesis, *FEBS Letters*, 579, 5, 963–968.
- Allen J. F., Martin W., 2007. Out of thin air, *Nature*, 445, 610–612.
- Allen J. P., Williams J. C., 2011. The evolutionary pathway from anoxygenic to oxygenic photosynthesis examined by comparison of the properties of photosystem II and bacterial reaction centers, *Photosynthesis Research*, 107, 59–69.
- Allwood A. C., Walter M. R., Kamber B. S., Marshall C. P., Burch I. W., 2006. Stromatolite reef from the Early Archean era of Australia, *Nature*, 441, 714–718.
- Allwood A. C., Kamber B. S., Walter M. R., Burch I. W., Kanik I., 2010. Trace elements record depositional history of an Early Archean stromatolitic carbonate platform. *Chemical Geology*, 270, 148–163.
- Aloisi G., 2008. The calcium carbonate saturation state in cyanobacterial mats throughout Earth's history. *Geochimica et Cosmochimica Acta*, 72 (24), 6037–6060.
- Altermann W., Kazmierczak J., Oren A., Wright D. T., 2006. Cyanobacterial calcification and its rock-building potential during 3.5 billion years of Earth history. *Geobiology*, 4, 147–166.
- Altermann W., 2008. Accretion, Trapping and Binding of Sediment in Archean Stromatolites—Morphological Expression of the Antiquity of Life, *Space Science Reviews*, 135(1–4), 55–79.
- Ananyev G. M., Zaltsman L., Vasko C., Dismukes G. C., 2001. The inorganic biochemistry of photosynthetic oxygen evolution/water oxidation, *Biochimica et Biophysica Acta*, 1503, 52–68.
- Anbar A. D., Holland H. D., 1992. The photochemistry of manganese and the origin of banded iron formations, *Geochimica et Cosmochimica Acta*, 56, 2595–2603.
- Anbar A. D., 2004. Iron stable isotopes: beyond biosignatures, *Earth and Planetary Science Letters*, 217, 223–236.
- Anbar A. D., Rouxel O. J., 2007. Metal Stable Isotopes in Paleoceanography. *Annual Review of Earth and Planetary Sciences*, 35, 717–746.
- Anbar A. D., Duan Y., Lyons T. W., Arnold G. L., Kendall B., Creaser R. A., Kaufman A. J., Gordon G. W., Scott C., Garvin J., Buick R., 2007. A Whiff of Oxygen Before the Great Oxidation Event?, *Science*, 317, 1903–1906.
- Armstrong R. A., Compston W., de Wit M. J., Williams I. S., 1990. The stratigraphy of the 3.5–3.2 Ga Barberton Greenstone Belt revisited: a single zircon ion microprobe study. *Earth and Planetary Science Letters*, 101, 1, 90–106.
- Arvestål E. H. M., 2013. Changes in Arsenic Levels in the Precambrian Oceans in Relation to the Upcome of Free Oxygen. Independent thesis Advanced level, Uppsala University,

Disciplinary Domain of Science and Technology, Earth Sciences, Department of Earth Sciences, Palaeobiology, Sweden.

- Ash R. D., Arden J. W., Wright I. P., Pillunger C. T., 1990. Recondite interstellar carbon components in the Allende meteorite revealed by preparative precombustion. *Geochimica et Cosmochimica Acta*, 54(2), 455-468.
- Awramik S. M., Barghoorn E. S., 1977. The Gunflint microbiota, *Precambrian Research*, 5, 121-142.
- Awramik S. M., 1992. The oldest records of photosynthesis. *Photosynthesis Research*, 33, 75-89.

B

- Bajwah Z. U., Seccombe P. K., Offler, R., 1987. Trace element distribution, Co:Ni ratios and genesis of the Big Cadia iron-copper deposit, New South Wales, Australia. *Mineralium Deposita*, 22, 292-300.
- Balk M., Bose M., Ertem G., Rogoff D. A., Rothschild L. J., Freund F. T., 2009. Oxidation of water to hydrogen peroxide at the rock-water interface due to stress-activated electric currents in rocks, *Earth and Planetary Science Letters*, 283, 87-92.
- Bare S. R., 2005. XANES Measurements and Interpretations. EXAFS Data Collection and Analysis Course, APS, July 26-29. UOP LLC, Des Plaines, Illinois, USA.
- Barghoorn E. S., Tyler S. A., 1965. Microorganisms from the Gunflint Chert, *Science*, 147(3658), 563-575.
- Barley M. E., Bekker A., Krapež B., 2005. Late Archean to Early Paleoproterozoic global tectonics, environmental change and the rise of atmospheric oxygen, *Earth and Planetary Science Letters*, 238, 1-2, 156-171.
- Barnicoat A. C., Henderson I.H.C., Knipe R.J., Yardley B.W.D., Napier R.W., Fox N.P.C., Kenyon A.K., Muntingh D.J., Strydom D., Winkler K.S., Lawrence S.R., Cornford C., 1997. Hydrothermal gold mineralization in the Witwatersrand basin. *Nature*, 386, 820-824.
- Bau M., Alexander B., 2006. Preservation of primary REE patterns without Ce anomaly during dolomitization of Mid-Paleoproterozoic limestone and the potential re-establishment of marine anoxia immediately after the "Great Oxidation Event". *South African Journal of Geology*, 109, 81-86.
- Baumgartner L. K., Reid R. P., Dupraz C., Decho A. W., Buckley D. H., Spear J. R., Przekop K. M., Visscher P. T., 2006. Sulfate reducing bacteria in microbial mats: Changing paradigms, new discoveries. *Sedimentary Geology*, 185, 131-145.
- Baymann F., Brugna M., Mühlenhoff U., Nitschke W., 2001. Daddy, where did (PS)I come from?, *Biochimica et Biophysica Acta*, 1507, 291-310.
- Beaumont V., Robert F., 1999. Nitrogen isotope ratios of kerogens in Precambrian cherts: a record of the evolution of atmosphere chemistry?. *Precambrian Research*, 96, 63-82.
- Bekker A., Holland H. D., Wang P. L., Rumble III D., Stein H. J., Hannah J. L., Coetzee L. L., Beukes N. J., 2004. Dating the rise of atmospheric oxygen, *Nature*, 427, 117-120.
- Benning L. G., Phoenix V. R., Yee N., Tobin M. J., 2004a. Molecular characterization of cyanobacterial silicification using synchrotron infrared micro-spectroscopy. *Geochimica et Cosmochimica Acta*, 68(4), 729-741.
- Benning L. G., Phoenix V. R., Yee N., Konhauser K. O., 2004b. The dynamics of cyanobacterial silicification: An infrared micro-spectroscopic investigation. *Geochimica et Cosmochimica Acta*, 68(4), 743-757.
- Benzerara K., 2014. Intracellular Ca-carbonate biomineralization is widespread in cyanobacteria. *Proceedings of the National Academy of Sciences*, 111 (30), 10933-10938.
- Bertine K. K., Turekian K. K., 1973. Molybdenum in marine deposits, *Geochimica et Cosmochimica Acta*, 37, 6, 1415-1434.
- Beukes N. J., Lowe D. R., 1989. Environmental control on diverse stromatolite morphologies in the 3000 Myr Pongola Supergroup, South Africa. *Sedimentology*, 36, 383-397.

- Beyssac O., Goffé B., Chopin C., Rouzaud J. N., 2002. Raman spectra of carbonaceous material in metasediments: a new geothermometer, *Journal of Metamorphic Geology* 20:9, 859-871.
- Björn L. O. and Govindjee, 2009. The evolution of photosynthesis and chloroplasts, *Current Science*, 96, 11, 1466-1474.
- Blankenship R. E., 1992. Origin and early evolution of photosynthesis, *Photosynthesis Research*, 33, 91-111.
- Blankenship R. E., Hartman H., 1998. The origin and evolution of oxygenic photosynthesis, *TIBS* 20, 23, 3, 94-97.
- Bontognali T. R. R., Vasconcelos C., Warthmann R. J., Dupraz C., Bernasconi S. M., McKenzie J. A., 2008. Microbes produce nanobacteria-like structures, avoiding cell entombment. *Geology*, 36 (8), 663-666.
- Bos M., Vrieling J.A.M., 2005. The influence of scattering processes in quantitative X-ray fluorescence analysis. *Analytica Chimica Acta*, 545, 92-98.
- Bosak T., Newman D. K., 2003. Microbial nucleation of calcium carbonate in the Precambrian. *Geology*, 31 (7), 577-580.
- Bosak T., Greene S. E., Newman D. K., 2007. A likely role for anoxygenic photosynthetic microbes in the formation of ancient stromatolites, *Geobiology*, 5, 119-126.
- Bosak T., Knoll A. H., Petroff A. P., 2013. The Meaning of Stromatolites, *Annual Reviews of Earth and Planetary Sciences*, 41, in press.
- Bowring S. A., Williams I. S., 1999. Priscoan (4.00±4.03 Ga) orthogneisses from northwestern Canada. *Contributions to Mineralogy and Petrology*, 134, 3-16.
- Boyd S. R., Hall A., Pillinger C. T., 1993. The measurement of $\delta^{15}\text{N}$ in crustal rocks by static vacuum mass spectrometry: Application to the origin of the ammonium in the Cornubian batholith, southwest England. *Geochimica et Cosmochimica Acta*, 57(6), 1339-1347.
- Boyd S. R., 2004. Determination of the Abundance and Stable Isotopic Composition of Trace Quantities of C and N in Geological Samples: The Practice and Principles of Stepped-Heating at High Temperature Resolution. in *Handbook of Stable Isotope Analytical Techniques*, Volume 1, P, A, de Groot (Editor), Part 1, Chapter 13, 256-271.
- Boyett M., Carlson R. W., 2005. ^{42}Nd Evidence for Early (>4.53 Ga) Global Differentiation of the Silicate Earth. *Science*, 309, 576-81.
- Brabec M. Y., Lyons T. W., Mandemack K. W., 2012. Oxygen and sulfur isotope fractionation during sulfide oxidation by anoxygenic phototrophic bacteria. *Geochimica et Cosmochimica Acta*, 83, 234-251.
- Brasier M. D., Green O. R., Jephcoat A. P., Klepepe A. K., Van Kranendonk M. J., Lindsay J. F., Steele A., Grassineau N. V., 2002. Questioning the evidence for Earth's oldest fossils, *Nature*, 416, 76-81.
- Braterman P. S., Cairn-Smith A. G., Sloper R. W., 1983. Photo-oxidation of hydrated Fe^{2+} —significance for banded iron formations, *Nature*, 303, 163-164.
- Braterman P. S., Cairn-Smith A. G., 1987. Photoprecipitation and the banded iron-formations — Some quantitative aspects, *Origins of Life and Evolution of the Biosphere*, 17 (3-4), 221-228.
- Brocks J. J., Logan G. A., Buick R., Summons R. E., 1999. Archean Molecular Fossils and the Early Rise of Eukaryotes, *Science*, 285, 1033-1036.
- Brocks J. J., 2001. Molecular fossils., In *McGraw-Hill Yearbook of Science & Technology*, McGraw Hill, 252-255.
- Brocks J. J., Buick R., Logan G. A., Summons R. E., 2003a. Composition and syngeneity of molecular fossils from the 2.78 to 2.45 billion-year-old Mount Bruce Supergroup, Pilbara Craton, Western Australia, *Geochimica et Cosmochimica Acta*, 67 (22), 4289-4319.
- Brocks J. J., Buick R., Summons R. E., Logan G. A., 2003b. A reconstruction of Archean biological diversity based on molecular fossils from the 2.78 to 2.45 billion-year-old Mount Bruce Supergroup, Hamersley Basin, Western Australia, *Geochimica et Cosmochimica Acta*, 67, 22, 4321- 4335.

- Brocks J. J., Pearson A., 2005. Building the biomarker tree of life. , *Reviews in Mineralogy and Geochemistry*, (eds. J. Banfield et al.) The Mineralogical Society of America, Chantilly. , 233-258.
- Brocks J. J., 2011. Millimeter-scale concentration gradients of hydrocarbons in Archean shales: Live-oil escape or fingerprint of contamination?, *Geochimica et Cosmochimica Acta*, 75 (11), 3196–3213.
- Bueno P., Varela J., Gimenez-Gallego G., del Rio L. A., 1995. Peroxisomal copper, zinc superoxide dismutase. Characterization of the isoenzyme from watermelon cotyledons. *Plant Physiology*, 108(3), 1151-1160.
- Buick R., Dunlop J.S.R., Groves D.I., 1981. Stromatolite recognition in ancient rocks: an appraisal of irregular laminated structures in an early Archean chert-barite unit from North Pole, Western Australia. *Alcheringa* 5, 161–181.
- Buick R., 1990. Microfossil Recognition in Archean Rocks: An Appraisal of Spheroids and Filaments from a 3500 M.Y. Old Chert-Barite Unit at North Pole, Western Australia, *Palaios*, 5(5), 441-459.
- Buick R., 2008. When did oxygenic photosynthesis evolve?, *Philosophical Transactions of the Royal Society B*, 363, 2731-2743.
- Bundeleva I. A., Shirokova L. S., Bénézeth P., Pokrovsky O. S., Kompantseva E. I., Balor S., 2012. Calcium carbonate precipitation by anoxygenic phototrophic bacteria. *Chemical Geology*, 291, 116-131.
- Busemann H., Alexander C. M. O. D., Nittler L. R., 2007. Characterization of insoluble organic matter in primitive meteorites by microRaman spectroscopy. *Meteoritics & Planetary Science*, 42, 1347–1416.
- Byerly G. R., Kröner A., Lowe D. R., Todt W., Walsh M. M., 1996. Prolonged magmatism and time constraints for sediment deposition in the early Archean Barberton greenstone belt: evidence from the Upper Onverwacht and Fig Tree groups. *Precambrian Research*, 78(1-3), 125–138.

C

- Cairns-Smith A. G., 1978. Precambrian solution photochemistry, inverse segregation, and banded iron formations. *Nature*, 276, 807-808.
- Campbell I. H., Allen C. M., 2008. Formation of supercontinents linked to increases in atmospheric oxygen, *Nature Geoscience*, 1, 554-558.
- Canfield D. E., 1998. A new model for Proterozoic ocean chemistry. *Nature*, 396, 450-453.
- Canfield D. E., Rosing M. T., Bjerrum C., 2006. Early anaerobic metabolisms, *Philosophical Transactions of the Royal Society B*, 361, 1819-1836.
- Canfield D. E., Poulton S. W., Narbonne G. M., 2007. Late-Neoproterozoic Deep-Ocean Oxygenation and the Rise of Animal Life. *Science*, 315, 92-95.
- Canfield D. E., Ngombi-Pemba L., Hammarlund E. U., Bengtson S., Chaussidon M., Gauthier-Lafaye F., Meunier A., Riboulleau A., Rollion-Bard C., Rouxel O., Asael D., Pierson-Wickmann A.-C., El Albani A., 2013. Oxygen dynamics in the aftermath of the Great Oxidation of Earth's atmosphere. *PNAS*, 110, 42, 16736–16741.
- Canup R. M., Asphaug E., 2001. Origin of the Moon in a giant impact near the end of the Earth's formation. *Nature*, 412, 708-712.
- Caro G., Bourdon B., Wood B. J., Corgne J., 2005. Trace-element fractionation in Hadean mantle generated by melt segregation from a magma ocean. *Nature*, 436, 246-249.
- Carstens H., 1986. Displacive Growth of Authigenic Pyrite. *Journal of Sedimentary Research*, 56(2), 252-257.
- Catling D., Zahnle K., 2002. Evolution of Atmospheric Oxygen. *Encyclopedia of Atmospheric Sciences*, (eds J. Holton, J. Pyle & J. Curry), Amsterdam, The Netherlands: Academic Press, 754-761.

- Catling D. C., Glein C. R., Zahnle K. J., McKay C. P., 2005. Why O₂ Is Required by Complex Life on Habitable Planets and the Concept of Planetary “Oxygenation Time”, *Astrobiology*, 5, 3, 451-438.
- Catling D. C., Claire M. W., 2005. How Earth's atmosphere evolved to an oxic state: A status report, *Earth and Planetary Science Letters*, 237, 1-20.
- Chambers J. E., 2004. Planetary accretion in the inner Solar System. *Earth and Planetary Science Letters*, 223, 241-252.
- Chen W.-J., Tao Y., Gu Y.-H., Zhao G.-W., 2001. Effect of lanthanide chloride on photosynthesis and dry matter accumulation in tobacco seedlings. *Biological Trace Element Research*, 79(2), 169-176.
- Chicarelli M. I., Hayes J. M., Popp B. N., Eckardt C. B., Maxwell J.R., 1993. Carbon and nitrogen isotopic compositions of alkyl porphyrins from the Triassic Serpiano oil shale. *Geochimica et Cosmochimica Acta*, 57(6), 1307-1311.
- Cinco R. M., McFarlane Holman K. L., Robblee J. H., Yano J., Pizarro S. H., Bellacchio E., Sauer K., Yachandra V. K., 2002. Calcium EXAFS Establishes the Mn-Ca Cluster in the Oxygen-Evolving Complex of Photosystem II, *Biochemistry*, 41, 43, 12928-12933.
- Clement B. G., Luther G.W., Tebo B. M., 2009. Rapid, oxygen-dependent microbial Mn(II) oxidation kinetics at sub-micromolar oxygen concentrations in the Black Sea suboxic zone. *Geochimica et Cosmochimica Acta*, 73, 18781889.
- Cloud P. E., 1965. Significance of the Gunflint (Precambrian) microflora, *Science*, 148, 3666, 27-35.
- Cloud P. E., 1968. Atmospheric and Hydrospheric Evolution on the Primitive Earth, *Science*, 160 (3829), 729-736 .
- Cloud P. E., 1973. Paleocological Significance of the Banded Iron-Formation, *Economic Geology*, 68 (7), 1135-1143.
- Cohen Y., E Padan E., Shilo M., 1975. Facultative Anoxygenic Photosynthesis in the Cyanobacterium *Oscillatoria limnetica*, *Journal of Bacteriology*, 123(3), 855-861.
- Collier R. W., 1985. Molybdenum in the Northeast Pacific Ocean, *Limnology and Oceanography*, 30(6), 1351-1354.
- Couradeau E., Benzerara K., Gérard E., Moreira D., Bernard S., Brown Jr. G. E., López-García P., 2012. An Early-Branching Microbialite Cyanobacterium Forms Intracellular Carbonates. *Science*, 336, 459-462.
- Craig J. R., Vokes M., Solberg T. N., 1998. Pyrite: physical and chemical textures. *Mineralium Deposita*, 34(1), 82-101.
- Croal L. R., Johnson C. M., Beard B. L., Newman D. K., 2004. Iron isotope fractionation by Fe(II)-oxidizing photoautotrophic bacteria, *Geochimica et Cosmochimica Acta*, 68 (6), 1227-1242.
- Crowe S. A., Døssing L. N., Beukes N. J., Bau M., Kruger S. J., Frei R., Canfield D. E., 2013. Atmospheric oxygenation three billion years ago, *Nature*, 501, 535-538.

D

- David J., Godin L., Stevenson R., O'Neil J., Francis D., 2009. U-Pb ages (3.8-2.7 Ga) and Nd isotope data from the newly identified Eoarchean Nuvvuagittuq supracrustal belt, Superior Craton, Canada. *Geological Society of America Bulletin*, 121, 150-163.
- Deditius A.P., Utsunomiya S., Renock D., Ewing R.C., Ramana C.V., Becker U., Kesler, S. E., 2008. A proposed new type of arsenian pyrite: Composition, nanostructure and geological significance. *Geochimica et Cosmochimica Acta*, 72, 2919-2933.
- Derry L. A., Jacobsen S. B., 1990. The chemical evolution of Precambrian seawater: Evidence from REEs in banded iron formations. *Geochimica et Cosmochimica Acta*, 54, 2965-2977.
- Des Marais D. J., 1997. Isotopic evolution of the biogeochemical carbon cycle during the Proterozoic Eon. *Organic Geochemistry*, 27(5-6), 185-193.

- de Wit M. J., Hart R. A., Hart R. J., 1987. The Jamestown Ophiolite Complex, Barberton Mountain Land: a section through 3.5 Ga oceanic crust. *Journal of African Earth Sciences*, 5, 681-730.
- de Wit M. J., Hart R. A., 1993. Earth's earliest continental lithosphere, hydrothermal flux and crustal recycling. *Lithos*, 30(3-4), 309-335.
- Dill H. G., Kemper E., 1990. Crystallographic and chemical variations during pyritization in the upper Barremian and lower Aptian dark claystone from the Lower Saxonian Basin (NW Germany). *Sedimentology*, 37, 427-443.
- Dowdle P. R., Oremland R. S., 1998. Microbial Oxidation of Elemental Selenium in Soil Slurries and Bacterial Cultures. *Environmental Science and Technology*, 32, 3749-3755.
- Dupraz C., Visscher P. T., Baumgartner L. K., Reid R. P., 2004. Microbe–mineral interactions: early carbonate precipitation in a hypersaline lake (Eleuthera Island, Bahamas). *Sedimentology*, 51, 745–765.

E

- Emmanuel E. S. C., Ramachandran A. M., Ravindran A. D., Natesan M., Maruthamuthu S., 2010. Effect of some rare earth elements on dry matter partitioning, nodule formation and chlorophyll content in *Arachis hypogaea* L. plants. *Australian Journal of Crop Science*, 4(9), 670-675.
- England G. L., Rasmussen B., Krapez B., Groves D. I., 2002. Palaeoenvironmental significance of rounded pyrite in siliciclastic sequences of the Late Archaean Witwatersrand Basin: oxygen-deficient atmosphere or hydrothermal alteration? *Sedimentology*, 49 (6), 1133–1156.

F

- Falkowski P. G., 2011. The biological and geological contingencies for the rise of oxygen on Earth, *Photosynthesis Research*, 107, 7-10.
- Farquhar J., Bao H., Thiemens M., 2000. Atmospheric Influence of Earth's Earliest Sulfur Cycle, *Science*, 289, 756-758.
- Farquhar J., Zerkle A. L., Bekker A., 2011. Geological constraints on the origin of oxygenic photosynthesis, *Photosynthesis Research*, 107, 11-36.
- Ferrari A. C., Robertson J., 2000. Interpretation of Raman spectra of disordered and amorphous carbon. *Physical Review*, 61, 14095–14107.
- Fisher W. W., Summons R. E., Pearson A., 2005. Targeted genomic detection of biosynthetic pathways: anaerobic production of hopanoid biomarkers by a common sedimentary microbe, *Geobiology*, 3, 33-40.
- Floor G. H., Roman-Ross G., 2012. Selenium in volcanic environments: A review. *Applied Geochemistry*, 27, 517-531.
- Folk R. L., Weaver C. E., 1952. A study of the texture and composition of chert. *American Journal of Science*, 250, 498-510.
- Folk R. L., 1980. *Petrology of sedimentary rocks*. Austin, Texas, Hemphill Publishing.
- Foucher F., Ammar M.-R., Westall F., 2015. Revealing the biotic origin of silicified Precambrian carbonaceous microstructures using Raman spectroscopic mapping, a potential method for the detection of microfossils on Mars. *Journal of Raman Spectrometry*, 46(10), 873–879.
- Fournelle J. H., Kim S., Perepezko J. H., 2005. Monte Carlo simulation of Nb Ka secondary fluorescence in EPMA: comparison of PENELOPE simulations with experimental results. *Surface and Interface Analysis*, 37, 1012-1016.

- Fralick P., Davis D. W., Kissin S. A., 2002. The age of the Gunflint Formation, Ontario, Canada: single zircon U–Pb age determinations from reworked volcanic ash. *Canadian Journal of Earth Sciences*, 39(7), 1085–1091.
- Frankel R. B., Bazylinski D. A., 2003. Biologically Induced Mineralization by Bacteria. *Reviews in Mineralogy and Geochemistry*, 54(1), 95–114.
- Franklin J. M., Shegelski R. J., 1982. Proterozoic geology of the northern Lake Superior area. Geological Association of Canada-Mineralogical Association of Canada, Filed Trip Guidebook, Trip 4.
- Frei, R., Gaucher, C., Poulton, S. W., Canfield, D. E., 2009. Fluctuations in Precambrian atmospheric oxygenation recorded by chromium isotopes, *Nature*, 461, 250-253.
- French B. M., 1973. Mineral Assemblages in Diagenetic and Low-Grade Metamorphic Iron-Formation. *Economic Geology*, 68(7), 1063-1074.
- Frizzo P., Rampazzo G., Molinaroli E., 1991. Authigenic iron sulphides in recent sediments of the Venice Lagoon (Northern Italy). *European Journal of Mineralogy*, 3(3), 603-612.
- Furnes H., de Wit M., Staudigel H., Rosing M., Muehlenbachs K., 2007. A Vestige of Earth's Oldest Ophiolite. *Science*, 315, 1704-1707.

G

- Gaillard F., Scaillet B., Arndt N. T., 2011. Atmospheric oxygenation caused by a change in volcanic degassing pressure, *Nature*, 478, 229-232.
- Garlick S., Oren A., Padan E., 1977. Occurrence of Facultative Anoxygenic Photosynthesis Among Filamentous and Unicellular Cyanobacteria, *Journal of Bacteriology*, 129(2), 623-629.
- Garrels R. M., Perry E. A., MacKenzie F. T., 1973. Genesis of Precambrian iron-formations and the development of atmospheric oxygen. *Economic Geology*, 68, 1173-1179.
- Garvin J., Buick R., Anbar A. D., Arnold G. L., Kaufman A. J., 2009. Isotopic evidence for an aerobic nitrogen cycle in the latest Archean. *Science*, 323, 1045-1048.
- Godfrey L. V., Falkowski P. G., 2009. The cycling and redox state of nitrogen in the Archean ocean. *Nature Geoscience*, vol. 2, 725-729.
- Goecke F., Jerez C. J., Zachleder V., Figueroa F. L., Bišová K., Řezanka T., Vítová M., 2015. Use of lanthanides to alleviate the effects of metal ion deficiency in *Desmodesmus quadricauda* (Sphaeropleales, Chlorophyta). *Frontiers in Microbiology*, 6(2), 1-12.
- Golubic S., Seong-Joo L., 1999. Early cyanobacterial fossil record: preservation, palaeoenvironments and identification. *European Journal of Phycology*, 34, 339-348.
- Goodwin A. M., 1956. Facies Relations in the Gunflint Iron Formation, *Economic Geology*, 51, 565-595.
- Grotzinger J. P., Rothman D. H., 1996. An abiotic model for stromatolite morphogenesis, *Nature*, 383, 423 - 425.
- Grotzinger J. P., Knoll A. H., 1999. Stromatolites in Precambrian Carbonates: Evolutionary Mileposts or Environmental Dipsticks?, *Annual Review of Earth and Planetary Science*, 27, 313-358.
- Guy B. M., Beukes N. J., Gutzmer J., 2010. Paleoenvironmental controls on the texture and chemical composition of pyrite from non-conglomeratic sedimentary rocks of the Mesoarchean Witwatersrand Supergroup, South Africa. *South African Journal of Geology*, 113 (2), 195-228.

H

- Hamade T., Konhauser K. O., Raiswell R., Goldsmith S., Morris R. C., 2003. Using Ge/Si ratios to decouple iron and silica fluxes in Precambrian banded iron formations. *Geology*, 31 (1), 35-38.

- Hannah J. L., Bekkerb A., Steina H. J., Markeya R. J., Holland H. D., 2004. Primitive Os and 2316 Ma age for marine shale: implications for Paleoproterozoic glacial events and the rise of atmospheric oxygen. *Earth and Planetary Science Letters*, 225, 43-52.
- Hartman, H., 1984. The evolution of photosynthesis and microbial mats: a speculation on banded iron formations. In: Cohen Y. Castenholz R.W., Halvorson H.O. (eds.), *Microbial Mats: Stromatolites*. New York, Alan Liss, 451-453.
- Hartman H., 1998. Photosynthesis and the origin of life, *Origins of Life and Evolution of the Biosphere*, 28(4-6), 515-521.
- Hazen R. M., Papineau D., Bleeker W., Downs R. T., Ferry J. M., McCoy T. J., Sverjensky D. A., Yang H., 2008. Mineral Evolution, *American Mineralogist*, 93, 1693-1720.
- Henke B. L., Gullikson E. M., David J. C., 1993. X-Ray Interactions: Photoabsorption, Scattering, Transmission, and Reflection at $E = 50-30,000$ eV, $Z = 1-92$. *Atomic Data and Nuclear Data Tables*, 54(2), 181-342.
- Herbel M. J., Switzer Blum J., Oremland R. S., Borglin S. E., 2003. Reduction of Elemental Selenium to Selenide: Experiments with Anoxic Sediments and Bacteria that Respire Selenoanions. *Geomicrobiology Journal*, 20, 587-602.
- Hoefl S. E., Kulp T. R., Stolz J. F., Hollibaugh J. T., Oremland R. S., 2004. Dissimilatory Arsenate Reduction with Sulfide as Electron Donor: Experiments with Mono Lake Water and Isolation of Strain MLMS-1, a Chemoautotrophic Arsenate Respirer. *Applied and Environmental Microbiology*, 70(5), 2741-2747.
- Hofmann H. J., 1969. Stromatolites from the Proterozoic Animikie and Sibley Groups, Ontario. *Geological Survey of Canada, Paper 68-69*, .
- Hofmann H. J., 1976. Precambrian microflora, Belcher Islands, Canada: Significance and systematics., *Journal of Paleontology*, 50(6), 1040-1073.
- Hofmann A., Bolhar R., 2007. Carbonaceous cherts in the Barberton greenstone belt and their significance for the study of early life in the Archean record. *Astrobiology*, 7 (2), 355-388.
- Hofmann A., Harris C., 2008. Silica alteration zones in the Barberton greenstone belt: A window into subseafloor processes 3.5-3.3 Ga ago. *Chemical Geology*, 257, 224-242.
- Hofmann A., Bekker A., Rouxel O., Rumble D., Master S., 2009. Multiple sulphur and iron isotope composition of detrital pyrite in Archaean sedimentary rocks: A new tool for provenance analysis, *Earth and Planetary Science Letters*, 286, 436-445.
- Holland H. D., 1984. *The chemical evolution of the atmosphere and oceans*, Princeton University Press.
- Holland H. D., 2002. Volcanic gases, black smokers, and the Great Oxidation Event, *Geochimica et Cosmochimica Acta* , 66, 21, 3811-3826.
- Holland H. D., 2006. The Oxygenation of the atmosphere and oceans, *Philosophical Transactions of the Royal Society B*, 361, 903-915.
- Deer W. A., Howie R. A., Zussman J., 1966. *An introduction to the rock-forming minerals*. Eds. Longman, London, 528pp.
- Hu G., Rumble D., Wang P., 2003. An ultraviolet laser microprobe for the in situ analysis of multisulfur isotopes and its use in measuring Archean sulfur isotope mass-independent anomalies, *Geochimica et Cosmochimica Acta*, 67 (17), 3101.
- Huertas M. J., López-Maury L., Giner-Lamia J., Sánchez-Riego A. M., Florencio F. J., 2014. Metals in Cyanobacteria: Analysis of the Copper, Nickel, Cobalt and Arsenic Homeostasis Mechanisms. *Life*, 4, 865-886.

J

- Jehlička J., Urban O., Pokorný J., 2003. Raman spectroscopy of carbon and solid bitumens in sedimentary and metamorphic rocks. *Spectrochimica Acta Part A: Molecular and Biomolecular Spectroscopy*, 59(10), 2341-2352.

- Johnson C. M., Beard B. M., Roden E. E., 2008. The Iron Isotope Fingerprints of Redox and Biogeochemical Cycling in Modern and Ancient Earth. *Annual Review of Earth and Planetary Sciences*, 36, 457-493.
- Johnson J. E., Webb S. M., Thomas K., Ono S., Kirschvink J. L., Fischer W. W., 2013. Manganese-oxidizing photosynthesis before the rise of cyanobacteria, *Proceedings of the National Academy of Sciences of the United States of America*, 110, 28, 11238-11243.
- Jørgensen B. B., Cohen Y., Revsbech N. P., 1986. Transition from Anoxygenic to Oxygenic Photosynthesis in a Microcoleus chthonoplastes Cyanobacterial Mat, *Applied and Environmental Microbiology*, 51, 2, 408-417.

K

- Kamber B. S., Webb G. E., 2001. The geochemistry of late Archaean microbial carbonate : Implications for ocean chemistry and continental erosion history. *Geochimica et cosmochimica Acta*, 65,15, 2509-2525.
- Kappler A., Newman D. K., 2004. Formation of Fe(III)-minerals by Fe(II)-oxidising photoautotrophic bacteria. *Geochimica et cosmochimica Acta*, 68, 6, 1217-1226.
- Kappler A., Pasquero C., Konhauser K. O., Newman D. K., 2005. Deposition of banded iron formations by anoxygenic phototrophic Fe(II)-oxidizing bacteria. *GSA Geology*, 33, 11, 865-868.
- Kasting J.F., 1993. Earth's Early Atmosphere, *Science*, 259, 920-926.
- Kato Y., Yamaguchi K. E., Ohmoto H., 2006. Rare earth elements in Precambrian banded iron formations: Secular changes of Ce and Eu anomalies and evolution of atmospheric oxygen . *Geological Society of America Memoirs*, 198, 269-289.
- Kaufman A. J., Johnston D. T., Farquhar J., Masterson AL .L., Lyons T. W., Bates S., Anbar A. D., Arnold G. L., Garvin J., Buick R., 2007. Late Archean Biospheric Oxygenation and Atmospheric Evolution. *Science*, 317, 1900-1903.
- Khorobrykh A., Dasgupta J., Kolling D. R. J., Terentyev V., Klimov V. V., Dismukes G. C., 2013. Evolutionary Origins of the Photosynthetic Water Oxidation Cluster: Bicarbonate Permits Mn²⁺ Photo-oxidation by Anoxygenic Bacterial Reaction Centers, *ChemBioChem*, 14 (14), 1725-1731.
- Kirk M. F., Holm T. R., Park J., Jin Q., Sanford R. A., Fouke B. W., Bethke C. M., 2004. Bacterial sulfate reduction limits natural arsenic contamination in groundwater. *Geology*, 32, 11, 953-956.
- Kirschvink J. L., Kopp R. E., 2008. Palaeoproterozoic ice houses and the evolution of oxygen-mediating enzymes: the case for a late origin of photosystem II, *Philosophical Transactions of the Royal Society B*, 363, 2755-2765.
- Klein C., Beukes N. J., 1992. Time distribution, stratigraphy, sedimentologic setting, and geochemistry of Precambrian iron-formations. In Schopf, J.W., and Klein, C., eds., *The Proterozoic biosphere*: New York, Cambridge University Press, 139-146.
- Kleine T., Münker C., Mezger K., Palme H., 2002. Rapid accretion and early core formation on asteroids and the terrestrial planets from Hf-W chronometry. *Nature*, 418, 952-955.
- Knauth L. P., 1994. Petrogenesis of chert. *Reviews in Mineralogy and Geochemistry*, 29, 233-258.
- Knoll A. H., 1985. Exceptional Preservation of Photosynthetic Organisms in Silicified Carbonates and Silicified Peats. *Philosophical Transactions of the Royal Society B*, 311, 111-122.
- Kok B., Forbush B., McGloin M., 1970. Cooperation of charges in photosynthetic O₂ evolution-I. A linear four step mechanism., *Photochemistry and Photobiology*, 11, 6, 457-475.
- Kolling D. R. J., Cox N., Ananyev G. M., Pace R. G., Dismukes G. C., 2012. What Are the Oxidation States of Manganese Required To Catalyze Photosynthetic Water Oxidation?, *Biophysical Journal*, 103, 313-322.

- Kohn M. J., Riciputi L. R., Stakes D., Orange D. L., 1998. Sulfur isotope variability in biogenic pyrite: Reflections of heterogeneous bacterial colonization?. *American Mineralogist*, 83, 1454–1468.
- Konhauser K., Hamade T., Raiswell M., Ferris F. G., Southam G., Canfield D. E., 2002. Could bacteria have formed the Precambrian banded iron formations?, *Geology*, 30, 12, 1079-1082.
- Konhauser K. O., Amskold L., Lalonde S. V., Posth N. R., Kappler A., Anbar A., 2007. Decoupling photochemical Fe(II) oxidation from shallow-water BIF deposition, *Earth and Planetary Science Letters*, 258, 87-100.
- Konhauser K., 2007. *Introduction to geomicrobiology*, Blackwell Publishing, Oxford.
- Konhauser K., Pecoits E., Lalonde S. V., Papineau D., Nisbet E. G., Barley M. E., Arndt N. T., Zahnle K., Kamber B.S., 2009. Oceanic nickel depletion and a methanogen famine before the Great Oxidation Event, *Nature*, 458, 750-753.
- Kopp R. E., Kirschvink J. L., Hilburn I. A., Nash C. Z., 2005. The Paleoproterozoic snowball Earth: A climate disaster triggered by the evolution of oxygenic photosynthesis, *Proceedings of the National Academy of Sciences*, 102, 32, 11131-11136.
- Koschinsky A., Hein J. R., 2003. Uptake of elements from seawater by ferromanganese crusts: solid-phase associations and seawater speciation. *Marine Geology*, 198, 331–351.
- Krajewski K. P., Luks B., 2003. Origin of “cannon-ball” concretions in the Carolinefjellet Formation (Lower Cretaceous), Spitsbergen. *Polish Polar Research*, 24, 217-242.
- Krüger M., Meyerdierks A., Glöckner F.O., Amann R., Widdel F., Kube M., Reinhardt R., Kahnt J., Böcher R., Thauer R.K., Shima S., 2003. A conspicuous nickel protein in microbial mats that oxidize methane anaerobically. *Nature*, 426, 878-881.
- Krüner A., Byerly G. R., Lowe D. R., 1991. Chronology of early Archaean granite-greenstone evolution in the Barberton Mountain Land, South Africa, based on precise dating by single zircon evaporation. *Earth and Planetary Science Letters*, 103, 41-54.
- Krupp R., Oberthür T., Hirdes W., 1994. The Early Precambrian Atmosphere and Hydrosphere: Thermodynamic Constraints from Mineral Deposits. *Economic Geology*, 89, 1581-1598.
- Kulp T. R., Pratt L. M., 2004. Speciation and weathering of selenium in Upper Cretaceous chalk and shale from South Dakota and Wyoming, USA. *Geochimica et Cosmochimica Acta*, 68(18), 3687–3701.
- Kulp T. R., Hoefft S. E., Asao M., Madigan M. T., Hollibaugh J. T., Fisher J. C., Stolz J. F., Culbertson C. W., Miller L. G., Oremland R. S., 2008. Arsenic(III) Fuels Anoxygenic Photosynthesis in Hot Spring Biofilms from Mono Lake, California. *Science*, 321, 967-970.
- Kump L.R., Kasting J. F., Barley M. E., 2001. Rise of atmospheric oxygen and the "upside-down" Archean mantle, *Geochemistry, Geophysics, Geosystems*, 2, 1525-2027.

L

- Labrot, P., 2006. *Microscopie à Force Atomique de Microfossiles Précambriens*. Thèse de Doctorat, Université d'Orléans, Orléans.
- Lancaster V. L., LoBrutto R., Selvaraj F. M., Blankenship R. E., 2004. A cambialistic superoxide dismutase in the thermophilic photosynthetic bacterium *Chloroflexus aurantiacus*. *Journal of Bacteriology*, 186(11), 3408-3414.
- Large R. R., Maslennikov V. V., Robert F., Danyushevsky L. V., Chang Z., 2007. Multistage Sedimentary and Metamorphic Origin of Pyrite and Gold in the Giant Sukhoi Log Deposit, Lena Gold Province, Russia. *Economic Geology*, 102, 1233–1267.
- Large R. R., Danyushevsky L., Hollit C., Maslennikov V., Meffre S., Gilbert S., Bull S., Scott R., Emsbo P., Thomas H., Singh B., Foster J., 2009. Gold and Trace Element Zonation in Pyrite Using a Laser Imaging Technique: Implications for the Timing of Gold in Orogenic and Carlin-Style Sediment-Hosted Deposits. *Economic Geology*, 104, 635-668.

- Large R. R., Halpin J. A., Danyushevsky L. V., Maslennikov V. V., Bull S. W., Long J. A., Gregory D. D., Lounejeva E., Lyons T. W., Sack P. J., McGoldrick P. J., Calver C. R., 2014. Trace element content of sedimentary pyrite as a new proxy for deep-time ocean-atmosphere evolution, *Earth and Planetary Science Letters*, 389, 209-220.
- Ledevin M., 2013. Les cherts Archéens de la ceinture de roches vertes de Barberton (3.5-3.2Ga), Afrique du Sud. Processus de formation et utilisation comme proxys paleo-environnementaux.. Thèse de Doctorat, Université Joseph Fourier, Grenoble, France.
- Ledevin M., Arndt N., Simionovici A., Jaillard E., Ulrich M., 2014. Silica precipitation triggered by clastic sedimentation in the Archean: New petrographic evidence from cherts of the Kromberg type section, South Africa. *Precambrian Research*, 255 (Part 1), 316-334.
- Lehmann M. F., Bernasconi S. M., Barbieri A., Mckenzie J. A., 2002. Preservation of organic matter and alteration of its carbon and nitrogen isotope composition during simulated and in situ early sedimentary diagenesis. *Geochimica et Cosmochimica Acta*, 66(20), 3573-3584.
- Lemelle L., Labrot P., Salomé M., Simionovici A., Viso M., Westall F., 2008. In situ imaging of organic sulfur in 700-800 Myr-old Neoproterozoic microfossils using X-ray spectromicroscopy at the S K-edge. *Organic Geochemistry*, 39, 188-202.
- Lepot K., Benzerara K., Brown Jr G. E., Philippot P., 2008. Microbially influenced formation of 2,724-million-year-old stromatolites, *Nature Geoscience*, 1, 118-121.
- Liang M.-C., Hartman H., Kopp R. E., Kirschvink J. L., Yung Y. L., 2006. Production of hydrogen peroxide in the atmosphere of a Snowball Earth and the origin of oxygenic photosynthesis, *Proceedings of the National Academy of Sciences*, 103 (50), 18896-18899.
- Lowe D. R., 1999. Petrology and sedimentology of cherts and related silicified sedimentary rocks in the Swaziland Supergroup. In: Lowe D. R., Byerly G. R., *The Geological Society of America Inc., Special Paper 329*, Chapter 3, 83-114.
- Lowe D. R., Byerly G. R., 1999a. Geologic Evolution of the Barberton Greenstone Belt, South Africa. *The Geological Society of America, Inc., Special Paper 329*.
- Lowe D. R., Byerly G. R., 1999b. Stratigraphy of the west-central part of the Barberton Greenstone Belt, South Africa. In: Lowe D. R., Byerly G. R., 42 (9), Chapter 1, 1-36.
- Lowenstam H., 1981. Mineral formed by organisms. *Science*, 211, 112-1131.
- Lowers H. A., Breit G. N., Foster A. L., Whitney J., Yount J., Uddin Md. N., Muneem Ad. A., 2007. Arsenic incorporation into authigenic pyrite, Bengal Basin sediment, Bangladesh. *Geochimica et Cosmochimica Acta*, 71, 2699-2717.
- Lumsden J., Hall D. O., 1975. Superoxide dismutase in photosynthetic organisms provides an evolutionary hypothesis. *Nature*, 257, 670-672.
- Luther G. W., III, Meyerson A. L., Krajewski J. J., Hires R., 1980. Metal sulfides in estuarine sediments. *Journal of Sedimentary Research*, 50(4), 1117-1120 .
- Lyons T. W., Reinhard C. T., Planavsky N. J., 2014. The rise of oxygen in Earth's early ocean and atmosphere. *Nature*, 506, 307-315.

M

- Maliva R. G., Knoll, A. H., Simonson B. M., 2005. Secular change in the Precambrian silica cycle: Insights from chert petrology. *Geological Society of America Bulletin*, 117, 7-8, 835-845.
- Matamoros-Veloza A., Peacock C. L., Benning L. G., 2014. Selenium Speciation in Framboidal and Euhedral Pyrites in Shales. *Environmental Science and Technology*, 14, 8972-8979.
- Mathis P., 1990. Compared structure of plant and bacterial photosynthetic reaction centers. Evolutionary implications., *Biochimica et Biophysica Acta*, 1018, 163-167.
- Mauzerall D., 1992. Light, iron, Sam Granick and the origin of life, *Photosynthesis Research*, 33, 2, 163-170.

- McInerney J. O., Cotton J. A., Pisani D., 2008. The prokaryotic tree of life: past, present. . . and future?, *Trends in Ecology and Evolution*, 23, 5, 276-281.
- McKay J. L., Pederson T. F., 2014. Geochemical response to pulsed sedimentation: Implications for the use of Mo as a paleo-proxy. *Chemical Geology*, 382, 83-94.
- McLennan S. M., 1989. Rare earth elements in sedimentary rocks; influence of provenance and sedimentary processes . *Reviews in Mineralogy and Geochemistry*, 21, 169-200.
- Merchant S. S., Helmann J. D., 2012. Elemental Economy: Microbial Strategies for Optimizing Growth in the Face of Nutrient Limitation. *Advances in Microbial Physiology*, 60, 91-210.
- Merz-Preiß, 2000. Calcification in cyanobacteria. In: Riding, R.E., Awramik, S.M. (Eds.), *Microbial Sediments.*, Springer-Verlag, Berlin, 51-56.
- Miller A.-F., 2012. Superoxide dismutases: Ancient enzymes and new insights. *FEBS Letters*, 586(5), 585-595.
- Miyano T., Klein C., 1986. Fluid behavior and phase relations in the system Fe-Mg-Si-C-O-H; application to high grade metamorphism of iron-formations. *American Journal of Science*, 286(7), 540-575.
- Mojzsis S. J., Arrhenius G., McKeegan K. D., Harrison T. M., Nutman A. P., Friend C. R. L., 1996. Evidence for life on Earth before 3,800 million years ago, *Nature*, 384 (6604), 55-59.
- Mojzsis S. J., Harrison T. M., Pidgeon R. T., 2001. Oxygen-isotope evidence from ancient zircons for liquid water at the Earth's surface 4,300 Myr ago. *Nature*, 409, 178-181.
- Mojzsis S. J., Coath C. D., Greenwood J. P., McKeegan K. D., Harrison T. M., 2003. Mass-independent isotope effects in Archean (2.5 to 3.8 Ga) sedimentary sulfides determined by ion microprobe analysis, *Geochimica et cosmochimica Acta*, 67, 9, 1635-1658.
- Moore J. N., Ficklin W. H., Johns C., 1988. Partitioning of arsenic and metals in reducing sulfidic sediments. *Environmental Science and Technology*, 22, 432-437.
- Mukasa S. B., Wilson A. H., Young K. R., 2013. Geochronological constraints on the magmatic and tectonic development of the Pongola Supergroup (Central Region), South Africa. *Precambrian Research*, 224, 268-286.
- Mulkiđjanian A. Y., Koonin E. V., Makarova K. S., Mekhedov S. L., Sorokin A., Wolf Y. I., Dufresne A., Partensky F., Burd H., Kaznadzey D., Haselkorn R., Galperin M. Y., 2006. The cyanobacterial genome core and the origin of photosynthesis, *Proceedings of the National Academeý of Sciences*, 103, 35, 13126-13131.

N

- Najafpour M. M., 2011. Amorphous Manganese-Calcium Oxides as a Possible Evolutionary Origin for the CaMn₄ Cluster in Photosystem II, *Origin of Life and Evolution of the Biosphere*, 41, 3, 237-247.
- Najafpour M. M., Isaloo M. A., Eaton-Rye J. J., Tomo T., Nishihara H., Satoh K., Carpentier R., Shen J.-R., Allakhverdiev S. I., 2014. Water exchange in manganese-based water-oxidizing catalysts in photosynthetic systems: From the water-oxidizing complex in photosystem II to nano-sized manganese oxides, *Biochimica et Biophysica Acta-Bioenergetics*, 1837, 9, 1395-1410.
- Navarro-González R., McKay C. P., Nna Mvondo D., 2001. A possible nitrogen crisis for Archaean life due to reduced nitrogen fixation by lightning, *Nature*, 412(6842), 61-64.
- Nier A. O., Gulbransen E. A., 1939. Variations in the Relative Abundance of the Carbon Isotopes, *Journal of the American Chemical Society*, 61 (3), 697-698.
- Nisbet E. G., Cann J. R., van Dover C. L., 1995. Origins of photosynthesis, *Nature*, 373, 479-480.
- Nisbet E. G., Fowler C. M. R., 1999. Archean metabolic evolution of microbial mats, *Proceedings of the Royal Society of London B*, 266, 2375-2382.
- Nisbet E., Fowler M., 2011. The evolution of the atmosphere in the Archaean and early Proterozoic, *Chinese Science Bulletin*, 56, 1, 4-13.

- Noffke N., Hazen R., Nhlenko N., 2003. Earth's earliest microbial mats in a siliciclastic marine environment (2.9 Ga Mozaan Group, South Africa), *Geology*, 31, 8, 673-676.
- Noffke N., 2008. Turbulent lifestyle: Microbial mats on Earth's sandy beaches - Today and 3 billion years ago, *Geological Society of America Today*, 18, 10, 4-9.
- Noffke N., 2010. *Geobiology: Microbial mats in sandy deposits from the Archean ear to today*. Springer-Verlag, Berlin Heidelberg, Eds..
- Noffke N., Christian D., Wacey D., Hazen R. M., 2013. Microbially Induced Sedimentary Structures Recording an Ancient Ecosystem in the ca. 3.48 Billion-Year-Old Dresser Formation, Pilbara, Western Australia, *Astrobiology*, 13, 12, 1103-1124.

O

- O'Day P.A., Vlassopoulos D., Root R., Rivera N., 2004. The influence of sulfur and iron on dissolved arsenic concentrations in the shallow subsurface under changing redox conditions. *PNAS*, 101, 38, 13703-13708.
- Ohmoto H., 1997. When did the Earth's atmosphere become oxic?, *The Geochemical News*, 93, 26-27.
- Ohmoto H., 2003. Non-redox Transformations of Magnetite-Hematite in Hydrothermal Systems. *Economic Geology, Scientific Communication*, 98, 157-161.
- Ohmoto H., Watanabe Y., Ikemi H., Poulson S. R., Taylor B. E., 2006. Sulphur isotope evidence for an oxic Archean atmosphere, *Nature*, 442, 908-911.
- Ojakangas R. W., Morey G. B., Southwick D. L., 2001. Paleoproterozoic basin development and sedimentation in the Lake Superior region, North America. *Sedimentary Geology*, 141-142, 319-341.
- Olson J. M., 1970. The evolution of photosynthesis, *Science*, 168 (3930), 438-446.
- Olson J. M., Pierson B. K., 1986. Photosynthesis 3.5 thousand million years ago , *Photosynthesis Research*, 9, 1-2, 251-259.
- Olson J. M., Pierson B. K., 1987. Origin and evolution of photosynthetic reaction centers, *Origin of Life and Evolution of the Biosphere*, 17, 3-4, 419-430.
- Olson J. M., 2001. 'Evolution of Photosynthesis' (1970), re-examined thirty years later, *Photosynthesis Research*, 68, 2, 95-112.
- Olson J. M., Blankenship R. E., 2004. Thinking about the evolution of photosynthesis, *Photosynthesis Research*, 80, 373-386.
- O'Neil J., Carlson R. W., Francis D., Stevenson R. K., 2008. Neodymium-142 Evidence for Hadean Mafic Crust. *Science*, 321, 1828-1831.
- Ono S., Eigenbrode J. L., Pavlov A. A., Kharecha P., Rumble III D., Kasting J. F., Freeman K. H., 2003. New insights into Archean sulfur cycle from mass-independent sulfur isotope records from the Hamersley Basin, Australia, *Earth and Planetary Science Letters*, 213, 15-30.
- Orange F., Westall F., Disnar J.-R., Prieur D., Bienvenu N., Le Romancer M., Defarge C., 2009. Experimental silicification of the extremophilic Archaea *Pyrococcus abyssi* and *Methanocaldococcus jannaschii*: applications in the search for evidence of life in early Earth and extraterrestrial rocks. *Geobiology*, 7, 1-16.
- Oremland R. S., Hollibaugh J. T., Maest A. S., Presser T. S., Miller L. G., Culbertson C. W., 1989. Selenate Reduction to Elemental Selenium by Anaerobic Bacteria in Sediments and Culture: Biogeochemical Significance of a Novel, Sulfate-Independent Respiration. *Applied and Environmental Microbiology*, 55(9), 2333-2343.
- Oren A., Padan E., 1978. Induction of Anaerobic, Photoautotrophic Growth in the Cyanobacterium *Oscillatoria limnetica*., *Journal of Bacteriology*, 133, 2, 558-563.
- Ormerod J., 1992. Physiology of the Photosynthetic Prokaryotes, In: Mann N. H. and Carr N. G. (eds), *Photosynthetic Prokaryotes*, Plenum Press, New York, 93-120.
- Osman D., Cavet J. S., 2008. Copper Homeostasis in Bacteria. *Advances in Applied Microbiology*, 65, 217-247.

P

- Papineau D., Mojzsis S. J., Karhu J. A., Marty B., 2005. Nitrogen isotopic composition of ammoniated phyllosilicates: case studies from Precambrian metamorphosed sedimentary rocks. *Chemical Geology*, 216, 37-58.
- Park R., Epstein S., 1960. Carbon isotope fractionation during photosynthesis, *Geochimica et Cosmochimica Acta*, 21(1-2), 110-126.
- Pavlov A. A., Kasting J. F., 2002. Mass-Independent Fractionation of Sulfur Isotopes in Archean Sediments: Strong Evidence for an Anoxic Archean Atmosphere, *Astrobiology*, 2, 1, 27-41.
- Payne J. L., McClain C. R., Boyer A. G., Brown J. H., Finnegan S., Kowalewski M., Krause Jr. R. A., Lyons S. K., McShea D. W., Novack-Gottshall P. M., Smith F. A., Spaeth P., Stempien J. A., Wang S. C., 2011. The evolutionary consequences of oxygenic photosynthesis: a body size perspective, *Photosynthesis Research*, 107, 37-57.
- Pearson V. K., Sephton M. A., Franchi I. A., Gibson J. M., Gilmour I., 2006. Carbon and nitrogen in carbonaceous chondrites: Elemental abundances and stable isotopic compositions. *Meteoritics & Planetary Science*, 41, 1899-1918.
- Perkins R. B., Piper D. Z., Mason C. E., 2008. Trace-element budgets in the Ohio/Sunbury shales of Kentucky: Constraints on ocean circulation and primary productivity in the Devonian-Mississippian Appalachian Basin. *Palaeogeography, Palaeoclimatology, Palaeoecology*, 265, 14-29.
- Perry Jr E. C., Lefticariu L., 2014. Formation and Geochemistry of Precambrian Cherts. *Treatise on Geochemistry 2nd Edition*, Elsevier Ltd, Chapter 9.5, 113-139.
- Peters K. E., Sweeney R. E., Kaplan I. R., 1978. Correlation of carbon and nitrogen stable isotope ratios in sedimentary organic matter. *Limnology and Oceanography*, 23(4), 598-604.
- Piper D. Z., Calvert S. E., 2009. A marine biogeochemical perspective on black shale deposition.. *Earth-Science Reviews*, 95, 63-96.
- Pisapia C., 2006. Identification de biosignatures structurales, chimiques et isotopiques à l'interface bactérie/minéral dans le système *Acidithiobacillus ferrooxidans*/pyrite. Thèse de Doctorat, Institut National Polytechnique de Lorraine, Nancy, France.
- Pizzarello S., Cooper G. W., Flynn G. J., 2010. The Nature and Distribution of the Organic Material in Carbonaceous Chondrites and Interplanetary Dust Particles. In: *Meteorites and the Early Solar System II*, 625-651.
- Planavsky N., Rouxel O., Bekker A., Shapiro R., Fralick P., Knudsen A., 2009. Iron-oxidizing microbial ecosystems thrived in late Paleoproterozoic redox-stratified oceans, *Earth and Planetary Science Letters*, 286, 230-242.
- Planavsky N. J., Bekker A., Rouxel O. J., Kamber B., Hofmann A., Knudsen A., Lyons T. W., 2010. Rare Earth Element and Yttrium compositions of Archean and Paleoproterozoic Fe formations revisited: New perspectives on the significance and mechanisms of deposition. *Geochimica et Cosmochimica Acta*, 74 (22), 6387-6405.
- Planavsky N. J., McGoldrick P., Scott C. T., Li C., Reinhard C. T., Kelly A. E., Chu X., Bekker A., Love G. D., Lyons T. W., 2011. Widespread iron-rich conditions in the mid-Proterozoic ocean. *Nature*, 477, 448-451.
- Planavsky N. J., Asael D., Hofmann A., Reinhard C. T., Lalonde S. V., Knudsen A., Wang X., Ossa Ossa F., Pecoits E., Smith A. J. B., Beukes N., Bekker A., Johnson T. M., Konhauser K. O., Lyons T. W., Rouxel O. J., 2014. Evidence for oxygenic photosynthesis half a billion years before the Great Oxidation Event, *Nature Geoscience*, 7, 283-286.
- Posth N. R., Huelin S., Konhauser K. O., Kappler A., 2010. Size, density and composition of cell-mineral aggregates formed during anoxygenic phototrophic Fe(II) oxidation: Impact on modern and ancient environments. *Geochimica et Cosmochimica Acta*, 74, 3476-3493.

- Posth N. R., Konhauser K. O., Kappler A., 2011. Banded Iron Formations. *Encyclopedia of Geobiology*, (Eds) J. Reitner, V. Thiel, Springer, 92-103.
- Poulton S. W., Fralick P. W., Canfield D. E., 2004. The transition to a sulphidic ocean, 1.84 billion years ago. *Nature*, 431 (7005), 173-177.
- Poulton S. W., Canfield D. E., 2011. Ferruginous Conditions: A Dominant Feature of the Ocean through Earth's History. *Elements*, 7, 107-112.

R

- Rademacher C., Masepohl B., 2012. Copper-responsive gene regulation in bacteria. *Microbiology*, 158, 2451-2464.
- Raiswell R., Plant J., 1980. The incorporation of trace elements into pyrite during diagenesis of black shales, Yorkshire, England. *Economic Geology*, 75, 684-699.
- Ramdohr P., 1958. New observations on the ores of the Witwatersrand in South Africa and their genetic significance. *Transactions of the Geological Society of South Africa*, 61, 1-50.
- Rasmussen B., Buick R., 1999. Redox state of the Archean atmosphere: Evidence from detrital heavy minerals in ca. 3250-2750 Ma sandstones from the Pilbara Craton, Australia. *Geology*, 27, 2, 115-118.
- Raymond J., Zhaxybayeva O., Gogarten J. P., Gerdes S. Y., Blankenship R. E., 2002. Whole-genome analysis of photosynthetic prokaryotes. *Science*, 298, 1616-1620.
- Raymond J., Zhaxybayeva O., Gogarten J. P., Blankenship R. E., 2003. Evolution of photosynthetic prokaryotes: a maximum-likelihood mapping approach. *Philosophical Transactions of the Royal Society of London B*, 358, 223-230.
- Raymond J., Blankenship R. E., 2008. The origin of the oxygen-evolving complex. *Coordination Chemistry Reviews*, 252, 377-383.
- Ridge P. G., Zhang Y., Gladyshev V. N., 2008. Comparative Genomic Analyses of Copper Transporters and Cuproproteomes Reveal Evolutionary Dynamics of Copper Utilization and Its Link to Oxygen. *PloS One*, 3(1), e1378.
- Riding R., 2000. Microbial carbonates: the geological record of calcified bacterial-algal mats and biofilms. *Sedimentology*, 47, 179-214.
- Riding R., Fralick P., Liang L., 2014. Identification of an Archean marine oxygen oasis. *Precambrian Research*, 251, 232-237.
- Roscoe S. M., 1996. Paleoplacer uranium gold, In: Eckstrand OR, Sinclair WD, Thorpe RI (eds) *Geology of Canadian mineral deposit types*, vol P-1. , Geological Society of America, *The Geology of North America*, Boulder, 10-23.
- Rosing M. T., 1999. ^{13}C -Depleted carbon microparticles in >3700-Ma sea-floor sedimentary rocks from west Greenland. *Science*, 283, 674-676.
- Roth A. S. G., Bourdon B., Mojzsis S. J., Toubou L. M., Sprung P., Guitreau M., Blichert-Toft J., 2013. Inherited ^{142}Nd anomalies in Eoarchean protoliths. *Earth and Planetary Science Letters*, 361, 50-57.
- Rouchy J. M., Monty C., 2000. Gypsum Microbial Sediments: Neogene and Modern Examples. In: Riding, R.E., Awramik, S.M. (Eds.), *Microbial Sediments*, Springer-Verlag, Berlin, 209-216.
- Rouxel O. J., Bekker A., Edwards K. J., 2005. Iron Isotope Constraints on the Archean and Paleoproterozoic Ocean Redox State. *Science*, 307 (5712), 1088-1091.
- Rouzaud J.-N., Deldicque D., Velde B., 2012. Raman Microspectrometry Study Of Carbonization Processes. First Promising Application In Archeology. Annual World Conference on Carbon (Carbon 2012), Krakow, Poland, 17-22 June, abstract #956.
- Roy S., 1997. Genetic diversity of manganese deposition in the terrestrial geological record. *Geological Society of London, Special Publications*, 119, 5-27.
- Roy S., 2006. Sedimentary manganese metallogenesis in response to the evolution of the Earth system. *Earth-Science Reviews*, 77(4), 273-305.

- Russell M. J., Hall A. J., 2006. The onset and early evolution of life, *Geological Society of America Bulletin-Memoirs*, 198, 1-32.
- Russell M. J., Allen J. F., Milner-White E. J., 2008. Inorganic Complexes Enabled the Onset of Life and Oxygenic Photosynthesis, In: *Photosynthesis, Energy from the Sun*, eds Allen J, Gantt E, Golbec J, Osmond B (Springer, Dordrecht, The Netherlands), 1187–1192.

S

- Sauer K., Yachandra V. K., 2002. A possible evolutionary origin for the Mn⁴ cluster of the photosynthetic water oxidation complex from natural MnO₂ precipitates in the early ocean, *Proceedings of the National Academy of Sciences of the United States of America*, 99(13), 8631–8636.
- Sauer K., Yano J., Yachandra V. K., 2008. X-ray spectroscopy of the photosynthetic oxygen-evolving complex, *Coordination Chemistry Reviews*, 252, 318–335.
- Schieber J., 2002. Sedimentary pyrite: A window into the microbial past. *Geology*, 30(6), 531-534.
- Schelble R. T., Westall F., Allen C. C., Brearley A. J., 2001. Hematite mineralized bacterial remnants: implications for Martian hematite deposits. *Lunar and Planetary Science XXXII*, conference abstract 1438.
- Schelble R. T., Westall F., Allen C. C., 2004. ~1.8 Ga iron-mineralized microbiota from the Gunflint Iron Formation, Ontario, Canada: implications for Mars. *Advances in Space Research*, 33(8), 1268–1273.
- Schidlowski M., Hayes J. M., Kaplan I. R., 1983. Isotopic inferences of ancient biochemistries: Carbon, sulfur, hydrogen and nitrogen.. In *Earth's Earliest Biosphere* (ed. J. W. Schopf), Princeton University Press, 149–186.
- Schidlowski M., 1988. A 3,800-million-year isotopic record of life from carbon in sedimentary rocks, *Nature*, 333, 313-318.
- Schidlowski M., 2000. Carbon Isotopes and Microbial Sediments, In: Riding, R.E., Awramik, S.M. (Eds.), *Microbial Sediments.*, Springer-Verlag, Berlin, 84-95.
- Schopf J. W., 1993. Microfossils of the Early Archean Apex Chert: New Evidence of the Antiquity of Life, *Science*, 260(5108), 640-646.
- Schopf J. W., Kudryavtsev A. B., Czaja A.D., Tripathi A. B., 2007. Evidence of Archean life: Stromatolites and microfossils, *Precambrian Research*, 158, 141–155.
- Schopf J. W., 2011. The paleobiological record of photosynthesis, *Photosynthesis Research*, 107, 87-101.
- Scott C., Lyons T. W., Bekker A., Shen Y., Poulton S. W., Chu X., Anbar A. D., 2008. Tracing the stepwise oxygenation of the Proterozoic ocean. *Nature*, 452, 456-460.
- Selles-Martinez J., 1996. Concretion morphology, classification and genesis. *Earth-Science Reviews*, 41, 177-210.
- Sephton M. A., 2002. Organic compounds in carbonaceous meteorites. *Natural Product Reports - Royal Society of Chemistry*, 19, 292-311.
- Severmann S., Johnson C. M., Beard B. L., Yevenes M., Huerta-Diaz M. A., Thamdrup B., Hoehler T., Welch S., 2004. Fe and S isotope variations in cyanobacterial mats: modern analogues of ancient stromatolites. *EOS Transactions*, 85, 47.
- Sforna M.-C., van Zuilen M. A., Philippot P., 2014. Structural characterization by Raman hyperspectral mapping of organic carbon in the 3.46 billion-year-old Apex chert, Western Australia. *Geochimica and Cosmochimica Acta*, 124, 18-33.
- Sforna M.-C., Philippot P., Somogyi A., van Zuilen M. A., Medjoubi K., Schoepp-Cothenet B., Nitschke W., Visscher P. T., 2014b. Evidence for arsenic metabolism and cycling by microorganisms 2.7 billion years ago. *Nature Geoscience*, 7, 811–815.
- Shapiro R. S., Konhauser K. O., 2015. Hematite-coated microfossils: primary ecological fingerprint or taphonomic oddity of the Paleoproterozoic?. *Geobiology*, 13, 209–224.
- Siebert C., Kramers J. D., Meisel Th., Morel Ph., Nägler Th. F., 2005. PGE, Re-Os, and Mo isotope systematics in Archean and early Proterozoic sedimentary systems as proxies for

- redox conditions of the early Earth, *Geochimica et Cosmochimica Acta*, 69, 7, 1787–1801.
- Siever R., 1957. The silica budget in the sedimentary cycle. *The American Mineralogist*, 42, 821-841.
- Siever R., 1992. The silica cycle in the Precambrian. *Geochimica et Cosmochimica Acta*, 56(8), 3265–3272.
- Simionovici A. S., Hubert A., Quitté G., Lemelle L., Ferroir T., Solé V. A., 2010. Semi-quantitative analysis of bulk chondritic material using X-ray fluorescence spectroscopy. *Proceedings of the Meteoritical Society Conference*, # 5149, New York., USA, July, 2010.
- Simionovici A. S., Beck P., Lemelle L., Hubert A., Quitté G., Westphal A., Schoonjans T., Vincze L., Solé V. A., Toucoulou R., Fihman F., Chazalnoel P., Viso M., 2012. Non-destructive multispectral imaging of Hazmat samples. *Proceedings of the Committee on Space Research (COSPAR) Conference*, 2012.
- Simionovici A., Hubert A., Lemelle L., Schoonjans T., Westall F., Hascke M. XRF quantification of undetected low Z elements by scattering in Earth & Planetary Sciences samples. *Analytical Chemistry*, in preparation, 2015.
- Smedley P. L., Kinniburgh D. G., 2002. A review of the source, behaviour and distribution of arsenic in natural waters. *Applied Geochemistry*, 17, 517–568.
- Smith B., 2007. The Paleo-environmental significance of the iron formations and iron-rich mudstones of the Mesoarchean Witwatersrand-Mozaan Basin, South Africa. Unpublished M.Sc. Thesis, University of Johannesburg, South Africa, 207pp.
- Solé V. A., Papillon E., Cotte M., Walter Ph., Susini J., 2007. A multiplatform code for the analysis of energy-dispersive X-ray fluorescence spectra. *Spectrochimica Acta Part B*, 62, 63-68.
- Stolz J. F., Basu P., Santini J. M., Oremland R. S., 2006. Arsenic and Selenium in Microbial Metabolism. *Annual Review of Microbiology*, 60, 107-130.
- Summons R. E., Powell T. G., Boreham C. J., 1988. Petroleum geology and geochemistry of the Middle Proterozoic McArthur Basin, Northern Australia: III. Composition of extractable hydrocarbons, *Geochimica et Cosmochimica Acta*, 52, 1747-1763.
- Summons R. E., Jahnke L. L., Hope J. M., Logan G. M., 1999. 2-Methylhopanoids as biomarkers for cyanobacterial oxygenic photosynthesis, *Nature*, 400, 554-557.
- Summons R. E., Bradley A. S., Jahnke L. L., Waldbauer J. L., 2006. Steroids, triterpenoids and molecular oxygen, *Philosophical Transactions of the Royal Society B*, 361, 951–968.
- Sweeney R. E., Liu K. K., Kaplan I. R., 1978. Oceanic nitrogen isotopes and their uses in determining the source of sedimentary nitrogen. In: Robinson BW (eds.), *Stable Isotopes in the Earth Sciences*, volume 220. DSIR Bulletin, Wellington, 9-26.

T

- Tamura N., Cheniae G., 1987. Photoactivation of the water-oxidizing complex in Photosystem II membranes depleted of Mn and extrinsic proteins. I. Biochemical and kinetic characterization, *Biochimica et Biophysica Acta-Bioenergetics*, 890(2), 179-194.
- Tang H.-S., Chen Y.-J., Santosh M., Zhong H., Yang T., 2013. REE geochemistry of carbonates from the Guanmenshan Formation, Liaohe Group, NE Sino-Korean Craton: Implications for seawater compositional change during the Great Oxidation Event. *Precambrian Research*, 227, 316–336.
- Tebo B. M., Johnson H. A., McCarthy J. K., Templeton A. S., 2005. Geomicrobiology of manganese(II) oxidation. *TRENDS in Microbiology*, 13(9), 421-428.
- Thode H. G., Monster J., Dunford H. B., 1961. Sulphur isotope geochemistry, *Geochimica et Cosmochimica Acta*, 25, 150-174.
- Thode H. G., 1991. Stable Isotopes in the Assessment of Natural and Anthropogenic Sulphur in the Environment, In: H.R. Krouse and V.A. Grinenko (Eds): *Stable Isotopes in the Assessment of Natural and Anthropogenic Sulphur in the Environment*. , SCOPE 43, Chapter 1. J. Wiley & Sons Publishers., 1-26.

- Tice M. M., Bostick B. C., Lowe D. R., 2004. Thermal history of the 3.5–3.2 Ga Onverwacht and Fig Tree Groups, Barberton greenstone belt, South Africa, inferred by Raman microspectroscopy of carbonaceous material. *Geology*, 32(1), 37–40.
- Tice M. M., Lowe D. R., 2004. Photosynthetic microbial mats in the 3,416-Myr-old ocean, *Nature*, 431, 549–552.
- Tice M. M., Lowe D. R., 2006. The origin of carbonaceous matter in pre-3.0 Ga greenstone terrains: A review and new evidence from the 3.42 Ga Buck Reef Chert, *Earth-Science Reviews*, 76, 259–300.
- Tissot F., Dauphas N., Reinhard C. T., Lyons T., Asael D., Rouxel O., 2012. Mo and U Geochemistry and Isotopes. Book Chapter, ?, ?.
- Tourney J., Ngwenya B. T., 2014. The role of bacterial extracellular polymeric substances in geomicrobiology. *Chemical Geology*, 386, 115–132.
- Tran R., Kern J., Hattne J., Koroidov S., Hellmich J., Alonso-Mori A., Sauter N. K., Bergmann U., Messinger J., Zouni A., Yano J., Yachandra V. K., 2014. The Mn4Ca photosynthetic water-oxidation catalyst studied by simultaneous X-ray spectroscopy and crystallography using an X-ray free-electron laser, *Philosophical Transactions of the Royal Society B*, 369, .
- Tribouillard N., Algeo T. J., Lyons T., Riboulleau A., 2006. Trace metals as paleoredox and paleoproductivity proxies: An update. *Chemical Geology*, 232, 12–32.
- Tuinstra F., Koenig J. L., 1970. Raman spectrum of graphite. *Journal of Chemical Physics*, 53, 1126–1130.
- Tyler S. A., Barghoorn E. S., 1954. Occurrence of Structurally Preserved Plants in Pre-Cambrian Rocks of the Canadian Shield. *Science*, 119, 606–608.
- Tyler S. A., Barghoorn E. S., Barrett L. P., 1957. Anthracitic Coal From Precambrian Upper Huronian Black Shale Of The Iron River District, Northern Michigan, *Geological Society of America Bulletin*, 68 (10), 1293–1304.

U

- Ueno Y., Isozaki Y., Yurimoto H., Maruyama S., 2001. Carbon isotopic Signatures of Individual Archean Microfossils(?) from Western Australia, *International Geology Review*, 43, 196–212.
- Ueno Y., Yurimoto H., Yoshioka H., Komiya T., Maruyama S., 2002. Ion microprobe analysis of graphite from ca. 3.8 Ga metasediments, Isua supracrustal belt, West Greenland: Relationship between metamorphism and carbon isotopic composition. *Geochimica et Cosmochimica Acta*, 66(7), 1257–1268.
- Ueno Y., Maruyama S., Yoshioka H., Isozaki Y., 2004. Carbon isotopes and petrography of kerogens in ~3.5-Ga hydrothermal silica dikes in the North Pole area, Western Australia, *Geochimica et Cosmochimica Acta*, 68(3), 573–589.
- Umena Y., Kawakami K., Shen J. R., Kamiya N., 2011. Crystal structure of oxygen-evolving photosystem II at a resolution of 1.9 Å, *Nature*, 473, 55–60.

V

- Van den Boorn S. H. J. M., van Bergen M. J., Nijman W., Vroon P. Z., 2007. Dual role of seawater and hydrothermal fluids in Early Archean chert formation: Evidence from silicon isotopes. *The Geological Society of America*, 35(10), 939–942.
- Van Kranendonk M. J., Webb G. E., Kamber B. S., 2003. Geological and trace element evidence for a marine sedimentary environment of deposition and biogenicity of 3.45 Ga stromatolitic carbonates in the Pilbara Craton, and support for a reducing Archaean ocean, *Geobiology*, 11, 91–108.

- Vasconcelos C., Warthmann R., McKenzie J. A., Visscher P. T., Bittermann A. G., van Lith Y., 2006. Lithifying microbial mats in Lagoa Vermelha, Brazil: Modern Precambrian relics?. *Sedimentary Geology*, 185, 175–183.
- van den Boorn S. H. J. M., van Bergen M. J., Nijman W., Vroon P. Z., 2007. Dual role of seawater and hydrothermal fluids in Early Archean chert formation: Evidence from silicon isotopes. *The Geological Society of America*, 35(10), 939–942.
- Vaughan D.J., Rosso, K.L., 2006. Chemical Bonding in Sulfide Minerals. *Reviews in Mineralogy and Geochemistry*, 61, 231-264.
- Volkov I. I., Fomina L. S., 1974. Influence of organic material and processes of sulfide formation on distribution of some trace elements in deep water sediments of the Black Sea. In: D. A. Ross and E. T. Degens (Editors), *The Black Sea – Geology, Chemistry, and Biology*, American Association of Petroleum Geologists, Memoir 20, 456–476.
- von Brun V., Mason T. R., 1977. Siliciclastic-carbonate tidal deposits from the 3000 M.Y. Pongola Supergroup, South Africa. *Sedimentary Geology*, 18, 245-255.

W

- Wacey D., Saunders M., Brasier M. D., Kilburn M. R., 2011. Earliest microbially mediated pyrite oxidation in ~3.4 billion-year-old sediments, *Earth and Planetary Science Letters*, 301, 393–402.
- Wacey D., McLoughlin N., Kilburn M. R., Saunders M., Cliff J., Kong C., Barley M. E., Brasier M. D., 2013. Nanoscale analysis of pyritized microfossils reveals differential heterotrophic consumption in the ~1.9-Ga Gunflint chert. *Proceedings of the National Academy of Sciences*, 110(20), 8020-8024.
- Waldbauer J. R., Sherman L. S., Sumner D. Y., Summons R. E., 2009. Late Archean molecular fossils from the Transvaal Supergroup record the antiquity of microbial diversity and aerobiosis, *Precambrian Research*, 169, 28-47.
- Walsh M. M., 1992. Microfossils and possible microfossils from the Early Archean Onverwacht Group, Barberton Mountain Land, South Africa. *Precambrian Research*, 54, 271-293.
- Walsh M. M., 2004. Evaluation of Early Archean Volcaniclastic and Volcanic Flow Rocks as Possible Sites for Carbonaceous Fossil Microbes. *Astrobiology*, 4(4), 429-437.
- Walter M. R., Buick R., Dunlop J. S. R., 1980. Stromatolites 3,400–3,500 Myr old from the North Pole area, Western Australia, *Nature*, 284, 443-445.
- Wang S., Mulligan C. N., 2008. Speciation and surface structure of inorganic arsenic in solid phases: A review. *Environment International*, 34, 867–879.
- Wang Y., Zhou M., Gong X., Liu C., Hong M., Wang L., Hong F., 2011. Influence of Lanthanides on the Antioxidative Defense System in Maize Seedlings Under Cold Stress. *Biological Trace Element Research*, 142(3), 819-830.
- Westall F., Boni L., Guerzoni E., 1995. The experimental silicification of microorganisms. *Palaeontology*, 38, 495-528.
- Westall F., 1997. The influence of cell wall composition on the fossilisation of bacteria and the implications for the search for early life forms. In: Cosmovici C. B., Bowyer S., Werthimer D. (Eds.), *Astronomical and Biochemical Origins and The Search For Life in The Universe*. Editori compositrici, Bolgna, 491-504.
- Westall, F., Steele, A., Toporski, J. Walsh, M., Allen, C., Guidry, S., Gibson, E., Mckay, D., Chafetz, H., 2000. Polymeric substances and biofilms as biomarkers in terrestrial materials: Implications for extraterrestrial samples. *Journal of Geophysical Research: Planets*, 105, 24511-24527.
- Westall F., de Wit M.J., Dann J., van der Gaast S., de Ronde C. E. J., Gerneke D., 2001. Early Archean fossil bacteria and biofilms in hydrothermally-influenced sediments from the Barberton greenstone belt, South Africa, *Precambrian Research*, 106, 93-116.

- Westall F., Folk R. L., 2003. Exogenous carbonaceous microstructures in Early Archaean cherts and BIFs from the Isua Greenstone Belt: implications for the search for life in ancient rocks. *Precambrian Research*, 126, 313-330.
- Westall F., Southam G., 2006. Early life on Earth, In: Benn K., Marccha J. C., Kondie K. C. (eds.) *Archean geodynamics and environments geophysical*, Monograph 164, AGU, Washington, 283-304.
- Westall F., de Ronde C. E. J., Southam G., Grassineau N., Colas M., Cockell C., Lammer H., 2006. Implications of a 3.472-3.333 Gyr-old subaerial microbial mat from the Barberton greenstone belt, South Africa for the UV environmental conditions on the early Earth, *Philosophical Transactions of the Royal Society B*, 361, 1857-1875.
- Westall F., Foucher F., Cavalazzi B., de Vries S. T., Nijman W., Pearson V., Watson J., Verchovsky A., Wright I., Rouzaud J.-N., Marchesini D., Anne S., 2011a. Volcaniclastic habitats for early life on Earth and Mars: A case study from 3.5 Ga-old rocks from the Pilbara, Australia, *Planetary and Space Science*, 59, 1093-1106.
- Westall F., Cavalazzi B., Lemelle L., Marrocchi Y., Rouzaud J.-N., Simionovici A., Salomé M., Mostafaoui S., Andrezza C., Foucher F., Toporski J., Jauss A., Thiel V., Southam G., Maclean L., Wirick S., Hofmann A., Meibom A., Robert F., Défarge C., 2011b. Implications of in situ calcification for photosynthesis in a 3.3 Ga-old microbial biofilm from the Barberton greenstone belt, South Africa, *Earth and Planetary Science Letters*, 310, 468-479.
- Westall, F., Cavalazzi, B., 2011. Biosignatures in rocks, In "Encyclopedia of Geobiology" V. Thiel, J. Reitner (Eds.), Springer, Berlin, 189-201.
- Westall, F., Campbell K.A., Breheret J.-G., Foucher F., Gautret P., Hubert A., Sorieul S., Grassineau N., Guido D. M., 2015. Archean (3.33 Ga) microbe-sediment systems were diverse and flourished in a hydrothermal context. *Geology*, 43(7), 615-618.
- Widdel F., Schnell S., Heising S., Ehrenreich A., Assmus B., Schink B., 1993. Ferrous iron oxidation by anoxygenic phototrophic bacteria. *Nature*, 362, 834-836.
- Wilde S. A., Valley J. W., Peck W. H., Graham C. M., 2001. Evidence from detrital zircons for the existence of continental crust and oceans on the Earth 4.4 Gyr ago. *Nature*, 409, 175-178.
- Wilson J. P., Woodward W. F., Johnston D. T., Knoll A. H., Grotzinger J. P., Walter M. R., McNaughton N. J., Simon M., Abelson J., Schrag D. P., Summons R., Allwood A., Andres M., Gammon C., Garvin J., Rashby S., Schweizer M., Watters W. A., 2010. Geobiology of the Late Paleoproterozoic Duck Creek Formation, Western Australia. *Precambrian Research*, 179, 135-149.
- Wilson A., Groenewald B., Palmer C., 2013. Volcanic and volcaniclastic rocks of the Mesoarchaean Pongola Supergroup in South Africa and Swaziland: distribution, physical characteristics, stratigraphy and correlations. *South African Journal of Geology*, 116(1), 119-168.
- Wille M., Kramers J.D., Nägler T.F., Beukes N.J., Schröder S., Meisel Th., Lacassie J.P., Voegelin A.R., 2007. Evidence for a gradual rise of oxygen between 2.6 and 2.5 Ga from Mo isotopes and Re-PGE signatures in shales, *Geochimica et Cosmochimica Acta*, 71 (22), 2417-2435.
- Williford K. H., Van Kranendonk M. J., Ushikubo T., Kozdon R., Valley J. W., 2011. Constraining atmospheric oxygen and seawater sulfate concentrations during Paleoproterozoic glaciation: In situ sulfur three-isotope microanalysis of pyrite from the Turee Creek Group, Western Australia. *Geochimica et Cosmochimica Acta*, 75, 5686-5705.
- Williford K. H., Ushikubo T., Schopf J. W., Lepot K., Kitajima K., Valley J. W., 2013. Preservation and detection of microstructural and taxonomic correlations in the carbon isotopic compositions of individual Precambrian microfossils. *Geochimica et Cosmochimica Acta*, 104, 165-182.
- Winter B. L., Knauth L. P., 1992. Stable isotope geochemistry of cherts and carbonates from the 2.0 Ga Gunflint Iron Formation: implications for the depositional setting, and the effects of diagenesis and metamorphism. *Precambrian Research*, 59, 283-313.
- Wood J. A., Dickey Jr J. S., Marvin U. B., Powell B., 1970. Lunar Anorthosites. *Science*, 167, 602-604.

Wu W., Swanner E. D., Hao L., Zeitvogel F., Obst M., Pan Y., Kappler A., 2014. Characterization of the physiology and cell – mineral interactions of the marine anoxygenic phototrophic Fe(II) oxidizer *Rhodovulum iodolum* – implications for Precambrian Fe(II) oxidation. *FEMS Microbiology Ecology*, 88 (3), 503-515.

X

Xie X., Byerly G. R., Ferrell R. E., 1997. Ilb trioctahedral chlorite from the Barberton greenstone belt: crystal structure and rock composition constraints with implications to geothermometry. *Contributions to Mineralogy and Petrology*, 126(3), 275-291.

Xiong J., Fischer W. M., Inoue K., Nakahara M., Bauer C.E., 2000. Molecular Evidence for the Early Evolution of Photosynthesis, *Science*, 289(5485), 1724-1730.

Xiong J., Bauer C.E., 2002. Complex evolution of photosynthesis, *Annual Review of Plant Biology*, 53, 503-521.

Y

Yachandra V. K., Sauer K., Klein M.P., 1996. Manganese Cluster in Photosynthesis: Where Plants Oxidize Water to Dioxygen, *Chemical Reviews*, 96(7), 2927-2950.

Yano J., Kern J., Sauer K., Latimer M. J., Pushkar Y., Biesiadka J., Loll B., Saenger W., Messinger J., Zouni A., Yachandra V. K., 2006. Where Water Is Oxidized to Dioxygen: Structure of the Photosynthetic Mn₄Ca Cluster., *Science*, 314(5800), 821-825.

Yano J., Yachandra V. K., 2014. Mn₄Ca Cluster in Photosynthesis: Where and How Water is Oxidized to Dioxygen, *Chemical Reviews*, 114, 4175-4205.

Yee N., Phoenix V. R., Konhauser K. O., Benning L.G., Ferris F. G., 2003. The effect of cyanobacteria on silica precipitation at neutral pH: implications for bacterial silicification in geothermal hot springs. *Chemical Geology*, 199, 83-90.

Z

Zahnle K., Claire M., Catling D., 2006. The loss of mass-independent fractionation in sulfur due to a Palaeoproterozoic collapse of atmospheric methane, *Geobiology*, 4 (4), 271-283.

Zehr J. .P., Oremland R. S., 1987. Reduction of Selenate to Selenide by Sulfate-Respiring Bacteria: Experiments with Cell Suspensions and Estuarine Sediments. *Applied and Environmental Microbiology*, 53(6), 1365-1369.

Zerle A.L., House C.H., Brantley S.L., 2005. Biogeochemical signatures through time as inferred from whole microbial genomes. *American Journal of Science*, 305, 467-502.

Zhang L., Zeng F., Xiao R., 2003. Effect of lanthanum ions (La³⁺) on the reactive oxygen species scavenging enzymes in wheat leaves. *Biological Trace Element Research*, 91(3), 243-252.

Zhu X. K., O'Nions R. K., Guo Y., Reynolds B. C., 2000. Secular Variation of Iron Isotopes in North Atlantic Deep Water. *Science*, 287 (5460), 2000-2002.

Annex

Annex 1: The biochemical processes of bacteria photosynthesis.

In Chapter I of this manuscript, we described in a simplified manner the biochemical processes of bacterial photosynthesis with the sole aim of gathering knowledge on the characteristic molecular component of the photosynthetic machinery and more specifically, on the chemical elements that they contain (mg, Fe, S, Cu, Mn, Ca...). This document presents another version of this section, in which the precise biological vocabulary is included.

1. Anoxygenic photosynthesis

Among the Bacteria, anoxygenic photosynthesis is carried out by the following groups, classified based on their pigment content and the type of electron donor they use: green sulfur bacteria, green non-sulfur bacteria, purple sulfur bacteria, purple non-sulfur bacteria and heliobacteria (Ormerod, 1992).

At the core of their photosynthetic machinery, all photosynthetic bacteria possess a molecular complex called “photosystem”, located in the cell membrane (Fig. I.1). Anoxygenic photosynthetic bacteria possess either one or the other of the two existing kinds of photosystems, called type 1 and type 2. In both cases, an electron transport chain is created between the three major components of the photosystem: (i) the reaction center, where the conversion of light energy to chemical redox energy takes place; electrons excited by this photochemical event are then cycled between (ii) a pool of ubiquinone molecules in the photosynthetic membrane playing the role of mobile electron carriers, and (iii) a transmembrane complex called cytochrome complex allowing the recycling of electrons.

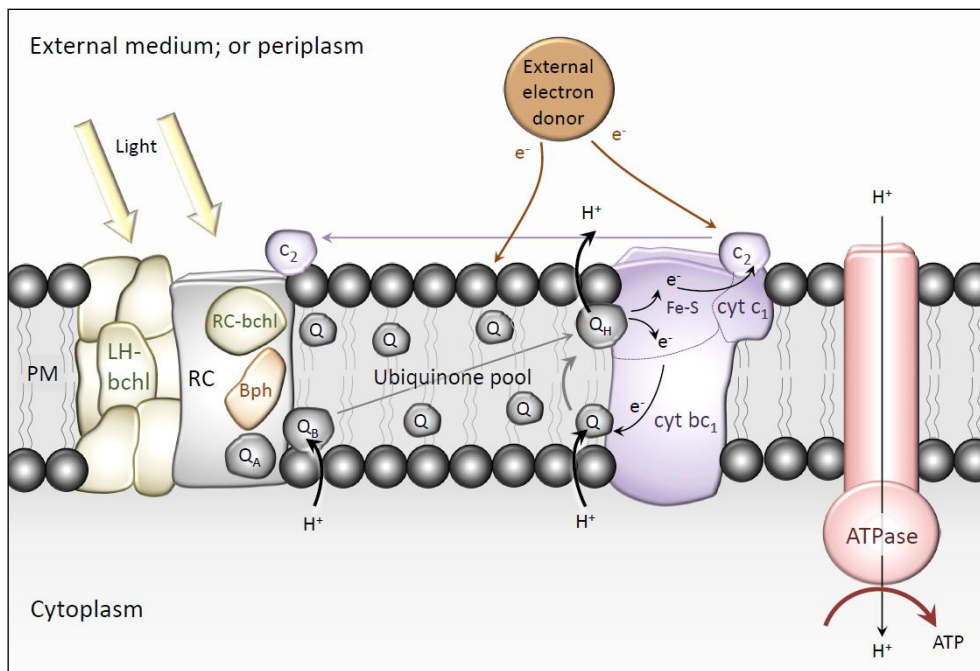


Figure I.1. Sketch of the type 2 photosystem and electronic transport chain in the membrane of a photosynthetic bacterium. PM: plasma membrane; LH-bchl: light-harvesting bacteriochlorophyll; RC: reaction center; RC-bchl: reaction center bacteriochlorophyll; Bph: bacteriopheophytin; Q: quinone molecule; Q_H: hydroquinone. Modified from Konhauser, 2007b.

During anoxygenic photosynthesis, light photons are collected by light-harvesting bacteriochlorophylls located in the membrane of the cell and are then transferred to the bacteriochlorophylls of the reaction center (henceforth called RC-bacteriochlorophylls). After this photochemical event, RC-bacteriochlorophylls become good electron donors. Excited electrons are transferred to the photosynthetic membrane where ubiquinone molecules, which are good electron acceptors, act as carriers and diffuse to the end-member transmembrane molecular complex called cytochrome bc₁. The latter contains iron able to alternate between the Fe(II) and Fe(III) states and possesses redox reactions sites to host both oxidation and reduction reactions on ubiquinone molecules allowing the transfer of electrons back to the ubiquinone pool for another cycle. This is called the “Q cycle”.

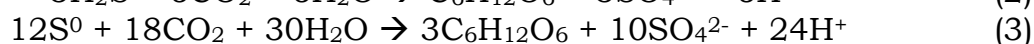
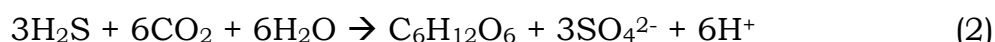
Specifically, the fully oxidized electron acceptor quinone molecule is reduced to hydroquinone with a simultaneous extraction of two protons from the cytoplasm. The hydroquinone diffuses to the cytochrome complex where it is oxidized back to quinone and both protons are released to the periplasm. This has the effect of creating a proton motive force between the cytoplasm and the periplasm. In the cytochrome complex, recently acquired electrons coming from the oxidation of the hydroquinone are transferred back to the ubiquinone pool for another cycle. The proton motive force created in the ubiquinone pool generates a proton gradient from the periplasm to the cytoplasm that supplies the ATP synthase enzyme, generating energy for the cell under the ATP form, via photophosphorylation.

The process by which ATP is generated differs between type 1 and type 2 photosystems. In both cases, ATP is produced as a consequence to the proton gradient created in the ubiquinone pool. In the type 2 photosystem, electrons are continuously cycled without any net input or consumption. The process is called cyclic photophosphorylation. In type 1 photosystem, the reaction center needs the input of electrons coming from external donors to become oxidized again and complete another cycle. In this case, the photophosphorylation is called noncyclic.

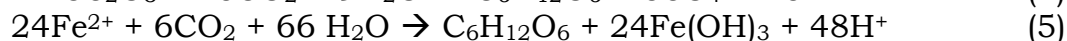
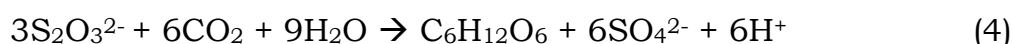
Apart from this, the principal difference between type 1 and type 2 photosystems lies in the composition of the acceptor molecule in charge of taking up the electrons transferred from the RC-bacteriochlorophyll after photo-oxidation.

Type 1 photosystem. In the case of green sulfur bacteria and heliobacteria that use a type 1 reaction center, acceptor molecules are iron-sulphur proteins. Via these Fe-S proteins, electrons excited from the RC1-bacteriochlorophyll (called P840, 840 being the wavelength in nm at which this bacteriochlorophyll absorbs the most) are directly transferred to an enzyme called ferredoxine NADP⁺ reductase allowing the generation of NADPH, the reductant required for the reduction of CO₂ to organic carbon. In the case of this type 1 photosystem, external electron donors step in so that the RC1-bacteriochlorophyll molecule does not remain in an oxidized state. Sulfur compounds such as H₂S, S⁰, S₂O₃²⁻ are thus used as electron donors to supply the reaction center with electrons. As it becomes reduced again, the reaction center is ready for another cycle.

Green sulfur bacteria, such as the *Chlorobium* genus, develop in sulfide-rich environments and are able to oxidize H₂S and elemental sulfur (S⁰) when H₂S is limiting. The reactions are as follows, with the intervention of light energy:

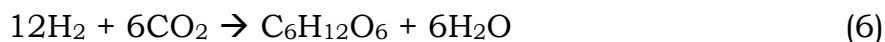


Chlorobium is also capable of using thiosulfate and ferrous iron (reactions (4) and (5)).



Type 2 photosystem. For purple bacteria and green non-sulfur bacteria that possess a type 2 reaction center, the excited electron is transferred from the RC2-bacteriochlorophyll (P870) to a bacteriopheophytin molecule and is then taken up by a quinone molecule (see Fig. I.1). In the cytochrome bc₁ complex, electrons that are not used to reduce quinone molecules for the Q cycle are transferred via a Fe-S protein to the cytochrome c₂ that acts as a shuttle in the periplasm and transfers the electrons back to the reaction center for a new cycle.

In bacteria using this type of photosystem, the production of the reductant NADPH is made possible by external electron donors. In an anoxic environment, electrons are stripped from H₂ (equation (6)), H₂S, S⁰, S₂O₃²⁻ and Fe²⁺, fed to the ubiquinone pool or directly to the cytochrome and are then transferred to the reaction center.



Green non-sulfur bacteria, e.g. the *Chloroflexus* genus, are filamentous and are often associated with cyanobacteria in microbial mats in the photic zone (PZ). Purple sulfur bacteria, such as *Chromatium*, however, are able to grow in deeper waters. This is made possible because their bacteriochlorophylls absorb at high wavelengths and because their red and purple carotenoids pigments allow them to use different wavelengths of light than those only penetrating the PZ. Even if they are very similar to purple sulfur bacteria, purple non-sulfur bacteria cannot develop in environments with a high concentration of H₂S. Genera such as *Rhodomicrobium* and *Rhodobacter* have the ability to use Fe²⁺ and H₂ as electron donors.

2. Oxygenic photosynthesis

The particularity of oxygenic photosynthesis lies in the fact that the electron donor used for the reduction of CO₂ is the water molecule. This “*small step for a bacterium, but a giant leap for biology and geochemistry*”, as rightly described by Allen & Martin (2007), completely revolutionized the photosynthetic pathway and the oxygenic photosynthesis by-product, oxygen gas, reworked the geobiochemical cycles of the entire planet.

To carry out oxygenic photosynthesis, the photosynthetic machinery must involve a reaction center capable, not only of oxidizing the H₂O molecule, but also of being sufficiently reducing to achieve carbon fixation from CO₂. Taken separately, the type 1 and type 2 photosystems involved in anoxygenic photosynthesis and described above do not have these abilities. Two coupled photosystems are necessary to carry out oxygenic photosynthesis. They are called photosystem I and photosystem II (PSI and PSII).

The other major improvement of the oxygenic photosynthetic machinery is the acquirement of the Water-Oxidizing Complex (WOC), also called Oxygen-Evolving Complex (OEC), in PSII. It consists of a manganese-calcium oxide cluster of the form Mn₄CaO₅, housed in a protein complex. Umena *et al.* (2011), have presented a high-resolution structure of this inorganic cluster with a resolution of 1.9 Å, shown in Figure I.2.

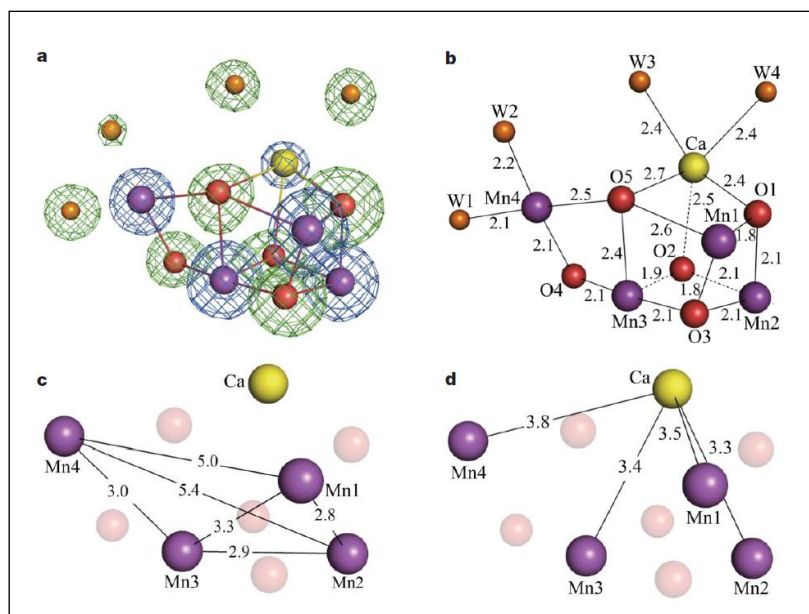


Figure I.2. High-resolution structure of the Mn_4CaO_5 cluster of the WOC in PSII. Distances are in angstroms. Calcium: yellow, oxygen: red, manganese: purple, water molecules: orange. From Umena *et al.*, 2011.

This Mn cluster is the active site for binding H_2O and splitting it into electrons and oxygen gas through what is known as the “Kok cycle” (Kok *et al.*, 1970; Fig. I.3). Mn atoms play the role of positive charge accumulators and are cycled between five different oxidation states called the S_i states ($i = 0 - 4$), S_0 being the less oxidized state and S_3 the most stable oxidized state. The release of O_2 occurs at the transition between S_4 and S_0 states (Fig. I.3). The structure of this cluster and the mechanisms for water splitting and oxygen release have been extensively studied by X-Ray spectroscopy analytical techniques (Yachandra *et al.*, 1996; Ananyev, 2001; Cinco *et al.*, 2002; Yano *et al.*, 2006; Sauer *et al.*, 2008; Umena *et al.*, 2011; Kolling *et al.*, 2012; Yano & Yachandra, 2014; Tran *et al.*, 2014) and are the subject of recent reviews (Sauer *et al.*, 2008; Yano & Yachandra, 2014; Najafpour *et al.*, 2014). However, whether the first cyanobacteria possessed an identical WOC remains unknown (discussed below in the section *Evolution of the Water Oxidizing Complex*).

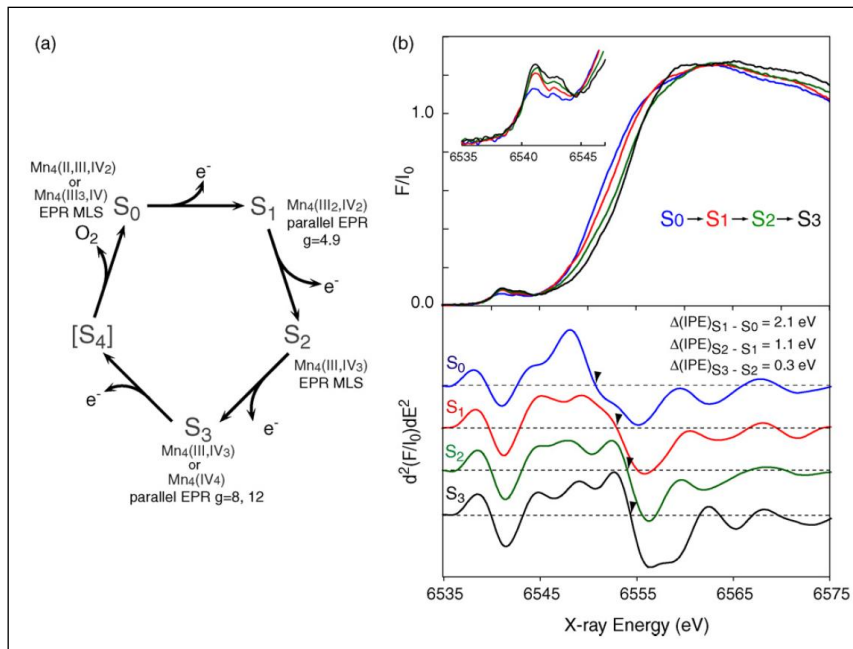
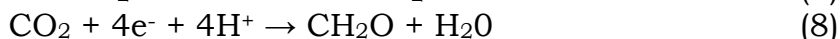
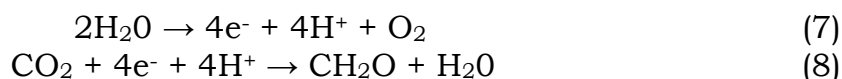


Figure I.3. The S-state Kok cycle and oxidation states of manganese monitored by X-ray absorption spectroscopy. From Sauer *et al.*, 2008.

Oxygenic photosynthesis begins in PSII when the chlorophyll *a* of the reaction center (RC-chlorophyll), called P680, receives the electrons coming from the splitting of water. This has the effect of producing O₂ via the Mn cluster of the WOC (through the S-state Kok cycle, Fig. I.3) and of transforming the chlorophyll into a reductant. Not unlike the anoxygenic photosynthetic process in type 2 photosystem, electrons are then taken up by a pheophytin molecule, transferred to the Q cycle, and then to the cytochrome called “bf”. The end-member of the electron transport chain of PSII, however, is a copper-containing molecule called plastocyanin. This is where the process departs from anoxygenic photosynthesis. Plastocyanin molecules do not return the electrons to the reaction center of PSII for another cycle. Instead, they are passed to the photo-oxidized RC-chlorophylls of PSI (P700) and dragged, along with newly donated electrons, into another transport chain involving chlorophyll and type 1 photosystem-like components: quinone, Fe-S proteins, and ferredoxins, the point at which electrons are used for the reduction of NADP⁺ to NADPH.

Just as in anoxygenic photosynthesis, ATP is synthesized as a result of the proton motive force generated during the Q cycle in the ubiquinone pool of the photosynthetic membrane. As electrons do not return to the reaction center due to the coupled PSII/PSI configuration, this method of making ATP is called noncyclic photophosphorylation.

In Bacteria, cyanobacteria are the only phylum representative of oxygenic photosynthesis. The overall reaction of oxygenic photosynthesis is reported by equation (1), but it can be decomposed as follows, where equation (7) represents the oxidation of water by the WOC, and equation (8) the generation of biomass via carbon fixation.



As photosynthesizers, cyanobacteria are necessarily restricted to the photic zone, where they develop either as cyanobacterial plankton in the open ocean, or as stratiform microbial mats or stromatolites in shallow aqueous environments, sometimes associated with anoxygenic photosynthesizers and other types of autotrophic and heterotrophic bacteria. With the splitting of the water molecule, cyanobacteria gained access to an unlimited source of electrons. The continuous input of O₂ in the environment led to the GOE, the reworking of Earth's geochemical cycles, the explosion of biodiversity, and of mineralogical diversity.

The following paragraph summarizes the evolutionary hypotheses on the emergence of oxygenic photosynthesis.

Annex 2: Bulk rock analyses by ICP-OES and ICP-MS.

(Next pages.)

Annex 2.1.

Age and locality	Sample / Other uses in this study	ICPOES data																						
		SiO2	TiO2	Al2O3	Fe2O3	MnO	MgO	CaO	Na2O	K2O	P2O5	LOI	Total	Sc	V	Cr	Co	Ni	Cu	Zn	Sr	Y	Zr	Ba
		wt%	wt%	wt%	wt%	wt%	wt%	wt%	wt%	wt%	wt%	wt%	wt%	ppm	ppm	ppm	ppm	ppm	ppm	ppm	ppm	ppm	ppm	ppm
3.33 Ga Josefsdal chert	12SA09 Optical microscopy; C and N isotopes analyses by stepped-combustion MS	99.61	0.01	0.12	0.08	0.02	0.01	0.02	0.02	0.04	0.009	0.31	100.23	0.2	3.0	5.9	0.8	6.8	9.2	4.7	0.9	0.3	3.5	21.1
	12SA16 Optical microscopy; Jos 2 FIB section for μ XRF analyses	99.29	0.01	0.15	0.22	0.02	0.05	0.05	0.01	0.05	0.009	0.23	100.09	0.4	4.4	20.6	1.1	14.7	44.2	31.5	0.4	0.4	5.6	3.2
2.9 Ga Pongola strom.	10SA01 Twin sample of 07SA01, 07SA02, 07SA03 used for SEM/EPMA ; C and N isotopes analyses by stepped combustion MS	89.15	0.13	3.11	1.02	0.05	1.32	1.59	0.03	1.02	0.015	3.15	100.59	2.0	22.8	38.1	4.5	19.0	28.0	9.3	17.4	3.2	42.9	138.8
1.88 Ga Gunflint chert	07CA05 Twin sample of GF-55-1 and GF-55-1b: C and N isotopes analyses by stepped-combustion MS	99.21	0.00	0.04	0.62	0.02	0.01	0.23	0.03	0.03	0.002	0.47	100.66	0.0	2.4	35.5	3.1	11.7	12.6	1.0	2.1	0.5	8.5	2.7
	07CA13 Optical microscopy; SEM/EPMA	95.31	0.01	0.03	0.29	0.14	0.06	1.56	0.01	0.03	0.008	1.87	99.31	0.1	4.0	3.1	2.8	4.4	10.5	4.0	3.3	1.3	5.5	42.8
	07CA16 Optical microscopy; SEM/EPMA	96.78	0.01	0.05	2.93	0.05	0.01	0.01	0.01	0.03	0.002	0.84	100.71	0.3	7.5	12.5	2.0	20.5	7.8	12.4	1.1	0.6	3.6	46.0

SB: Schreiber Beach; KF: Kakabeka Falls; MM: Mink Mountain

Annex 2.2.

		ICPMS Data																									
Age and locality		TiO2	V	Cr	MnO	Fe2O3	Co	Ni	Cu	Zn	Ga	Rb	Sr	Y	Zr	Nb	Mo	Sn	Cs	Ba	La	Ce	Nd	Sm	Eu	Gd	
		%	ppm	ppm	%	%	ppm	ppm	ppm	ppm	ppm	ppm	ppm	ppm	ppm	ppm	ppm	ppm	ppm	ppm	ppm	ppm	ppm	ppm	ppm	ppm	
3.33 Ga Josefsdal chert	12SA09	0.01	2.6	9.1	0.01	0.05	1.8	4.9	5.6	5.2	0.4	0.6	0.9	0.3	4.2	0.28	0.25	0.47	0.02	23.1	0.96	0.34	0.27	0.07	0.02	0.06	
	12SA16	0.01	2.8	20.6	0.02	0.20	1.3	16.3	42.0	32.0	0.5	1.2	0.5	0.4	4.3	0.32	0.37	1.10	0.04	2.2	0.44	0.54	0.22	0.05	0.02	0.05	
2.9 Ga Pongola strom.		0.13	25.4	38.4	0.05	1.04	3.3	14.2	22.4	8.5	5.9	44.6	17.0	3.1	37.2	2.46	0.26	10.55	1.61	136.4	8.50	14.54	4.73	0.63	0.12	0.61	
1.88 Ga Gunflint chert	SB	0.01	2.8	36.4	0.02	0.68	2.1	13.1	13.2	1.7	0.4	0.3	1.6	0.4	6.2	0.49	0.62	0.36	0.06	2.3	0.38	0.55	0.40	0.09	0.03	0.08	
	KF	0.01	2.3	5.6	0.14	0.34	3.1	3.3	12.7	4.4	0.7	0.5	3.5	1.0	4.9	0.32	0.25	0.42	0.07	48.1	1.70	1.64	0.94	0.21	0.06	0.22	
	MM	0.01	5.0	15.3	0.05	3.13	2.0	20.6	6.2	10.2	0.4	0.7	1.2	0.6	4.3	0.43	0.46	0.90	0.08	48.3	3.29	7.20	2.00	0.28	0.06	0.21	

SB: Schreiber Beach; KF: Kakabeka Falls; MM: Mink Mountain

Annex 2.3. ICP-MS results from a ~3.4 Ga silicified komatiitic basalt (AO2), and from a cherty layer (“white”) and an organic matter-rich layer (“black”) of sample 99SA07 from the 3.33 Ga Josefsdal Chert.

	silic. kom basalt	99SA07 2 (white)	99SA07 3 (black)
SiO ₂	91,87	95,539	94,917
TiO ₂	0,61	0,312	0,237
Al ₂ O ₃	3,11	2,715	2,217
Fe ₂ O ₃	1,23	0,163	0,248
MnO	0,05	< L.D.	0,002
MgO	0,24	0,169	0,351
CaO	0,10	< L.D.	< L.D.
Na ₂ O	0,00	< L.D.	< L.D.
K ₂ O	0,75	0,873	0,747
P ₂ O ₅	0,09	< L.D.	< L.D.
LOI	0,84	0,71	0,744
Total	98,89	100,481	99,46301
Sc	13,70		
V	103,59	60,48	52,41
Cr	821,06	695,8	646
Co	46,75	8,938	21,68
Ni	189,44	29,33	78,54
Cu	20,48	11,89	15,28
Zn		31,22	17,69
Ga		3,901	3,316
Rb	16,87	23,64	19,01
Sr	6,50	3,015	< L.D.
Y	5,79	4,922	3,659
Zr	38,00	22,1	19,24
Nb	4,11	1,224	0,998
Mo		0,743	1,84
Sn		1,279	0,489
Cs	0,30	0,547	6,109
Ba	48,23	32,47	25,57
La	3,20	6,214	4,146
Ce	8,92	10,1	6,909
Pr	1,35	1,387	0,906
Nd	6,69	5,891	3,512
Sm	1,62	1,091	0,687
Eu	0,53	0,399	0,243
Gd	1,64	0,933	0,546
Tb	0,22	0,143	0,086
Dy	1,27	0,827	0,584
Ho	0,24	0,167	0,119
Er	0,61	0,464	0,361
Tm	0,08	0,069	0,052
Yb	0,52	0,473	0,376
Lu	0,08	0,076	0,058
Hf	0,93	0,573	0,582
Ta	0,34	0,113	0,075
W		0,358	< L.D.
Pb	1,46	1,746	1,7039
Th	0,37	0,412	0,271
U	0,20	0,198	0,125
As		8,539	10,21
Cd		< L.D.	< L.D.
Sb		12,99	11,26

Axelle HUBERT

Signatures chimiques et mineralogiques de la photosynthèse oxygénique dans les sédiments de l'Archéen et du Paleoproterozoïque

L'émergence des bactéries photosynthétiques oxygéniques (BPO), ou cyanobactéries, est probablement l'évènement le plus important de l'histoire de la Terre, depuis l'apparition de la vie elle-même. Par la libération d'O₂ dans l'environnement, les BPO ont conduit à l'oxygénation de notre planète, jusqu'alors anoxique, et au développement de la vie complexe. Cependant, cette évolution n'est toujours pas datée.

Dans cette étude, j'ai cherché à identifier des signatures chimiques spécifiques aux BPO, *in situ* à l'échelle du µm, dans des tapis microbiens fossiles datant de 3,45 à 1,88 Ga, recouvrant ainsi une période allant de la Terre anoxique à la Terre oxygénée après le « *Great Oxidation Event* » (GOE). Nous avons utilisé la microscopie optique, la spectroscopie Raman, le MEB/EDX, l'EPMA, la µ-XRF à rayonnement synchrotron (SR-XRF), et des analyses isotopiques. Une nouvelle méthode de quantification élémentaire pour SR-XRF, ainsi qu'une nouvelle méthodologie de préparation d'échantillons ont été développées. Les résultats obtenus par EPMA et µ-XRF montrent que, dans certains contextes de déposition, un enrichissement en lanthanides (par exemple La, Sm, Gd) de cellules fossiles, et un enrichissement en Cu de pyrites diagenétiques formées en association avec des BPO, pourraient représenter des signatures chimiques spécifiques aux BPO. Suite à ces résultats, je propose que les BPO ont évolué entre 3,33 et 2,98 Ga. Je propose que les techniques élémentaires telles que l'EPMA et la µ-XRF sont les techniques les plus appropriées pour trouver des signatures chimiques spécifiques aux BPO et contraindre leur émergence dans le temps.

Mots-clés : photosynthèse oxygénique bactérienne, GOE, cherts Précambriens, éléments traces, EPMA, µ-XRF

Chemical and mineralogical signatures of oxygenic photosynthesis in Archean and Paleoproterozoic sediments

The evolution of oxygenic photosynthetic bacteria (OPB) is probably the most important biological event of Earth's history since the emergence of life itself. The release of their by-product O₂ in the environment, which was globally anoxic, fundamentally changed the face of the Earth and led to the development of complex life. However, the specific timing of this evolutionary step remains unclear.

This study is based on the search for *in situ* chemical signatures of OPB at the microbial (µm) scale, within fossilized microbial photosynthetic mats in Archean and Paleoproterozoic sediments dated between 3.45 Ga and 1.88 Ga, *i.e.* spanning the anoxic Earth to the aftermath of the GOE. We used optical microscopy, Raman spectroscopy, SEM/EDS, EPMA, synchrotron radiation µ-XRF, and isotope analytical techniques. The µXRF results were improved by the use of a new sample preparation method and a new quantification method, both developed during this study. Results obtained by EPMA and µXRF show that, under certain depositional contexts, enrichment in lanthanides (such as Sm, La and Gd) in individual OPB cells, as well as a Cu enrichment in diagenetic pyrites formed in association with OPB, may represent chemical signatures of OPB. I propose that OPB evolved sometime between 3.33 Ga and 2.98 Ga. Also, I argue that elemental techniques such as EPMA and µ-XRF are the most suitable techniques to find chemical signatures of OPB and constrain the timing of their emergence.

Key words: bacterial oxygenic photosynthesis, GOE, Precambrian cherts, trace elements, EPMA, µ-XRF



Centre de Biophysique Moléculaire,
CNRS Orléans,
Rue Charles Sadron, 45071 Orléans

